AGARD

ADVISORY GROUP FOR AEROSPACE RESEARCH & DEVELOPMENT

7 RUE ANCELLE, 92200 NEUILLY-SUR-SEINE, FRANCE

AGARD CONFERENCE PROCEEDINGS 569
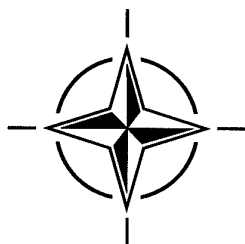
Thermal Mechanical Fatigue of Aircraft Engine Materials

(la Fatigue thermomécanique des matériaux constitutifs des moteurs d'avion)

Papers presented at the 81st Meeting of the AGARD Structures and Materials Panel, held in Banff, Canada 2-4 October 1995.
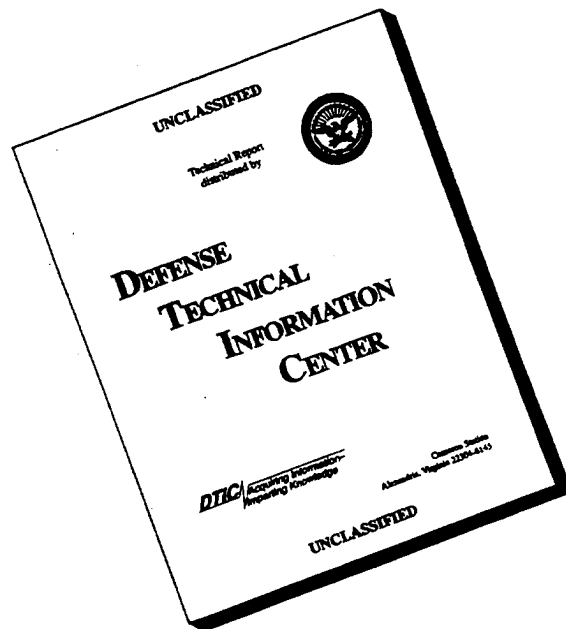
19960408 082

NORTH ATLANTIC TREATY ORGANIZATION

Published March 1996

Distribution and Availability on Back Cover

DISCLAIMER NOTICE

THIS DOCUMENT IS BEST
QUALITY AVAILABLE. THE
COPY FURNISHED TO DTIC
CONTAINED A SIGNIFICANT
NUMBER OF PAGES WHICH DO
NOT REPRODUCE LEGIBLY.

The Mission of AGARD

According to its Charter, the mission of AGARD is to bring together the leading personalities of the NATO nations in the fields of science and technology relating to aerospace for the following purposes:

— Recommending effective ways for the member nations to use their research and development capabilities for the common benefit of the NATO community;

— Providing scientific and technical advice and assistance to the Military Committee in the field of aerospace research and development (with particular regard to its military application);

— Continuously stimulating advances in the aerospace sciences relevant to strengthening the common defence posture;

— Improving the co-operation among member nations in aerospace research and development;

— Exchange of scientific and technical information;

— Providing assistance to member nations for the purpose of increasing their scientific and technical potential;

— Rendering scientific and technical assistance, as requested, to other NATO bodies and to member nations in connection with research and development problems in the aerospace field.

The highest authority within AGARD is the National Delegates Board consisting of officially appointed senior representatives from each member nation. The mission of AGARD is carried out through the Panels which are composed of experts appointed by the National Delegates, the Consultant and Exchange Programme and the Aerospace Applications Studies Programme. The results of AGARD work are reported to the member nations and the NATO Authorities through the AGARD series of publications of which this is one.

Participation in AGARD activities is by invitation only and is normally limited to citizens of the NATO nations.

The content of this publication has been reproduced
directly from material supplied by AGARD or the authors.

Published March 1996

Printed by Canada Communication Group
45 Sacré-Cœur Blvd., Hull (Québec), Canada K1A 0S7

Thermal Mechanical Fatigue of Aircraft Engine Materials

(AGARD CP-569)

Executive Summary

Many engine components may be subject to Thermal Mechanical Fatigue (TMF). For example, engine start-up and shut-down leads to severe cyclic thermal-mechanical loading of turbine blades. However, turbine blades lifing is a very complex process due to the difficulties of predicting their state of stress and strain.

Currently there is no standard test practice for TMF testing although there is a tremendous knowledge base among the various materials/structures research groups scattered throughout private, government, and academic sectors. Very little of this knowledge and experience has been shared or pooled in an attempt to standardize a testing methodology. Work in progress to develop a standard practice for TMF testing was reported. In addition, a program under the auspices of the International Standards Organisation, involving Canada, France, Germany, Italy, The Netherlands, Sweden, Switzerland, United Kingdom and the United States, and directed towards developing a test standard for TMF was described.

Because the critical issues may be material-dependent, an ideal program would test two materials. For aerospace applications the program should utilize testing of a cast single crystal superalloy blade alloy and a wrought polycrystalline superalloy.

A number of lifing models have been developed. A study of their applicability to various materials, predictive capability, cost, etc., should be undertaken in one comprehensive program. AGARD should establish a Task Force to examine the various lifing methodologies since the predictive capability has an impact on the examination and service intervals of military engines as well as the cost of service.

La fatigue thermomécanique des matériaux constitutifs des moteurs d'avion

(AGARD CP-569)

Synthèse

De multiples organes moteur sont sujets à la fatigue mécanique thermique (TMF). Pour en citer un exemple, le démarrage et l'arrêt d'un moteur provoquent des sollicitations thermomécaniques cycliques sévères au niveau des aubes de turbine. Cependant, la prévision de la durée de vie des aubes de turbine est une opération très onéreuse en raison des difficultés rencontrées pour la prédiction de leur état de contrainte et de déformation.

A l'heure actuelle il n'existe aucune méthode d'essai normalisée permettant de mesurer la fatigue mécanique thermique TMF malgré la base de connaissances énorme que représentent les différentes équipes de chercheurs en structures et matériaux présentes dans l'ensemble des secteurs privés, gouvernementaux et universitaires. Très peu d'efforts ont été faits pour partager ou mettre en commun ces connaissances et ce savoir-faire pour obtenir une méthodologie d'essais normalisée. Des travaux en cours sur le développement d'une méthode normalisée pour les essais TMF ont été signalés. En outre, des informations ont été communiquées concernant un programme qui vise l'établissement d'une norme d'essai TMF, créé sous l'égide de l'Organisation internationale de normalisation (ISO) et faisant intervenir le Canada, la France, l'Allemagne, l'Italie, les Pays-Bas, la Suède, la Suisse, le Royaume-Uni et les Etats-Unis.

Etant donné que les principales questions à résoudre risquent de concerner les matériaux, le programme idéal prévoirait des essais pour deux types de matériaux: pour les applications aérospatiales un tel programme devrait comprendre des essais sur un alliage pour aubes de turbine, composé dans un cas d'un superalliage monocristallin coulé, et dans un autre cas d'un superalliage polycristallin forgé.

Un certain nombre de modèles de prévision de durée de vie ont été développés. L'examen de leur applicabilité à différents matériaux, leur capacité de prédiction, leur coût etc... a été proposé dans le cadre d'un programme unique global. Pour ce faire, l'AGARD doit créer une équipe spéciale pour examiner les différentes méthodologies de prévision de durée de vie, puisque la capacité de prévision a un impact direct sur la périodicité du contrôle et de l'entretien des moteurs militaires, ainsi que sur le coût de cet entretien.

Contents

Preface

Aircraft engine components experience severe operating conditions, often involving complex combinations of cyclic mechanical stress, cyclic temperature and varying environmental conditions. Thus, in addition to mechanically induced cracking, cracking may also be caused by or accelerated by thermally induced stress and aggressive environmental conditions. The damage incurred by components under such conditions is known as thermal mechanical fatigue (TMF).

At the 81st Meeting of the AGARD Structures and Materials Panel, the SMP held a Specialists' Meeting on Thermal Mechanical Fatigue of Aircraft Engine Materials. The purpose of the meeting was to review the state-of-the-art experience in experimental methods as well as approaches to analytical modelling of damage accumulation and growth in metallic gas turbine engine materials under TMF conditions.

The Specialists' Meeting consisted of four sessions:

— Impact of TMF

— Testing Methodology

— Damage Mechanisms

— Analytical Modelling/Lifing Methods

On behalf of the Structures and Materials Panel, I would like to thank the authors, session chairmen and technical evaluation reporters whose participation made possible the success of the Specialists' Meeting.

Dr. Jeffrey Waldman
Chairman, Sub-Committee on
Thermal Mechanical Fatigue
of Aircraft Engine Materials

Structures and Materials Panel

Chairman: Prof. O. Sensburg
Chief Engineer
Daimler Benz Aerospace
Militaerflugzeuge LM2
Postfach 80 11 60
81663 Munich
Germany

Deputy Chairman: Prof. S. Paipetis
Prof. of Applied Mechanics
School of Engineering
Dept. of Mechanical Engineering
University of Patras
26110 Patras
Greece

SUB-COMMITTEE MEMBERS

Chairman: Dr. J. Waldman
Dept. of Materials Engineering
Drexell University
32nd and Chestnut Streets
Philadelphia, PA 19104
USA

Members:

P. Armando	—	FR	J.P. Immarigeon	—	CA
H.J.G. Carvalhinhos	—	PO	R. Kochendörfer	—	GE
L. Chesta	—	IT	A. Lasalmonie	—	FR
E.E. Gdoutos	—	GR	H.H. Ottens	—	NE
H. Goncalo	—	PO	G. Papakonstantinou	—	GR
C.R. Gostelow	—	UK			
P. Heuler	—	GE			

PANEL EXECUTIVE

TECHNICAL EVALUATION REPORT

E.A. Starke, Jr.
Department of Materials Science and Engineering
University of Virginia
Charlottesville, VA 22901 USA

and

C. A. de Moura Branco
Instituto Superior Teccnico/CEMUL
av Rovisco Pais
1096 Lisbon, Portugal

1. SUMMARY

This report provides a technical evaluation of the Specialists' Meeting on "Thermal Mechanical Fatigue of Aircraft Engine Materials," held during the 81st meeting of the AGARD Structures and Materials Panel on October 2-6, 1995 in Banff, Canada.

2. CONTENTS OF PRESENTATIONS

2.1 Impact of Thermal Mechanical Fatigue

Many engine components may be subject to TMF, for example engine start-up and shut-down leads to severe cyclic thermal-mechanical loading of turbine blades. The papers by Lasalmonie and Cook et al, described the importance of using TMF tests that are representative of service conditions when evaluating materials for engine components. The authors noted that creep, fatigue and oxidation damage are operating in turbine blades during service and complex interactions exist between the various damage mechanisms. They pointed out that it is usually impossible to conduct TMF tests at the cyclic rate that is experienced in a gas turbine engine. The slow test frequency that is usually used affects both the amount of data obtained in the cyclic range of interest, and the accuracy of determining the effect of oxidation, coatings, etc., on crack initiation and propagation. Cook et al suggested that the evaluation of TMF should include obtaining isothermal data and developing correlation's that would encompass the operational variables and deformation and failure modes that would most likely occur in service. The challenge using this approach is the selection of the isothermal temperature to determine failure for a specific TMF cycle since damage is strongly affected by the temperature selected. This will make TMF testing much easier to perform and hence the TMF testing methodologies will become accessible to an increasing number of users.

2.2 Testing Methodology

Verrilli et al reviewed this topic and noted that currently there is no standard test practice for strain-controlled TMF testing although there is a tremendous knowledge and experience base among the various materials/structures research groups scattered throughout private, government, and academic sectors. Very little of this knowledge and experience has been shared or pooled in an attempt to standardize a testing methodology. Work in progress to develop a standard practice for TMF testing, including an ASTM inter-laboratory test program and a European collaborative activity designated as COST, was reported. In addition, a program under the auspices of ISO involving Canada, France,

Germany, Italy, The Netherlands, Sweden, Switzerland, United Kingdom and the United States, and directed towards developing a test standard for TMF was described.

2.3 Damage Mechanisms

A number of papers were presented describing the specific damage mechanisms in various materials, including coated and uncoated superalloys (single and polycrystalline), monolithic and composite titanium alloys, and ceramics. Testing procedures included high and low temperature LCF, in-phase (maximum temperature coincides with the maximum mechanical strain) and out-of-phase (maximum temperature coincides with minimum mechanical strain) TMF, and the influence of environment, e.g. oxygen. The importance of various testing parameters, e.g. heat-up rate, creep-fatigue interactions, in-phase, out-of-phase, sample geometry, etc. was discussed. The effects of microstructural features, e.g. internal porosity, oxidized carbides, shearable precipitates, were also examined. The importance of considering microstructural changes due to service exposure when modeling damage for life prediction was emphasized. Damage mechanisms depend on the specific material and testing conditions and, therefore, damage models and TMF models need to be material dependent. The importance of oxidation in time dependent failures where intergranular cracking dominates was not emphasized. The contributions of oxidation induced cracking and creep induced cracking are difficult to separate and more work should be carried out in order to develop a reliable damage model able to quantify these two damage mechanisms.

2.4 Analytical Modeling/Lifing Methods

Turbine blade lifing is very difficult due to the difficulties of predicting the state of stress and strain caused by the intricate geometrical features such as internal passages and film cooling holes and by uncertainties in transient temperature distributions. Harrison et al pointed out that any model aimed at producing acceptable turbine blade life predictions must examine the loading cycles in detail, and take into account how variables such as the stress and inelastic strain at each area of the blade varies with time. They suggested combining non-linear codes, which characterize the behavior of a material under all loading conditions, with time-stepping analyses of large blade models associated with complex engine cycles, all backed up by lifing algorithms which continuously calculate the rate of life consumption.

Life prediction assessments for TMF generally use (1) strain-life or stress-life approaches or a combination of both, (2) continuum damage approaches and (3) microcrack rate approaches. Nicholas described the use of a linear damage summation approach for the prediction of crack growth rates under TMF. The methodology involved the addition of growth rates due to cyclic and time-dependent mechanisms. He examined three different classes of materials; Inconel 718 - a creep brittle material, Ti-24Al-11Nb - a creep ductile material, and a metal matrix composite SCS-6/Ti-6Al-2Sn-4Zr-2Mo. Parameters were added to the model to account for the combined effects of environment and retardation due to blunting. The linear summation model appeared to have reasonable good capability for prediction and correlation of crack growth rates in all three classes of materials examined.

Meersmann et al proposed a life prediction assessment based on inelastic work ij $ijin$. They assumed that the driving force for the propagation of nucleated cracks in metals is a function of the shear and normal stresses acting on the crack plane. In multiaxial loading conditions the magnitude of the stresses depends on the strain paths. A global measure which includes all of these parameters is the inelastic work $ijijin$ at Nf/2. Using this approach, Meersmann et al were able to show that the von Mises-hypothesis is

applicable to the deformation behavior of IN 738 LC (conventional cast) during TMF loading. They also showed that the J2 - theory is applicable to TMF-loading.

Heine et al described a life prediction approach that utilized 3D finite element output and applied a simplified constitutive model to predict the stress extremes of a TMF cycle in an advanced single crystal alloy. They used a simplified constitutive model to capture the first order effects of yielding and time dependent relaxation and showed that first order stress-strain analysis is sufficient for initial design iterations as the detailed transient conditions are not typically fully defined. Their model can be useful when time constraints limit the use of comprehensive constitutive models. Schubert et al developed a constitutive equation that describes the deformation behavior by using internal variables which concern microstructural features. Their equation utilizes user materials routines (UMAT) in the finite element code ABAQUS. They used this methodology to calculate the temperature distribution and compute the stress strain behavior for internally cooled model blades of IN 783 LC. The comparison of experimental results with the mathematical prediction was reasonably close. However, due account should be given in this model to the effects of stress ratio and oxidation as pointed out by Branco et al. A very innovative paper was presented by Marchand et al who reported on a computer model able to predict the microstructural material response to TMF from input data of the microstructural properties of the material. One drawback of this approach is the difficulty of providing the appropriate input data. However, the approach seems to have a great potential for development and should be pursued further.

3. CONCLUSIONS AND RECOMMENDATIONS

The process of TMF standardization has started. ISO is in the process of drafting a standard, and data from two TMF inter-laboratory test programs has been analyzed. This data indicates that some issues need to be addressed when formulating a robust TMF standard. The maximum allowable variation in factors such as specimen geometry (tubular, solid, etc.), gage section temperature gradients, phase shift between the temperature and strain waveforms, temperature range and limits during test duration, and specimen surface finish on life and deformation behavior need to be quantified.

Another inter-laboratory test program is needed. Using results of previous test programs and collective experience of experts in this field, a test program should be formulated to specifically address areas of concern. Involvement of AGARD is highly desired. Ideally, a single laboratory that is willing to perform additional, follow-up tests in order to examine the suspected sources of scatter in the inter-laboratory results, should be selected. In this way, all critical issues can be identified and maximum allowable variations in these factors can be quantified.

Because the critical issues may be material dependent, an ideal program would test two materials. For aerospace applications the program should utilize testing of a cast single crystal superalloy blade alloy and a wrought polycrystalline superalloy.

Work needs to continue on the study of damage mechanisms that occur during TMF. It is quite evident that the mechanisms are material dependent but various features which aid in oxidation, pores, cracks in coatings, etc., are important in most materials.

However, damage mechanisms that occur under various loading conditions and in different environments for the different materials used in engine applications should be quantified. This information is important for the development of accurate lifing methodologies.

A number of lifing models have been developed. A study of their applicability to various materials, predictive capability, cost, etc., should be undertaken in one comprehensive program. AGARD should establish a Task Force to examine the various lifing methodologies since the predictive capability impacts examination and service intervals of military engines as well as the cost of service.

THERMOMECHANICAL FATIGUE IN GAS TURBINE ENGINES : THE REASONS OF A CONCERN

A. LASALMONIE*, F. PELLERIN**, D. FOURNIER**

Snecma
Materials and Processes Department
B.P 81, 91003 EVRY CEDEX - France

**Turboméca*
Materials and Techniques Department
64511 BORDES - France

1. Introduction

The improvement of the performance of gas turbine engines for military aircrafts or helicopters has been the result of a continuous evolution in the materials properties and the technology of the components. For example the improvement of the specific thrust was obtained through on increase in the temperature level of the turbine : the gas temperature in the SNECMA M53 P2 (year 1970) which was around 1520K on the HP vanes has grown up to 1850K in the M88 engine (year 1989)(Fig.1) still higher temperatures will be needed in future military engines. New, more efficient cooling technologies were developed for the hottest components [HP turbine vanes and blades] which induce very high thermal stresses. Simultaneously the engines became smaller, more compact, so that the temperature gradients as well as thermal inertia were strongly modified compared to previous engines.

The result of this evolution is that the alloys experience complicated stress and temperature cycles ; the life prediction based on isothermal characterisation is no more satisfactory ; indeed classical isothermal tests (monotonic or cyclic) do not discriminate enough for behaviour validation and are sometimes unrealistic to describe damage mechanisms (1).

In the case of the helicopter engines, technological evolutions contributed also to more severe temperature gradients (Fig.2) : as an example the centrifugal injection chamber of the Arriel and Makila engines gave very homogeneous temperatures in the combustion chamber. On the contrary the reverse flow injection chamber of the Arrius engine induces higher heterogeneities and gradients.

This paper presents in more details the TMF concerns on the components which are submitted to the highest temperatures.

2. Thermal mechanical fatigue in turbine blades

The evolution of turbine blades technology is a good illustration of the problem described above : until 1960, solid uncooled blades were used in military and civil aircraft engine. this blades were made of equiaxed alloys such as Nimonic 90 and later IN100 (Fig.3).

The temperature level was below 950°C and the temperature gradients were low so that the life of the blades could be predicted using isothermal fatigue models. This is still the case for BP Turbine blades in aircraft engines and in blades for helicopter engines which are too small to have cooling cavities. Cooling technologies were introduced around 1965 first in equiaxed blades (i.e the turbine blades in IN100 of M53-P2) and later in DS blades and vanes. In this case the rupture was always due to creep damage or isothermal fatigue.

A few cases of TMF cracks were identified but were exceptional and probably due to extreme working conditions. Now highly cooled single crystalline components are widely used in military and commercial aircraft engines.

In this case the temperature in the metal can reach 1150°C with high gradients and stresses specially during the transients.

As a consequence the alloys experience :

- damaging stress and temperature cycles
- microstructural evolutions such as rafting of the γ' structure
- environmental damaging (corrosion, oxidation).

Due to the complex anisothermal conditions the comparison between alloys is not easy. Great care must be taken to compare with the same deformation-. temperature or stress-temperature cycles.

The influence of the various parameters can be summarized as follows :

a) TMF cycle and the role of the coating

The actual cycle changes with the geometry, location, and cooling technology. even in cases of identical stress and temperatures variations some cycles can be much more damaging.

At SNECMA, a 4 slope cycle representative of the leading edge of a blade is used (Fig.4a). With such a cycle Fig.5 shows that the TMF life of the alloys increased continuously when going from equiaxed to DS an single crystals alloys. Previous studies have shown that the protective coating which is deposited on the blades may strongly affect the TMF response of the alloy. indeed this coating is essentially an aluminide intermetallic with a ductile to brittle transition around 700°C. When the TMF cycle has large tensile stresses in the brittle domain, the damaging mechanism is completely modified due to multiple cracking of the coating. This is the reason why a different cycle (Fig.4b) is also used with high tensile stress below 700°C. This cycle is called W. As an example Fig.6 shows that the TMF life of the same coated alloy (AM1) is much smaller in the case of cycle 4b than 4a.

b) The effect of oxidation

Oxidation contributes strongly to the degradation (3) : in bare alloys the TMF life is controlled by fatigue-oxidation interactions. In the case of the 4 slope cycle (Fig.4a) the TMF resistance of the single crystalline alloys should be more dependent upon the oxidation behaviour than upon the creep resistance. As a result LCF isothermal test at the temperature of the maximum stress, or at the average temperature are not representative of the TMF life ; it is also necessary to have good intrinsic oxidation strength for the alloys.

Although the TMF resistance of the alloys was improved (Fig.5) cases of TMF damages are now found in single crystalline cooled blades. Some cases are expected in the future if TMF is not considered in the lifing with the actual stress temperature cycles.

3. TMF in combustion chambers

In the combustion chambers the deformations are due to the thermal stresses. The chambers are always coated by a sprayed thermal barrier, which decreases both the temperature level on the metal and the thermal gradients.
The average temperature levels are typically 150°C lower than on the HP turbine vanes. The gradients and, as a consequence, the stresses can however be large near geometrical singularities and eventually at some hot areas when the gas temperature is not homogeneous. Centrifugal injection is thus more favourable for temperature distribution than reverses flow. Cases of fatigue cracks in the chambers are observed but it is not clear if it must be associated with non isothermal fatigue.

4. CONCLUSION

TMF is observed mainly in highly cooled components working in very hot atmospheres such as HP turbine single crystalline vanes and blades.
A good prediction of TMF Life must fullfil the following criteria :
- The cycles must be representative of the actual cycles.
- The cycles can vary with the location in the same component.
- If the temperature can be expermentally measured, the strain or stress cycle has to be calculated, which implies reliable thermal and mechanical models.
- The ductile to britte transition of the coating is an important parameter
- the effect of oxidation must be assessed.

BIBLIOGRAPHY :

[1] : J.Y GUEDOU, Y. HONNORAT
in "Thermomechanical fatigue behaviour of materials"
ASTM STP1186, H. Schitoglu Ed.
ASTM Philadelphia (1993) p157-175

[2] J.C LAUTRIDOU, J.Y GUEDOU, J. DELAUTRE
International Symposium on "Fatigue under Thermal and Mechanical Loading"
Petten (NL) - May 1995

[3] J.C LAUTRIDOU, J.Y GUEDOU, J.DELAUTRE
This conference

FIGURES

Technology of turbine :

Thrust 95 KN	HP turbine vanes : cooled MARM 509	T : 1520 K
Length 5m	HP Turbine blades cooled IN 100	T : 1480 K
Weight 1500 Kg	LP Turbine blades cooled IN 100	T : 1350 K

Fig. 1a

Technology of turbine :

Thrust 75 - 105 KN	HP turbine vanes : cooled AM1 single crystals Tgas : 1850°K
Length 3,5m	HP Turbine blades : cooled AM1 single crystals 1800°K
Weight 900Kgs	LP Turbine blades : cooled DS200 single crystals 1720°K

Fig. 1b

Figure 1 : a) Temperature and technology in the M53-P2 engine
b) Temperature and technology in the M88 engine
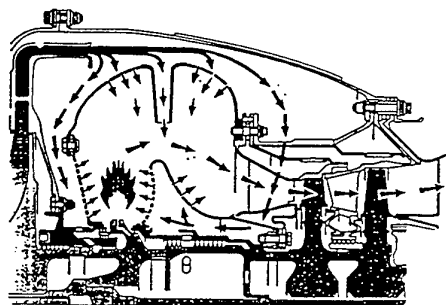
Figure 2 :
a) Combustion chamber of an Arriel Engine
(Centrifugal injection)
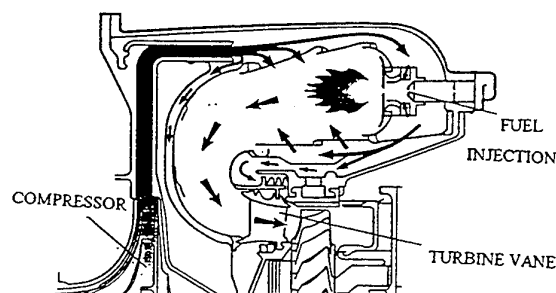
Figure 2 :
b) Combustion chamber of an Arrius Engine
(Reverse flow)

FIGURES
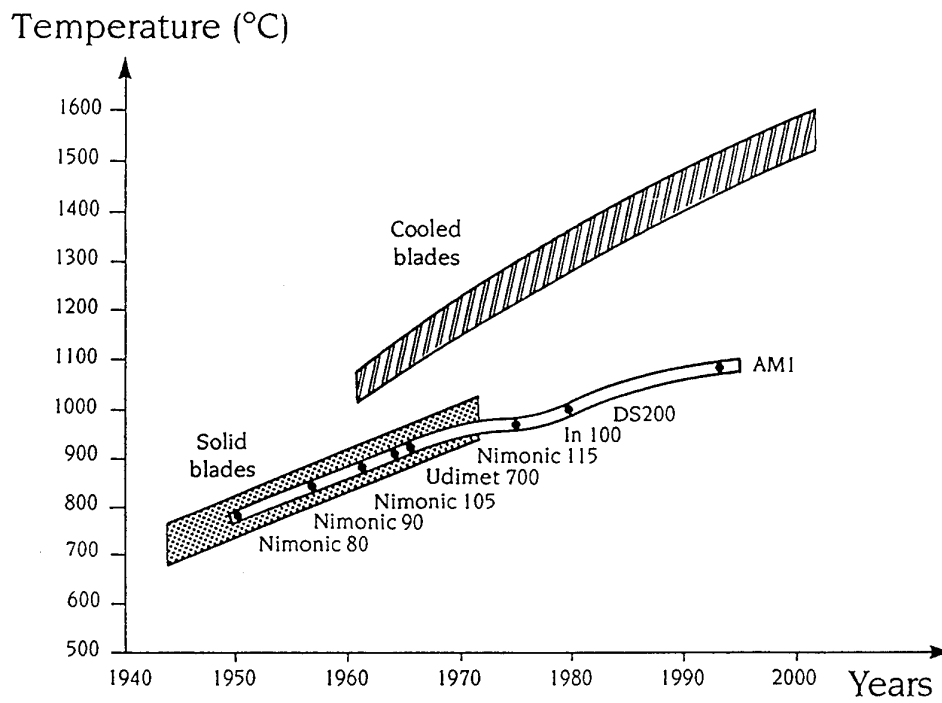
Temperature (°C)

Figure 3 : Temperature capability of the blade alloys
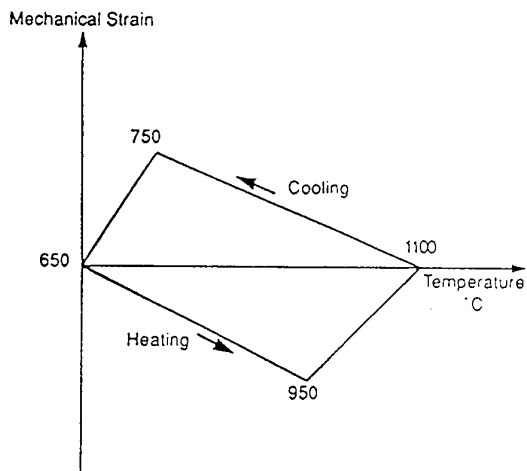
Fig. 4a
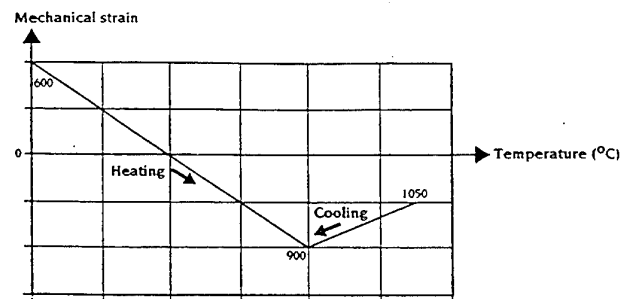
Fig. 4b

Figure 4 : Typical TMF cycles
a) 4 slope cycle
b) "W" TMF cycle

FIGURES
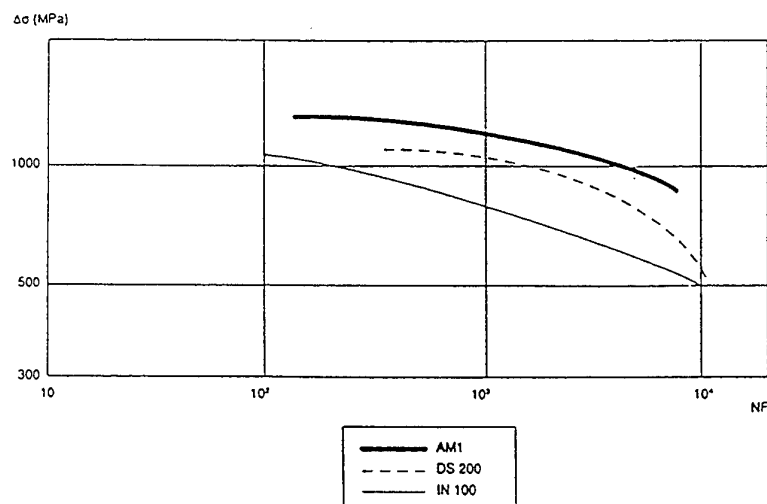
Figure 5 : Δσ (N) TMF lives of IN100 - DS200 - AM1
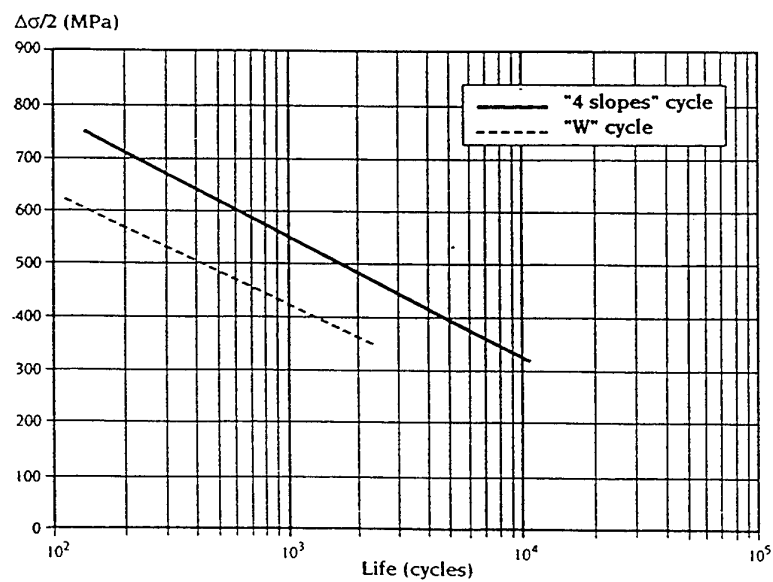
Figure 6 : TMF life of coated AM1 in the case of cycles 4a and 4b.
Lower life for cycle 4b is due to cracking of the coating due to the tensile stress in the brittle domain.

TMF Experience With Gas Turbine Engine Materials

T.S. Cook
GE Power Generation
Schenectady, New York
USA

J.H. Laflen, R.H. Van Stone, P.K. Wright
GE Aircraft Engines
Mail Stop A406, Evendale
Ohio 45215, USA

Abstract

Standard design and analysis methods for determining fatigue life involve using fatigue data generated under isothermal conditions. The large temperature variations in the turbine section of gas turbine engines promote an interest in the effect of temperature cycling on fatigue life. Consequently, thermo mechanical fatigue (TMF) tests have been conducted on a variety of materials to determine the effects of temperature cycling on fatigue crack initiation and growth. This paper reviews enhanced test methods, the results of such tests, life prediction methods, and makes recommendations for future work.

Introduction

From a fatigue perspective, gas turbine engine components experience a complex combination of stress, temperature, time and material effects ranging from transient multiaxial stresses to complex strain-temperature-time behavior of anisotropic materials. Several of these factors have been research topics which will continue to be studied for the foreseeable future. One of these factors is thermo mechanical fatigue (TMF) which is the topic of this meeting. The authors of this paper have been involved in evaluating the effects of TMF for several years, and it is the purpose of this paper to summarize these efforts.

There are three basics topics that will be discussed each representing a different facet of TMF research:

- TMF Crack Initiation Test Results and Correlations
- Experimental Developments
- TMF Crack Growth Behavior

The emphasis of this review will be to illustrate comparisons of isothermal and TMF test results as interpreted through conventional analytical methods. Included in the discussion are indications of factors that lead to differences between isothermal and TMF tests and factors that require additional work.

TMF Crack Initiation Test Results and Correlations

Owing to exposure to hot gas temperatures, high pressure turbine components of gas turbine engines can operate at temperatures exceeding 1093C. Such demands have led to the use of nickel-base superalloys which exhibit sufficient mechanical strength at such temperatures. Nevertheless, the behavior of these alloys can show strong time dependent behavior at the highest cycle temperatures while exhibiting time independent behavior at the lower cycle temperatures. An additional consideration at lower temperatures is the brittle behavior of environmental coatings used on turbine blades and vanes which has been shown to lead to premature cracking in TMF tests [1]. During steady engine operation, local areas can exhibit creep and subsequently significant changes in the cyclic mean stresses.

An added consideration is the phasing between temperature and stress or strain that occurs in TMF. The usual engineering practice for predicting TMF life is to select a temperature which is "most" damaging to the material and base the analysis on the isothermal fatigue data at that temperature. In thermal stress situations, the mechanical stress can reach peak compression at maximum temperature; while in

predominantly mechanically loaded situations, the maximum strain tends to occur at maximum temperature. The former situation is an example of an out of phase relationship between strain and temperature, while the latter is in phase. All types of such phasing are possible including clockwise and counterclockwise "baseball diamonds". An example of the influence of strain and temperature phasing on fatigue life is illustrated by the results of a study on wrought nickel-base alloy Inconel 718. Four cycles were tested, linear in and out of phase and the clockwise and counterclockwise diamond cycle. It was felt that this would provide a test of any TMF model since both the clockwise and the counterclockwise diamonds have their maximum stress at an intermediate temperature but approach the maximum temperature point from different directions.

The experimental program was conducted using hollow cylindrical bars and induction heating to cover the temperature range 343 to 650 C. Forced air cooling was not employed which necessitated a slow frequency of 0.25 cpm. The test results are shown in Figures 1 and 2. Figure 1 compares the linear in and out of phase results with the isothermal results at the maximum and minimum temperature and the same test frequency. The maximum temperature isothermal results would correctly predict the in phase cycle but would be very conservative in predicting the out of phase cycle. Figure 2 makes the same comparison for the diamond cycles. The figure shows that the counterclockwise cycle is much more damaging than the clockwise cycle. This finding is at odds with that of Embley and Russell [2] who found roughly the same life for the two cycles for a cast alloy, IN 738. Again, the use of the maximum temperature isothermal LCF curve would produce a good prediction for the counterclockwise cycle but a very conservative one for the clockwise cycle.

The hysteresis loops from the tests were examined to see if mean stress effects could be discerned. All of the tests produced roughly the same cyclic stress-strain curves. The mean stress showed the usual pattern with the in and out of phase tests having a negative and positive mean stress, with the in phase having the larger absolute value. The clockwise cycle had no mean stress while the counterclockwise cycle

had a small negative value. In all cases, the out of phase and clockwise diamond cycle had the highest stress and the longest life. This shows that the maximum (or mean) stress is not the primary factor in determining the life for TMF cycles on Inconel 718.

In addition to the differences in life, an examination of the fracture surface displayed significant differences in behavior. The in phase surface is entirely intergranular while the out of phase is entirely transgranular. Apparently, the simultaneous application of the high strain and temperature caused the cracking to favor the grain boundaries. The two diamond specimens were mixed in appearance but the counterclockwise surface was predominantly intergranular while the clockwise surface is predominately transgranular.

To apply quantitatively the results of TMF crack initiation tests to the prediction of component life, it is necessary to have a model, or correlation method for the experimental results. The development of such a model should consider a correlation of isothermal data, consideration of the appropriate mechanisms, and mathematical representation of the damage process. Conceivably, a method could work over different temperature ranges or for a specific type of strain-temperature phasing depending on the deformation and failure modes. Additionally, it would be possible for synergistic effects to prohibit the correlation of isothermal and TMF data. For example, it has been suggested that additional deformation modes may be induced through TMF cycling [3]. Time dependent phenomena can be manifested through both rate dependent deformation as well as rate dependent failure effects, and it may be necessary to account for both effects. While a successful method should reflect these complications, it must be consistent with the level of analysis that is used to analyze gas turbine engine hardware. The authors' work on DS Rene' 80H and Rene' 80 illustrates an approach and the limitations of trying to correlate isothermal and TMF data.

Through the evaluation of several life methods [4] for hot section applications, it was found [5] that one approach seemed to correlate the isothermal behavior of Directionally Solidified,

DS, Rene' 80H over a large range of temperatures. The Ostergren Frequency Damage method [6], is expressed by the equation

$$\sigma_t \Delta\varepsilon_i = A[N_i \nu^k]^c$$

where σ_t is the maximum tensile stress, $\Delta\varepsilon_i$ is the inelastic strain range, ν is the frequency (in the case of hold times, the reciprocal of cyclic period), A is a constant, k and c are exponents, and N_i is cycles to crack initiation. In Reference 5, the results of a single linear regression applied to a series of isothermal DS Rene'80H data showed that the Ostergren parameter is effective in correlating the data over a range of test conditions including temperature and hold times in tension and compression. That the method was so successful in correlating isothermal conditions suggests that it could be applied to TMF test conditions.

In order to evaluate the approach for application to TMF, the Ostergren method was used to correlate a series of isothermal conventionally cast Rene' 80 data taken from [1] assuming that one fit would adequately correlate all temperatures. Figure 3 shows a comparison of the correlated and actual life from a regression analysis of the Rene' 80 data based on the Ostergren method and the assumption that the constants are independent of temperature (in the figure, frequency modified life is defined as $N_i\nu^k$). All together, there are 122 isothermal data from 650 to 1093C with a range of hold times and strain rates. That the data are correlated so well, strongly implies that the Ostergren parameter correctly captures the dominant damage mechanisms in this material. There are limitations with this approach for these materials. Typically, beyond about 1000 cycles, the inelastic strain ranges become very small. This is reflected in the correlation shown in Figures 3 in the longer life regions where the method tends to over predict the actual life. A second concern is that this method would require accurate predictions of the maximum tensile stress and the inelastic strain range which in turn requires accurate constitutive models.

In phase, out of phase, and clockwise diamond TMF data are available for Rene' 80 from [1];

the Ostergren correlation was used to predict the TMF data with the results plotted in Figure 4. While most of the data are captured within factors of two, the data with larger temperature excursions and higher strain rates lie significantly outside this scatter range. These data (the ones inside the box in Figure 4) were found to have annular coating cracking, an effect which was not captured in the uncoated data base. It appears that the combination of low temperature brittle coating and high temperature stress relaxation can produce a condition that leads to lower specimen life than encountered in isothermal test conditions. Considering the overall correlation, and the complexity of conducting TMF experiments, it should be concluded that the method is an excellent reflection of the behavior of this alloy. Nevertheless, the experimental results also imply that there is a potential synergism between high and low temperature behavior that should be considered when conducting TMF experiments.

Experimental Developments

An issue that transcends the test results is the experimental approach. As is well known, the TMF experimental procedure is compromised by the conflicting goals to conduct an experiment with a fast frequency while minimizing the thermal gradients and hence the thermal stresses. In order to adequately control specimen temperature, the requirement is usually that testing be done at slow cyclic rates. Typically, it is impossible to conduct TMF tests at the cyclic rate that is experienced in a gas turbine engine. However, a slow test frequency makes it impossible to collect significant amounts of data in the range of interest, 30-50,000 cycles. This means that the TMF applied inelastic strain have to be larger than what is experienced by the operating component. In addition, when the isothermal data is examined at high and low frequencies, much of the time dependence tends to disappear at smaller strains. Hence any model based on the data generated at large inelastic strains may be inappropriate for component applications. To combat this difficulty, a new test facility is

required to obtain data in the long life, low strain regime.

The objective was to develop a controlled test method that would provide measured data at a rate fast enough to economically test up to 10^5 cycles. The approach taken was to employ a conventional servomechanical test frame with an appropriate rapid heating and cooling system. A preliminary design with impingement cooling and induction heating was developed and analyzed. The heat transfer analysis indicated that the system would be capable of cycle times on the order of 15 seconds. A prototype system was constructed and is shown in Figure 5. The system consists of a pressurized annular chamber containing holes to provide the impingement cooling. The chamber is constructed of non-coupling material so the induction coil can be placed inside it. Access ports provide an entry for the extensometer arms and the fiber optics for temperature monitoring.

A solid specimen with thermocouples was placed in the test frame and temperature data collected. Figure 6 shows a typical waveform achieved; the data is taken at the center and top of the gage section. Similar measurements were taken over the bottom of the gage section. The figure shows that the goal of a coil design that achieving minimal axial gradients over the gage section was accomplished. Other measurements were made to ensure that heating and cooling gradients were not developed in the circumferential direction. A cycle of eighteen seconds with linear ramps and slight rounding of the ends was produced. Based on the temperature measurements, the preliminary heat transfer coefficients were refined and a transient thermal stress analysis was conducted. The induction heating, a near surface effect, was treated as a surface heat flux. The analysis matched the ramp times and end point temperatures as shown in Figure 6. During the cycle, the analysis underpredicts the temperature on cooling, but overestimates the heating ramp.

Following these temperature measurements, the system was cycled extensively to determine its stability. There was concern that the air currents would disturb the instrumentation and prevent the control system from achieving a quasi-steady state. These fears proved

unfounded as the system ran over 50,000 cycles in load and strain control with no stability problems. Both in and out of phase cycles and two mean strains were tested for the temperature range 204-590C.

While the system proved its capability, the problem of data analysis and interpretation remained. Since the specimen is being rapidly cycled, temperature gradients exist in the radial direction of the bar. There are also gradients in the axial direction but these were eliminated in the gage section and do not affect the control section. The finite element analysis was used to account for the stresses produced by the radial temperature gradients. The analysis showed that the temperature cycle achieves stability within a few cycles, so the associated stress cycle is also stable and the stress and strain at a given location in the gage section determined. This value is then available to correlate the failure data. While the value of stress "adjustment" is small for the cases studied, on the order of 80 MPa in the cycles examined to date, it must be accounted for and could be larger in other, more complex, cycles.

TMF Crack Growth Behavior

Much like crack initiation, it is extremely important to be able to model the growth of cracks during TMF cycles. Crack growth is an important property for use in damage tolerant applications such as the Air Force ENSIP program and field management programs for fracture critical components. In these cases, it is important to determine the impact of the large temperature variations on isothermal crack growth predictions in order to provide confidence in the damage tolerance analysis. The approach to crack growth can be somewhat different because the damage process is the opening of the crack as compared to deformation and presumably inelastic strain accumulation for crack initiation. As with crack initiation testing, the large majority of the tests are isothermal. However, limited tests have been performed under TMF type of loading

conditions. Two examples will be reported in this paper; both are for disk applications.

Several nonisothermal crack growth verification tests were performed in a double edge notch Rene '95 specimen [7] with a crack growing from one side. Three specimens were cycled with an overpeak at 399C (750°F) followed by a hold time cycle at 649C (1200°F) as shown schematically in Figure 7. This type of test was performed for various overpeaks and hold times. The lives were predicted using a linear elastic fracture mechanics methodology including consideration of cyclic crack growth, time-dependent crack growth, and the benefits of overpeak retardation. The basis of this model is the linear superposition of cyclic and static crack growth and is reported elsewhere [8]. The results of six of these tests are shown in Figure 7 where the predicted lives are shown plotted against the experimentally measured crack propagation lives. The life of each specimen was predicted in three ways: (1) cyclic only (no time dependent prediction), (2) cyclic + static (no retardation benefit), and (3) cyclic + static + retardation. These results show that time-dependent behavior must be considered to accurately predict the experimental conditions, but if retardation is not used, the predicted lives may be excessively conservative. Comparing the cyclic + static + retardation predictions to the experimental lives shows that this life methodology tends to accurately predict the observed crack growth behavior.

In a separate study [9], the crack growth properties of Inconel 718 under inelastic cycling conditions were measured and correlated using fracture mechanics. For TMF crack growth, unlike the nonisothermal conditions which were discussed above, it was found necessary to utilize nonlinear fracture mechanics to correlate the results. The results summarized here are for tests performed under in and out of phase TMF conditions as well as crack growth through a temperature gradient. The test specimen was a single edge notch geometry cycled under gage section displacement (strain) control. In addition to the control displacement, the crack mouth opening displacement (CMOD), back face displacement, and load were measured. Using the gage displacement as a boundary condition, a nonlinear finite element analysis, including node release to model crack advance,

was performed on each test. A number of fracture mechanics parameters, including four path independent integrals, were calculated for each specimen as a function of crack length. The finite element analysis was validated by comparing the calculated CMOD and loads to the experimentally measured values. Once validated, the experimentally measured Inconel 718 crack growth rates were plotted as a function of the calculated parameters; Kishimoto's integral [10], ΔJ^*, is shown in Figure 8. The ability of the other integrals to correlate the data was about the same or slightly less. Figure 8 shows that the large majority of the tests could be adequately correlated using the ΔJ^* values. It is especially noteworthy that it was possible to correlate the isothermal baseline data, 538C, and the 427-649C in and out of phase TMF data into a narrow scatter band. The ability of the path integral to correlate the three data sets is promising but additional strain and temperature cycles must be examined to determine the generality of this observation. Note also that the crack growth test data covers only region 2; extension of the correlation to lower growth rates will also require more data.

The integrals were less successful in correlating crack growth through the temperature gradient. Figure 8 shows the gradient data points lie considerably above the other values. However, in [9], the calculated CMOD values were almost a factor of 2 less than the measured values. This suggests that the finite element analysis may not adequately model the experiment. Thermal gradients occur frequently in hot path structures so a further examination of this case is required.

A similar type of analysis was performed for a series of Hastelloy-X TMF crack growth tests reported in the literature[11]. It was found that for a given temperature range, several of the path independent integrals could adequately correlate the behavior.

The computation of path integrals to correlate the test data is straight forward but it does necessitate the use of nonlinear finite element analyses to accurately capture the crack tip response. Creep and nonlinear constitutive behavior must be characterized and included in the structural analysis. While such nonlinear

analyses are not routinely performed by designers, critical components must receive special attention and be analyzed using these more advanced techniques.

The challenge remaining for this approach is to determine a "rule" for the selection of the isothermal temperature to predict crack growth for a specific TMF cycle. Since the growth rate in nickel-base alloys is strongly affected by the temperature, this requirement must be met if this predictive methodology is to be used in an engineering application.

Conclusions

This paper has shown that TMF results can be correlated or at least understood through studies of the underlying mechanisms. The extent to which the mechanisms are mirrored in the predictive methodology determines the accuracy of the technique. This was illustrated in the analysis of the Rene' 80 isothermal and TMF data using the Ostergren method. The method resulted in reasonable predictions except when coating cracking (which was not modeled) was a significant factor in the life of the test. Similarly, an analysis of crack growth data under nonisothermal conditions showed that as long as all of the factors were included in the analysis (e.g. retardation and inelastic effects) then the effects could be correlated. An exception was crack growth in a thermal gradient field which was not well understood. The conclusion then is that TMF testing has provided an excellent tool for validating predictive methodology while pointing out limitations that require further work.

As the authors see it, TMF testing should be used as a verification tool to insure that the life analysis prediction techniques are suitable for the stress and temperature histories that will be experienced in the hardware that is being designed. The process would include obtaining isothermal data, and developing correlations that would encompass the operational variables. This would include evaluating and including the active deformation and failure modes that are most likely to occur in service. The final step

would be to perform TMF testing to validate the isothermal methodology to insure that additional mechanisms do not disturb the correlation in some important operational regime.

In this regard, a new test technique was described that shows the promise of being able to conduct TMF experiments at a faster cyclic rate than has used in most previous test programs. This method will allow the efficient evaluation of life parameters and mechanisms in life ranges that have not been explored. As discussed above, isothermal test results suggest that the mechanisms will change in the longer life range, so determining the limiting factors in this region will provide needed validation of the current life analysis methods.

References

1. Mc Knight, RL, Laflen, JH, Spamer, GT,"Turbine Blade Tip Durability Analysis,"NASA CR 165268, NASA Lewis, February 1982

2. Embley, GT, Russell, ES, "Thermal-Mechanical Fatigue of Gas Turbine Bucket Alloys," Proceedings, First Parsons International Turbine Conference, Dublin, Institute of Mechanical Engineers, pp157, 1984.

3. Bhattachar, V, Stouffer, D, "A Constitutive Model for the TMF Response of Rene' 80," Sixth NASA Thermo Mechanical Fatigue Workshop, NASA-Lewis, 1991.

4. Laflen, JH, Cook, TS, "Equivalent Damage - A Critical Assessment," NASA CR 167874, NASA Lewis, November 1982.

5. Wright, PK, Laflen, JH, "Influence of Cyclic Conditions on the LCF Behavior of a DS Superalloy" Presented at Designing with Advanced Superalloys, Sponsored by TMS-AIME, October 4, 1983, Philadelphia, Pa.

6. Ostergren, WJ, "Correlation of Hold Time Effects in Elevated Temperature Low Cycle Fatigue Using a Frequency Modified Damage Function,"1976 ASME-MPC Symposium on Creep-Rupture Interaction, MPC-3, December 1976, pp.179-202.

7. Van Stone, R.H., Gilbert, M.S., Gooden, O.C., and Laflen, J.H., "Constraint-Loss Model for the Growth of Surface Cracks", Fracture Mechanics: Nineteenth Symposium, ASTM STP 969, T.A. Cruse, Ed., American Society for Testing and Materials, Philadelphia, 1988, pp 637-656

8. Van Stone, R.H., Gooden, O.C., and Krueger, D.D., "Advanced Cumulative Damage Modeling", Contract Report AFWAL-TR-88-4146, GE Aircraft Engines, Cincinnati, Ohio, September 1988

9. Kim, K.S., and Van Stone, R.H., "Elevated Temperature Crack Growth", Final Report, NASA Contract NAS3-23940, GE Aircraft Engines, Cincinnati, Ohio, April 1992

10. Kishimoto, K., Aoki, S. and Sakada, M., "On the Path-Independent Integral - J", Engineering Fracture Mechanics, Vol. 13, 1980, pp. 841-850

11. Meyers, G.J., "Fracture Mechanics Criteria for Engine Hot Section Components", Final Report, NASA CR-167896, United Technologies Corporation, Pratt and Whitney Aircraft Engine Group, May 1982

2-8
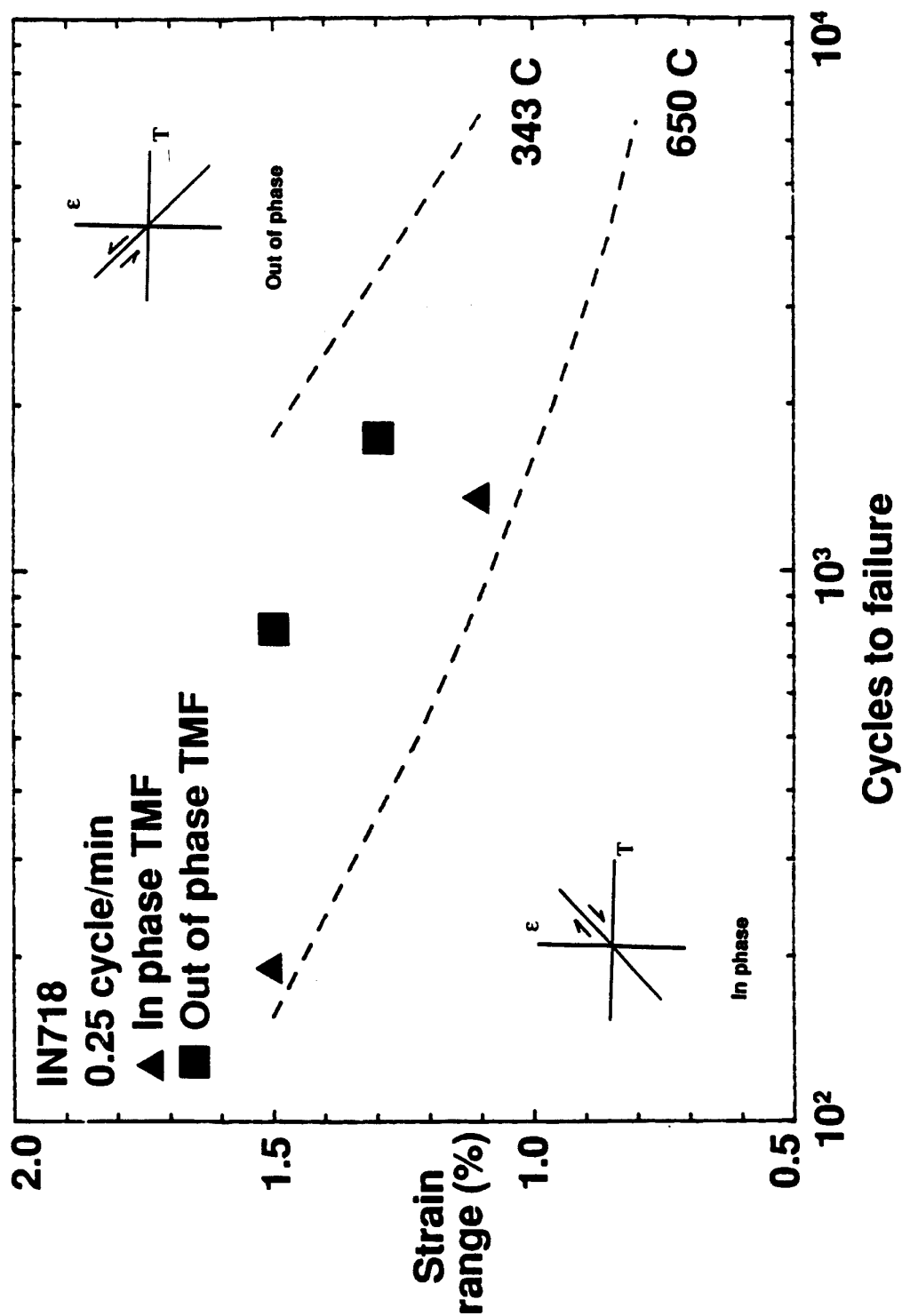
Figure 1

Comparisons of In and Out of Phase TMF Tests With Isothermal Curves
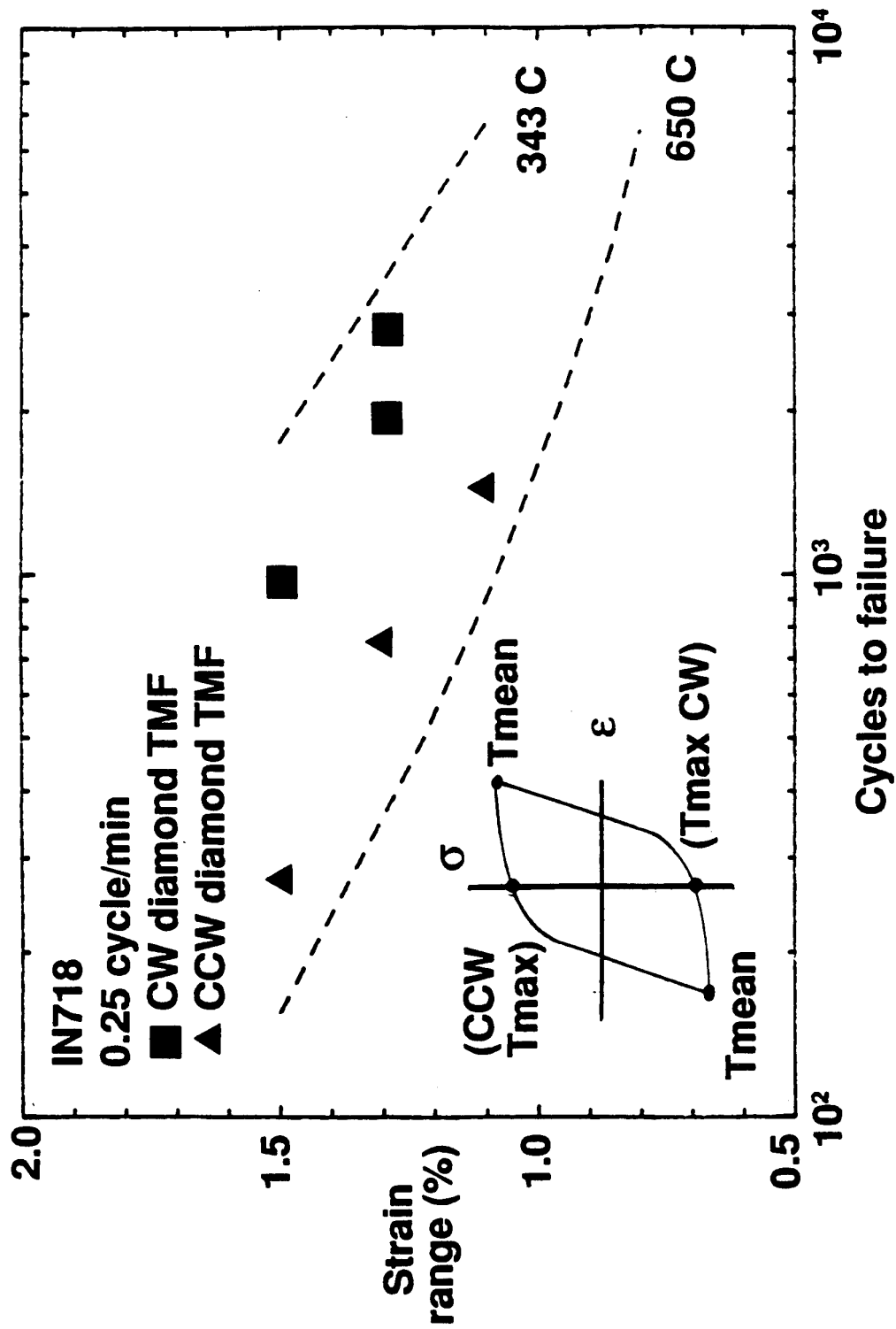
Figure 2

Comparisons of Clockwise and Counter Clockwise TMF Tests With Isothermal Curves

Correlation of Isothermal Rene 80 LCF Data Using the Ostergren Parameter
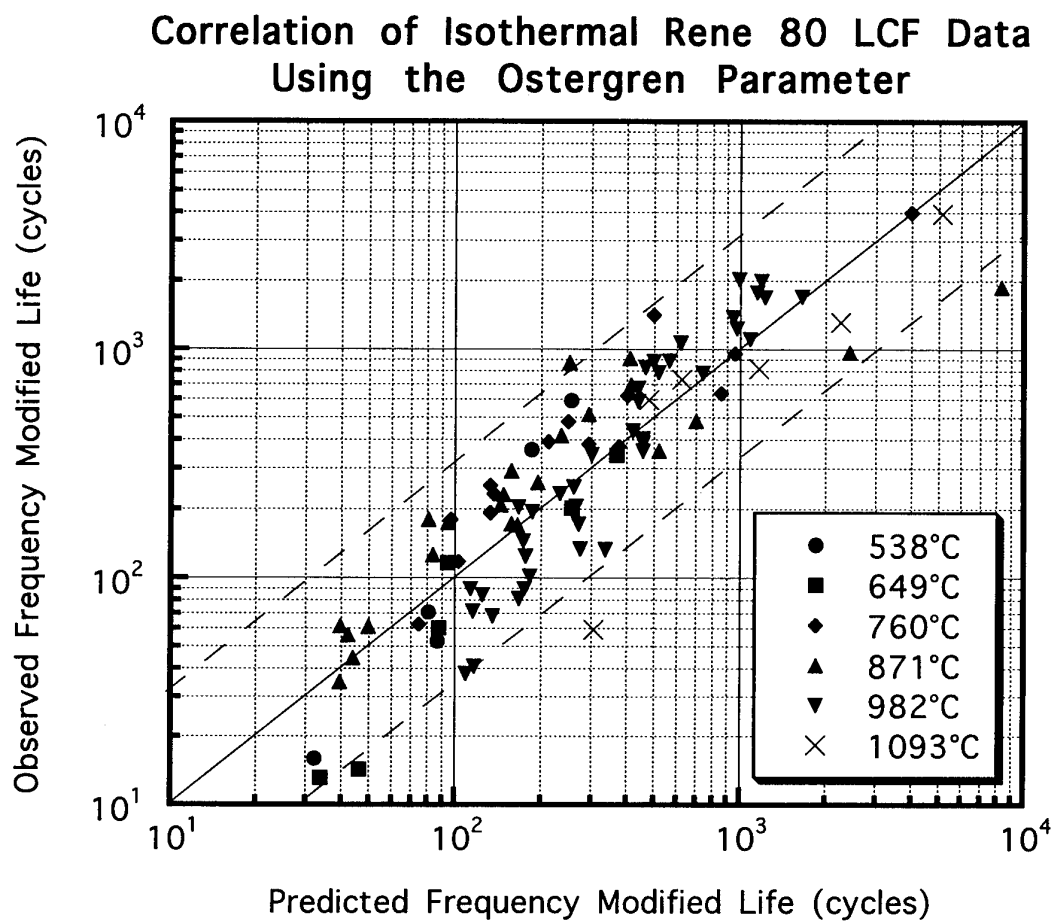
Figure 3

Correlation of Isothermal Rene' 80 LCF Data Using the Temperature Independent Ostergren Parameter
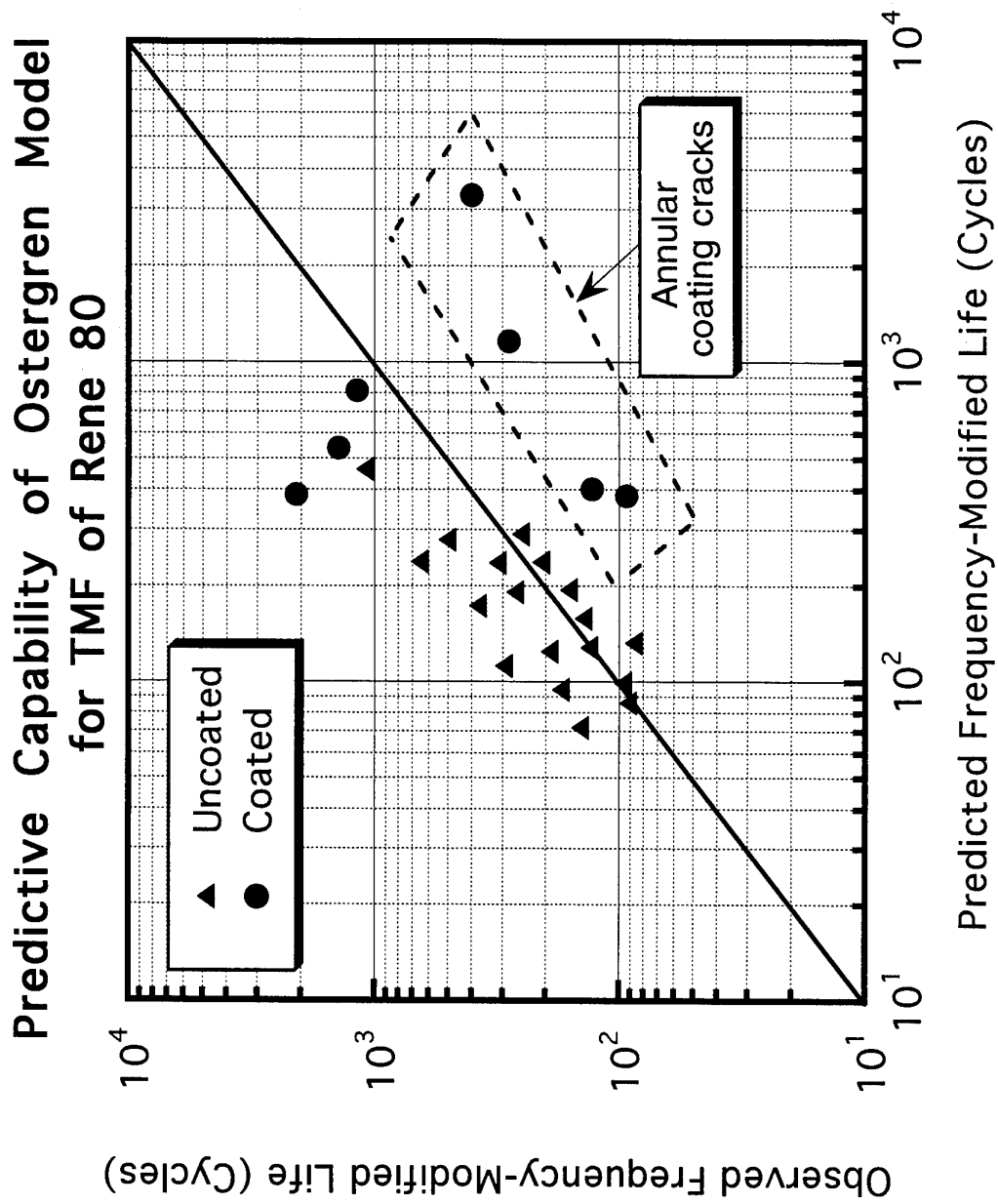
Figure 4

Predictive Capability of the Temperature Independent Ostergren Model for TMF of Rene' 80

FORCED—AIR
COOLING PLENUM

1. TEST SPECIMEN
2. COOLING PLENUM
3. EXTENSOMETER
4. INDUCTION COIL
5. AIR JETS
6. AIR INLET
7. MACHINE GRIPS
8. ACCESS TUBES
9. EXHAUST AIR

Figure 5

Schematic of Forced -Air Cooling Plenum TMF Experimental Set-up

Figure 6

Circumfirential Temperature Variation During Cooling Transient

Figure 7

Comparison of Predicted to Observed Crack Growth Life During Overload and
Temperature Cycling

Figure 8

Comparison of TMF and Inelastic Crack Growth Correlated by ΔJ^*

Thermal Mechanical Fatigue and its Effect on Combustor Design

R.L. Sikorski
Aero Propulsion and Power Directorate
Wright Laboratories
Wright Patterson AFB, OH 45433, USA

ABSTRACT

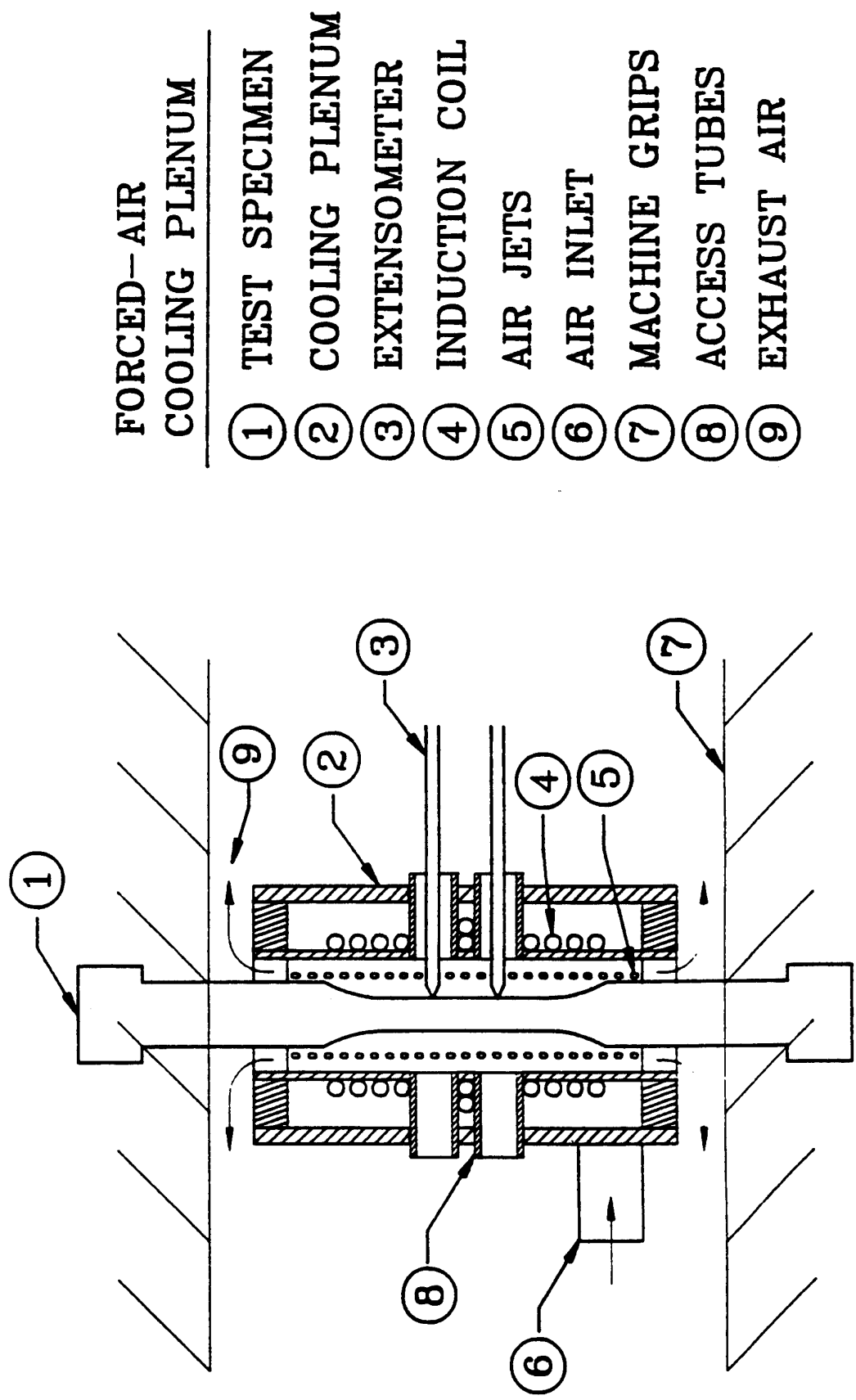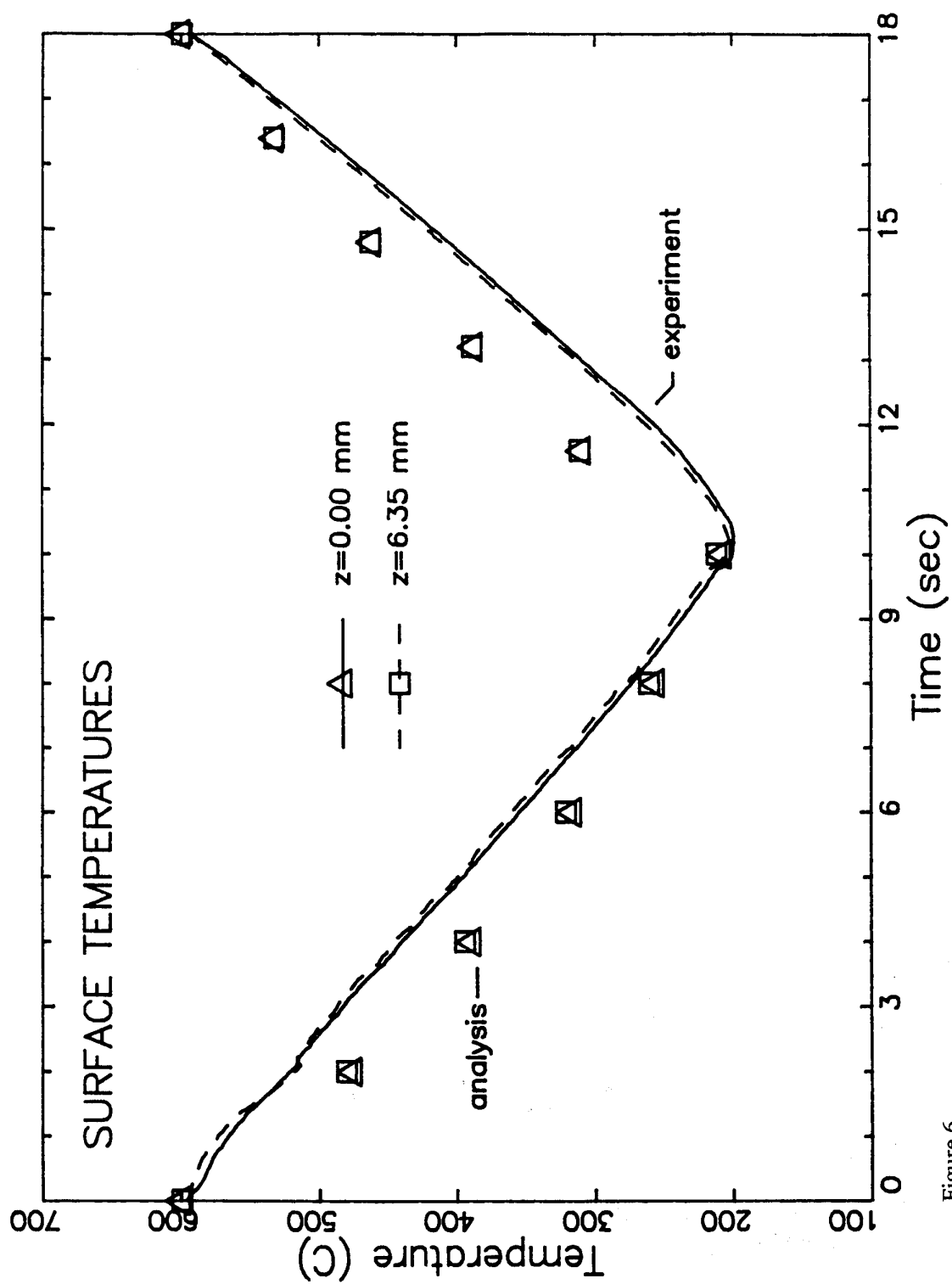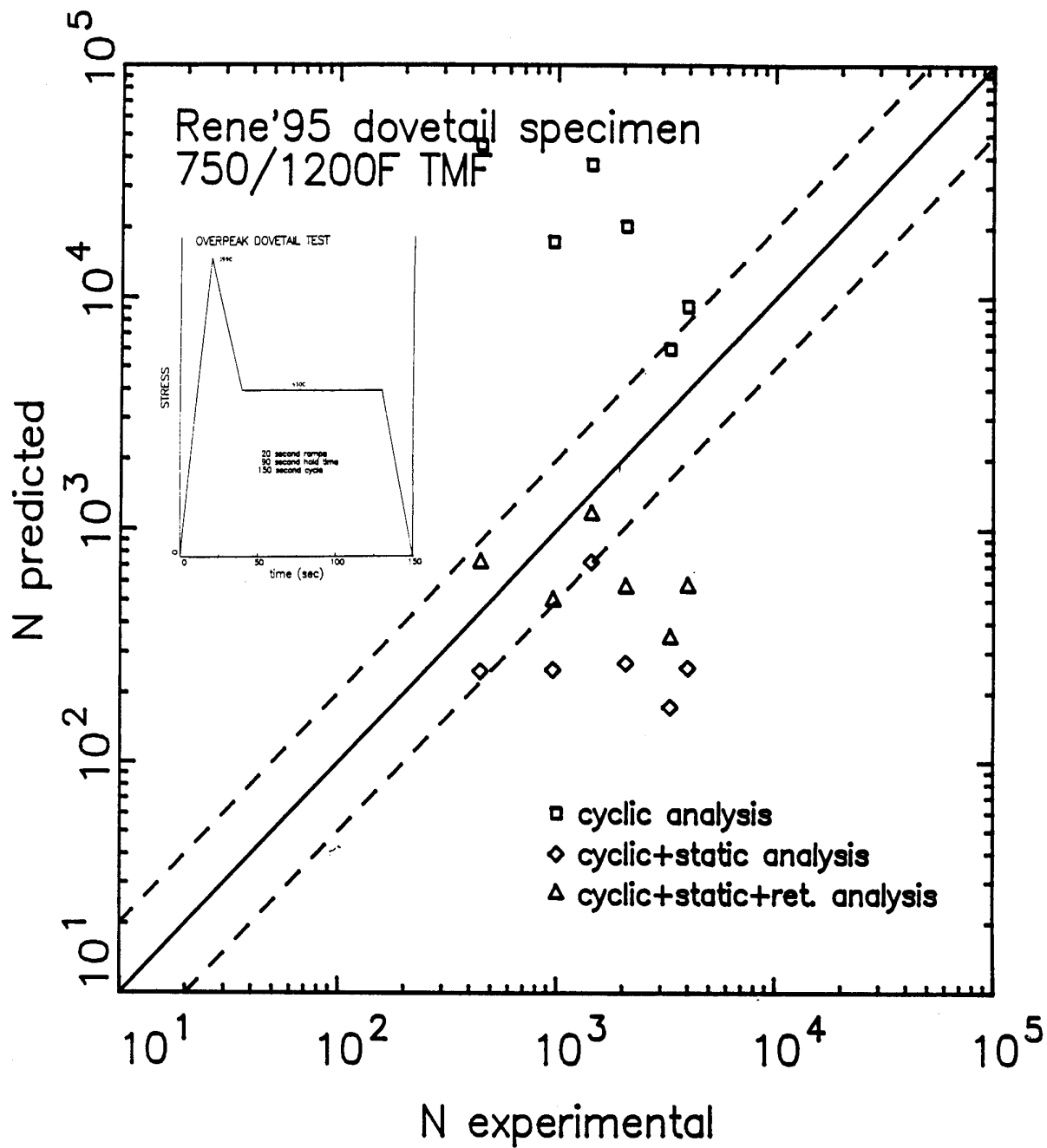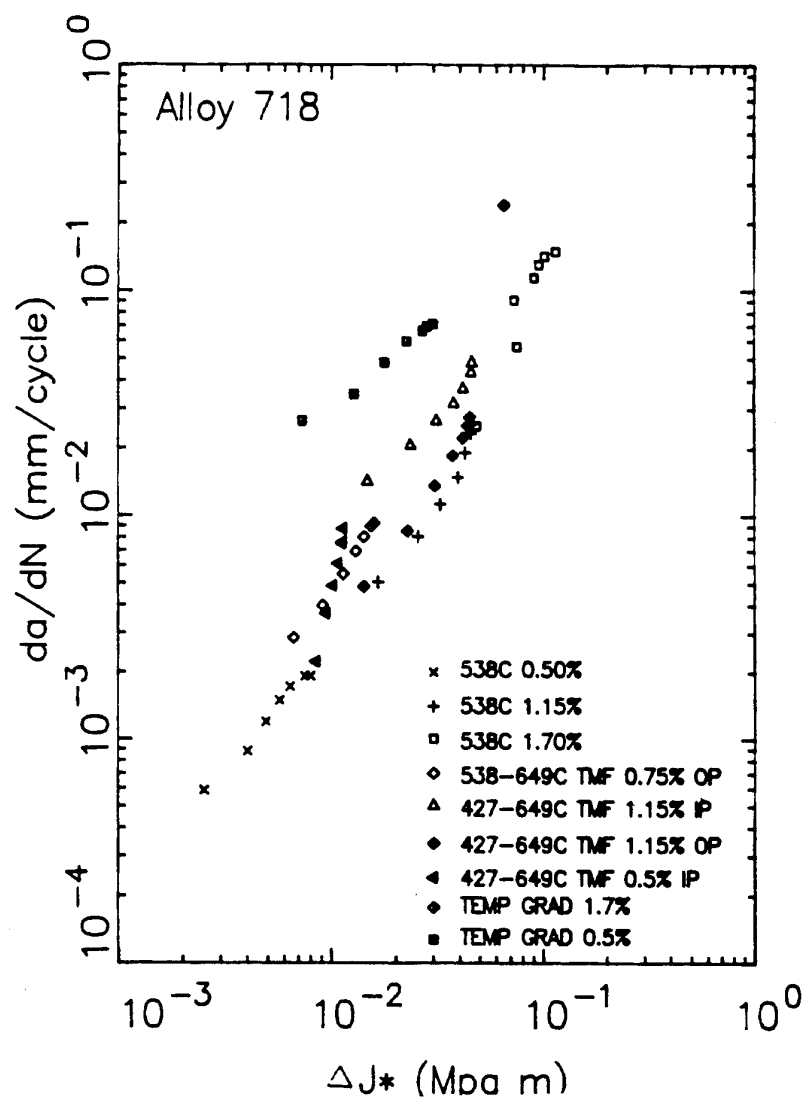In the past, a typical combustor design consisted of single-wall 360° rings with film cooling introduced periodically along the length of the combustor wall. This type of construction, coupled with dilution and cooling hole discontinuities, created high local thermal stresses. The pressure levels also affected the radiation such that as pressure increased, thermal gradients and thus thermal stresses increased. Mechanical loads and stresses were directly proportional to the pressure loading in the combustor. The combination of these thermal and mechanical stresses caused premature failures in the combustor liners. Evidence indicates that dividing components into segments reduces mechanical load and thermal variations significantly. Combustor liner segments are supported by a load bearing structure such that pressure levels have a small effect on the segmented liner. These segments can also grow both axially and circumferentially, thus reducing thermal gradients in the liner. The resulting reduction in stress lowers the possibility of a catastrophic failure in the component. The purpose of this paper is to trace the history of segment combustors, examining their role in today's technology, and to explore development for the future.

1   THE PROBLEM

Thermal mechanical fatigue (TMF) is one of the leading causes of premature failure in conventional, single-walled, 360° ring combustor liners. As the name suggests, high levels of thermal and mechanical stresses on the liner can accumulate over time and cause the liner to fail. So, where do these stresses come from?

At the heart of the problem is the liner's location between the combustion zone and the combustor bypass air. The side of the liner that is exposed to the hot combustion gases expands much more than the side facing the relatively cool bypass air. In the conventional liner, where the two sides comprise a single structure, this difference in thermal expansion causes the liner to try to flatten out, while the liner's 360° ring construction and its attachment to the engine structure constrain it from doing so, resulting in increased liner mechanical stress. Local rich zones resulting from imperfect mixing of the fuel and air can produce hot streaks which can lead to steep temperature gradients in the liner. These potentially damaging temperature gradients can also occur when the liner cooling flow is disrupted by the dilution air jets.

The engine pressure environment is a mixed blessing for the liner. On the one hand, it produces the necessary pressure drop across the liner to drive the liner cooling flow that helps to keep the liner temperature to within materials limits. On the other hand, that same pressure drop also represents a major mechanical load on the liner. Moreover, the high pressure inside the combustion zone increases the amount of heat transferred to the liner by raising combustion gas density and the level of radiation output from the combustion process.

Finally, there is the engine cycle. In a typical mission, the engine can be cycled from idle to high power and back again a number of times, causing the engine temperatures and pressure to do likewise. The resulting fluctuations in liner stresses can greatly magnify the amount of damage they can inflict. This effect is intensified by an increase in the number of engine cycles experienced by the liner, whether it's brought about by a change in the mission requirements or an increase in the liner's life requirement.

2   MANRATED SEGMENTED LINERS

The early 70's saw the birth of a revolutionary new concept: the segmented liner (Fig. 1) First developed
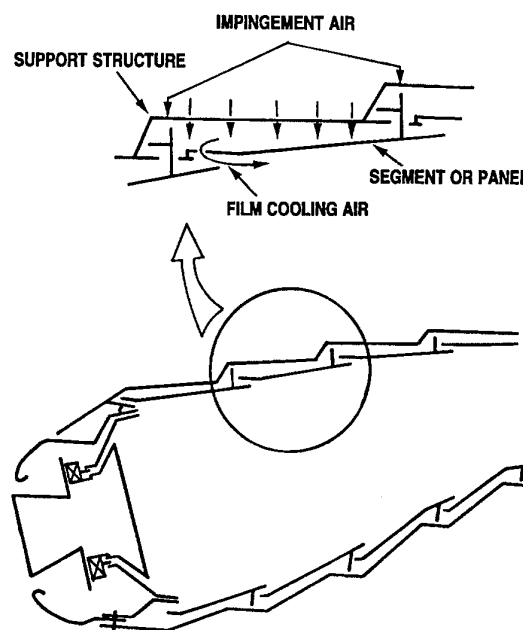

Fig. 1 - Segmented Liner

for large manrated engines where liner TMF was becoming a significant safety concern, this design divides the hot and cold sides of the liner into two mechanically isolated parts, which has the effect of splitting up the thermal and mechanical loads. The cool side is now the mechanical load bearing member (called the structural shell). The hot side, which bears the brunt of the high combustion gas temperatures, is further segmented into roughly rectangular panels to accommodate the greater axial and circumferential expansion experienced by the hotter parts. In addition, carefully placed metering holes in the structural shell help to direct the cooling air onto the panels' backsides. A slight overlap between consecutive rows of panels allows cooling air to be fed between the rows and laid down as a cooling film on the face of the succeeding panel row. That same air is also used to cool the trailing edge of the preceding row panel. This multiple use of the cooling has the effect of reducing the amount of cooling flow required to keep the panel temperatures to within the materials limits.

Both GE and P&W developed their own versions of the segmented liner. GE called their version the shingle® liner while P&W dubbed theirs the FLOATWALL™ liner. Both designs have proved to be hugely successful during the extensive cyclic engine testing carried out by these companies. However, the early prototypes were not very practical. Problems included a huge increase in parts counts and weight compared to the conventional, single-walled, machined ring liners. When one factored in the cost of the labor intensive assembly process, it was no wonder that the designers had a tough time convincing their respective managements of the efficacy of this design approach.

Fortunately for the combustor world, there were those who persevered, and their persistence finally paid off when P&W subsequently came with an improved FLOATWALL™ design which addressed at least some
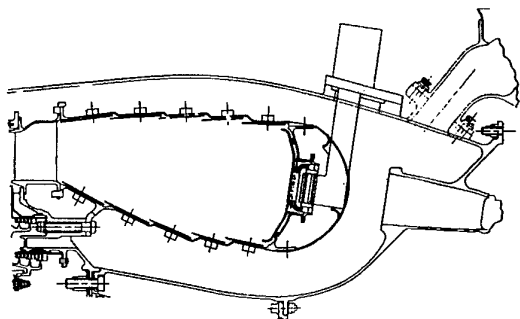

Fig. 2 - FLOATWALL™ Liner

of these issues. In their new FLOATWALL™ design (Fig. 2), they modified the panel attachment scheme to make the panels easier to attach and detach, and they so arranged the panels that the individual panels could be removed without necessitating the complete disassembly of the liner. This greatly facilitated the removal and installation process and cut down on the labor cost. At the same time, they lightened the panels by making them thinner and stiffened them by adding cooling pins to their backsides, which also had the effect of improving the heat transfer effectiveness of the liner cooling flow. This enabled the combustor designers to reduce the amount of cooling flow they had budgeted for the liner by as much as 30% relative to the conventional machined ring liners, without sacrificing liner life. This preservation of liner life was amply demonstrated when a FLOATWALL™ liner of the type that is currently in use in the F100-PW-229 survived a 4,000-TAC cycle[*] endurance test with minimal liner distress.

3   EXPENDABLE SEGMENTED LINERS

At about the same time, the Garrett Engine Company developed a segmented liner concept for their expendable engine combustor. Because expendable engines have fewer safety requirements and shorter life
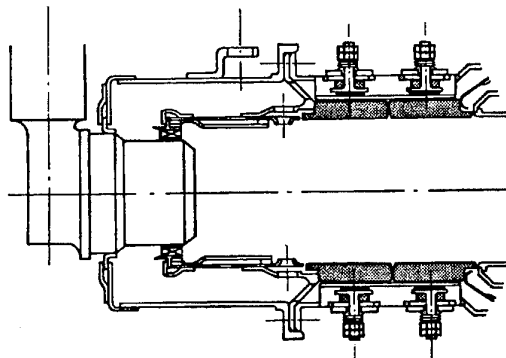
Fig. 3 - Segmented Ceramic Liners

expectancies, Garrett was able to make their segments out of the riskier but higher temperature capable ceramic materials. (Fig. 3) The higher temperature capabilities of the ceramic materials enabled Garrett to use backside cooling only for their segmented ceramic liner. It was also hoped that the ceramic material's lower density would provide the potential for reducing the liner weight. Unfortunately, because ceramic parts have to be beefed up to make up for the lower materials

---

[*] An engine cycle, equivalent to one OFF to MAX to OFF cycle.

strength, that weight reduction still remains a potential to this day.

4 ADVANCED SEGMENTED LINERS

In an effort to further reduce the weight of their FLOATWALL™ liner, P&W added COMPGLAS® panels. COMPGLAS® is a composite ceramic material made of SiC fibers and an Aluminosilicate matrix. This liner has successfully undergone extensive cyclic engine testing, Although the COMPGLAS® never went beyond the development phase, it did form the basis of another of P&W's panel concepts.

In recent years, as engine thrust to weight requirements rose, the combustor liner temperature crept up as well, until P&W felt that the cooling capacity of their metal FLOATWALL™ liner could no longer keep up. That was when P&W modified the ceramic FLOATWALL™

Fig. 4 - Tiled Ceramic Panel

liner design to include monolithic ceramic tiles imbedded in the COMPGLAS® panels. These new tiled panels utilized the higher temperature capability of the monolithic ceramic materials and the relative toughness of the COMPGLAS® material. For this approach to succeed, the method used to attach the ceramic tiles to the COMPGLAS® panels had to be loose enough to allow for the difference in thermal expansion but tight enough to keep the tiles in place during engine operation. The resulting tiled panel liner showed some promise during combustor rig testing, but further materials development will be needed before such a design can be put into an engine.

5 WHAT'S NEXT?

While the segmented liner goes a long way towards solving the problem of thermal mechanical fatigue, its weight and complexity are still obstacles to its widespread acceptance. The problem is that we need

the durability and life advantages that this design approach can offer, but we can't afford the associated costs. Moreover, because increasing engine thrust to weight goals are driving up engine temperatures and pressures, that need has intensified to the point where combustor liner durability has become one of the critical areas in advanced engine development.

I believe that the keys to success lie in two areas. First, we need tougher high temperature capable materials which will withstand the sort of environment they will face in advanced engine combustors. Efforts in this area are ongoing, of which the NASA Enabling Propulsion Materials program is the largest. Secondly, better analytical tools are needed both to design better liners and to better predict their heat transfer characteristics. It is hoped that such tools will facilitate the development of the next generation combustor liners.

ACKNOWLEDGMENT

Standardization Activities in TMF Test Methodologies

M.J. Verrilli*, M.G. Castelli**, J. Bressers***, R.L.T. Oehmke****

*NASA Lewis Research Center, 21000 Brookpark Road, Cleveland, Ohio, 44135 USA
**NASA LeRC/NYMA, 21000 Brookpark Road, Cleveland, Ohio, 44135 USA
***Joint Research Centre, EC, P.O. Box 2, 1755 ZG Petten, The Netherlands
****MTS Systems Corp., 14000 Technology Drive, Eden Prairie, MN, 55344 USA

1. SUMMARY

No standard test practice currently exists for strain-controlled thermomechanical fatigue (TMF) testing. This paper discusses recent activities which lay the foundation for standardization of TMF test methods. Specifically, the paper documents the results of two interlaboratory TMF test programs, identifies key TMF symposia and workshops, and discusses efforts toward drafting a TMF standard test practice.

2. INTRODUCTION

Thermomechanical fatigue (TMF) data is recognized as essential for of characterization of deformation and life modeling of materials experiencing combined thermal and mechanical loads during service (1). Since no standard practice exists for TMF testing, experimentalists generally resort to using various aspects of isothermal low cycle fatigue (LCF) standards (2-5). Unfortunately, these standards do not address many of the critical issues involved in TMF testing, leaving such matters without guidelines and completely dependent upon the experimentalist's discretion. Thus, potential for variability in the resulting TMF data is significant, as a result of both the complexities of TMF and the diversity of approaches taken.

The objective of this paper is to present the work in progress to develop a standard practice for strain-controlled TMF testing. Specific objectives are: 1) present the results of interlaboratory TMF test programs; 2) identify key symposia and workshops on TMF behavior; 3) present approaches and issues of consensus for a TMF test methodology; and 4) discuss the issues needed to be resolved and efforts required to develop a TMF standard.

3. ASTM INTER-LABORATORY TMF TEST PROGRAM

3.1 Introduction

An interlaboratory program on deformation behavior was conducted under the auspices of the ASTM Committee on Fatigue (E08). The specific objectives of the program were to conduct preliminary in-phase and out-of-phase TMF experiments under strain control and to identify possible variations in the stress-strain response as measured by different laboratories. Four laboratories participated in the program, namely Mar-Test, Inc., General Electric Aircraft Engines, NASA Lewis Research Center, all of the U.S., and Joint Research Centre-Petten, The Netherlands.

3.2 Material and Specimens

The material selected for this program was Haynes 188, a wrought cobalt-base superalloy. The as-received material was in the form of 19 mm diameter round bars, with equiaxed grains ranging in size from 46 to 65 microns. The Haynes 188 was supplied by a single source from one heat of material to eliminate as much as possible any material variation. Each laboratory tested a specimen of their own design as shown in Fig. 1.

3.3 Test Procedures

Four strain-controlled TMF experiments were performed by each participant. A triangular waveform and a cycle period of 400 s was used. Two in-phase and two out-of-phase tests were conducted, all using the same mechanical strain range of 1%. The minimum temperature of the TMF cycle was 500 C, and the maximum was 900 C. Strain measurement and control was performed using axial extensometry. All participants used direct induction heating of the specimens and natural convection and conduction for cooling (i.e., no forced air cooling).

To control the mechanical strain range and rate, a thermal strain compensation technique is required. The following procedure was used by each

participant. The specimen temperature was cycled between 500 and 900 C under zero load to obtain the thermal strain increments, ϵ^{th}_i, versus temperature or time. Using the following equation

$$e_i = \epsilon^m_i + \epsilon^{th}_i \qquad (1)$$

the total strain increment (e_i), required for the desired mechanical strain increment (ϵ^m_i) was obtained. Total strain is the controlled variable.

As the main objective of the program was to compare cyclic stress-strain behavior during TMF, tests were run for a minimum of 50 cycles. Under these conditions, life was expected to exceed 50 cycles. For the same mechanical strain range, fatigue life at 927 C is about 1500 cycles, and TMF life using a temperature range of 316 to 760 C was more than 500 cycles (6).

3.4 Results
Fig. 2(a) compares the in-phase TMF stress-total strain hysteresis loops generated by each of the four laboratories. Two in-phase and two out-of-phase tests were conducted by each participant, but for clarity, only one experiment by each is shown in Fig. 2. Data for cycle 20 is shown. Excellent agreement of all the data is seen, with the biggest strain difference between any of the four hysteresis loops of about 0.1%. The stress-mechanical strain comparison for the same cycle (Fig. 2(b)) also shows very good agreement. The agreement seen for this cycle was observed for cycles 1 through 50.

Fig. 2(c) is the comparison of the out-of-phase TMF stress-total strain hysteresis loops for cycle 20. Although the hysteresis loops vary slightly in shape, the biggest strain difference is also about 0.1%. Reducing the same data to stress versus mechanical strain (Fig. 2(d)) collapses the four hysteresis loops, yielding less scatter, with the difference in the strain at any point on the loops of less than 0.05%. As observed for the in-phase data, the agreement of the various laboratory's data was consistent through 50 cycles.

A plot of the peak tensile and compressive stresses as a function of cycle number for all the in-phase TMF tests is shown in Fig. 3(a). (Remember that for these in-phase TMF tests, the peak tensile strain is attained at 900 C and the peak compressive strain at 500 C). Data for the duplicate tests by each laboratory are shown. The tensile peak stress

approaches saturation after 15 cycles and the scatter between the data sets decreases from about 60 MPa at cycle 1 to 40 MPa at cycle 10. The scatter remains about 40 MPa until the end of the tests, cycle 50. The compressive peak stress continuously hardens throughout the tests, although the rate of hardening decreases after cycle 10. Also, the scatter in measured compressive peak stresses decreases from about 80 MPa at cycle 1 to about 40 MPa at cycle 50. Note that the data from individual laboratories is self-consistent, with the exception of the compressive stress response from one laboratory.

A plot of the peak tensile and compressive stresses as a function of cycle number for all the out-of-phase TMF tests is shown in Fig. 3(b). (Note that for these out-of-phase TMF tests, the peak tensile strain is attained at 500 C and the peak compressive strain at 900 C). The stress response mirrors that observed for the in-phase cycle in temperature, that is, continuous hardening at 500 C and stress saturation after about 15 cycles at 900 C. Also, the 500 C and the 900 C peak stresses are about the same for both cycle types. Excluding the data shown as solid diamonds, the scatter between the data sets in the stress measurements for these tests is lower than that obtained under in-phase testing.

The data shown as solid diamonds in Fig. 3(b) differs from the average of the rest of the data due to material history effects. This test was stopped after a few cycles due to a drift of the temperature, and then restarted. Data from the restart in shown in this figure. Note that even though the tensile (500 C) stress response deviates, the compressive (900 C) response collapses with the rest of the data after a few cycles.

3.5 Discussion and Results
As seen in Figs. 2 and 3, good agreement of both in-phase and out-of-phase TMF deformation data exists for all participants. There were, however, differences in the test procedures employed by the four participants.

Each participant used a different specimen design. Three of the specimen designs (Fig.1a-c) utilized a cylindrical gage section. The fourth design had a rectangular gage section (Fig. 1d).

All participants used an initial tensile-going straining direction at the start of the in-phase tests.

Laboratories 2 and 4 started the out-of-phase tests in a compression-going direction, but laboratories 1 and 3 used a tensile-going direction. In spite of these two different initial straining directions, only small differences were seen in the stress response (Fig. 3).

Two methods were used for compensation of thermal strains during the tests. During the thermal cycling of specimens prior to the start of the TMF tests, laboratories 3 and 4 measured the thermal expansion strain as a function of specimen temperature, and utilized this function for compensation. Laboratories 1 and 2 used a function of the thermal strains versus time to obtain the required mechanical strains versus time. The data indicates (Fig. 2) that for these test conditions, both methods yielded nominally the same stress-mechanical strain response.

The good correlation of all the TMF deformation data, in spite of differences in test procedure, may be due to several reasons. One may be the test conditions employed. Stress relaxation appears to play an important role in the deformation behavior at the hottest portion of the cycle as can been seen in the TMF hysteresis loops (Fig. 2). Also, material history effects did not change the 900 C peak stress response during the 400 second cycles (Fig. 3). Thus, the ability to discern differences in test results between the four laboratories was probably masked, at least for the hot part of the cycles, by stress relaxation.

Another reason for good agreement may be the precise manner in which each participant performed the tests. This can be seen by examining additional data reported by the participants, such as the elastic modulus (E) versus temperature data measured before every test. For a given laboratory, the variation of E was less than 6 % from the mean value at a given temperature. If the data from all the participants is pooled, the standard deviation of E is less than 6 % of the mean value at a given temperature. Bonacuse and Kalluri (7) also measured E versus temperature for the same material, Haynes 188. For seven specimens tested at 800 C, they reported a 2 % variation of E from the mean value. Note that their data was generated utilizing one specimen design tested on one LCF machine, while the round robin data was generated using four specimen geometries tested at four different laboratories.

The results show that the test conditions and procedures employed yielded excellent agreement of the deformation response under strain-controlled in-phase and out-of-phase TMF cycles. However, for most applications, the objective of TMF tests is to determine life data. Thus, additional interlaboratory testing is needed to determine the scatter of life data using these procedures.

4. ADDITIONAL EFFORTS IN TMF TEST STANDARDIZATION AND MATERIAL BEHAVIOR

4.1 Interlaboratory Test Program in the Framework of COST 501-II

In addition to the ASTM-organized TMF deformation test program discussed in section 3, several other ongoing activities are making significant contributions to the area of TMF test standardization. In particular, an interlaboratory round robin organized in 1992 within the framework of the European collaborative activity designated as COST (COST 501 round II - Working package 5) (8) examined the life of an ODS alloy subjected to the proto-typical TMF cycle given in Fig. 4 prior to embarking on an extended test and research program on this material. The specific material selected was ODS alloy MA 760 with the composition of Ni-19.66Cr-5.97Al-7.92Mo-3.5W-1.0Fe-0.043C-0.011B-0.74Z-0.284N-1.03Y_2O_3 (wt. %). The laboratories participating in the round robin were the MPI fur Materialforschung (Stuttgart, Germany), CNR-ITM (Milano, Italy), Escole des Mines (Paris, France) and Joint Research Centre (EC Petten, Netherlands). Each laboratory used their own specimen design, varying from the traditional hollow cylindrical sample with a 1 to 1.5 mm wall thickness, to a flat squared sample of cross-section 3 x 12 mm and a solid cylindrical sample with a 7 mm diameter.

Results from this program are given in Table 1 and plotted in Fig. 5 as the open symbols (8). A scatter of a factor of nearly 10x in life, and of the order of 25% on the maximum and minimum stress levels achieved in the cycle at half life was noted. Given that scatter in a corresponding isothermal round robin program on the same material with the same participants was smaller (8), it seemed reasonable to conclude that the wide scatter was caused by differences in testing procedure (including specimen surface finish) and the material variability. The suggestion of variability within the

testing material was supported by the measured differences in elastic modulus (E), see Table 1. To test this hypothesis, a second round robin was set up using the same specimen geometry of hollow, cylindrical samples machined from a single bar section. The results are listed in Table 2 and plotted in Fig. 5 as the filled symbols. With the exception of the longest living specimen (tested by 1D14), of which the internal surface was polished, all specimens were tested in the as-received condition. The longest and shortest living 1D14 specimens failed from the outside and from the inside (initiation at machining mark), respectively. The two samples tested by 5CCR1 failed from the outside, whereas multiple in- and outside initiation sites were reported for the sample tested by 5F2. The scatter in cyclic life was 3.5x, which may have been partly due to differences in surface finish. The scatterband width of the minimum and maximum stress level response was of the order of 30%. The fact that the specimens were machined from the same bar section and the limited variability in E, combined with the relatively small scatter observed between specimens taken from different bars in a related isothermal LCF round robin (8) suggested that material variability was not the primary cause for scatter in the TMF lives. It was concluded that the differences in the prescribed temperature / strain levels and non-uniformity over the specimen gage length were the main factors contributing to the scatter of both stress response and lifetime, whilst specimen surface finish was a major cause for the observed scatter in life. The outcome of the round robin illustrated the need for a TMF testing standard which should specify tolerances on the above mentioned factors.

4.2 Key TMF Symposia and Workshops

One means by which widespread experience in TMF testing is pooled is through the holding of specialized symposia and workshops.

The 1993 workshop "Practicalities of TMF Testing" at Derby (UK) was organized by the High Temperature Mechanical Testing Committee (HTMTC) to provide a forum for exchange of information; approximately 25 laboratories in Western Europe involved with this developing area of testing were in attendance. Issues discussed included thermal and mechanical aspects of the test, heating and temperature control, strain measurement and control, etc. An overview entitled "Taking the Test in Thermo-mechanical

Fatigue" can be found in Materials World, vol. 2, 1994, pp. 468-470.

The international symposium "Fatigue under Thermal and Mechanical Loading" held at Petten (the Netherlands) in 1995 covered mechanisms, mechanics, modeling, and experimental techniques of both thermo-mechanical and thermal fatigue loading (9).

ASTM sponsored two international symposia on the TMF behavior of materials, the most recent one in 1994 in Phoenix (U.S.). Progress in the understanding, testing and modeling of both high temperature alloys and titanium matrix composites were included in the symposia. The proceedings are published as ASTM Special Technical Publications (10,11).

A series of informal workshops on TMF behavior of materials has been organized by NASA Lewis Research Center in the U.S. Seven workshops have been held since 1981, with the purpose of disseminating recent advances among U.S. aerospace organizations in the areas of test methods, mechanisms, deformation modeling, and life prediction under TMF loadings.

5. CURRENT TMF TEST STANDARDIZATION ACTIVITIES

5.1 Introduction
As previously stated, a widely accepted test standard, such as any one of the many cited for isothermal LCF testing, does not currently exist for TMF testing. This may seem surprising given that controlled TMF testing, where a uniform stress-strain-temperature field is achieved over a specified gage section (in principal), can be found in the literature from over 35 years ago (12). Further, TMF testing is commonly included in most high temperature material characterization programs, particularly in the area of gas turbine engine applications. Thus, although there is a tremendous knowledge and experience base among the various materials/structures research groups scattered throughout private, government, and academic sectors, very little of this knowledge and experience has been shared or pooled in an attempt to standardize a testing methodology. Consequently, data generated from these relatively expensive, time-consuming tests may not be readily accepted from one research group to the next, potentially leading to either a tremendous

duplication of work, or a misuse/misinterpretation of the data. Efforts are currently aimed at correcting this shortcoming through the proposal of a standard approach to TMF testing.

5.2 Approach

Under the auspices of ISO, technical experts representing at least 9 countries (Canada, France, Germany, Italy, The Netherlands, Sweden, Switzerland, United Kingdom, and United States) and their various standards organizations are meeting to establish an international standard practice for the TMF testing of metallic materials; this group is designated ISO TC164/SC5/WG9. To date, three meetings have been held with the main objectives of compiling a list of the various widespread approaches and methodologies for conducting TMF testing and to establish a consensus on fundamental issues.

As expected, the approaches employed among the various laboratories for the many parameters involved with TMF testing (e.g., specimen design, heating methodologies, temperature control and measurement, strain control and measurement, temperature-strain phasing) are too numerous to discuss here. Rather, the intent here is to present a few of the key issues unique to TMF testing and convey areas of consensus.

5.3 Scope

As a result of a consensus of the ISO TC164 /SC5/WG6 group, the scope of a standard test practice for TMF testing would be subject to the following limits. The test practice would only apply to uniaxially loaded, uniform gage length specimens. Testing would be limited to strain-controlled cycling under any strain R ratio. Any cyclically- constant phase shift between temperature and mechanical strain would be acceptable. Specimen heating rates would only be limited by a specification which limits the temperature gradient in the specimen gage section. Different specimen heating and cooling rates can be incorporated.

5.4 Areas of Consensus

To date, agreement among the members of the ISO group has been reached for three specific aspects of a proposed standard TMF test method. These areas of consensus are methods used for thermal cycling, temperature/ strain phasing, and thermal strain compensation.

5.4.1 *Thermal Cycling*

Commonly-used specimen heating techniques were deemed acceptable. These include the use of direct induction, indirect induction (susceptor), and quartz-lamp systems. Other methods, such as direct resistance heating, cannot be used.

Temperature measurement and general control techniques will be very similar to those specified in LCF test standards. Temperature gradients over the axial gage section will be specified based on those existing under thermal cycling (dynamic) conditions and not those existing under static conditions prior to test initiation.

5.4.2 *Phasing Accuracy*

The temperature/mechanical component phasing accuracy will be specified via an allowable phase-angle error or time-shift error based on the response waveforms. This value can be calculated at all points throughout the cycle.

5.4.3 *Thermal Strain Compensation*

As stated earlier, a thermal strain compensation technique is required if the mechanical strain range and rate are to be specified and controlled under strain controlled conditions. Two compensation techniques are deemed acceptable and are illustrated by the following equations:

$$e_i = \epsilon^m_i(t) + \epsilon^{th}_i(t) \qquad (2)$$

$$where \ \epsilon^{th}_i(t) \neq Constant$$

$$e_i = \epsilon^m_i(t) + \epsilon^{th}_i(T) \qquad (3)$$

The method represented by equation (2) is the most commonly employed. Here the thermal strain is "pre-recorded" as a function in time and subsequently used/recalled as a function of time throughout the test for appropriate compensation. This technique captures the non-linear effects associated with both a non-linear CTE and non-constant temperature-response rate.

The method represented by equation (3) calculates the real-time thermal strains based upon a real-time measurement of the temperature. An appropriate functional relationship between temperature and thermal strain is established prior to the TMF test. This function is used for subsequent thermal strain compensation. Note that for modern digitally-controlled test systems, equation 3 can be easily

employed, however, equation 2 is often easier to implement when using an analog-controlled system.

6. CONCLUSIONS

1. The requirement for a standard practice for TMF testing is illustrated by the extensive collaborative activities in the area of TMF of materials, including several on-going symposium, interlaboratory test programs, and efforts to draft a standard.

2. Data from two interlaboratory test programs were presented. Results show critical aspects of TMF testing where strict tolerances are required to ensure consistent life data, such as specimen surface finish and uniform dynamic temperature gradients in the specimen gage section.

3. ISO has begun the process of developing a test standard by identifying and reaching consensus on some key issues unique to TMF.

7. REFERENCES

1. Halford, G.R.,"Chapter 6: Low-Cycle Thermal Fatigue," in Thermal Stresses II, Edited by R.B. Hetnarski, Elsevier Science Publishers B.V., 1987.

2. ASTM E606-92, "Standard Practice for Strain-Controlled Fatigue Testing," 1994.

3. Thomas, G.B., Hales, R., Ramsdale, J., Suhr, R.W., and Sumner, G.,"A Code of Practice for Constant-Amplitude Low Cycle Fatigue Testing at Elevated Temperatures," Fatigue Fract. Engng. Mater. Struct., vol. 12, no. 2, pp. 135-153, 1989.

4. Amzallag, C., Kono, H., and Endo, T., "Recommendation pour la practique des essais de fatigue oligocyclique a deformation imposee," RE 90 601, Unirec, France, 1990.

5. ISO document #ISO/TC 164/SC5/WG2/N1, "Metallic materials - Fatigue testing, Axial strain-controlled low-cycle method (project 12106)," working document, Sept. 1993.

6. Halford, G.R., Saltsman, J.F., and Kalluri, S.,"High Temperature Fatigue Behavior of Haynes 188," NASA C.P. 3012, pp. 497-509, 1988.

7. Bonacuse, P.J. and Kalluri, S., "Elevated Temperature Axial and Torsional Fatigue Behavior of Haynes 188," ASME J. Eng. Mater. and Tech., vol. 117, April 1995, pp. 191-199.

8. Bressers, J. and Timm, J., "Prediction of Lifetime under Simulated Service Loads," Final Report Work Package 5, COST 501--round II, EuCo/MCS/03/94, March 1994, pp. 19-58.

9. Bressers, J., Remy, L., Steen, M., and Valles, L.J. (eds.), proceedings of the international symposium "Fatigue under Thermal and Mechanical Loadings: Mechanisms, Mechanics, Modeling," May 22-24, 1995, Petten, the Netherlands, Kluwer Academic Publishers 1996.

10. Sehitoglu, H.,(ed.),"Thermo-Mechanical Fatigue Behavior of Materials," ASTM STP 1186, Am. Soc. Testing and Mater., Philadelphia, PA, 1993.

11. Verrilli, M.J. and Castelli, M.G., (eds.)" Thermo-Mechanical Fatigue Behavior of Materials: Second Symposium," ASTM STP 1263, Am. Soc. Testing and Mater., Philadelphia, PA, 1996.

12. Carden, A.E., and Slade, T.B., "High-temperature Low-cycle Fatigue Experiments on Hastelloy X," Fatigue at High Temperature, ASTM STP 459, Am. Soc. Testing and Mater., Philadelphia, 1969, pp. 111-129.

Table 1. TMF data on ODS alloy MA 760 from the COST 501-II round robin test program (10). Different bar stock and specimen geometries used by the participants. The mechanical strain range employed was 0.8±0.01 %.

Project	Specimen Geometry	σ_{max} MPa	σ_{min} MPa	$\Delta\sigma$ MPa	E, GPa			N_f cycles
					R.T.	550 C	1050 C	
5CCR1	flat 12 x 3 mm	510	-830	1340				720
II1	solid cyl., 7 mm dia.	420	-999	1419				280
5F2	hollow cyl., 1 mm wall thickness	400	-890	1290	199	172	106.5	201
1D14	hollow cyl., 1.5 mm wall thickness	530	-909	1440	214	186	117	1200
1D14	solid cyl., 7 mm dia.	470	-925	1395		193		920

Table 2. TMF data on ODS alloy MA 760 from the COST 501-II round robin test program (10). Hollow cylindrical specimens with a 1 mm wall thickness machined from one bar were used by all participants. The mechanical strain range employed by all was 0.8±0.01%.

Project	σ_{max} MPa	σ_{min} MPa	$\Delta\sigma$ MPa	E, GPa			N_f cycles	Remarks
				R.T.	550 C	1050 C		
5F2	400	-890	1290	199	172	106.5	201	as received
5CCR1	560	-901	1461		191	106	407	as received
5CCR1	572	-732	1304				377	as received
1D14	523	-845	1375	220	195	122	704	polished
1D14	514	-965	1499	226	195	116	202	as received

(A)

(B)

(C)

(D)

Figure 1. Specimen designs used by the four participants of the ASTM-organized TMF deformation test program. All dimensions in mm, except the thread pitch of specimen (a).
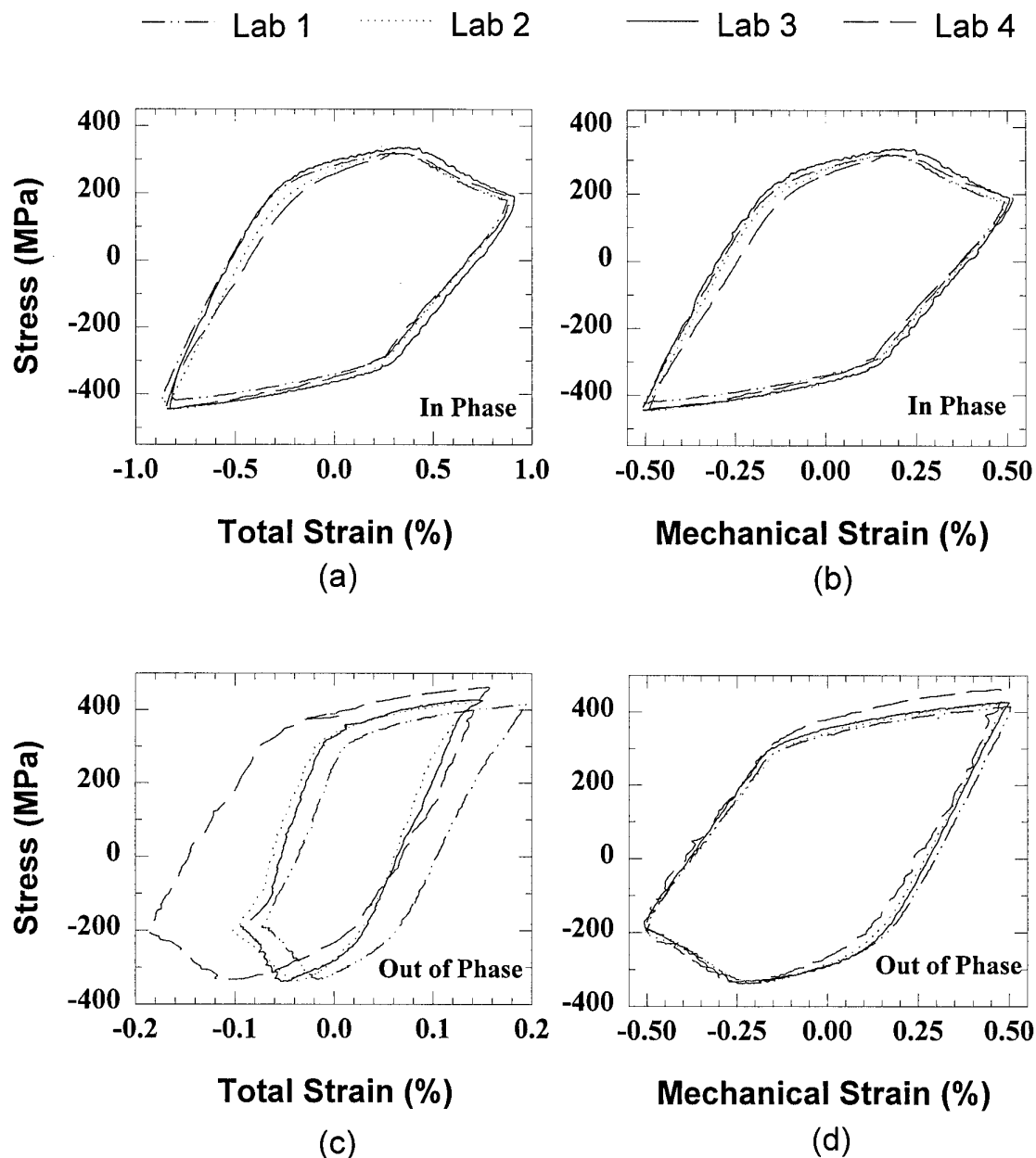
Figure 2. Comparison of the hysteresis loops generated by the four participants of the ASTM interlaboratory test program on strain-controlled TMF cycling of alloy Haynes 188: a) stress vs. total strain for in-phase TMF; b) stress vs. mechanical strain for in-phase TMF; c) stress vs. total strain for out-of-phase TMF; d) stress vs. mechanical strain for out-of-phase TMF. Data shown is for cycle 20.
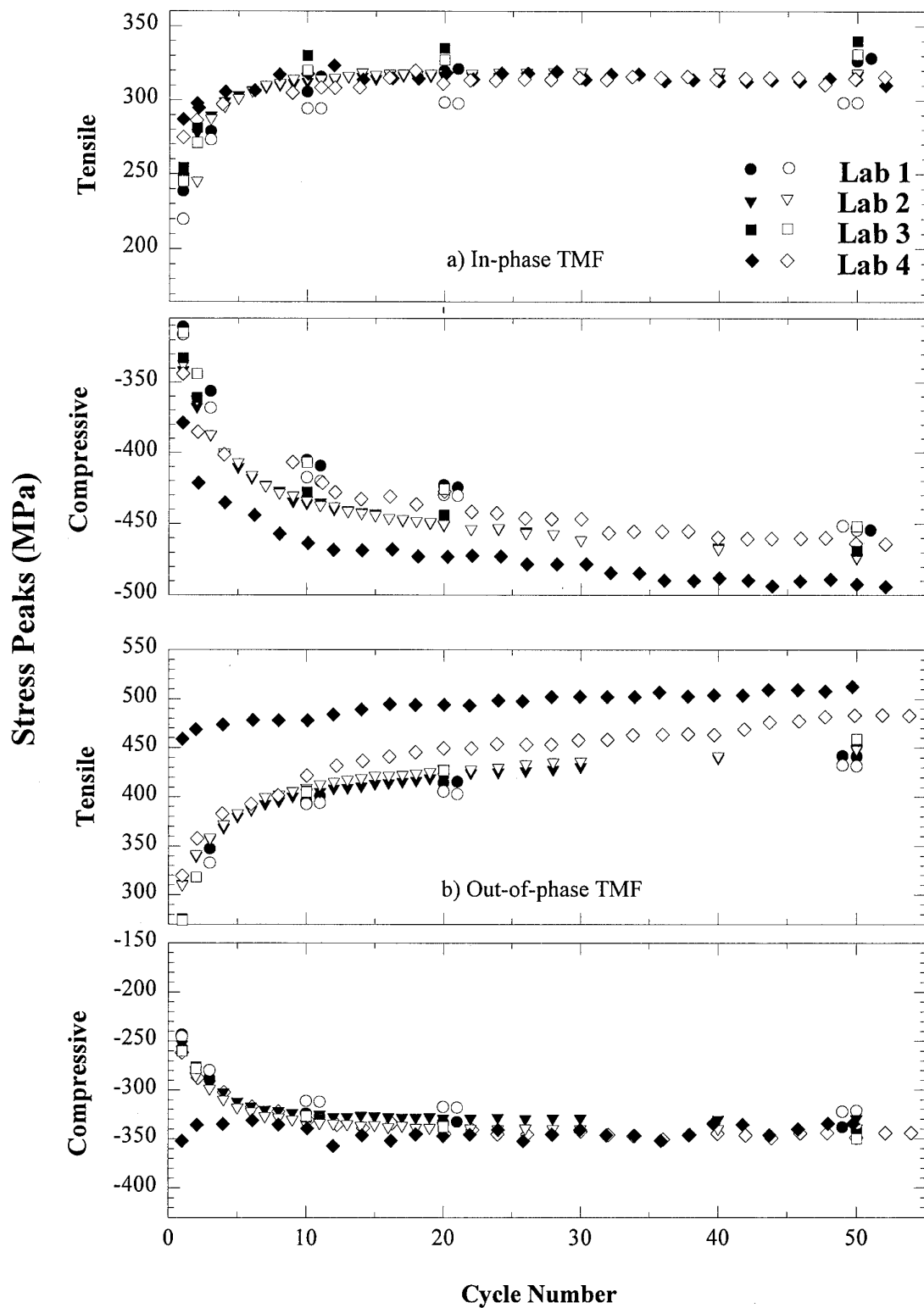
Figure 3. Comparison for peak stresses vs. cycle number for the ASTM interlaboratory program on alloy Haynes 188. Data for duplicate tests by each laboratory are shown.
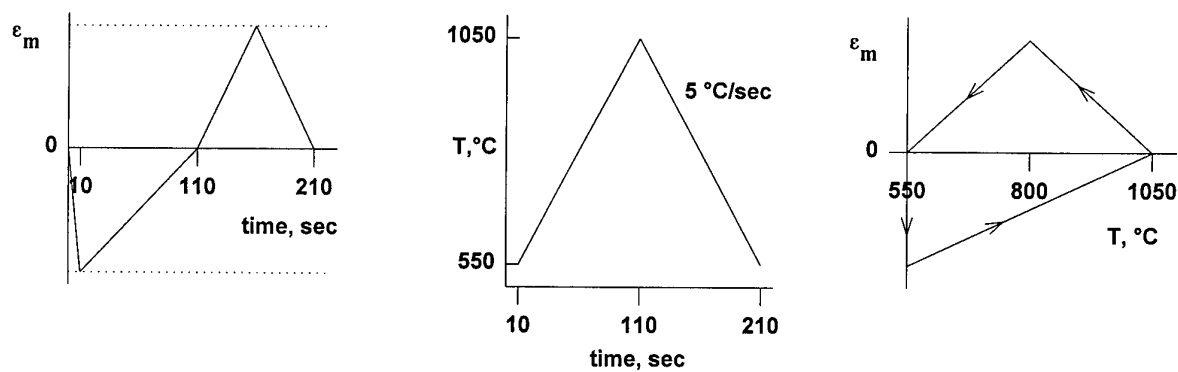
Figure 4. TMF cycle utilized for the interlaboratory testing of ODS alloy MA 760 conducted under the COST 501-II framework (8).
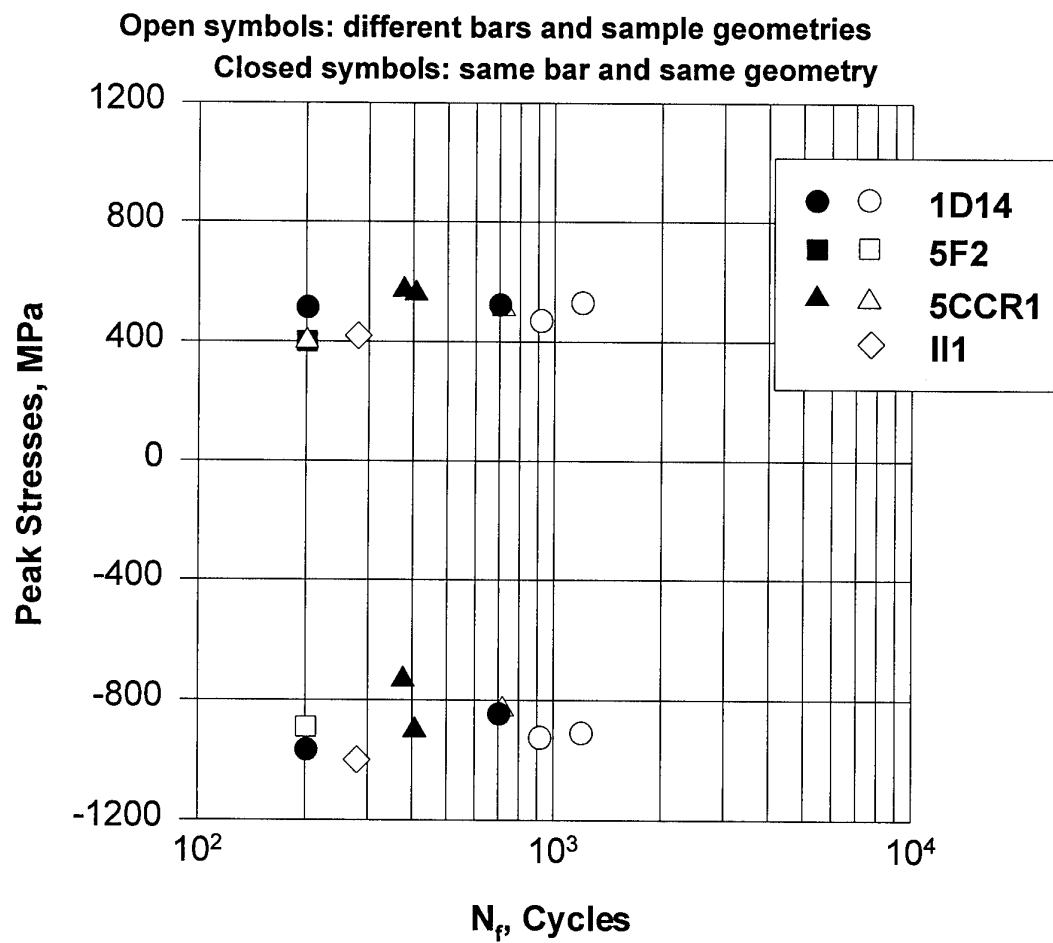

Figure 5. S-N results for the TMF interlaboratory test program of ODS alloy MA 760 conducted under the COST 501-II framework (8).

ELEVATED TEMPERATURE FATIGUE OF IN718: EFFECTS OF STRESS RATIO AND FREQUENCY

BY

C. Moura Branco
Lisbon University of Technology (IST)
1096 Lisbon Codex, Portugal

and

J. Byrne
University of Portsmouth
Portsmouth PO 13DJ, UK

ABSTRACT

The paper presents a combined analysis of the influence of stress ratio, frequency (hold time) on the fatigue crack growth in IN718 at 600°C. Fatigue crack growth rate (FCGR) data is presented for three stress ratio values (0.05, 0.5 and 0.8) and several values of hold time at maximum load ranging from 10 to 600s. FCGR data is also presented for sustained load where oxidation damage and creep failure mechanisms dominate. A preliminary assessment is presented of the transition frequency behaviour from transgranular dominant cracks to intergranular dominant. SEM observations show that specific types of failure can occur for different combinations of stress ratio and frequency.

INTRODUCTION

The nickel base superalloy IN718 is generally used in the turbine discs of aeroengines (1,3). The results reported in this paper were obtained in a standard grade IN718, i.e., with the conventional casting and forging route followed by the standard annealing and ageing treatment.

Isothermal fatigue tests are much less expensive and easier to carry out than thermal-mechanical tests, and the data obtained in the isothermal tests allows a straight comparison of material performance and can also make a screening of the most relevant parameters that might affect the fatigue behaviour of these alloys. The treatment of creep cracking may require the use of different fracture mechanics parameters, including C* (4,5).

The mechanical behaviour at high temperature of Ni based superalloys has been covered in a extensive number of publications (6). Some good reviews in the subject are available dealing in detail with the crack propagation behaviour of these materials (7,11). Most of the work presented concerns the growth of long cracks (more than 0.25-0.5 mm length) in the regions I and II of the fatigue crack growth rate (FCGR) diagram (da/dN against ΔK or K_{max}). Some important results on the behaviour of short cracks have been published also (12).

Despite the fact that the FCGR behaviour of N_i base superalloys is documented in the literature there are still areas which need clarification and also systematization is needed for the gathering and treatment of the data available.

Recent work carried out by Byrne and coworkers (13,14) in Waspalloy at temperatures up to 650°C under conditions of cyclic fatigue, cyclic dwell and static loading (creep) have shown no significant effect of dwell at peak load on fatigue crack growth rates for the temperature of 550°C, where the main failure mechanism detected was transgranular fatigue cracking. However, at 600 and 650°C severe increases in fatigue crack growth rate and also a sharp transition to intergranular cracking were observed under dwell-cycling conditions. The application of a linear summation model (15), to correlate dwell-cycling fatigue crack growth rates at 650°C, gave good results for the predictions based on the summation of static load and fatigue data.

Branco has published the results of a fatigue life study on compressor and turbine discs (16). Work at CEMUL/IST in this field started in 1989 resulting from a crack propagation study in nickel base superalloys of used engine turbine discs of the Portuguese Air Force fleet. In that work fatigue life predictions were made and inspection intervals were defined (17,18).

Under AGARD P94 project the work was to complement the research at Portsmouth University (PU), testing in another nickel based super alloy (IN718 at 600°C), under similar testing conditions and specimen geometries. The tests were fatigue cycling with trapezoidal load wave (Fig. 1) at different stress ratios (R=0.05, 0.5 and 0.8) and dwell times. Creep tests were also performed to enable the fatigue modelling to be carried out. The results were published (19) for the tests carried out at R=0.05.

This paper presents the results of the preliminary study of the influence of stress ratio and dwell time with the aim to obtain the transition frequencies for the change in fracture mode from transgranular to mixed and mixed to

intergranular. Micromechanisms of failure were also studied with the SEM.

2. SUMMARY OF THE EFFECTS OF FREQUENCY AND HOLD TIME ON FCGR.

This summary is based on a review recently published by the authors (20).

2.1 Effects of Frequency

The general trends found from the reviewed literature, (7-11,20) and specially for IN718, with regard to the effects of frequency on FCGR are shown below.
1) FCGR per cycle increases with decrease in frequency or increase in total cycle time (t_T)
2) Crack growth rate can be divided into three regimes:
   i) **Cycle dependent or frequency independent** at high frequencies (where from the literature, high frequencies can be regarded as approximately $f>1$ Hz where f is the total cyclic frequency.
   ii) **Frequency dependent** (mixed mode region).
   iii) **Time dependent or frequency independent** at low frequencies or long cycle times (approximately $f<0.1$ Hz).
3) Low frequencies or time dependent effects normally promote an intergranular fracture mode.
4) High frequencies or cycle dependence normally promotes transgranular fracture mode.
5) Increasing the temperature and/or ΔK (or K_{max}) for a given frequency, increases the FCGR.
6) Increasing ΔK or K_{max} decreases the cycle time (or increases the frequency) at which the transition from frequency dependent to cycle dependent effects occur and subsequent fracture mode transition occurs.

2.2 Effects of Hold Time

It is widely reported that the addition of a hold time at maximum load to a fatigue cycle tends to increase the crack growth rate per cycle in Alloy 718, as well as in a number of other nickel base superalloys (20).

However an increase in hold time at maximum load at **low ΔK values** and low loads can cause growth rates to decrease rapidly with time to the extent that there is complete crack arrest. This phenomenon is thought to be due to creep relaxation but has yet to be quantified (21,22).

A few special conditions do not show the same trend of increase in growth rate with longer hold times.

(i)   When hold time occurs at other than maximum load (i.e., at minimum load).
(ii) When specialized heat treatments are used and (or) temperatures are high enough to promote microscopic changes within the material (23).

In this latter case it was found that microstructures with very small grain size and different δ particle distribution, such those found in the direct aged (DA) IN718, enhanced the resistance to environmentally assisted creep crack growth in

comparison with the standard processed IN718. So a lack of effect of hold time on crack growth rates was obtained in the DA IN718 (23,24).

(iii) In the low ΔK region (near the threshold ΔK_O) (23,24). This effect is due to increasing extents of oxide-induced closure at the longer dwell times and if creep effects occur, the enhancement of crack growth by creep is offset by extensive intergranular branching deflection at longer hold times (24).

For elevated temperatures between 500 and 700°C, hold time at maximum load appears to have only one effect clearly understood:

(i)   If the frequency of the base cycle, $f<f_c$ a fracture mode transition frequency, and a hold period at maximum load is added then there is a measurable acceleration in the FCGR per cycle (Fig. 2). When $f<f_c$ the regime is time or frequency dependent and the resulting fracture mode is intergranular. f_c is defined as a transition from the cycle dependent transgranular regime to the frequency dependent mixed regime where intergranular cracking begins.

If $f>f_c$ an increase in FCGR per cycle is expected to occur depending on the amount of hold time, stress ratio, temperature and ΔK or K_{max} values. FCGR per cycle will not increase with the hold time at maximum load if crack blunting effects due to excessive creep or building up of oxide products at the crack tip lead to crack arrest.

The combined effects on FCGR base line frequency and dwell time are not described in the literature and a joint investigation is in progress to assess the influence of these parameters (25,26).

2.2.2 Effects of hold time at minimum load

There are several studies where hold time retarded crack growth instead of accelerating it and even contribute to total crack arrest. This had been observed when hold times occur at other than maximum load (20).

For **low R values and $K_{min}<K_{th}$** hold period at minimum load for low R (R=0.05) caused an increase in da/dN relative to zero hold time. For **low and medium values of R and $K_{min}>K_{th}$** in general it has been observed that hold times at minimum load only produce an increase in the FCGR. For **medium values of R and $K_{min}<K_{th}$.** FCGR decreases with increasing ΔK and in some cases the decrease in FCGR caused crack retardation and arrest to occur. This behaviour was attributed to crack tip blunting resulting from creep deformation at a Kmin level slightly below that required for creep crack growth.

Effects of thermal exposure

In tests at short frequencies and (or) long dwell times prolonged thermal exposure occurs and this may lead to microstructural alterations in the material due to overaging effects. FCGR properties may degrade during

the testing and hence results will be affected by this behaviour. Results reported in (27), and obtained for IN718, have shown that in the specimens subjected to a prior thermal exposure of overageing during 800 hours at a constant temperature of 650°C, the FCGR resistance increased in comparison with the specimens tested without the overaging treatment. This aspect is currently under investigation (24,25).

3. EXPERIMENTAL

The specimens were supplied by DRA (formerly RAE) in Farnborough, UK).

The chemical composition of the IN718 supplied, was 56.5 wt% N_i, 19 wt% Cr, 0.9 wt% Ti, 0.6 wt% Al, 20 wt% Fe, 3 wt% Mo. The mechanical properties are presented in (19).

The CT specimens (Fig. 1) for the fatigue tests had a nominal thickness (B) of 13 mm. The details of the corner cracked specimens (CC) can be seen in Fig. 1. In this specimen the fatigue crack grew from a quarter circular corner crack with 0.25 mm radius ($a_0=c_0=0.25$ mm).

The fatigue and sustained load tests were carried out in a computer controlled servohydraulic fatigue machine with ±100 kN dynamic load capacity. Two series of tests were performed. The first used a trapezoidal load waveform with 1s for each step (frequency of 0.25 Hz) both at R=0, R=0.5 and R=0.8, i.e., 1s loading time, 1s of unloading time and 1s of dwell time at minimum and maximum load. The second used a similar load waveform, with dwell times at maximum load for R=0.05 with different magnitude ranging from 1 to 600s (1, 10, 30, 60, 90, 120, 300 and 600s).

Two techniques were used to monitor fatigue crack growth, crack marking and potential drop (PD).

For R=0.5 and 0.8 tests were carried out at f=10Hz and with the dwell times of 1s and 300s only. For continuous crack growth measurements the DCPD technique was employed. The AGARD testing procedures for the use of potential drop equipment to measure crack length at high temperature, were used (28). To convert the voltage ratios to crack length, calibration curves were obtained for the CT and CC specimens.

For the CT specimens the stress intensity factor was calculated with the ASTM equation (29). For the CC specimens the Pickard formulation (30) was used to compute the stress intensity factors at the surface points of the corner crack.

The creep crack growth rate tests were carried out in accordance with the guidelines defined in the appropriate ASTM specification (31). In this project no analysis of C* was carried out. The creep behaviour under C* based on the analysis of the displacements will be one of the main topics of study in the AGARD SMP follow-on project to P94, Project P111.

4. RESULTS AND DISCUSSION

4.1 Baseline fatigue results for R=0.05

The baseline fatigue results for R=0.05 and f=0.25 Hz are plotted in Fig. 3 using the Paris law, the modified Paris law and the Forman equation (32).

The modified Paris law takes into account the behaviour in region I, i.e. slow crack growth near the threshold. The equation is

$$\frac{da}{dN}=C_1(\Delta K-\Delta K_o)^{m_1} \tag{1}$$

where C_1 and m_1 are the experimental constants and ΔK_o is the appropriate value of the threshold for crack propagation.

The Forman equation is

$$\frac{da}{dN}=\frac{A(\Delta K)^P}{K_c(1-R)-\Delta K} \tag{2}$$

where A and p are experimental constants and K_c is the fracture toughness of the material.

The correlation of the results with the modified Paris law is shown in Figure 3. A good fit of the data was obtained for regions I and II, better than that given by the Paris law. The values of C_1 and m_1 in equation (1) are $C_1=1.42\times10^{-5}$ and $m_1=1.163$. For ΔK_o a value of 11MPa√m was taken from the data published by King (7) for IN718 with a grain size of 30μm, very close to the actual grain size measured in the tested material.

Despite the fact that FCGR equations with threshold term (equation 1) give the best correlarion with experimental data, (Fig. 3), its use is limited due to the experimental difficulty of obtaining threshold values at low frequencies or long dwell times.

The correlation with the Forman equation is good in regions II and III. In region III a poor correlation was obtained with both the Paris law and the modified Paris law. The best fit values of A and p in the Forman equation were $A=1.46\times10^{-3}$ and p=0.761. The modified Paris law, with the threshold term, seems to provide the best correlation for the fatigue crack growth rate in IN718 under the specified testing conditions.

In this work crack arrest/blunting secondary effects were found reflected in the data in Fig. 3.

The da/dN equation given by Tomkins (33) is used as a conservative upper bound for the data when the mechanism of crack growth is by decohesion striations. The equation is

$$\frac{da}{dN}\approx\frac{\delta}{2}\approx\frac{\Delta K^2}{4E\sigma_y} \tag{3}$$

where δ is the crack tip opening displacement, E is Young's modulus and σ_y is the yield stress. In other work (34) equation (4) is claimed to give the best fit with measured striation spacing in IN718 in the range 316-650°C.

$$\frac{da}{dN}=6\left(\frac{\Delta K}{E}\right)^2 \qquad (4)$$

The values of C, using the data obtained for this alloy (Fig. 3), were found to be 1.41×10^{-6} mm per cycle with equation (3) and 2.08×10^{-7} mm per cycle with equation (4). This value is very close to the value of $C=2.72\times10^{-7}$ mm/cycle obtained in the present work. Since the values of m were also very close to 2 (2.11) the rupture mechanism is by transgranular striations and this was confirmed by SEM observations at the fracture surface.

4.2 Influence of stress ratio and frequency including dwell time

The transition frequencies change with stress ratio and an increase of stress ratio, R (increase of K_{max}) at constant ΔK gives an increase of mean load. Hence the creep or time dependent component increases. For this reason for high stress ratios better correlations of FCGR are obtained with K_{max} (35). The influence of stress ratio can also be explained in terms of crack closure. Increasing R leads, for the same ΔK, to increased values of ΔK_{ef} in the loading cycle.

Mainly for the two reasons mentioned above FCGR increases with R. Also the transition frequency, f_c, increase with increasing K_{max} or R, i.e., a higher R value is able to promote the transition of failure mode from transgranular to intergranular, to occur at a higher frequency.

An alternative way of plotting FCGR data is in terms of ΔJ or J_{max}. The present data was obtained for bulk or nominal stresses in the elastic regime. Hence LEFM is basically valid and in this case, $\Delta J \equiv \Delta G$.

Data available in the literature seems to indicate reduced scatter when FCGR is plotted as a function of ΔJ (36).

Fig. 4 shows the combined da/dN; ΔK plot of the specimens tested for R=0.5 and 0.8. For the correlation with Paris law the initial set of data points were not considered since those are outside the behaviour of region II. The acceleration of crack growth in the early part of the curve is not a threshold effect but is resulting from crack growth still within the plastic region of the notch.

Details about the da/dN; ΔK, da/dt; K_{max} and a da/dN against ΔJ and da/dt against J_{max} equations are given in (25).

For R=0.8 (Fig. 4) da/dN increases with the decrease in frequency, i.e., when the dwell time of 5 minutes was introduced in the loading cycle, da/dN has increased by a factor of 20, in comparison with the results for the 0.25 Hz, and near three orders of magnitude against the results

obtained at 15 Hz FCGR per cycle increases with decreasing frequency and increasing stress ratio. However only a very small effect of stress ratio was found in the higher frequency of 15Hz. Note that increasing the stress ratio from 0.5 to 0.8 has led to very similar increases of da/dN, both for the frequencies of 0.25 and 0.033Hz (5 minutes dwell). Hence, after a certain frequency is attained, it looks that the increase in FCGR per cycle with the stress ratio is proportional.

The data obtained in the creep tests (da/dt vs. K) is plotted in Fig. 5. The straight lines of the Paris law for da/dt; K_{max} refer also to the stabilized growth of region II of crack propagation.

The effect of frequency for R=0.05 and for the dwell times of 1, 120 and 300s, is depicted in Figs. 6 and 7. The lines are the best fit to experimental data points. It is seen that FCGR per cycle increases as the test frequency decreases or dwell time increases. The increase in da/dN is higher when f increases from 0.25 to 0.033 Hz (5 minutes dwell at peak load) than from 15 to 0.25 Hz. Hence, time at maximum load makes a substantial contribution for this effect. The da/dt K_{max} plots (Fig. 7) show that there is a compression of the data of Fig. 6. Now FCGR per time is higher in the higher frequency. The creep curve (Fig. 7) gives lower crack growth rates very close to the curve for 5 minutes dwell. Therefore, and in agreement with the findings reported in the literature (20), for sufficiently long dwell times at maximum load, FCGR will not depend on the dwell time, and failure will be extensively intergranular as it will be shown later.

The equivalent plots of da/dt against J_{max} are given in Fig. 8 (R=0.05). As happened before with K_{max}, (Fig. 7) da/dt is higher for the higher frequencies when plotted against J_{max}. It is seen that J_{max} provides a better correlation parameter than K_{max} reducing to a great extent the variations of da/dt with frequency detected in the (da/dt; K_{max}) plot (Fig. 7).

The variation of da/dN with frequency (dwell time) for a constant $K_{max}=40MPa\sqrt{m}$ is plotted in Fig. 9. da/dN increases when the dwell time was increased but increases when R is decreasing. The data follows closely a linear relationship between log da/dN and log f.

In the frequency diagram, and for R=0.05, the three zones refered above can be defined, time dependent, mixed and cycle dependent. The tests carried out with dwell times of 1, 10, 30 and 60s produced mixed type failures. The dwell times in excess of 90s were clearly intergranular. Cyclic dependent behaviour was obtained for frequencies above 1Hz. For R=0.5 and 0.8 only two regions seem to have been obtained in the diagram (Fig. 9), and only one transition frequency is clear. This looks to be in line with the data obtained in (37,38). Additional tests are in progress to define more exactly the range of transition frequencies. The data in Fig. 9 can be correlated with a general equation of the type

$$\frac{da}{dN}=Cf^\alpha(K_{max})^n \qquad (5)$$

where α is the frequency or dwell time dependent exponent (37).

The modelling work is in progress in order to predict the creep-fatigue crack growth rates from superposition of creep and pure fatigue components. Work is already under way in this area and superposition models (15,37-40) are being investigated.

4.3 Fractography. Mechanisms of crack growth

Fig. 10 shows for a ΔK value of 25MPa$\sqrt{m}$, and R=0.05 the transition between the fatigue crack at 10Hz (right) under continuous cycling, and the crack of the immediate load cycle, with 10 seconds dwell. Both cracks are essentially transgranular but there is an increase in surface roughness in the dwell area due to the higher crack growth rate in the 10s dwell zone (Fig. 9). Small areas of secondary cracking appear in the dwell zone. Hence these two testing conditions produce failures that are mainly within the cycle dependent region.

Fracture surfaces in specimens tested at R=0.5 and 5 minutes dwell at maximum load are depicted in Fig. 11 a,b. Fig. 11 a) shows the transition between the fatigue crack under baseline fatigue at 10Hz and the dwell crack. In the base line fatigue transgranular crack growth is dominant and fatigue striations are noticeable in some grains. Intergranular cracking is predominant in the dwell zone (lower half) as evidenced in more detail in Fig. 11 b). Secondary cracking can be seen in Fig. 11b) and cracks along the grain boundaries are covered with oxidation products. Damage by oxidation is the most plausible failure mechanism and very little creep seems to be occurring since reduced cavitation and grain boundary cycling was detected at this dwell time.

For R=0.8, (K_{max}= 45MPa$\sqrt{m}$) and with the same dwell time of 300s at maximum load, a fracture surface is shown in Fig. 12a). Intergranular cracking is again dominant due mainly to oxidation damage. Increasing the frequency to 0.25 Hz (1s dwell time) gives widespread transgranular cracking although some secondary cracking is apparent at this dwell time (1s) which is not so apparent at the stress ratio of R=0.05 (Fig. 10). The increase in stress ratio from R=0.05 to 0.8 enhanced the intergranular cracking and has increased the surface roughness (compare Figs. 12b) with 10). When the frequency was increased to 10Hz the fracture surface appearance has changed to a predominant transgranular mode (Fig. 12c). However, and even at this frequency, a few secondary cracks were detected (Fig. 12c). Note that secondary cracking was not observed at 10Hz both for R=0.05 (Fig.10) and R=0.5 Fig. 11). Also, there is a distinct reduction in surface roughness when the frequency is changed (Fig. 12).

The relevance of the creep process to the intergranular nature of failure detected at high R values (Figs. 11a and 12a) is currently being assessed in tests carried out under longer dwell times. Additionally an analysis of creep displacement data (31) obtained in the specimens tested at longer dwell times is in progress.

Fracture surfaces of the specimens tested under sustained load are illustrated in Fig. 13), b). Thus, Fig. 13a) is the

transition between the fatigue precrack at 10Hz and the creep crack. The creep fracture is intergranular. Evidence of intergranular cracking is shown in Fig. 13b). Oxidation damage is also apparent in the central area. In Fig. 13c) taken in an area with a high K_{max} of 65MPa$\sqrt{m}$, slip bands within the grain are shown which look like fatigue striations. Some second phase particles are visible, both inside the grain and mostly scattered at the grain boundary. Note that the particles were not transversed by the crack.

5. CONCLUSIONS

1- Fatigue crack growth rate at 600°C in the nickel based superalloy IN718 was shown to increase both with the dwell time at maximum load and stress ratio. A preliminary assessment of these effects have shown that testing at high stress ratio can change considerably the fracture mode from transgranular to intergranular.

2- FCGR was shown to give appropriate correlations with the maximum values of the stress intensity factor, K_{max}, and of the J integral, J_{max}.

3- Modelling of FCGR data for one stress ratio (0.05) was achieved with the modified Paris equation.

4- SEM observations at the fracture surfaces have shown mainly intergranular type fractures at long dwell times but more transgranular fractures were obtained with the increase in frequency or decrease in dwell time. A transition type behaviour of the FCGR and fracture surface appearance with the dwell time was detected and further work will continue in this area.

ACKNOWLEDGMENTS

REFERENCES

(1)- Hammond, C., Nutting, J., "The physical metallurgy of superalloys and titanium alloys", Met. Sci., 1977, pp. 474-490.

(2)- Jeal, R. H., Met. Mater., 1985, pp.528-538.

(3)- Meatham, G., "Superalloys in gas turbine engines", The Metallurgist and Materials Technologist, September 1982, pp. 387-392.

(4)- Landes, J.D. and Begley, J., "A fracture mechanics approach to creep cracking", in Mechanics of Crack Growth, ASTM STP 590, American Society for Testing and Materials, 1976, pp.128-148.

(5)- Smith, D.J. and Webster, G.A., "Estimates of the C* parameter for crack growth in creeping materials", in Elastic-plastic Fracture (Eds. C.F. Shih and P. Goudas), Vol. I, ASTM STP803, American Society for Testing and Materials, 1983, pp. I-654-I-674.

(6)- Webster, G.A., Ainsworth, R.A., "High temperature component life assessment", Ed. Chapman & Hall, UK, 1994.

(7)- King, J.E., "Fatigue crack propagation in nickel-base superalloys: effects of microstructure, load ratio and

temperature", Mat. Sci. Technol., 3, 1987, pp.750-764.

(8)- Webster, G.A., "High temperature fatigue crack growth in superalloy blade materials", Mat. Sci. Technol., 3, 1987, pp. 716-725.

(9)- Pineau. A., "Mechanisms of creep-fatigue interactions", in Advances in Fatigue Science and Technology, (Eds. C. Moura Branco and L. Guerra Rosa), Kluwer Academic, Doordrecht, The Netherlands, 1989, pp. 283-313.

(10)- James, L.A., "Fatigue crack propagation in alloy 718; a review", Proc. Int. Conf. Superalloy 718-Metallurgy and applications, Ed. E. A. Laria, The Minerals, Metals & Materials Society, USA, 1989, pp. 499-515.

(11)- Skelton, P., Byrne, J., Hall, R.F., "Crack growth in nickel base superalloys in the temperature range, 550-700°C, A review", Int. report, University of Portsmouth, Department of Mechanical and Manufacturing Engineering, UK, 1994.

(12)- Grabowski, L. and Yates, J.R., "The effect of specimen geometry on short crack growth behaviour of a nickel based superalloy", Int.J. Fat., July 1992, pp.1-6.

(13)- Byrne, J., Alabraba, M., Grabowski, L., Hussey, I.W., "Influence of dwell at peak load on elevated temperature fatigue crack growth in Waspalloy", Proc. 6th Int. Conf. Mechanical Behaviour of Materials, Kyoto, Japan, Vol. 4, 1991, pp.367-381.

(14)- Byrne, J., Hall, R., Grabowski, L., "Elevated temperature crack growth in nickel base superalloys", in Behaviour of Defects at High Temperature", ESIS15, Eds. R. A. Ainsworth and R. O. Skelton, 1993, Mechanical Engineering Publications, London, UK, pp. 367-381.

(15)- Gayda, J., Grabb, T.P., Miner, R.V., "Fatigue crack propagation of nickel base superalloys at 650°C", in "Low Cycle Fatigue", ASTM STP942, Eds. H. D. Solomon, G.R. Halford, L.R. Kaisand and B.N. Leis, ASTM, 1988, pp.293-309.

(16)- Branco, CM., "Damage tolerance of critical engine components", Proc. 1st Spanish-French Meeting on Fracture, Aiguablava, Spain, Ed. Spanish Group on Fracture, Madrid, 1992, pp.337-342.

(17)- Pires, J.C., "Fatigue life assessment of critical components in aeroengines", (in portuguese), MSc Thesis, IST, Department of Mechanical Engineering, Technical University of Lisbon, 1991.

(18)- Branco, C.M., Pires, J.C., "Fatigue analysis of the TF-30 engine" (in portuguese), Proc. 3rd Portuguese Congress on Fracture, Lisbon, IST, 1989, Paper No. 20, Ed. Portuguese Society of Materials.

(19)- Branco, C.M., Byrne, J., "Fatigue behaviour of the nickel base super alloy IN718 at elevated temperature", Mat. High Temp., 12, 4, 1994, pp.261-268.

(20)- Branco, C.M., Hodkinson, V., Byrne, J., "Elevated temperature fatigue of Ni base superalloys", NATO ASI "Mechanical Behaviour of Materials at High Temperature", Sesimbra, Portugal, 12-22 September, to be published by Kluwer ASI Series.

(21)- Lynch, S.P., Radtke, T.C., Wicks, B.J., Byrnes, R.T., "Fatigue crack growth in nickel base superalloys at 500-700°C, I- Waspalloy", Fat. Fract. Eng. Mat. Struct., 17, 3, 1994, pp.297-311.

(22)- Sadananda, K., Shahinian, P., "Hold time effects on high temperature fatigue crack growth in Udimet 700", J. Met. Sci., 13, 1978, pp.2347-2357.

(23)- Lynch, S.P., Radtke, T.C., Wicks, B.J., Byrnes, R.T., "Fatigue crack growth in nickel based superalloys at

500-700°C, II- Direct aged alloy 718", Fat. Fract. Eng. Mat. Struct., 17, 3, 1994, pp.313-325.

(24)- Woolin, P., Knott, J.F., "Effects of temperature and environment on the long crack growth behaviour of IN718", Proc. ICF7, 7th International Conference on Fracture, Houston, Texas, USA, Ed. K. Salama et al, Pergamon Press, Vol. 2, 1989, pp.1859-1868.

(25)- Branco, C.M., "Fatigue behaviour of nickel base superalloys under dwell conditions", Final Report of AGARD P94 project, CEMUL/IST, Technical University of Lisbon, April 1995.

(26)- Hodkinson, V., "Modelling fatigue crack growth at elevated temperature in nickel base superalloys", Int. report, Dept. Mechanical Engineering, University of Portsmouth, UK, 1995.

(27)- Zheng, D., Ghonem, H., "Influence of prolonged thermal exposure in intergranular fatigue crack growth behaviour in alloy 718 at 650°C", Met. Trans., 23A, 1992, pp.3169-3171.

(28)- AGARD/SMP, WG26, "High temperature cyclic behaviour of aerospace materials", April 1991.

(29)- Annual book of ASTM Standards, "American Society for Testing and Materials", E647-93, 1993.

(30)- Pickard, A. C., "The application of three dimensional finite element methods to fracture mechanisms and fatigue life prediction", Ed. EMAS, UK, 1986.

(31)- ASTM E 1457-92, Standard test methods for measurement of creep crack growth rates in metals", 1992.

(32)- Forman, R., Kearnley, A.J., Engle, K.R., "Numerical analysis of crack propagation in cyclic loaded structures", J. Bas. Eng., 19, 1967, p.459.

(33)- Tomkins, B.J., Trans ASME, J. Eng. Mat. Tech., 1975, 97, p.289.

(34)- Mills, W.J., James, L. A., ASME Paper 18-WA/PVP-3, 1978, p.25.

(35)- Dimopoulus, V. Nikbin, K.M., Webster, G.A., "Influence of cyclic to mean load ratio on creep fatigue crack growth", Met. Trans., 19A, 1988, pp.873-880.

(36)- Ohtami, R., Kitamura, T. Nitta, A., Kuwabara, K., "High temperature low cycle fatigue crack propagation and life laws of smooth specimens derived from the crack propagation laws", in "Low-Cycle Fatigue", Eds. H. Solomon, G. R. Halford, L.R., Kaisand and B. N. Leis, ASTM STP942, 1988, pp.1163-1180.

(37)- Nicholas, T., Mall, S., "Elevated temperature crack growth in aircraft engine materials", in "Advances in Fatigue Lifetime Predictive Techniques", ASTM STP 1122, Eds. M. R. Mitchell, R. W. Landgraff, 1992, pp.143-157.

(38)- Weerasooriya, T., "Effect of frequency on fatigue crack growth rate of IN718 at high temperature", in ASTM, 19th Symposium Fracture Mechanics, ASTM STP 969, Ed. T. A. Cruse, 1988, pp. 907-923.

(39)- Skelton, R.P., "Damage factors during high temperature fatigue crack growth", in "Behaviour of Defects at High Temperatures", ESIS15, Mechanical Engineering Publications, 1993, pp.191-218.

(40)- Skelton, R.P., Byrne, J., "Prediction of frequency effects in high temperature fatigue crack growth using damage factors", Mat. High Temp., 12, 1, 1994, pp. 67-74.
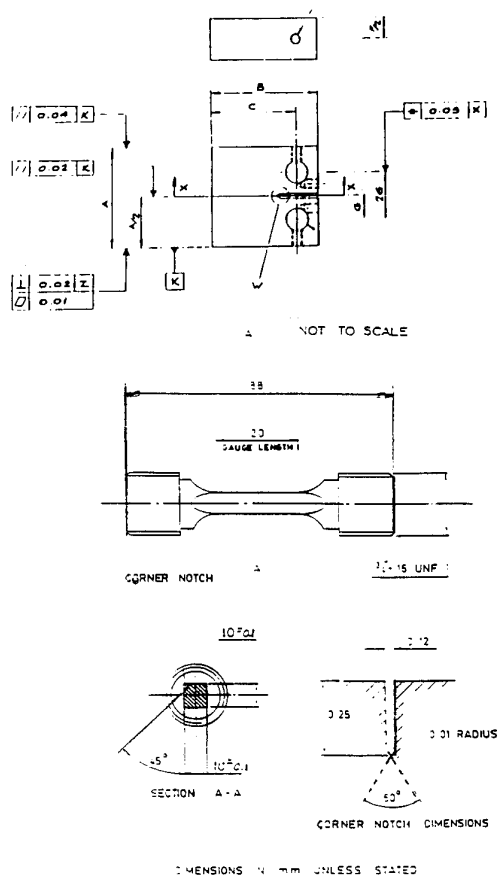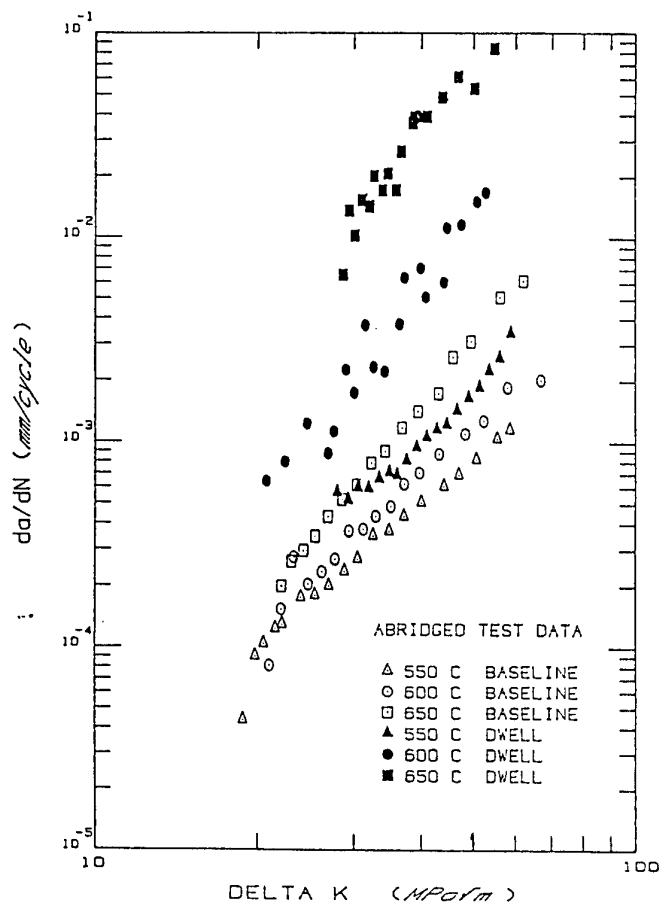
FIG. 1 - CT and CC specimens. IN718

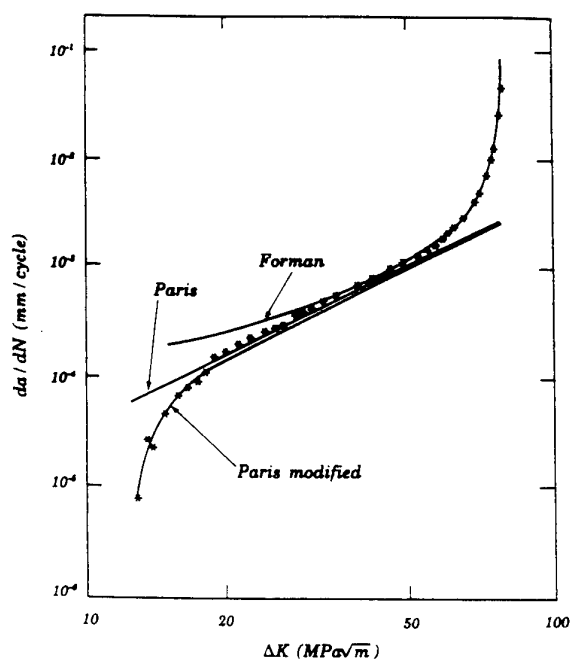FIG. 2 - da/dN against ΔK data. Waspalloy. CC specimens (14).

FIG. 3 - da/dN against ΔK plot. IN718. f = 0.25 Hz. T = 600°C. R = 0.05
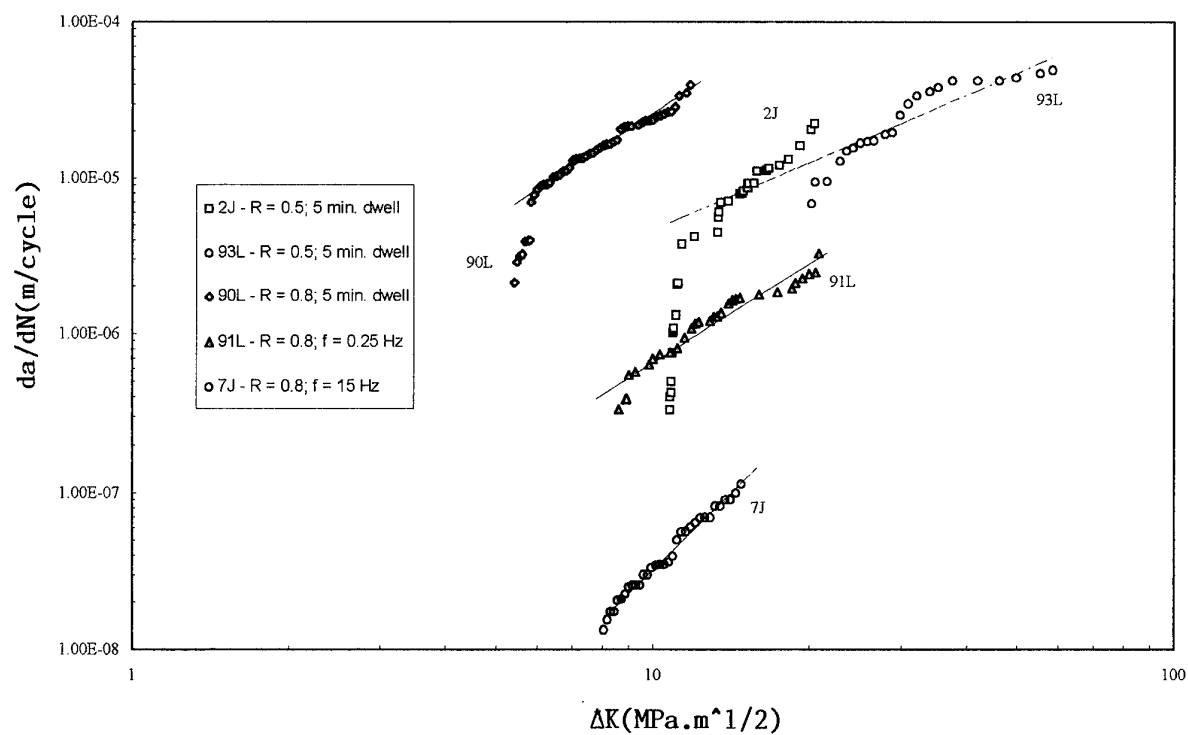
FIG. 4 - da/dN against ΔK data. R = 0.5 and 0.8. T = 600°C. IN718.

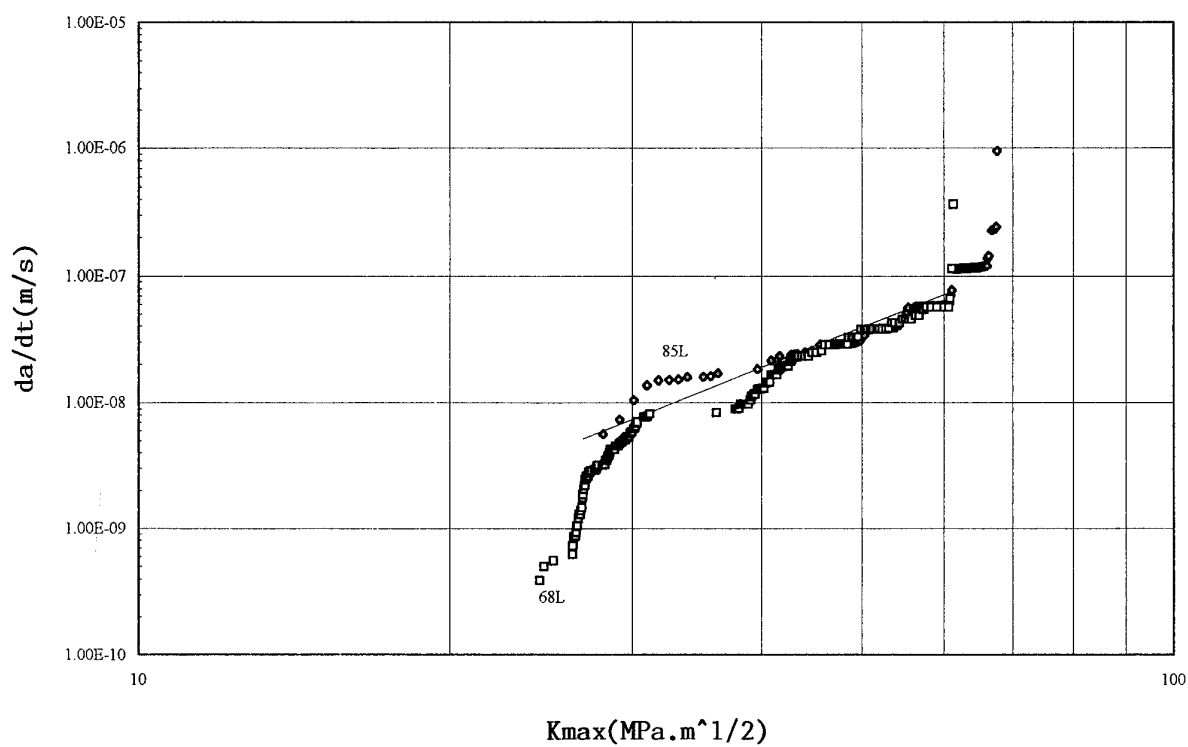

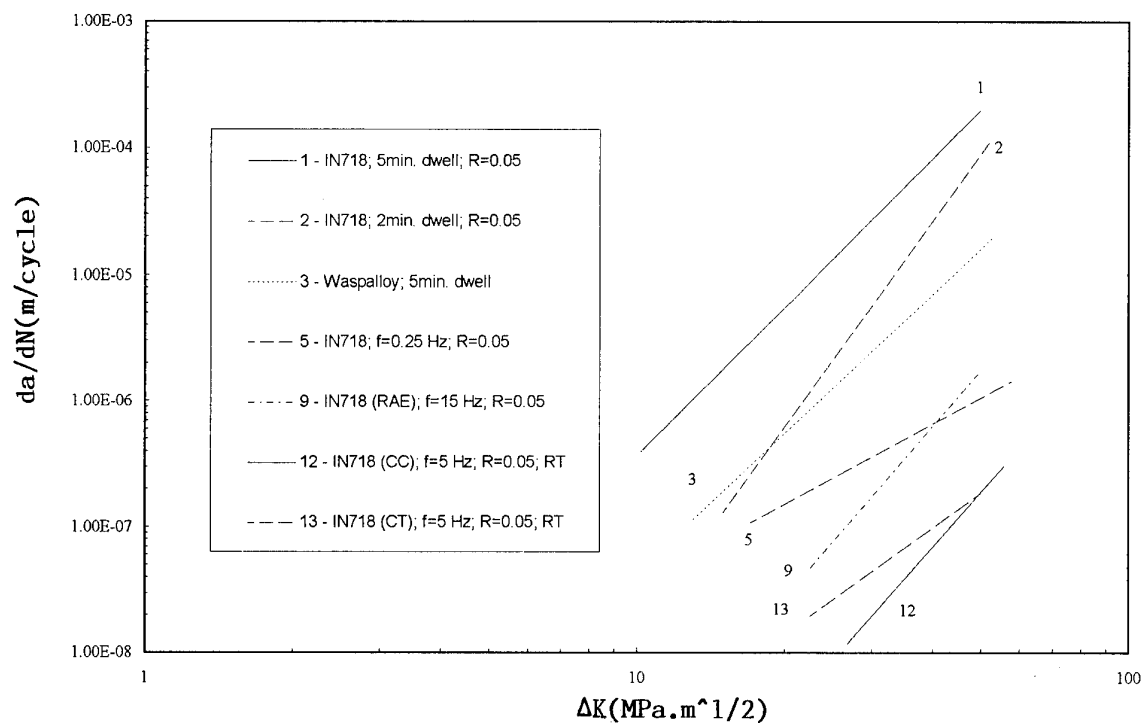FIG. 5 - da/dt against K_{max}. Creep tests. IN718. T = 600°C. CC specimens.

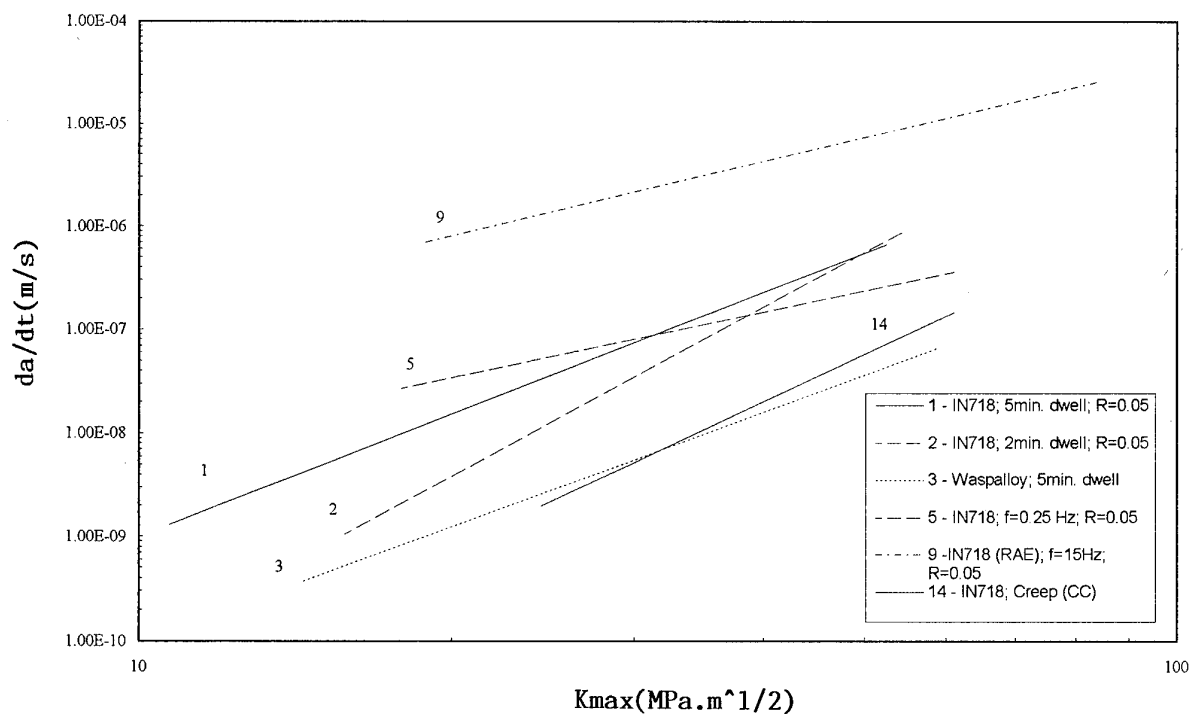FIG. 6 - da/dN against ΔK plots for R = 0.05. T = 600°C. IN718.

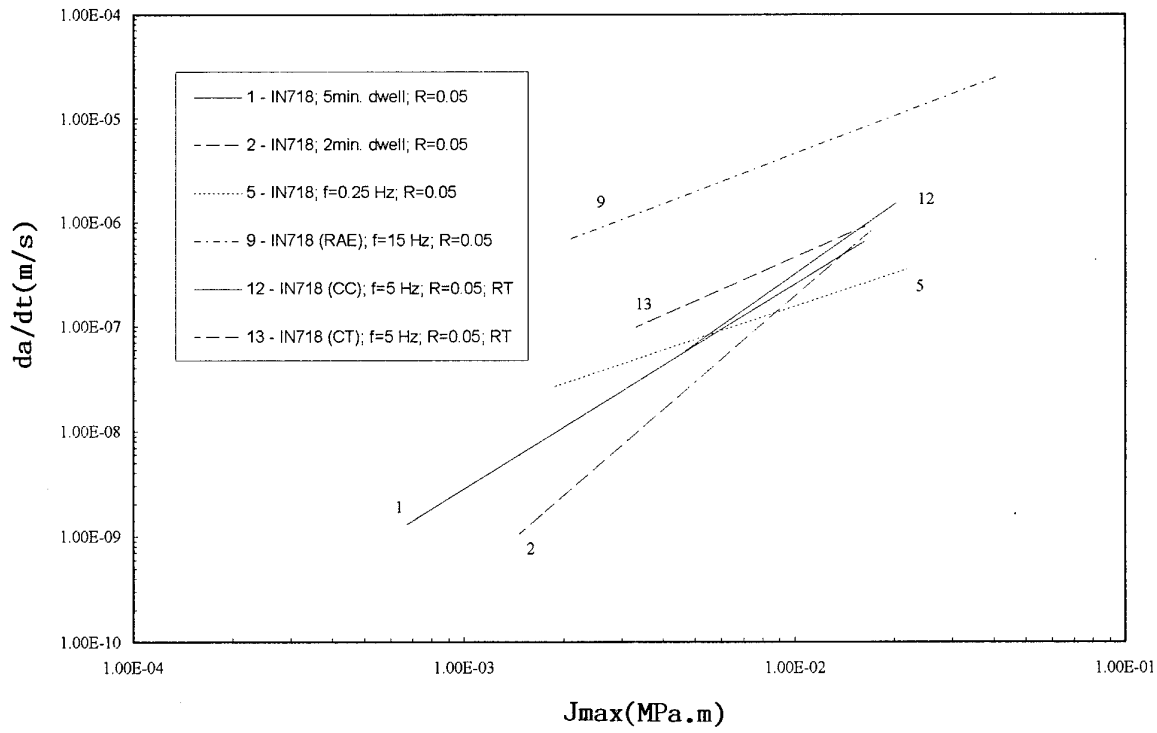FIG. 7 - da/dt against K$_{max}$ plots for R = 0.05. T = 600°C. IN718.

FIG. 8 - da/dt against J_{max} plots for R = 0.05. T = 600°C. IN718

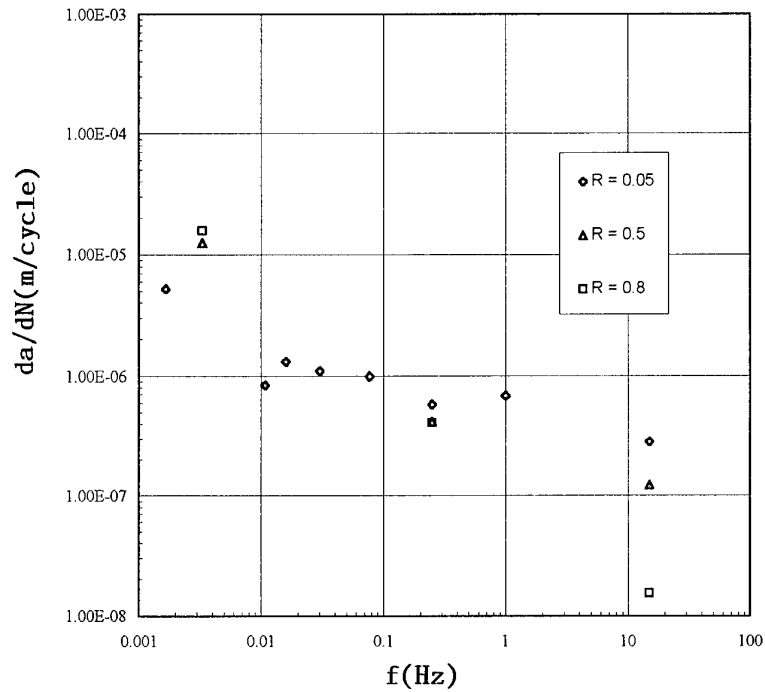FIG. 9 - da/dN against frequency (dwell time) for K_{max} = 40 MPa $\sqrt{m}$.
R = 0.05, 0.5 and 0.8. IN718. T = 600°C.
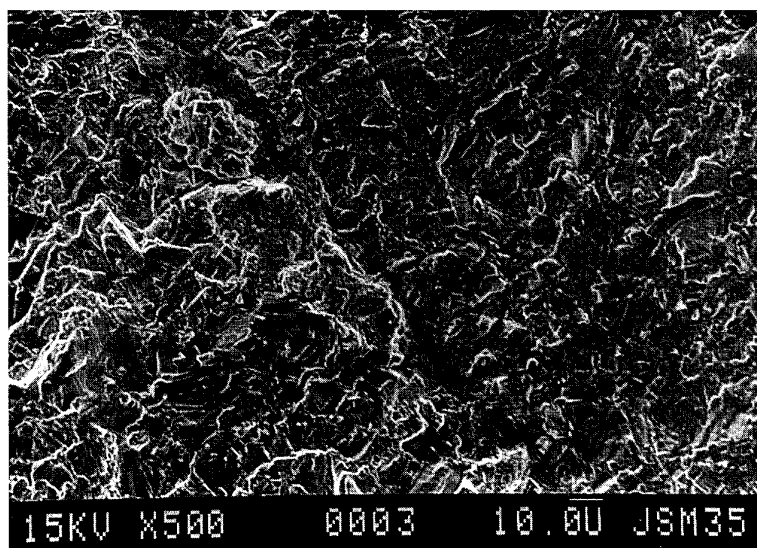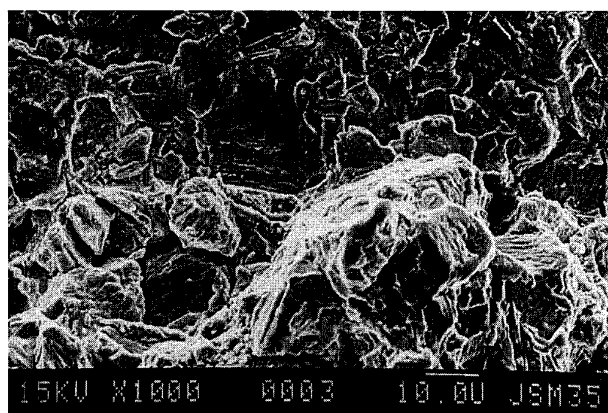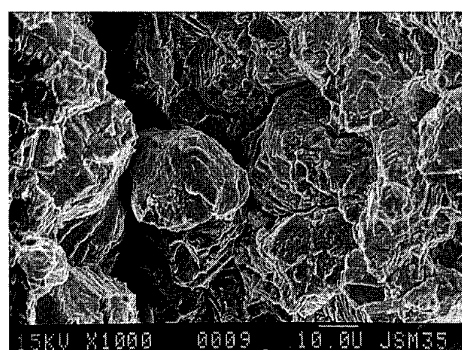
Fig. 10- Transition between the fatigue crack at 10Hz and the fatigue crack with 10s dwell time at maximum load. $\Delta K=25MPa\sqrt{m}$. R=0.05. T=600°C. IN718.
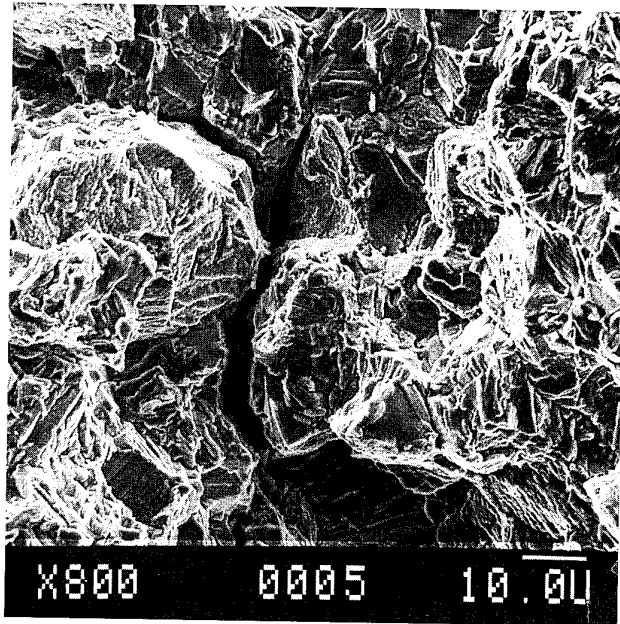

(a)

(b)

Fig. 11a)- Transition between the fatigue crack at 10Hz and the crack with 300s dwell time at maximum load. R=0.5. T=600°C. IN718. $\Delta K40MPa\sqrt{m}$. b) View of the dwell crack only. $\Delta K=60MPa\sqrt{m}$.
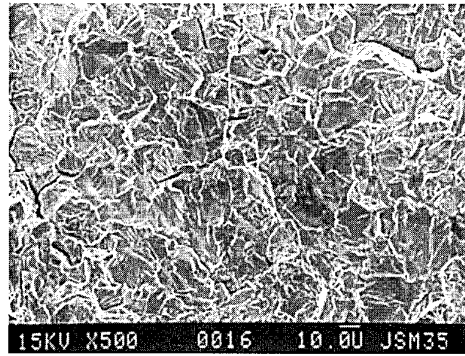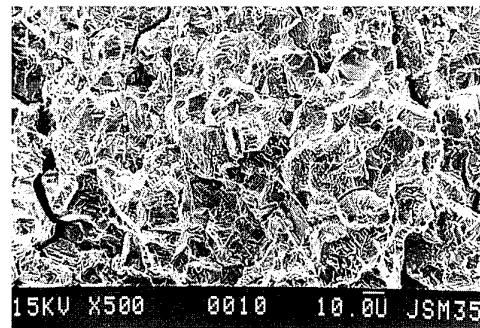
Fig. 12- Fracture surfaces of specimens tested at R=0.8. 600oC. IN718. a) 300s dwell time at maximum load. b) f=0.25Hz (1s dwell time). c) f=10Hz (continuous cycling.)

Fig. 13- a) Sustained loads cracks (creep) at 600°C. IN718. b) Low magnification of intergranular cracking. K_{max}=40MPa$\sqrt{m}$. c) Slip based band formation within a grain (K_{max}=66MPa$\sqrt{m}$).

NON-ISOTHERMAL FATIGUE: METHODS, RESULTS AND INTERPRETATION

C.C. Engler-Pinto, Jr.
M. Blümm
F. Meyer-Olbersleben
B. Ilschner
F. Rézaï-Aria
Laboratory of Mechanical Metallurgy
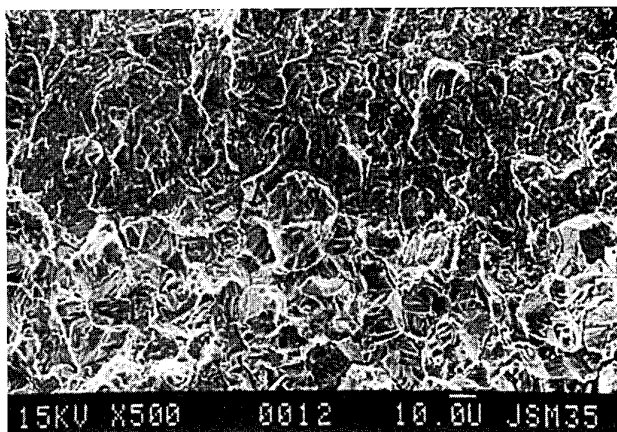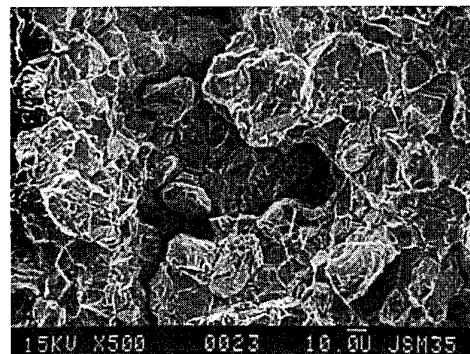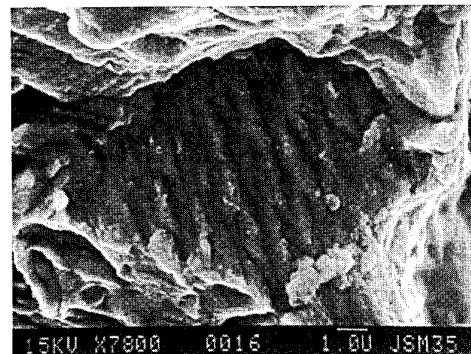Swiss Federal Institute of Technology
CH - 1015 Lausanne

SUMMARY

Non-isothermal fatigue is one of the life limiting factors of the turbine blades in-service. Thermal fatigue (TF) and thermo-mechanical (TMF) fatigue are two basic tests used for non-isothermal assessments of materials. In this investigation both TF and TMF tests are conducted. The mechanical strain at the wedge tip of blade-shaped TF specimens is measured as a function of temperature and applied as the basic TMF cycle. Crack initiation life and total life in TF and TMF are compared for CMSX-6. It is observed that the life under TF experiment is lower than TMF for the test conditions investigated. The effect of the thermal gradient fluctuation on the crack initiation life is reported for CM247LCDS. It is shown that a Miner's cumulative linear law can accommodate the effect of the variation of the thermal gradient on the remaining thermal fatigue life.

NOMENCLATURE

TF	thermal fatigue
TMF	thermo-mechanical fatigue
LCF	low cycle fatigue
DZ	γ'-depleted zone
T_{max}	maximum temperature of thermal cycle
T_{min}	minimum temperature of thermal cycle
ΔT	temperature range ($T_{max} - T_{min}$)
ε_{max}	maximum mechanical strain
ε_{min}	minimum mechanical strain
$\Delta\varepsilon_m$	mechanical strain range ($\varepsilon_{max} - \varepsilon_{min}$)
$\Delta\sigma$	stress range ($\sigma_{max} - \sigma_{min}$)
N_f	total fatigue life; number of cycles to form a 1 mm crack depth
N_i	crack initiation life — number of cycles to form a 0.1 mm crack depth
N_p	crack propagation life ($N_f - N_i$)

1   INTRODUCTION

Turbine blades experience many transient regimes of start-up/shut-down operations in their life. Thermal gradients arising during these regimes produce a complex thermal and mechanical fatigue loading [1] which limit their in-service life by a non-isothermal low cycle fatigue process.

Both thermal fatigue [2] and thermo-mechanical fatigue experiments can be used in the laboratory [3] to simulate the temperature–strain history of a critical element in a blade. The TF blade-shaped and tubular TMF specimens are in general used, Fig. 1.

The stress-strain loops are calculated for blade-shaped TF specimens but they can directly be measured under TMF tests. The results of the calculation depend however upon the constitutive law and boundary conditions considered [4]. The simple in-phase (IP) or out-of-phase (OP) and more complicated cycles such as diamond [5] and non symmetric diamond [6] cycles (the maximum and minimum strains/stresses are attained at intermediate temperatures) are proposed for TMF investigations.

In spite of being two complementary non-isothermal fatigue laboratory tests the TF and TMF results are generally compared solely to the high temperature isothermal LCF results. No systematic comparison or link has been established yet between TF and TMF mainly because of the difficulty in measuring stresses and strains on blades or blade-shaped TF specimens.

In this paper he effect of the thermal gradient on TF-life of CM247LCDS is reported. Two thermal fatigue rigs inducing different
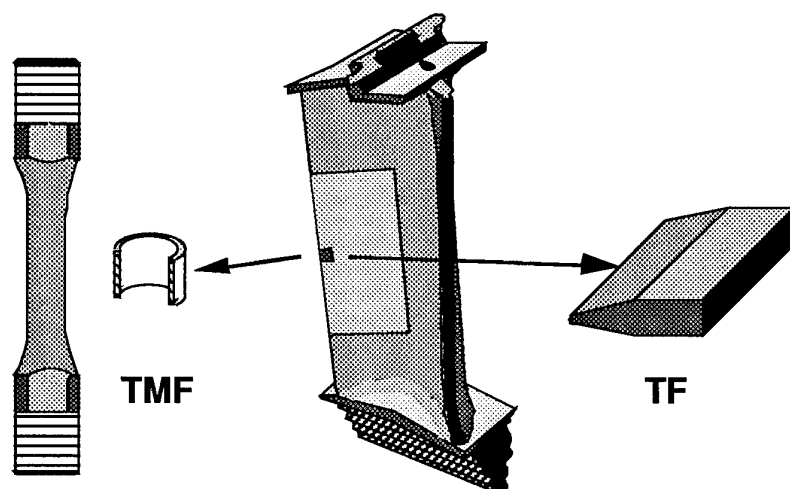
Figure 1: Laboratory thermo-mechanical fatigue and thermal fatigue tests used for non-isothermal fatigue investigations of turbine blades.

thermal gradients are used. On the other hand the results of TMF investigations on CMSX-6 are reported. The basic TMF-cycle is deduced from the *measured* (instead of calculated) TF temperature–strain loops. TF and TMF crack initiation life and total life are evaluated for a maximum temperature of thermal cycle of 1100°C. The TMF results are compared to the ones obtained previously on SRR99 [7].

2 MATERIALS AND EXPERIMENTAL PROCEDURES

Alloys

CMSX-6 and CM247LCDS are respectively a single crystal and a low carbon content directionally solidified nickel based superalloys. Their chemical compositions are given in Table 1. CMSX-6 was received as cast slabs (50*30*7 mm) and solid bars (Ø20*150 mm). CM247LCDS was received as large cast slabs with about 120*114*18 mm dimensions.

TF test procedure and specimen

The TF tests were carried out on blade-shaped single edge wedge specimens, Fig. 2a. They were cut from the cast slabs by electroerosion machining, then ground parallel to the edge and polished (1 μm diamond paste). The [001] crystallographic orientation of each single crystal TF specimen was determined by the Laue method. It was within 6° in the direction of the thin edge for all specimens. For CM247LCDS, the elongated grains were parallel to the edge of the TF specimens.

Two similar thermal fatigue rigs consisting of a high frequency (HF) oscillator for heating and a nozzle for forced air cooling were developed [7-8]. The TF specimens are totally unconstrained during thermal cycling, Figure 3. Two 6.0 kW Hüttinger solid state induction generators working at two different frequencies (200 kHz and 3000 kHz) were employed.

Table 1:   Chemical composition of CMSX-6 in weight %.

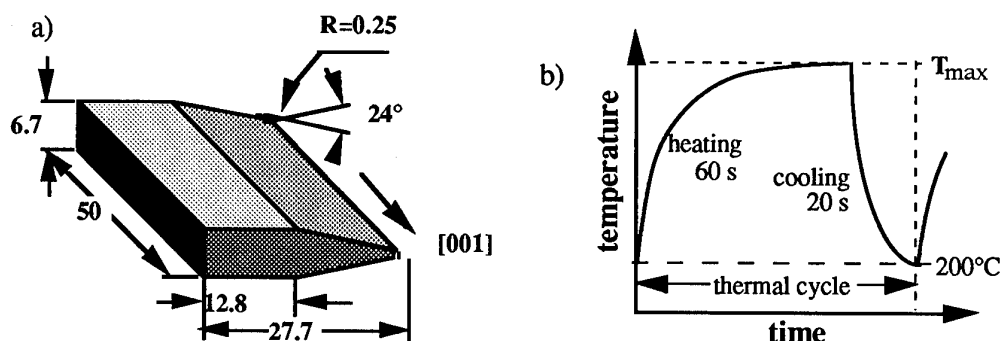| Ni	Co	Cr	Al	Ti	Mo	Ta	Hf	C
Bal.	5.0	9.9	4.8	4.7	3.0	2.1	0.08	0.006
Bal.	9.5	8.1	5.6	0.7	0.5	3.2	1.4	0.07

Figure 2: (a) Thermal fatigue specimen (dimensions in mm), (b) thermal fatigue cycle.

The different skin depths lead to two different thermal gradients without changing the specimen geometry. Therefore, two different temperature-strain histories were generated at the wedge tip of the TF specimens for an identical temperature-time cycle, Fig. 2b. A Chromel-Alumel (type K) thermocouple spot-welded at 0.5 mm from the edge was used to monitor the test. The temperature was controlled by means of a programmable Eurotherm 818P controller.

TF Temperature-strain cycles

As shown in Fig. 3, a special extensometer device with a total freedom of movement in the horizontal plane was set-up using a MTS transducer for measuring the strain during TF tests [7-8]. The strain at the wedge tip was measured as a function of time and temperature over 50 mm and over 20 mm within the central part of the TF specimen [7].
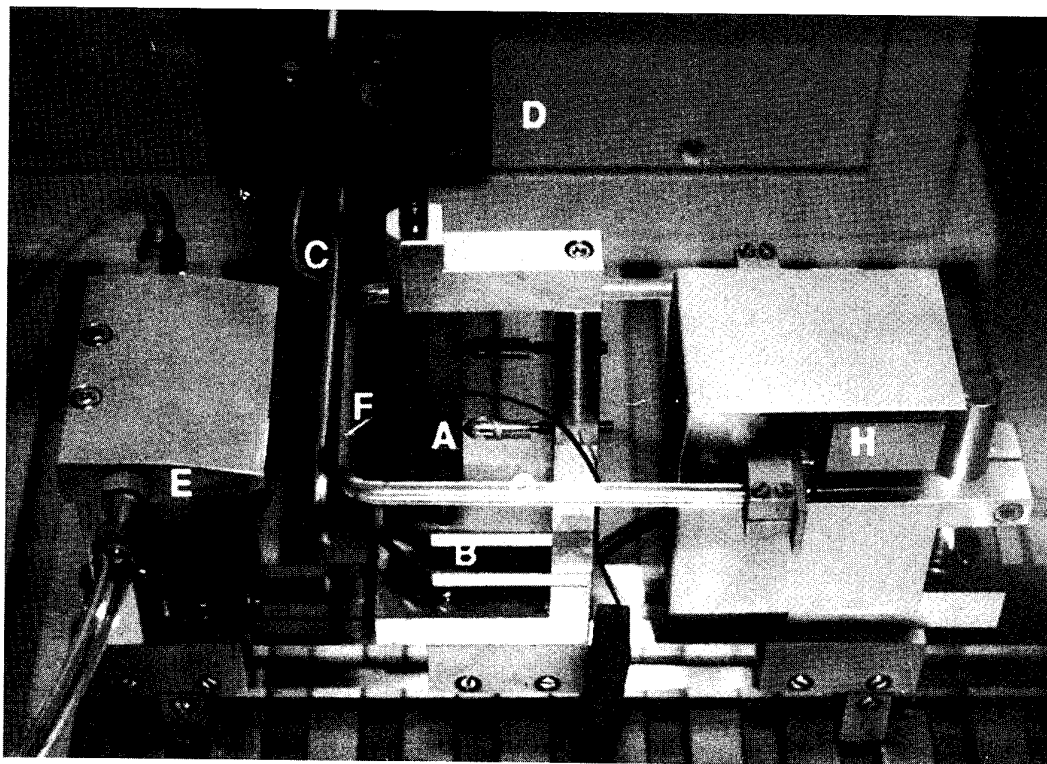

Figure 3: View of the thermal fatigue rig with (A) specimen, (B) specimen support, (C) induction coil, (D) HF-generator, (E) air nozzle, (F) thermocouple and (G, H) extensometer device.

The temperature-strain loops measured on 20 mm for both TF rigs are compared in Fig. 4 (T_{max}=1100°C). The mechanical strain range, $\Delta\varepsilon_m$, is different for each TF rig. The 3000 kHz TF rig with higher thermal gradient induces a wider mechanical temperature-strain loop. The hysteresis loops are thus named "high gradient" or "high strain" for 3000 kHz and "low gradient" or "low strain" cycles for 200 kHz TF rig. The temperature-strain loops have shown that the central part of the wedge tip is subjected to a more damaging TF loading, which confirms the experimental evidences that cracks initiate mostly in the middle region of the TF specimens [9].

TMF specimen and test procedure

The TMF tests were performed on hollow specimens, Fig. 5. The hole was cut by electroerosion and honed. The external surface was turned and mechanically polished along the longitudinal direction (1 μm diamond the longitudinal direction (1 μm diamond paste).

The tests were performed in a conventional closed-loop servo-hydraulic fatigue testing machine MFL (100 kN) specially adapted for TMF tests under total strain control, Fig. 6. The experiments were monitored by a Hewlett-Packard micro-computer (Apollo 715) connected to a Data Acquisition System
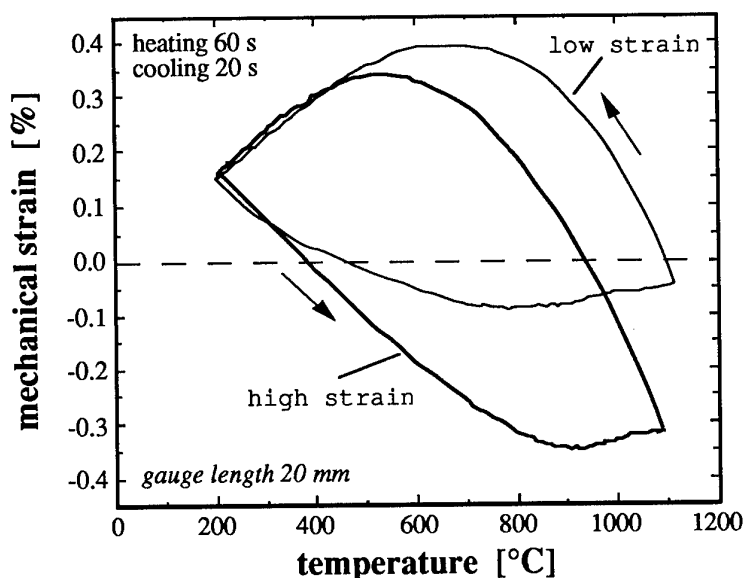

Figure 4: Measured temperature-strain loops of the high strain cycle (3000 kHz) and the low strain cycle (200 kHz).
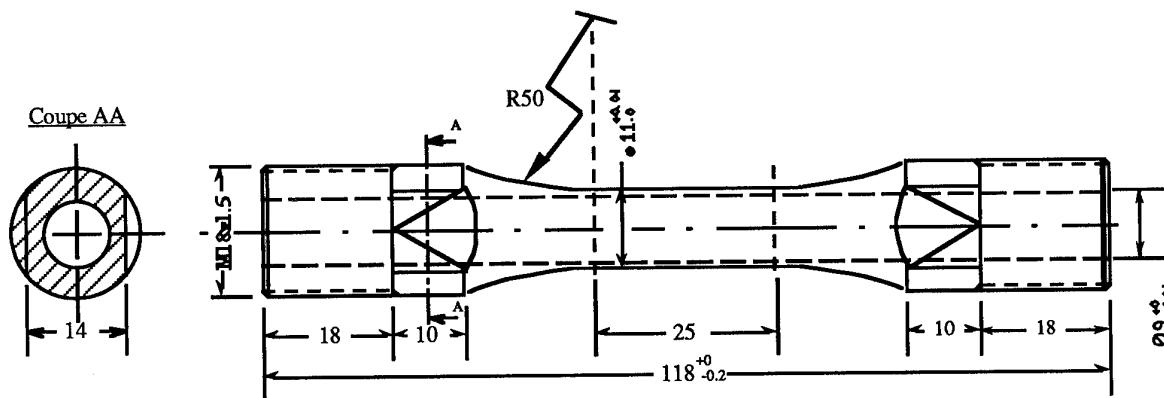

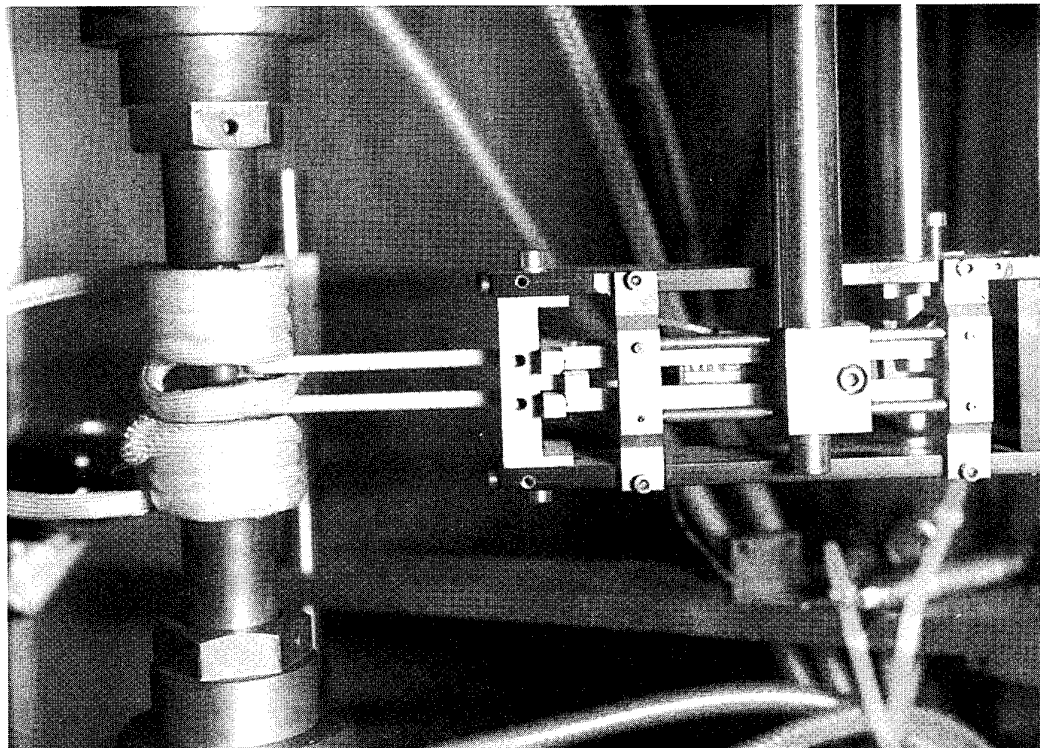Figure 5: Tubular thermo-mechanical specimen (all dimensions in mm).

Figure 6: Thermo-mechanical fatigue test facility.

(HP3852A). The specimens were heated by a HF generator (Hüttinger IG5/200, 6.0 kW, 200 kHz), connected to a Eurotherm 906S closed loop temperature controller and naturally cooled. A software was developed using the Hewlett-Packard VEE-Test environment. A 10°C/s linear heating and cooling rate was used. The thermal gradient through the specimen thickness was less than 10°C. A Maurer QPMR 85-d bi-colour pyrometer monitored the tests. Details of test procedure and schema are given in [10].

3   RESULTS AND DISCUSSIONS

Cumulative TF-life

Blades experience variable thermal gradient during operation. Therefore, a critical element experiences a variable temperature-strain history. At our knowledge the effect of the fluctuation of the thermal gradient on TF-life is not reported in the literature. This was mainly because the change of the thermal gradient was possible only by changing either the temperature-time history of the thin edge of the TF specimens (e.g., T_{max}, T_{min}, heating or cooling periods, etc.) or the specimen geometry. The TF-rigs used in our laboratory permit to incur two different thermal gradients in one specimen geometry under similar temperature-time cycle imposed to the thin edge (i.e., the critical element), Fig. 2b.

The effect of the thermal gradient (i.e., temperature-strain history) on the cumulative TF-life of CM247LCDS was investigated. Figure 7 shows the crack initiation and propagation curves of CM247LCDS under both TF-rigs. TF crack initiation life (0.1 mm crack depth, N_i) was 1950 cycles (mean value) for the high gradient (high strain) TF test and 20000 cycles for low gradient (low strain) test. In a sequential scenario two specimens were first cycled to about 0.25 to 0.3 fraction of the N_i-life under one of the two TF-rigs (500 cycles for high strain and 6600 cycles for low strain tests) and then experiments were continued on the other TF-rig till the initiation of a crack.

Figure 8 shows that a Miner's linear damage law can accommodate the cumulative TF-life under variation of the thermal gradient (i.e., temperature-strain history) when the same temperature-time history is applied to the thin edge of the TF-specimens.
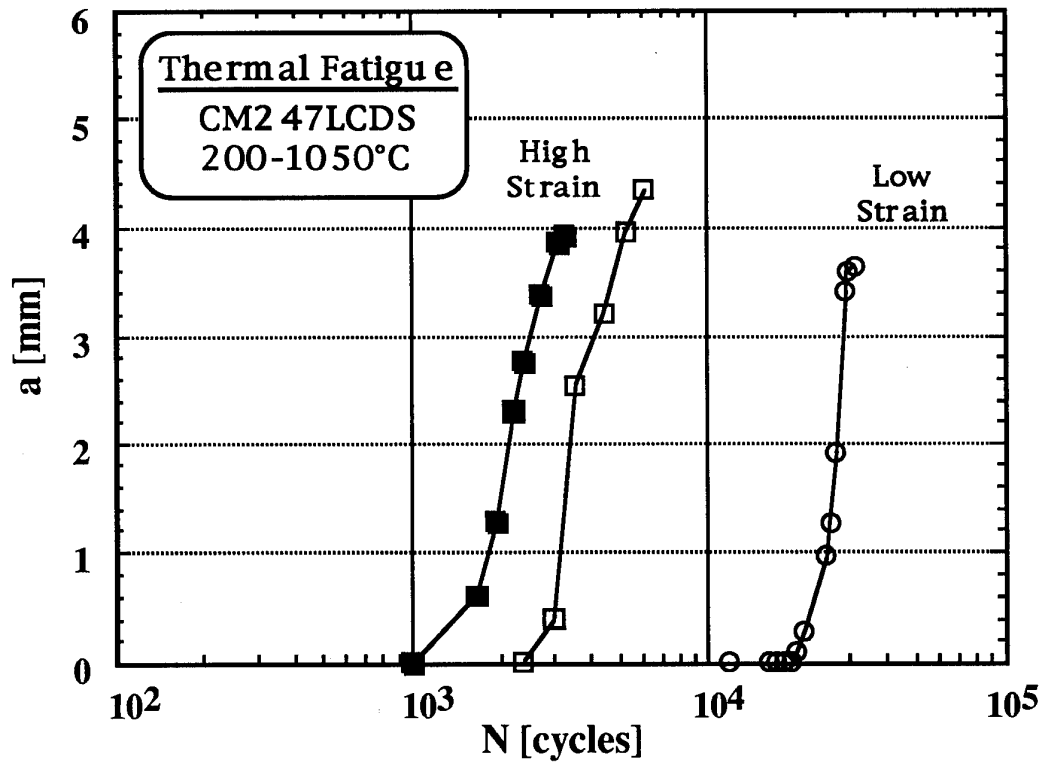
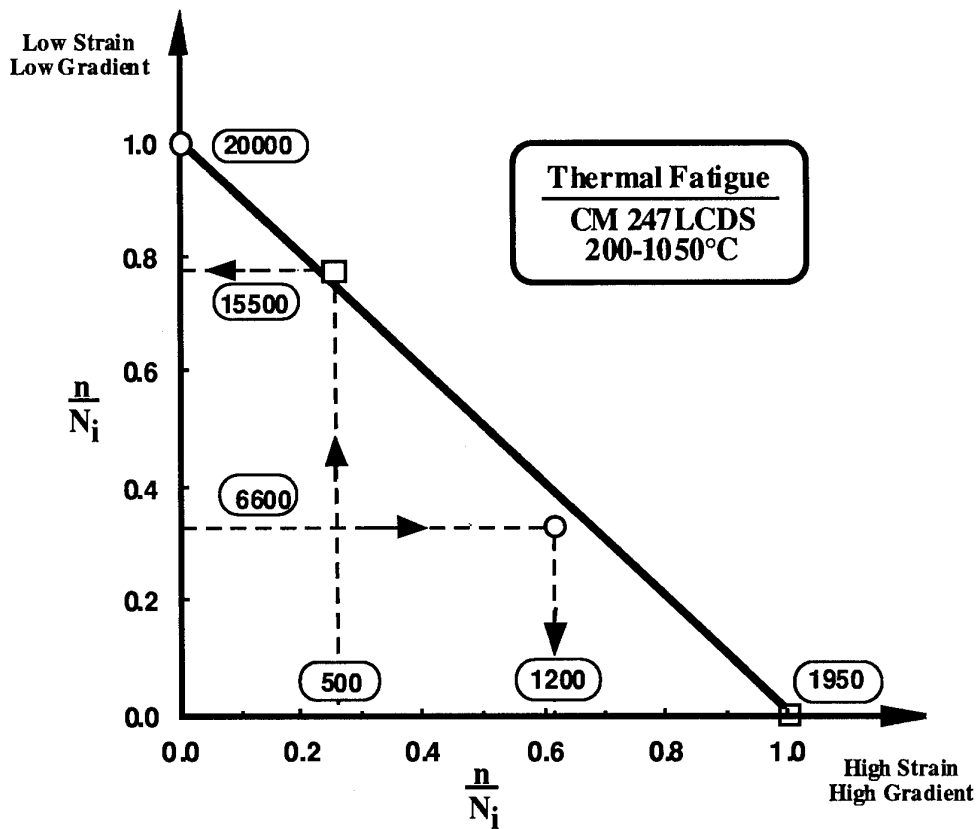Figure 7: Thermal fatigue cracking two TF-rigs.

Figure 8: The effect of the fluctuation of the thermal gradient on the remaining TF crack initiation life.

This sequential testing can reproduce the cumulative damage of the trailing edge of a cooled blade for example which experiences constant inlet gas temperature but its internal temperature changes. Other sequential tests are under progress to assess the effect of the change of the T_{max} on the TF crack initiation life.

The crack initiation was intergranular under both test conditions and did not change by the sequential TF testing.

Comparison between TF and TMF

To compare the life of CMSX-6 under TF and TMF, the same T_{max} of 1100°C was chosen. While T_{min} was 200°C in TF, it was raised to 600°C on TMF tests because the total period of a TMF cycle 200°↔1100°C without forced cooling is too long. Therefore, the TF temperature-strain cycle was truncated and simplified for TMF as illustrated in Fig. 9.

The total fatigue life (N_f) was defined as the number of cycles to form a 1 mm crack depth, which corresponds to the TMF
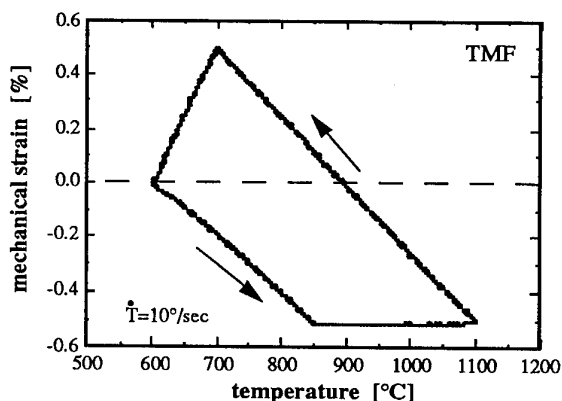
Figure 9: TMF temperature-strain cycle based on TF measurements.

specimen wall thickness. The crack initiation life, N_i, was defined as the number of cycles required to form a 0.1 mm crack depth. The replica method was used to determine the crack initiation and propagation in TMF [10], while in TF the microscopic measurements were made directly on the specimens.

The TF and TMF lives of CMSX-6 are compared to SRR99 tested under similar conditions [11] in Figs. 10a–d. The stress range presented in Figs. 10b and 10d for

the TF tests were obtained from the TMF experiments ran between 200°↔1100°C using non truncated measured TF temperature-strain cycle. It can be seen that, for the test conditions investigated, TF loading results in a shorter life for both life criteria. Further TMF experiments should however be performed at lower strain ranges.

During TF and TMF testing of CMSX-6 the oxide-scale spalling was observed, in particular at the wedge tip of the TF specimens under "low strain" loading (the specimen is exposed to a higher number of thermal cycles). The resistance of the oxide-scale to spalling in CMSX-6 is lower than in SRR99 [7-9], leading to a significantly lower TF and TMF resistance for lower values of $\Delta\varepsilon_m$. In fact, when $\Delta\varepsilon_m$ is low and the life is longer, the oxidation damage plays an important role in the overall fatigue damage.

As shown in the life cycle curves (Fig. 10), a large part of the total fatigue life is consumed in crack initiation (about 50–70%). For both TF and TMF tests, it was observed that more cracks initiated in CMSX-6 than in SRR99. The observation of the replicas has revealed that, under TMF cycling, cracks initiate on sub-surface oxidised microporos.

The microstructure of the nickel based superalloys consists of a nickel-rich fcc γ-phase strengthened by a large volume fraction of γ'-phase. During isothermal and non-isothermal fatigue and before crack initiation, an oxide-scale and its corresponding γ'-depleted zone are created. In addition the γ-γ' microstructure changes under both TF or TMF loading.

The micro-mechanical behaviour and resistance of this "composite-like" layer, which is in fact a "sub-surface process zone", determines the fatigue life of the alloy [12]. The overall resistance of this composite layer depends on the resistance of the oxide-scale, of the DZ, of the interface between the oxide scale and DZ (adherence resistance) and the resistance of the altered γ-γ' microstructure.

The stress concentration ahead of a sub-surface pores combined with the loss of resistance of the DZ and with the fragility of the oxide scale constitute the predominant mechanism of crack initiation for the conditions investigated.
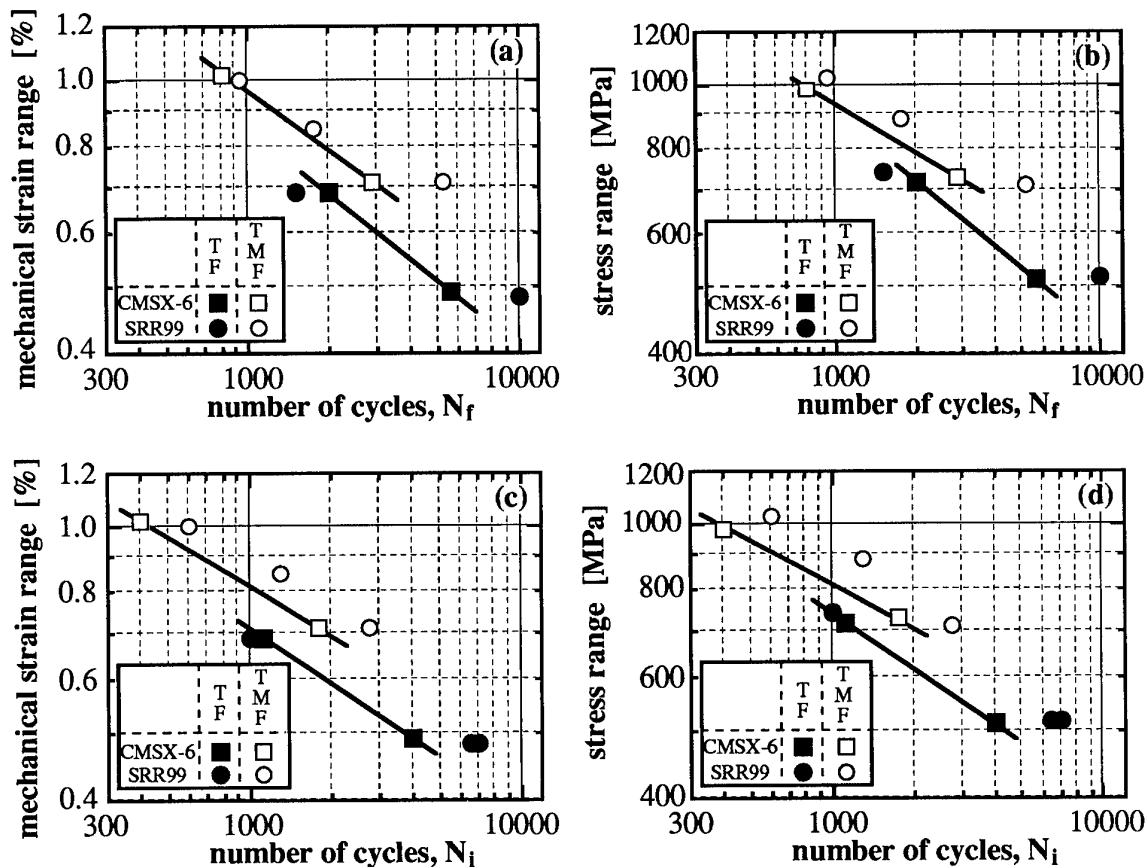
Figure 10: Total life of TF and TMF as a function of: (a) strain range and (b) stress range; and crack initiation life of TF and TMF as a function of (c) strain range and (d) stress range.

To rationalise the difference observed between the TF and the TMF live, three important aspects are considered and summarised below:

- First, the strain rates during the thermal shocks in TF are much higher than the maximum TMF strain rate.

- Second, the geometry of the specimens is different: the TF specimen wedge tip radius (0.25 mm) is much smaller than the external radius of TMF specimens (5.5 mm). Therefore, the wedge tip is more sensitive to the notch effect of a cast microporosity, what means that a higher stress intensity factor is expected in a TF specimen.

- Third, the temperature ranges are different: 900°C for the TF-cycle and 500°C for the TMF cycle. Given the "composite" nature of the microstructure near the surface, the mismatch of thermal expansion between the oxide, γ'-depleted zone and the alterated base material will enhance the interfacial stress experienced. As this effect increases with increasing ΔT, TF tests tend to be more damaging.

4   SUMMARY

The thermal fatigue and thermo-mechanical fatigue behaviour of CMSX-6 was investigated. The strain was measured at the wedge tip of TF specimens and used as a new TMF cycle. Both strain and stress range versus life curves show that under test condition reported the TF-life is shorter than TMF life. Thermal fatigue investigations on CM247LCDS have revealed that the effect of the variation of thermal gradient (i.e., temperature-strain history) on the remaining life of a blade-shaped specimen can be accommodated by a Miner's cumulative linear law.

5   ACKNOWLEDGEMENTS

6   REFERENCES

1.   Coney M.H., "Thermal Fatigue Cycling in Turbine Blades", High Temperature Technology, Vol. 8, No. 2, 1990, pp. 115-120.

2.   Glenny E., "The Influence of Specimen Geometry on Thermal Fatigue Behaviour", *in* "Thermal and High Strain Fatigue", The Institute of Metals, London, 1967, pp. 346-363.

3.   Hopkins S.W., "Low-Cycle Thermal Mechanical Fatigue Testing", *in* "Thermal Fatigue of Materials and Components", ASTM STP 612, D.A. Spera and D.F. Mowbray, Eds., American Society for Testing and Materials, 1976, pp. 157-169.

4.   Mallet O., Kaguchi H., Ilschner B., Meyer-Olbersleben F., Nikbin K., Rézaï-Aria F. and Webster G.A., "Influence of Thermal Boundary Conditions on Stress-Strain Distribution Generated in Blade-Shaped Samples", Int. Fatigue Vol. 17, N° 2, 1995, pp. 129-134.

5.   Kraft S., Zauter R. and Mughrabi H., "Aspects of High-Temperature Low Cycle Thermomechanical Fatigue of a Single Crystal Nickel-Base Superalloy", Fatigue Fract. Engng. Mater. Struct., Vol. 16, No. 2, 1993, pp. 237-253.

6.   Malpertu J.L. and Rémy L., "Influence of Test Parameters on the Thermal-Mechanical Fatigue Behaviour of a Superalloy", Metallurgical Transactions A, Vol. 21A, 1990, pp. 389–399.

7.   Meyer-Olbersleben F., Engler-Pinto Jr. C.C. and Rézaï-Aria F., "On Thermal Fatigue of Nickel-Based Superalloys", To be published *in* "Thermo-Mechanical Fatigue Behavior of Materials: 2nd Volume", ASTM STP 1263, Michael J. Verrilli and Michael G. Castelli, Eds., American Society for Testing and Materials, Philadelphia, 1994.

8.   Meyer-Olbersleben F., Goldschmidt D. and Rézaï-Aria F., "Investigation of the thermal fatigue behaviour of single-crystal nickel-based superalloys SRR99 and CMSX-4," *in* "Seventh International Symposium on Superalloys, 92", TMS, Seven Springs Mountain Resort, Champion, Pennsylvania, 1992, pp. 785-794.

9   Meyer-Olbersleben F. "Thermische Ermüdung einkristalliner Nickelbasis-Legierungen", Dissertation thesis No. 1255, Swiss Federal Institute of Technology, Lausanne, 1994.

10.   Engler-Pinto Jr. C.C., Härkegård G., Ilschner B., Nazmy M.Y., Noseda C., Rézaï-Aria F., "Thermo-mechanical Fatigue Behaviour of IN738LC", *in* "Materials for Advanced Power Engineering 1994", Kluwer Academic Publishers, Part I, 1994, pp. 853-862.

11.   Engler-Pinto Jr. C.C., Meyer-Olbersleben F. and Rézaï-Aria F., "Thermo-Mechanical Fatigue Behaviour of SRR99", To be published *in* "International Symposium on: Fatigue under Thermal and Mechanical Loading-Mechanisms, Mechanics and Modelling", Petten, The Netherlands, 1995, May 22-24.

12.   Meyer-Olbersleben F., Goldschmidt D. and Rézaï-Aria F., "The Relationship Between Oxidation Driven γ'-Depletion Zone and Thermal Fatigue Crack Initiation Life of SRR99", *in* "International Conference on Corrosion-Deformation Interactions CDI'92", Editions de physique, Les Ulis, Fontainebleau, 1992, pp. 543-551.

THERMAL FATIGUE, A USEFUL TOOL TO ASSESS LOW CYCLE FATIGUE DAMAGE IN SUPERALLOYS FOR COMPONENTS EXPERIENCING THERMAL TRANSIENTS

A. Köster, E. Chataigner and L. Rémy,
Centre des Matériaux, Ecole des Mines de Paris,
URA CNRS 866, B.P. 87,
91003 EVRY Cedex, France

SUMMARY

A thermal fatigue facility using a lamp furnace is described. This test is intended to simulate thermal shocks on a simple structure, and is shown to be a useful tool to investigate the damage evolution in superalloys exposed to temperature transients up to 1100°C. This is illustrated by the study of two nickel-based superalloys : a wrought superalloy used for rocket engine, and a single-crystal superalloy (AM1) used for jet engine blades.

The effect of the specimen geometry and of a coating on fatigue life and failure mechanisms are described. Comparisons with thermal-mechanical fatigue results show the necessity of thermal fatigue tests for studying high temperature materials.

A heat transfer analysis and a stress analysis are made for two geometries of wedge type specimens. The temperature history of the thin edge as well as the stress-strain hysteresis loops are so computed. These computations are used for lifetime prediction. In the case of the wrought superalloy, TF experiments are found in good agreement with lifetime predictions and TMF test results.

1. INTRODUCTION

Thermal-Mechanical Fatigue (TMF) was considerably developed over the last ten years due to the decrease in cost and the increase in performances of microcomputers [1]. A TMF facility basically requires a LCF fatigue machine with high temperature equipment, a microcomputer and appropriate software and instrumentation. Thus it remains an expensive testing facility and conducting experiments requires a lot of care and experience. One of the major benefits of this testing technique is to get stress-strain loops under anisothermal conditions besides life to crack initiation. However this requires to keep volume element conditions and in particular to minimise temperature gradients in specimen cross-section. In superalloys this can be achieved only using a moderate temperature rate about 5°C/s (at most 10°C/s) even when using hollow specimens.

Most facilities use only natural cooling and when one studies gas turbine components, this is only appropriate for hot cycles. Cold cycles which are the more severe require most often forced cooling.

Thermal Fatigue (TF) testing was not very much investigated over recent years though it is basically complementary of the TMF test. This test uses a simple structure (such as a wedge) and obviously shows the advantages and drawbacks of component-like tests. This test simulates more closely the behaviour of a real

component and has almost no limitation on temperature rate (within the capabilities of heating/cooling systems). Such a TF facility was developed in our laboratory designing a lamp furnace with six 1500W-light bulbs and a cooling system with forced air at 8 bar. Wedge specimens were used as in previous studies on the SNECMA rig (with flame heating) [2] or by other groups using fluidized bed facilities [3].

Application of this facility is shown in two cases : for a wrought nickel base superalloy used for rocket engine blades using a temperature cycle between 30°C and 750°C, and for a coated nickel base single crystal superalloy used for jet engine blades using a temperature cycle between 30°C and 1100°C.

2. THERMAL FATIGUE TESTS

2.1 Test materials

The bulk of the experimental work was carried out with two nickel-based superalloys.

The first one is a wrought nickel base superalloy used for rocket engine blades. Specimens (described in next section) were cut by electro-discharge machining from a solid bar (Ø80 mm). This polycrystal superalloy was fully heat treated to obtain two sizes of γ'-precipitates, the largest being 200 nm.

The second one is the single crystal nickel-based superalloy AM1 used by SNECMA for jet engine advanced blades. The chemical composition of AM1 is given in the table 1. This single crystal was received as cast solid plates in the fully heat treated condition with cubic γ'-precipitates of about 450 nm edge length. Some specimens were studied in a coated condition which consists in a chromising and aluminising treatment followed by a heat treatment to give the same distribution of γ'-precipitates as in uncoated AM1.

Table 1 : Chemical composition of AM1 in weight %.

Ni	Ta	Cr	Co	W	Al	Mo	Ti
63.4	8.3	7.6	6.4	5.4	5.5	2.1	1.3

2.2 Test specimen design

The TF tests are carried out on single-edge wedge specimens with an edge radius of 0.25 mm and a maximal thickness of 6.7 mm.

For the wrought superalloy, two geometries were tested as shown in figure 1 : the one with a total width of 27.6 mm (FT-S) is a standard single-edge wedge specimen [3] and the other is 50 mm wide (FT-L). The larger geometry was employed to increase the thermal gradient during TF testing, and consequently to reduce the lifetime of specimen by increasing stresses and strains.

Only FT-S specimens were used for the study on coated and uncoated AM1, and the specimens were machined such that the angle between the low-modulus <001> direction and the longitudinal axis is less than 5°.
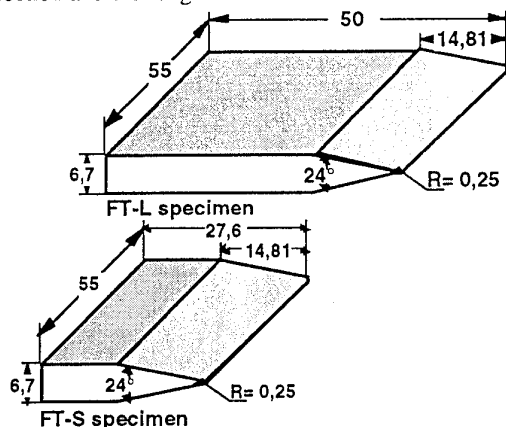

Figure 1 : Geometry of Thermal Fatigue specimens.

The edge area of specimens was mechanically polished parallel to their longitudinal axis using diamond paste down to 3 μm to facilitate metallographic observations.

2.3 Thermal fatigue facility

The TF test consists of alternately heating and cooling the leading edge of specimen. While thermal cycling, the specimen is totally free to expand or to contract so that only mechanical strains resulting from the thermal gradients are seen by the specimen.

Closed-loop temperature cycling is achieved using a thermocouple spot welded at the mid point of the leading edge at 1.5 mm from the radius. The temperature cycle is obtained by programming a temperature controller which lets the user define T_{max}, T_{min}, the temperature rate, the number of cycles.

The thermal fatigue rig we used for these studies was specially designed for single-edge wedge specimens.

Heating is provided by a radiation furnace with six 1500-W light bulbs (figure 2). It has no thermal inertia. The specimen leading edge is placed in the centre of the furnace on an adjustable holder that kept the tested structure in position without mechanical loading. The furnace was designed to focus lamp radiation on a small area of about 6 mm in diameter, to maximise the thermal gradient in the specimen .
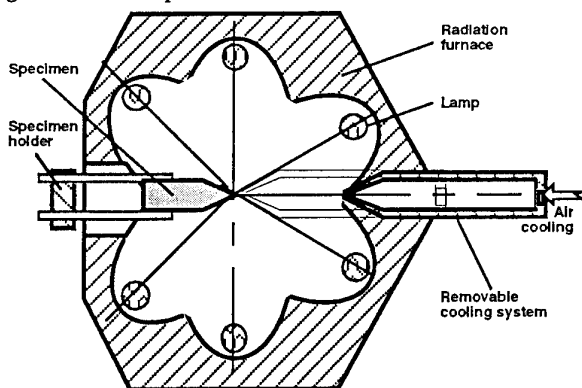

Figure 2 : Schematic drawing of the thermal fatigue rig used in testing the wedge-shaped specimens.

The cooling system consists of a removable nozzle which moves during the thermal cycle. When the furnace is heating, the nozzle is in a backward position, and when the cooling sequence begins, a pneumatic actuator moves the cooling system near to the specimen (at about 3 mm). The cooling was ensured by forced blowing of cold air at 8 bar on the specimen leading edge.

2.4 Thermal fatigue testing techniques

In evaluating the relative merit of each materials, it is therefore important to simulate the service conditions as closely as possible.

For the wrought superalloy used for aerospace turbine blades, a thermal cycle was defined between 30°C and 750°C (fig 3) in agreement with finite element analysis. This aerospace thermal cycle is composed of heating stage at a maximum temperature of 750°C during 60 s following by a cooling sequence down to 30°C at 30 s.

AM1 single crystals were cycled using an aeronautical thermal cycle between 30°C and 1100°C which corresponds to the thermal loading of jet engine blades. The thermal cycle was composed by a 60 s heating sequence and a cooling sequence fixed at 20 s as shown in figure 3.
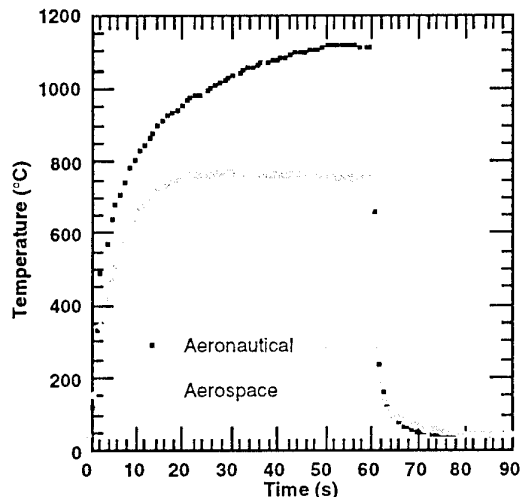
Figure 3 : Temperature of the thin edge cycle of TF specimens.

Tests were regularly interrupted and specimens were examined by scanning electron and optical microscopy to investigate the crack initiation and propagation mechanisms.

The criterion of crack initiation was taken as the first appearance of a 0.2 mm crack length at the leading edge of the specimen.

3. EFFECT OF THE SPECIMEN SIZE

An increase in the size of a particular shape increases the transient temperature gradients and is therefore likely to decrease the endurance.

Thermal-fatigue tests were carried out on the wrought nickel based superalloy specimens using the aerospace cycle. The results of these tests, reported in figure 4, show that the endurance progressively decreases with the increase of the specimen width.

The crack initiation life is 2.5 times shorter for the FT-L

specimen than for the FT-S specimen. Lives for initiation are 800 cycles and 2100 cycles respectively, using the criterion for initiation previously described. The crack growth rate quickly increases for the FT-L specimen, and is always higher than that of FT-S specimen. The crack growth rate for FT-S decreases when the crack has reached a length of 3 mm whilst it is constant for FT-L from 0.4 to 4 mm. It is likely that the propagation rate for this specimen geometry should decrease after 5 mm crack length due to the mechanical loading conditions.

Crack length a (mm)

Figure 4 : Evolution of the longest crack (a) vs. cycles under thermal fatigue between 25°C and 750°C.

Metallographic examination was carried out on each specimen tested. The nature of the thermal-fatigue failures was found to be indepe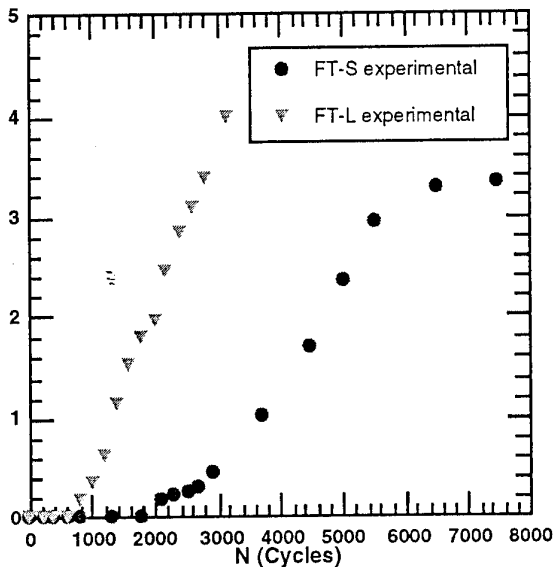ndent of the size of the specimen. Failure of the FT-S specimen was characterised by many intergranular cracks originating at the leading edge. On FT-L specimen, only a few cracks (3) are observed which are intergranular too. The observation of fracture surfaces has revealed that all cracks initiated from grain boundaries at the wedge tip of the TF specimens (figure 4 a).
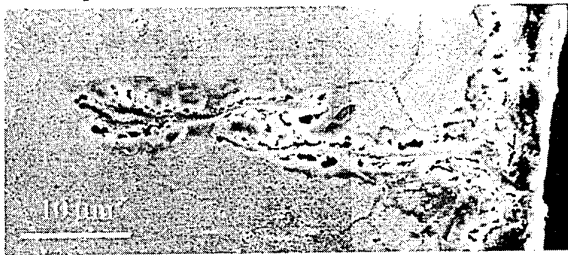
Figure 4 a : Thermal-fatigue crack in transversal section of FT-S wrought superalloy specimen.

All cracks are oriented perpendicular to the principal loading direction and the crack front is semi-circular (figure 4 b). The crack propagation is mainly intergranular for both geometries, but transgranular propagation was observed for FT-S after 2.5 mm of crack length that corresponds to the decrease in crack propagation rate.
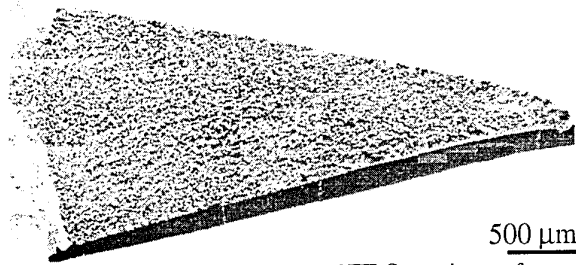
Figure 4 b : Fracture surface of FT-S specimen after 7500 cycles of thermal-fatigue.

4. EFFECT OF COATING UNDER TF LOADING
4.1 Crack initiation
The crack initiation in coated [001] AM1 specimens should be described as follows:
- first, failure occurred in the coating layer. A number of randomly dispersed transgranular cracks were observed in the coating layer, initiating at the surface of the thin edge (figure 5 a) perpendicular to the longitudinal axis.
- then, these micro-cracks (10 μm thick) were grown from the surface through the thickness. The cracks have a « horseshoe » shape after coating cracking and became semi-elliptical when the crack front advances.
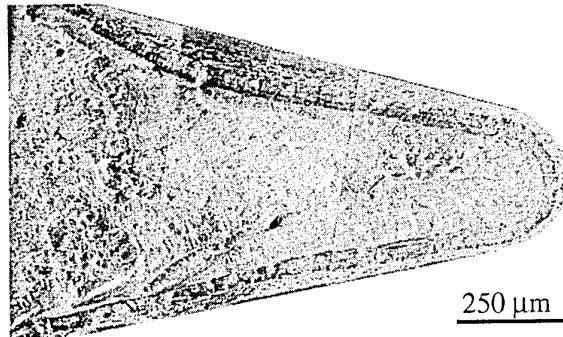
Figure 5 a : SEM observation of major crack in a coated [001] specimen under TF ($N_i = 245$, $N_t = 3100$).

All the cracks in bare AM1 initiate at a large casting micropore at the surface or in the subsurface area of TF specimen thin edge, near the leading edge as shown in figure 5 b.
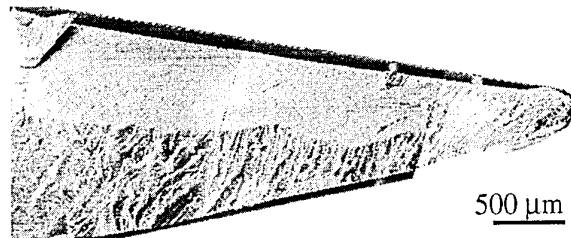
Figure 5 b : SEM observation of major crack in a [001] specimen under TF ($N_i = 800$, $N_t = 1959$).

4.2 Crack growth
Figure 6 shows the evolution of the longest cracks for bare and coated TF specimens.
The comparison between the aluminised and the bare single crystal superalloy shows a detrimental influence of the coating on the TF life to crack initiation.

Crack length a (mm)
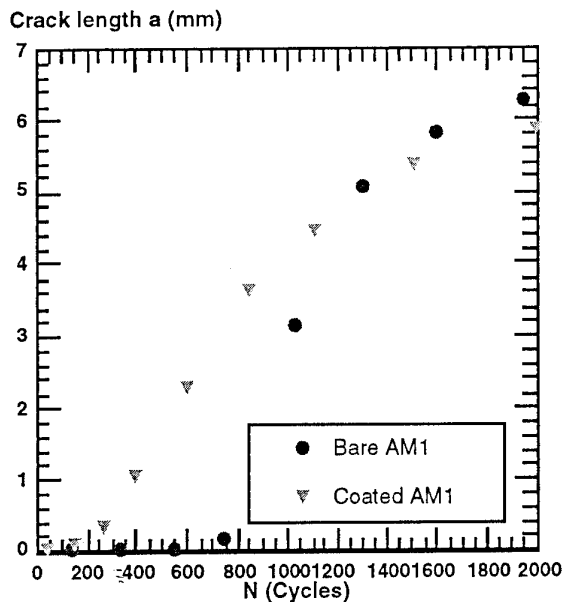
Figure 6 : Evolution of the longest crack depth (a) vs. number of cycles in bare and coated AM1 specimens.

In coated AM1, cracks were observed after a few thermal cycles (<<150) when in bare specimens, cracks initiate around 650 cycles. For a crack initiation criterion at 0.25 mm, the lifetime of coated specimen was more than 3 times shorter than the bare one in spite of a crack propagation rate for the coated single crystal always lower than the one of bare superalloy. A decrease of the crack growth rate was observed for both specimens when cracks have a length of about 4 mm due to decreasing of the mechanical loading conditions far from the leading edge.

5. THERMAL AND MECHANICAL ANALYSIS

Usually, TF is used to compare the thermal cycling endurance of different materials under various test conditions. To estimate the temperature-stress-strain history of critical elements and test lifetime predictions, a thermal and mechanical analysis is necessary like in a component. However in most cases only temperature can be measured though in recent work [9] the total strain was measured directly at the thin edge of TF structures.

5.1 Thermal analysis

In order to perform a heat transfer analysis, several thermocouples (K type) were spot-welded along the mid-section of each specimen geometries. The temperatures from these thermocouples were recorded along a stabilised thermal cycle using a micro-computer. Examples of surface temperatures obtained from FT-S specimens are shown in figures 7 and 8 for the aerospace cycle and the aeronautical cycle respectively.

The transient temperature map of the structures was obtained using a 2-D analysis with a finite element code modelling half the middle section (symmetry). Specific heat (C_p), thermal conductivity (k) and coefficient of thermal expansion are used in calculations as functions of temperature. The thermal loading of the specimens was described with convective film cooling (h_i) and radiation heat flow ($\emptyset_i$) which vary with the location (i) in the

specimen. The results for these computations with FT-S geometry are shown in figures 10 and 11 for the aerospace cycle and the aeronautical cycle respectively.
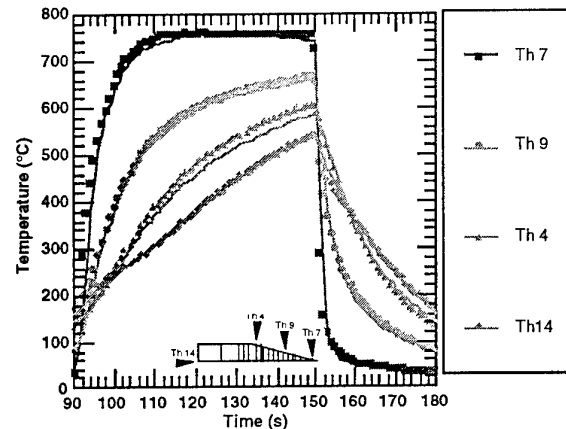
Figure 7 : Experimental and computed temperature profiles for FT-S geometry and aerospace thermal cycle.
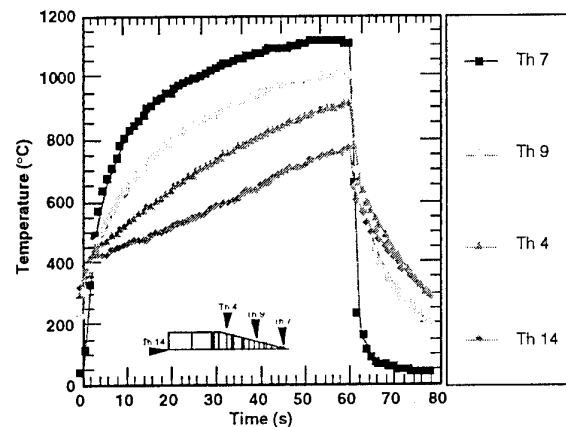
Figure 8 : Experimental temperature profiles for FT-S geometry and aeronautical thermal cycle.

The comparison between the calculated and the experimentally measured temperatures along the section of specimens shows for the most part of the thermal cycle a good agreement, with a maximum difference of 20°C. The results from the thermal analyses were used as an input for the mechanical stress-strain analysis.

5.2 Mechanical analysis

The mechanical behaviour of the two materials was modelled using constitutive equations. In that way, a viscoplastic Chaboche model with internal variables was used to simulate the stress-strain behaviour of the two superalloys [6,10]. For the wrought superalloy, the constitutive equations are written at a macroscopical scale; for the AM1 single crystal, the fairly similar equations was written at the level of the slip systems. In this model, the strain is partitioned into an elastic and a viscoplastic part :

$$\varepsilon_m = \varepsilon_e + \varepsilon_v \tag{1}$$

Under uniaxial loading, the viscoplastic constitutive equations are written as:

$$\dot{\varepsilon}_v = \left\langle \frac{|\sigma - X| - R_v}{K} \right\rangle^n \ Sign(\sigma - X_v) \qquad (2)$$

$$with \ \langle a \rangle = \max(0, a)$$

$$X = X_1 + X_2 \qquad (3)$$

$$X_1 = C_1 \ \alpha_{1v} \qquad (4)$$

$$where \ \dot{\alpha}_{1v} = \dot{\varepsilon}_v$$

$$X_2 = C_2 \ \alpha_{2v} \qquad (5)$$

$$where \ \dot{\alpha}_{2v} = \dot{\varepsilon}_v - D_2 \alpha_{2v} \ \dot{v} \ and \ \dot{v} = \left| \dot{\varepsilon}_v \right|$$

$$R_v = R_0 + Q(1 - e^{bv}) \qquad (6)$$

where ε_v is viscoplastic strain, $\dot{\varepsilon}_v$ the rate of viscoplastic strain and v the cumulated viscoplastic strain. Kinematic hardening is described by means of two kinematic variables (X_1 and X_2). R_v represents the elastic domain radius . Young's modulus (E(T)) and Poisson's coefficient (v) were measured by means of tensile tests at several temperatures.

The materials parameters K, n, C_1, C_2, D_2, R_0, Q and b were identified in the full temperature range of TF cycles from LCF and TMF test results [5,7,11] by numerical methods (see [9,11]). An example of the simulated stress-strain loops is shown in figure 9 for TMF test under the wrought superalloy used in this study.

Stress (MPa)
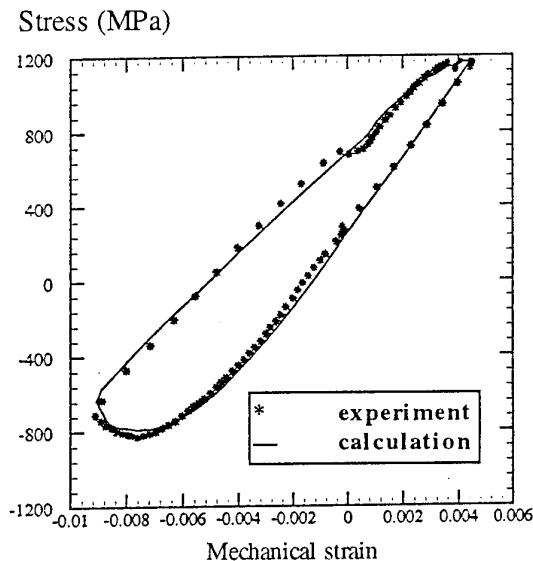
Figure 9 : Comparison between experimental and computed stress-strain loops from wrought superalloy TMF test.

The identified constitutive equations were used in a finite element code to calculate strains and stresses using previous thermal analysis for the different specimen geometries and the two materials using the same mesh as for thermal analysis.

Examples of the results obtained for the wrought superalloy during a mechanical stabilised cycle (20th) are presented in figures 10 and 11 for FT-S and FT-L specimens.
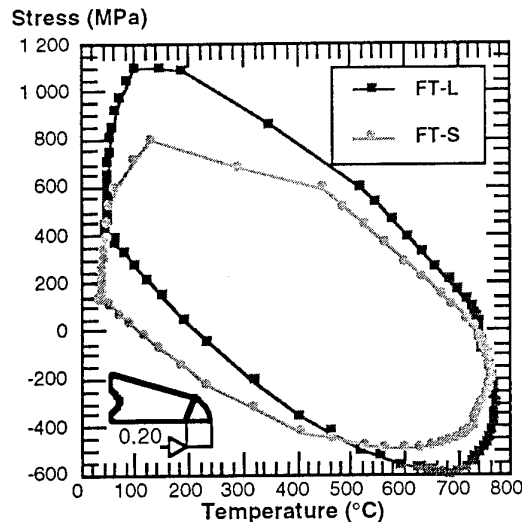
Figure 10 : Calculated stress-temperature loops for the first element of FT-S and FT-L geometries.

These loops are the average of temperature, stress and strain along 0.2 mm from the leading edge. Thanks to the low temperature-stress-strain variation, this first element could be considered as a volume element. The stresses generated by thermal cycling are higher at the thin edge of FT-L specimen than for FT-S specimen, and the mean stresses are tensile for both geometries. The mechanical and inelastic strains on the one hand, and the mean strain which is compressive, on the other hand, are larger in the FT-L and FT-S specimen geometries respectively. Inelastic strains are observed up to 5.6 mm and 11 mm from the leading edge of the FT-S geometry and FT-L geometry, respectively.
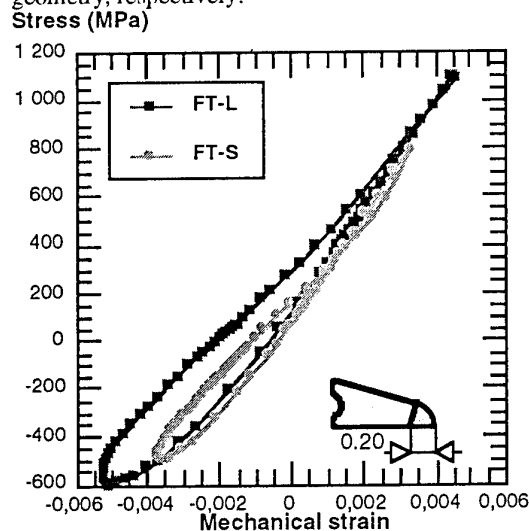
Stress (MPa)

Figure 11 : Calculated stress-mechanical strain loops in the case of wrought superalloy for the first element of FT-S and FT-L geometries.

Results obtained for the coated AM1 single crystal during a mechanical stabilised cycle (20th) are presented in figures 12 and 13 for FT-S geometry. These loops are drawn considering the average of temperature, stress and strain along 0.2 mm from the leading edge. The maximum stress generated by thermal cycling is observed

at 200°C and the minimum stress around 800°C. Comparatively, the maximum and the minimum stresses were observed at 700°C and 950°C respectively during TMF tests. The mean stress and the mean strain are tensile for the first elements near the leading edge. Inelastic strains are observed up to a few millimetres from the leading edge of the specimen.

Stress (MPa)
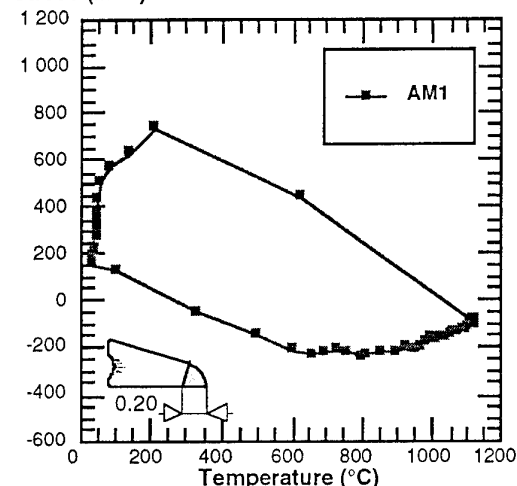
Figure 12 : Calculated stress-temperature loops in the case of coated AM1 for FT-S geometry.

Stress (MPa)
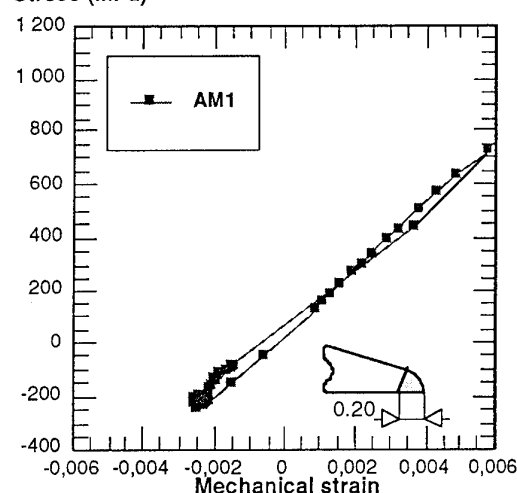
Figure 13 : Calculated stress-mechanical strain loops in the case of coated AM1 for FT-S geometry.

6. ESTIMATION OF DAMAGE DURING TF

In this section, two methods for damage evaluation will be exposed for the wrought superalloy.

A way to assess to the damage during TF tests is to compare TF tests to TMF tests results in the same temperature range using similar failure criteria (failure of a volume element). This is done in figure 14 which shows a Manson-Coffin diagram (using the inelastic strain range) obtained from volume element TMF tests in the temperature range between 100°C and 750°C. The TF crack initiation life corresponds to the number of thermal cycles required to reach a 0.2 mm crack length. The Manson-Coffin diagram shows that the lifetime obtained with the two geometries are close in agreement with the

TMF results. Consequently, the Manson-Coffin relation for TMF loading gives a good prediction of the TF specimen life.

Plastic strain (%)
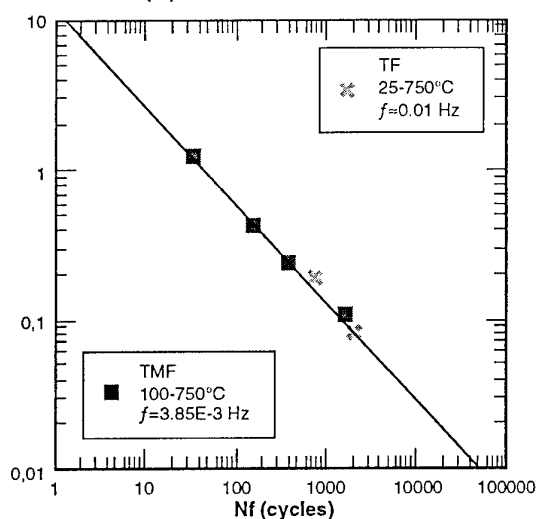
Figure 14 : Lifetime comparison between TMF (100°C-750°C) and TF (30°C-750°C) tests.

The lifetime of TF specimens was also calculated using a fatigue-creep damage model. In this model [see 12, 13], the total damage rate results from the cumulation of creep (D_C) and fatigue (D_F). Damage coupling is ensured by the total damage dependence of each damage rate :

$$dD = dD_C + dD_F \qquad (8)$$

$$dD_C = f_C(\sigma, D, T) \ dt \ \ et \ \ dD_F = f_F(\sigma_M, \overline{\sigma}, D, T) \ dN$$

where σ, σ_M, $\overline{\sigma}$ are the current stress, maximum stress and mean stress respectively.
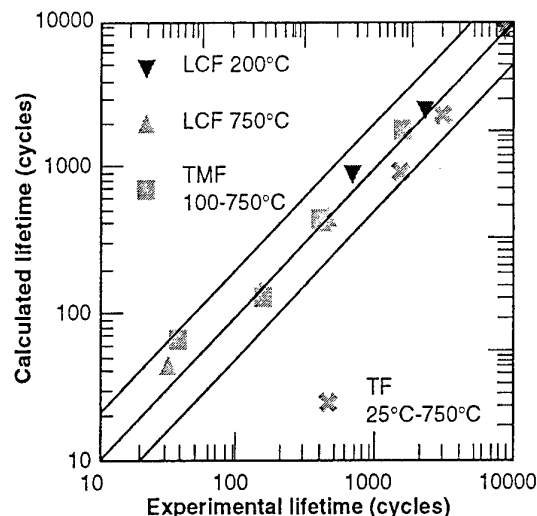
Figure 15 : Comparison between calculated life of LCF, TMF, TF specimens and experimental data.

This model had to be defined for the whole temperature range of TF tests. This was done by numerically identifying model parameters on LCF at high frequency and creep results. Lifetime prediction for volume element tested under LCF at low frequency and TMF conditions was in good agreement with the experiment as shown in

figure 15.
Eq (8) was used to compute the life of the first element at the leading edge of the TF specimen, which is compared to experimental data to 0.2 mm crack depth in figure 15. Predictions tend to be slightly conservative, but are pretty good, within a factor of two of the experimental results.

7. INFLUENCE OF A COATING ON THE FATIGUE LIFETIME UNDER THERMAL TRANSIENTS

In this study of TF resistance of [001] single-crystal of AM1 superalloy, a severe cold cycle between 30°C and 1100°C was used. This could be done easily using severe cooling in a test structure.
On the other hand, such a temperature range is much more difficult to achieved using a TMF test. Since a TMF test is supposed to be a volume element test, no thermal gradient is allowed in specimen cross section.
TMF tests can be used more easily to investigate a hot thermal shock cycle, such as from 600°C to 1100°C. A counterclockwisediamond type cycle was so used in recent investigations of bare [5] and coated [4] AM1 single-crystal. Hollow cylindrical specimens with 1 mm wall thickness, 11 mm external diameter and 25 mm gauge length were used with a surface finishing as described in earlier publications [1,5,6,11].
The TMF cycle used was intended to simulate a « hot » thermal loading experienced by the leading edge of a blade and is depicted in figure 16. A mechanical strain-temperature loop was used from 600°C to 1100°C with peak strains at intermediate temperature : 950°C in compression on heating and 700°C in tension on cooling. Tests were stopped when the major crack grows through wall thickness or slightly before 1 mm depth.
The lifetime of bare and coated specimens of [001] AM1 single crystal is plotted versus the mechanical strain range and the stress range in figures 17a and 17b for this TMF cycle between 600°C and 1100°C.
No significant difference is observed between bare and coated specimens using this cycle. The major crack in these TMF specimen initiate at casting micropores which are located in the sub-surface area for both bare and coated specimens.
The life to initiate a major crack 0.2 mm in depth under TF between 30°C and 1100°C is reported on figures 17a and 17b. The life to crack initiation in the bare specimen compares fairly well between TMF (600°C <=> 1100°C) and TF (30°C<=>1100°C). This is no longer the case for coated specimen where the more severe TF cycle gives rise to a strong reduction in lifetime as compared to TMF by a factor of four.

Figure 17a : Variation of the TMF total lifetime with the mechanical strain range for the [001] orientation.

Figure 17b : Variation of the TMF total lifetime with the stress range for the [001] orientation.

This difference is linked with the existence of a ductile-brittle transition in the intermetallic coating layer. The detailed interpretation of this difference is still in progress and is beyond the scope of this paper.
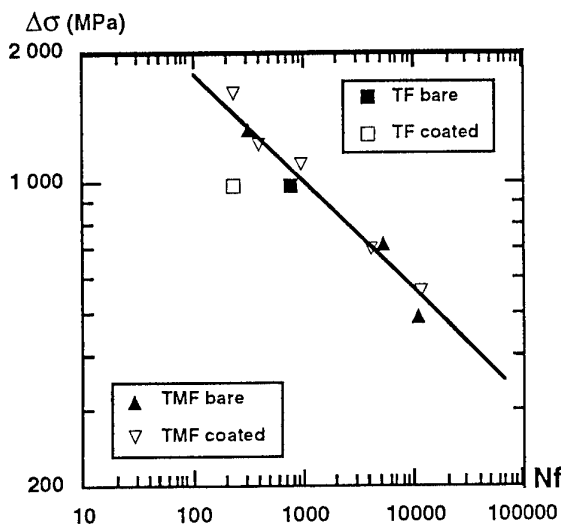

Figure 16 : Thermal-Mechanical Fatigue cycle for bare and coated AM1.

This comparison definitely demonstrates the importance of the TMF cycle on the lifetime of coated components. Therefore, laboratory tests have to simulate as closely as possible the thermal-mechanical loading of coated components.
Under these circumstances the old-fashioned TF test may be somewhat more useful than the TMF test which is much more popular these days.

8. CONCLUSIONS

A thermal fatigue facility was build up using a radiation furnace and an air forced cooling system. This TF facility, which is much less expensive than a TMF facility, allows to study damaging mechanisms under TF in the temperature range between 30°C-1100°C with a great versatility by controlling the temperature history on specimens.
TF tests were performed using two specimen geometries and two nickel-based superalloy (a wrought superalloy and a single-crystal) under different thermal cycles representative of actual loading conditions. The effect of the geometry on crack initiation and growth was shown. The influence deleterious of a coating that did not appear during TMF tests, has been revealed by TF tests. The damaging mechanisms were clearly identified and described.
A finite element analysis was made to compute the temperature-strain-stress history for each specimen. The mechanical analysis was performed using results from thermal computations and volume element test results to identify the material mechanical behaviour.
In the case of the wrought superalloy submitted to an aerospace cycle, the TF life to initiate a major crack 0.2 mm deep in depth was computed using two damage models. The one based on TMF results in combination with a Manson-Coffin relation ship was shown to give good predictions of TF data. The other one, based on fatigue-creep damage cumulation, was shown to give pretty good agreement with experiment.

9. ACKNOWLEDGEMENTS

10. REFERENCES

[1] KÖSTER A., FLEURY E., VASSEUR E. and REMY L., Thermal-Mechanical Fatigue Testing, *Automation in Fatigue and Fracture : Testing and Analysis, ASTM STP 1231*, C. AMZALLAG, Ed., American Society for Testing and Materials, Philadelphia, 1994, pp. 563-580.

[2] REZAÏ-ARIA F., FRANÇOIS M., REMY L., Thermal fatigue of MAR-M509 superalloy, *Fatigue Fract. Eng. Mater. Struc.*, 1988, pp. 277—289.

[3] GLENNY E., A study of the thermal-fatigue behaviour metals, Paper No 2010, *Journal of the Institute of Metals*, 1970, pp. 449-461.

[4] CHATAIGNER E., REMY L., Influence d'un revêtement protecteur (C1A) sur la tenue en fatigue d'aubes de turbine monocristallines, *Journées de Printemps, SF2M*, 1995, to be published.

[5] FLEURY E., REMY L., Behaviour of Nickel-Base superalloy single crystals under Thermal-Mechanical Fatigue, *Metal. Trans., vol. 25 A, 1994, pp. 99-109*.

[6] CHATAIGNER E., REMY L., Thermo-Mechanical fatigue behaviour of coated and bare nickel-based superalloy single crystals, *Second symposium :Thermomechanical fatigue behaviour of materials, Phoenix - Arizona, 14-15 November 1994, ASTM*, American Society for Testing and Materials, 1994, to be published.

[7] CHATAIGNER E., Influence d'un revêtement protecteur (C1A) sur la tenue en fatigue d'aubes de turbine monocristallines, *Ph. D. Thesis, Ecole des Mines de Paris*, 1995, to be published.

[8] REZAI F. MEYER-OLBERSLEBEN F., GOLDSCHMIDT D., Investigation of the thermal fatigue behaviour of single-crystal nickel based superalloy SRR99 and CMSX-4, *Superalloys 92 - 7th international symposium on superalloys*, Sevensprings Mountain resort, Champion, Pennsylvania, 20-24 September 1992, S. D. ANTOLOVICH et al. Ed., 1992, pp.785-794.

[9] KÖSTER A, LAURENT G, REMY L, Analysis of thermal fatigue tests for superalloy components, *Fatigue under thermal and mechanical loading*, J. BRESSERS, L. REMY Ed., European Commission J.R.C. and S.F.2.M, Petten, 1995, to be published.

[10] KÖSTER A., Fatigue of a nickel base superalloy for aerospace turbine blades: application to lifetime prediction, *Ph. D. thesis*, ENSMP, 1995, to be published.

[11] HANRIOT F., CAILLETAUD G., REMY L, Mechanical behaviour of a nickel-base superalloy single crystal, *High temperature constitutive modelling - Theory and Application*, A.D. FREED and K.P. WALKER Ed., ASME, 1991, Book No. H00667, pp. 139-150.

[12] CHABOCHE J.-L., Low cycle fatigue and life predictions, *ASTM STP 770*, C. AMZALLAG, B.N. LEIS AND P. RABBE, Ed., ASTM, Philadelphia, 1982, pp. 81-104.

[13] CAILLETAUD G., CHABOCHE J.-L., Lifetime predictions in 304 stainless steel by damage approach, *ASME*, Orlando(USA), 27 June - 1st July 1982.

EFFECTS OF CYCLE TYPE AND COATING ON THE TMF LIVES OF CMSX6

J. Bressers[1], J. Timm[1], E. Affeldt[2], A. Bennett[3]

[1]Institute for Advanced Materials, Joint Research Centre, P.O.Box 2, 1755 ZG Petten, The Netherlands.

[2]MTU Motoren und Turbinen Union München, Postfach 50 06 40, 80976 München, Germany

[3]Rolls-Royce plc, P.O.Box 31, Derby DE24 8BJ, United Kingdom.

ABSTRACT
Strain controlled thermo-mechanical fatigue cycles simulating the temperature-strain-time history at critical locations of blades of advanced aero gas turbines are applied to the single crystal nickel based alloy CMSX6 in the uncoated and PtAl coated conditions. The TMF cycle selection includes a -135°lag cycle and an in-phase cycle, with various R_ε-ratios, $T_{min}=300°C$, and $T_{max}=1050°C$ and 850°C,respectively. The cycle-specific stress response is analyzed and discussed in terms of the accumulation of inelastic strain during the TMF tests. The number of cycles for initiating microcracks is measured by means of a computer vision system. Various modes of crack initiation and crack growth are observed and correlated with the TMF cycle type, with the strain range imposed, and with the ductile/brittle behaviour of the coating. The differences in TMF lives are discussed in terms of the material and TMF parameters.

LIST OF SYMBOLS

ε total strain
ε_{th} thermal strain
ε_m mechanical strain
$\Delta\varepsilon_m$ mechanical strain range
R_ε mechanical strain ratio
T_{min} lower temperature
T_{max} upper temperature
l   crack length
N   number of cycles
N_f number of cycles to 66% of max. stress

INTRODUCTION
Single crystal nickel based alloys are widely used as blade materials in aero gas turbine blades because of their excellent resistance to high temperature deformation. Tailoring of their chemical composition towards improving the high temperature strength has resulted in a reduced oxidation resistance. Coatings such as Platinum-aluminides formed by a diffusion process are applied in order to provide the blades with adequate protection against environmental degradation.
The major cause of failure in current single crystal blades of aero gas turbines is thermally induced stresses, which result from thermal strains over the blade thickness caused by temperature gradients during heating and cooling cycles. Isothermal mechanical fatigue data, which

are traditionally used for blade design purposes, do not account for the damage and failure processes occurring in blades exposed to thermal fatigue cycles. Moreover, blades provided with PtAl coatings are expected to display a non-isothermal fatigue behaviour because of the ductile-brittle transition of the coating at intermediate temperatures. Actual blade behaviour is more closely simulated by thermo-mechanical fatigue (TMF) tests, which are designed to reproduce the temperature and strain cycles seen by critical volume elements of the blade. As opposed to isothermal fatigue testing, the coated test specimen is repeatedly cycled through the ductile-brittle transition temperature of the coating during TMF cycling, which gives rise to different damage and failure mechanisms.

In a number of studies the nature and the extent of the influence of the presence of the coating on the mechanical performance of nickel based superalloys has been investigated. Either detrimental or beneficial/neutral effects on specific, isothermally-measured mechanical properties of the substrate were reported [1-8]. When subjected to TMF cycling, the presence of a coating can be detrimental [9] or beneficial [10-11] to the TMF life. However, the sparse data reported so far are not comparable in terms of coating types, substrates, temperatures and loading cycles, making an interpretation of the results rather difficult. As part of a study into the TMF behaviour of single crystal nickel based alloys in the uncoated and PtAl coated conditions, the effect of the TMF cycle type and the influence of the presence of the coating on the TMF life, and the associated crack initiation and failure modes have been investigated and are reported here.

EXPERIMENTAL DETAILS

Material
Single crystal CMSX6 of industrial quality

has been selected as the substrate material for all of the TMF testing reported in this paper. Its chemical composition is given in Table 1. Following the solution heat treatment of the 25 mm diameter single crystal blanks, these are machined into TMF test specimens. The PtAl coated test specimens are given a coating diffusion treatment of 1 h at 1100°C in an Ar atmosphere, and a 16 h ageing heat treatment at 870°C in Ar.

TABLE 1-Chemical composition of CMSX6 (in wt.%)

Al	Co	Cr	Mo	Ta	Ti
4.85	5.0	10.0	3.0	2.0	4.75

C	Zr	B	Si	Hf	Ni
0.02	0.08	0.03	0.02	0.01	bal

The crystallographic orientation of the long axis of the test specimens is within 10° of <001>. The microstructure of CMSX6 consists of approximately 70 vol.% of γ' phase in a γ matrix, with an average size of 0.6-0.7 µm. In addition carbides are observed, along with interdendritic porosity. The top layer of the coating consists of a mixture of PtAl and NiAl while the internal part is composed of NiAl which is understoichometric in Al. Near the coating-substrate interface an interdiffusion zone with Cr-Mo and W rich types of carbides exists.

Thermo-mechanical fatigue test procedure
The thermo-mechanical fatigue tests are carried out on a computer controlled

servohydraulic testing machine. The test specimen is heated by means of direct induction. Control of the testing machine and of the high frequency generator, and data acquisition are performed by means of a dedicated computer system, using a graphical programming language for constructing hierarchically ordered command and data acquisition software modules.

The TMF test specimen has a cylindrical end geometry and a solid gauge length with a rectangular cross section of 12mmx3mm in order to enable observation of the surface by means of an optical microscope during testing. The edges of the gauge length section of the coated (and uncoated) specimens are rounded in order to promote good adherence of the coating. The surface finish in the gauge length of the substrate material is R_a=0.05 µm. Coated specimens are tested in the as received condition without any further surface modification treatment.The coating cross section is taken into account when calculating stresses on the coated specimens.

The sample temperature is controlled by means of a thermocouple spotwelded to the specimen surface outside the gauge length, in order to inhibit premature crack formation in the gauge section as the result of spot welding damage. A calibration procedure is used to obtain the correct temperature at the centre of the gauge length, in conjunction with a pyrometer for double checking of the temperature. Strains are measured by means of a longitudinal extensometer, with the limbs spanning a gauge length of 10 mm.

All tests are carried out in total strain control between mechanical strain limits. The temperature is varied linearly with time and synchronously in-phase, or with a 135° phase lag with respect to the mechanical strain. The mechanical strain ε_m is defined as

$$\varepsilon_m = \varepsilon - \varepsilon_{th} \tag{1}$$

where ε and ε_{th} are the total and thermal components of the strain, respectively. The two cycle types are shown schematically in Fig.1 .

Tests with different R-ratios are performed i.e. R_ε=-∞ and R_ε=0 in the case of the -135°lag tests, and R_ε=0 in the case of the in-phase tests. The minimum cycle temperature is 300°C. The maximum cycle temperature varies from 850°C in the in-phase tests to 1050°C in the -135°lag tests. Generalized plane-strain as well as 3D Finite Element calculations confirm that
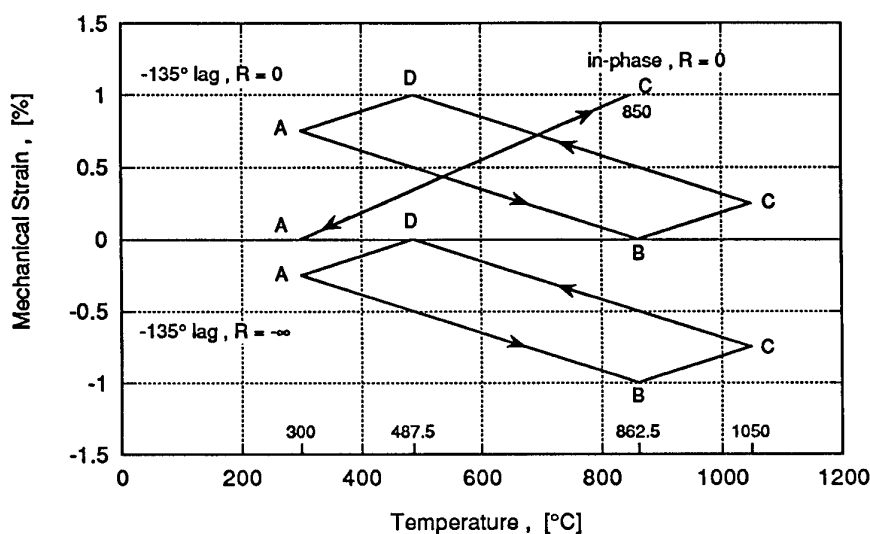
Fig.1-Schematic representation of the TMF cycle types

these cycle types mimic the strain-temperature conditions at the most critical blade locations. For example, the -135°lag, R=-∞ tests simulate a hot spot condition.

In order to approach in-service heating and cooling rates of blades as realistically as possible, a compromise between high rates and an acceptable temperature gradient over the specimens' gauge length had to be made. Specimen heating and cooling rates were set at 25°C/s and 12.5°C/s respectively, resulting in a maximum temperature gradient over the gauge length of ±15°C. The corresponding maximum deviation from zero of the stress measured during cycling under thermal strain control is well within ±10 MPa. Forced cooling during the larger part of the downward branch of the cycle is required in order to enable the cooling rate of 12.5°C/s to be achieved. Cycle periods are 90s and 66s for the out-of-phase and in-phase tests, resulting in mechanical strain rates of approximately 3×10^{-5} s^{-1} and 1.5×10^{-5} s^{-1} during the heating and cooling parts of the cycle respectively . In view of the modest strain rate sensitivity of the material and of the small changes in strain rate involved, the effect on the mean stress of halving the strain rate between the heating and cooling ramps is estimated to be less than 20 MPa.

Prior to each TMF test the temperature dependence of the E-modulus for the test specimen involved is measured at intervals of 100°C, up to the maximum temperature of the TMF cycle. The thermal expansion of the specimen is recorded as a continuous function of the temperature whilst heating and cooling the specimen at the same rate as in the actual TMF test. All tests are started at 300°C.

Crack Initiation and Growth

One of the reasons for adopting a flat specimen geometry is related to the use of a computer vision system for the non-intrusive, in-situ monitoring of the initiation and growth of microcracks during the TMF tests. The surface of the test specimen is optically imaged at preselected cycle numbers, at a magnification which enables microcracks approximately l=15-30 μm long to be detected under the oxidizing conditions of the test. The images are digitized and stored for post processing. Image acquisition occurs in a fully automated, computer controlled manner. All the operational parameters of the system are user defined.

RESULTS AND DISCUSSION

Stress Response

Fig.2 shows the evolution of the characteristic cycle stresses with cycle number N at points A to D (see Fig.1) for each of the three TMF cycle types, measured on an uncoated specimen at a mechanical strain range $\Delta\varepsilon_m$=0.65%. The stress response is not influenced by the presence of the coating.

In the -135°lag, R_ε=-∞ test the material exhibits a saturation stage which sets in after a fraction of the cyclic life of the order of N/N_f=0.1 has elapsed. Prior to saturation a pronounced shift of all the cycle stresses towards more positive values is noted. The stress range assumes a constant value of nearly 1100 MPa from the first cycle onwards.

In the -135°lag, R_ε=0 test and in the in-phase test a primary stage of tensile softening/compressive hardening is observed, which is more pronounced in the in-phase testing condition. Subsequently the material response changes to another regime of either gradual or pronounced tensile softening/compressive hardening in the -135°lag, R_ε=0 and in the in-phase test conditions respectively, from N/N_f = 0.1 onwards. The corresponding stress range in the -135°lag, R_ε=0 test condition slightly increases to nearly 1100 MPa before stabilizing at approximately N/N_f =0.02. In the in-phase test the stress range increases slightly up to appoximately 1050 MPa.
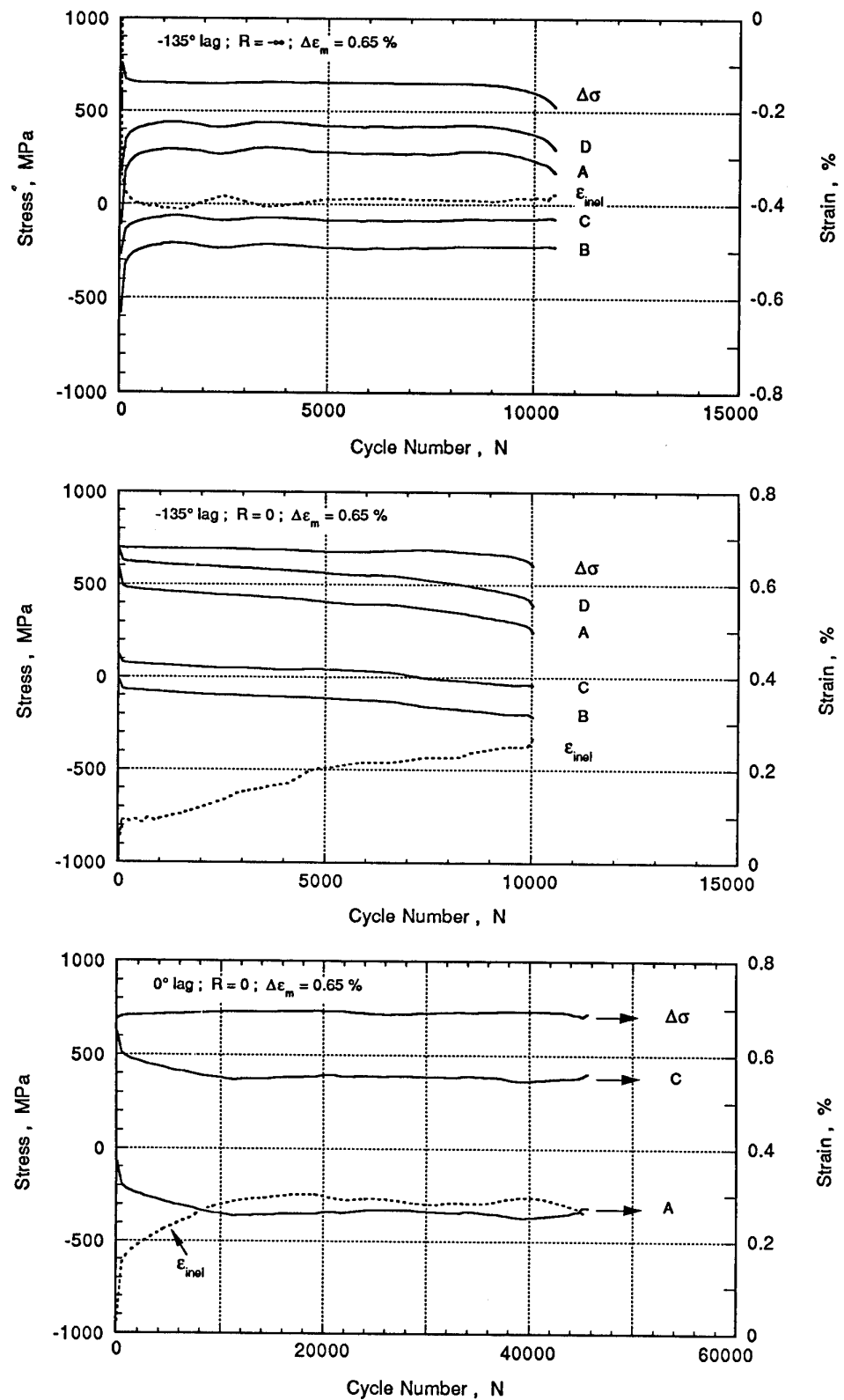
Fig.2-Evolution of the characteristic cycle stresses with number of cycles for the various TMF cycle types, $\Delta\varepsilon$=0.65%.

Fig.2 also displays the evolution with the cycle number N of the momentary value of the inelastic strain at the end point A (see fig.1) of each cycle. The changes of the inelastic strain within each cycle are not shown. The inelastic strain accumulation during cycling is the result of plastic deformation/creep occurring in specific parts of the TMF cycle. The inelastic deformation has to be balanced by an increased elastic strain in reversing the cycle, which explains the cycle-specific hardening/softening behaviour of the material. It is obvious from both the -135° TMF cycle types that the extreme differences in the stress levels of the $R_\varepsilon=0$ and $R_\varepsilon=-\infty$ tests vanish early in the life, resulting in relatively small differences beyond $N/N_f=0.1$. This behaviour is comparable to that observed in another single crystal alloy (SRR99), and is discussed in more detail in [11].

TMF Lives

A relatively small fraction of the TMF life is spent in initiating microcracks. Initiation is defined as the cycle number N_i where cracks with a length on the surface of $l=30\mu m$ are measured, a definition which is dictated by the resolution of the computer vision system. The TMF life is defined as the cycle number N at which the maximum cycle stress has decreased to 2/3 of the saturation stress level. The fraction of life required for initiation ranges from <1% to 5% in nearly all the -135°lag tests of coated and uncoated CMSX6, with the exception of tests at small strain ranges. For the in-phase tests cracks initiate at sub-surface porosity in uncoated CMSX6 and both at the surface and at sub-surface pores in coated material. Precise N_i data for sub-surface initiation are not available because of the type of monitoring technique used. A conservative estimate of N_i/N_f, based on the observation of the first surface breaking of sub-surface initiated cracks, suggests values of the order of <30%.

Effect of TMF cycle type on the life of uncoated CMSX6

The lives of the uncoated CMSX6 are plotted in fig.3 as a function of the mechanical strain range Δe_m. The in-phase cycle yields a substantially longer life when compared to the lives of the -135°lag cycles. No effect of the R_ε ratio on life is noted for the -135°lag tests, which is consistent with the observation that the stress levels in both the $R_\varepsilon=0$ and $R_\varepsilon=-\infty$ tests approach comparable values early in

Fig.3-Influence of TMF cycle phasing and of R_ε ratio on life for uncoated CMSX6

the tests.

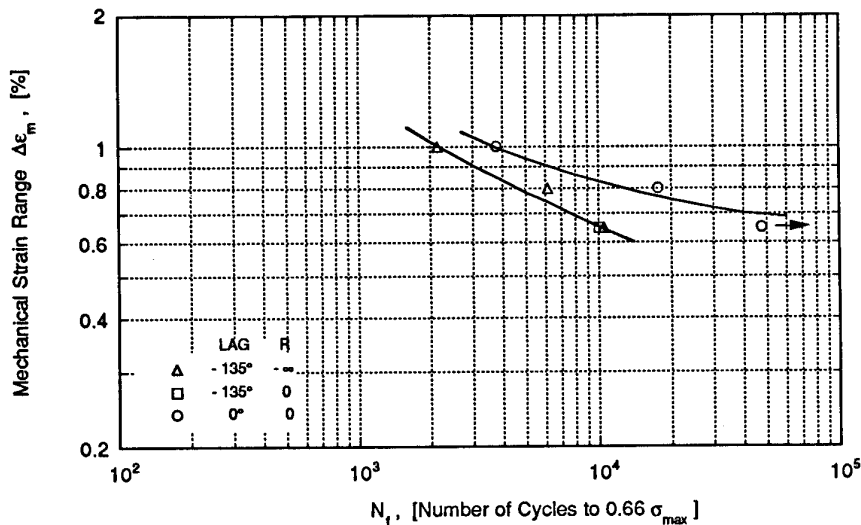Apart from the disparities in terms of stress response and deformation between the various cycle types, pronounced differences also exist in terms of crack initiation and crack growth mechanisms. In the -135°lag cycle tests multiple cracks initiate at the side faces of the test specimen, prior to $N/N_f=0.05$. The process of crack initiation appears frequently to be associated with the preferential oxidation of microstructural features located in stringers along the long axis of the test specimen, resulting in oxide hillocks protruding from the surface, which are cracked, see fig.4a. There is some evidence that these preferred sites of crack initiation, which are located on top of the interdendritic zones, are associated with casting porosity. Crack growth starts off in stage II, changing to stage I later on. The crack tip environments observed in specimen cross sections suggest a growth mechanism whereby oxide films, repeatedly formed in the high temperature part of the TMF cycle, are disrupted by crack extension in the intermediate/low temperature part of the cycle where the stress is at and near its maximum.

In the in-phase tests cracks initiate at pores in the bulk of the specimen, see fig.4b, growing in stage II in an environment shielded from oxidation during a relatively large part of the life. Surface piercing of some of the sub-surface growing cracks, and their exposure to the air environment results in an acceleration of the crack growth rate as the result of thermally activated oxidation (12). Concurrent with the initiation of cracks at internal porosity, oxide hillocks form on the outer surface of the specimen, creating potential sites for external crack initiation. The competition between internal and external cracking will be influenced by the possible occurrence of an oxide induced closure effect at surface initiated cracks which may give rise to an increase of the threshold for crack growth. This would necessitate a crack initiated at an oxide hillock to overcome a larger initial crack size relative to a pore initiated crack before growth can start. Both the lower maximum cycle temperature (850°C versus 1050°C for the -135°lag cycle) and the initiation and the growth of cracks in an oxygen-free environment during a relatively large fraction of the life will contribute to extending the lives of the in-phase tests relative to the -135°C tests. However, the situation is more complex because the high tensile stresses which drive the crack forward are experienced at high versus low temperature respectively in the in-phase and -135°lag tests.
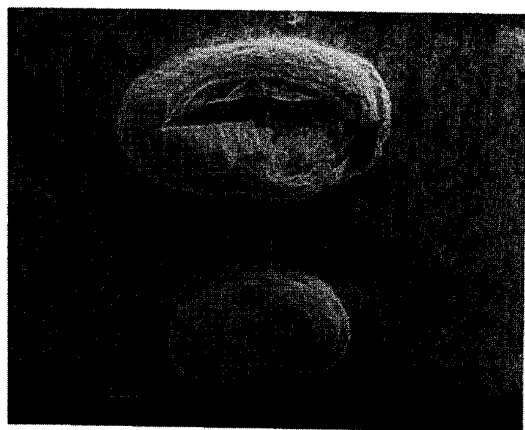
Fig.4a-Crack initiation at oxide hillock on the surface for the -135°lag cycle
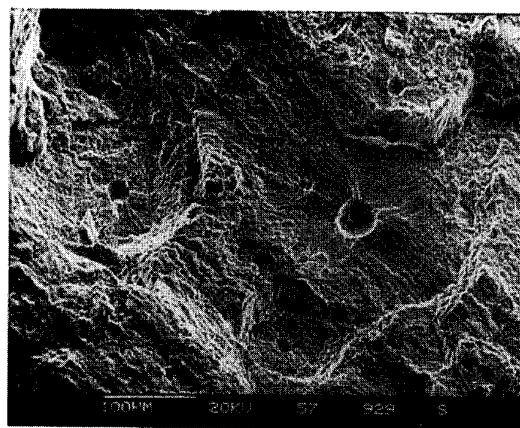
Fig. 4b- Crack initiation at internal porosity for the in-phase cycle.
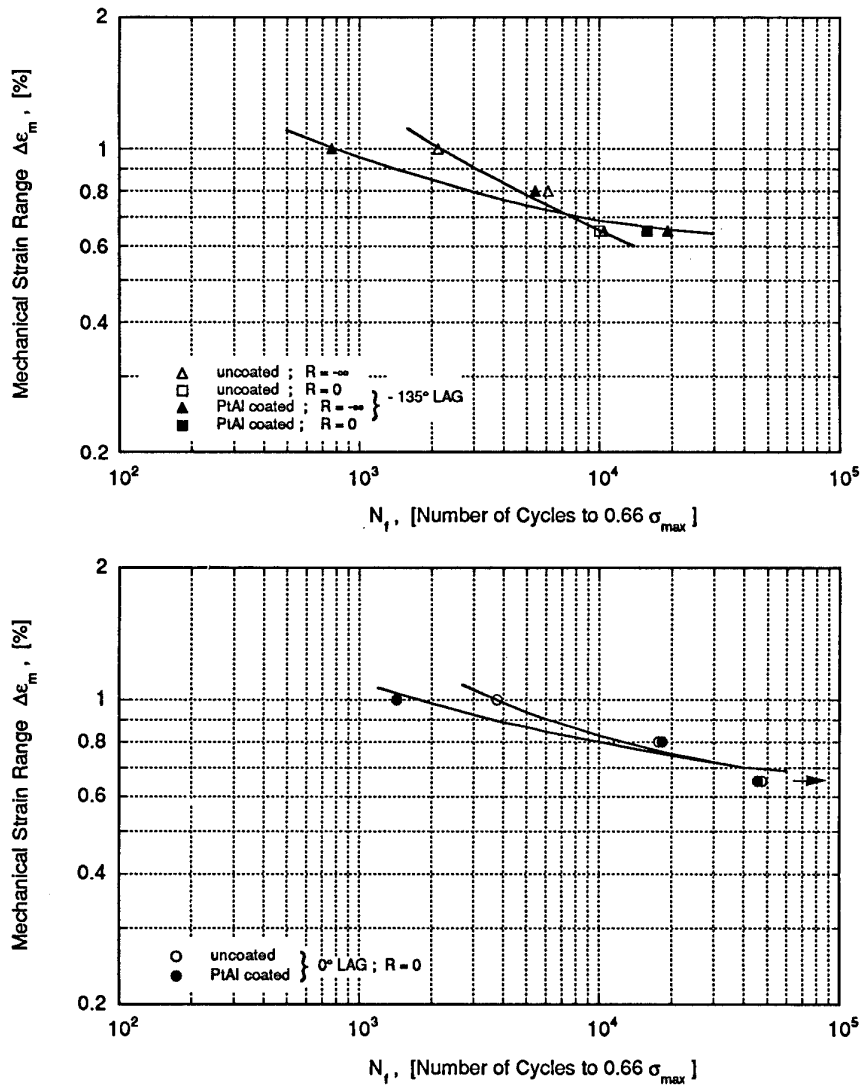
Fig.5-TMF lives for uncoated and PtAl coated specimens for the in-phase tests (lower) and for the -135°lag tests (upper)

Effect of the coating on the life of SRR99

The influence of the presence of the PtAl coating on the TMF life is shown in fig.5. The presence of the PtAl coating results in a life reduction at high strain ranges and in similar lives at intermediate strain ranges relative to the uncoated CMSX6. Whereas the life for the in-phase cycle shows no effect of the coating at intermediate and low strain ranges, the presence of the coating increases the life in the case of the -135°lag tests.

The effect of the coating on the TMF lives can be rationalized in terms of the cracking mechanisms associated with the presence of the coating. Investigation of the fracture surfaces shows brittle fracture of the coating at the high strain ranges. A network of parallel, equidistant cracks spanning the entire width of the specimen develops early in the life (line initiation). An example of the resulting fracture surface of a -135°lag tested specimen is shown in fig.6. This brittle cracking mechanism affects the TMF
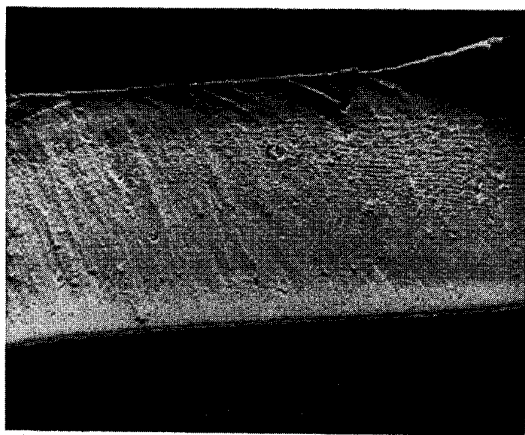
Fig.6-Part of the fracture surface of a coated specimen tested at -135°lag, $\Delta\varepsilon_m$=1%

in various ways. The depth of the brittle cracks at initiation is equal to the coating thickness of 50 μm, which generally exceeds the depth of point-initiated cracks associated with oxide hillocks or pores of less than 100 μm, giving rise to higher stress intensity factors. A similar effect results from the fact that the geometry factor in the Paris law expression for ΔK is 1.12 for the brittle line crack, versus 0.66 for the deepest point of a semi-circular crack of the same depth initiating at an oxide hillock or a pore in the point mode. Finally, because the shape of the different cracks is preserved during growth, the life crack increment required to cause specimen failure is smaller for line initiated cracks than for semi-circular cracks. All three factors contribute to the observed life reduction. These effects vanish at a strain level where the cracking mechanism of the coating changes from the line initiation mode to the point initiation mode, observed at intermediate and small strain ranges. In the intermediate and low strain range regime the different cracking mechanisms typical for in-phase and -135°lag cycling now become life controlling. For the in-phase tests the life is controlled by the initiation and growth of cracks at internal porosity in the substrate material, irrespective of the presence of the coating. For the -135°lag cycle cracks

initiate in the point mode at oxide hillocks, the formation of which is slowed down in the PtAl coated specimens relative to the uncoated CMSX6 because of the better oxidation resistance of the coating.

CONCLUSIONS

1.TMF testing with -135°lag cycles and strain ratios of R_ε=0 and R_ε=-∞ leads to comparable saturated stress levels after approximately 10% of the life has elapsed, resulting in a negligible influence of the R_ε-ratio on the TMF life. TMF testing with an in-phase cycle in combination with a strain ratio of R_ε=0 results in a different hardening/softening behaviour.

2.Cracks in uncoated specimens TMF tested with a -135°lag cycle initiate at surface locations which show preferential oxidation.

3.In-phase TMF cycles cause crack initiation and growth from internal porosity, resulting in longer lives compared to -135°lag cycling.

4.PtAl coated CMSX6 has a shorter life than uncoated CMSX6 for both in-phase and -135°lag conditions at high strain ranges, due to the brittle cracking of the coating.

5.At intermediate strain ranges the presence of the PtAl coating does not affect the TMF life because the brittle cracking mechanism does not any longer operate.

6.The presence of the PtAl coating causes life lenghtening for the -135°lag cycle at low strain ranges, due to its protective role in terms of hindering the formation of oxide hillocks.

7.For in-phase cycling, the presence of the PtAl coating has no effect on the TMF life at low strain ranges because the life is controlled by the initiation and growth of cracks from internal porosity.

ACKNOWLEDGEMENTS

REFERENCES

[1] Strang, A. and Lang, E., "Effect of coatings on the mechanical properties of superalloys", in R. Brunetaud et al. (eds.), *High Temperature Alloys for Gas Turbines 1982*, D. Reidel Publishing Co., 1982, pp 469-506.

[2] Strangman, T.E., Fuji, M. and NGuyen-Dinh X., in Gell et al. (eds.), *Superalloys 84*, The Metal Society, AIME, 1984, pp 795-804.

[3] Wood, M.I. and Restall, J.E., "The mechanical properties of coated nickel based superalloy single crystals", in W.Betz et al. (eds.), *High Temperature Alloys for Gas Turbines and other Applications*, D. Reidel Publishing Co., 1986, pp 1215-1226.

[4] Grünling, H.W., Schneider K. and Singheiser, L., "Mechanical properties of coated systems", *Mater. Sci. Eng.*, Vol. 88, 1987, pp 177-189.

[5] Veys J.-M. and Mevrel, M., "Influence of protective coatings on the mechanical properties of CMSX 2 and Cotac 784", *Mater. Sci. Eng.*, Vol.88, 1987, pp 253-260.

[6] Veys, J.-M. and Mevrel, R., "Creep and high cycle fatigue properties of coated CMSX 2", in T. Khan and A. Lasalmonie (eds.), *Advanced Materials and Processing Techniques for Structural Applications*, ONERA, 1988, pp 168-178.

[7] Au, P., Dainty, R.V. and Patnaik, P.C. in T.S. Sudarshan and D.G. Bhat (eds.), Isothermal low cycle fatigue properties of diffusion aluminide coated nickel and cobalt based superalloys, *Surface Modification Technologies III*, TMS, 1990, pp 729-748.

[8] Bain, K.R. "The effect of coatings on the thermo-mechanical fatigue life of a single crystal turbine blade material", AIAA / SAE / ASME / ASEE *21st Joint Propulsion Conference*, Monterey (Ca), July, 1985.

[9] Bernard, H. and Remy, L., "Thermal mechanical fatigue damage of an aluminide coated nickel base superalloy", in H.Exner and V.Schumacher (eds.), *Advanced Materials and processes EUROMAT_* 1989, pp 529-534.

[10] Guedou J.-Y. and Honnorat, Y., "Thermo-mechanical fatigue of turboengine blade superalloys", in *Thermomechanical Fatigue Behaviour of Materials*, ASTM STP 1186, ed. H. Sehitoglu, San Diego, Oct. 1991, pp 157-175.

[11] Bressers J., Timm J., Williams S., Bennett A., and Affeldt E., "Effects of cycle type and coating on the TMF lives of a single crystal nickel-based gas turbine blade alloy" in *Thermomechanical Fatigue Behaviour of Materials*, ASTM STP 1263, eds. M.J. Verrilli and M.G. Castelli, American Society for Testing and Materials, Philadelphia, to be published

[12] Affeldt E., Timm J., Bennett A., Importance of Crack Growth to damage under TMF Loading, in J. Bressers, L. Rémy, M. Steen and L.J. Vallés (eds.), *Proceedings of the Symposium Fatigue under Thermal and Mechanical Loading*, Petten May, 1995, Kluwer, to be published

DAMAGE MECHANISM ASSESSMENT ON TURBINE BLADES SUPERALLOYS THROUGH TMF TESTS

J.C. LAUTRIDOU, J.Y. GUEDOU, J. DELAUTRE

Snecma
Materials and Processes Department
B.P. 81, 91003 EVRY CEDEX - France

1. INTRODUCTION

The greatest advance in metal temperature and stress capability for turbine blades in the last 30 years has been the result of the development of directionnally solidified single crystal superalloys. Two groups of alloys, called first and second generation, have been developed. The second generation alloys were essentially developed to improve the creep resistance and the long time phase stability in order to allow increased operating temperatures.Creep resistance is not the only property to be considered for life prediction. In complex shaped highly cooled turbine blades, stresses of thermomechanical origin may become at least as important as the centrifugal stress causing the creep of the material during the stabilized regime of the engine cycle. Those thermomechanical stresses are generated in particular during aircraft take off and landing operations. A limited amount of work has been done to compare the performance of the two generations of single crystals alloys regarding thermomechanical fatigue resistance.

The aim of the present study was to compare the mechanical properties of four single crystals superalloys belonging to the first (AM1, AM3) and second generation (MC2, CMSX4). In order to get a complete comparison, creep rupture, and thermal mechanical fatigue (TMF) tests were carried out.

2. MATERIALS AND HEAT TREATMENTS

AM1 is a french patented [1] first generation single crystal alloy introduced by SNECMA for turbine blading in the military M88 engine. AM3 is also a first generation single crystal [2] which offers very attractive properties due to its low density (8.25×10^3 kg/m^3). MC2 is a second generation single crystal, developed by ONERA [3], which has the particularity to be rhenium free. CMSX4 developed by CANNON MUSKEGON corporation [4] is, as the majority of second generation single crystals, a rhenium containing alloy (3 % wt). The chemical compositions of these four single crystals used in this investigation are shown in table 1. The single crystal bars with their axis oriented in the [001] direction were given the heat treatments shown in table 2. Those heat treatments produce a homogeneous distribution of cuboïdal γ' precipitates with a mean size of 0,5 µm for AM1, 0,4 µm for AM3 and MC2, and of 0,3 µm for CMSX4

3. RESULTS AND DISCUSSION

3.1. Creep properties

An extensive characterization of the creep-rupture strength of the four alloys was conducted between 760°C and 1150°C employing specimens machined from cylindrical bars of 10 mm in diameter. The creep capability of the alloys is compared in Fig.1.It appears from this comparison that the two second generation single crystals, CMSX4 and MC2, exhibit the highest resistance especially as soon as the testing temperature is higher than 1000°C. CMSX4 is better than MC2 at temperatures lower than 1000°C but the difference between these alloys is small at higher temperatures, MC2 being better than CMSX4 in the range 1050°C to 1100°C and CMSX4 being better than MC2 at 1150°C. The better behaviour of CMSX4 can be attributed to the beneficial effect of rhenium which is known to reduce rates of diffusion and thus retards coarsening of the γ' strengthening phase [5]. The particular behaviour of MC2, which is rhenium free, can be attributed to γ and γ' strengthening by a particularly high level respectively of molybdenum and titanium as compared to the other alloys [3].The temperature advantage of CMSX4 over AM1 varies from 25°C around 850°C to 50°C around 1150°C.

3.2. Thermal mechanical fatigue properties

3.2.1 Uncoated materials
Hollow cylindrical fatigue specimens (9 mm internal diameter) were machined from bars of 20 mm in diameter. All the materials were investigated in the bare condition. The tests were performed within the Centre d'Essais Aéronautiques de Toulouse, and the experimental procedure used was close to that of SNECMA which has been shown elsewhere [7]. The TMF cycle used for this study is presented in Fig.2.

It consists of a triangular temperature cycle between 650°C and 1100°C associated with an alternate four slopes strain wave ($R\varepsilon = -1$). The frequency of this cycle is 5.6×10^{-3} Hz (180 s per cycle). This cycle was defined to simulate the temperature and strain histories at the leading edge of a turbine blade.The four uncoated materials have been submitted to the same cycle under the same strain range ($\pm$ 0,5 %),up to macroscopic crack initiation that is determined by a 20 % maximum tensile load decrease after stabilization.The results of two tests on each alloy are shown in Fig.3, illustrating a better fatigue resistance of AM1,AM3 and MC2 as compared to CMSX4 which exhibits on average a reduction of life of a factor 2.

Two kinds of investigation were made in order to try to explain the particular behaviour of CMSX4. At first an examination of the stress-strain hysteresis loops at mid life was made for the four alloys. No major difference was observed between the alloys concerning stress and plastic strain amplitudes. Secondly, fractographic examinations of failed specimens were performed. These investigations reveal that for each alloy crack initiation sites were located at the oxide scale on the surface of specimens. This is in agreement with the results obtained by others [6] on Ni-base single crystals tested in TMF at the same strain range. These observations support the view that long lives under TMF or thermal fatigue are mainly controlled by fatigue oxidation interactions and that the TMF resistance cannot be compared with LCF lives obtained at a temperature close to the maximum peak stress of the TMF cycles because the damage mechanisms are not the same. As pointed out by Fleury and Remy [6] LCF isothermal tests at high temperature, close to the maximum temperature of the TMF cycle, should be more representative of damage mechanisms operating in TMF tests. Consequently, the TMF resistance of bare materials should be more dependent on the oxidation behaviour of the material rather than on its creep resistance.

3.2.2 Coated materials

Aluminide coating has been shown to improve TMF life on superalloys [8] especially at low strain levels corresponding to the longer lives due to their beneficial effect against oxidation.The same kind of TMF tests as mentioned earlier have been performed in the same loading condition on AM1 chromium-aluminium coated specimens (AM1 + CA). The results are compared to the previous ones obtained on bare specimens on Fig.3. A mean life improvement of a factor of 2 is observed as compared to bare AM1. On these specimens crack initiation sites were observed at the interface between the Cr-Al coating and the single crystal material. An illustration of this phenomenon is shown in Fig.4.

The coating first cracks, then an oxide develops at the interface between the coating and the substrate and finally a crack propagates into the substrate until rupture.The coating will prevent oxidation of the substrate provided it can withstand the mechanical loading without cracking. It is therefore very important to know the ductile-brittle transition temperature of the coating and to make sure that the TMF cycle of actual blades does not enter the brittle range to prevent the coating from cracking at the very first cycle and thus protect the substrate from localised oxidation.To measure the effect of such a situation another TMF cycle was applied. This new TMF cycle (cycle "W") is shown in Fig.5 where it can be seen that it contains a peak stress at the lowest temperature (600°C) which is within the brittle domain of the coating.

Several tests were performed on AM1 chromium-aluminium coated specimens. The results are compared in Fig.5 to those obtained on coated AM1 under comparable strain conditions but with the four slopes TMF cycle previously used.It appears that a life reduction factor of 3 ,with respect to the coated material using the "4 slopes"TMF cycle, is obtained when the "W" cycle is applied. The metallurgical examination of the specimens (see Fig.7) shows that a great number of straight cracks have crossed the coating and are growing into the substrate perpendicularly to the applied stress. This is attributed to the brittleness of the coating at the lowest cycle temperature which leads to its rupture in the very first cycles.The single crystal is thus no longer protected against oxidation and the fatigue life is thus considerably reduced. Moreover multiple cracking of the coating leads to the development of a circumferential crack at the surface of the specimen which undoubtedly contributes to a further reduction of life due to a geometrical effect.This clearly shows that, in some operating conditions, the coating cannot prevent the single crystal from oxidation and demonstrates the necessity of developing single crystals of good intrinsic resistance to the fatigue oxidation damage that operates in TMF.

4. CONCLUSION

Creep and TMF fatigue tests have been performed on four turbine blade single crystal superalloys. The main objective of the study was to compare the mechanical properties of first and second generation single crystals. The superior creep resistance at high temperature of the second generation single crystals (MC2 and CMSX4) over the first generation (AM1 and AM3) was confirmed. Under TMF cycling,which is representative of service operating conditions of turbine blades, the damage is associated predominantly with the oxidation-fatigue interaction. In bare condition, the second generation single crystals are not found to show better results than the first generation , CMSX4 even presenting the lowest results. The TMF fatigue resistance of aluminide coated AM1 was found to be better than that of bare AM1 when the specimens were not stressed into the

brittle domain of the coating, but was substantially reduced in the opposite situation.

It is clear that creep, fatigue and oxidation damage are operating in turbine blades during service and that complex interactions exist between those mechanisms. This indicates that the development of single crystal superalloys cannot only be based on the achievement of a high creep resistance , and that it is also necessary to evaluate the TMF resistance of materials in the bare and coated conditions. The development of prediction models that would explicitly treat interactions between those damage mechanisms would also be of great help for the optimisation of future materials.

References

[1] Bachelet, E. and Lamanthe, G. - National Symposium Single Crystals Superalloys, Villard de Lans, France - 1986

[2] Khan "Recent Developments and Potential of Single Crystal Superalloys for advanced turbine blades" in High Temperature Alloys for Gas Turbines and Other Applications, Dordrecht, Holland,1986, pp. 21-50

[3] Caron P., Khan T., Development of a new nickel based single crystal turbine blade alloy for very high temperatures. European Conference on Advanced Materials and Processes- Aachen (FRG) (Nov. 1989)

[4] K. Harris, G.L. Ericksson, R.E. Schwer "Development of CMSX-4 for Small Gas turbines, TMS-AIME, Fall Meeting, Philadelphia, PA, 3 oct. 83

[5] Giamei A.F., Anton D.L. Rhenium additions to a Ni-base superalloy : Effects on microstructure, Met Trans A, 16A (nov. 85) pp 1997-2005

[6] Fleury E., Remy L. Thermal-Mechanical fatigue behaviour of Nickel base superalloy single crystals Proceedings of ICF 7 - Houston, Texas - March 1989 - pp 133 - 1140

[7] Guedou J.Y., Honnorat Y., Thermomechanical Fatigue of turbo-engine blade superalloys - ASTM - STP 1186 Philadelphia, 1993, pp 157-175

[8] Bernard, H. and Remy, L. High Temperature Materials for Power Engineering, Kluwer Academic Publishers, Liege, Belgium, 1990, pp 1185-1194

TABLE 1. Nominal compositions (wt %) of the single crystal superalloys

☐	Ni	Co	Cr	W	Al	Ta	Mo	Ti	Re
MC2	base	5,08	7,89	7,99	5,05	5,96	2,11	1,49	-
CMSX4	base	9,70	6,47	6,50	5,63	6,50	0,56	1,01	2,9
AM3	base	5,61	8,04	4,91	5,86	3,43	2,20	2,00	-
AM1	base	6,5	7,8	5,7	5,2	7,9	2	1,1	-

TABLE 2.Heat treatments conditions

ALLOY	AM1	AM3	MC2	CMSX4
solution treatment	1300°C/3h	1305°C/3h	1315°C/3h	multi-step from 1277°C to1321°C (16h)
precipitation treatment	1100°C/5h	1050°C/16h	1100°C/5h	1080°C/4h
aging treatment	87°C/16h	850°C/24h	850°C/24h	870°C/16h

**Stress for rupture
in 300 hours (MPa)**

Figure 1 showing creep-rupture capability comparison with curves for AM1, MC2, CMSX4, and AM3 plotted against Temperature (°C) from 800 to 1150.
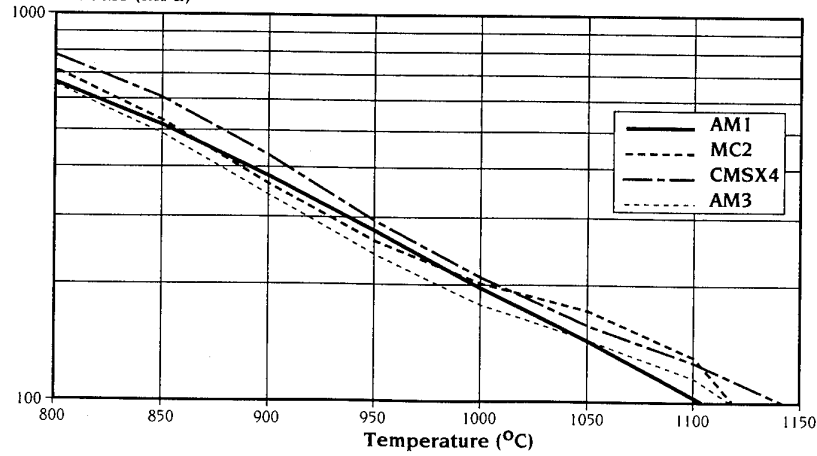
*Figure 1.*Creep-rupture capability comparison

Mechanical strain

Figure 2 showing "4 slopes" TMF cycle definition with Cooling and Heating arrows, temperature points at 650, 750, 950, 1100 plotted against Temperature (°C).
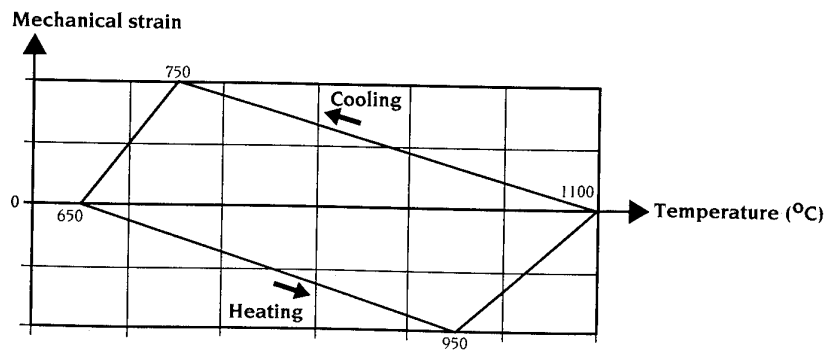
Figure 2."4 slopes" TMF cycle definition

Life (cycles)

Figure 3 bar chart showing TMF lives comparison for CMSX4, AM3, AM1, MC2 (Bare materials) and AM1 (Coated), with label "4 slopes" TMF cycle $\Delta\varepsilon_m = \pm 0,5\%$.

*Figure 3.*TMF lives comparison

*Figure 4.*Illustration of fatigue crack initiation on
coated AM1 under TMF("4 slopes" cycle)
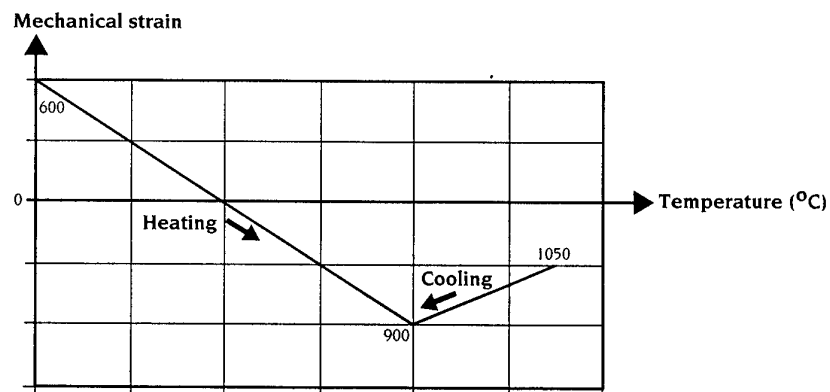
Figure 5."W" TMF cycle definition
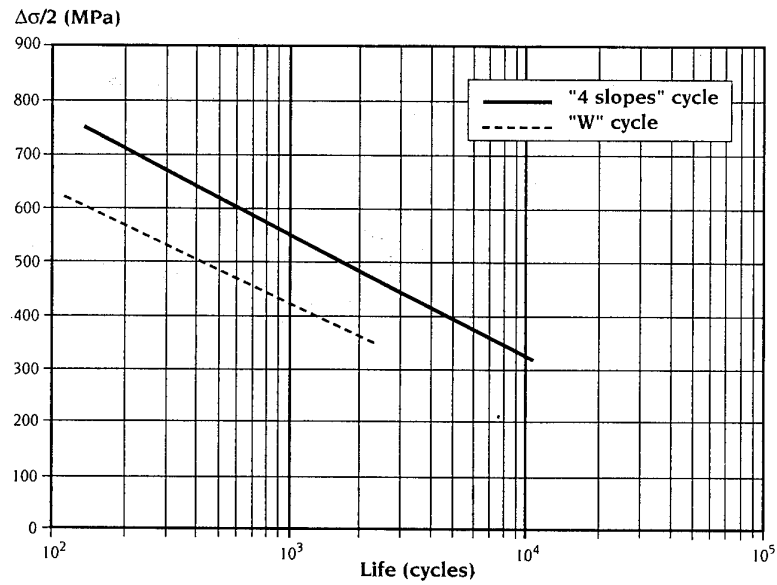
Figure 6. Influence of TMF cycle definition on life for
coated AM1
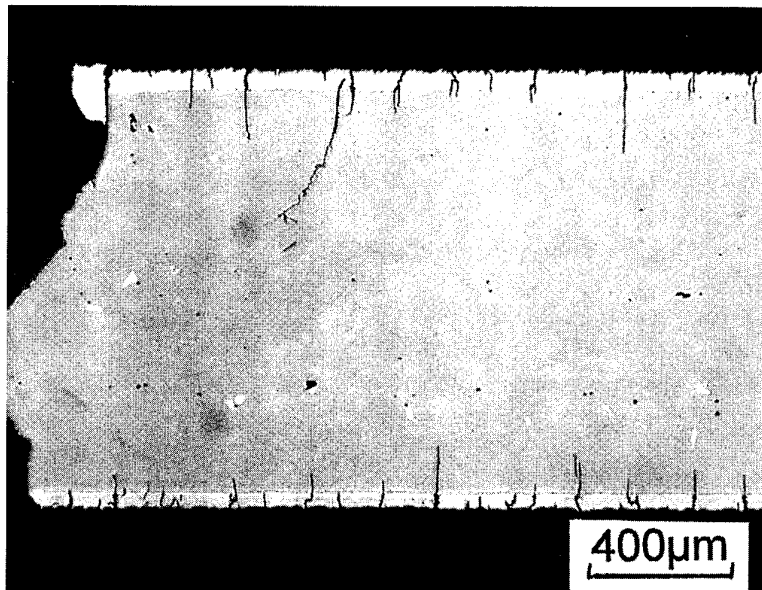
Figure 7. Illustration of fatigue crack initiation on
coated AM1 under TMF ("W" cycle)

DEFORMATION AND FAILURE MECHANISMS OF DS CM 247 LC UNDER TMF AND LCF LOADING

C. Sommer, M. Bayerlein and W. Hartnagel
ABB Corporate Research Centre
P.O. Box 10 13 32
D-69003 Heidelberg
Germany

SUMMARY
The deformation, crack initiation and crack propagation behavior of DS CM 247 LC in longitudinal and transverse orientation under LCF loading at 500°C to 1000°C and TMF loading (400-1000°C out-of-phase cycle) is described in this paper and discussed under the aspect of TMF life time prediction.

Different deformation and damage mechanisms were found for low temperature LCF, high temperature LCF and TMF loading. The deformation and damage behavior under TMF loading incorporates characteristics typical for low temperature LCF as well as characteristics typical for high temperature LCF. Cutting of γ' as well as interfacial network formation is observed. Cracks were found to initiate at strongly oxidized carbides similar to what is observed under high temperature LCF, the crack propagation however is a mixture of crystallographic and non-crystallographic crack growth. Cyclic plastic deformation at low temperatures (under low temperature LCF as well as under TMF loading) was found to be very detrimental.

The coincidence between TMF life data and LCF life data at a temperature close to the upper temperature of the TMF cycle on a total strain and equal strain rate basis m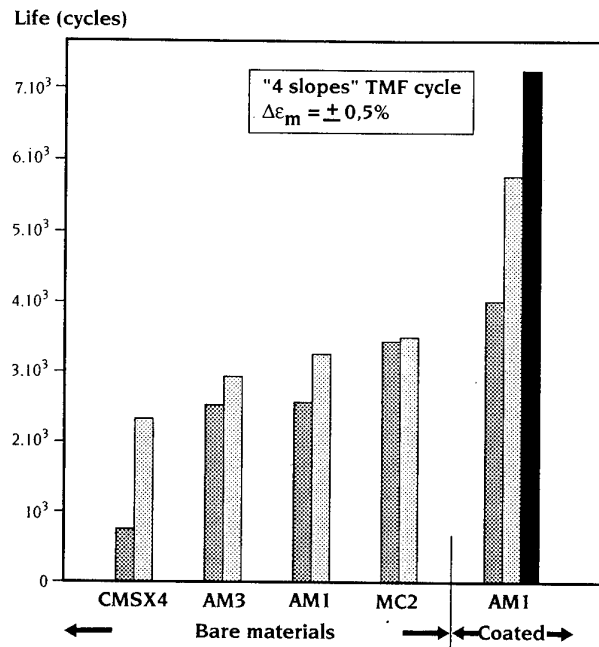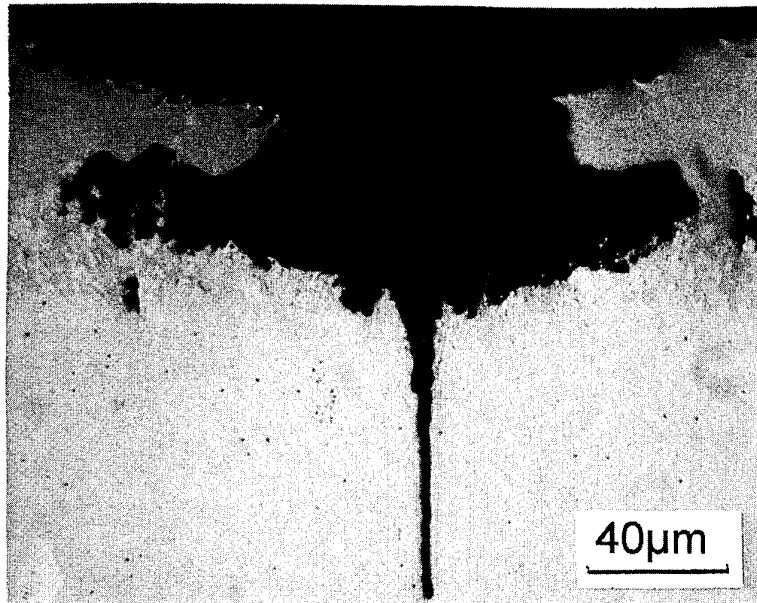aybe related to the oxidation controlled crack initiation mechanism which is identical for both types of loading or has to be regarded as fortuitous.

1. INTRODUCTION
In a recent paper by the authors phenomenological damage parameters for TMF life prediction have been evaluated and the question of TMF life prediction based upon LCF life data has been treated [1]. It has been shown that for this type of TMF loading which is typical for a volume element close to the surface of a cooled gas turbine blade
- TMF life data can be well correlated with both Total strain and Smith-Watson-Topper parameter.
- Inelastic strain related parameters like Manson-Coffin or the Ostergren parameter did not provide adequate results.
- TMF life (out-of-phase, 400-1000°C) can be adequately described by LCF life data obtained at 950°C on total strain and equal strain rate basis (cf. fig. 1).

Figure 2 shows a Manson-Coffin plot of plastic strain range $\Delta\varepsilon_{pl}$ vs. number of cycles until crack initiation for LCF loading at 500°C, 850°C, 950°C, 1000°C and TMF out-of-phase loading at 400-1000°C. Plastic deformation was found to be the more detrimental the lower the temperature.

It is evident that TMF lives and LCF lives obtained at 500°C are close to each other on a plastic strain range basis, whereas there is no correlation with high temperature LCF data.

The current paper provides some evidence on the deformation and failure mechanisms behind these apparently contradictory observations concerning the mechanical behavior. This is important 1. to understand the phenomenological findings and 2. to be aware of the limitations of a phenomenological description under complex loading conditions (especially when fatigue life data are transferred from a lab cycle to service conditions).

Only very limited information is available in literature on the deformation and damage mechanisms of DS materials, especially for DS CM 247 LC and under TMF loading conditions. The basic deformation mechanisms described for SX materials (cf. e.g. [2, 3]) of course are valid also for DS materials.

2. EXPERIMENTAL DETAILS

2.1 Material
The nominal composition of DS CM 247 LC in weight % is Ni: bal., Cr: 8.1, Co: 9.2, Mo: 0.5, W: 9.5, Ta: 3.2, Ti: 0.7, Al: 5.6, Zr: 0.01, B: 0.01, C: 0.07, Hf: 1.4. The material was used in the fully heat-treated condition. The microstructure consisted mostly of cuboidal γ'-particles with a size of 0.55 μm embedded in the γ-matrix. The volume fraction of γ' was approximately 70 %. The alloy was provided in form of slabs with the longitudinal direction being parallel to [001]. The maximum angular deviation from [001] was limited to 15°.

2.2 Testing
Threaded cylindrical specimens with a diameter of 10 mm and a gauge length of 30 mm were machined out of slabs in longitudinal (0°) and transverse (90°) direction. Isothermal LCF tests and TMF tests were run on closed-loop servohydraulic testing machines which were equipped with 200 kHz induction heating facilities. Temperature was measured with a thermocouple which had been locally rolled to facilitate fixing around the circumference in the middle of the specimen. For strain measurement a strain gauge system with 15 mm distance between the ceramic tips was applied. The specimens were subjected to controlled temperature-strain-time cycles using commercial software.

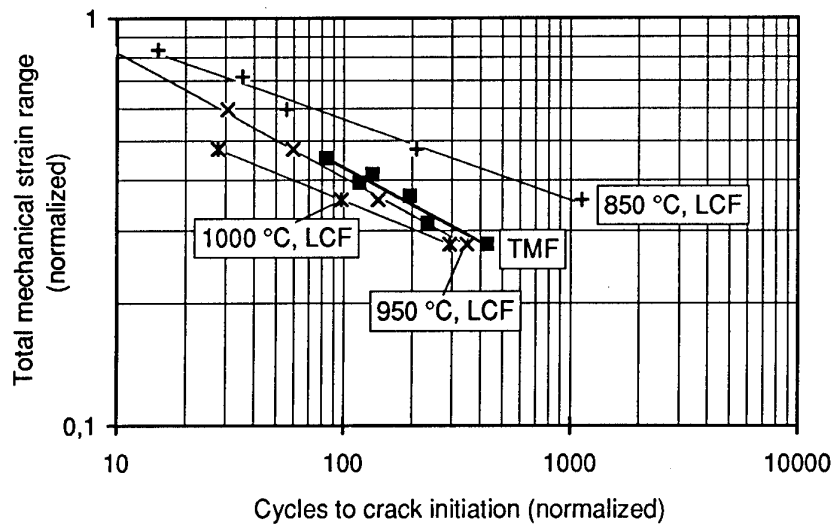Fig. 1: TMF and LCF life data in normalized $\Delta\varepsilon_t$ - N_i (2%) representation. LCF lives corrected to frequency of TMF tests, from [1].
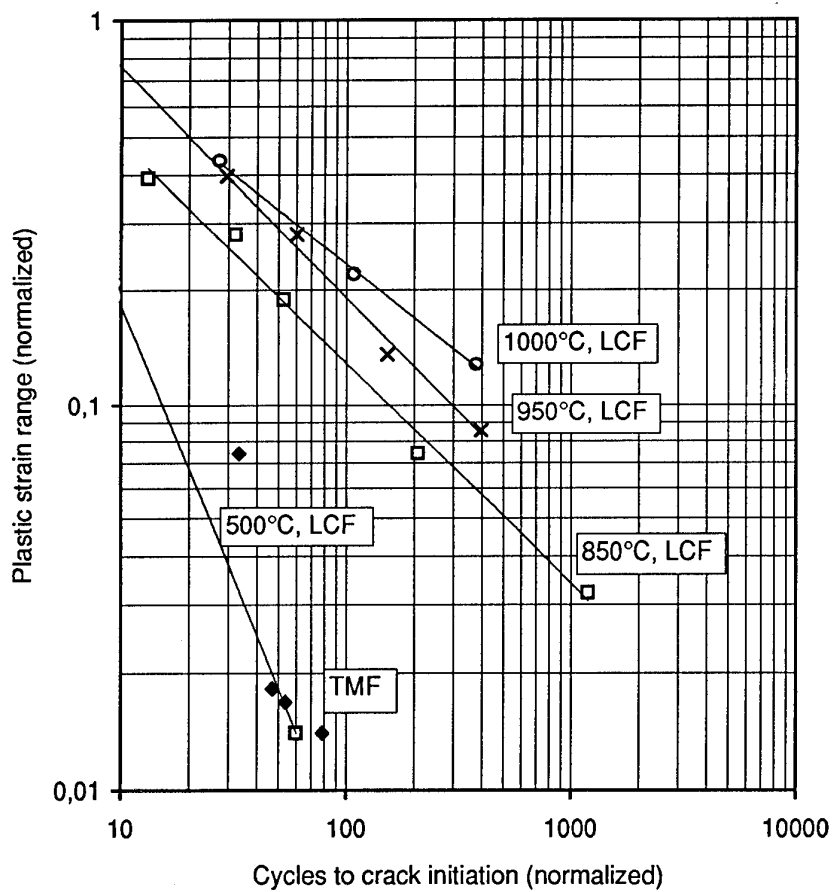

Fig. 2: Manson-Coffin-behavior of DS CM 247 LC under LCF and TMF (out-of-phase, 400-1000°C) loading.

Isothermal LCF tests were performed according to ASTM E 606. Testing temperatures were 500°C, 850°C, 950°C and 1000°C. All tests were conducted under total strain control with various total strain ranges $\Delta\varepsilon_t$ and a constant strain rate of 6 %/min.

The TMF tests were performed with temperature cycles between 400°C and 1000°C, a heating/cooling rate of 3.8 K/s, $R\varepsilon = -\infty$ and a frequency of $3.2 \cdot 10^{-3}$ s^{-1}. Cooling was achieved by heat flux through the grips. No forced cooling was applied in order to achieve a low dynamic axial temperature gradient (maximum 1 K/mm in the gauge length covered by the extensometer). All tests were carried out for various mechanical strain ranges $\Delta\varepsilon_m$ with temperature and mechanical strain being out-of-phase. The number of cycles to crack initiation $N_i(2\%)$ was determined at a decrease of the tensile stress by 2%, the number of cycles to failure N_f at a decrease by 50%.

2.3. Fractographic and microstructural investigations

In order to characterize deformation mechanisms with regard to slip systems, dislocation density, slip localization and γ'-dislocation interaction bulk material of specimens deformed until failure was investigated by transmission electron microscopy (TEM). All investigations were carried out on longitudinal sections, i.e. the stress axis (approximately parallel to the <001> direction) lies in the plane of the section. The secondary orientation is random.

The γ' degradation has been characterized on longitudinal sections of specimens cyclically deformed until failure by means of scanning electron microscopy (SEM). The γ' morphology has been made visible by an oxalic acid etching. Information on the γ' degradation was also gained by the TEM investigations.

The crack initiation under fatigue loading has been characterized by evaluation of the fracture surfaces and the original surfaces of failed specimens by means of optical microscopy (OM) and SEM. Some additional information on crack iniation could be gained also by the evaluation of short cracks in longitudinal sections.

The crack propagation has been characterized by evaluation of fracture surfaces and longitudinal sections by OM and SEM. The orientation of crystallographic facets on the fracture surface was determined by means of Laue X-ray back reflection technique.

3. RESULTS

3.1. Deformation mechanisms

The dislocation structures observed under LCF loading are in coincidence with the results reported in literature for the respective temperatures. Nevertheless, some representative figures are shown and described in the following section, since these results are important for the comparison with the dislocation structures that develop under TMF loading.

Dislocation - γ' interaction
Under LCF loading at 500°C Orowan bowing of the dislocations in matrix channels was observed (fig. 3a).

Cutting of γ' by coupled superpartial dislocations on sharp slip bands was found (figs. 3a).

Under LCF loading at 850°C only matrix / interface dislocations were found (fig. 3b) with the exception of loading with very high plastic strain ranges where also cutting of γ' by coupled superpartial dislocations was observed. The cutting is however less localized, the character of slip is more homogenous than at 500°C. Thermally activated dislocation climb and cross slip is active above 850°C.

Under LCF loading at 950°C and 1000°C all mobile dislocations were localized in the matrix channels (figs. 3 c, d). Immobile dislocations were present in the γ-γ' interfaces where they minimize the misfit strains between γ and γ'.

Under TMF loading (400°C - 1000°C, out-of-phase) dislocation structures were observed which originate from both low temperature and high temperature deformation: cutting of γ' by superpartial dislocations as well as interfacial networks were observed (figs. 4 a, b). Figure 5 shows slip bands adjacent to a crack in the vicinity of the disastrous crack, i.e. at a site of locally increased cyclic plastic deformation.

Dislocation densities
The dislocation density in fatigue loaded specimens is strongly dependent on temperature and plastic strain range as would be expected.

Also the distribution of dislocations in γ, γ' and the γ-γ' interface is strongly dependent on temperature. At 500°C the dislocations are located mainly in the matrix channels and partly in γ', whereas at high temperatures the development of dislocation networks in the γ-γ' interface is observed, especially for higher test durations.

In TMF loaded specimens the dislocation distribution is different from low temperature LCF as well as from high temperature LCF behavior. The dislocation density in γ and in the γ-γ' interface is similar to high temperature LCF. The dislocation density in γ' however is similar to LCF at 500°C.

Table I gives an qualitative overview of the dislocation densities in γ, γ' and the γ-γ' interface in dependence of temperature and strain range.

Slip localization
Besides the overall dislocation densities the character of slip and the slip localization is important for a correlation with the mechanical behavior. Slip is very planar and much stronger localized to sharp slip planes at 500°C (cf. fig. 3a). At high temperatures slip is more wavy and much more homogenous (cf. e.g. fig. 3c).

3.2 Change of γ' morphology

The initial γ' size and morphology is not stable under long term temperature exposure. More or less isotropic coarsening is observed for high temperature loading without or with symmetrical stress (LCF).
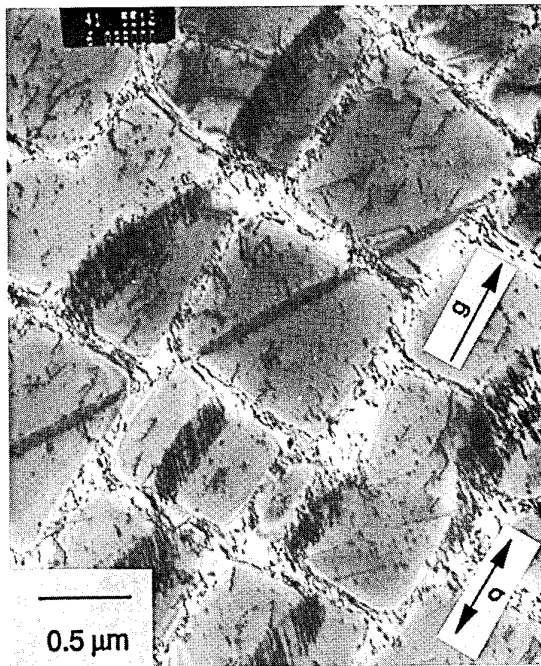
a) 500°C, $\Delta\varepsilon_{pl}$ = 0.15%: Cuboidal γ′. High dislocation density. Dislocations spread in matrix channels und cut γ′. Sharp slip bands.
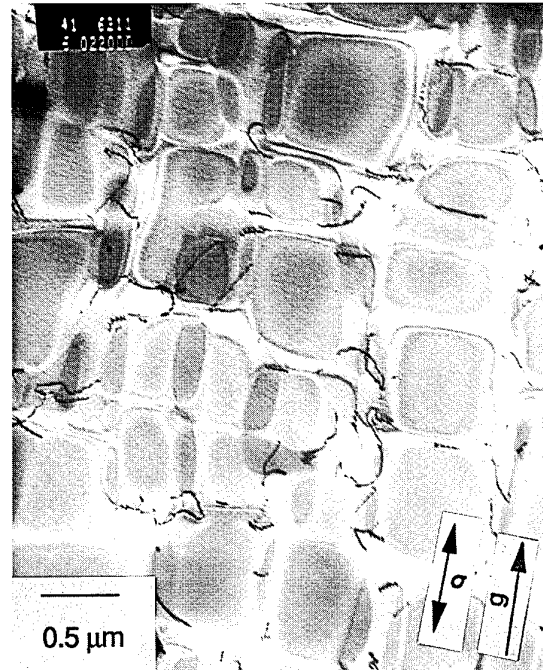
b) 850°C, $\Delta\varepsilon_{pl}$ = 0.14%: γ′ nearly cuboidal. Low dislocation density. Dislocations in matrix channels.
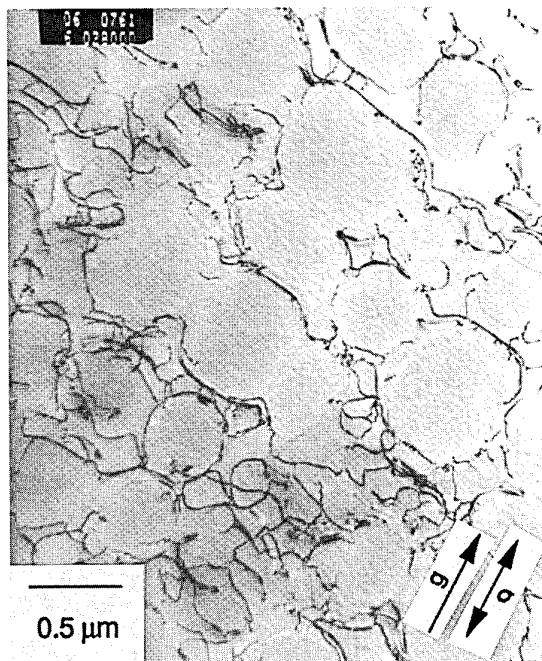
c) 950°C, $\Delta\varepsilon_{pl}$ = 0.28%: Edges of γ′ rounded. Dislocations in matrix channels, mainly at γ-γ′ interface.
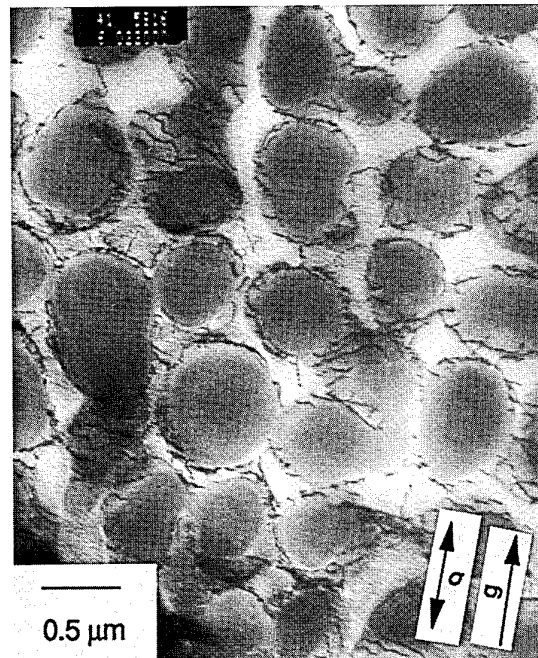
d) 1000°C, $\Delta\varepsilon_{pl}$ = 0.31%: γ′ rounded. Low dislocation density. Dislocations preferentially in γ-γ′ interface. Beginning of network formation.

Fig. 3: Dislocation structure and morphology of γ′ precipitations in LCF loaded specimens. TEM, bright field.
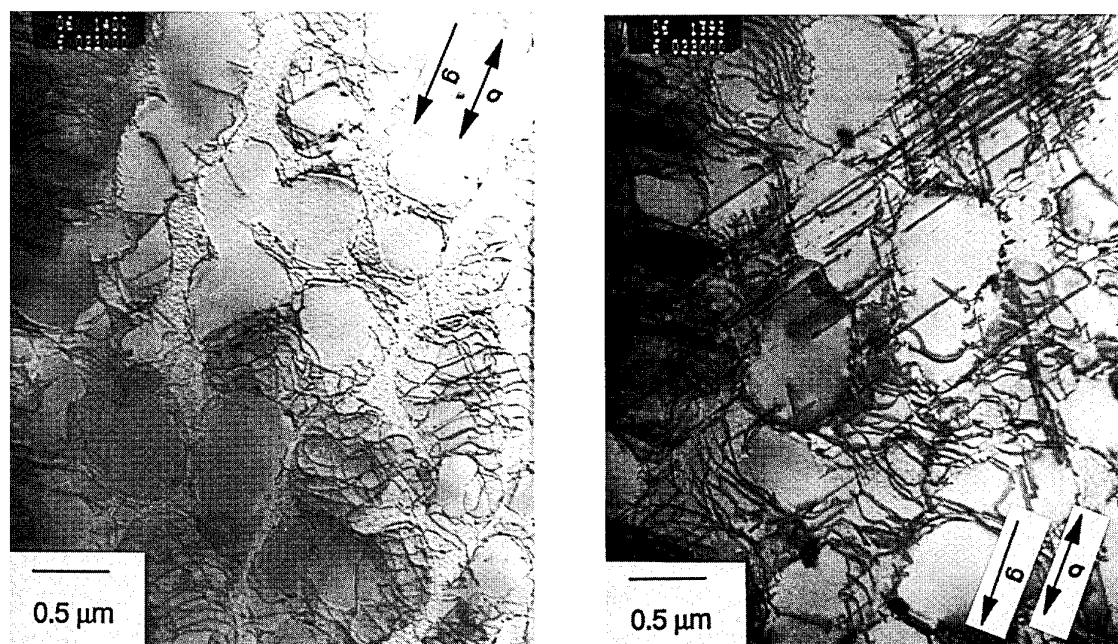
a) network formation

b) dislocations cutting γ′

Fig. 4 : Dislocation structure and morphology of γ′ precipitations in TMF loaded specimen. Out-of-phase, 400-1000°C, $\Delta\varepsilon_m$ = 1.04%: $\Delta\varepsilon_{pl}$ = 0.01%:

Table 1: Dislocation densities in γ, γ′ and γ-γ′ interface in LCF and TMF loaded specimens

Temperature	Strain range	Dislocation density in		
		γ	γ-γ′ interface	γ′
500°C	low	high	low	medium
500°C	high	very high	low	high
850°C	low	low	very low	very low
850°C	high	medium	low	low
950°C/1000°C	low	low	low to medium	zero
950°C/1000°C	high	low	medium	zero
TMF 400-1000°C	low	very low to low	medium	low
TMF 400-1000°C	high	low	medium	low to medium

Under thermal exposure with an uniaxial stress component or an unsymmetrical stress amplitude directional coarsening and rafting is found. This holds especially for creep loading. The directional coarsening or rafting perpendicular to the tensile stress axis is generally found in Ni-base superalloys with a negative γ-γ′ misfit (DS CM 247 LC, CMSX-4). The rafting is primarily a stress induced phenomenon. Under low stresses with or without low dislocation activity long straight rafts are found, whereas zig-zag rafts are formed under creep loading with considerable dislocation movement.

An example for the directional coarsening of γ′ under TMF loading is presented in fig. 5. Since compressive stresses develop at the maximum temperature of the TMF cycle no rafts perpendicular to the stress axis, but rods parallel to the stress axis appear. Short times at high temperatures are sufficient for directional coarsening (the total duration at temperatures above 900°C in this test was only 15 h). In fig. 5 also slip bands adjacent to a crack in the vicinity of the disastrous crack are apparent. Within these slip bands a breakdown of the ordered rafted γ′ morphology can be observed. Note the sharp slip lines (marked) with a γ′ displacement.

Both coarsening and rafting of γ′ affect the interaction of dislocations with the γ′ precipitations and thus the mechanical behavior (cf. e.g. [3, 7]).

Fig. 5: γ'-morphology after TMF-loading, out-of-phase, 400-1000°C, $\Delta\varepsilon_m = 1.04\%$, Raftening parallel to stress axis and slip bands adjacent to crack. SEM. Oxalic acid etching.

3.3. Damage mechanisms

Crack initiation

Fatigue crack initiation is strongly dependent on temperature and especially at high temperatures on the orientation of the material (longitudinal - transverse).

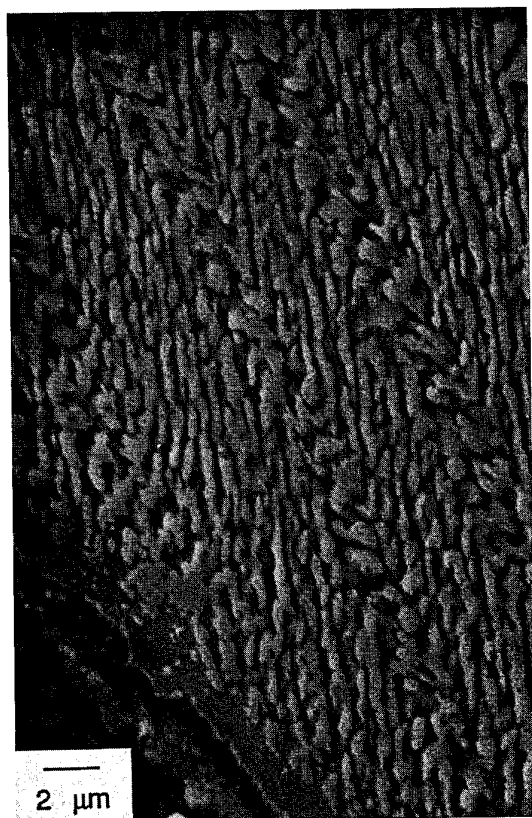At 500°C (low temperature behavior) casting porosity was found to be the most common crack initiation site in longitudinal as well as in transverse specimens, cf. fig. 6a. The pores which had initiated cracks leading to failure were typical casting micropores. This observation is in coincidence with results on DS and SX Ni-base superalloys [6, 8]. Grain boundaries were found to play a minor role as crack initiation site, also in transverse specimens. The material was observed to be very sensitive to surface defects under 500°C LCF loading. Cracks were found to initiate at thermocouple spot welds even in the fillet radius or the specimens shaft with a cross section 2.1 times higher than the cross section of the gauge length. As a consequence a different method for the adaption of the thermocouple has been used.

At temperatures above 850°C (high temperature behavior) oxidized carbides, cf. fig. 6b, and grain boundaries were observed to be the most common crack initiation sites. Crack initiation at casting porosity was found to play a minor role. The role of oxidation for crack initiation is not yet clear. Tests in vacuum are planned to clarify this point. Due to the high number of surface carbides numerous potential crack initiation sites exist under high temperature LCF loading.

Grain boundaries were found to be an important crack initiation site in transverse specimens under LCF loading at high temperature. A grain boundary intersecting the surface of a longitudinal specimen could also as an crack initiation site.

The crack initiation behavior under 400-1000°C TMF loading was found to be very similar to the high temperature LCF behavior. Cracks were generally observed to initiate at strongly oxidized surface carbides, cf. fig. 7. This is also reported for conventional cast IN100 under TMF cycling [9]. The fatal crack was found to grow together from multiple crack initiatiation sites. These observations are in coincidence with results reported on single crystal Ni base superalloys subjected to TMF loading with a -135°-phase shift cycle [10]. In transverse specimens cracks were found to initiate both at oxidized carbides and at grain boundaries.

Crack propagation

Also the fatigue crack propagation behavior was found to depend strongly on temperature.

Under 500°C LCF loading initial crack propagation occured non-crystallographic and perpendicular to the stress axis (mode I), cf. fig. 6a, 8a. The further crack propagation was mainly a crystallographic mode II crack growth on slip planes, cf. fig. 8a. This type of crack propagation is often referred to as "stage I" fatigue crack growth. Crack propagation occurred on {111} planes as similarly reported in literature (cf. e.g. [6, 11]). In this mode the crack grows due to shear stresses parallel to the crack path. The crystallographic crack growth can be correlated with the deformation behavior observed for the low temperature range: The crack propagates along the sharp slip bands with high dislocation activity. The transition from the non-crystallographic mode I to the crystallographic mode II seems to occur the sooner the higher the strain amplitude. Also in transverse specimens mainly crystallographic fatigue crack growth was observed under low temperature low cycle fatigue.

Under 850°C - 1000°C LCF loading only non-crystallographic crack growth was found. In longitudinal specimens cracks deeper than appr. 0.2 mm were observed to grow preferentially along eutectics and carbides, cf. fig. 8b. The resulting fracture surface is relatively rough. Grain boundaries were found to deflect cracks from a growth direction approximately perpendicular to the stress axis. In transverse specimens longer cracks were found to spread preferentially along grain boundaries.

Under 400-1000°C TMF loading a mixture between crystallographic and non-crystallographic crack propagation was observed for cracks with a crack depth of more than 0.2-0.3 mm, cf. fig. 9. The fracture surface consisted partly of small crystallographic facets. The original surface of the specimen revealed slip traces at the tips of small cracks. These features are an indication for low temperature crack propagation, especially if the high
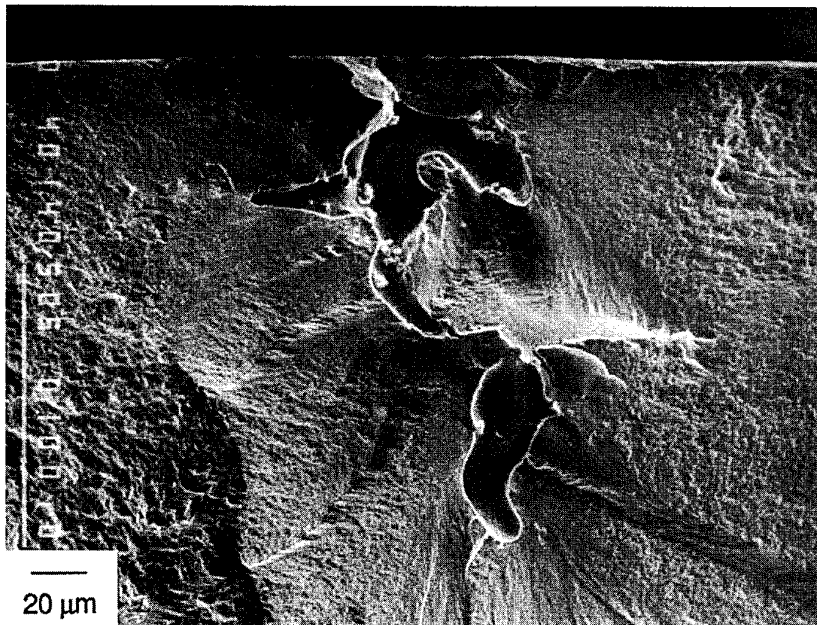
a) 500°C, $\Delta\varepsilon_t$ = 1.2%, fracture surface: crack initiation at casting porosity.
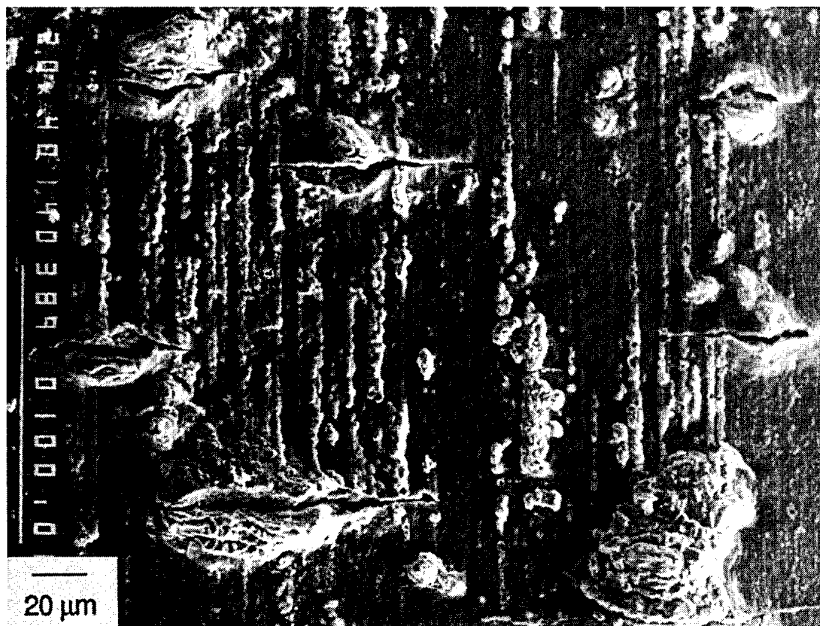
b) 950°C, $\Delta\varepsilon_t$ = 0.9%, specimen surface: crack initiation at strongly oxidized carbides.

Fig. 6: Crack initiation under LCF loading.
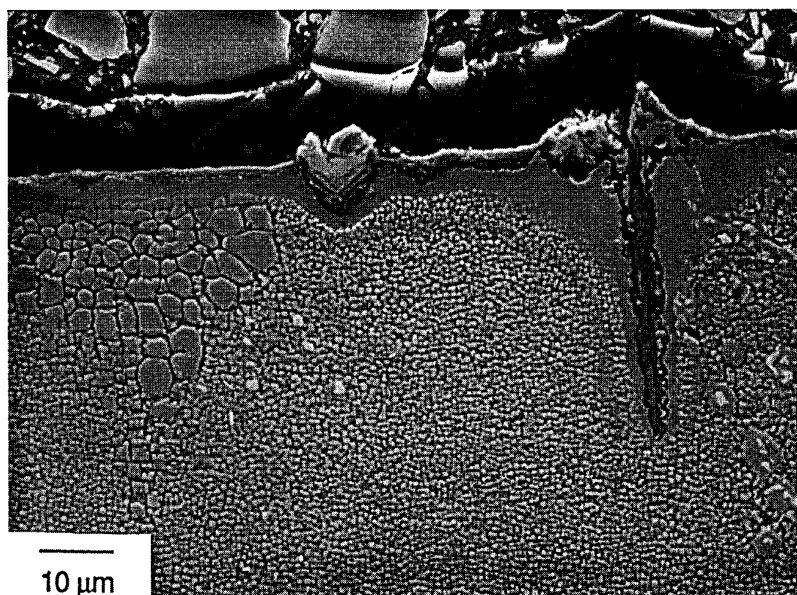
Fig. 7: Crack initiation under TMF loading, out-of-phase, 400°C - 1000°C, $\Delta\varepsilon_m$ = 0.79%, longitudinal section, oxalic acid etching: crack initiation at strongly oxidized carbides.

tensile stresses which develop at the low temperatures under out-of-phase TMF loading are taken into consideration. In transverse specimens longer cracks were found to propagate preferentially along grain boundaries under TMF loading similar to what is found under high temperature LCF loading.

4. DISCUSSION

Neither the good coincidence of TMF lives wizh LCF lives obtained at the maximum temperature of the TMF cycle on a total strain basis (cf. fig. 1) nor the relatively good coincidence of TMF lives and low temperature LCF lives on a plastic strain range basis (cf. fig. 2) are reflected by coincidence of deformation and failure mechanisms. The results presented in this paper clearly show that TMF loading incorporates deformation and failure mechanisms typical for the low temperature regime as well as mechanisms typical for the high temperature regime. Table 2 summarizes the similarities and differences.

4.1 Detrimental effect of slip localization at low temperatures

The slopes of the Manson-Coffin curves for LCF loading at 500°C and for TMF loading are very steep, the Manson-Coffin-exponent m = -1.4 for LCF at 500°C is considerably lower than values commonly found for ductile metals (m = -0.5...-0.6) or even for high strength steels (m = -0.9...-1.2) [5]. The reduction of lives for isothermal fatigue tests at 500°C compared to the fatigue lives at higher temperatures is the more pronounced the lower the plastic strain range. For 850°C and 950°C "normal" slopes of the Manson-Coffin curves were found for DS CM 247 LC.

In contrast to high strength steels the high sensitivity against cyclic plastic deformation is not reflected by a low tensile ductility for DS CM 247 LC. Rather DS CM 247 LC exhibits a tensile elongation of about 15 % at 500°C, so it

shows no brittle behavior. Rather, the high sensitivity against cyclic plastic deformation is a consequence of the pronounced cyclic slip localization in sharp slip bands with strong localized damage, whereas the slip is much less localized in tensile deformation.

Thus, the coincidence of low temperature LCF and out-of-phase TMF loading with regard to Manson-Coffin behavior can be attributed to the lack of stress relaxation at the crack tip and the localization of deformation. The higher stress at the crack tip is expected to lead to higher crack propagation rates.

Evaluations presented in an earlier paper on the phenomenological damage parameters for TMF life prediction [1] showed that inelastic strain based parameters did not provide adequate results for TMF life prediction. This was explained by the relatively high measurement error compared to the relatively low plastic strain ranges observed. A further aspect is that plastic deformation is not homogenously distributed in the material. The macroscopically measured plastic strain range does consequently not reflect the deformation mechanisms on the microstructural scale. Plastic strain range was also found to be an unsuitable parameter for correlation of LCF data obtained at 600°C on DS CM 247 and DS Rene80H [6].

From the present results it has to be concluded that cyclic plastic deformation under stabilized conditions, i.e. after the initial cycles, has to be avoided by an appropriate design.

4.2 Damage mechanisms controlling TMF life

The crack initiation behavior showed a high similarity between TMF and high temperature LCF behavior whereas the deformation behavior and the crack propagation behavior were found to be different. The different
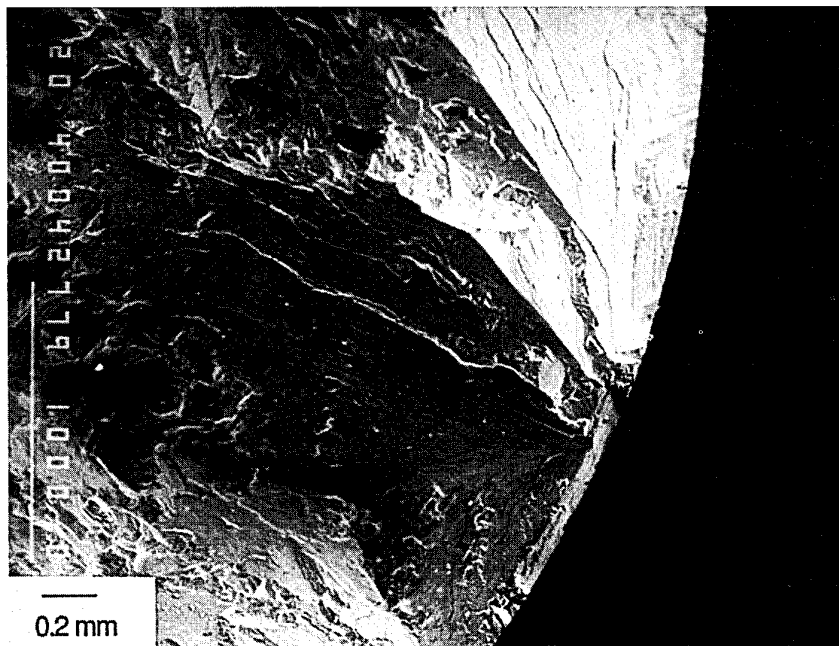
a) 500°C, $\Delta\varepsilon_t$ = 1.8%: crystallographic crack propagation.
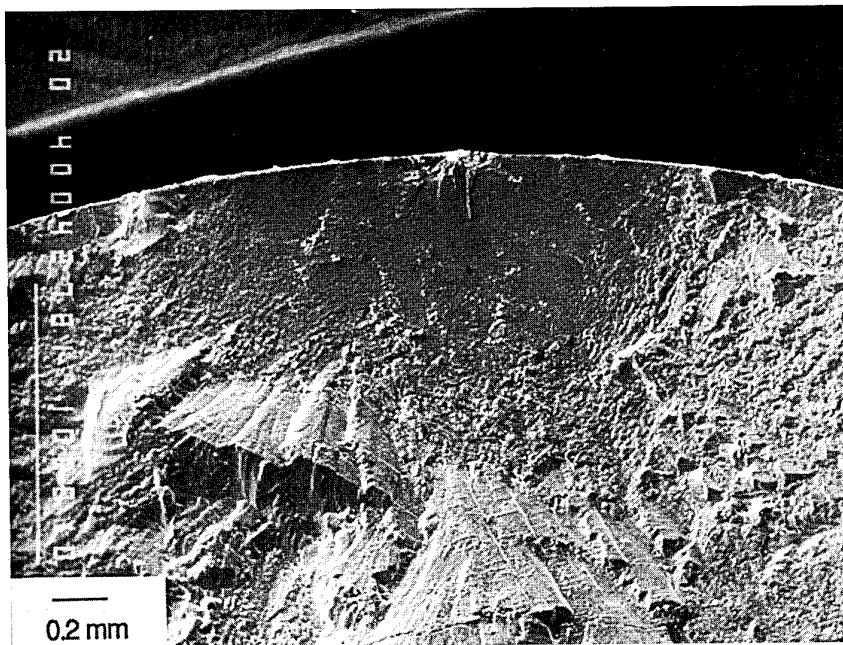
b) 850°C, $\Delta\varepsilon_t$ = 0.9%: mode I crack propagation.

Fig. 8: Crack propagation under LCF loading, fracture surfaces.
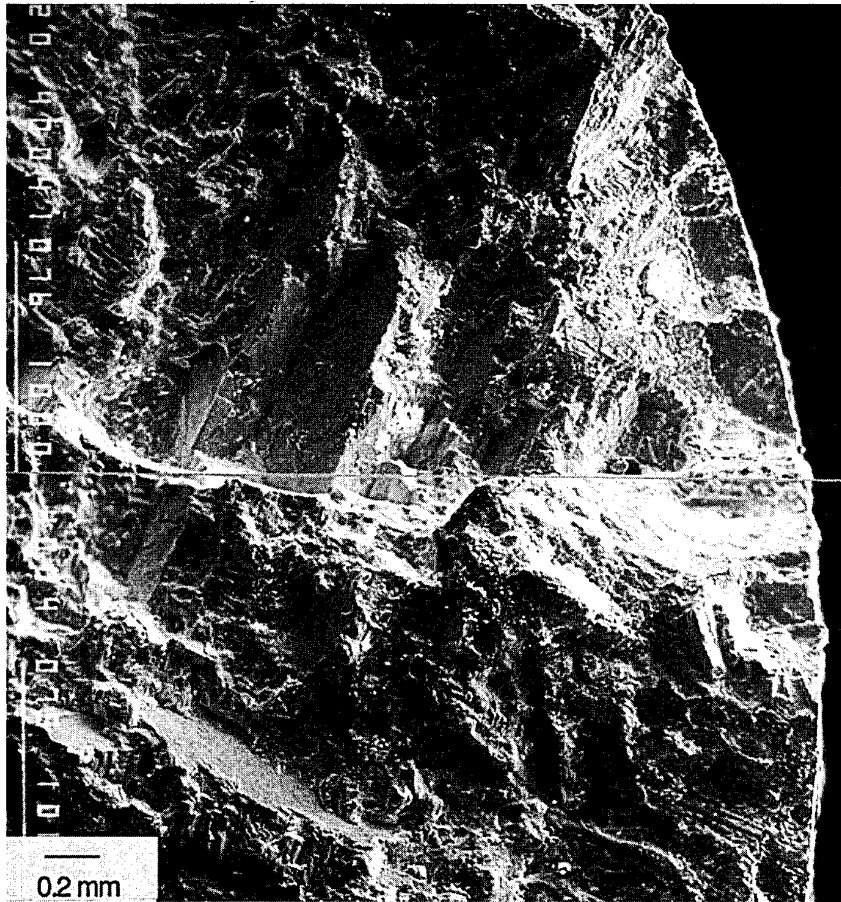
Fig 9: Crack propagation under TMF loading, out-of-phase, 400°C - 1000°C, $\Delta\varepsilon_m$ = 0.79%, fracture surface: mixed mode crack propagation, partly crystallographic facets.

Table 2: Overview of deformation and damage mechanisms observed under LCF and TMF loading

Mechanism	Low temperature LCF	High temperature LCF	TMF
Deformation mechanism	Planar slip Orowan bowing Cutting of γ' Slip partially localized in slip bands.	Wavy slip, cross-slip, climb Dislocation network formation in γ-γ' interface	Cutting of γ' Partial slip localization Network formation in γ-γ' interface
Crack initiation longitudinal	Casting porosity Grain boundaries Surface defects	Oxidized surface carbides Grain boundaries Casting porosity	Oxidized surface carbides Grain boundaries
Crack initiation transverse	Casting porosity Grain boundaries Surface defects	Grain boundaries Oxidized surface carbides	Grain boundaries Oxidized surface carbides
Crack propagation longitudinal	Crystallographic (mode II)	Non-crystallographic (mode I)	Mixture of modes I and II
Crack propagation transverse	Crystallographic (mode II)	Non-crystallographic (mode I) Grain boundaries	Non-crystallographic (mode I) Grain boundaries

deformation mechanisms were not found to be reflected in different crack initiation mechanisms. Since crack initiation is observed at strongly oxidized carbides both under TMF and under high temperature LCF loading it can be concluded that oxidation processes are relevant for crack initiation independent of the stress state at high temperature. A oxidation mechanism for crack initiation and early crack propagation aspects is discussed under life prediction aspects by Arana et al. [12].

The role of the crack initiation and early crack propagation phase (up to 0.3 mm) in quantitative terms is unclear. Informations on the damage evolution are important for the selection of adequate life prediction rules and for damage monitoring in engine components.

The experimental techniques necessary for such a quantification are arduous since only replication techniques can be used. Literature results which quantify the different stages of fatigue life are scarce. From the results of Okazaki et al. [6] for LCF loading of DS CM 247 LC at 600°C can be concluded that about 2/3 of the fatigue life ($N_f \approx 5500$) are spent for crack initiation and early crack propagation and 1/3 is spent for the further propagation. However, these findings cannot be read across to the high temperature behavior since at 600°C an oxidation mechanism probably does not play a dominant role.

The situation is of course different for real engine components which are applied with an oxidation resistant surface coating avoiding surface carbide oxidation. Tests on DS CM 247 LC with an MCrAlY overlay coating [13] showed a prolongation of LCF life at 1000°C by a factor of 2 as compared to bare base material. TMF life, however, was considerably reduced due to early coating crack initiation at the low temperature regime of the TMF cycle. These results clearly indicate the importance of the crack initiation phase for component life time prediction. For the case of coated components a TMF life prediction by LCF data obtained at the maximum temperature of the cycle may provide non-conservative results due to the fact that the crack initiation mechanisms are different.

From the fact that oxidation is one of the relevant mechanisms controlling TMF life it should be concluded that TMF life models have to consider oxidation by an appropriate term.

5. CONCLUSIONS

The deformation and failure mechanisms observed under TMF loading incorporate features typical for low temperature LCF as well as features typical for high temperature LCF. Cutting of γ' as well as formation of a dislocation network in the γ-γ' interface is observed. Crack initiation is found at strongly oxidized surface carbides, similar to high temperature LCF. For crack propagation however a mixture of crystallographic (mode II) crack growth typical for low temperature LCF and of mode I crack growth following carbides and eutectics typical for high temperature LCF was observed. The sensitivity against plastic deformation is similar to low temperature LCF.

On this background the coincidence between TMF and LCF life data at a temperature close to the maximum temperature of the TMF cycle on a total strain and equal strain rate basis

can be interpreted in two ways: Either the oxidation controlled crack initiation and early crack growth that is found to be the only identical mechanism for high temperature LCF and TMF loading is life controlling which has to be finally clarified, or the coincidence has to be regarded as fortuitous.

Additional tests have to be carried out to better quantify the proportions of fatigue life spent during the crack initiation and early crack growth phase (up to 0.2 mm) versus the further crack propagation phase to settle a deeper understanding which damage mechanisms are really relevant for TMF life. Furthermore tests in vacuum could support the understanding of the role of oxidation.

LITERATURE

1   Bayerlein, M., Hartnagel, W. and Sommer, C., "Phenomenological Damage Parameters for TMF Life Prediction of DS CM 247 LC", in Proc. of Int. Symp. on "Fatigue under Thermal and Mechanical Loading", May 22-24, 1995, Petten, in press.

2   McLean, M., "Directionally Solidified Materials for High Temperature Service", The Metals Society, 1983, pp 151-205.

3   Caron, P., Ohta, Y., Nakagawa, Y.G. and Khan, T., "Creep Deformation Anisotropy in Single Crystal Superalloys", in: "Superalloys 1988", ed. by Reichman, S., pp 215-224.

4   Duhl, D.N., "Directionally Solidified Superalloys", in: "Superalloys II", ed. by Sims, C.T., Stoloff, N.S. and Hagel, W.C., New York, 1987, pp 189-214.

5   Polak, J., "Cyclic Plasticity and Low Cycle Fatigue Life of Metals", Materials Science Monographs 63, Elsevier, 1991, pp 286-292.

6   Okazaki, M., Tabata, T. and Nohmi, S., "Intrinsic Stage I Crack Growth of Directionally Solidified Ni-Base Superalloys during Low-Cycle Fatigue at Elevated Temperature", Met. Trans. A 21 A, 1990, pp 2201-2208.

7   Baldan, A., "Relationship between Rafted γ' Morphology and Creep Resistance of a Nickel-Based Superalloy", in: "Superalloys 1992", ed. by Antolovich, S.D. et al., pp 647-656.

8   Anton, D.L., "Low Cycle Fatigue Characteristics of <001> and Randomly Aligned Superalloy Single Crystals", Acta metall. 32, 1984, pp 1669-1679.

9   Malpertu, J.L. and Remy, L., "Thermomechanical Fatigue Behavior of a Superalloy". In: "Low Cycle Fatigue", ed. by H. D. Solomon et al., ASTM STP 942, 1988, pp 657-671.

10 Affeldt, E.E., Timm, J. and Bennett, A., "Importance of Crack Growth to Damage under TMF Loading", in Proc. of Int. Symp. on "Fatigue under Thermal and

Mechanical Loading", May 22-24, 1995, Petten, in press.

11 Goldschmidt, D., "Einkristalline Gasturbinen-schaufeln aus Nickelbasis-Legierungen", Mat.-wiss. u. Werkstofftech. 25, 1994, pp 373-382.

12 Arana, M., Martinez-Esnaola, J.M. and Bressers, J., "Crack Propagation and Life Prediction in a Nickel-Based Superalloy under TMF Conditions", in Proc. of Int. Symp. on "Fatigue under Thermal and Mechanical Loading", May 22-24, 1995, Petten, in press.

13 Sommer, C., Kowalewski, R., Mughrabi, H. and Bayerlein, M., unpublished results, 1995.

A Summary of Damage Mechanisms and Mechanical Property Degradation in Titanium Matrix Composites Subjected to TMF Loadings

Michael G. Castelli
NYMA, Inc.
NASA Lewis Research Center Group
21000 Brookpark Road, MS 49-7
Cleveland, Ohio 44135
U.S.A.

1. SUMMARY

An overview of thermomechanical fatigue (TMF) deformation, damage progression, and life is presented for multiple laminates of continuous SiC fiber reinforced titanium matrix composites (TMCs). Fundamental behaviors resulting from in-phase (IP) and out-of-phase (OP) TMF loadings are addressed with particular emphasis on the micromechanical damage mechanisms leading to macroscopic failure. This is accomplished through detailed microstructural examinations using both fractography and metallography. Further, macroscopic measures of damage progression based on mechanical property degradation are examined through data collected using an advanced TMF test technique which allows explicit measurements of the macroscopic *i*) isothermal static moduli and *ii*) coefficient of thermal expansion (CTE) as functions of the TMF cycles. Zero-tension TMF life results indicate analogous trends for both [0] and [0/90] TMC laminates. High stress IP TMF and mid to low stress OP TMF loadings are life-limiting in comparison to maximum temperature isothermal conditions. Dominant damage mechanisms changed with cycle type. Damage resulting from IP TMF conditions produces measurable decreases in static moduli but only minimal changes in CTE occur. Microstructural damage is dominated by extensive [0] fiber cracking with sparse matrix damage and no surface initiated cracking. Under OP TMF conditions, notable static moduli and CTE degradations are experienced. Here, conditions promote environment enhanced surface initiated cracking. The [0/90] TMC also exhibits matrix cracking initiated at debonded [90] fiber/matrix interfaces. Both laminates show little to no [0] fiber cracking. Zero-tension TMF of a [90] TMC reveals significant changes in both the static moduli and CTE under IP and OP conditions. Mechanical property degradation patterns are very similar to those exhibited under isothermal loadings. Further, damage mechanisms promoted by isothermal, IP TMF and OP TMF loadings are essentially identical, consisting of debonding at the fiber/matrix interface followed by matrix cracking which initiates at the debond and propagates transverse to the applied load.

2. INTRODUCTION

Over the past several years, continuous silicon carbide fiber reinforced titanium matrix composites (SiC-TMCs) have been the focus of many research programs aimed at evaluating these materials for high-temperature aeronautics and aerospace applications. Specifically, the use of theses materials in future super- and hypersonic flight vehicles and advanced propulsion systems is viewed as a critical enabling technology. As the vast majority of such applications involve combined cyclic stress and temperature conditions, it is essential to characterize and evaluate material behavior under thermomechanical fatigue (TMF) loadings with the ultimate goal of developing robust deformation and damage/life models applicable to in-service conditions. This task is no small challenge, as the material deformation and damage behaviors of SiC-TMC laminates are complicated by the vastly different thermal and mechanical properties of the constituents. Further, many of these complexities, such as the coefficient of thermal expansion (CTE) mismatch and matrix load shedding, are particularly highlighted under TMF conditions where dominant damage mechanisms have been shown by several investigators to be functions of not only the load-temperature phasing, but also the multitude of additional environmental and mechanical test parameters [refs. 1-8].

If TMF damage/life modeling for this class of materials is to be entirely successful, the fundamental microscopic damage mechanisms and their resulting impact on macroscopic mechanical properties and structural integrity must be well understood and accurately represented. Otherwise, reliable predictions of the multiaxial TMF behaviors resulting from proto-typical component loadings will not be possible. Investigations examining TMF damage/failure mechanisms in SiC-TMCs, generally do so in terms of the various observations made through metallographic and fractographic analyses, and most often on specimens cycled to complete fracture. Though this information is extremely useful for identifying the damage mechanisms, it is often times only qualitative, and has generally not been presented in conjunction with quantifyable degradations of the macroscopic mechanical properties. The difficulty associated with linking mechanical property degradation to observed microstructural damage arises from the fact that, unlike data generated under isothermal conditions, TMF data are not easily reduced to obtain critical properties, such as material stiffness (hereafter referred to as E). This results from

several conditions, one of which is the continuously dynamic temperature, which promotes a continuous change in E. Further, and more difficult to account for, is the high potential for the composite CTE to degrade with damage [see refs. 9 & 10], which causes the thermal strain range corresponding to the TMF cycle to change. It follows that without real time quantitative thermal strain information, mechanical strain information cannot be accurately reduced from the total strain component, and without the mechanical strain component, E cannot be measured. A select few studies can be cited where a measure of E or modulus degradation is given as a function of TMF cycles [refs. 2 & 3]; however, this measurement is subject to assumptions associated with a non-degrading thermal strain response, and further, is approximated from the dynamic temperature TMF stress-strain response.

To overcome the difficulty of quantifying property degradation during TMF, a specialized test technique was developed to assess i) the real-time mechanical and thermal strain components and ii) isothermal static stiffness as functions of accumulated TMF cycles, that is, progressive TMF damage states (ref. 9). Fully automated explicit isothermal E and CTE measurements were introduced into a TMF test without disturbing the specimen or significantly altering the test conditions. By tracking these two key mechanical properties, unique insights were gained into the ongoing TMF damage progression with quantitative trends established for damage/life model characterization and verification [refs. 11-13]. Thus, the objective of this study is to present a summary of the dominant damage mechanisms and mechanical property degradations in TMCs subjected to TMF loadings. Three SiC-TMC laminates will be discussed. Deformation and life behaviors will be briefly examined. TMF damage and failure mechanisms will be summarized through observations made using optical and scanning electron microscopy (SEM) analyses of fracture surfaces and metallographic sections, along with the presentation of mechanical property degradations (i.e., E and CTE) to assist in quantifying the state of material damage.

3. MATERIAL AND TEST DETAILS

For the purposes of summarizing the TMF damage mechanisms in TMCs, three laminates will be examined, namely [0]$_4$, [90]$_8$, and [0/90]$_s$. All of the laminates were continuously reinforced with SCS-6 fibers, a SiC fiber manufactured by Textron Specialty Materials, USA, with a nominal diameter of 140 μm. Two ß-titanium alloys were used in this study, that is, *TIMETAL* 21S {nominal composition Ti-15Mo-3Nb-3Al-0.2Si (wt. %)} and Ti-15-3 {nominal composition Ti-15V-3Cr-3Al-3Sn (wt. %)}. The [0]$_4$ and [0/90]$_s$ laminates were SCS-6/*TIMETAL* 21S and the [90]$_8$ TMC was SCS-6/Ti-15-3. The TMC panels were fabricated by hot isostatic pressing alternate layers of the Ti alloy foil and SCS-6 fiber mats; TiNb ribbon was used as crossweave material in the fiber mats to ensure fiber spacing and alignment during consolidation. The [0]$_4$ and

[90]$_8$ TMCs had a nominal fiber volume ratio of 35% and the [0/90]$_s$ laminate was slightly higher at 39%. The four and eight ply laminates had nominal thicknesses of 1 and 2 mm, respectively. Coupon test specimens were cut from the panels and given alloy microstructure stabilization heat treatments (8 hrs in vacuum at 621°C for the *TIMETAL* 21S TMCs; 24 hrs in vacuum at 700°C for the Ti-15-3 TMC). Additional material details can be found in refs. 11-13.

All TMF tests were conducted in laboratory air on a computer-controlled servo-hydraulic test system equipped with water-cooled grips. The tests were load-controlled, zero-tension (R$_\sigma$ = 0) with triangular waveforms for both load and temperature commands. The selection of load controlled R$_\sigma$ = 0 is not one which is necessarily the most representative of anticipated conditions within a given component, but rather it is necessitated by the thin plate material-specimen geometry if one desires to conduct the tests without the use of buckling guides. Note, the use of buckling guides in a TMF test would likely introduce insurmountable complications, compromising the controlled nature of the test, particularly in regards to dynamic temperature gradients and reasonable cycle periods. In-phase (IP) and out-of-phase (OP) loadings were examined and were defined as 0° and 180°, respectively, time phase shifts between the load and temperature waveforms. Axial strain measurements were made over a centrally located 12.7 mm gage length with a water-cooled extensometer mounted on the edge of the specimen. Intrinsic K-type thermocouples were used for temperature monitoring and closed-loop control. For the [0]$_4$ and [0/90]$_s$ TMCs, a cyclic period of 3 min and a temperature cycle of 150 to 650°C was used; for the [90]$_8$ TMC a cyclic period of 2 min and a temperature cycle of 200 to 427°C was used. For purposes of reporting number of cycles to failure (N$_f$) or fatigue life, specimen failure was defined as complete fracture of the specimen.
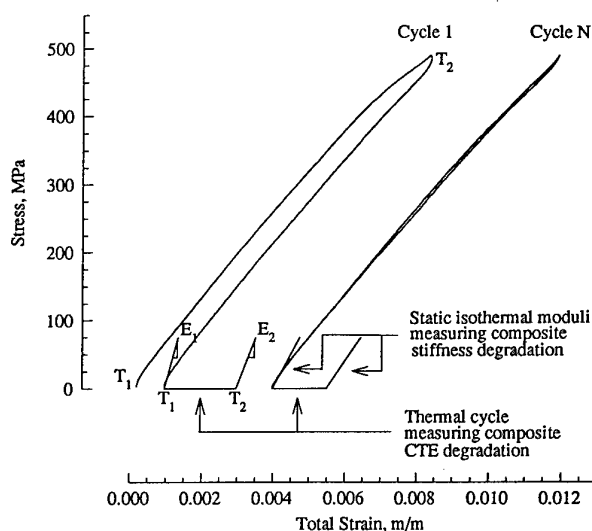

Fig. 1-Advanced TMF test technique enabling explicit measurement of isothermal E and CTE values.

The TMF test technique used in this study [ref. 9] to quantify both the E and the CTE degradations during TMF testing is shown graphically in Fig. 1. After each TMF cycle designated for data collection, the specimen was subjected to a thermal cycle under zero load, represented by the horizontal line from T_1 to T_2 at zero load. This thermal cycle allowed the real-time or "current" thermal strain properties of the composite to be explicitly measured with the high temperature extensometer. At the extremes of the thermal cycle (e.g., 150 and 650°C), the temperatures were briefly stabilized and small "elastic" loads were applied; these loadings are represented by the stress-strain lines in Fig. 1 with slopes marked E_1 and E_2. This allowed explicit measurement of the "current" isothermal material stiffness at both temperature extremes. Note that the E measurements are essentially a Young's modulus measurement with the maximum stress levels used to obtain E kept relatively small (80 MPa) to facilitate a linear-elastic response.

It is important to emphasize that E is defined here as the slope of the initial stress-strain response initiated from zero macroscopic load at an isothermal temperature. As measured, these E values may differ from those which can be estimated at comparable temperature points along the TMF deformation loops. For example, during an IP TMF test on the [0/90] TMC, the E_{650} value as measured by the technique discussed, will likely differ from the tangent modulus at 650°C taken from the deformation loop, which occurs at the maximum cyclic stress. These two measurements potentially represent vastly different states of [90] fiber/matrix (F/M) interface separations, crack openings, constituent stresses, and temperature gradients over the gage section (static versus dynamic), all of which strongly impact the slope of the stress-mechanical strain response. Consequently, for a composite material, the "stiffness" values are dependent upon the convention used to make the measurement, and must be interpreted appropriately. The convention employed here was felt to represent the most explicit and informative approach.

Several benefits were realized from this test technique. First, the "real-time" thermal strain information was essential for an accurate post-test assessment of the mechanical strain response; this fact will become evident after discussing the mechanical deformation behavior and CTE degradation data. Second, the CTE and isothermal E measurements provide a definitive quantitative measurement for tracking the TMF damage progression. Third, measurement of the isothermal E values enables direct stiffness degradation/damage comparisons between TMF and isothermal fatigue loadings.

4.0 RESULTS AND DISCUSSION

Prior to discussing the various TMF behaviors of TMCs, it is worthwhile to point out that the specific alloys used in the SiC-TMCs (in the present case, TIMETAL 21S and Ti-15-3) have little to no influence on the damage mechanisms resulting from the fatigue loadings. That is to say, that for any given SiC-TMC system, the mechanistic and

phenomenological behaviors resulting from fatigue loadings are qualitatively identical [ref. 14]. This fact enables the concept of a "model material" for this class of materials, meaning that the behavior of any one continuously reinforced SiC-TMC sufficiently represents the fundamental behaviors of all other continuously reinforced SiC-TMCs. Of course, quantitative variations in behaviors can be evidenced among the multitude of SiC-TMCs; however, even these differences have been found to be minimal [ref. 14]. Thus, in general, the TMF damage mechanisms discussed herein for the three laminates can be taken to apply to all TMCs with those respective laminate architectures.

4.1 TMF Deformation and Life

Representative deformation behaviors for IP and OP TMF are shown in Fig. 2 for the $[0]_4$ TMC with a maximum cyclic stress, S_{max} of 1000 MPa. Selected progressive cycles
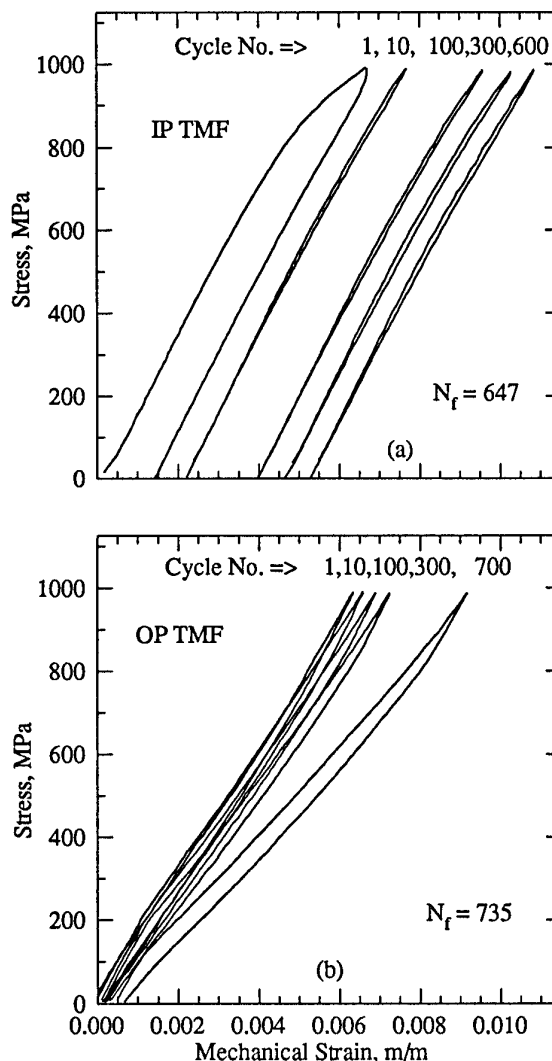

Fig. 2-Deformation of SCS-6/TIMETAL 21S $[0]_4$ during IP and OP TMF with ΔT = 150-650°C and S_{max} = 1000 MPa.

from the first to slightly prior to failure are shown to reveal several aspects of the deformation behaviors, including individual cycle hysteresis and overall stiffness with their progressive changes, and the cumulative strain ratchetting. Further, note that the strain values plotted are mechanical, that is, the total strains less the "true" thermal strains as determined by the test methodology discussed above.

As evidenced from Fig. 2a, IP zero-tension TMF loadings introduce conditions which are highly conducive to strain ratchetting. At equivalent S_{max} levels, this behavior is often amplified over that found under T_{max} isothermal conditions because of the increasing stiffness on the unload (due to the decreasing temperature) which likely tends to minimize the degree of stress reversal in the matrix. The excessive strain ratchetting under IP TMF is consistent for all of the laminates examined here, as it is strongly related to the R_σ = 0 test condition (The effect of control mode and R-ratio are examined in ref. 15 under isothermal conditions.). In laminates containing [0] fibers, matrix load shedding to the fibers results from the Ti alloy's time dependent stress relaxation behavior at elevated temperatures. In the [90] laminate where the stiff [0] fibers are not present to restrain the deformation process (in the loading direction), the strain ratchetting behavior is more closely associated with a traditional view of viscoplastic ratchetting, enhanced by the ongoing internal damage (to be discussed). Upon examining the slopes of the IP TMF stress-strain curves, some degree of stiffness degradation is generally apparent for the [90] (most obvious) and [0/90] laminates; however, a quantitative assessment is complicated by the dynamic temperature conditions, strain ratchetting, states of F/M debonding, and other factors which dictate the instantaneous slope at various points along the stress-strain response. In contrast, the IP TMF deformation of the [0] laminate, as shown in Fig. 2a, does not exhibit a discernable change in stiffness. The discussion later will show that there actually is a modest decrease in E which occurs early in cyclic life where the majority of strain ratchetting is observed.

In contrast to IP TMF loadings, OP loadings do not generally promote excessive strain ratchetting, as OP maximum loading occurs at T_{min} where matrix load shedding and viscoplastic material behavior is much less pervasive. Fig. 2b shows a representative OP deformation response for a [0] laminate with S_{max} = 1000 MPa. In general, only minor increases in minimum cyclic strain occur throughout the OP tests indicating the lack of strain ratchetting. The maximum strain values, however, typically reveal clear increases, indicating decreases in the overall "TMF stiffness". This is most obvious in laminates containing [0] fibers where damage mechanisms are significantly different from those under IP TMF conditions.

TMF life results for the [0]₄, [90]₈, and [0/90]ₛ TMCs are plotted in Fig. 3. In general, R_σ = 0 TMF life trends of SiC-TMCs can be separated into two groups which are delineated by the presence/absence of [0] fibers. For laminates containing [0] fibers, IP TMF loading conditions
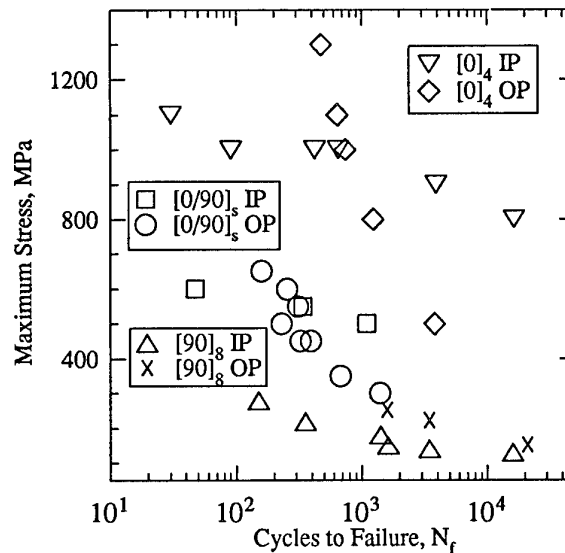
Fig. 3-TMF Life behavior of SiC-TMC laminates.

are found to be life-limiting under relatively high S_{max} conditions where the strain ratchetting mechanisms mentioned above lead to excessive strains resulting in relatively short cyclic lives. The IP and OP TMF life trends cross at some "mid" S_{max} level, below which OP conditions result in shorter cyclic lives. These trends are illustrated in Fig. 3 for the [0] and [0/90] laminates, and have also been shown for [0/±45/90] laminates [refs. 3 & 6]. Of course, the exact crossing stress will be a function of the specific test parameters, such as ΔT and cyclic period. Also apparent from Fig. 3 is that the S_{max}-N_f trends exhibited under IP TMF conditions have a very shallow slope in comparison to those revealed under OP TMF conditions. That is, the IP TMF lives show a much stronger stress dependence. Very little data are available on the TMF behavior of SiC-TMCs without [0] fibers; however, the limited data suggest a clear distinction. As shown in Fig. 3, within the S_{max}-N_f regime examined for the [90] laminate, no crossover between IP and OP TMF is apparent. In this case, the IP TMF conditions appear to be consistently more damaging, resulting in shorter cyclic lives. Also note that the stress dependence is nominally the same. Verrilli and Lerch [ref. 16] conducted a limited study on the TMF behavior of a [±30] TMC, where, similar to the [90] behavior, no crossover in the IP and OP life trends was evident, and the stress dependence and damage mechanisms were nominally the same. The reason for this trend, and the trends exhibited by the other [0] containing laminates will become evident upon discussion of the damage mechanisms.

4.2 TMF Damage in [0] TMCs
Of the laminates to be discussed, the [0] SiC-TMCs have been the focus of the majority of detailed microstructural analysis documenting the TMF damage mechanisms in comprehensive fashion [refs. 17-19]. These mechanisms will be briefly reviewed here and associated with observed mechanical property degradation.

0.1 mm

Fig. 4-Fiber cracking typical of IP TMF in [0] SiC-TMCs.

4.2.1 Microstructural Damage

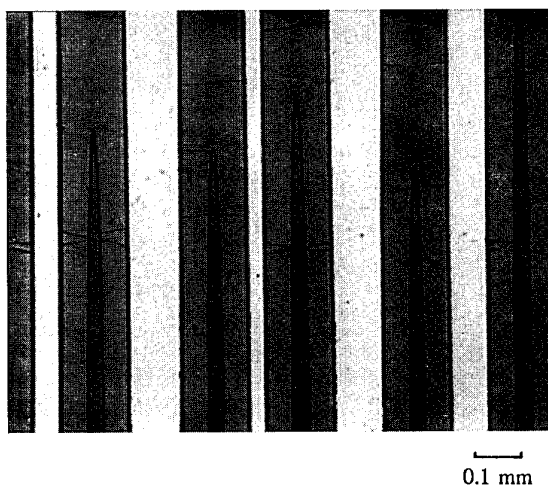In-Phase TMF - Detailed microstructural examinations of specimens subjected to IP TMF loadings reveal a single dominant damage mode, namely, fiber cracking predominantly transverse to the loading direction. Specimens destructively examined very early in expected TMF life [ref. 11] (10% N_f) reveal fiber cracking, such as that shown by the longitudinal section into the specimen width, Fig. 4. Initial damage generally consists of relatively fine cracks, most often visible only in the Si rich "outer" portion of the SiC fiber. Although some degree of highly localized F/M debonding is likely associated with the fiber crack locations, it is usually not visible on the metallographic mounts. The identification of fiber cracking very early in cyclic life is consistent with observations made by Neu and Roman [ref. 20] where acoustic emission (AE) indications suggested numerous fiber breakage events on the first IP TMF cycle at moderate TMF life S_{max} levels. Specimens examined at mid-to-late stages of anticipated TMF life do not reveal a clear progression of damage. In comparison to initial damage states, it is possible that the later damage states exhibit *i*) more numerous fiber cracks, *ii*) smaller un-broken fiber lengths between cracks, and *iii*) larger openings in the axial fiber cracks [ref. 11]; however, a comprehensive study confirming these observations with at least modest quantitative significance is lacking.

It can be said, however, that in both late stages of damage progression and failed specimens, there is a consistent absence of matrix fatigue cracking. This observation is consistent over a multitude of stress levels/cyclic lives examined. Given the relatively high ductilities of most Ti alloys, and the tendency for viscoplastic stress relaxation at elevated temperatures, the matrix is able to shed significant load to the stiff elastic SiC fibers which essentially impose a strain controlled environment for the matrix. As a result, the matrix undergoes only moderate loads and strains under IP TMF loadings, as noted by several of the authors

previously cited. Thus, the high S_{max}-short life regime experienced under IP TMF loadings is generally attributed to excessive strain ratchetting due to matrix load shedding, which eventually results in a pure tensile overload, rather than a traditional view of material fatigue. Further, as a result of the lack of matrix cracking, environmental degradation under IP TMF appears to be suppressed (in comparison to OP TMF) [ref. 5].

Out-of-phase TMF - In contrast to IP TMF, microstructural damage observed in [0] SiC-TMCs under OP TMF conditions is dominated by surface initiated matrix cracking. To document the evolution of the microstructural damage, specimens were cycled to various percentages of N_f and destructively examined [ref. 11]. As was the case for IP loadings, damage is generally evident very early in cyclic life. At 10% expected N_f, numerous, very fine surface initiated matrix cracks are evident around the full perimeter of the rectangular cross-section. With continued cycling, the cracks are found to propagate transverse to the loading direction, both along the surface and into the specimen thickness. Unlike the IP TMF specimens, OP TMF specimens examined at progressive life intervals reveal an orderly progression of damage. Also, enhanced degradation resulting from the oxidizing environment (matrix embrittlement) appears to play a significant role, as oxidation patterns and oxide spikes always accompany the matrix cracking. The effect of an oxidizing environment on OP TMF [ref. 5] and OP non-isothermal fatigue [ref. 21] was shown to be significant, and predominantly dictated by the maximum temperature within the cycle (as opposed to ΔT) [ref. 21]. For the specific S_{max} examined in ref. 11 and shown in Fig. 2, the surface initiated cracks reach the outer fiber rows at approximately 60% N_f. Of course, it should be understood without stating that the specific rate of crack propagation will be strongly dependent upon the particular test conditions. However, note that all [0] TMC data available to date under OP TMF conditions reveal the dominant damage mechanism of surface initiated matrix
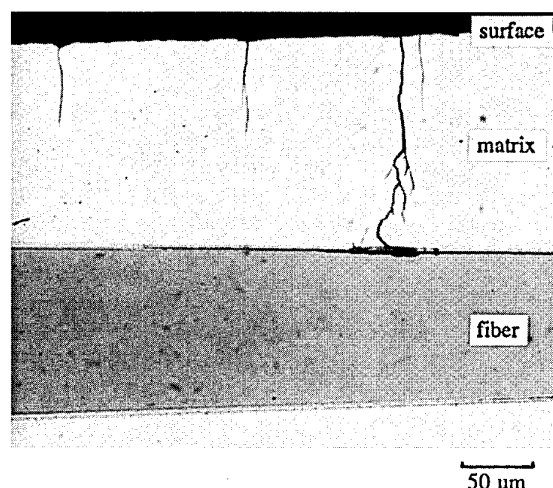

50 μm

Fig. 5-Surface initiated crack reaching outer fiber row during OP TMF of [0] SiC-TMC.

cracking, either with or without the enhanced degradation of an oxidizing environment. At late stages of OP TMF damage, the cracks have generally reached the outer fiber rows, with many of the dominant cracks exhibiting branching such as that illustrated in Fig. 5 by the longitudinal section into the thickness. Also shown in this figure is the debonding at the F/M interface which results. In later stages of damage such as that shown, and in sections taken from failed specimens, no fiber cracking is evident. Thus, crack bridging takes place to the extent that cracks are able to propagate into the specimen thickness prior to the final overload failure event. Fracture surfaces generated under OP TMF conditions generally reveal an outer "ring" of oxidized fatigue cracking, with the inner area exhibiting tensile failure characteristics [ref. 1].

4.2.2 Mechanical Property Degradation

In-Phase TMF - As previously stated, the TMF test technique enabled explicit measurement of isothermal E and CTE values as functions of accumulated TMF cycles; these data are shown in Figs. 6a and 6b, respectively, for an IP TMF test with S_{max} = 1000 MPa [ref. 11]. Note that the isothermal E measurements for this one test are represented in Fig. 6a by two sets of data consisting of the isothermal E values measured at the temperature extremes of the TMF cycle, that is, E_{150} and E_{650}. This representative trend reveals that IP TMF damage promotes a relatively small, but detectable stiffness degradation with the magnitude of degradation comparable at both temperature extremes; this will be found to contrast the OP TMF degradation. As alluded to in the introduction, this degradation is often not obvious from the deformation data, as the slope of the stress-mechanical strain data is often complicated by strain ratchetting, the dynamic temperature condition, and/or a changing thermal strain component. Using a simple rule of mixtures interpretation and noting from above that IP TMF damage is dominated by fiber cracking, it is easily shown that a reduction of the effective fiber contribution to the composite stiffness will promote reductions of comparable magnitudes in this measurement at 150 and 650°C. This arises from the fact that the SCS-6 fiber stiffness is relatively insensitive to temperature over this range. This may not suggest that the fiber stiffness is actually decreasing, but rather that the *effective fiber contribution* to the composite stiffness is decreasing. This effect may result from fiber cracking and highly localized debonding associated with the crack locations. As typical of all of the IP TMF conditions examined, the data reveal that the stiffness degradation occurs very early in cyclic life where the strain ratchetting is most severe, and tends to stabilize quickly. In general, the degree of initial stiffness degradation increased with increasing S_{max}. Degradation of the CTE during IP TMF (Fig. 6b) reveals that the [0] TMC experiences only a small decrease in mean CTE with S_{max} = 1000 MPa, representing a change in the thermal strain range of approximately 100 μm/m. These relatively small changes were again representative of the typical damage state found under IP TMF conditions. Note, however, the similarity in

trends with the stiffness degradation and strain ratchetting, as the majority of change occurs early in cyclic life.

Out-of-phase TMF - Shown in Figs. 7a and 7b, are the E and CTE degradations measured during an OP TMF test with S_{max} = 1000 MPa. Several noteworthy trends are evident in Fig. 7a concerning the E degradations. First, the E values measured from the OP test do not degrade equally, but rather, the E_{150} values ultimately degrade much more severely, even to the point where the E_{150} and E_{650} are essentially equal just prior to failure (that is, in a highly damaged state). The discussion above reveals that the dominant damage in [0] TMCs under OP TMF loading is matrix damage in association with minimal fiber cracking. Again, using a simple rule of mixtures approach to composite stiffness, one notes that the contribution of the matrix is much greater at 150°C than at 650°C. This comes from the fact that the stiffness of the *TIMETAL* 21S matrix
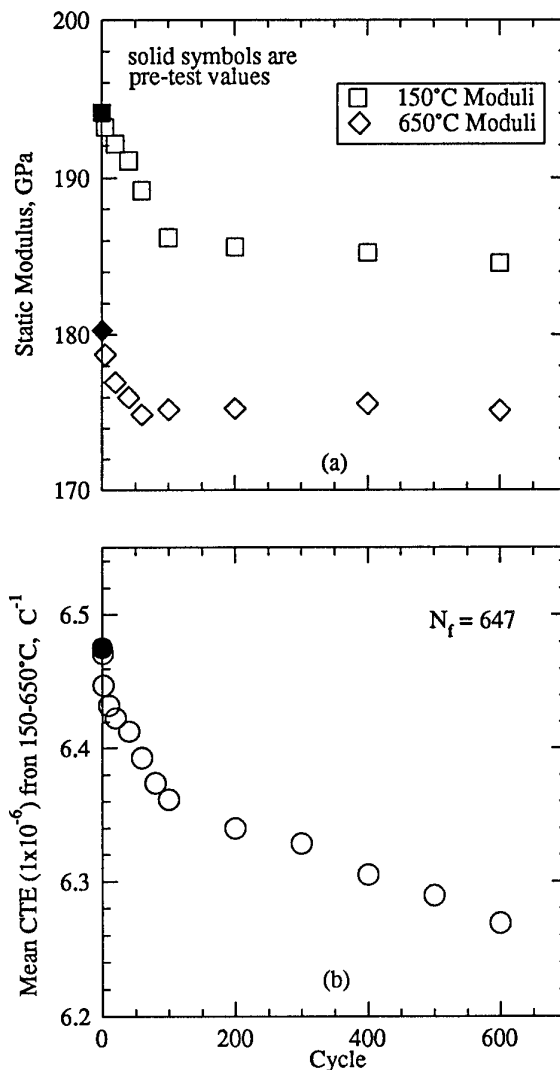

Fig. 6-Degradation of a) E and b) mean CTE during IP TMF of a [0] SiC-TMC: ΔT=150-650°C, S_{max}=1000 MPa.

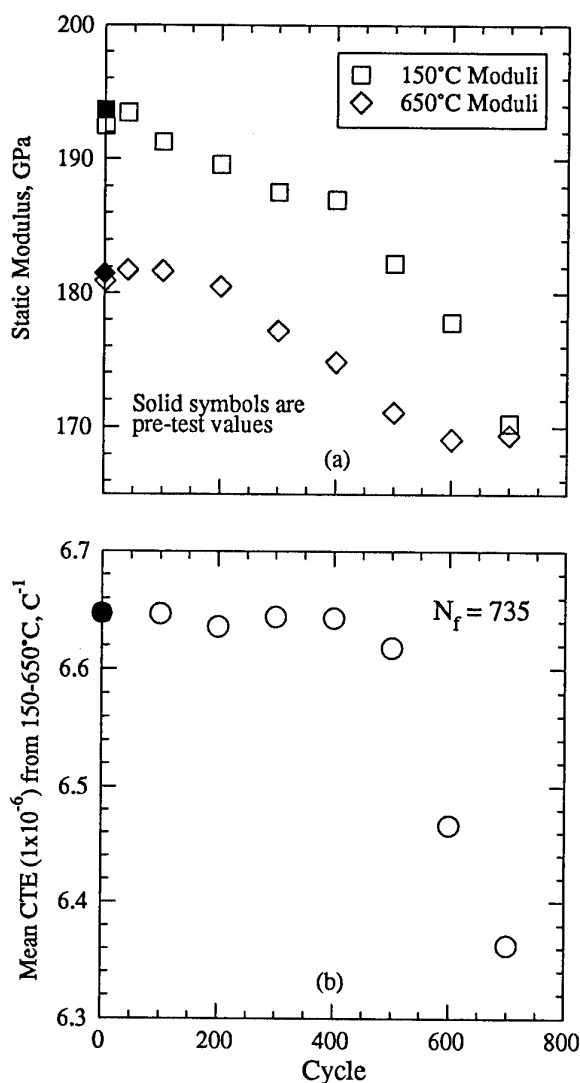Fig. 7-Degradation of a) E and b) mean CTE during OP TMF of a [0] SiC-TMC: ΔT=150-650°C, S_{max}=1000 MPa.

Fig. 7a also reveals that a slight degradation is detected by the E_{150} very early in life, likely indicating the very early surface crack initiations. Again, the fact that the E_{150} measurements detect this damage and the E_{650} measurements do not should be understood from the discussion above. Also, there is potential for high temperature measurements to mask matrix damage because of crack closure. That is, given the CTE mismatch between the fiber and the matrix, and the relaxation of originally tensile longitudinal residual stresses in the matrix (induced during cool-down from consolidation), compressive stresses can be induced in the matrix upon raising the temperature, potentially closing matrix cracks which could be open at lower temperatures [see ref. 9 for case in point]. Also recall from the discussion of the microstructural damage that for the specific test discussed, the surface initiated matrix cracks reached the outer fiber rows at approximately 60% N_f. Notice that the E_{150} data, in particular, appear to degrade at a relatively constant slope up to approximately 60% N_f, subsequent to which the degradation accelerates, exhibiting an increased rate. This suggests that the E degradation trends are indicating the point when the major cracks reach the fibers and F/M debonding and crack bridging occurs.

Degradation of the macroscopic CTE of the [0] TMC during OP TMF with S_{max} = 1000 MPa is shown in Fig. 7b. The mean CTE of the TMC is seen to be essentially constant and then the property degrades a relatively small degree to a total degradation of approximately 5 percent prior to failure. Note that the degradation of this "structural" property begins at approximately the 60% N_f point when again, debonding and crack bridging occur. Additional results where CTE degradation was monitored reveal that this measurement is a good indicator of matrix dominated damage, particularly at relatively low S_{max} levels where matrix crack growth can mature and dominate the cross-section prior to overload failure. In such cases, the degradation of this property has been observed to be as high as 25% [ref. 9].

4.3 TMF Damage in [90] TMCs

4.3.1 Microstructural Damage

A representative SEM fractograph taken from a [90] specimen subjected to OP TMF conditions is shown in Fig 8. Unlike [0] SiC-TMCs, [90] SiC/TMCs do not exhibit any damage/failure mechanisms that are unique to any one cycle type, including isothermal, IP, and OP TMF [ref. 12]. Fractographs taken from all three loading conditions reveal exclusive internal crack initiations at F/M interface locations. Oxidized matrix fatigue cracking dominates all of the fracture surfaces. The extent of oxidation at surface locations is modest in comparison to that which occurs at internal cracked matrix locations. The exposed [90] fibers along the cut edges of the specimen appear to serve as oxygen "pipelines" to the numerous cracks propagating from the F/M interfaces. Fracture surfaces from moderate to low stress specimens reveal the most extensive cracking, with numerous F/M interface initiation points and very little matrix area exhibiting ductile-tensile failure. Fig. 8 reveals a fracture surface generated from a relatively high S_{max} OP

is strongly dependent upon temperature in this temperature range [E_{150} = 110 and E_{650} = 67 GPa]. Given this fact, and considering a continual degradation of the effective matrix contribution in the presence of undamaged fibers, the relative degradation of the composite E_{150} values will be greater than that experienced by the composite E_{650} values. Further, in a case where the matrix approaches a "completely" damaged state, the composite E values at both temperature extremes will degrade to similar quantities, given that the SCS-6 fiber stiffness is relatively insensitive to temperature over this temperature range [E_{150} = 388 and E_{650} = 370 GPa]. It is important to note, however, that other factors, such as constituent stresses existing at zero macroscopic load, can influence this measurement and complicate a rule-of-mixtures interpretation [see ref. 11 for examples].

Fig. 8-SEM fractograph from [90] SiC-TMC under OP
TMF: ΔT=200-427°C, S_{max}=250 MPa.

Fig. 9-Degradation of the E values during IP and OP TMF
of a [90] SiC-TMC: ΔT=200-427°C, S_{max}=150 MPa.

TMF loading condition. Here too, multiple fatigue cracks
are initiated at the F/M interfaces; however, the extent of
crack propagation is slightly reduced as a result of the
greater S_{max} promoting a tensile overload failure prior to
complete through-the-thickness transverse cracking. Thus,
distinct "strips" exhibiting ductile microvoid coalescence are
often created along approximate centerlines of the matrix
layers during the final tensile failure event, as shown in Fig.
8. Similar features are also evident under relatively high
stress isothermal and IP TMF conditions. Metallographic
mounts were examined from both longitudinal and
transverse sections revealing damage consistent with
observations made from the fracture surfaces [ref. 12]. No
surface matrix cracking or fiber splitting, and minimal
transverse fiber cracking is evident. Matrix cracking
initiated at the F/M interfaces is present at a majority of the
fibers. Using a clock face to represent a transverse view of
the fiber, where the uniaxial loading direction corresponds
to the 6 and 12 o'clock positions, the vast majority of
cracks initiate between the 2 to 4 and 8 to 10 o'clock
positions, and propagate transverse to the loading direction
into the matrix. Given the consistent failure mechanisms
between the various loading types, it is reasonable that the
IP and OP TMF life trends presented in Fig. 3 exhibit
comparable slopes and do not cross, as is found in the [0]
and [0/90] SiC-TMCs.

4.3.2 Mechanical Property Degradation

In similar fashion to that presented for the [0] TMC, E
degradations as a functions of the TMF cycles are presented
in Fig. 9. Note, a log scale is used to facilitate the
simultaneous presentation of both an IP and an OP TMF
test conducted with S_{max} = 150 MPa. Also, recall that the
temperature extremes of the TMF cycle are 200 and 427°C.
In general, first-cycle E degradations are comparable for
both the IP and OP loadings. This first-cycle degradation is
likely associated with the initial F/M bond failure which
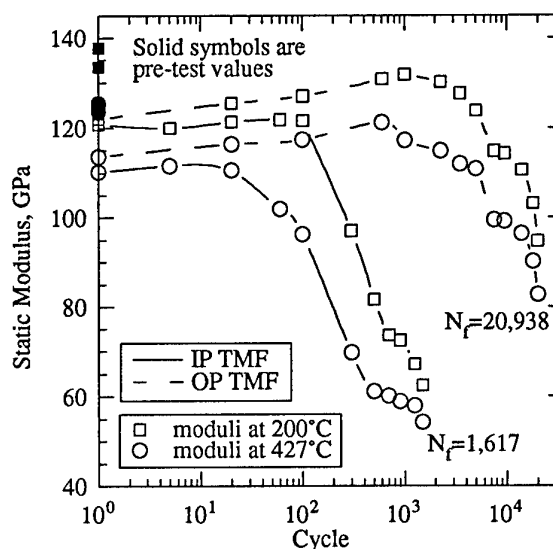occurs on the first loading cycle. However, from that point

on, the IP TMF E values tend to degrade much earlier in
cyclic life; this is in agreement with the fatigue life
behaviors and reveals that the IP cycle was considerably
more damaging. Note that for both IP and OP conditions
the moduli at 427°C begin to degrade prior to those
measured at 200°C. This may have been indicative of
cracks opening at the higher temperatures, as well as being
related to the state of residual stresses in the specimen. As
may be obvious, without the presence of the [0] fibers (i.e.,
fibers in the loading direction], the concept of matrix load
shedding/stress relaxation in the loading direction does not
apply. By comparing the first-cycle stiffness degradation
experienced in the TMF tests ($\approx$10% change) to that which
is found in an isothermal test with S_{max} = 150 MPa ($\approx$32%
change) it becomes apparent that isothermal loadings are
more damaging [ref. 12]. Although not plotted in Fig. 3,
the isothermal lives of this [90] SiC-TMC at T_{max} (i.e.,
427°C) are generally less than those experienced under IP
TMF conditions. The cause for this result is likely the
same mechanism which causes the IP TMF to be more
detrimental than the OP TMF. That is, the simultaneous
high-temperature high-load conditions serve to enhance the
viscoplastic strain ratchetting and crack growth, causing the
maximum strain accumulation at failure in the isothermal
and IP TMF tests to be more than twice that experienced
under comparable OP TMF conditions. Further, the
isothermal tests will experience enhanced environmental
degradation (given identical damage mechanisms to TMF),
as the material is constantly exposed to T_{max} conditions.

Degradations of the composite mean CTEs for the S_{max} =
150 MPa IP and OP TMF tests are shown in Fig. 10. As
TMF damage accumulates, the mean CTE in the [90] TMC
increases. Although this result may seem initially
surprising, it can be easily understood by examining a
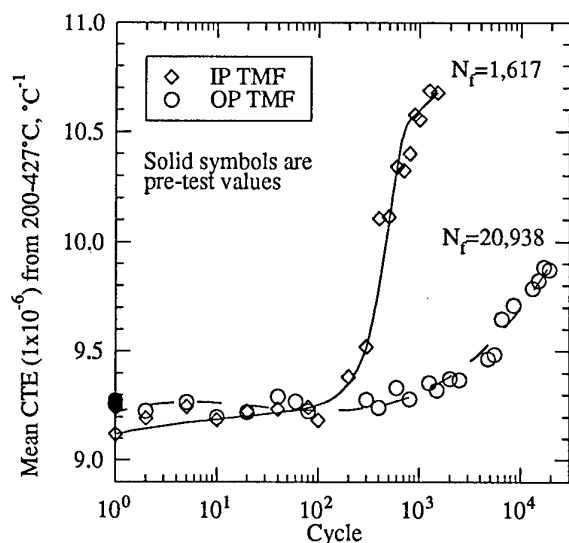simple expression for the composite CTE in the [90] or

Fig. 10-Degradation of the CTE values during IP and OP TMF of a [90] SiC-TMC: $\Delta T=200\text{-}427°C$, $S_{max}=150$ MPa.

transverse direction (i.e., CTE_T), that is,

$$CTE_T = (1 + v_f) \, CTE_f \, V_f + (1 + v_m) \, CTE_m \, V_m - CTE_L \, v_L$$

where v and V are Poisson's ratio and volume fraction, respectively, and subscripts f, m, and L represent the fiber, matrix, and composite longitudinal direction, respectively. If the ensuing damage introduces a decrease in restraint along the composite longitudinal direction (the last term), it can be seen from the equation above that the CTE_T will increase. Experimental results discussed earlier on the [0] SiC-TMCs clearly reveal that both the CTE_L and E_L decrease with ensuing TMF damage where matrix cracking is present. Further, gross debonding will have the effect of eliminating the fiber contribution to this term, allowing the CTE_T to reflect the higher CTE_m value. Also note that the increases in CTE_T directly correspond to the decreases in E shown for the respective tests given in Fig. 9.

4.4 TMF Damage in [0/90] TMCs

The dominant damage/failure mechanisms present in [0/90] SiC-TMCs vary as a function of cycle type. As suggested by the trends established in the fatigue life plot, Fig. 3, many of the mechanisms are similar to those found in [0] TMCs. However, additional damage mechanisms are introduced by including fibers transverse to the loading direction, most notably, cracking initiated at the [90] F/M interfaces, such as that found in the [90] SiC-TMCs. As before, the microstructure damage will be discussed initially, as this information will add insight to the interpretation of the macroscopic property degradation curves.

4.4.1 *Microstructural Damage*

For comparison purposes, metallographic observations made from isothermal testing at 650°C on this [0/90]$_s$ TMC [ref. 22] will be briefly summarized. Fracture surfaces from all stress levels reveal environment enhanced internal matrix

cracking. Oxidation patterns on the fracture surfaces and extensive metallography indicate that the matrix cracks initiate at [90] F/M interfaces and propagate normal to the loading in the specimen thickness direction. Based on the extent of internal oxidation it is evident that the [90] fibers serve as oxygen conduits along the F/M interfaces, enhancing internal environment assisted matrix cracking. Surface initiated matrix cracking cannot be identified at any of the stress levels investigated. Metallographic mounts reveal that essentially all [90] F/M interfaces are debonded. Longitudinal sections taken from [0] fiber plies reveal little or no [0] fiber cracking or debonding. In general, a single dominant damage mode is revealed: environment enhanced matrix cracking initiated exclusively at the [90] F/M interfaces.

In-phase TMF - Fracture surfaces taken from IP TMF specimens revealed distinct and unique features relative to those found under isothermal and OP conditions. All IP TMF fracture surfaces exhibit ductile matrix failure over the entire cross-section. Matrix in contact with the [90] fibers reveals a relative increase in oxidation (based on discoloration), again confirming the oxygen "piping" effect noted under isothermal conditions. However, fatigue cracking initiated at the [90] F/M interfaces is not evident on the fracture surfaces. A relative increase in [0] fiber pullout is also visible. In general, all IP TMF features closely resemble those produced by monotonic tensile failures, a trend identical to that exhibited by [0] SiC-TMCs. Comprehensive metallography on failed specimens reveals global debonding of the [90] fibers in the loading direction. Limited matrix cracks, predominantly transverse to the loading direction, are found to initiate at [90] F/M interfaces, but their relative size and number are greatly reduced from those produced under comparable isothermal and OP TMF conditions. SEM of the specimen surfaces reveal no surface cracking, confirming the fractographic observations. The dominant damage present under IP TMF conditions is clearly extensive [0] fiber cracking, as shown in Fig. 11 by the longitudinal section exposing a [0] fiber
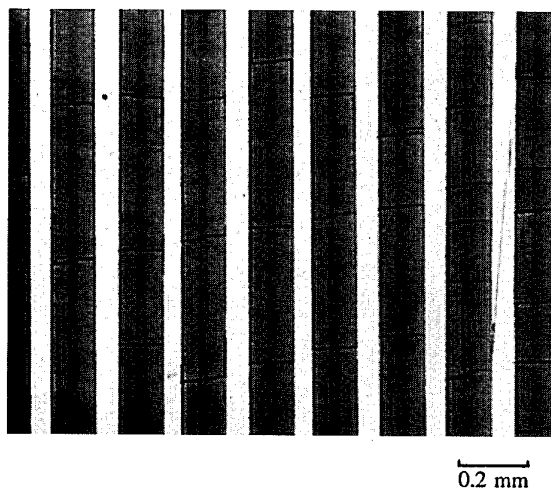

0.2 mm

Fig. 11-[0] fiber cracks from IP TMF in [0/90] SiC-TMC.

ply. The majority of fibers appear to be broken into lengths of 200 to 400 μm, suggesting a relationship to a characteristic load development length. Close inspections at high magnifications reveal that the cracks typically stop (or begin) at the interfaces of the outer carbon/carbon coating of the SCS-6 fibers and do not reach (or start at) the interfaces of the reaction zone/carbon coating. Note, however, that the exact initiation points of the fiber cracks are unclear because the fibers are always found to be cracked across their full diameter. Metallography on IP TMF specimens interrupted prior to failure reveal that the [0] fiber cracking occurs relatively early in cyclic life (≈20% N_f) [ref. 13].

Out-of-phase TMF - OP TMF conditions introduced a mechanism not present under 650°C isothermal or IP TMF loadings, namely, surface initiated fatigue cracking. Fracture characteristics and oxidation patterns strongly suggest crack initiation points at both surface and [90] F/M interface locations. Oxidized cracks initiated at the surface appear to propagate transversely (i.e., through the thickness) in toward the [0] fibers, and oxidized cracks initiated at the [90] F/M interfaces propagate transversely out toward the [0] fibers. Upon failure, a "strip" of matrix exhibiting ductile failure characteristics is created along the centerline of the [0] fibers as shown in Fig. 12. These ductile strips are most notable under high and mid S_{max} levels, as under relatively low S_{max} conditions, surface initiated and [90] F/M interface initiated cracks are able to meet at the [0] fibers prior to overload failure, creating fracture surfaces which are fatigue cracked through the entire thickness. SEM of the specimen surfaces and thorough metallography confirmed the fracture surface indications of extensive surface cracking transverse to the loading direction. In general, the number of visible surface cracks increases with increasing S_{max}; however, relatively low S_{max} conditions tend to produce cracks exhibiting a more torturous path with increased crack branching. The majority of [90] fibers exhibit multiple crack initiations, and as previously

observed under IP TMF conditions, all [90] fibers exhibit some degree of debonding in the loading direction. Sections exposing the [0] ply reveal a complete absence of [0] fiber cracking. Metallography on OP test specimens interrupted prior to failure reveal that both surface and [90] F/M interface initiated cracks occur extremely early in cyclic life (as early as ≈7% of the expected N_f) [ref. 13].

4.4.2 *Mechanical Property Degradation*
In-phase TMF - Under IP TMF conditions, first cycle E degradations are evident, and similar in magnitude to those found under T_{max} (i.e., 650°C) isothermal fatigue conditions and OP TMF conditions (a drop of ≈6% with S_{max} = 500 MPa) [ref. 13]. For all tests conducted on this material, the degree of initial stiffness degradation is more closely related to S_{max} rather than cycle type, and in general, is found to increase with increasing S_{max}. It is likely that this initial stiffness degradation is strongly associated with the [90]
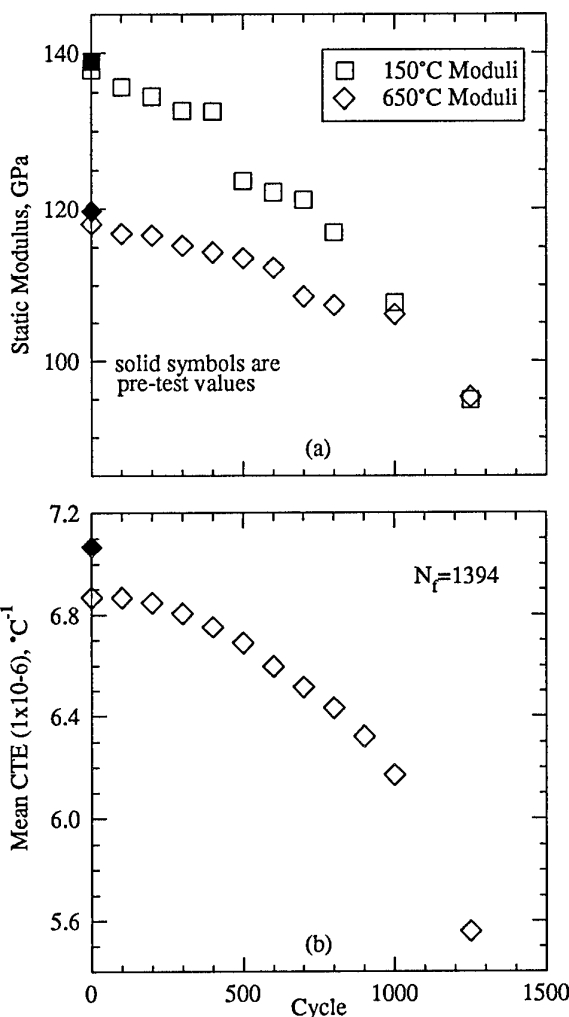

Fig. 12-SEM fractograph from [0/90] SiC-TMC under OP TMF: ΔT=150-650°C, S_{max}=300 MPa.

Fig. 13-Degradation of a) E and b) mean CTE during OP TMF of a [0/90] SiC-TMC: ΔT=150-650°C, S_{max}=300 MPa.

F/M debonding. However, subsequent to first-cycle drops, E degradation trends are generally unique to the specific cycle type. A comparison between S_{max} = 500 MPa IP TMF and 650°C isothermal tests reveals that although the N_f values are not significantly different (1000 and 1500, respectively) and the first-cycle E_{650} degradations are essentially identical, the damage progression is notably different. Prior to failure, the isothermal specimen experiences a 13% degradation in E_{650}, whereas, the IP TMF specimen experiences a 26% drop in this same property. This, in spite of the fact that the environmental degradation is heightened in the isothermal case where the material is constantly held at 650°C and the IP TMF specimen is thermally cycled from 150 to 650°C. (This statement is corroborated by a qualitative assessment of the relative oxidations of the specimen surfaces and fracture surfaces.). This highlights the enhanced damage progression introduced by the synergistic effects associated with TMF conditions. As was found in the [0] SiC-TMCs, IP TMF promotes similar degradation behaviors in the E_{150} and E_{650} values. Also, note that the microstructural damage is very similar, that is, predominantly [0] fiber cracking. Thus, many of the same rationalizations used in the discussion above for the [0] TMC adequately apply to the [0/90] TMC.

In general, for the [0/90] SiC-TMC, damage resulting from IP TMF loadings produces a relatively small decrease in the mean CTE early in cyclic life. This property appears to quickly stabilize and remain essentially constant throughout the cyclic life of the specimen, again, much like the [0] TMC. Although a significant degree of stiffness degradation takes place as a likely result of [90] F/M debonding and associated damage progression, it appears that the impact of this type of damage on the macroscopic CTE is minimal. This suggests an overriding influence of the [0] fiber when no gross [0] fiber debonding is apparent and matrix cracking is modest.

Out-of-phase TMF - In contrast to the [0/90] IP TMF behavior, the E values measured under OP TMF conditions do not degrade equally, but rather, the E_{150} or "low" temperature E values degrade more severely, such as those shown in Fig. 13a. This trend is most evident under mid to low S_{max} values where the progression of matrix cracking through the cross-section is extensive prior to the effective overload failure. For the OP TMF test presented (i.e., S_{max} = 300 MPa), the composite E values at both temperature extremes are essentially equal just prior to failure where the material is in a highly damaged state. Again, the similarities between the trends established here and those observed for the [0] TMC are outstanding and because the damage mechanisms are similar (i.e., extensive matrix damage in the absence of [0] fiber breakage), the rationalization used above can be essentially duplicated here.

Also in contrast to the IP TMF condition, cyclic damage resulting from OP TMF conditions appears to have a notable effect on the composite CTE, as shown in Fig. 13b.

Degradation of this macroscopic property is again most pronounced and severe under mid to low S_{max} values (i.e., conditions which resulted in relatively long lives). Fig. 13b illustrates that under OP conditions with S_{max} = 300 MPa, this property experiences a degradation of 22%. The extensive matrix damage in the presence of undamaged [0] fibers allows the composite mean CTE to tend towards the lower CTE dictated by the [0] fibers. The magnitude of degradation will of course be strongly influenced by the relative percentage of [0] fibers and the remaining transverse stiffness imposed by the [90] fibers. It is apparent that under loading conditions which promote extensive matrix cracking, measurement of the CTE degradation provides a straightforward quantitative means for tracking the progression of composite damage.

5.0 ACKNOWLEDGEMENTS

6.0 REFERENCES

1. Castelli, M.G., Bartolotta, P.A. and Ellis, J.R., "Thermomechanical Testing of High-Temperature Composites: Thermomechanical Fatigue Behavior of SCS-6/Ti-15-3," *Compos. Mat.: Testing and Design (Tenth Vol.), ASTM STP 1120*, Glen C. Grimes, Ed., Philadelphia, PA, 1992, pp. 70-86.

2. Neu, R.W. and Nicholas, T. Effect of Laminate Orientation on the Thermomechanical Fatigue Behavior of Titanium Matrix Composites. *J. of Compos. Tech. and Res.*, Vol. 16, No. 3, Jul., 1994, pp. 214-224.

3. Aksoy, S., "Stiffness Degradation in Metal Matrix Composites Caused by Thermomechanical Fatigue Loading," *J. of Eng. for Gas Turbines and Power*, Vol. 116, No. 3, Jul. 1994.

4. Russ, S.M., Nicholas, T., Bates, M. and Mall, S., "Thermomechanical Fatigue of SiC/Ti-24Al-11Nb Metal Matrix Composites," *Failure Mechanisms in High Temp. Compos. Mat.*, AD-Vol. 22, G.K. Haritos, G. Newaz, and S. Mall, Eds., ASME, NY, 1991, pp. 37-43.

5. Bartolotta, P.A., Kantzos, P., Verrilli, M.J. and Dickerson, R.M., "Environmental Degradation of an Intermetallic Composite During Thermomechanical Fatigue," *Fat. 93*, Vol. 2, J.P. Bailon and J.I. Dickson, Eds., 1993, pp. 1001-1006.

6. Majumdar, B.S. and Newaz, G.M., "Thermomechanical Fatigue of a Quasi-Isotropic Metal Matrix Composite," *Compos. Mat.: Fat. and Frac. (Third Volume), ASTM STP 1110*, T. Kevin O'Brien, Ed., Philadelphia, PA, 1991, pp. 732-752.

7. Johnson, W.S., Mirdamadi, M. and Bahei-El-Din, Y.A, "Stress-Strain Analysis of a $[0/90]_{2s}$ Titanium Matrix Laminate Subjected to a Generic Hypersonic Flight Profile," *J. of Compos. Tech. and Res.*, Vol. 15, No.4, Winter 1993, pp. 297-303.

8. Mall, S., Hanson, D.G., Nicholas, T. and Russ, S.M. Thermomechanical Fatigue Behavior of a Cross-Ply SCS-6/β21-S Metal Matrix Composite. *Constitutive Behav. of High Temp. Compos.*, MD-Vol. 40, B.S. Majumdar, G.M. Newaz, and S. Mall, Eds. ASME, 1992, pp. 91-106.

9. Castelli, M.G., "An Advanced Test Technique to Quantify Thermomechanical Fatigue Damage Accumulation in Composite Materials," *J. of Compos. Tech. and Res.*, Vol 16, No. 4, Oct., 1994, pp. 323-328.

10. Hashin, Z., "The Effect of Microcracking on Thermal Expansion and Cyclic Stress-Strain Relations of Composites," *Microcracking-Induced Damage in Composites*, ASME, AMD-Vol. 111, Nov., 1990, pp. 35-40.

11. Castelli, M.G., "Characterization of Damage Progression in SCS-6/*TIMETAL* 21S $[0]_4$ Under Thermomechanical Fatigue Loadings," *Life Prediction Methodology for Titanium Matrix Composites, ASTM STP 1253*, W.S. Johnson, J.M. Larsen, and B.N. Cox, Eds., Philadelphia, PA, 1995.

12. Castelli, M.G., "Thermomechanical and Isothermal Fatigue Behavior of a $[90]_8$ Titanium Matrix Composite," In: *Proc. of ASC 8ᵗʰ Tech. Conf. on Compos. Mat., Mechanics, and Processing*, Technomic Pub., Lancaster, PA, Oct., 1993, pp. 884-892.

13. Castelli, M.G., "Thermomechanical Fatigue Damage/Failure Mechanisms in SCS-6/Timetal 21S $[0/90]_s$ Composite," *Compos. Eng.*, Vol 4, No. 9, 1994, PP. 931-946.

14. Arnold, S.M. and Castelli, M.G., "What Constitutes a Model Material? A LeRC Structural Fatigue Branch Perspective," In: *HITEMP Review 1995: Advanced High Temperature Engine Materials Technology Program*, NASA Report CP-10178, Vol. II, Oct., 1995, paper 35a.

15. Lerch, B.A., and Halford, G.R., "Effects of Control Mode and R-Ratio on the Fatigue Behavior of a Metal Matrix Composite," *Mat. Sci. and Eng.*, special issue, Proc. of TMS/ASM Symp. on Mechanisms and Mechanics of MMC Fatigue, 1995.

16. Verrilli, M.J. and Lerch, B.A., "Thermomechanical Fatigue Behavior of an Angle Ply Titanium Matrix Composite," In: *HITEMP Review 1993: Advanced High Temperature Engine Materials Technology Program*, NASA Report CP-19117, Vol. II, Oct., 1993, pp. 38:1-10.

17. Gabb, T.P., Gayda, J., Bartolotta, P.A., and Castelli, M.G., "A Review of Thermomechanical Fatigue Damage Mechanisms in Titanium and Titanium Aluminide Matrix Composites," *Int. J. of Fatigue*, Vol. 15, No. 5, 1993, pp. 413-422.

18. Castelli, M.G. and Gayda, J, "An Overview of Elevated Temperature Damage Mechanisms and Fatigue Behavior of a Unidirectional SCS-6/Ti-15-3 Composite," DE-Vol. 55, *Reliability, Stress Analysis, and Failure Prevention*, ASME, 1993, pp. 213-221.

19. Neu, R.W., "Thermomechanical Fatigue Damage Mechanism Maps for Metal Matrix Composites," *Thermomechanical Fatigue Behavior of Materials: 2nd Vol. ASTM STP 1263*, M.J. Verrilli and M.G. Castelli, Eds., Philadelphia, PA, 1995.

20. Neu, R.W. and Roman, I., "Acoustic Emission Monitoring of Damage in Metal Matrix Composites Subjected to Thermomechanical Fatigue," *Compos. Sci. and Tech.*, Vol. 52, 1994, pp. 1-8.

21. Gayda, J., Gabb, T.P. and Lerch, B.A., "Fatigue-Environment Interactions in a SiC/Ti-15-3 Composite," *Int. J. of Fat.*, Vol. 15, No. 1, 1993, pp. 41-45.

22. Castelli, M.G., "Isothermal Damage and Fatigue Behavior of SCS-6/Timetal 21S $[0/90]_s$ Composite at 650°C," NASA Report CR-195345, Cleveland, OH, June, 1994.

TMF RESPONSE OF Ti-48Al-2V ALLOY AND ITS COMPOSITE

E. U. Lee

Naval Air Warfare Center
Aircraft Division
Patuxent River, MD 20670-5304, U. S. A.

SUMMARY

The fatigue behavior of a Ti-48Al-2V alloy and its composite, reinforced with particulate TiB_2, was investigated under in-phase thermal-mechanical cycling and isothermal cycling. In the thermal-mechanical fatigue (TMF) tests, the temperature was cycled between a minimum temperature T_{min}, 100°C, and a maximum temperature T_{max}, ranging from 750°C to 1400°C; the cyclic stress ranges were 2.8 - 28 MPa and 4.2 -42 MPa. Employing the identical cyclic stress ranges, isothermal fatigue (IF) tests were conducted at a T_{max}. The lower the T_{max} and the smaller the stress range, the longer was the TMF and IF lives for the Ti-48Al-2V alloy and its composite. IF inflicted damage earlier than TMF in the Ti-48Al-2V alloy, whereas their damaging effects were similar in the composite. Both materials had similar TMF resistance, but the composite showed greater IF resistance than Ti-48Al-2V alloy. The TMF mechanism is nucleation and growth of voids in interlamellar plate, twin and grain boundaries, their linkage, intergranular separation, and disintegration of lamellar structure.

INTRODUCTION

Current advances in the technology of titanium aluminide and its composite have made their properties attractive for a variety of applications. The attractive properties include high strength-to-density ratio, high specific modulus, retention of high strength and modulus at elevated temperatures, good creep resistance and non-burning characteristics (1-5). Consequently, new applications keep arising and they are becoming potential structural materials in demanding service environments. One example is their use at elevated temperatures. In this application, they replace superalloys, which have high densities and impose penalties on weight-critical structures (6,7).

Many engineering components, operating at elevated temperatures, are often subjected to fluctuating temperatures and loads, and are susceptible to isothermal fatigue (IF), thermal fatigue, or/and thermal-mechanical fatigue (TMF) damage. Such a damage is costly. TMF has been a serious concern of aerospace (8-11), power generation (12, 13), ground transportation (14, 15) and ceramics (16) industries. Major TMF parameters for various materials have been known to be the range and frequency of fluctuating temperature and load, maximum temperature, hold time, specimen geometry, coefficient of thermal expansion, material property, metallurgical change and environment (17, 18). However, few studies have been reported on the TMF of newly emerged titanium aluminides and their composites. Furthermore, response of these materials to TMF loading is of considerable research interest. The objective of this study was to investigate the TMF response of a Ti-48Al-2V alloy, consisting of two titanium aluminides Alpha-2 and Gamma, and its composite, and to identify the TMF mechanism.

IF life data at the maximum temperature of a TMF cycle have been used to predict TMF lives, though the IF test does not capture some of the significant TMF parameters. Some investigators (19-25) have found TMF to be more damaging than IF at the maximum temperature, while others (26-30) have noted the opposite effect. In this study, the TMF behavior of a Ti-48Al-2V alloy and its composite was also compared with the IF behavior.

EXPERIMENTAL PROCEDURE

1. Material and Specimen

The specimen materials were 102 mm x 102 mm x 13 mm (4 in. x 4 in. x 1/2 in.) plates of a Ti-48Al-2V alloy and its composite, reinforced with 7.5 pct volume fraction of TiB_2 particles. The plates were initially produced by vacuum hot pressing powders of the matrix alloy Ti-48Al-2V and its $(TiB_2)_p$-reinforced composite. Subsequently, they were subjected to hot isostatic pressing at 1400°C under 207 MPa (30 ksi) for 4 hours to eliminate or minimize cavities.

The plates were machined into rectangular sheet specimens, 98 mm (3 7/8 in.) long, 13 mm (1/2 in.) wide and 3 mm (1/8 in.) thick.

2. Fatigue Test

A rectangular sheet specimen was gripped by water-cooled stainless-steel jaws in the vacuum (10^{-5} torr) chamber of a Gleeble 1500 thermal-mechanical test machine. (The Gleeble 1500 machine is controlled by a computer system, which provides signals necessary to run thermal-mechanical test programs simultaneously through a closed loop servo system.) The exposed length of the specimen between the jaws was 30 mm. The specimen was resistance-heated by passing electric current through it and was loaded hydraulically. A Pt-PtRh thermocouple was spot-welded on the mid-span of the specimen, and was used to monitor and control the temperature of the heated zone.

In the TMF test, the temperature was cycled between the minimum temperature T_{min} = 100°C and a maximum temperature T_{max}, ranging from 750 to 1400°C. Simultaneously the specimen was also subjected to tension-tension loading with a load ratio 0.1. The applied cyclic stress ranges were 2.8 - 28 MPa and 4.2 - 42 MPa. The fluctuating temperature and load had triangular waveforms with the maximum temperature at the maximum load, i. e., in-phase cycling. On the one hand, in the IF test, only the load changed cyclically at a given temperature, which is identical to the T_{max} of a TMF cycle. For both tests, the cycle time was 8 minutes, and the temperature and load cycles were computer-controlled. The fatigue life N is defined as the number of loading cycles required to fracture the specimen.

3. Metallographic and Fractographic Examination

Specimens were polished and etched with Keller's reagent, and the microstructures were examined in an optical microscope. The fracture surface morphology was characterized in an AMR 1000 scanning electron microscope, operated at an accelerating voltage of 20 kv.

RESULTS

1. Fatigue Behavior

The variation of fatigue life, N, with T_{max} is shown for the matrix alloy Ti-48Al-2V in Fig. 1. The TMF life increases with decreasing T_{max} at a given stress range. The TMF life is greater for a lower stress range. Similar features are observable for the composite, as shown in Fig. 2. With decreasing T_{max}, the TMF and IF lives increase for both the matrix alloy and its composite. The relationship can be expressed by an equation of the form $T_{max} = A \cdot N^{-b}$, where A and b are constants. These figures indicate that the TMF life is longer than the IF life in the matrix alloy at all temperatures employed but only at higher temperatures in the composite. At lower temperatures, the TMF and IF lives are essentially identical in the composite.

The TMF lives of the matrix alloy and its composite are compared for a given applied stress range (4.2 - 42 MPa) in Fig. 3. They are similar, indicating that the addition of 7.5 pct volume fraction of TiB_2 particles has little effect on the TMF life. The IF lives of the matrix alloy and the composite are compared for a given stress range (4.2 - 42 MPa) in Fig. 4. The composite has slightly greater resistance to IF than the matrix alloy.

2. Metallographic and Fractographic Characteristics

   a. Micrographs of As-Received Materials

The microstructures of the as-received matrix alloy of Ti-48Al-2V and its composite are shown in Fig. 5. The as-received matrix alloy has a fully lamellar microstructure, consisting of alternating plates of two titanium aluminides, Alpha-2 and Gamma. The composite has TiB_2 particles distributed throughout the matrix of lamellar microstructure and its grain size is smaller than that of the matrix alloy.

b. Post-TMF Micrographs and Fractographs

SEM fractographs of a matrix alloy specimen and a composite specimen, which were subjected to TMF, are shown in Fig. 6. These fractographs exhibit voids, linking along and across the lamellar plate boundaries, and cracking along the interface of a TiB_2 particle.

SEM fractographs of a matrix alloy specimen, which was subjected to TMF over a temperature range of 100 - 1100°C and a stress range of 2.8 - 28 MPa, were shown in Fig. 7. These fractographs show twins (fine parallel lines) in lamellar plates; voids and their linkage along twin boundaries; and secondary cracking along twin and interlamellar plate boundaries.

Micrographs of matrix alloy and its composite specimens, which were subjected to TMF of temperature range 100 - 850°C and stress range 4.2 - 42 MPa, are shown in Fig. 8. These micrographs show voids, their linkage and cracking along grain boundaries. These observations are supported by SEM fractographs of a matrix alloy specimen, which was subjected to TMF in the temperature range 100 - 900°C and stress range 4.2 - 42 MPa. The fractographs show intergranular fracture and dimples on grain boundaries, Fig. 9.

DISCUSSION

1. Fatigue Resistance

The IF life at the maximum temperature of a TMF cycle is found to be shorter than the TMF life in the matrix alloy at all temperatures employed and in the composite only at higher temperatures. At lower temperatures, the TMF and IF lives are essentially identical in the composite. A group of researchers (15, 19-25, 29-32) found the TMF life shorter than the IF

life at a maximum temperature, whereas the others (10, 13, 26-28, 33) found the opposite was the case. Sehitoglu (15) studied the TMF behavior of 1070 steel under T_{min}, ranging from 150°C to 500°C, and T_{max}, ranging from 450°C to 700°C. He found TMF more damaging than IF at the T_{max}. Majumdar (29) conducted TMF tests between 427°C and 593°C on Type 304 stainless steel. His results show that in-phase TMF is the most damaging, followed by IF at the maximum temperature, which in turn is followed by out-of-phase TMF, and finally, the least damaging of all, IF at the minimum temperature. He (31) also performed in-phase TMF and IF experiments on a $(0, + 45,90)_s$ Ti-15-3/SCS-6 composite under load control. In the TMF test the temperature cycling was done between 315°C and 649°C, and the IF test at 649°C. He found the TMF life significantly shorter than the IF life when comparison was made either on a stress-range or a gross mechanical strain-range basis. Karayaka (32) noted that the 100°C to 300°C TMF lives of unreinforced and SiC_p-reinforced aluminum 2XXX-T4 alloy are shorter than the IF lives corresponding to the T_{max} of the cycle. However, the IF lives at 200°C are shorter compared to 100°C to 200°C TMF lives. Jaske (19) investigated the TMF behavior of an AISI 1010 steel at three range of temperatures: 93-316°C, 93-427°C and 93-538°C. His result shows that the TMF life is much less than the IF life and there is little difference in fatigue life between in-phase and out-of-phase cycling. Sheffler (30) conducted TMF tests in ultrahigh vacuum on Type 304 stainless steel and A286 alloy at a temperature range of 600-1200°F and IF tests at 1200°F. He found the in-phase and out-of-phase TMF lives shorter than the IF lives for both materials. Bill (20) performed TMF tests on polycrystalline MAR-M 200 over a cyclic temperature range of 500 to 1000°C. Inelastic strain ranges of 0.03 to 0.2% were imposed on the specimens. TMF lives were found to be significantly shorter than IF life at the maximum cycle temperature, and in-phase cycling was more damaging than out-of-phase cycling. Fujino (22) carried out TMF tests in the temperature range 373-873°K for a low carbon steel and in the range 473-1023°K for a Type 304 stainless steel. His results show that both in-phase and out-of-phase TMF lives are shorter than the IF life at a temperature equal to the mean temperature of thermal cycle but the TMF lives are, in some cases, shorter than IF lives at a

temperature equal to the maximum temperature of the thermal cycle. Kuwabara (23) investigated the TMF behavior of Type 304 stainless steels in the temperature range 473-823°K and the IF behavior at 823°K. He found the in-phase and out-of-phase TMF lives shorter than the IF life at a given strain range. Nicholas (33) observed that the crack growth rate is smaller in the TMF of an Inconel 718 for a temperature range between 427°C and 649°C than in the IF at 649°C. Kuwabara (13) also investigated the TMF behavior of a Type 304 stainless steel in a temperature range between 200°C and 550°C, and reported longer TMF life than the IF life at the maximum temperature. Pernot (10) carried out a 649°C IF test and a 316°C to 649°C in-phase TMF on a Ti-24Al-11Nb alloy. His results show that the crack growth rate for the IF is slightly higher than that for the in-phase TMF at a given value of stress intensity range.

The results of this study indicate that the TMF resistance is similar in the matrix alloy and its composite while the IF resistance is greater in the composite. The observations of the other investigators varied. Karayaka (32) reported substantial improvements in the fatigue life of an aluminum 2XXX-T4 alloy with reinforcement SiC_p under both TMF and IF loading conditions. Gayda (34) studied the fatigue behavior of unidirectional Ti-15-3/SCS-6 composites at 300°C and 550°C, and observed that the composite has a longer IF life than the matrix alloy on a stress-range basis. He suggested that the fatigue life probably was not matrix dominated but was more likely governed by fiber-matrix interface characteristics.

2. Micrographic and Fractographic Features

The post-TMF micrographic and fractographic features observed in this study are: voids on interlamellar plate, twin and grain boundaries; interlamellar, translamellar and intergranular void linkage; intergranular cracking; and disintegration of lamellar structure. Similar observations were made by others. Karayaka (32) reported the presence of voids on the grain boundaries and within the grains in unreinforced and SiC_p-reinforced aluminum 2XXX-T4 alloys, which were subjected to IF at 200°C. He did not observe any preferential void formation around the SiC particles. However, he noticed that intergranular crack growth becomes pronounced

in unreinforced and reinforced materials during in-phase TMF. Furthermore, the fatigue crack initiation sites for the reinforced material were found to be in the matrix phase for most of the loading conditions. Neu (35) found occurrence of crack and void coalescence and intergranular cracking along pearlite colony boundaries in 1070 steel during in-phase TMF. Sheffler (36) conducted TMF and IF tests in ultrahigh vacuum (1 x 10-7 torr) on Type 304 stainless steel and A286 alloy. The T_{min} and T_{max} were 316°C and 649°C for the Type 304 stainless steel and 316°C and 593°C for the A286 alloy, respectively. He found severe grain boundary cavitation in both alloys under in-phase TMF. Boismier (18) investigated the TMF and IF behavior of Mar-M247 nickel-based superalloy in the temperature range 500°C to 871°C, and observed intergranular cracking for in-phase TMF and transgranular crack growth during IF. Nicholas (33) observed intergranular crack growth occurring in the increasing load portion of the cycle, during the TMF of an Inconel 718. Marchand (37) conducted in-phase and out-of-phase TMF tests between 400°C and 925°C for a cast superalloy B-1900+Hf and observed interdendritic cracking.

Also reported was that during creep-fatigue or TMF, voids nucleate, grow and link together in grain boundaries (38, 39). The nucleation of a void is attributed to the formation of vacancy clusters of a critical size under the influence of interface tensile stress (38, 40). Voids nucleate preferentially at heterogeneous sites, such as grain boundaries, where the critical vacancy cluster size is smaller and vacancy diffusion is more rapid. Apparently not only the grain boundaries but also the interlamellar plate and twin boundaries act as the heterogeneous nucleation sites for voids during thermal-mechanical cycling in the current specimen materials.

3. TMF Mechanism

On the basis of the observed pre- and post-TMF micrographic and fractographic features, a TMF mechanism is proposed for the Ti-48Al-2V alloy and its composite: (1) nucleation and growth of voids on interlamellar plate, twin and grain boundaries, (2) interlamellar, translamellar and intergranular linkage of growing voids, (3) secondary cracking along interlamellar plate and

twin boundaries, (4) intergranular cracking, and (5) disintegration of lamellar structure. The schematic of the mechanism is shown in Fig. 10.

CONCLUSIONS

1. The relationship of TMF and IF lives N with T_{max} for a given stress range can be expressed by an equation of the form $T_{max} = A \cdot N^{-b}$, where A and b are constants.

2. For a given T_{max}, the larger the applied stress range, the shorter is the TMF life for both of the matrix alloy and its composite.

3. The IF life at a given T_{max} is shorter than the TMF life in the matrix alloy at all temperatures employed and in the composite only at higher temperatures. At lower temperatures, the IF and TMF lives are essentially identical in the composite.

4. The resistance to TMF is similar in the matrix alloy and its composite, but the IF resistance is greater in the composite than in the matrix alloy.

5. The mechanism of TMF is nucleation and growth of voids on interlamellar plate, twin and grain boundaries, their interlamellar, translamellar and intergranular linkage, intergranular separation, and disintegration of lamellar structure.

REFERENCES

1. Wright, I. C. and Caluer, A. H., "Study of Intermetallic Compounds Task A: Dispersion-Hardened TiAl", Technical Report AFML-TR-76-107, Air Force Materials Laboratory, Wright-Patterson Air Force Base, OH, July 1976.

2. Bhatt, D. D., Meyers G. E. and Hoffmanner, A. L., "Rolling, Forming, and Joining Titanium Aluminide Sheet", Technical Report AFML-TR-78-59, Air Force Materials Laboratory, Wright-Patterson Air Force Base, OH, May 1978.

3. Blackburn, M. J. and Smith, M. P., "The Understanding and Exploitation of Alloys Based on the Compound TiAl (Gamma Phase)", Technical Report AFML-TR-79-4056, Air Force Materials Laboratory, Wright-Patterson Air Force Base, OH, May 1979.

4. O'Connell, T. E., "Study of Intermetallic Compounds", Technical Report AFML-TR-79-4177, Air Force Materials Laboratory, Wright-Patterson Air Force Base, OH, December 1979.

5. Lipsitt, H. A., "Titanium Aluminides - An Overview", in "Proceedings of the Materials Research Society Symposia on High Temperature Ordered intermetallic Alloys", Pittsburgh, PA, 39, 1985, pp. 351.

6. Kampe, S. L., Bryant, J. D., and Christodoulou, L., "Creep Deformation of TiB_2-Reinforced Near-Gamma Titanium Aluminides", Met. Trans. A, 22A, Feb. 1991, pp. 447-454.

7. Bartollotta, P. A. and Verrilli, M. J., "Thermomechanical Fatigue Behavior of SiC/Ti-24Al-11Nb in Air and Argon Environments", NASA Technical Memorandum 105723, August 1992.

8. Marchand, N. J., Pelloux, R. M., and Ilschner, B., "A Fracture Mechanics Criterion for Thermal-Mechanical Fatigue Crack Growth of Gas Turbine Materials", Engineering Fracture Mechanics, 31, 3, 1988, pp. 535-551.

9. Halford, G. R., Verrilli, M. J., Kalluri, S., Ritzert, F. J., Duckert, R. E., and Holland, F. A., "Thermomechanical and Bithermal Fatigue Behavior of Cast B1900 + Hf and Wrought Haynes 188", NASA Technical Memorandum 4225, April 1991.

10. Pernot, J. J., "Thermal-Mechanical Fatigue Testing of a Titanium-Aluminide Alloy", MS Thesis, AFIT/GAE/AA/87D-18, Air Force Institute of Technology, Dayon, OH, December 1987.

11. Cook, T. S., Kim, K. S., and McKnight, R. L., "Low Cycle Fatigue", ASTM STP 942, Solomon, H. D., Halford, G. R, Kaisand, L. R., and Leis, B. N., Eds., American Society for Testing and Materials, Philadelphia, PA, 1988, pp. 692-708.

12. Koizumi, T. and Okazaki, M., "Crack Growth and Prediction of Endurance in Thermal-Mechanical Fatigue of 12Cr-Mo-V-W Steel", Fatigue of Engineering Materials and Structures, 1, 1979, pp. 509-520.

13. Kuwabara, K., Nitta, A., and Kitamura, T., "Thermal-Mechanical Fatigue Life Prediction in High-Temperature Component Materials for Power Plant", in "Advances in Life Prediction Method", Woodford, D. A. and Whitehead, J. R., Eds., American Society of Mechanical Engineers, New York, 1983, pp. 131-141.

14. Sehitoglu, H. and Morrow, J-D., "Characterization of Thermo-Mechanical Fatigue", ASME PVP, 71, 1983, pp. 93-109.

15. Sehitoglu, H. and Karasek, M., "Observations of Material Behavior Under Isothermal and Thermo-Mechanical Loading", Trans. ASME, 108, April 1986. pp. 192-198.

16. Kamiya, N. and Kamigaito, O., "Prediction of Thermal Fatigue Life of Ceramics", Journal of Materials Science, 14, 1979, pp. 573-582.

17. Sehitoglu, H., "Constraint Effect in Thermo-Mechanical Fatigue", Journal of Engineering Materials and Technology, 107, July 1985, pp. 221-226.

18. Boismier, D. A. and Sehitoglu, H., "Thermo-Mechanical Fatigue of Mar-M247: Part 1 - Experiments", Trans. ASME, 112, Jan. 1990, pp. 68-79.

19. Jaske, C. E., "Thermal-Mechanical, Low-Cycle Fatigue of AISI 1010 Steel", in "Thermal Fatigue of Materials and Composites", ASTM STP 612, Spera, D. A. and Mowbray, D. F., Eds., American Society for Testing and Materials, Philadelphia, PA, 1976, pp. 170-198.

20. Bill, R. C., Verrilli, M. J., McGraw, M. A. and Halford, G. R., "Preliminary Study of Thermomechanical Fatigue of Polycrystalline MAR-M 200", NASA Technical Paper 2280, Feb. 1984.

21. Stentz, R. H., Berling, J. T. and Conway, J. B., "A Comparison of Combined Temperature and Mechanical Strain Cycling Data with Isothermal Fatigue Results", Proc. First Int. Conf. on Structural Mechanics in Reactor Technology, Berlin, 1.5, part 5/1, Sept. 1971.

22. Fujino, M. and Taira, S., "Effect of Thermal Cycle on Low Cycle Fatigue life of Steels and Grain Boundary Sliding Characteristics", in "Mechanical Behavior of Materials", eds. K. J. Miller and R. F. Smith, 2, Pergamon Press, New York, NY, 1980, pp. 49-58.

23. Kuwabara, K. and Nitta, A., "Thermal-Mechanical Low-Cycle Fatigue Under Creep-Fatigue Interaction on Type 304 Stainless Steels", in "Mechanical Behavior of Materials", eds. K. J. Miller and R. F. Smith, 2, Pergamon Press, New York, NY, 1980, pp. 69-78.

24. Kuwabara, K. and Nitta, A., "Effect of Strain Hold-Time of High Temperature on Thermal Fatigue Behavior of Type 304 Stainless Steel", 1976 ASMC-MPC Symposium on Creep-Fatigue Interaction, ed. R. M. Currran, American Society of Mechanical Engineers, New York, Dec. 1975, pp. 161-177.

25. Newaz, G. M., Majumdar, B. S., and Brust, F. W., "Thermal Cycling Response of Quasi-Isotropic Metal Matrix Composites", Trans. ASME, 114, April 1992, pp. 156-161.

26. Skelton, R. P., "Environmental Crack Growth in 0.5Cr-Mo-V Steel During Isothermal High Strain Fatigue and Temperature Cycling", Materials Science and Engineering, 35, 2, 1978, pp. 287-298.

27. Taira, S., "Relationship Between Thermal Fatigue and Low-Cycle Fatigue at Elevated Temperature", Fatigue at Elevated Temperatures, ASTM STP 520, American Society for Testing and Materials, 1973, pp. 80-101.

28. Forrest, P. G., "The Use of Strain Cycling Tests for Assessing Thermal Fatigue Resistance", Applied Materials Research, 4, 4, Oct. 1965, pp. 239-246.

29. Majumdar, S., "Thermomechanical Fatigue of Type 304 Stainless Steel", in "Thermal Stress, Material Deformation, and Thermo-Mechanical Fatigue", Sehitoglu, H. and Zamrik, S. Y., Eds., ASME, New York, NY, PVP-vol. 123, 1987, pp.31-36.

30. Sheffler, K. D., "Vacuum Thermal-Mechanical Fatigue Behavior of Two Iron-Base Alloys", in "Thermal Fatigue of Materials and Components", ASTM STP 612, Spera, D. A. and Mowbray, D. F., Eds., American Society for

Testing and Materials, Philadelphia, PA, 1976, pp. 214-226.

31. Majumdar, B. S. and Newaz, G. M., "Thermomechanical Fatigue of a Quasi-Isotropic Metal Matrix Composite", in "Composite Materials: Fatigue and Fracture (Third Volume), ASTM STP 1110, O'Brien, T. K., Ed., American Society for Testing and Materials, Philadelphia, PA, 1991, pp. 732-752.

32. Karayake, M. and Sehitoglu, H., "Thermomechanical Fatigue of Particulate-Reinforced Aluminum 2xxx-T4", Met. Trans. A, 22A, March 1991, pp. 697-707.

33. Nicholas, T., Heil, M. L., and Haritos, G. K., "Predicting Crack Growth Under Thermo-Mechanical Cycling", International Journal of Fracture, 41, 1989, pp. 157-176.

34. Gayda, J., Gabb, T. P., and Freed, A. D., "The Isothermal Fatigue Behavior of a Unidirectional SiC/Ti Composite and the Ti Alloy Matrix", NASA Technical Memorandum 101984, NASA Lewis Research Center, Cleveland, OH, April 1989.

35. Neu, R. W. and Sehitoglu, H., "Thermomechanical Fatigue, Oxidation, and Creep: Part I. Damage Mechanisms", Met. Trans. A, 20A, Sept. 1989, pp. 1755-1767.

36. Sheffler, K. D., "Vacuum Thermal-Mechanical Fatigue Behavior of Two Iron-Base Alloys", in "Thermal Fatigue of Materials and Components", ASTM STP 612, Spera, D. A. and Mowbray, D. F., Eds., American Society for Testing and Materials, Philadelphia, PA, 1976, pp. 214-226.

37. Marchand, N., L'Esperance, G., and Pelloux, R. M., "The Thermal-Mechnical Cyclic Stress-Strain Response of Cast B-1900+Hf", in "Low Cycle Fatigue", ASTM STP 942, Solomon, H. D., Halford, G. R., Kaisand, L. R., and Leis, B. N., Eds., American Society for Testing and Materials, Philadelphia, PA, 1988, pp. 638-656.

38. Raj, R., "Nucleation of Cavities at Second Phase Particles in Grain Boundaries", Acta Metallurgica, 26, 1978, pp. 995-1006.

39. Min, B. K. and Raj, R., "Hold-Time Effects in High Temperature Fatigue", Acta Metallurgica, 26, 1978, pp. 1007-1022.

40. Argon, A. S., Chen, I. W., and Lau, C. W., "Proceedings of a Symposium Sponsored by the TMS-AIME Mechanical Metallurgy Committee at the Fall Meeting of The Metallurgical Society of AIME", Pelloux, R. M. and Stoloff, N., Eds., The Metallurgical Society of AIME, Warrendale, PA, Sept. 18-19, 1979, pp. 46-81.
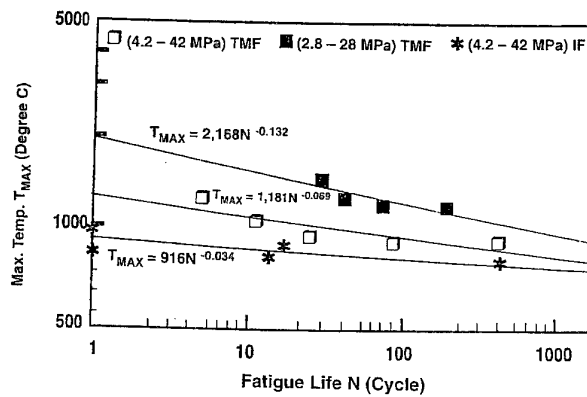
Fig. 1 - Variation of fatigue life N with T_{max} in matrix alloy Ti-48Al-2V.
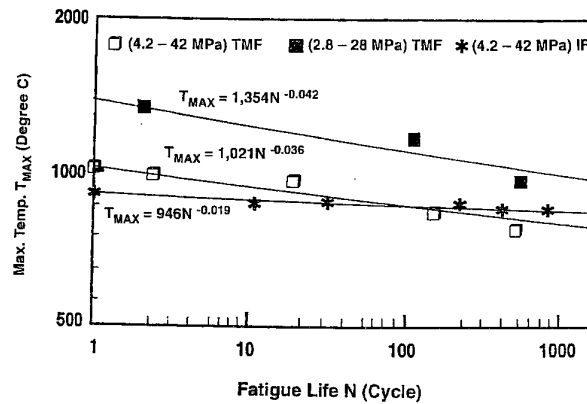
Fig. 2 - Variation of fatigue life N with T_{max} in composite of Ti-48Al-2V alloy reinforced with TiB_2 particles.
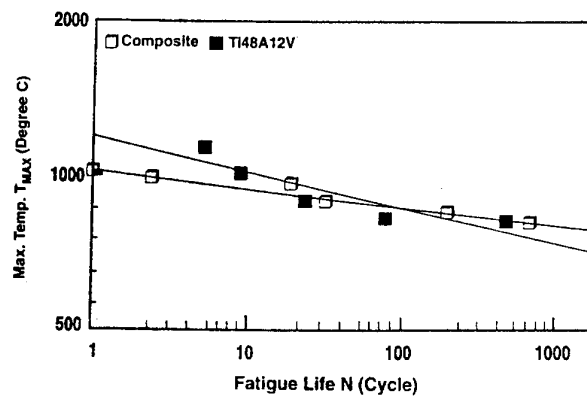
Fig. 3 - TMF lives of matrix alloy and its composite.
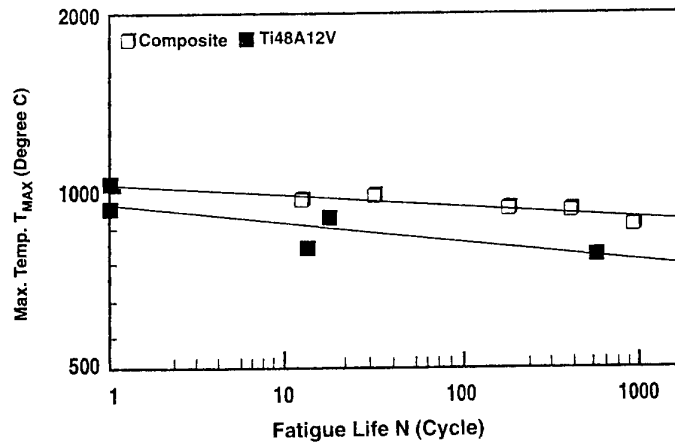
Fig. 4 - IF lives of matrix alloy and its composite.

Ti-48Al-2V alloy   (Ti-48Al-2V) + 7.5 vol% TiB$_2$ composite

Fig. 5 - Pre-TMF Micrographs of Ti-48Al-2V alloy and its composite.
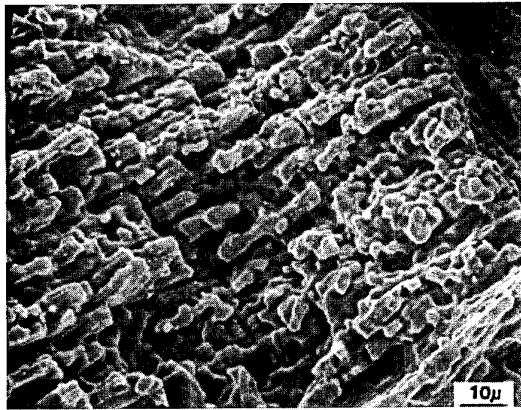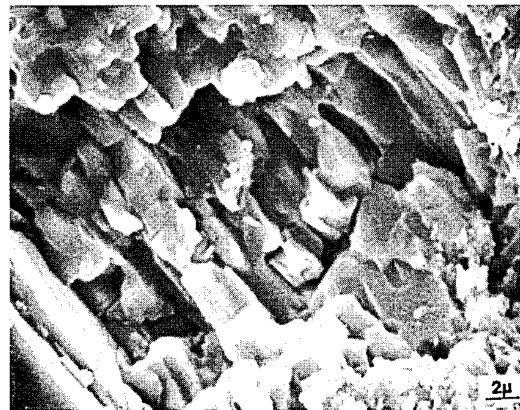
Ti-48Al-2V alloy   (Ti-48Al-2V) + 7.5 vol% TiB$_2$ composite

(100-1400°C, 2.8-28 MPa)   (100-850°C, 4.2-42 MPa)

Fig. 6 - Post-TMF SEM fractographs of Ti-48Al-2V alloy and its composite, showing voids, their linkage, and cracking along interface of a TiB$_2$ particle.
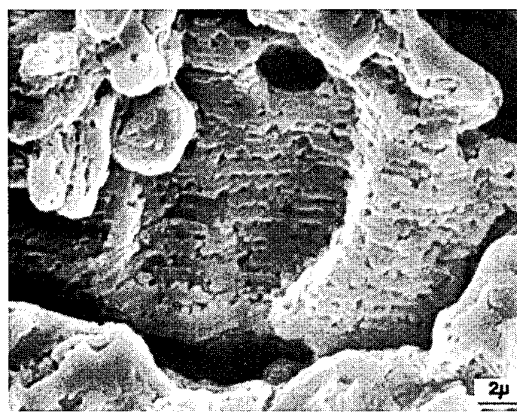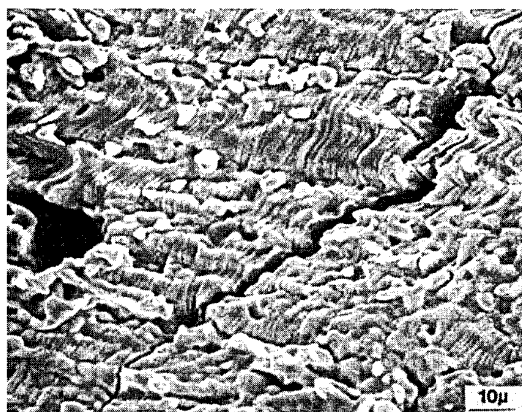
Fig. 7 - Post-TMF SEM fractographs of Ti-48Al-2V alloy, showing twins, voids and their linkage along twin boundaries, and secondary cracking along twin and interlamellar plate boundaries.
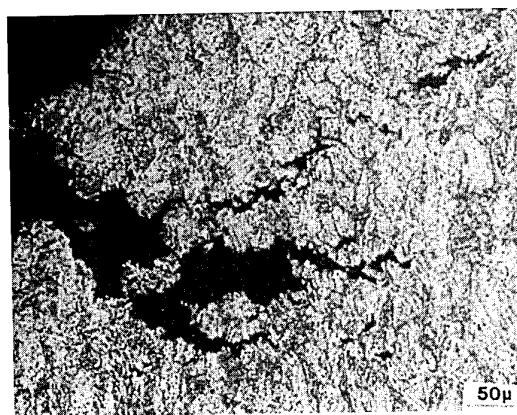
Ti-48Al-2V alloy   (Ti-48Al-2V) + 7.5 vol% TiB$_2$ composite

Fig. 8 - Post-TMF micrographs of matrix alloy and its composite, showing voids, their linkage, and cracking along grain boundaries.

Fig. 9 - Post-TMF SEM fractographs of matrix alloy, showing intergranular fracture.
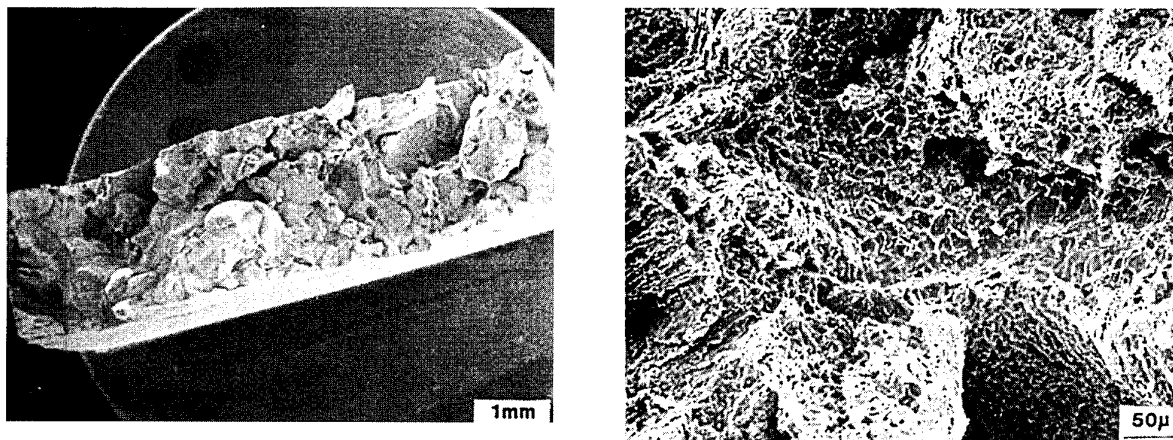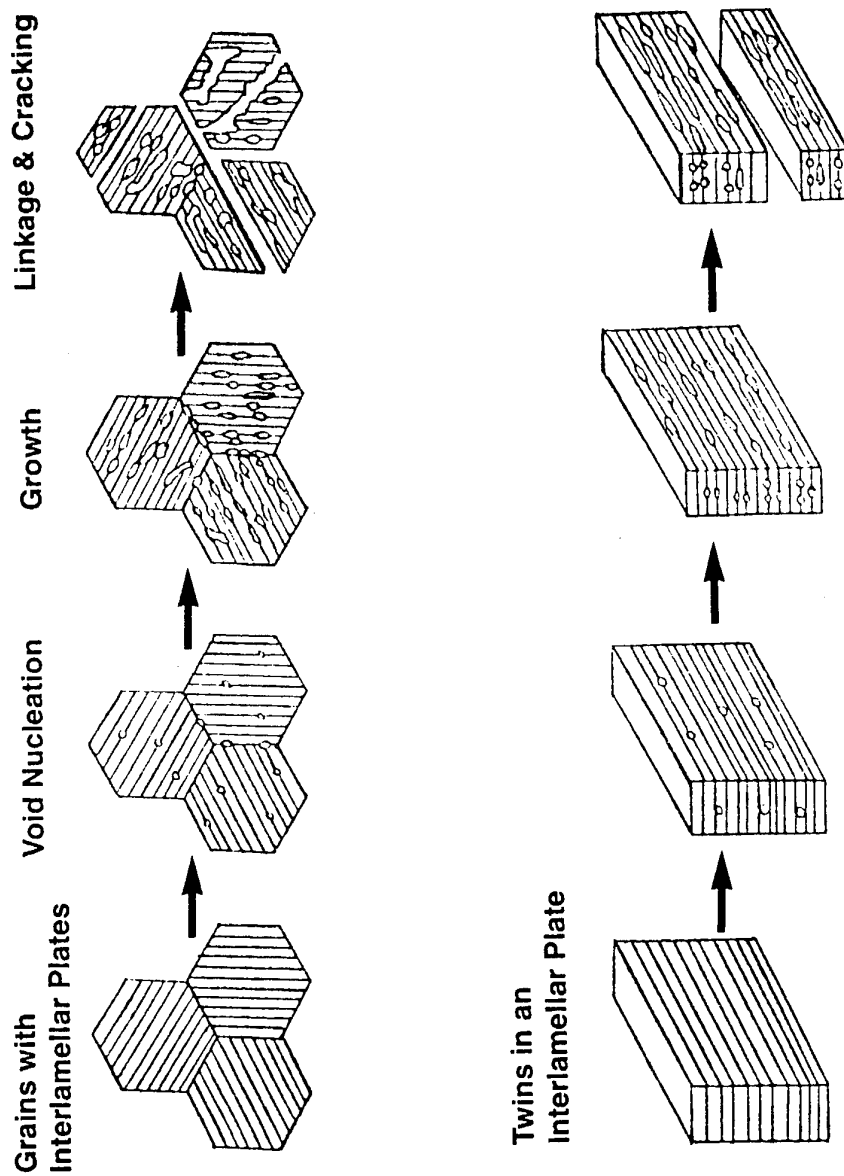
Fig. 10 - Schematic of TMF mechanism.

Damage mechanisms for thermomechanical fatique of aircraft engines materials.

Yu.A. Nozhnitsky,
R.A. Doulnev,
V.G. Soudyrin
Central Institute of Aviation Motors (CIAM)
2, Aviamotornaya st, 111250, Moscow, Russia.

1. SUMMARY

There are presented the main lines of the conducted in CIAM investigations of thermomechanical fatique of aircraft engine parts materials.

Based on a generalization of the results of extensive experimental investigations, it is suggested the strength criterion for non-isothermal cyclic loading with creep effect in every cycle involving two limiting characteristics:

- value of the limiting material deformation, (ε_f^{*})

determined in the conditions of single-cycle reverse loading at temperature changing by the Tmin→ Tmax → Tmin regime, and value of limiting creep

strain (ε_{fc}^{*}) determined in the cyclic creep conditions.

The analytical methods for determining a stress-strain state and the approaches for estimating a life in case of thermomechanical loading of turbine SC-alloy blades and coated blades are worked out.

2. INTRODUCTION

Many parts of aircraft engines, mainly turbine and combustion chamber components, are operated under conditions of cyclic action of mechanical loads and temperature. In this connection over many years in CIAM there are conducted the investigations of thermomechanical fatique. Major directions of these investigations are:
- working out of methods and experimental investigations of thermomechanical fatique of aircraft engine materials,
- elaboration of life models and criterions for strength of material under thermomechanical fatique,
- development of analytical methods for determining a stress- strain state and estimating life of components.

A broad spectrum of materials is under investigation, involving super alloys (including nickel single-crystal alloys are among them), ceramic, carbon-carbon, and metallic composite materials.

Below some results of the damage investigations performed for alloys under thermocyclic loading and also the approaches used for estimating stress-strain state and life of turbine single crystal material blades and coated blades are considered.

3. STRENGTH CRITERION FOR THERMAL-CYCLIC LOADING.

The investigations of the process of static and cyclic non-isothermal loading have been perfomed. Cyclic loading at a varying temperature has been studied for three conditions:
- sign-constant cyclic loading (without of strain reverser),
- sign-varible (reversive) cyclic loading,
- cyclic loading with holdings under load in extreme cycle points.
There have been investigated thirteen schemes of loading for different disc and blade materials of Russian aircraft engines in the temperature range 20-950°C.

Experimental investigations have shown that for non-isothermal sign-constant straining of high-temperature aviation alloy, it is not met the suggestion saying that there is a common generalized strain surface F(σ,ε,T) = 0, plotted from the strain-stress curves σ = f (ε) at constant temperature values. Fig. 1 illustrates, as an example, some results obtained. Loading without strain reverser has shown that, like static loading, the influence of temperature change in cycle manifests itself in the shift of strain-ctress diagram from common strain surface. Such examples are given in Fig.2, Fig.3, and in the last case the value of preliminary strain εo was varied. Table 1 presents the qualitative results of this tests. The shift of strain-stress diagrams can be supposedly explained by the fact that the plasticity value of the studied high-temperature alloys non-monotonically changes, with temperature (Fig.4). If the plasticity decrease ("fall-through") takes place in the range between Tmin and Tmax of the cycle, then the going of strain process through this zone manifests itself in the form of shift of non-isothermal straining diagram from the generalized strain surface, plotted for the T = const condition.

It is of more impotance the study of this influence in case of loading with strain reversing and going of stresses from a compression area to a tension area

or in a inverse sequence.This regime is the most real for the part areas under load, i.e., turbine blade edges, disc rims, etc.In addition to the above -stated influence of going through the area of decreased plasticity, it is realized in this regime the plastic straining in the compression area which coincides often with demonstration of minimum material plasticity. The experimental investigations have shown that in so doing for investigating the high-temperature nickel-base alloys a considerable decrease in the residual plasticity is observed.The preliminary compression at maximum cycle temperature $T_{max}=750^{\circ}C$ has resulted in a considerable (two times and more) decrease in residual strain with following rupture by tensioning load with simultanuous decrease of temperature from 750° to $100^{\circ}C$ (Fig .5). This effects is expressed weaker for more strength and less plastic alloys, however, it reveals itself rather stably also and in this case. The specific feature is that it takes place when the material compression is made in the billets even before manufacturing specimens.It makes sense only the fact that this process is perfomed at a temperature close to that where the plasticity "fall through" is observed.

Regime of non-isothermal loading with strain reversing includes a twofold change in strain sign: material was subjected at the first stage to tensioning at minimum cycle temperature, then to compression at an increasing temperature up to T_{max} value, after which a cooling was performed with simultaneous load increase from σ_{Tmax} up to ultimate value at tensioning (Fig.6). The final value of residual strain has been always less than the value determined in standard experiments performed at constant temperature and without strain reversing. Thus, the results of experiments show that in case of non-isothermal cyclic loading when a portion of material straining process is realized under conditions unfavourable for it (in compression area at a damaging temperature), it is necessary to take into account this effect made on the following straining process.So in this case the usage of residual strain determined in standard experiments for the criterion equations is not justified.The damaging effect of the preliminary compression made on the properties in the following tensioning has been noticed in a number of investigations performed (D. Yao and V.Mundze, D. Drakker, N.N.Davidenkov and P.S.Sakharov, and others), but the material behaviour has not been considered in connection with non-isothermal loading.

Based on generalization of the results of extensive experimental investigations it is suggested the next modified form of strength criterion for non-isothermal cyclic loading:

$$\int_{N} \frac{dN}{N\left(\varepsilon_{f}^{*}, \Delta \varepsilon_{ir}\right)} + \sum_{i=1}^{N} \frac{\Delta \varepsilon_{ic}}{\varepsilon_{fc}^{*}} = 1 \qquad (1)$$

where $\Delta \varepsilon_{ir}$- strain range in cycle, $\Delta \varepsilon_{ic}$ - creep strain in cycle, ε_{f}^{*}- limiting strain value determined in the conditions of single cycle reverse non-isothermal loading, ε_{fc}^{*} - limiting creep strain value determined inthe cycling loading conditions.The value ε_{f}^{*} depends on extreme cycle temperatures T_{max}, T_{min}, values of preliminary strain of tension ε_{t} and compression ε_{com}, and, as well as, on a strain rate ε. It should be defined by the scheme Fig.7. This scheme shows that the residual strain characterizing the material plasticity life, determined not by standard experiments, but for (1/4 + 1) cycle. The addition of one full cycle in this process reflects the specific feature of the process of non-isothermal cyclic loading of material in the parts subjected to a thermal-fatigue damage. The up-to-date testing machines, equipped with the systems of programmed heating and loading, enable to realize cycle, shown in Fig.7 and determine the residual plasticity value $\varepsilon_{f}^{*} = \varepsilon^{t-com-t}$.

The problem available regards the selection of the ε_{com} and ε_{t} strain values. By sense of the tests they should be taken maximum possible, however, practically their values are limited by the area of uniform straining of specimen. From this point of view it is reasonable to use specimens of with striction in the mid-part.

Creep strains $\Delta \varepsilon_{ic}$ are developed in every cycle and finally result in an accumulation of static damage, ε_{fc}^{*} - total creep strain, corresponding to a failure moment, determined in cycling loading conditions, i.e. under creep conditions during cyclic loading. It is worth of noting, that the relaxation process in these conditions slightly differs from the relaxation performed in stationary conditions: the known dependence $\sigma = \sigma_{0}^{*} e^{-kt}$, which is derived from McWell's elastic-viscous body model,rearranged for the cyclic loading conditions in the form:

$$\sigma = \sigma_{0}^{*} e^{-kt^{a}} \qquad (2)$$

where k, a -are there coefficients that depend on temperature.

For the materials that have been investigated, this dependences are established. Omitting here the description of the cyclic relaxation process under conditions of " rigid " loading, that has been investigated in detail but presents the subject of separate discussion, it is worth to note once again the necessity of investigation of the obtained in cyclic creep conditions of ε_{fc}^{*} value in the criterion equation as a limiting characteristic attributed to static damage.

The experimental materials confirming the advisability of using the criterion (1) in calculations have been obtained and also have been performed

the life calculations for some parts have been performed. In view of limited volume of the present paper these data are not given here. Table 2 gives the result of processing the experimental data obtained when high temperature alloys were tested for thermal fatigue. The total damade corresponding to a failure moment (d $_\Sigma$=1) was calculated with the use of Eq.(1). The range of d$_\Sigma$ values, considering the spread, is within range 0,6 - 1,4, as regards mean values, within range 0,7 - 1,2; this is quite acceptable for practical calculations, in view of usially introduced life margin.Table 2 presents the mean values of cyclic damage determined for the regime of thermal-cyclic loading without static damade using the known L. Coffin, S. Manson, B. Langers equations, as well as, by the method described in the given paper with the use of plasticity characteristics which was defined by the sceme shown in Fig.7. It is only in the last case when the calculated damage values are close to 1, i.e. correspond to the experimental data.

For the regime of thermal-cyclic loading by cycles of different duration, the total damage may be expressed not in terms of strains, but in terms of relative values of time and number of cycles. If d$_t$, d$_N$ are the fractions of static and cyclic damage, the total damage :

$$d_\Sigma = d_t + d_N \tag{3}$$

Experimental investigations of a great number of aviation materials performed in the temperature range up to Tmax = 1200° C and corresponding operational loads, have shown that there is a mutual damaging effect made by one type of loading on another type, and the hypothesis of linear summation of damagies when static and non-isothermal cyclic loads act simultaneously is not executed.So:

$$d_t^{\alpha} + d_N^{\beta} = 1 \tag{4}$$

where α, β < 1. The α and β values are defined. The minimum values for all investigated materials and operating temperatures can be taken as α_{min}, β_{min} = 0,25.The establishment of this fact that the α and β parameters of the rule (4) do not depend on a loading level is rather important. Nonlinearity of damage accumulation in the terms of number of cycles and time of loading is reflected in Eq.(1) too. Experiments of other authors also confirmed that TMF damage accumulation is not a linear process.

4. CONSTITUTIVE AND LIFE PREDICTION MODELS FOR SINGLE-CRYSTAL AND DIRECTIONALLY - SOLIDIFIED TURBINE BLADES.

There are developed the constitutive and life prediction models intended for the turbine blades that are cast of the anisotropic single-crystal (SC) and directionally-solidified (DS) superalloys [1]

which allow to analyse a stress-strain state of blades and estimate their lives with the limited available number of experimental data on these materials anisotropy properties. The SC- and DS-materials constitutive models are based on modified Hill's theory of plasticity for orthotropic materials and on an associative flow rule.

For SC-materials having a cubic symmetry, Hill's plasticity surface (potential) in a space of stresses is described by the equation:

$$\Phi(\sigma_{ij}) = 1/2[(\sigma_x - \sigma_y)^2 + (\sigma_y - \sigma_z)^2 + (\sigma_z - \sigma_x)^2]$$

$$+ k_p(\tau_{xy}^2 + \tau_{yz}^2 + \tau_{zx}^2) - \sigma_{<001>}^2 = 0, \tag{5}$$

where

$$k_p = [(\sigma_{<001>T}/\sigma_{<n>T})^2 - f]/g + 1 \tag{6}$$

- coefficient of plastic anisotropy of SC-material.

In formulae (5),(6): $\sigma_{<001>T}$, $\sigma_{<n>T}$ -yield stresses of SC-material in the <001> and <n> directions; $\sigma_{<001>} = \sigma_{<001>}(\lambda)$ - current yield stress of SC- material in the <001> direction; $\lambda = \int \sigma_{<001>} d\varepsilon_{<001>}^P$ - hardening parameter; $d\varepsilon_{<001>}^P$ - increment of plastic strain in the <001> direction.

According to Hill's theory, a plasticity anisotropy is determined based on an yield condition and remains invariant in case of plastic flow (isotropic hardening). The modification suggested is that the coefficient of plastic anisotropy k_p in Eq.(5) at a numerical solution of incremental plastic flow problem for every i-loading step is determined by the formula:

$$k_p = k_p^{(i)} = [(\sigma_{<001>}(\lambda_{i-1})/\sigma_{<n>}(\lambda_{i-1}))^2 - f]/g + 1, \tag{7}$$

where: $\sigma_{<001>}(\lambda_{i-1})$, $\sigma_{<n>}(\lambda_{i-1})$ - current values of SC-material yield stress in the <001> and <n> directions, corresponding to the hardening parameter λ_{i-1} for the previous (i-1) - loading step.

In formulae (6),(7)

$$f = f(\varphi, \psi) = \cos^4\psi(\cos^4\varphi + \sin^4\varphi) + \sin^4\psi;$$
$$g = g(\varphi, \psi) = \cos^4\psi \sin^2\varphi \cos^2\varphi + \cos^2\psi \sin^2\psi,$$

where: φ, ψ - angles that define the <n> direction about the crystallographic axes x,y,z (Fig.8).

The formula (6) is derived from (5) for the case of uniaxial crystal tensioning in the <n> direction. This formula assumes a piece-isotropic hardening of SC- material that simulates its anisotropic hardening approximately .

Such approach may be used also for thermal - cyclic loading, if solving the task relative to the stress and strain ranges and using the cyclic stress-strain curves $\Delta\sigma_{<n>} = \Delta\sigma_{<n>}(\Delta\varepsilon_{<n>})$, obtained in TMF tests.

For this case it is applied an approximate way, when the stress and strain ranges remain constant in the loading cycles and only mean stresses and strains vary in the cycle due to creep effect when holding at maximum cycle temperature.

Creep strains are defined by the way similar to the above-stated, assuming an availability of potential for creep strain rates in the form of surface, like Hill's plasticity surface (5).

For describing the SC-material creep- rupture damage and TMF damage surfaces when a stress state is complex, it is suggested to use the surfaces, like Hill's yield surface following from (5) when $\sigma_{<001>} = \sigma_{<001>T}$. In this case creep- rupture damage, such as yield surface, is described in space of stresses σ_{ij}, and TMF damage surface - in space of elastic-plastic strain ranges $\Delta\varepsilon_{ij}$. Then instead of yield stresses for creep-rupture damage surface it is necessary to use creep-rupture stresses taken from creep-rupture curves at the given temperature and time and for TMF damage surfaces - total elastic-plastic strain ranges taken from TMF curves at given thermal-cyclic regime and numbers of cycles for the <001> and <n> directions respectively.

The moment at which a local crack is created in a SC-blade may be estimated on the hypothesis of summation of static creep- rupture (d_t) and cyclic (d_N) damages from the condition (4). Due to unsufficiency of experimental data for SC alloys the values $\alpha=\beta=1$ are using now.

It makes sense to define the values of anisotropy coefficients of the considered mechanical properties for every point of SC-blade cast with the primary orientation <001> (the majority of SC-blades attribute to this class) using the experimental data on SC-material mechanical properties for the orientations $0\leq\varphi\leq\pi/4$, $\psi=0$, that correspond to the side <100> - <110> of standard stereographic triangle. Such suggestion looks like reasonable, as one of the main stresses (longitudinal - σ_z) available in the cooled SC-blade wall always acts in the direction <001> (or very close to it), and the second one (transversal - σ_s) acts in the directions close to the directions like <100>, <110> and intermediate ones ($0\leq\varphi\leq\pi/4$; $\psi=0$) depending on location of the point in the blade airfoil (Fig.8).

Minimum number of directions for which there should be known the standard mechanical properties of SC-materials is equal two here. Along with the <001> direction it is considered to be preferable the <100> direction, in the vicinity of wich, as a rule, the SC-material creep-rupture strength and TMF characterstics are the worst.

Fig.9 illustrates the results of the calculational estimation of static (d_t) and thermal-cyclic (d_N) damages of SC-blade for different azimuthal (secondary) orientations of single crystal in the plane of mean cross-section of blade airfoil that

have been performed on the basis of the above-presented constitutive and life prediction models. Based on these calculations there has been defined the optimal secondary orientation which provides the largest life for SC-blade. This secondary orientation was realized in a manufacturing casting blade process.

For DC-materials one may use the plasticity surface corresponding to the materials having a transversal-isotropic symmetry of mechanical properties:

$$\Phi(\sigma_{ij}) = 1/2[(\sigma_y - \sigma_z)^2 + (\sigma_z - \sigma_x)^2 - (\sigma_x - \sigma_y)^2 - 2\tau_{xy}^2]$$

$$+ k_{pt}[(\sigma_x - \sigma_y)^2 + 4\tau_{xy}^2] + k_{pz}[\tau_{yz}^2 + \tau_{zx}^2] - \sigma_z^2 = 0, (8)$$

where $k_{pt} = (\sigma_{zT}/\sigma_{tT})^2$; $k_{pz} = (\sigma_{zT}/\tau_{ztT})^2$- coefficients of plastic anisotropy for DS-material; $\sigma_{zT}, \sigma_{tT}, \tau_{ztT}$ - yield stresses of DS-material respectively in tensioning in the longitudinal (z) and transversal (t) directions, as well as, in torsioning around longitudinal direction; σ_z - current yield stress in longitudinal direction. All other principal aspects, stated above, are applicable also to DS-materials.

5. LIFE PREDICTION MODELS FOR CORROSION-RESISTANT AND THERMAL-BARRIER COATINGS OF TURBINE BLADES.

The experimental-calculational method is worked out for investigation of TMF of hot-temperature corrosion-resistant coatings on turbine blades. This method is founded on TMF tests of continuous cylindrical coated specimens conducted till occurrence of the first TMF cracks in the coating and on the calculational determination of elastic-plastic strain ranges in the coating that have resulted in its cracking. The TMF tests are conducted by the scheme with load adjustment (LA TMF-test) for pure elastic straining of base specimen material performed in a special rig enabling to provide an independent control by load and temperature, including synchronized changing load and temperature with any given phase shift between them. The specimen elastic straining conditions permissible for TMF tests of corrosion-resistant coatings, as the developed elastic-plastic strains occur in these coatings (especially in plastic overlay coatings) even with pure elastic straining of the substrate. Such approach is all the more applicable to SC- blades, considering the fact that plastic strains generally don't occur (or they are minor) in the walls of these blades with the exception of small stress concentration zones, due to relatively low value of modulus of elasticity for the <001> orientation and high value of yield stress of SC - superalloys.

The possibility for tests with elastic specimen straining permits the usage of LA TMF-test scheme that is more simple and convenient in practical realization in comparison with the scheme of strain control (SC TMF-test). The main advantage of the

LA TMF- test scheme resides in removal of the necessity of providing constant temperature along the specimen axis, required to specimen strain control by extensometer. Quite the reverse, for LA TMF - tests of coated specimens, the nonuniformity of temperature along the specimen length with maximum temperature value in a mean area of working zone is required. This results in location of coating cracking zone and makes the control over crack onset considerably easier. Further important outcome here is high specimen heating rate at LA TMF-tests, in comparison with the SC TMF-tests. It results in a contraction of test time duration. Test rig, developed in CIAM for conducting LA TMF - tests of specimens, provides a specimen's heating rate in the range 20-50 OC/sec by passing the current of industrial frequency 50 Hz through the specimen, and its cooling rate in the range 20-30 °C/sec with water cooling of catches. Temperature non-uniformity is 600-700 °C along the specimen length. The tests are carried out till the emergency of the first crack of depth 0,1 mm and lehgth 0,3-0,5 mm in the coating under out-of-phase change of load and temperature and symmetric cycle of load change without holding at maximum cycle temperature. By the test data there are plotted the TMF curves $\Delta\varepsilon = =\Delta\varepsilon(N_{Rc})$,where $\Delta\varepsilon$ - elastic strain range of specimen, N_{Rc}- number of thermal cycles to appearance of the first crack in the coating. Further with the use of the developed constitutive model [2] there are calculated the ranges of intensity of elastic-plastic strains in the coating $\Delta\varepsilon_{ic}$ and plotted the TMF curves $\Delta\varepsilon_{ic} = \Delta\varepsilon_{ic}(N_{Rc})$ directly for the coating. As an example Fig.10 shows the hysteresis loop of elastic-plastic straining of NiCrAlY overlay EB-PVD coating applied on specimen casted of DS-superalloy ZhS26 VSNK, that is obtained with use of developed constitutive model [2] for out- of -phase thermal-mechanical cyclic loading of specimen ($\sigma=+200$ MPa$\to$-200 MPa$\to$+200 Mpa; T=300 °C$\to$1100 °C $\to$ 300 °C).

The TMF curves obtained for hot-temperature corrosion-resistant coatings can be used further to predict life of this coatings in the operational conditions, as well as when designing the coatings. Fig. 11 presents the results of the calculational estimation of thermal-cyclic life of some overlay coatings applied on outer blade surface. From this one can see that the chemical composition of coatings significantly affects their thermal-cyclic fatigue. The difference in thermal-cyclic life between the coatings with different chemical compositions and consequently with different thermal-physical and mechanical properties can attain two orders.

The experimental-calculational method is developed to analyze TMF of thermal-barier coatings (TBC). This method involves the experimental determination of a number of thermal cycles (or time) to spalling of a TBC's ceramic layer from specimen surface during periodic heatings in the furnace without load and cooling in air of the continuous cylindrical specimens of different diameters with TBC's applied to their side surfaces , as well as, the calculated determination of normal stresses, spalling TBC's ceramic layer from blade surface in the actual operating coditions.

As an criterion for estimating TBC's life it is used the following condition:

$$\sigma_a = \sigma_a(\,N_{Rc},\,T_a,\,t_c\,) = \begin{cases} \sigma_n, & \text{if } \sigma_n > 0; \\ \\ 0, & \text{if } \sigma_n \le 0, \end{cases} \qquad (9)$$

where σ_n - normal stress, spalling ceramic layer off substrate, σ_a - ultimate spalling stress, breaking ceramic layer off substrate upon accumulation of certain running time in hours and cycles (adhesive strength), T_a - temperature of holding a specimen in furnace, t_c - time of holding in furnace in every cycle, N_{Rc} - number of thermal cycles to the spalling of ceramic layer. Normal stresses σ_n for different areas of outer blade surface are defined by calculations according to special technique [3] taking into account the blade creep and plastic strains. The σ_n stress is positive if it spalls ceramic layer from blade surface and negative - if it presses this layer to blade. The ultimate spalling stress σ_a is evaluated for cylindrical specimens of different diameters from the formula:

$$\sigma_a = E_c(\alpha_{Tc} - \alpha_T)(T - T_a)(\delta/R)/(1 - \mu_c) \qquad (10)$$

and corresponds to a number of thermal cycles of heating in a furnace with holding and cooling in air till the spalling of the TBC's ceramic layer from these specimens. In this formula E_c, α_{Tc}, μ_c - respectively modulus of elasticity, coefficient of thermal expansion and Poisson's ratio for the TBC's ceramic layer, α_T - coefficient of thermal expansion of blade material, $T = 20$°C - temperature of air-cooled specimen, R and δ - radius of specimen external surface and thickness of ceramic layer respectively. The spalling of ceramic layer generally takes place in the cooling semi-cycle. Fig. 12 shows example of life assessment of ZrO_2 / NiCrAlY TBC's ceramic layer at the leading edge of cooled SC turbine blade in the operational conditions (time to spalling $t \approx 265$ hours) .

6. TMF TESTS OF COOLED TURBINE BLADES.

Special test rig is developed in CIAM for conducting TMF- tests of full-scale cooled turbine blades. At this test rig there can be simulated the conditions of thermal-mechanical loading for the mean zone of turbine cooled blade airfoil. Scheme of load and temperature control of this rig is the same as for specimen LA TMF test rig described above. The centrifugal foce for mean cross-sections of blade airfoil is simulated by application of appropriate load to the shroud which is set with the use of servohydraulic system. If blade has not

shroud then a technological shroud has to be welded to blade for applying loading. Thermal stresses in mean cross-sections of cooled blade are simulated by means of creation of tempetature field in them which is close to the actual one. Corrosive attack of environment medium can be simulated by using a covering of appropriate chemical composition for a blade. A superficial heating of blade is performed with the use of high-frequency induction heating of its external surface layer. Here used a high-frequency generator of maximum electromagnetic oscillation frequency 440KHz enables to release more than 80% main quantity of thermal energy in the external surface blade layer of 0,1 mm in thickness. Blade cooling is performed by passing a cooling air through the blade. Simulation of the non-uniform temperature field in the given blade cross-section is accomplished in the following way. Inductor having a variable width along its length is designed using the given steady temperatyre field for the considered cross-section of mean zone of blade airfoil. Such inductor of variable profile provides the given temperature non-uniformity along the external contour of blade cross-section (clearanse between inductor and blade surface is everywere the same). Further it is carried out the preparation of one "tuned up" blade outer surface with thermocouples in the considered cross-section. An inner surface of cooled blade is not strain gauged. The investigations accomplished before have shown that when cooling air flow is defined properly, the value of blade inner surface temperature measured during tests differs from the calculated one not more than 5-10°C. The controlling thermocouple is located below the inductor. The blade is fixed in the testing machine clamps. Adjusted flow-air is supplied to cool the blade on the inside. The warming-up rate is adjusted to the operating conditions. An agreement between the given temperature field and the temperature field obtained with an induction heating in the given blade cross-section is ensured by changing the inductor profile .

Upon running the test regimes on a "tuned-up" blade, there are carried out TMF- tests of the conventional blades. Only one thermocouple welded below the inductor is used in these blades to adjust the temperature change cycle. Actual maximum blade temperature is controlled by pyrometer. Stable reproduction of temperature field on all tested blades is ensured by special splitted turning construction of inductor that is installed with the same clearance about every blade in the batch under test. Crack initiation period is visually controlled while occuring a crack, resistance to Foucault currents increases and the crack begins to shine brightly in the high-frequency electromagnetic field. Continuous monitoring over the surface is accomplished by videocamera involving a periodic recording of display on a video magnetic tape recorder. On periodic visual monitoring, a crack is detected in blade outer surface, and this crack initiation is refined when watching the available recordings. An example of application of the stated rig is given in Table 3, which presents the results of the experimental and calculational TMF analysis of cooled SC- blade casted with <001> and <111> primary orientations. It is important that relative values are close in both cases.

Refferences
1. V.K. Kostege, V.A. Khalturin, V.G. Soundyrin. "Mathematical Models of Gas Turbine Engines and their Components". - Advisory Group for Aerospace Research & Development AGARD-LS-198, NATO, December 1994, France.

2. Yu.A. Tamarin, E.B. Kachanov, V.G. Soundyrin. "Gas Corrosion and Thermal Fatigue of Protective Coatings for Turbine Blades". - Proc. of Intern. Symp. "High-Temperature Corrosion and Protection", June, 26-30, 1990, Shenyang, China.

3. V.G. Soundyrin, Yu.A. Tamarin, V.Yu. Kanaev. "Stress Calculation the Ceramic Thermal Barrier Coatings for cooled Turbine Blades". - Proc. of Intern. Colloquium on Mechanics of Creep Brittle Materials-2, 1991, Leicester, England.

Table 1. Qualitative results of cyclic tests.
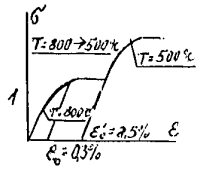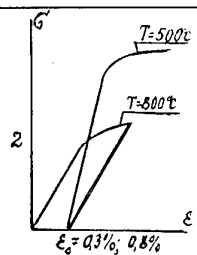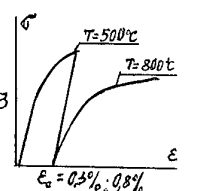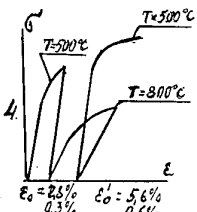
Regime of loading	Specific features of straining process in comparison with isothermal loading		Notest
	at T=500°C=const	at T=800°C=const	
1	Considerable decrease of residual strain, minor increase in strength limit.	Considerable decrease in residual strain.	Curve is located above the strain surface.
2	Increase in strength limit is proportional to ε_0 value. Decrease in residual strain.	The same	Similar result are obtainedat T=800°C and 700°C. The curve is located above the strain surface.
3	Preliminary straining does't make an effect on the following strain process.	Minor decrease in yield strength. Residual strain and strength limit coincide with the given values.	Similar results are obtained at T=800°C and 700°C. The curve approaches to the strain surface underside.
4	Considerable decrease in residual strain, minor increase in strength limit.	Decrease in residual strain at ε_0=2,8 and 5,6% and increase at ε_0=0.3% and 0.6%.	

Table 2   Mean values of cyclic damage for some high-temperature alloys determined from different dependencies   ($T_{min}=20^oC$)

Calculated dependence Alloy, T_{max}	L.Coffin	S. Manson	B.Langer	Dependence (1)
KhN77TYuR 750°	0.48	0.43	0.53	0.93
KhN73MBTYu 750°	0.40	0.50	0.34	1.09
ZhS6U 950°	0.82	0.51	0.48	1.01
KhN56VMTYu 850°	0.72	0.28	0.58	0.83

Table 3 Experimental and calculational TMF analysis data for cooled turbine blades

Primary orientation	Number of thermocycles to crack (calculation)	Number of thermocycles to crack (experiment)
<001>	987	1166
<111>	264	284
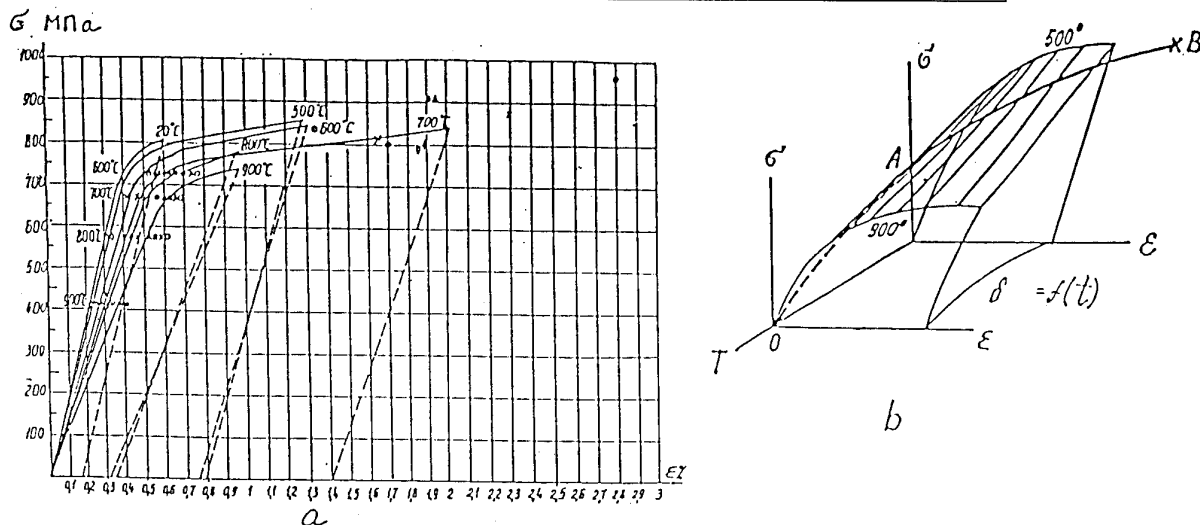
Fig.1Test results of ZhS6K alloy under isothermal (curves) and non-isothermal (900° C→500 °C, experimental points) loading.

a) 1-T = 20°C; 2-500°C, 3-600°C, 4-700°C, 5-800°C, 6-900°C.

×- specimen №1;   ◊ - № 2 ;   • - №9.

b) location of the ε = f (σ, T_{var}) curve relative to the surface of isothermal straining.
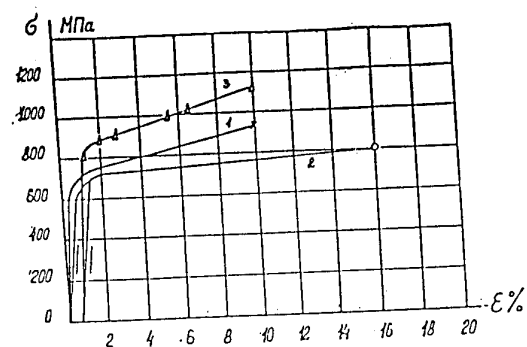
Fig.2 Single-cycled non-isothermal loading of
KhN70VMTYuF alloy by 900→500°C regime.
1-T=500°C, 2-T= 800°C, 3-T= 800→500°C.
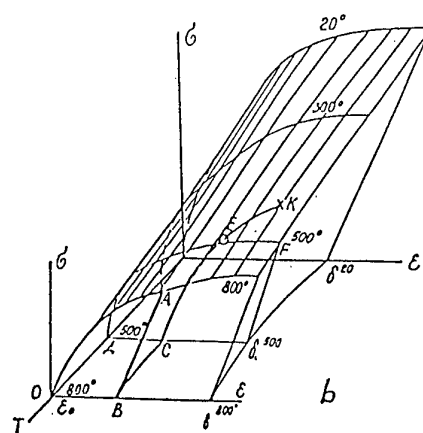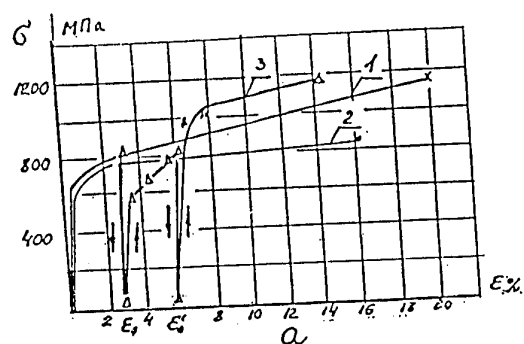
Fig.3 Strane diagram for KhN70VMTYuF alloy with double temperature change:
   a) 1-T = 500°C, 2-T = 800°C, 3-T=500°C→800°C→500°C;
   b) location of the ε= f(σ, Tvar) curve relative to the serface of isothermal straining.
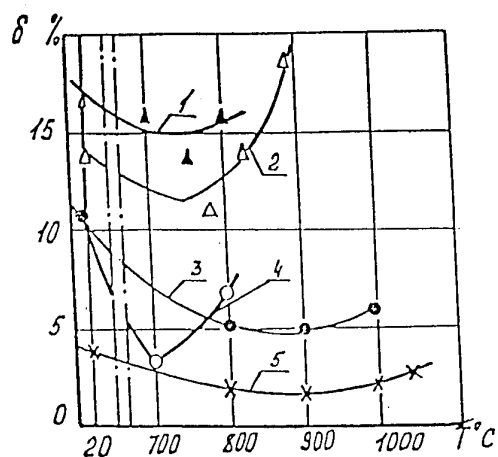
Fig.4 Effect of test temperature on value of residual
plasticity: 1 - N77TYuR, 2 - Rene (from technical
papers), 3 - VZhL12U, 4 KhN77TYu, 5 - ZhS6U.
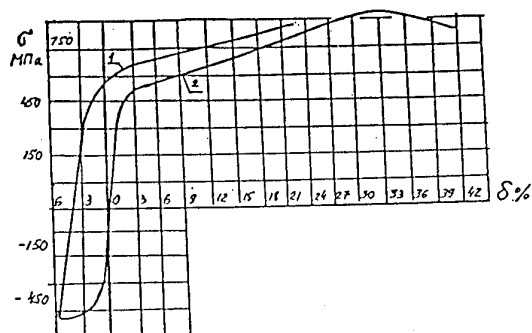
Fig.5 Effect of preliminary compression at
temperature T=750°C on value of residual strain
for KhN77TYuR alloy.   T=500°C→100°C.
1 - with preliminary compression
2 - without preliminary compression
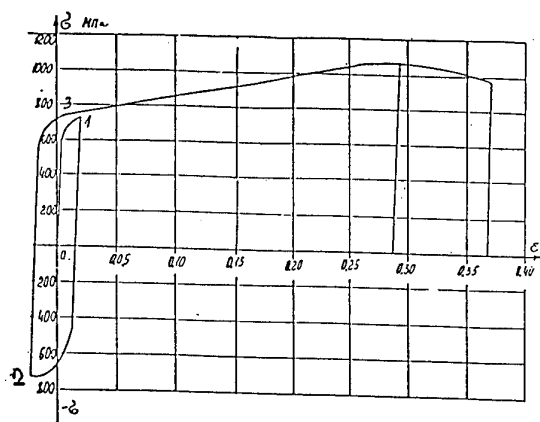
Fig.6 Cyclogram of non-isothermal loading for KhHN77TYuF alloy (point 1 - T= 20ºC, point 2 - T=750ºC, point 3 - T=20ºC).
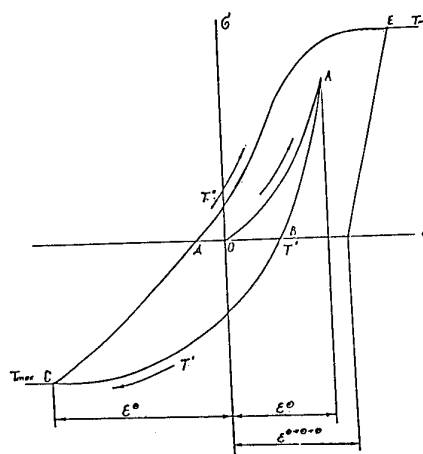
Fig.7 Scheme of the experiment to determine the limiting plasticity characteristicunder non-isotheral loading
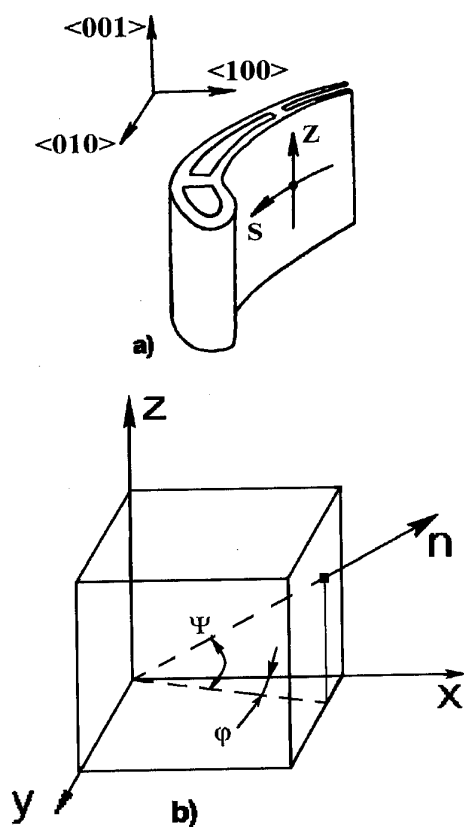
Fig.8. Scheme of the single-crystal turbine blade.
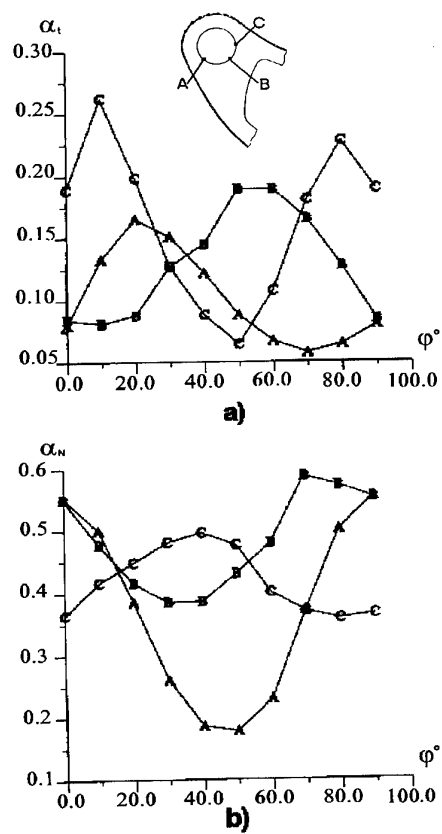
Fig.9. Static damage α_t (a) and cyclic damage α_N(b) vs angle φ of secondary orientation in SC-blade:
A - in point A; B - in point B; C - in point C.

STRESS σ, MPa

STRAIN ϵ

× - METAL   + - COATING
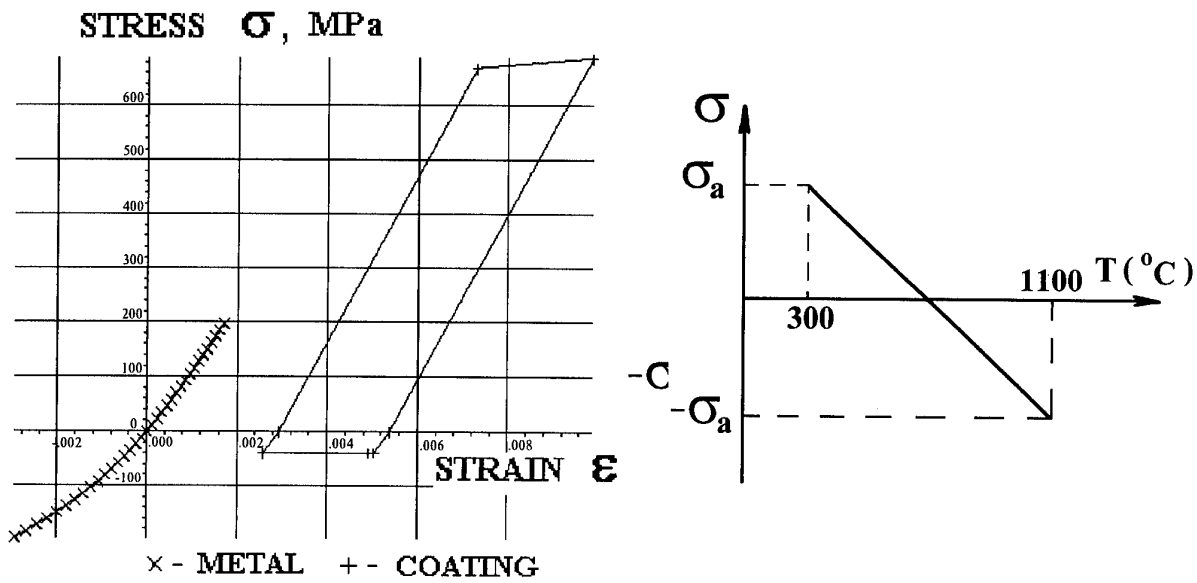
Fig.10. Hysteresis loops for Ni22Cr11AlY coating and ZHS26 VSHK DS-superalloy casted
specimen for out-of-phase: test conditions

N_{Rc}, cycles

Numbers of points, N
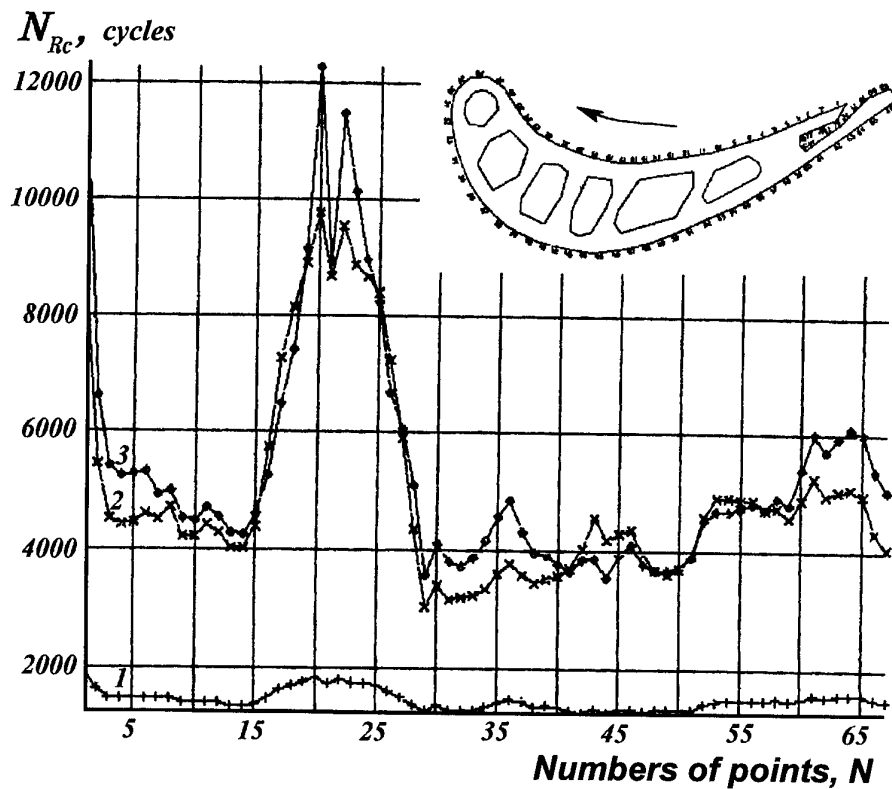
Fig.11. Number of cycles N_{Rc} to TMF cracking of the overlay coatings in different points of blade
outer surface. (1- Ni20Cr5AlY; 2- Ni22Cr11AlY; 3- Ni8Co20Cr11AlY).
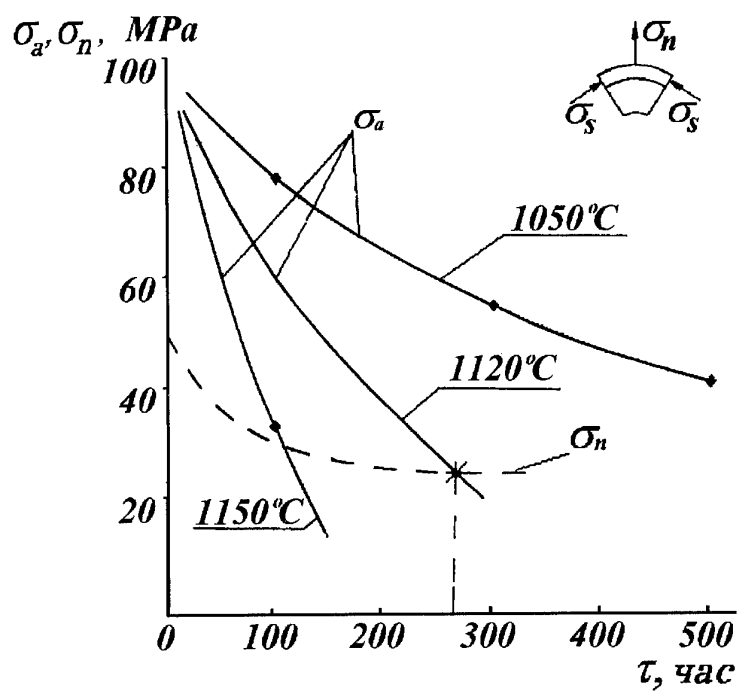
Fig.12. Experimental ultimate spalling stress σ_a and calculated normal stress σ_n (dotted line)
in ZrO_2 - 8%Y_2O_3/ Ni - 22%Cr - 11%Al - Y TBC ceramic layers (leading edge of
cooled turbine blade casted of ZHS32 SC-superalloy).

Axial-Torsional, Thermomechanical Fatigue Behavior
of Haynes 188 Superalloy

Peter J. Bonacuse
Materials Research Engineer
U.S. Army Research Laboratory
Vehicle Propulsion Directorate
NASA Lewis Research Center
21000 Brookpark Rd., Mail Stop 49-7
Cleveland, Ohio 44135-3191, USA

and

Sreeramesh Kalluri
Senior Research Engineer
NYMA, Inc.
NASA Lewis Research Center
21000 Brookpark Rd.
Cleveland, Ohio 44135-3191
USA

1. SUMMARY

The results of axial-torsional, thermomechanical fatigue experiments on thin walled tubular specimens fabricated from the wrought cobalt-base superalloy Haynes 188 are presented. The fatigue test matrix consists of uniaxial, thermally in-phase (maximum temperature coincides with the maximum mechanical strain) and thermally out-of-phase (maximum temperature coincides with the minimum mechanical strain) experiments; a torsional thermomechanical experiment; a mechanically in-phase (maximum axial mechanical strain occurs at the same point in time as the maximum torsional strain), thermally in-phase experiment; a mechanically in-phase, thermally out-of-phase experiment; a mechanically out-of-phase (maximum axial mechanical strain occurs when the torsional strain passes through zero), thermally in-phase experiment; and a mechanically out-of-phase, thermally out-of-phase experiment. In all the experiments the minimum temperature was 316°C and the maximum temperature was 760°C. The axial mechanical strain range in all experiments but the torsional experiment was 0.8%. The torsional strain range in all experiments with an axial strain component was 1.4%. Four multiaxial life models are used to predict the fatigue lives of these experiments. Using 760°C fatigue life parameters, derived from previous axial and torsional experiments on the same heat of Haynes 188, it was found that the von Mises equivalent strain range and Modified Multiaxiality factor

approaches predicted the thermomechanical fatigue lives to within a factor of two of the experimentally observed fatigue lives for all experiments except for the thermally in-phase axial-torsional experiments. Predicted thermomechanical fatigue lives by the Smith-Watson-Topper and the Fatemi-Socie-Kurath parameters were also within a factor of two of the experimental observed fatigue lives, except for the mechanically out-of-phase tests. In general, the largest deviations from the experimentally observed lives were exhibited by the Fatemi-Socie-Kurath model.

2. INTRODUCTION

To determine if various multiaxial life models, which have been typically derived from room temperature fatigue data, are applicable to materials at elevated temperatures, some experimental substantiation is necessary. This is especially true in the case of non-isothermal loading conditions. To address this issue, several axial-torsional thermomechanical fatigue (AT-TMF) experiments have been performed on a cobalt base superalloy, Haynes 188. The test matrix, the experimental techniques, and the testing apparatus are briefly described.

Four life prediction models have been used to estimate the fatigue lives of these experiments. The models chosen can be separated into two groups: two are based on an effective strain range, and two are based on the definition of a "critical plane" on which both stress and

strain act to accumulate damage. The effective strain range models are: the von Mises equivalent strain range model, and the modified Multiaxiality Factor approach. The two critical plane models are a modified Smith-Watson-Topper model and the Fatemi-Socie-Kurath model.

3. EXPERIMENTAL PROGRAM

The following sections will provide an overview of the experimental program that generated the data for this report. Specific details of the experimental program, the facilities, and experimental techniques employed are discussed in detail elswhere [1-4].

3.1 Material Description

Wrought cobalt-base superalloy, Haynes 188, was supplied by a commercial vendor in the form of hot rolled, solution-annealed, round bars with a nominal diameter of 50.8 mm. The chemical composition of the superalloy in weight percent is as follows: <0.002 S; 0.002 B; 0.012 P; 0.1 C; 0.4 Si; 0.034 La; 0.75 Mn; 1.24 Fe; 13.95 W; 21.84 Cr; 22.43 Ni; and the balance is cobalt. The grain size of the supplied material ranges from 45 to 65 μm. This same heat of material was used in previous investigations to perform high temperature isothermal axial-torsional fatigue experiments [1,2] and an intermediate temperature isothermal axial-torsional fatigue study [3].

3.2 Experimental Details

3.2.1 Test Specimen

Thin-walled, tubular specimens with an outer diameter of 26 mm, an inner diameter of 22 mm, and with a uniform gage section of 25 mm [1-4], were machined from the round bar stock. The outer surface of each tubular specimen was polished such that the final polishing marks were parallel to the longitudinal axis of the specimen. The cylindrical bore of each specimen was finished with honing operation to prevent fatigue cracking from the inner surface.

3.2.2 Test Equipment

The experiments described herein were performed on an MTS axial-torsional load frame. A 50 kVA induction heating system was used for specimen heating. In the AT-TMF tests, the constant temperature rate thermal cycle had a maximum temperature of 760°C, a minimum temperature of 316°C and a cycle period of 600 seconds. A special algorithm was employed to ensure that the specimen gage section temperature was kept to within 6°C of the desired temperature at any given point in the thermal cycle. A commercially available, water cooled extensometer equipped with quartz probes was used to measure axial and shear strains. All tests were conducted in strain

control. The entire process was computer controlled with a MS-DOS based microcomputer. Data within a AT-TMF cycle were acquired at 0.6 sec intervals for axial and torsional load, strain, and stroke as well as specimen temperatures. This data were stored to disk at logarithmic intervals. Further details of the AT-TMF testing technique can be found in ref. 4.

3.2.3 Test Matrix

In planning these experiments, a nomenclature was established to distinguish each unique axial-torsional thermomechanical testing condition. When the mechanical strains were proportional (in-phase) this type of test was designated as Mechanically In-Phase (MIP) and when the strains were non-proportional, in this case 90° out-of-phase, the test was designated as Mechanically Out-of-Phase (MOP). Correspondingly, when the axial mechanical strain cycle was in-phase with the temperature the test was designated as a Thermally In-Phase (TIP) experiment and when the axial mechanical strain cycle was 180° out-of-phase with the temperature the test was designated as a Thermally Out-of-Phase (TOP) experiment. Combining these four types of experiments (which are mutually exclusive by pairs) the four axial-torsional TMF experiments listed in Table 1 are obtained (MIPTIP, MIPTOP, MOPTIP, and MOPTOP). In addition, two axial mechanical strain range only and one torsional strain range only TMF experiments were performed. In the axial tests, one test was thermally in-phase while the other test was thermally out-of-phase. In all three cases, the servocontroller with an uncommanded strain history was left in load control at zero load.

3.2.4 Failure Criteria

The failure criteria at the outset of the test matrix was a 10% load drop in either the axial or torsional peak loads from a previously recorded cycle. This criteria was found to be inadequate because specimens failed catastrophically before a 10% reduction in the cyclic loads occurred.

This might be due to the extensive hardening of this material under combined thermomechanical and axial-torsional loading. The load drop criteria was reduced to 5% in an attempt to preclude the extensive deformations that typically occur when large cracks are allowed to form. The reported failure lives are the life to the load drop or the life to specimen separation, which ever occurred first.

4. ANALYSIS OF DATA

In this section, the fatigue lives observed in the AT-TMF experiments were estimated using four multiaxial

life prediction models. The cyclic lives predicted by these models were then compared to the experimentally observed cyclic lives.

4.1 Multiaxial Fatigue Life Models

The following sections describe four multiaxial fatigue life models and the application of these models to axial-torsional thermomechanical fatigue test data.

4.1.1 *von Mises equivalent strain range*

The von Mises equivalent strain range model assumes that the state of strain in a component can be transformed into a scalar quantity by means of the von Mises yield criteria, and that this scalar can then be used as an equivalent uniaxial strain to predict the fatigue life. Reference [5] provides specific details for the implementation of this fatigue life model. For axial-torsional experiments the von Mises equivalent strain range is defined as:

$$\Delta \varepsilon_{eq} = \sqrt{\Delta \varepsilon^2 + \frac{3}{4(1+v_{eff})^2} \Delta \gamma^2} \qquad (1)$$

where $\Delta \varepsilon$ and $\Delta \gamma$ are the maxima of the differences between a peak strain and the recorded strains around a cycle. The effective Poisson's ratio (v_{eff}) in equation (1) is defined as follows for a thermomechanical fatigue test:

$$v_{eff} = \left[\frac{\Delta \varepsilon_e v_e + \Delta \varepsilon_p v_p}{\Delta \varepsilon} \right]$$

$$where: \quad \Delta \varepsilon_e = \left| \frac{\sigma_{T_{max}}}{E_{T_{max}}} - \frac{\sigma_{T_{min}}}{E_{T_{min}}} \right| \qquad (2)$$

$$and: \quad \Delta \varepsilon_p = \Delta \varepsilon - \Delta \varepsilon_e$$

In equation (2), v_e and v_p are the elastic and plastic Poisson's ratios. The stresses and elastic moduli are those corresponding to the temperatures indicated by the subscripts. The elastic Poisson's ratio, v_e, did not change significantly between 760°C and 316°C for Haynes 188. Therefore, v_e at 760° was used in the analysis. For the torsional TMF test, v_{eff} was assumed to be 0.5.

The life model for the von Mises equivalent strain range is described by the following equation:

$$\Delta \varepsilon_{eq} = B(N_f)^b + C(N_f)^c \qquad (3)$$

where the coefficients B and C and the exponents b and c are determined from isothermal uniaxial data. These parameters are found by performing linear least-squares fits of elastic strain range vs. log(N_f) (B and b) and plastic strain range vs. log(N_f) (C and c). The results are plotted in Figure 1. For comparison, isothermal uniaxial fatigue curves corresponding to 316°C and 760°C are also plotted in this figure. The figure clearly shows that the TMF data fell closer to the 760°C life curve.

4.1.2 *Modified Multiaxiality factor approach*

The Modified Multiaxiality Factor approach is an adaptation of the von Mises equivalent strain range method that compensates for the apparent change in ductility due to the presence (or relative absence) of hydrostatic stress [1]. The equation for this model is as follows:

$$\Delta \varepsilon_{eq} = \frac{B}{MF^{(b/c)}}(N_f)^b + \frac{C}{MF}(N_f)^c \qquad (4)$$

where the multiaxiality factor is derived from the triaxiality factor, TF, in the following equation (given in terms of axial-torsional loading) :

$$MF = \frac{1}{2 - TF} \quad ; \; TF \le 1$$

$$MF = TF \quad ; \qquad TF \ge 1 \qquad (5)$$

$$and: \; TF = \frac{\sigma}{\sqrt{\sigma^2 + 3\tau^2}}$$

where σ and τ are the axial and shear stresses, respectively. The coefficients (B and C) and exponents (b and c) are the same as those used in the von Mises equivalent strain range model. The implementation of this fatigue life model for combined axial-torsional loading conditions was discussed in detail in Ref. 2.

In Figures 2 and 3, the Modified Multiaxiality Factor Model predictions are plotted using fatigue parameters derived from 316°C isothermal fatigue data (Fig. 2) and 760°C isothermal fatigue data (Fig. 3). In both figures, curves are plotted for values of the multiaxiality factor of 1 (axial loading only) and 0.5 (torsional loading only). Note that each axial-torsional combined loading test has a different multiaxiality factor, which lies somewhere between 0.5 and 1.0.

The predictions of the Modified Multiaxiality Factor approach based on the 760°C isothermal data are also closer to the AT-TMF data than those based on the 316°C data.

4.1.3 *Modified Smith-Watson-Topper Parameter*

This critical plane approach is a modification to the method originally proposed by Smith-Watson-Topper as a mean stress correction in fatigue life prediction [6]. As proposed by Socie [7], it is intended for use on materials that initiate cracks in planes perpendicular to the maximum normal strain plane. Although originally reported in terms of strain amplitude based parameters it is presented here in terms of the range based parameters used in the von Mises equivalent strain range model:

$$\Delta\varepsilon_1\sigma_1^{max} = \frac{BCE}{2}(N_f)^{b+c} + \frac{B^2E}{2}(N_f)^{2b} \qquad (6)$$

The terms $\Delta\varepsilon_1$ and σ_1^{max} are the maximum principal strain range and the maximum normal stress acting on the maximum principal strain range plane. E is the elastic modulus.

For all the AT-TMF tests, the computed values for the Smith-Watson-Topper parameter, $\Delta\varepsilon_1\cdot\sigma_1^{max}$, are plotted against the observed cyclic lives in Figure 4. Also presented in the figure are the model predictions computed from the isothermal fatigue life constants at both 316°C and 760°C. As in the case of the von Mises parameter, the 760°C fatigue constants provide a better approximation to the TMF data.

4.1.4 *Fatemi-Socie-Kurath model*

This plane specific model was proposed by Fatemi and Socie [8] for use when the material shows a propensity for crack initiation and microcrack propagation on maximum shear strain planes. The equation for the model has been altered from its original form to reflect range based (as opposed to amplitude based) fatigue parameters:

$$\gamma_{max}(1+k\frac{\sigma_n^{max}}{\sigma_y}) = \left[1+\frac{kEB}{4\sigma_y}(N_f)^b\right]\cdot$$
$$\left[(1+v_e)\frac{B}{2}(N_f)^b + (1+v_p)\frac{C}{2}(N_f)^c\right] \qquad (7)$$

where k is a constant determined through the correlation of uniaxial and torsional fatigue data. In the case of Haynes 188 this constant was determined to be 1 in the fatigue life range of interest. The maximum shear strain, γ_{max}, was determined by examining many planes at every collected data point around the fatigue cycle. The maximum normal stress, σ_n^{max}, was the largest normal stress on the maximum shear strain plane.

In Figure 5, the TMF data are displayed in terms of the Fatemi-Socie-Kurath parameter, $\gamma_{max}(1+k\frac{\sigma_n^{max}}{\sigma_y})$, versus the observed cycles to failure. As in the previous figures, the model prediction (also presented in Fig.5) most closely approximating the TMF data is that computed with the 760°C isothermal fatigue data.

4.2 Discussion of Results

In calculating the fatigue lives of AT-TMF experiments using the life models described, a method for incorporating the effect of temperature on fatigue life must be devised as it is not explicitly addressed. As a first approximation, the maximum or another temperature within the TMF cycle, including the minimum, may be used to evaluate the model constants provided that uniaxial fatigue data exist for the chosen temperature. As can be seen in figure 1 the fatigue lives of the AT-TMF tests clustered closer to the 760°C life curve than the 316°C life curve. It was therefore determined that the 760°C fatigue parameters would be used to predict the fatigue lives for the four life models examined. As stated previously, uniaxial fatigue tests were performed on the same heat of material, with the same specimen geometry, as that used in this study. The life curves for all the models were determined from the uniaxial fatigue data generated at 760°C.

The von Mises equivalent strain parameter, using the 760°C isothermal fatigue constants, predicts the cyclic lives under most thermomechanical and axial-torsional loading conditions to within approximately a factor of two (Fig. 6). The thermally in-phase axial-torsional experiments are slightly over predicted and the torsional test is marginally under predicted. Both of these phenomena have been observed in uniaxial TMF experiments and isothermal torsional experiments, respectively. The under prediction of torsional experiments has led to the genesis of many of the multiaxial fatigue life models.

The Modified Multiaxiality Factor (MMF) approach also predicted most of the cyclic lives to within a factor of two of the observed lives. The MMF approach improved the prediction of the torsional TMF test over the von Mises equivalent strain range parameter (Fig. 7). However this approach also over predicted the thermally in-phase AT-TMF tests.

The Smith-Watson-Topper (SWT) model in addition to slightly over predicting the thermally in-phase tests, marginally under predicted cyclic lives of the axial thermally out-of-phase, the MIPTOP, and the MOPTOP tests (Fig. 8). Overall, the prediction of the

SWT parameter seemed to have a larger scatter than either the von Mises or the MMF approaches. As in the the previous two models, SWT parameter had its worst prediction for the MOPTIP experiment.

The Fatemi-Socie-Kurath (FSK) model predicted the cyclic lives to within approximately a factor of two with the exception of the two mechanically out-of-phase experiments (Fig. 9). At worst, in the case of the MOPTIP experiment, the FSK parameter over estimated the fatigue life by a factor of 16.

The TMF data set presented in this paper is limited, in terms of the temperature extremes and strain range regimes explored. However, all the life prediction models investigated over predicted the fatigue life of the MOPTOP test. In general, the thermally in-phase test lives were slightly over predicted. A possible explanation may the relative lack of time dependent deformation (creep strain) in the isothermal data at 760°C (from which the model constants are obtained). The uniaxial, isothermal, fatigue experiments were performed with a cycle period that was 10 seconds as opposed to 600 seconds for the AT-TMF experiments. This difference in cycle period allowed significantly larger amounts of creep strain to occur at the hot end of the TMF cycle than occurred in the high temperature (760°C) isothermal experiments. Since the presence of creep strain is well known to decrease the fatigue life, this may explain the over prediction of the thermally in-phase tests. This hypothesis, and other observed trends, must be confirmed by conducting additional AT-TMF tests different temperature extremes and strain ranges.

5. CONCLUSIONS
For this material, using fatigue parameters derived from isothermal data generated at the peak temperature of the TMF cycle produced better estimations of the TMF fatigue lives than parameters derived from lower temperature isothermal fatigue data.

Of the four fatigue life models used to evaluate the axial-torsional TMF data the von Mises equivalent strain range approach seemed to provide the best predictions. The Modified Multiaxiality Factor approach did not significantly improve the TMF life predictions over the Von Mises equivalent strain range model.

In general, all of the fatigue life models evaluated in this report were unconservative when predicting the lives of the thermally in-phase axial-torsional experiments. The Fatemi-Socie-Kurath model also over predicted the life of the mechanically out-of-phase, thermally out-of-phase experiment.

6. REFERENCES

[1] Bonacuse, P. J. and Kalluri, S., "Elevated Temperature Axial and Torsional Fatigue Behavior of Haynes 188," Journal of Engineering Materials and Technology, Vol. 117, April 1995, pp. 191-199.

[2] Kalluri, S. and Bonacuse, P. J., "In-Phase and Out-of-Phase Axial-Torsional Fatigue Behavior of Haynes 188 at 760°C," Advances in Multiaxial Fatigue, ASTM STP 1191, D. L. McDowell and J. R. Ellis, Eds.,1993, pp. 133-150.

[3] Kalluri, S. and Bonacuse, P. J., "Estimation of Fatigue Life under Axial-Torsional Loading," Material Durability/Life Prediction Modeling: Materials for the 21ˢᵗ Century, PVP-Vol. 290, ASME, 1994, pp. 17-33.

[4] Kalluri, S. and Bonacuse, P. J., "An Axial-Torsional, Thermomechanical Fatigue Testing Technique," presented at ASTM symposium on Multiaxial Fatigue and Deformation Testing Techniques, May 15, 1995 (to be published in ASTM STP 1280, 1996).

[5] "Case 1592-7," Cases of ASME Boiler and Pressure Vessel Code, American Society of Mechanical Engineers, New York, 1975, pp. 388-389.

[6] Smith, K. N., Watson, P., and Topper, T. H., "A Stress Strain Function for the Fatigue of Metals," Journal of Materials, Vol. 5, No. 4, 1970, pp. 767-778.

[7] Socie, D. F., "Multiaxial Fatigue Damage Models", Journal of Engineering Materials and Technology, Vol. 109, No. 4, 1987, pp. 293-298.

[8] Fatemi, A., and Socie, D. F., "A Critical Plane Approach to Multiaxial Fatigue Damage Including Out-of-Phase Loading," Fatigue and Fracture of Engineering Materials and Structures, Vol. 11, No. 3, 1988, pp. 149-165.

Table 1: Axial-Torsional Thermomechanical Fatigue Test Matrix

Test Type	Axial Strain Range $\Delta\varepsilon$ [%]	Shear Strain Range $\Delta\gamma$ [%]	Mechanical Phase Shift ϕ [°]	Thermal Phase Shift θ [°]
Axial TMF In-Phase	0.8	0.0	0	0
Axial TMF Out-of-Phase	0.8	0.0	0	180
Torsional TMF	0.0	1.4	0	0
MIPTIP	0.8	1.4	0	0
MIPTOP	0.8	1.4	0	180
MOPTIP	0.8	1.4	90	0
MOPTOP	0.8	1.4	90	180
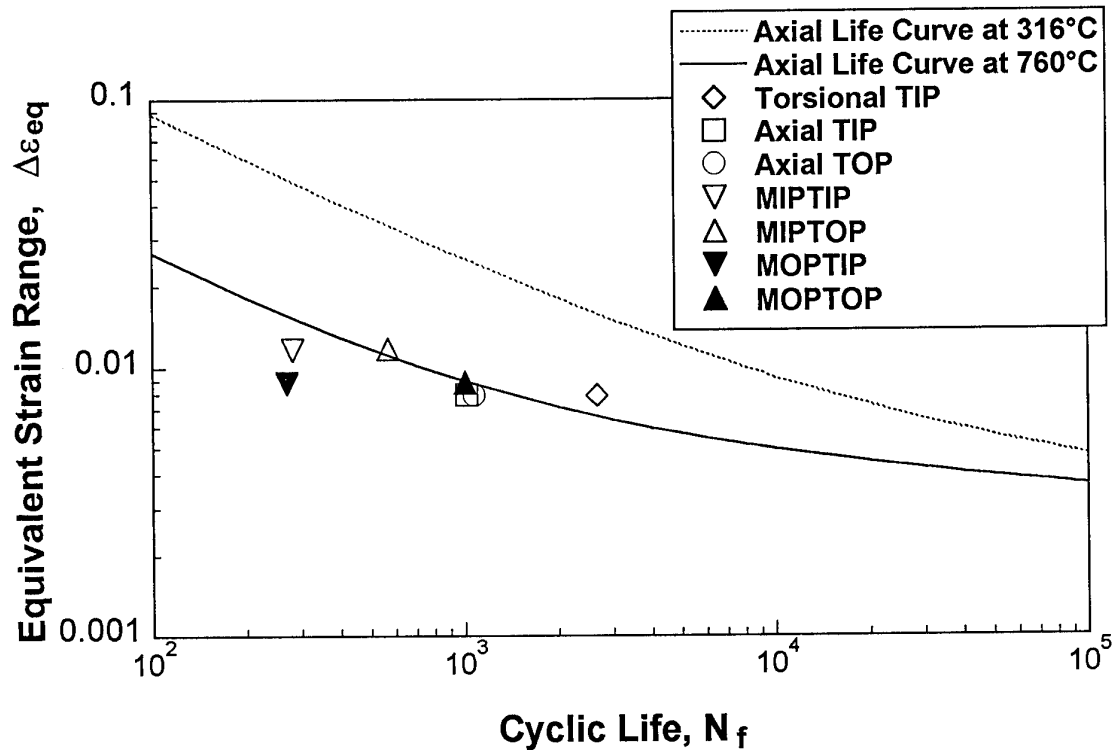
Figure 1: von Mises equivalent strain range vs. life for thermomechanical fatigue tests with isothermal uniaxial fatigue life curves at 316° and 760° C.
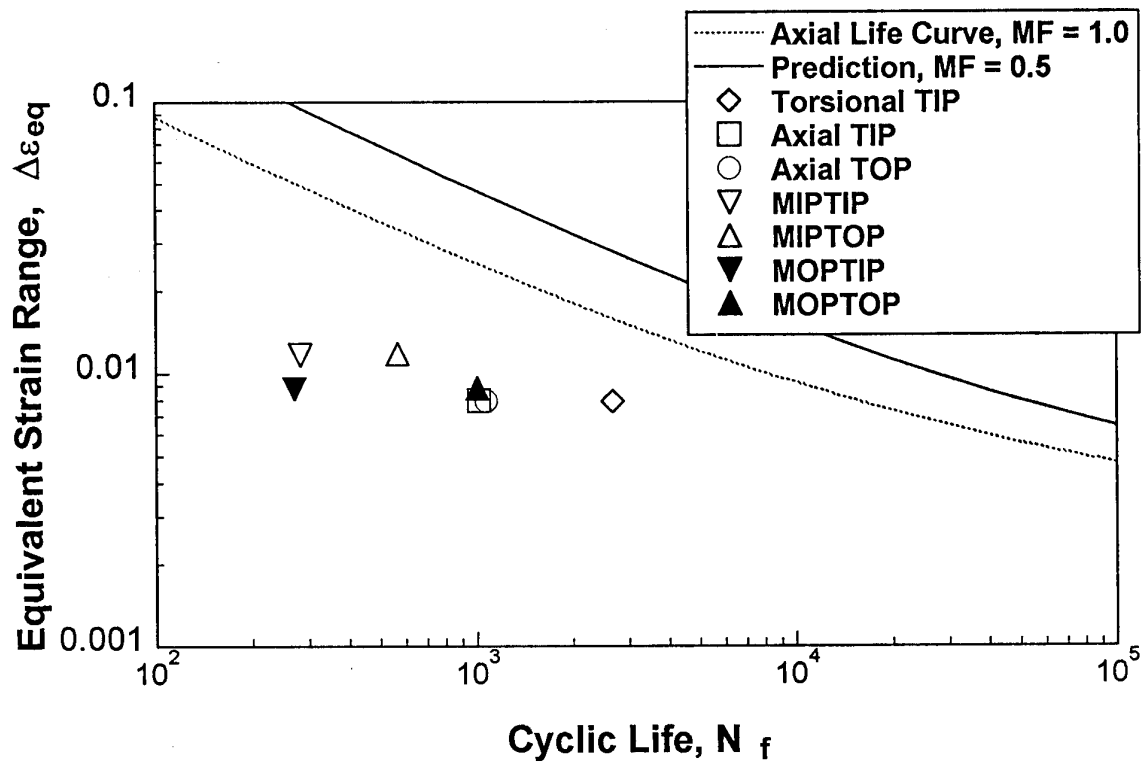
Figure 2: Modified Multiaxiality Factor Predictions using constants from 316°C fatigue life data
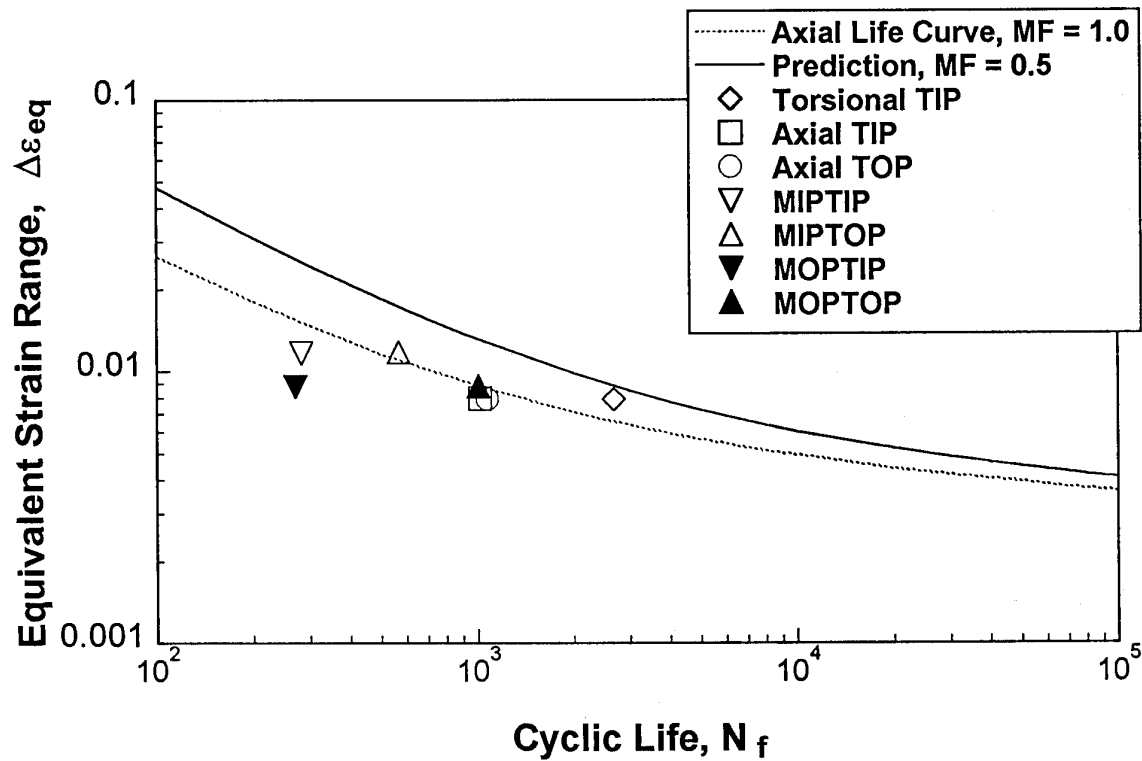
Figure 3: Modified Multiaxiality Factor Predictions using constants from 760°C fatigue life data
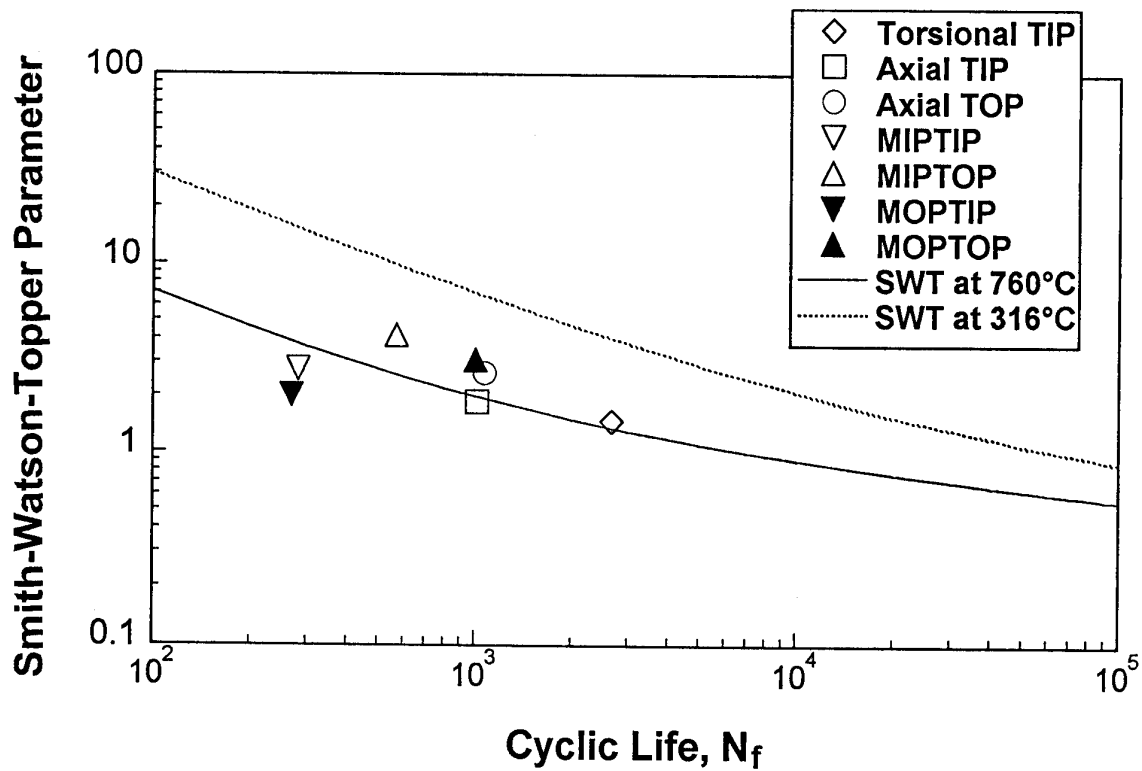
Figure 4: Smith-Watson-Topper parameter vs. life with model evaluated at 316° and 760° C
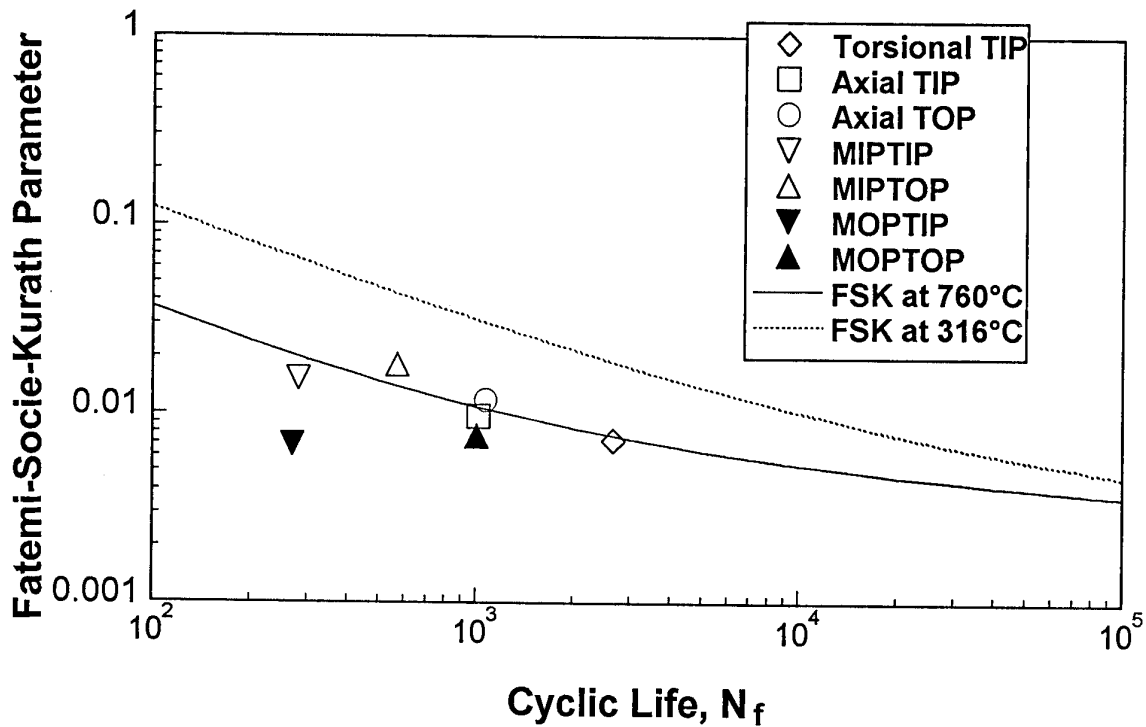
Figure 5: Fatemi-Socie-Kurath parameter (using 760°C yield stress) vs. life with model evaluated at 316° and 760° C
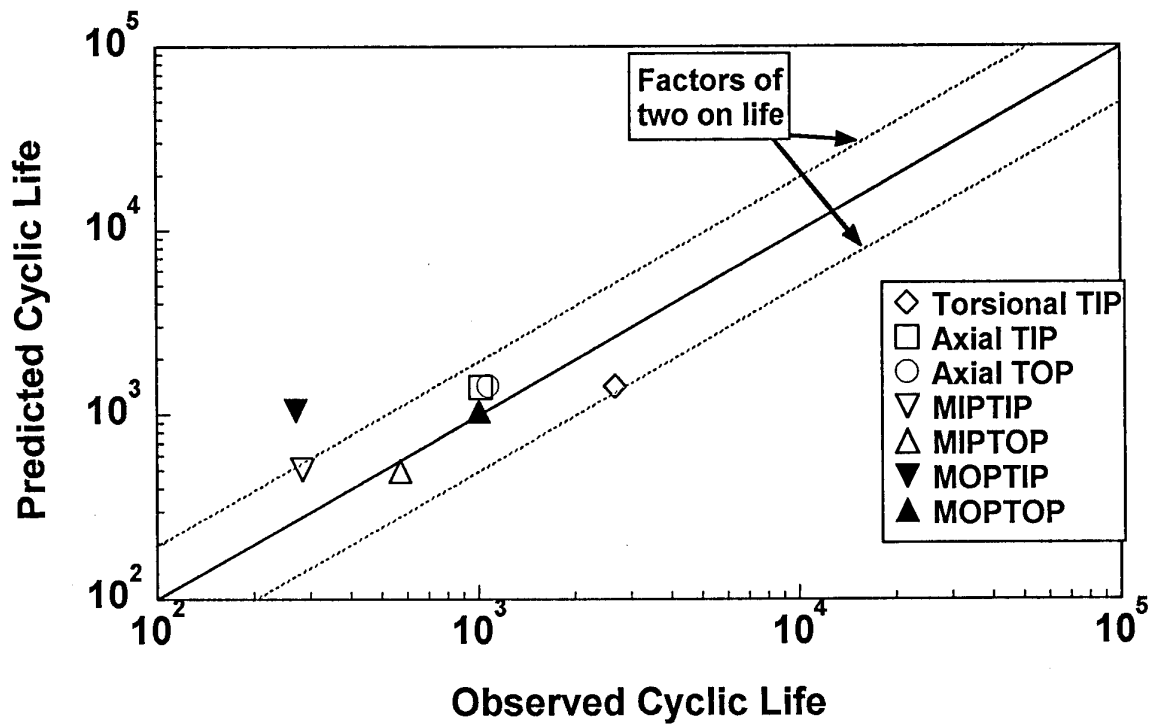
Figure 6: Observed vs. predicted fatigue life for the von Mises equivalent strain range method
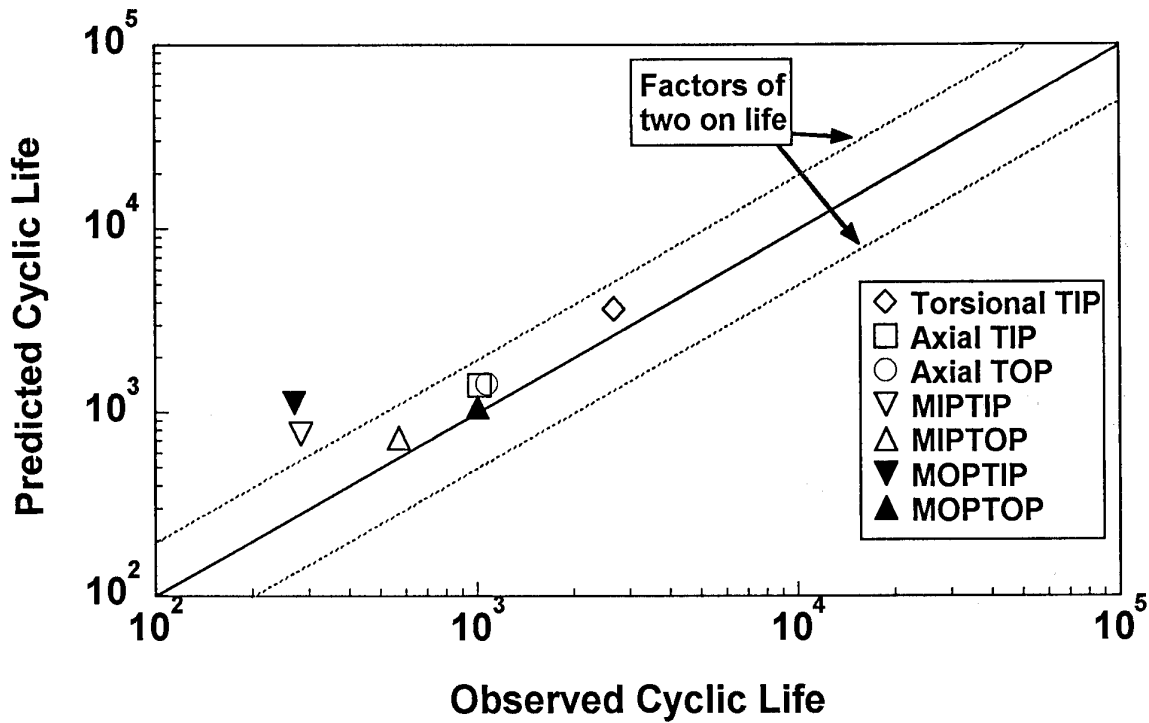
Figure 7: Observed vs. predicted fatigue lives for the modified multiaxiality factor approach
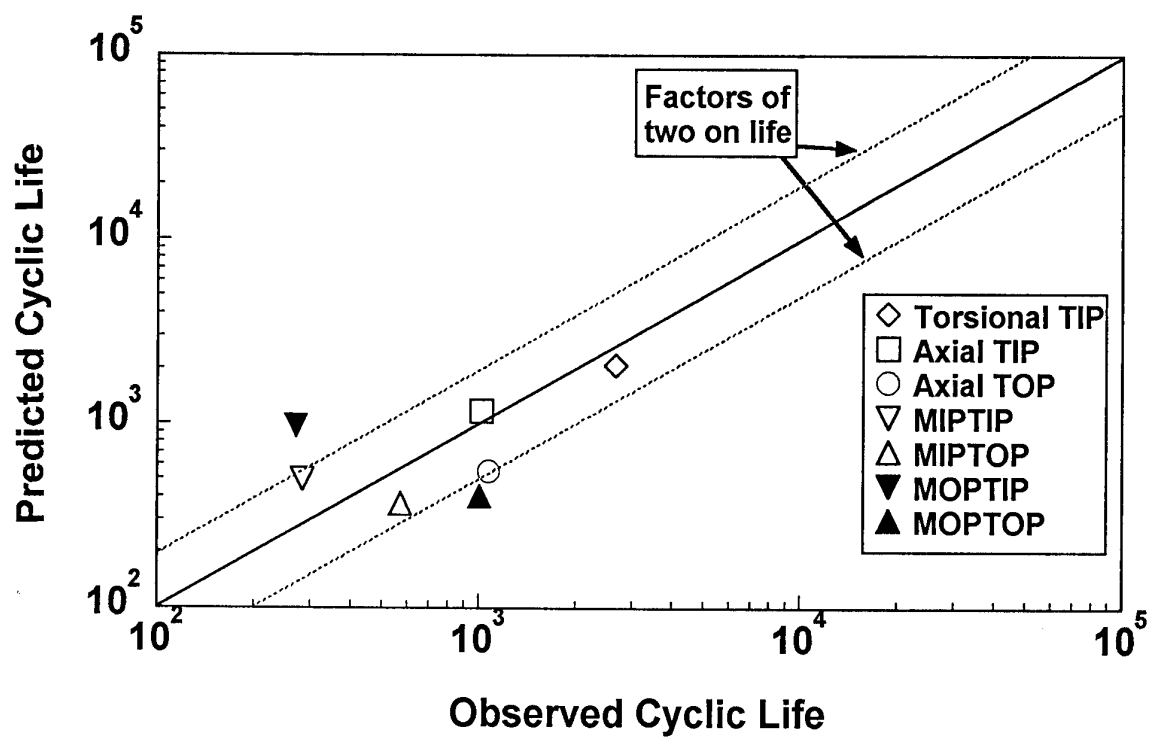
Figure 8: Observed vs. predicted fatigue lives for the modified Smith-Watson-Topper model
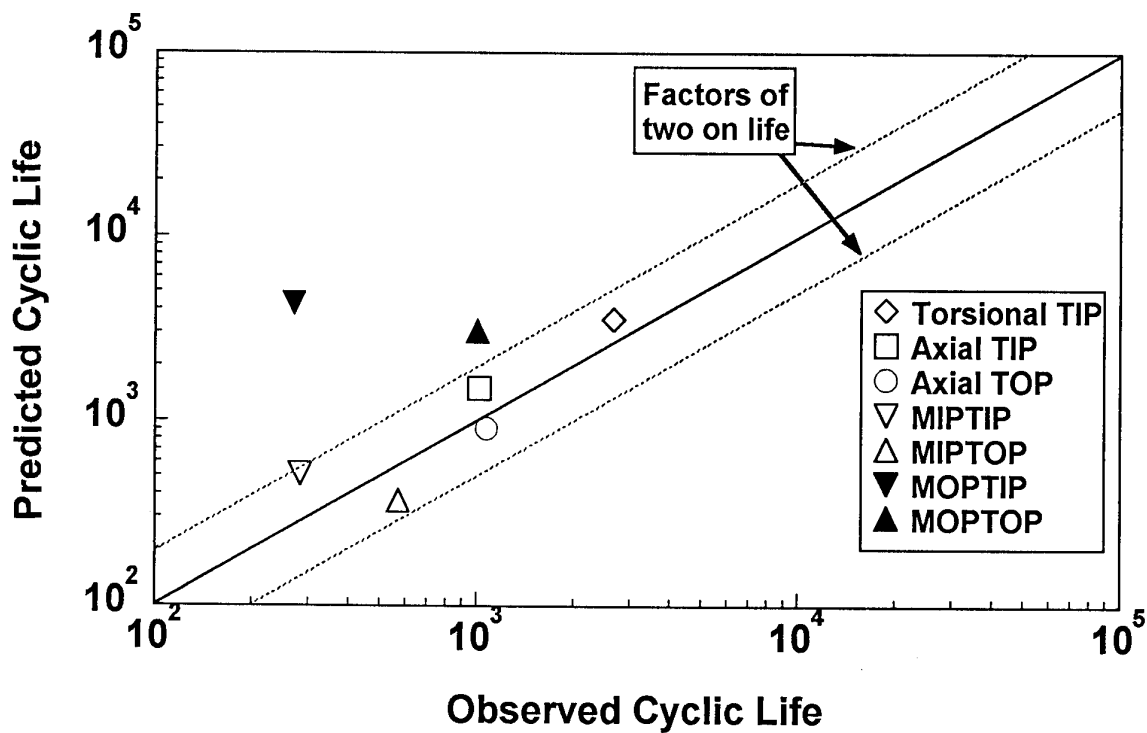
Figure 9: Observed vs. predicted fatigue lives for the Fatemi-Socie-Kurath model using 760°C σ_y

MODELLING OF THERMOMECHANICAL FATIGUE IN AERO ENGINE TURBINE BLADES

G.F. Harrison[1], P.H.Tranter[1] and S.J. Williams[2]

[1] Defence Research Agency, Pyestock, Farnborough,
Hampshire, GU14 0LS, UK
[2] Rolls-Royce plc, PO Box 31, Derby, DE2 8BJ, UK

1. ABSTRACT

The paper discusses the major parameters influencing the design of aero engine high pressure turbine blades and their contribution to the thermomechanical fatigue (TMF) behaviour of these blades. Procedures for calculating transient temperatures and the role of such temperatures in determining thermomechanical stresses are considered.

In turn, having established the major parameters influencing the TMF behaviour of the blade, both stress and strain based life prediction models are considered. In-phase and out-of phase TMF test results of both plane and coated specimens are presented and the implications for lifing models are discussed. Finally, the form of future TMF models are briefly considered.

2. INTRODUCTION

One of the most challenging tasks facing today's engineer is the design of high pressure turbine blades for advanced gas turbine aero engines. These blades are required to operate in extremely hostile environments and in gas temperatures now approaching 1800K. Since such temperatures are considerably above the melting points of even the most advanced current aero engine materials, it is essential that the blades have adequate internal cooling passages and associated cooling air flows to maintain the temperatures at sustainable levels (typically not greater than 80% of the metal solidus temperatures). Thus, in addition to the combined mechanical loadings of centrifugal and gas bending forces, the cooled blade experiences significant thermal loads which vary markedly over small distances in the blade cross section and which change rapidly throughout the engine operating cycle. Indeed, these rapidly changing external conditions can result in transient temperatures and induced thermal stresses of sufficient severity to cause failure in extremely short periods. Since the damage produced in such situations is controlled by the cumulative effects of the transient temperature differences and because of its cyclic nature, it has been termed "thermal fatigue", where only thermal stresses are involved, or TMF, where both the thermal and mechanical loadings contribute to failure. Although transient thermal stresses make a significant contribution to the stresses operating in aero engine discs, their dominant contribution concerns the influence they have on the behaviour and integrity of turbine blades and this paper addresses only the latter situation.

3. BLADE DESIGN REQUIREMENTS

It is instructive to reflect briefly on the major factors influencing the design process since the turbine blade that enters service is a compromise solution to a number of conflicting requirements each of which may contribute to the overall TMF behaviour.

Aerofoil design is probably the primary consideration since it is essential for the blade to generate sufficient power to drive the compressor at maximum efficiency. Aspects that influence design include the aircraft role, (civil or military application), and the number of stages required in the proposed design configuration. Within the context of the current paper it is sufficient to note that aerodynamic factors influence blade lives by dictating blade geometry, thus fixing the level of induced stresses and thereby ultimately determining the failure modes and failure locations.

For advanced gas turbine engines, where turbine entry temperatures can be significantly above the incipient melting temperatures of available blade materials, cooling of first stage nozzle guide vanes and HP turbine rotor blades is an essential requirement. However compromises again have to be made between the ideals of cooling design and the requirements of blade manufacture. As well as introducing stress concentration features, cooling passages contribute to the substantial variations in temperatures which occur over small regions of the blade cross section. Both aspects compound the difficulties of accurate blade life determination.

Mechanical integrity is the final design consideration since having met aerodynamic and blade cooling requirements, the blade must have the ability to withstand the imposed static and cyclic stresses. Although many factors affect mechanical design the

two of importance in respect to the current paper are (i) the combined thermomechanical load state within the blade and (ii) the inherent strength of the blade material.

4.   MODELLING TRANSIENT TEMPERATURES AND STRESSES

A detailed knowledge of the transient temperature distribution throughout an engine cycle is a pre-requisite to the analysis of local stresses and strains. Indeed accurate TMF life calculations in particular depend on the reliability of temperature predictions, since it is these transient changes which bring about the reverse thermal stresses and inelastic flow which characterise thermal fatigue damage.

The advent of supercomputers has meant that transient and steady state heat transfer analyses can now be performed by advanced 3D finite element codes. Analysis models vary markedly in complexity, however, it is frequently considered that the heat flux is entirely within the selected blade section, no spanwise heat conduction being allowed. The heat transfer is assumed to be by convection and the secondary radiation terms may or may not be included. External gas stream temperatures and heat transfer coefficients may be input to the programme using calculated velocity distributions and assuming turbulent boundary layers. To account for the effects of internal cooling, a heat balance sum can be performed. Such an approach may make allowance for the rise in the temperature of the cooling air as it passes in the spanwise direction down the blade. Complex cooling system designs still have to be modelled in a highly idealised manner and calculated temperatures are generally adjusted against instrumented thermocouple and thermal paint rig tests.

The calculated temperature distributions throughout the blade (and their variation throughout the service mission) can be used as input information for the subsequent thermomechanical stress calculation. Prior to such an analysis it is necessary to identify appropriate constitutive equations to model material behaviour. Temperature dependent stress-strain curves and an appropriate law to model the creep behaviour of the blade material over the whole of the temperature range experienced by the blade form part of the essential input information. Typically, with a blade mesh of only about 1000 elements, to model only 2 simple transient cycles can take 30000 seconds core time on a Cray II computer. Although non-linear modelling of the blade behaviour throughout its total service life is therefore not yet computationally viable, nevertheless it is essential to model sufficient flight cycles until approximate "shake down" conditions have been established. In such cases, assumptions have to be made as to the effect of cycling on the material yield surface. This is particularly relevant in the transient stress analysis of turbine blades where reverse plastic flow can be induced during the acceleration and subsequent deceleration portions of the flight cycle. Typically, kinematic or isotropic hardening assumptions are adopted, the option depending on information obtained from the appropriate material database.

To illustrate the origins of thermal stresses, the blade can be considered to be composed of a series of chordwise sections each consisting of a set of columns which are fixed at the base with the free elements forming the plane section top surface. With the assumption that plane sections must remain plane, as the columns expand and contract under the combined mechanical and thermal loads, at any instant in the thermal cycle, each column will impose constraints on the free expansion of its neighbours and vice-versa. The associated spanwise stresses are wholly thermal in origin. They are self equilibrating, internal to the blade and add to or subtract from the externally applied centrifugal loadings. Although demonstrating the nature of the thermal stresses, such a simple model takes no account of thermal stresses in the plane of the aerofoil or of shear stresses and recent 3D finite element stress analyses at DRA have shown that these transverse stresses can be of a significant magnitude.

In practice, during the acceleration from ground idle to maximum take-off conditions, gas temperatures rise rapidly. For a cooled HP turbine blade, surface temperatures quickly follow but the temperature rise of the cooled central core is considerably slower and less extreme. Constraints imposed by this cooler and stronger core mean that the leading and trailing edges cannot attain free expansion levels and compressive thermal stresses build up until both plastic flow and creep deformation are experienced. These flow processes, plus a reducing thermal differential, act to decrease further the level of compressive stresses.

During the landing and shutdown sequences, blade surface cooling and the free contraction of the leading and trailing edges is now inhibited by the core section but in this case both the thermal and mechanical stresses may be tensile. Tensile creep again acts to reduce these stresses. However the creep contributions are rapidly terminated as blade temperatures fall below critical levels and subsequent fall may well lead to increased plastic flow. The net effect of such temperature variations is that, during each flight cycle, different regions of the blade section are subjected to differing reversed stresses and strains. It is the repetition of these together with the accumulation of creep during the cruise phase that lead to eventual TMF failure.

In the stress analysis of such situations, it is convenient to replace the thermal elements by 20 noded isoparametric brick stress elements. This element type is appropriate because the displacement field at any point within such an element is quadratic which results in the calculated strain components varying linearly across the element. The service mission cycle under consideration is generally subdivided into several load-time steps and tangent or initial stiffness models applied to calculate the elastic-plastic strain distributions occurring during any increment. Sufficient iterations are applied until preset convergence criteria are satisfied. In addition, to requiring a non linear behaviour model for the material, a creep analysis requires an equation of state to describe equivalent damage when conditions change from one set of stress-strain-temperature conditions to another. Frequently, for isotropic materials, Von Mises stress and either time hardening or strain hardening assumptions are adopted. The creep strain increment is then determined from the stresses computed after the plastic solution has been completed. However, where TMF is the primary consideration, the effects of the cruise phase of a mission are minimal and can therefore be modelled in a condensed form. Thus, it may be possible to consider only a simple cycle which commences at ground idle and comprises acceleration to maximum take-off conditions and a hold period at a steady state cruise condition followed by deceleration back to ground idle. The approach generally adopted is therefore to run such analyses at least until shakedown, i.e. until a stabilised stress-strain hysteresis loop is obtained, and then apply fatigue and creep damage criteria to estimate the remaining life.

5.   COATING RESPONSE TO TRANSIENT STRESSES AND TEMPERATURES

For coated blades, in practice, a shortfall in life compared with bare alloy testing at the same conditions may be observed, and is generally associated with early cracking of the coating. To determine whether or not the coating will crack involves the calculation of shaken down stress values. In general the coefficients of thermal expansion are higher for the coating than the substrate blade material, which means that the coating stresses are more compressive. The consequences of this for in-phase engine cycles are shown in Figure 1 and for out of phase cycling in Figure 2.

Figure 1 is typical of the response of a position on a turbine blade leading edge and shows the change in strain response with cycling. The relatively poor creep properties of the coating will cause an early shakedown of the coating stresses in the manner shown. It should be noted that the coating will then be in compression during almost the whole of the engine cycle, and is

therefore unlikely to crack. An exception to this would be if a brittle coating were subjected to a combination of high mechanical loading and residual stresses from the coating deposition process. This could occur on the first loading cycle before the stresses had an opportunity to creep relax.

Figure 2 is typical of the response where the coating is constrained by the cooled inner surface of the blade. The loading on the coating at this location is obviously much more severe than at an in-phase area because the stresses during most of the engine cycle are tensile. In addition, there exists the possibility that the tensile strength of the coating at low temperatures may be exceeded. Even in situations where the coating tensile strength is not exceeded, coating cracking will almost always be expected before substrate cracking because of the former's much higher ratio of running stress to material mechanical properties (this suggests an explanation for the observed reduction in coated specimen lives compared to those for bare alloy for all out-of phase TMF cycles and has important consequences both for TMF testing and for turbine blade design).

The monitoring of coating cracking during TMF testing is also important since this should allow the behavioural constants in predictive equations to be calculated for the coating and for the substrate in the presence of a crack.

On the design side, the matching of coatings and substrates is obviously extremely important. The aim should be to reduce the likelihood of generating high residual coating stresses at low temperatures following shakedown by using a coating with a lower coefficient of thermal expansion than the substrate on which it is applied.

6.   EFFECT OF MISSION PROFILE ON CRITICAL REGION STRESS VARIATION

There is of course no single cycle which accurately identifies the most damaging feature of the blade in every instance and individual cycles are very dependent on blade geometry, rates of heating and cooling, maximum metal temperatures and material properties etc. Mission cycles analysed should therefore be based on typical service experience or on an identified design duty cycle.

The resistance of a blade to TMF depends on the magnitudes of the stresses and strains experienced by the different regions of the blade throughout its service life. Figure 3 illustrates a typical stress-temperature-time profile predicted for a coated aerofoil response to external conditions imposed in the DRA thermal shock rig. Figure 4 shows the calculated stress-time and

temperature-time responses of a local area in the leading edge of a turbine blade and used as input parmeters in the DRA TMF rig. In the analyses creep was allowed to occur during both the steady state cruise phase and in conjunction with plastic flow, during the acceleration and deceleration phases of the cycle. Indeed the significant creep damage induced during the transient phases in Figure 4 is illustrated qualitatively in Figure 5 by superimposing the calculated stress and temperature combinations onto the creep rupture database for the material (an assumption being made that compressive creep characteristics are identical to tensile behaviour).

It has been illustrated that in TMF, temperature has two important roles. In conjunction with the blade geometry, transient temperatures control the level of induced thermal stresses however the damage incurred during this process is also a function of the temperature at which the most severe combined thermomechanical stresses are experienced by the blade. The point must be emphasised that many analyses of mission profiles only allow for creep during steady state conditions, however the importance of creep processes during the transient phases must also be considered.

7.   LIFE PREDICTION MODELS

7.1   Isothermal Stress Based

Figures 1 to 5 illustrate that large transient thermal strains can be generated by the thermal shock, however Figure 5 also identifies the most adverse transient temperature combinations. Indeed, by representing the transient stresses and temperatures in Figure 4 as a discrete number of time steps Δt, and using these in conjunction with the creep rupture data in Figure 5, simple life fraction concepts can be applied to quantify the creep damage[1]. Hence, extending the creep model used in the non linear stress analysis and assuming life fraction concepts, the qualitative information in Figure 5 can be used to determine quantitatively the cyclic transient creep life fraction, L_f, consumed during the mission in the expression :

$$L_f = \sum_{1,1}^{n,m} \frac{\Delta t}{t_r} \qquad (7.1)$$

where Δt is the time interval at any particular stress and temperature,
and t_r is the life to rupture of a creep test at the same stress and temperature.

Such analyses show that for the mission profile selected, during the cooling part of the cycle where the mechanical and thermal loads both produce tensile stress contributions, the creep damage imposed can be more than three times that incurred during heating,

where, despite the mechanical load still being tensile, the thermal load produces a compressive stress contribution.

In the above approach to thermomechanical analysis, only creep induced damage situations have as yet been considered. However, although the creep damage assumption is probably valid for certain locations of HP turbine blades, for other locations and for LP turbine and compressor blades, significant thermal transients may be experienced but at substantially lower temperatures, thus leading to the possibility of transient temperature plasticity induced low cycle fatigue (LCF) damage. A problem arises in identifying an effective failure stress range during a transient thermal cycle. It transpires that although proof stress or elastic modulus may be expected to be more appropriate parameters from a physical point of view, for up to moderately elevated temperatures, there is a strong correlation between fatigue behaviour and tensile strength. Hence, as shown in Figure 6, fatigue results at several temperatures can be normalised if the stresses are expressed as fractions of the temperature dependent tensile strength. A corollary of this is that under transient temperature loading, such an approach can be used to identify the effective fatigue stress range and indeed to identify the most appropriate temperature and stress range for an isothermal estimation of transient temperature LCF life[2] .

Using a Robinson-Miner linear damage approach the total thermal fatigue cyclic life, N_{tf}, can be quantified through the equally simple expression :

$$N_{tf} = \frac{1}{\sum_{1,1}^{n,m} \frac{\Delta t}{t_r}} + \sum_{1}^{n} \frac{N}{N_f} \qquad (7.2)$$

In conjunction with strain hardening, the DRA creep model allows a simple expression to be derived for repeated tension high temperature LCF behaviour.

The expression is of the form[3] :

$$t_f = \left(\frac{\beta}{\kappa}\right) t_c \qquad (7.3)$$

where t_c is the creep time to failure at stress, s, and temperature, T,
   $-\kappa/\beta$ is the slope of the rupture line in Figure 3,
and t_f is the cyclic time to failure under cyclic loading to max conditions s,T.

This approach leads to the expression :

$$N_f = \left(\frac{\beta}{\kappa}\right) t_c f \qquad (7.4)$$

where f is the loading frequency.

Similar expressions have been derived for push-pull loading and also to incorporate the effects of dwell[4].

7.2   Isothermal Strain Based

The results from the finite element stress analyses discussed earlier demonstrate that inelastic deformation occurs at high temperatures as a result of two distinctly different processes - plastic strain and creep strain. Hence, any reversed inelastic strain induced during TMF cycling may involve either or both processes at each end of the stress strain hysteresis loop. Appropriate damage models must be able to accommodate such behaviour.

In an attempt to develop his low temperature fatigue model for elevated temperature applications, Coffin introduced a frequency term ν to give[5]

$$\Delta \varepsilon_T = \Delta \varepsilon_p + \Delta \varepsilon_\varepsilon$$
$$= C_2 (N_f \nu^{K-1})^{-\beta} + \frac{A'}{E} N_f^{-\beta_1} \nu^{K_1} \qquad (7.5)$$

where material specific properties enter the above equation via a ductility value 'C$_2$' and a strength value 'A''. Constants 'K' and 'K$_1$' reflect the extent to which frequency of cycling is important. Indeed if K = 1 and K$_1$ = 0 the frequency terms are eliminated and the equation becomes similar to that of Manson's "Universal Slopes" where

$$\varepsilon_T = D^{0.6} N_f^{0.6} + \frac{3.5 \sigma_u}{E} N_f^{0.12} \qquad (7.6)$$

It is possible to represent any closed hysteresis loop by a combination of four types of strain range of which in any one case a maximum of three are possible. These are :

1   tensile plasticity reversed by compressive plasticity, $\Delta\varepsilon_{pp}$
2   tensile creep reversed by compressive creep, $\Delta\varepsilon_{cc}$
3   tensile creep reversed by compressive plasticity, $\Delta\varepsilon_{cp}$
4   tensile plasticity reversed by compressive creep, $\Delta\varepsilon_{pc}$

In the strainrange partitioning[6] (SRP) approach, each of these forms of inelastic strain range has its own relationship with the number of cycles to failure and so

can be represented in a form similar to the basic Manson-Coffin relationship. Once a hysteresis loop has been partitioned into its inelastic components, the life prediction stage assumes a linear damage summation rule of the form :

$$\frac{1}{N_f} = \frac{F_{pp}}{N_{pp}} + \frac{F_{pc}}{N_{pc}} + \frac{F_{cp}}{N_{cp}} + \frac{F_{cc}}{N_{cc}} \qquad (7.7)$$

where F_{pp} (etc) is the fraction of the total inelastic strain that is e_{pp} (etc) and N_{pp} (etc) is the number of cycles to failure of a test conducted at a strain range Δe_{pp}. Typical life relationships for the different basic strain loops are shown in Figure 7.

For blades in service, any plastic component of strain is likely to be near the lowest temperature in the cycle. However, the four component SRP life relationships are frequently established at the peak temperature. Hence, before the information can be used in any lifing calculation it is necessary to adjust the strain levels to reflect the tensile plastic straining capacity at this lower temperature rather than tensile ductility effective at any higher temperature. This is the basis behind the ductility normalised extension to SRP[7].

Recently, a further extension based on a fracture mechanics model has been proposed[8]. The formulation of the basic equations are as follows :

(i)   For PP strain ranges, the crack propagation rate is found to correlate well with a conventional non-linear time independent J integral equation of the form :

$$da / dN = C_f \Delta J^{m_f} \qquad (7.8)$$

(ii)   For PC strain ranges, experimental results indicate that compressive deformation does not alter appreciably the crack propagation observed during PP cycling and hence an equation similar to that for PP cycling can be used to correlate the data.

(iii)   For CP strain ranges, crack propagation exhibits time dependency and the rate of propagation is now related to a creep parameter (either J^* or C^*)[8], and the equation has the form :

$$da / dt = C_c J^* \qquad (7.9)$$

where the term J^* is defined as a modification of the Rice integral in which strain and displacement are replaced by their respective rates of change, J^*. If the equation is integrated during the tensile portion of the

cycle, the time based crack propagation equation can be converted to the cycle based equation :

$$da/dN = C_c \, \Delta J_c \qquad (7.10)$$

where

$$\Delta J_c = \int_0^{t_0} J^* dt \qquad (7.11)$$

and $(0 - t_0)$ is the increasing portion of the tensile loading period of the cycle.

(iv)   For CC strain ranges, compressive creep deformation can alter considerably the tensile creep response. In doing this, the J-integral is altered along with the crack propagation rate. However the form of expression governing CC fatigue is similar to CP fatigue. Figure 8 shows schematically the fracture mechanics relationships for heat resistant alloys in CP and CC fatigue and PP and PC fatigue.

For several materials the basic life equations are insensitive to temperature suggesting that it may be possible to apply directly the isothermal SRP life relations in TMF life prediction.

8.   TMF MODEL VALIDATION VIA TESTING

The final validation of any form of lifing model should be against engine service experience, but for a number of reasons, this becomes extremely difficult. In practice, full 3D thermomechanical transient blade analyses, such as described earlier, require simplifications in both the modelling of the aerofoil geometry and in the thermal and mechanical loadings. In addition, the mission cycles flown by the engine may vary significantly from those assumed in the analysis. Unfortunately, errors arising from assumptions in the modelling and from inaccuracies in the calculated transient blade temperatures, are hard to datum against engine values. It is therefore very difficult to establish whether any discrepancy between calculated and demonstrated lives has arisen from the mission analysis or from inadequacies in the characterisation of the damage mechanisms of the material.

8.1   Stress Based Life Prediction Models

A full transient analysis using the DRA creep model and applying strain hardening concepts, provides an expression of the form[1] :

$$N_{tf} = \cfrac{t_{ref}}{\Delta t\left[1 + \sum_1^n \left(\cfrac{\sigma}{\sigma_{ref}}\right)^{\beta/\kappa}\left[\cfrac{T' - T_{ref}}{T' - T}\right]^{20}\right]} + \sum_1^n \cfrac{N}{N_f}$$

$$(8.1)$$

where T' is a temperature dependent constant,
and t_{ref} is the rupture life at a selected reference stress s_{ref}, and reference temperature T_{ref}.

In Figure 9 such an equation has been used to predict the lives of a set of experimental TMF tests conducted using cycle profiles similar to those shown in Figure 4. The accurate correlation between theoretical predictions and experimental results supports the contribution of creep failure mechanisms in TMF life prediction of blade lives.

8.2   Strain Based Life Prediction Models

Figure 10 shows two sets of results from out-of phase strain controlled TMF tests on uncoated material[9,10]. Both sets of results consist of three tests performed at similar mechanical strain ranges but at different ratios of minimum to maximum strain. The detailed test cycles and materials are different in the two sets of results, but these are unlikely to affect the observed life trends associated with changing R-ratio.

A life correlation simply based on strain range alone would obviously predict no variation with changing R-ratio. A parameter using the maximum and minimum strains in the cycle would also be inadequate, because the lives calculated for $R = 0$ loading conditions would be shorter than for $R = -1$ in both sets of results. These strain controlled tests again illustrate the importance of the actual stress levels induced since in such strain controlled TMF tests the recorded stresses generally settle down to approximately constant levels, the values being determined by the details of the loading cycle and the inelastic behaviour of the material. It must be noted that such modelling does not account for any strain ratchetting/growth of the blade and which could make a significant contribution to the final failure.

Hence it has been found that during the initial TMF cycles, creep relaxation may occur to an extent that the amount of creep strain associated with each subsequent cycle becomes negligible, as expressed in equation (7.8). In this situation the behaviour of the material during the remainder (i.e. majority) of the test will be elastic, and a correlation may be expected if the overall life is assessed against a parameter similar to either J or ΔK.

Considering the low strain range results of Figure 10 as an example, the first step is to determine the shakedown stress-temperature histories as shown schematically in Figure 11. For low total strains, the $R=-\infty$ exhibits stress relaxation at higher temperature and the $R=0$ relaxes at the lower temperature. Although there is more total inelastic deformation exhibited in the $R=-\infty$ at shakedown, the higher peak stress encountered under $R=0$ conditions results in greater rates of LCF life consumption. A suitable parameter to describe this behaviour quantitatively is given by the normalised shaken down stress range, 'mean stress' corrected to take account of the relative magnitudes of the tensile and compressive stresses. A suitable normalising property is found to be the 0.1% proof stress, since this value marks the boundary between the material's elastic and plastic behaviour. Thus:

$$F = \left\{ \left(\frac{\sigma}{PS_{0.1}}\right)_{MAX} - \left(\frac{\sigma}{PS_{0.1}}\right)_{MIN} \right\} \left(1 - \frac{(\sigma/PS_{0.1})_{MIN}}{(\sigma/PS_{0.1})_{MAX}}\right)^m \quad (8.2)$$

where σ is the value of shaken down stress,
and m is the Walker coefficient for the material.

An alternative situation is where stabilisation of the strain loops occurs by the inelastic creep strain accumulated during the hot part of each cycle being completely reversed by cold plasticity, as expressed in equation (7.9).

For the high strain conditions a ductility exhaustion argument can be used to explain the relative lives. For most of the test duration, the three higher strain range tests shown in Figure 10 should now be experiencing similar loading conditions i.e. for high strains, the shakedown hysteresis loops of the $R=-\infty$, $R=-1$ and $R=0$ are virtually identical. However the strain consumed during shakedown of the $R=-\infty$ is largest and has the greatest influence on total life consumption. In all cases the amount of inelastic strain accumulated per cycle will also be equal, although the amount of residual ductility will differ. Considerably more inelastic strain per cycle is experienced during shakedown of the $R=-\infty$ test than in the corresponding $R=0$ test and this is reflected in the lower life under the former test conditions.

A lifing parameter to describe this behaviour may therefore be formulated as

$$C = \frac{\Delta\varepsilon_o}{\varepsilon_f - \varepsilon_o} \quad (8.3)$$

where $\Delta\varepsilon_o$ is the amount of inelastic strain incurred per cycle once the stresses have stabilised,
  ε_f is the creep ductility,
and ε_o is the total inelastic strain incurred prior to stabilisation.

Such observations have resulted in a UK approach broadly similar to the fracture mechanics based SRP discussed earlier and where the overall crack growth rate during a test can be calculated by a summation of cycle and time dependent effects as shown below.

$$\left\{\frac{da}{dN}\right\}_{Total} = \left\{\frac{da}{dN}\right\}_{\substack{J\,Integral \\ Controlled}} + \left\{\frac{dt}{dN} \bullet \frac{da}{dt}\right\}_{C^*\,Controlled}$$

$$(8.4)$$

The overall crack growth rate can be expressed as:

$$\left(\frac{da}{dN}\right)_{TOTAL} = gF^l + hC^m \quad (8.5)$$

where g, h, l and m are material constants.

For uniaxial loading, the model may be adequately represented through creep and plasticity algorithms based on lower temperature tensile behaviour.

In the application of the method to a turbine blade assessment, C and F are determined at the point in the loading history where the change in peak stress over a chosen number of cycles drops below a pre-determined value. In the case of single crystal superalloys, where a full viscoplastic model including the effects of anisotropy is required, the values of the constants g and l can be found from the analysis of low temperature isothermal strain controlled LCF tests and the constants h and m, associated with the parameter C, by analysing high stress/strain range high temperature LCF tests.

Typical comparisons of both in-phase and out-of-phase TMF strain controlled test results with model predictions are given in Figure 12. The in-phase predictions are in good agreement with the test results. A reason for the conservative predictions of high strain out-of phase tests could be that the model predicts slightly greater plastic strain accumulation at lower temperatures than occurs in practice.

9. CONCLUDING REMARKS

Few tasks in engineering pose as many varied and complex problems as turbine blade lifing. Predictions of the state of stress and strain are made difficult by intricate geometrical features such as internal passages and film cooling holes and by uncertainties in transient

temperature distributions. The effects of localised creep and engine performance deterioration also cause this stress distribution to change significantly with time. Additionally there is the need to understand how the metallurgical damage mechanisms vary depending on the applied loading and how they are modified by external factors such as the presence of a coating or an oxide film.

In recent years proposed lifing models have become progressively more sophisticated, with more of the identified lifing variables being incorporated. In today's highly competitive aero engine business, however, cost is a major factor and with several different choices of both blade material and oxidation resistant coating available, a lifing model which requires large test matrices for each combination is impractical. As shown, however, the correlation of blade lives to easily calculable parameters such as strain range is too much of an over-simplification.

It is clear is that any model aimed at producing acceptable turbine blade life predictions must examine the loading cycles in detail, and take into account how variables such as the stress and inelastic strain at each area of the blade varies with time. The future therefore seems to lie in combining non-linear codes which characterise the behaviour of a material under all loading conditions with time-stepping analyses of large blade models associated with complex engine cycles, all backed up by lifing algorithms which continuously calculate the rate of life consumption. The analysis of TMF test results is an essential ingredient in the development of these algorithms, and an important step in the fuller integration of mechanical integrity considerations into the design process.

REFERENCES

1   G. F. HARRISON, J. E. GOODWIN, R. S. DENNIS: Laboratory simulation of thermal fatigue, Int Conf Society of Environmental Engineers Fatigue Group V1 No 16 1-14 1976.

2   G. F. HARRISON: Deformation and fracture of some nickel based gas turbine alloys, PhD thesis, University of London 1975.

3   G. F. HARRISON, M. G. COCKROFT: The effects of cycle parameters on high temperature low cycle fatigue, 1974, AGARD CP 155, Paper 4 1-13.

4   G. F. HARRISON, G. P. TILLY: The state and cyclic creep properties of three forms of a cast Nickel Alloy, Int Conf on Creep and Fatigue in elevated temperature applications. 222.1-9. I Mech Eng, Sheffield, 1974.

5   L. F. COFFIN: Fatigue at high temperature, ASTM STP 520, 1972, 5-34.

6   S. S. MANSON, G. R. HALFORD, M. H. HIRSCHBERG: Creep fatigue analysis by strain-range partitioning, NASA TM X-67838, 1971.

7   G. R. HALFORD, J. F. SALLSMAN, M. H. HIRSCHBERG: Ductility normalised strain range partitioning life relationships for creep-fatigue life predictions, NASA TM 73737, 1977.

8   T. KITAMURA, G. R. HALFORD: A non linear high temperature fracture mechanics basis for strain range partitioning, NASA TM 4133, 1989.

9   R. S. NELSON and J. F. SCHOENDORF: Creep fatigue life prediction for engine hot section materials (isotropic) - fourth year progress review, NASA Report N89-12914, 1986.

10   J. BRESSERS and M. M. BUCKLEY: Thermomechanical and isothermal fatigue of coated and uncoated nickel-based single crystal superalloys, Rolls-Royce plc, private report, 1990.
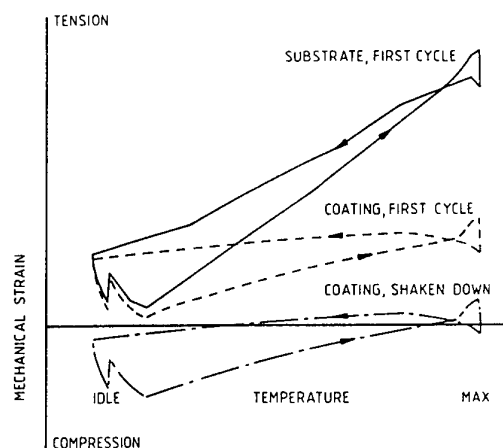
Figure 1

Coating cyclic strain response -
In phase substrate strain temperature loop.
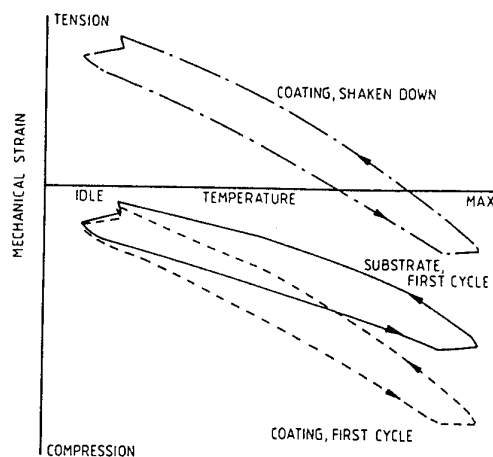
Figure 2

Coating cyclic strain response -
Out of phase strain temperature loop.
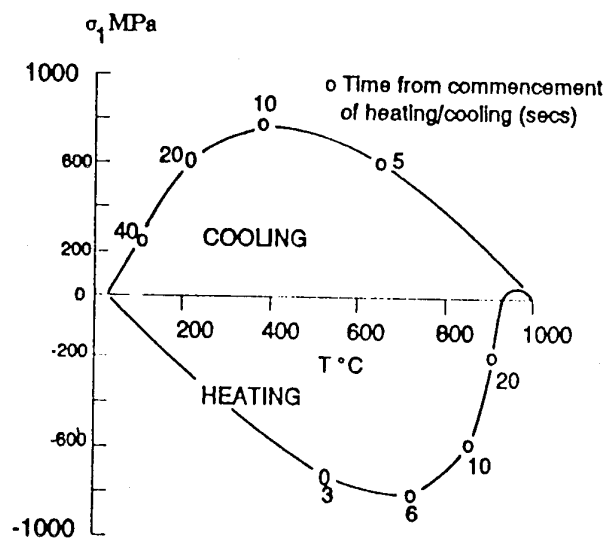
Figure 3

Predicted stress temperature-time responses
on an aerofoil leading edge tested in
the DRA thermal shock rig.
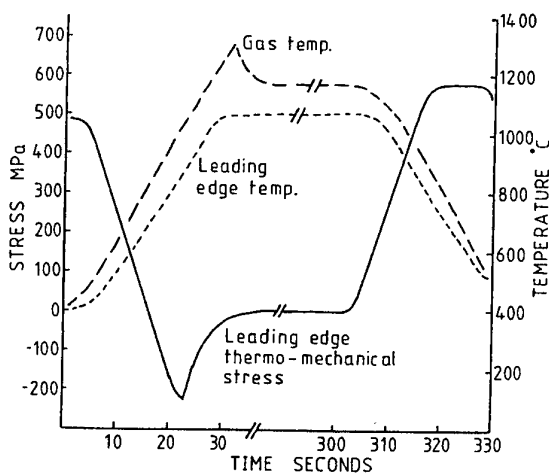
Figure 4

Predicted typical leading edge loading
sequence used in the DRA TMF rig.
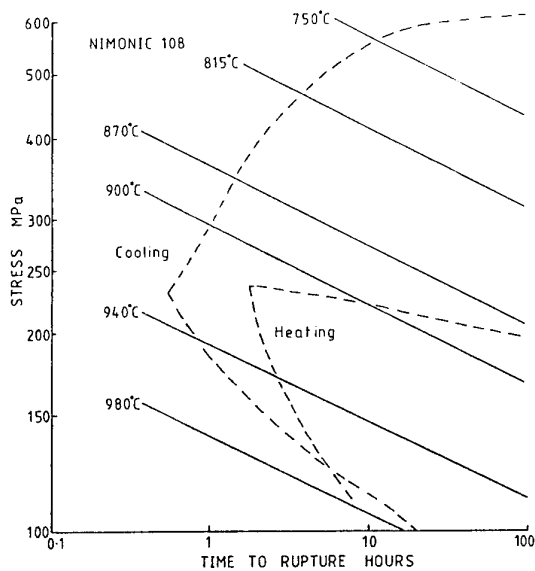
Figure 5
TMF loading sequence superimposed onto
creep rupture map for the turbine blade
alloy NIM 108.
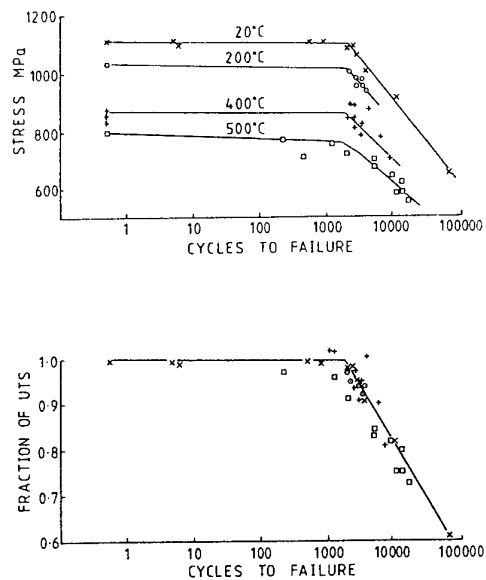
Figure 6
Conventional and normalised elevated
temperature LCF results for H46 stainless steel.
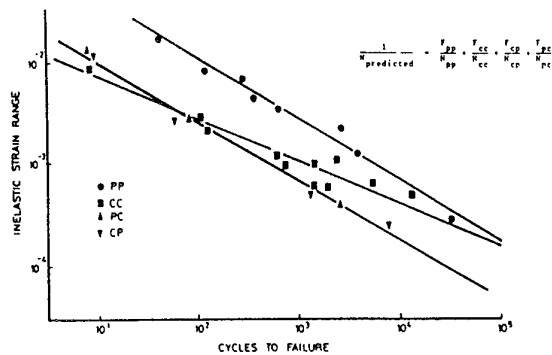
Figure 7
Basic SRP fatigue life lines
for NIM 90 at 180°C.
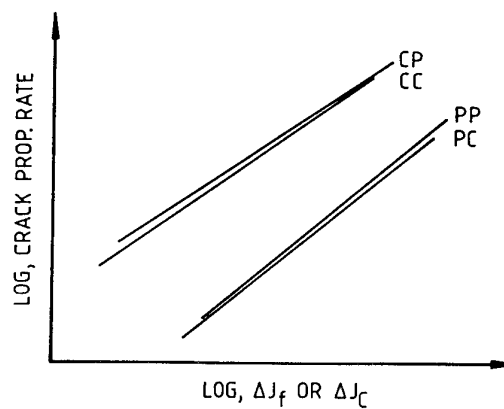
Figure 8
Schematic illustration of fracture mechanics
relationships for basic SRP strain relationships.
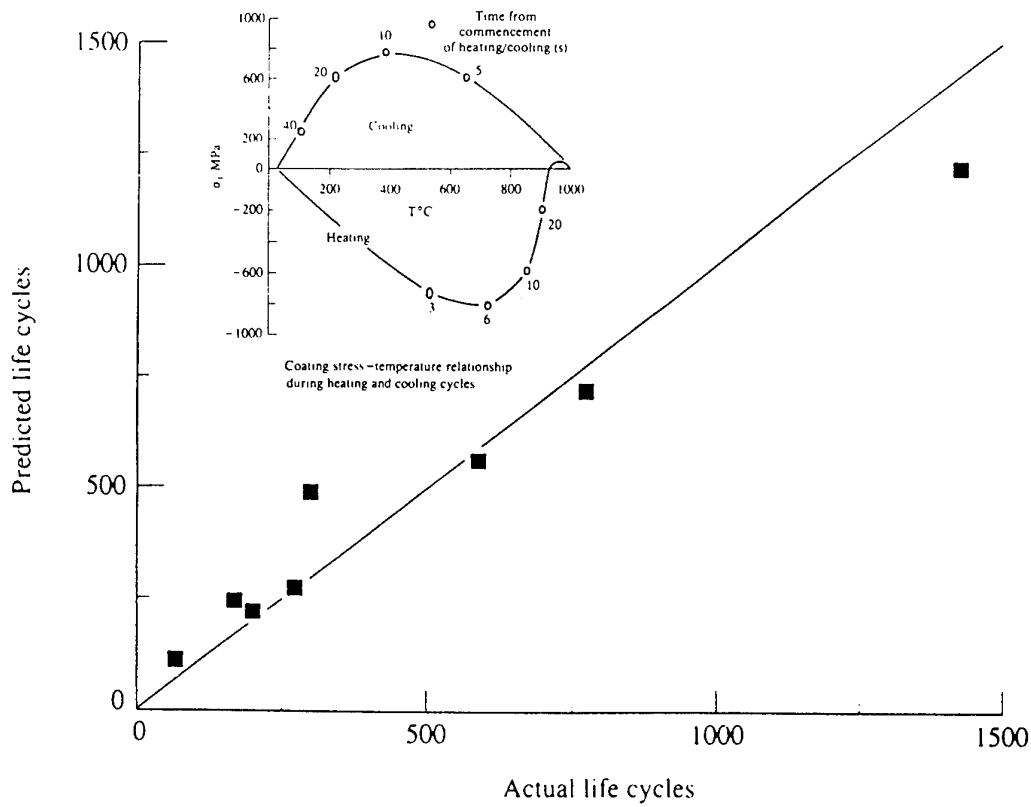
Figure 9
Comparison of experimental and stress based
predictions of TMF life for NIM 108.
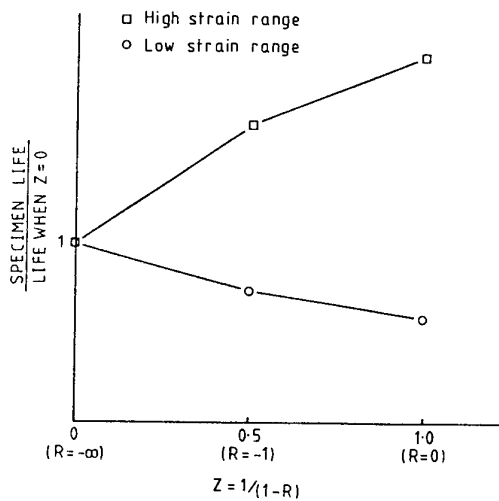
Figure 10
Out of phase TMF results under low and high
mechanical strains and different R-ratios
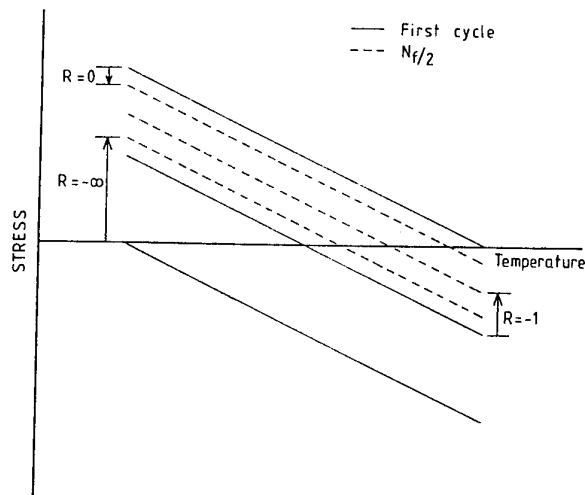
Figure 11
Schematic illustration of the effect of R-ratio
on the shakedown stress cycle for low strain range
out of phase TMF loads.
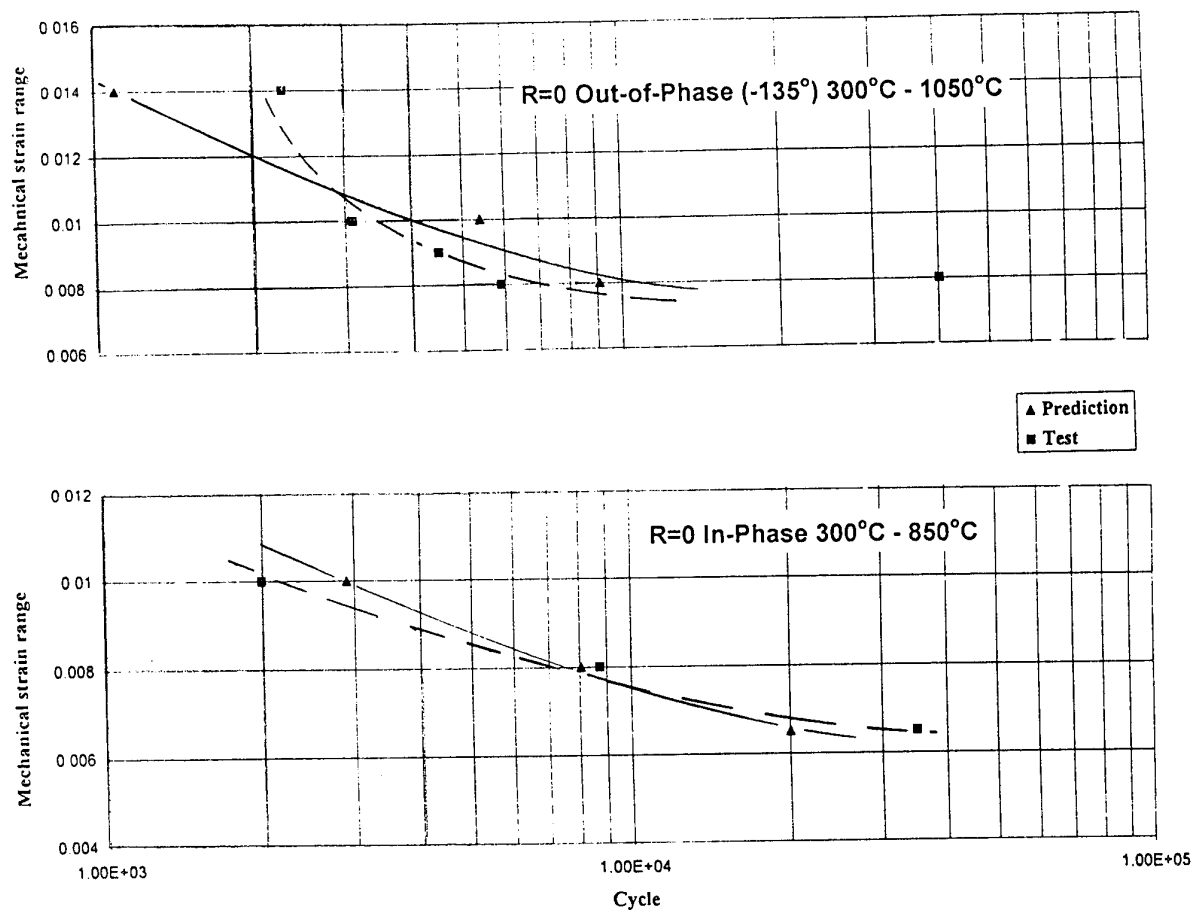
Figure 12
Comparison of both in phase and out of phase TMF strain controlled
SRR 99 test results with strain based model predictions.

MODELLING OF THERMOMECHANICAL FATIGUE INCLUDING
PHASE TRANSFORMATIONS

S. Boire-Lavigne[1]
S. Gendron[1]
N.J. Marchand[2]
J.P. Immarigeon[3]

[1] Formerly Graduate Students, Ecole Polytechnique, Dep. of Mater. Engineering, P.O. Box 6079, Station "Centre-Ville", Montreal, Canada H3C 3A7. Now Project Engineer, AMRA Technologies, 4700 de la Savane, Suite 300, Montreal, Quebec, Canada H4P 1T7

[2] Senior Research Engineer, AMRA Technologies, 4700 de la Savane, Suite 300, Montreal, Quebec, Canada H4P 1T7

[3] Chief Materials, NRC Institute for Aerospace Research, Montreal Road , Ottawa, Ontario, Canada K1A 0R6

ABSTRACT

Typical gas turbine and jet engine hot section components are subjected to severe environment along with variable thermal and mechanical loading histories. Furthermore, stress induced morphological transformations of the materials have been observed to occur during turbine engine operations with the amount of transformation a function of the thermal-mechanical history. At present, the popular models for thermal-mechanical fatigue (TMF) life predictions are based on creep-fatigue interactions and do not explicitly contain environmental and microstructural transformation features. In this paper, a novel framework and process simulation software, which explicitly tracks the evolution of the microstructure (including dislocations structures) is presented. In essence, this model described the overall behavior of a material as the weighted average of the mechanical responses of the present phases (or dislocation structures). Dynamic recovery is modeled by explicitly describing the transformations of a "hard structures" to a "soft structure" in agreement with the basics concepts of dislocations dynamics. The effectiveness of this novel multi-structure approach will be demonstrated through modeling the TMF behavior of René 80.

1. INTRODUCTION

The continuous search for better performance and fuel economy in structural components operating in high temperature environments has resulted in further increases in operating temperatures. Assessment of component integrity under complex non-proportional thermomechanical loadings, requires detailed knowledge of the operating environment and the ability to predict the structural response for these loadings [1-2].

With the advent of increasing computing power, the capabilities to perform nonlinear analyses has also significantly increased. This power, together with the demand and or requirement for predictability and reliability of performance, puts the emphasis on realistic and accurate models of the deformation behavior and on the damage accumulation laws. It should be emphasized that the prime objective of the constitutive models is not to determine the deformation of structures per se, but rather to provide the necessary inputs to the integrity assessment schemes and models. Typically, the life assessment schemes require quantities such as stress range, mean stress, inelastic strain including percentage of creep and plasticity, mean stress

relaxation, ratchetting strain, etc. Therefore, it is paramount that the predictive capability of the constitutive models be capable of predicting the actual phenomena (occurring during operating conditions) with reasonable accuracy [3-4].

Traditionally, the stresses and strains are computed at mid-life and provided as inputs to the life predicting schemes under the assumption that they prevail throughout the life time of the component. While these methods can be adequate for cyclically neutral materials or low temperature applications, they always lead to highly inaccurate life predictions when there are cycle-dependent property changes as observed in most high temperature engineering materials [5-7]. Also, these methods assume the existence of a typical cycle throughout the life of a structure and this is not realistic for most loading spectrums [6-7]. Notwithstanding oxidation effects, microstructural transformations also occur during engine operations [8]. For instance, most nickel-base alloys experience microstructural aging above 1700°F, such as γ' precipitates coarsening [8-9], dynamic strain aging, the apparition of brittle phases [11], etc. Dislocation structures are also known to evolve during operation cycles from planar types to cell types with the corresponding mechanical response of the materials to further straining completely different from its original state [12-13]. The most important point here is that the material after some time in service is different from its original state and thus cannot be described with the same constitutive equations. At present, the development of physically and mechanically based predictive schemes for TMF is in its infancy.

The purpose of this paper is to present a novel approach to predicting the TMF response of materials with special emphasis on nickel-base superalloys. In fact, a new general unified framework, capable of describing and predicting microstructural transformations in both metal working processes and/or during service operation, is presented. The similarities as well as the fundamental differences between the proposed model and the existing schemes and models will be highlighted. The physical significance (i.e. the mechanisms underlying the phenomena) of the parameters used in the model will be pointed out. The effectiveness of this general framework is illustrated through modeling the evolution of the microstructure of a nickel-base superalloy during operating service conditions.

2.0 CONSTITUTIVE MODEL
2.1 Generalities

Most commercial alloys contain a heterogeneous microstructure consisting of two or more metallurgical phases. A number of different microstructures can be encountered but, in general, they fall into the two classes illustrated in figure 1.

Hence, figure 1.a shows the aggregated type of two-phase structure in which the size of the second-phase particles are of the order of the grain size of the matrix. The other general type of structure is the dispersed two-phase structure (see figure 1.b) in which each particle is completely surrounded by a matrix of a single orientation (grain). Generally, the particle size of the second phase is much finer for the dispersed structure and may be of submicroscopic dimensions in the early stages of precipitation. The theories of strengthening in dispersion-hardened alloys have been studied thoroughly and most theories model the overall behavior using one set of constitutive equations (for the back stress and the drag stress) in which some of the material constants are a function of the particle size and distribution. This approach is also used in the present framework, that is, the dispersed-structures are treated as single phase materials in which the materials' constants are changed (or updated) to reflect the actual distribution of the second-phase particles.
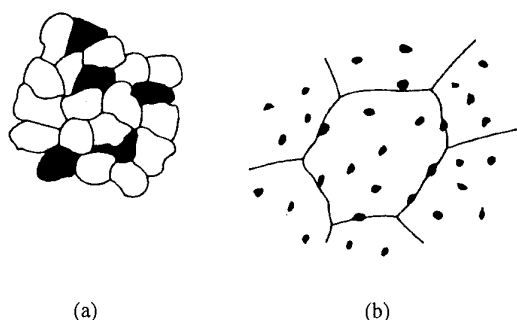

(a) (b)

Figure 1. General types of two-phase microstructures. (a) Aggregated structure, (b) dispersed-structure

In a multi-phase aggregated alloy, each phase contributes a certain amount to the overall properties of the aggregate. If the contributions of each phase are independent, then the properties of the multiphase alloy will be a weighted average of the properties of the individual phases. For example, the density of a two-phase alloy is equal to the sum of the volume fraction of each phase times its density. However, for the structure-sensitive mechanical properties, the overall properties of the aggregate are generally influenced by interactions between the two-phases.

At present, there are two simple hypotheses to compute the properties of a two-phase alloy from the properties of individual ductile phases. If it is assumed that the stress in each phase is equal, the average strain in the alloy, for a given stress, will increase linearly with the volume fraction of the second-phase, i.e.

$$\varepsilon_{avg} = X_1 \cdot \varepsilon_1 + X_2 \cdot \varepsilon_2 \qquad (1)$$

with X_1 the volume fraction of phase 1, and $X_1+X_2 =1$. An alternative hypothesis is to assume that the two phase are subjected to equal strain. The average stress in the alloy at a given strain is then given by

$$\sigma_{avg} = X_1\sigma_1 + X_2\sigma_2 \qquad (2)$$

Both hypotheses are simple approximations, and the strengths of alloys containing two ductile phases should lie somewhere between the values predicted by the two models (equations 1 and 2). Nevertheless, a mismatch strain (coherency strain) or a mismatch stress needs to be introduced to avoid unacceptable strain or a stress jump at interfaces[14].

2.2 Constitutive Model-General Framework

First, the model assumes that the material is an aggregated structure with up to five different phases with these phases, parents or by-products of the neighboring phases. For example, one can imagine a steel component having a microstructure consisting of austenite, perlite, ferrite, bainite and martensite. Furthermore, each of these phases can assume two states of deformation (structure) or a combination of these two states. Hence, each phase can take a low energy dislocation state (e.g. carpet structure) or a high energy dislocation state (e.g. cell structure). While phase transformation can occur without plastic deformation (depending on temperature, nucleation rate, etc.), structure transformation from low to high energy requires mechanical deformation. Thus, the model explicitly assumes that phase or structure transformations can occur, given the right combination of temperature, stress gradient, strain, etc. In this sense, the proposed model is a true multi-phase/multi-structure formulation. Figure 2 shows a schematic of the multi-phase approach.
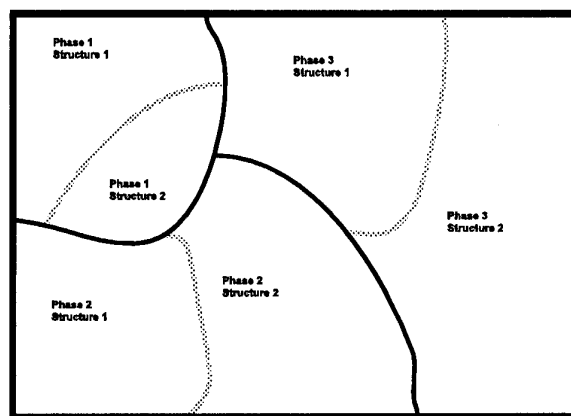
Figure 2. Schematic showing the multi-phase/multi-structure approach. Note here the 3 phases, each with two structures.

In essence, the computation at each integration point (i.e. for the associated volume) consists of (1) an evaluation of the phase and structure distributions, (2) solving for each phase and structure, (3) averaging the material's response, and (4) re-assembling and solving for the entire structure. Figure 3 summarizes the proposed approach.
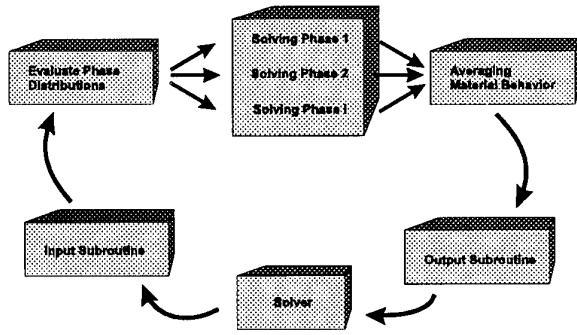
Figure 3. Phase Multi-Structure Constitutive Scheme

2.3 Multi-Phase Formulation

Since up to five phases are assumed to exist simultaneously (at least one phase), and since the overall behavior of the material at a given integration point is passed to a finite element solver, an averaging procedure is required. Here it is assumed that the average behavior can be obtained with the following equations[1]:

$$\underline{\dot{\varepsilon}} = \underline{\dot{\varepsilon}}_i \tag{1}$$

$$\underline{\sigma} = \sum_{i=1}^{n} X_i \underline{\sigma}_i \tag{2}$$

$$\underline{\underline{H}} = \sum_{i=1}^{n} X_i \underline{\underline{H}}_i \tag{3}$$

$$X_i = X_k^{ph} X_j^{st} \tag{4}$$

$$\sum_{k=1}^{n/2} X_k^{ph} = 1 \tag{5a}$$

$$\sum_{j=1}^{2} X_j^{st} = 1 \tag{5b}$$

Equation 1 assumes that the total strain rates in each phase and structure are the same. Equation 2 gives the average stress field as a function of the respective stress field of each phase and structure. Equation 3 gives the average jacobian ($\underline{\underline{H}}$) as a function of each phase and structure. Equation 4 gives the volume fraction of the ith substructure respective to the total volume element, while equations 5a and 5b express the fact that

---

[1] $\underline{A}$ means that A is a second order tensorial variable; $\underline{A}_i$ is a second order tensor associated to the ith structure, $\underline{\underline{H}}$ is a fourth order tensor; n is the total number of phases and structures, X_k^{ph} is the volume fraction of the kth phase, X_j^{st} is the volume fraction of the jth structure.

the summations of phases and the summation of substructures (for each phase) should be unity.

Because the multiphase approach has been implemented in a fully updated Lagrangian finite element code, only the average stress field (Kirchhoff stress $\underline{\sigma}$) and the average jacobian ($\underline{\underline{H}} = \partial \Delta \underline{\sigma} / \partial \Delta \underline{\varepsilon}$) need to be passed at each iteration. In other words, the constitutive modeling is handled separately from the solver, which function is to optimize the displacement and temperature fields throughout the finite element model. However, to solve for the constitutive behavior of each phase and substructure, the flow rules, and evolutionary equations for each phase and substructure must be prescribed.

2.4 The Thermomechanical Model

All the phases and substructures are assumed to have the same essential features, i.e. (1) a flow rule and (2) evolutionary equations for the internal state variables. The flow rule, or strain rate equation, give the plastic strain rate ($\underline{\dot{\varepsilon}}^p$) in terms of the effective stress, the internal variables (e.g. K and $\underline{\underline{\Omega}}$), and the temperature ., i.e.

$$\underline{\dot{\varepsilon}}^p = \phi\left(\underline{S}, \underline{\underline{\Omega}}, K, T\right) \underline{\underline{\Sigma}} = \phi\left(\underline{S}, \underline{\underline{\Omega}}, K, T\right)\left(\frac{3}{2}\underline{S} - \underline{\underline{\Omega}}\right) \tag{6}$$

where $\underline{\underline{\Sigma}}$ is the effective stress tensor;

         $\underline{S}$ is the deviatoric stress tensor;

         $\underline{\underline{\Omega}}$ is the back stress tensor;

         K   is the drag stress (viscous stress);

and $\phi(\ )$ is the plastic multiplier which is a function of $\underline{S}, \underline{\underline{\Omega}}, K$ and T.

Equation 6 represents the associated flow rule for the translated Von Mises surface in a rate independent model. It also accounts for the non-coaxiality associated with non-proportional loadings; i.e. between $\underline{\dot{\varepsilon}}^p$ and the deviatoric stress $\underline{S}$ (a requirement for most practical problems).

It is important to re-emphasize the conceptual framework for this model. Here, two internal variables are chosen as a minimum set per structure. One, associated with deformation induced anisotropy, is called "back stress" and is given by the second-order tensor $\underline{\underline{\Omega}}$. Physically the back stress $\underline{\underline{\Omega}}$ is the residual stress field embedded in the material at the crystal-lattice level due to deformation, i.e. due to dislocation pile-ups in the crystallites (grains). The back stress affects the magnitude of the superimposed applied stress ($\underline{S}$) needed to produce additional plastic flow. The other internal variable (K) is associated with isotropic hardening effects. It is often perceived as a viscous drag stress , implying that the resistance to dislocation glide is dependent upon the deformation or on the dislocation structure. It can be shown thoroughly that these two

internal variables are associated with microstructurally local stresses produced by dislocation arrangements [15].

Actually, the model accepts three different types of formulations for the plastic multiplier $\phi(\ )$, respectively;

$$\phi(\ ) = \frac{\left(\dfrac{\Sigma}{K}\right)^n}{\Sigma} \tag{7a}$$

$$\phi(\ ) = B\frac{\left\{\exp\left(\dfrac{\Sigma}{K}\right) - 1\right\}}{\Sigma} \tag{7b}$$

$$\phi(\ ) = \frac{\sinh\left(\dfrac{\Sigma}{K}\right)^n}{\Sigma} \tag{7c}$$

with $\overline{\Sigma} = \sqrt{\dfrac{2}{3}\left(\dfrac{3}{2}\underline{\underline{s}} - \underline{\underline{\Omega}}\right) : \left(\dfrac{3}{2}\underline{\underline{s}} - \underline{\underline{\Omega}}\right)}$, the norm of the effective stress tensor.

Equations 7a and 7b are the well-known power law and exponential formulations while Equation 7c is the hyperbolic sine formulation. Figure 4 shows a comparison between these three formulations. As can be seen both the power law and hyperbolic sine increase rapidly after reaching a critical value while the exponential law increases steadily. Note that both the exponential and power laws have sound fundamental basis [16] while the hyperbolic sine law is often used to bridge the varying behavior as a function of stress (or overstress) [17]. Hence, it can be shown from first principle, that for dislocation-glide and twinning, the exponential form is more appropriate. On the other hand for dislocation-creep and diffusion-creep mechanisms, a power law form is appropriate to describe the behavior.
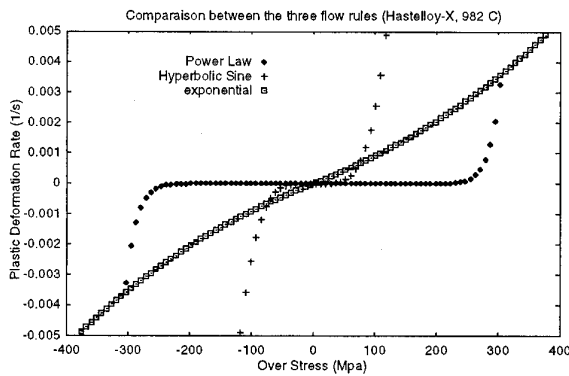
The general framework of the evolutionary equations for the internal variables is directly based on the Bailey-Orowan theory [18], which assumes that deformation occurs under two simultaneously competing mechanisms: a hardening process which proceeds with deformation, and a recovery process proceeding with time (at a given temperature). The evolution rate of the internal variable is then the difference between the hardening rate and the recovery rate. For each phase and structure the following set of evolutionary equations is used

$$\dot{K} = A\,f(t,T) \tag{8a}$$

$$\underline{\underline{\dot{\Omega}}} = h\,\underline{\dot{\varepsilon}}^{p} - a \cdot \overline{\Omega}^{m-1}\left(\underline{\underline{\Omega}} - \frac{\Omega}{\overline{\overline{\Omega}}}\Omega^0\right) \tag{8b}$$

where $\overline{\Omega} = \sqrt{\dfrac{2}{3}\underline{\underline{\Omega}} : \underline{\underline{\Omega}}}$

Equation 8a assumes that the drag stress for a given phase in a structure can only vary as a function of time and temperature. This is to account for precipitation and coarsening in dispersed-structures. In other words, the drag stress is a constant (for a given phase and structure) unless there are changes in the distribution of the precipitates. For example, K can have the following form [19]

$$K = K^0(T) + A(T)\sqrt{\frac{f}{d}} \tag{9}$$

where f is the volume fraction and d the average particle diameter as a function of time. $K^0(T)$ and $A(T)$ are constants which depends on temperature only. Thus, if f and d change due to coarsening/dissolution (e.g. Greewood-Wagner coarsening law[19]), then K changes accordingly. The present formulation accommodates all these possibilities.

Equation 8b shows that the back stress has one dynamic hardening term which depends on the plastic strain rate and one thermal softening term. Obviously, the thermal recovery term alone cannot account for the saturation (stage II) of the stress - strain curve which is shown schematically in Figure 5.

Figure 4. Comparison between the three flow rules. The exponent for the hyperbolic and power laws is 4.
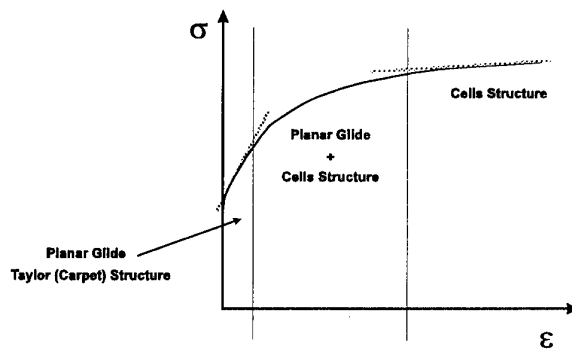

Figure 5. Typical stress-strain curve (single phase)

Thus, most models (if not all) view the introduction of a dynamic recovery term as essential for proper multiaxial generalization and proper correlation of experimental uniaxial data. Hence, the dynamic recovery term is often introduced as

$$\dot{\underline{\underline{\Omega}}} = h\left(\underline{\underline{\Omega}}, K\right)\dot{\underline{\varepsilon}}^{P} - r\left(\overline{\Omega}, T\right)\underline{\underline{\Omega}} - \dot{d}\left(\underline{\underline{\Omega}}, \dot{\underline{\varepsilon}}^{P}, T\right)\underline{\underline{\Omega}} \quad (9)$$

As one can see, the dynamic recovery function depends both on the back stress and plastic strain rate tensors. However, there is a fundamental problem with using the plastic deformation or plastic strain rate as variables controlling the dynamic recovery term. This is because $\underline{\underline{\varepsilon}}^{P}$ cannot be used as internal variables to describe the state of a material since the same $\underline{\underline{\varepsilon}}^{P}$ (using various loading histories) can be associated with different dislocation structures. The physical justification for using a dynamic recovery term is unclear except for the vague notion that it should be related to stress-assisted cross slip. Furthermore, in the field of dislocation dynamics, there is no model or equation to describe such phenomena [20]. However, models and equations exist to describe dislocation structures such as planar-type and cell-type structures. Dynamic recovery is implicitly assumed to be a transient phenomena in which the material undergo a transformation from a low to a high energy dislocation structure. Thus, any model claiming to have sound physical basis should not be using a dynamic recovery term in the evolutionary equations for the internal variables (drag or back stress). Thus, the present formulation goes into this direction, because it explicitly assumes that the behavior of a material is controlled by:

(1) The kinetics of creation and annihilations of dislocations;

(2) The transformation (or evolution) of the dislocation structures from one type to another.

The typical stress-strain behavior shown in Figure 5 is assumed to be composed of two linear hardening stages, each corresponding to given dislocations structure. The first stage is associated with planar-type structures while the second stage is associated with cell structures. Within each stage the principle of similitude applies. This principle of similitude states that a given structure will shrink with increasing deformation and stress until it reaches a critical amount of strain energy at which point it starts to transform into another structure capable of accommodating higher strain energies [20-21]. Accordingly, the two stages are separated by regime where both structures coexist in agreement with most observations [20-22]. Thus, the dynamic recovery term, which is required and present in almost every advanced constitutive model, is not necessary in the present formulation. This is because the mechanisms leading to dynamic recovery are modeled explicitly through structure transformation.

Thermal recovery of the back stress is given the form

$$a \cdot \overline{\Omega}^{m-1}\left(\underline{\underline{\Omega}} - \frac{\underline{\underline{\Omega}}}{\overline{\Omega}}\Omega^{0}\right) \quad (10)$$

where Ω^{0} is the lowest value sustained by a given dislocation structure. For a planar-like structure Ω^{0} is close to zero while for a cell-type structure, Ω^{0} is close to the critical strain energy

associated with the onset of structure transformation. Equation 10 implies that the recovery rate increases with increasing value of $\underline{\underline{\Omega}}$ but also assumes that the overall back stress tensor decreases isotropically as shown in figure 6
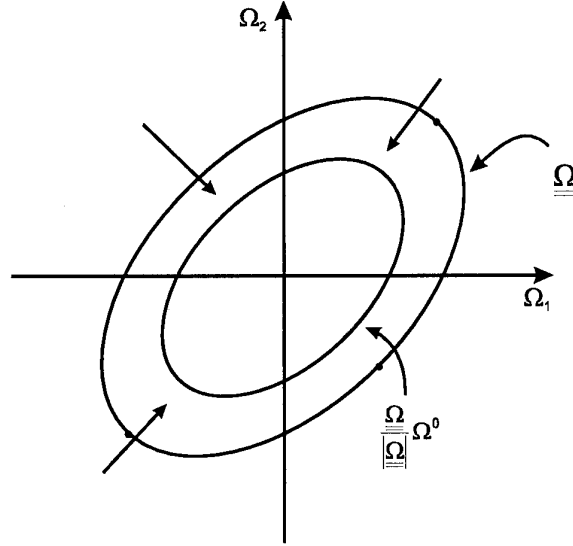
Figure 6. Isotropic recovery of the back stress

2.3 Structure Transformation

As we have seen, each type of phase and dislocation structure is given a specific constitutive behavior, which include a flow rule and an evolutionary law for the back stress (composed of a hardening rate and a thermal recovery rate). We must now prescribe a transformation law to account for the passage from a low to a high energy dislocation structure. At the moment, there is no solid theoretical background to model these transformations, although a multitude of experimental observations can assess for the occurrence of these transformations. Because the triggering of stress-assisted multiple cross slip is believed to be associated with the onset of transformation[20-22], the transformation law should contain the back stress and the plastic strain rate, two factors known to drastically influence cross-slip. The equation proposed to model structure transformation is

$$X_{2} = 1 - \exp\left\{-\left(\frac{W}{W^{t}}\right)^{v}\right\} \quad (11)$$

with

$$W^{t} = B\left(\frac{\dot{\overline{\varepsilon}}^{P}}{\dot{\varepsilon}^{0}}\right)^{C} \quad (12a)$$

and

$$W = \int \underline{\underline{\Omega}}: d\underline{\underline{\varepsilon}}^{P} \quad (12b)$$

Here, X_2 is the volume fraction of cell structure ($0 \leq X_2 \leq 1$), while B, c, $\dot{\varepsilon}^0$ and v are material constants which vary with temperature. W^t is the critical energy per unit volume which can be sustained by a planar structure before transformation.

2.4 Phase Transformations

As stated earlier, the present framework models explicitly the aggregated structures. These structures are the results of allotropic transformations of which the kinetics are controlled by nucleation and growth mechanisms. On the other hand, dispersed structures are modeled as single phase/two-structures materials. Coarsening/dissolution of the particles is accounted for by proper evolution of the drag stress (see Eq. 8a) or, in the case of rafting, by proper change of the constants in the back stress equation (see Eq. 8b). To model allotropic phase transformation, almost every (if not all) existing models use an Avrami's type equation [23], i.e.

$$X_i = 1 - \exp\left(-k_i t^{n_i}\right) \tag{13}$$

where X_i is the volume fraction of the ith phase, k_i and n_i are constants which depend on the physics of the ith transformation, and t is the time (or re-actualized time). The fundamental problem with this approach is that time is used as a state variable. Thus, depending on the thermo-mechanical history experienced by the material, the time can have different meaning. To avoid this problem, the concept of incremental transformation was developed [24]. In this new approach for phase transformation, time is not a state variable. Here, the nucleation and growth rates are continuously updated as a function of the thermomechanical history. Combining the nucleation and growth rates yields the incremented rates of transformation, i.e.

$$\dot{X}_i = f_i\left(\underline{\varepsilon}, \underline{\dot{\varepsilon}}, \underline{\sigma}, T, d, etc\right) \tag{14}$$

Equation 14 recognizes that many allotropic phase transformation are known to depend on strain, stress, temperature, grain size (d), etc. Note that the mechanical variables, such as $\underline{\varepsilon}$ and $\underline{\sigma}$, are not explicit state variables for X_i. In fact, their effect is to modify the nucleation and growth rates which are the true state variables for X_i. Note that the concept of incremental transformation is akin to the concept of incremental plasticity (or viscoplasticity) in which the mechanical state ($\underline{\varepsilon}$ and $\underline{\sigma}$) of a given material is dictated by the thermomechanical history (changes in rates) and not by time. Hence, the volume fraction and sizes of the phases at a given time, depend on the previous thermomechanical history and not on time per se. Incremental transformation will not be described further because this would go beyond the scope of this paper. However, it can be mentioned that homogenous as well as heterogeneous nucleation rates (at boundaries, edges, corners, etc.) are already accounted for, while interface-controlled, diffusion-controlled and eutectoid-type growths, are also all accounted for in the present framework [24].

3.0 NUMERICAL IMPLEMENTATION

Notwithstanding the equations used to described structure and phase transformations (i.e. Eq 11,12 and 14), the proposed formulation shows that twelve (12) differential equations need to be solved simultaneously for each structure (of each phase) as indicated by Equations 6 and 8b. The standard numerical procedure is to use a Self-Adaptive Forward Euler (SAFE) scheme[25]. As formulated, both the flow rule (whatever the exact form) and the evolutionary equation of $\underline{\underline{\Omega}}$ can be classified as nonhomogeneous nonlinear first order ordinary differential equation, i.e. of the form

$$\underline{\dot{y}} + \dot{a}(t)\,\underline{y} = \underline{f}(t) \tag{15}$$

Usually, to obtain the solution to Equation 15, the initial values $\underline{y}(t + \Delta t) = 0$ have to be prescribed. The numerical solution can be performed in discrete time steps Δt, starting from a known solution at time t. The time step Δt is the current finite element global time increment and can be divided into N equal subincrements. The integration of the system in Equation 15 is then performed by using forward differences with a smaller step size as

$$\underline{y}(t + \Delta t) = \underline{y}(t) + \left(\frac{\Delta t}{N}\right)\underline{f}(t) \tag{16}$$

The above equation is repeated N times and the solution of $\underline{y}$ at time t+Δt is obtained. The above equation implies that N must be selected depending on the magnitude of the change in strain for every subincrement.

It must be emphasized here that the robustness of this scheme (speed at which convergence is achieved) is strongly dependent on the form of the differential equations. Hence, whether an exponential form or a power law is used, there can be a significant difference on the computational time required for convergence. Furthermore, the analytical form chosen for the dynamic recovery term (which is used in most advanced constitutive models) renders the sets of differential equations highly nonlinear and extremely stiff. In these cases, very small time steps are required in order to use standard numerical integration techniques to solve these equations without loss of stability.

To alleviate this problem, it was decided to use an asymptotic integration scheme. The fundamental concept in obtaining a uniformly valid asymptotic integration scheme to equation 15, is to convert the constitutive equations into integral forms. With the integrated form of each flow rule and state variable, the asymptotic expansion can be used to represent each integral. The final forms appear in recursive relations which need to be solved by a Newton-Raphson iterative technique. It can be shown [26] that the general asymptotic solution to equation 15 is

$$\underline{y}(t + \Delta t) = \underline{y}(t)\,e^{-\Delta a} + \Delta\underline{f}\left(\frac{1 - e^{-\Delta a}}{\Delta a}\right) \tag{17}$$

with

$$\Delta a = \dot{a}(t) \cdot \Delta t \qquad (18a)$$

$$\Delta \underline{f} = \underline{\dot{f}}(t) \cdot \Delta t \qquad (18b)$$

Hence the flow rule can be rewritten as

$$\left(\underline{\dot{s}} - \frac{2}{3}\underline{\dot{\Omega}} \right) + \dot{Q}\left(\underline{s} - \frac{2}{3}\underline{\Omega} \right) = 2\mu \cdot \underline{\dot{e}} - \frac{2}{3}\underline{\dot{\Omega}} \qquad (19)$$

which reduces to Equation 15 if

$$\underline{y} = \left(\underline{s} - \frac{2}{3}\underline{\Omega} \right) \qquad (20a)$$

$$\dot{a}(t) = \dot{Q} = 3\mu \cdot \phi \qquad (20b)$$

$$\underline{f}(t) = 2\mu \cdot \underline{e} - \frac{2}{3}\underline{\Omega} \qquad (20c)$$

The most important thing to notice is that the asymptotic formulation of the flow rule is independent of the form chosen for the plastic multiplier ϕ. This is not the case with the standard integration procedures used in conjunction with other constitutive models.

The evolutionary equation of the back stress can be rewritten as:

$$\underline{\dot{\Omega}} + a \cdot \overline{\Omega}^{m-1}\left(1 - \frac{\Omega^0}{\overline{\Omega}} \right)\underline{\Omega} = h \cdot \underline{\dot{\epsilon}}^p \qquad (21)$$

which also reduces to equation 15 if

$$\underline{y} = \underline{\Omega} \qquad (22a)$$

$$\dot{a}(t) = a\overline{\Omega}^{m-1}\left(1 - \frac{\Omega^0}{\overline{\Omega}} \right) \qquad (22b)$$

$$\underline{f}(t) = h \cdot \underline{\dot{\epsilon}}^p \qquad (22c)$$

The following compares the standard and the asymptotic approaches to solving the constitutive behavior of each phase and structure:

Standard approach

$$\left. \begin{array}{l} \underline{\dot{y}} + \dot{a}(t)\,\underline{y} = \underline{\dot{f}}(t) \\[2mm] \underline{\dot{z}} + \dot{b}(t)\,\underline{z} = \underline{\dot{g}}(t) \end{array} \right\} \quad \text{12 equations.}$$

Asymptotic integration approach

$$\underline{y}(t + \Delta t) = \underline{y}(t)\,e^{-\Delta a} + \Delta\underline{f}\left(\frac{1 - e^{-\Delta a}}{\Delta a} \right)$$

$$\underline{z}(t + \Delta t) = \underline{z}(t)\,e^{-\Delta b} + \Delta\underline{g}\left(\frac{1 - e^{-\Delta b}}{\Delta b} \right)$$

6 x 2 equations.

Hence, the asymptotic integration encapsulates the interaction between tensor components into Δa and Δb. It is then possible to solve for the tensor components of the flow rule and back stress independently by a double iteration process using a Newton-Raphson algorithm. This numerical procedure (asymptotic integration method) was found to be at least ten (10) times faster than Newton-Raphson method, while as fast and more stable than SAFE method. This was achieved whatever the analytical form chosen for the plastic multiplier[27].

4.0 NUMERICAL EXAMPLES AND COMPARISONS

To demonstrate the capabilities and robustness of the present framework (including the constitutive model and numerical integration scheme), a 3-D finite element model was used to simulate one quarter of a solid specimen made of René 80, an alloy used for jet engine turbine blades. The material's constants were extracted from tensile curves, creep curves, stress relaxation curves and low cycle fatigue stress-strain loops, all taken from the literature [28]. The physical properties such as thermal conductivity, specific heat, expansion coefficient, elastic modulus, etc, were obtained from a NASA report [29].

4.1 Isothermal hysteresis behavior at 980°C

Using the parameters obtained from uniaxial tests (tensile, creep, and stress relaxation) the load response under varying strain histories were computed. For each strain history, the full cycle of load, consisting of three loading portions was imposed as follows: step 1 - loading ($o < \epsilon \le \epsilon_{max}$); step -2 unloading ($\epsilon_{max} > \epsilon \ge -\epsilon_{max}$); and step 3 - loading ($-\epsilon_{max} < \epsilon \le \epsilon_{max}$). The time for each step was adjusted such that the total strain rate was equal to 5×10^{-5} s^{-1}, 5×10^{-3} s^{-1} and 5×10^{-2} s^{-1} (Figure 7). Comparison of CPU time indicates that the proposed asymptotic integration scheme is very efficient computationally. Note that greater accuracy will always be obtained with the asymptotic integration because of the iterative nature of the scheme, as compared to the SAFE scheme which is of a non-iterative type.

4.2 Thermomechanical fatigue behavior

In order to predict the life of turbine and combustor components realistically, the lifing engineer must have a precise knowledge of the stress-strain hysteresis behaviour at the critical fatigue locations (with the corresponding loadings occurring at that site). The purpose of modelling TMF is twofold, firstly to assess the predictive capability of the proposed multistructure/multiphase approach as compared to experimental data reported elsewhere[29] and secondly to

demonstrate the capability of the asymptotic integration scheme in handling nonisothermal loading paths.
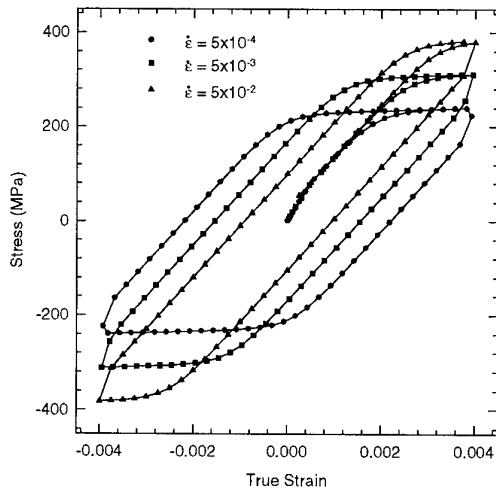
Figure 7. Hysteresis loop predictions of the model for René 80, Temperature 980°C, strain rate 5×10^{-4} s^{-1}, 5×10^{-3} s^{-1}, 5×10^{-2} s^{-1}.

Here we considered an open non-symmetrical TMF cycle as shown in Figure 8. The temperature holds about 1100 °C for 250 s. The strain, which was also varied, holds at -0.33% for the same period. Note that this thermomechanical history (about 18.6 min) mimics a typical engine's mission cycle (takeoff, cruise, landing, and taxi) of 3 to 4 hr. This thermal cycle time was broken up into seven segments (see Figure 8).

The results using our multi-structure approach and asymptotic integration scheme are presented in Figure 9 along with the experimental results. As can be seen, the computed results agree with the experimental results. The difference between the predicted and observed behaviors is attributed to the fact that the parameters used in the models were obtained from experiments involving various Rene80 with different microstructures. Although not shown here, the multi-structure approach combined with a standard fully implicit Newton-Raphston method was also used to compute the TMF response. Hence the 12 differential equations were solved simultaneously. It was decided not to use the SAFE scheme because it is not an iterative process.
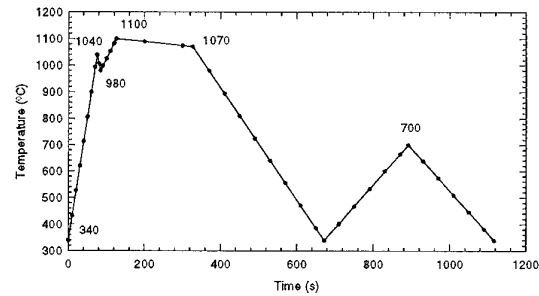
(a)
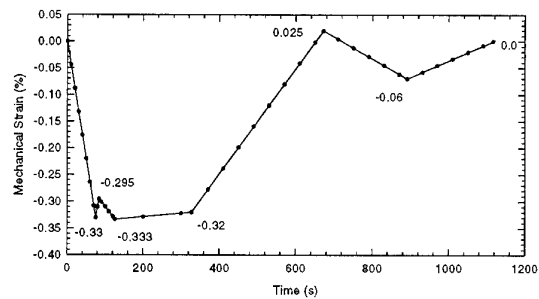
(b)
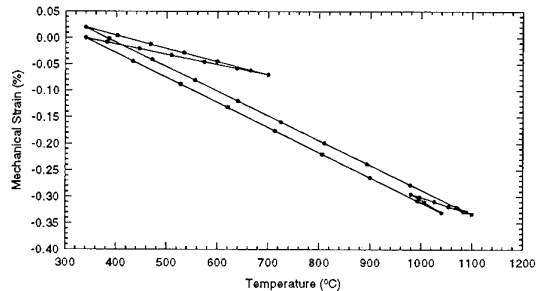
(c)

Figure 8. Open nonsymetrical thermomechanical fatigue loading cycle[29].
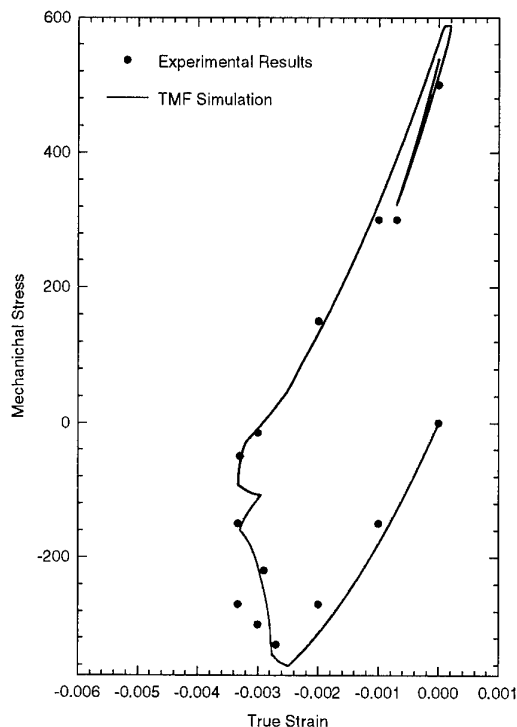
Figure 9. Thermomechanical fatigue loop predictions.

In fact, the use of a SAFE scheme for large scale analysis with complex loading histories is questionable since it is a subincremental noniterative approach. Hence, the error that occurs in each time step of a large scale analysis may be sizable and cumulative [26]. Because of the iterative approach of the asymptotic integration scheme and of the fully implicit Newton-Raphson method, error is not accumulated. However, comparison of the CPU times shows the asymptotic integration scheme to be 10 to 20 times faster than the fully-implicit Newton-Raphson (with the same accuracy).

5.0 CONCLUSIONS

A novel multistructure-multiphase approach to model viscoplasticity of solids was presented. In this framework, the evolution of the microstructure (including dislocation structures) is described explicitly. Transformation laws for structures transformation are given as well as the flow rules and evolutionary laws for the state variables (back stress and drag stress) of each structure. These laws and equations stem from the basic concepts of dislocation dynamics.

An asymptotic implicit integration scheme is proposed for solving the flow rule and evolutionary equations for each phase and structure. Concerning this scheme it can be said that:

- it is iterative without a high computational cost;

- the algorithm is stable for large time increment;

- the results are less user-dependent (less affected by the analytical form of the differential equations);

- the algorithm is accurate and efficient.

The multi-structure/multi-phase formulation can handle almost any kind of phase transformations occurring in solids. This framework is particularly suited for problems where phase transformations are expected, including oxidation problems, heat treatments, high temperature forging , etc.

6.0 REFERENCES

1. Nissley D.M., T.G. Meyer T.G. and Walker K.P., "Life Prediction and Constitutive Models for Engine Hot Section Anisotropic Materials Programs",NASA CR-189223,1992.

2. Thulin E.D., Howe D.C. and Singer I.D., "Energy Efficient Engine High Performance Turbine", NASA Report CR-165608 Pratt & Whitney Group, East Hartford, CT, 1982

3. Moreno V., Nissley D.M. and Lin L.S., "Creep-Fatigue Life Prediction for Engine Hot Solution Materials", NASA Report CR-174844, Pratt Whitney Group, East Hartford, CT, 1984

4. McDonnell D., Antolovich S.D. and Oehmke R.L.T., Nucl. Engng. J. Design, vol 133, 1992, pp. 383-399

5. Remy L., Rezai-Aria F., Danzer F. and Hoffelner W., ASTM STP 942, ed. by H.D. Solomon et al., American Society for Testing and Materials, Philadelphia, PA, 1988, pp. 1115-1132.

6. Larsen J. and Nicholas T., Engng. Fract. Mech., vol.22, 1984, pp. 713-730

7. Larsen J. and Nicholas T., "Engine Cyclic Durability by Analysis and Testing", AGARD specialists Meeting, Netherland, June 1984.

8. Draper, Hull D. and Dreshfield R., Met. Trans., vol. 20A, 1993, pp. 683-688

9. Mackay R. and Ebert L.J., Superalloys 84, ed. By M. Gell and al., pub. by AIME, 1984, pp. 135-144.

10. Radavich J.F. and Korth G.E., Superalloys 1992, ed. by Antolovich S.D. and al., pub. by AIME, 1992, pp. 497-506

11. Aimone P.A. and McCormick R.L., Superalloys 1992, ed. by Antolovich S.D. and al, pub. by AIME, 1992, pp. 817-824.

12. Raquet M., Antolovich S.D. and Kelly-Payne R., Superalloys 84, pub. by AIME, 1984, pp. 231-241.

13. Antolovich S.D., Liu S. and Baur R., Met. Trans., vol 12A, 1981, pp. 473-481.

14. Eshelby J.D., Proc. Royal Soc. London, vol. 241A, 1957, pp. 891-898.

15. Kocks U.F., "Constitutive Equations in Plasticity", ed. by Argon A.S., MIT press, 1975, pp. 81-115.

16. Kocks U.F., Argon A.S. and Ashby M.F., Prog. Mater.Sci., vol 19, 1975, 219 p.

17. Miller A.K., J. Engng Mater & Techno., vol 96, 1976, pp. 97-110.

18. Poirier J.-P., "Plasticité à haute température des solides cristallins", Eyrolles Press, 1976, Chapter 9.

19. Meyers M.A. and Chawla K.K., "Mechanical Metallurgy: Principles and Applications", Prentice-Hall, 1984, Chapter 11.

20. Kuhlmann-Wilsdorf D., Mater. Sci. & Engng., vol. 113A, 1989, pp. 1-41.

21. Kuhlmann-Wilsdorf D., Met. Trans., vol 16A, 1985, pp. 2091-2108.

22. Mughrabi H., "Constitutive Equations in Plasticity", ed. by Argon A.S., MIT Press, 1975, pp. 199-250.

23. Porter D.A. and Easterling K.E., "Phase Transformations in Metals and Alloys", Van Nostrand Reinhold Int., 1981.

24. Malenfant E., "Transformation microstructurale des métaux sous chargement thermomecanique", M.Sc.A., Ecole Polytechnique (Dec 1995).

25. Cassenti B.N., "Research and Development Program for the Development of Advanced Time-Temperature Dependent Constitutive Relationships-Theoretical Discussion", NASA CR-168191-VOL-1, 1983.

26. Chulya A. and Walker K.P., Int. J. for Num. Methods in Engng., vol. 32, 1991, pp. 385-418.

27. Boire-Lavigne S., "Formulation d'un modèle constitutif incluant les effets des transformations microstructurales", M.Sc.A. Thesis, Ecole Polytechnique de Montréal, November 1995.

28. Ramaswamy V.G., "A Constitutive Model for the Inelastic Multiaxial Cyclic Response of a Nickel Base Superalloys Rene-80", NASA CR-3998,1986.

29. McKnight R.L., Laflen J.H. and Spamer G.T., "Turbine Blade Tip Durability Analysis", NASA CR-165268, 1981.

FATIGUE CRACK GROWTH UNDER TMF

T. Nicholas
USAF Wright Laboratory Materials Directorate
Wright-Patterson AFB, OH 45433, USA

SUMMARY

The use of a linear damage summation approach for the prediction of crack growth rates under thermomechanical fatigue (TMF) is summarized. The methodology involves the addition of growth rates due to cyclic and time-dependent mechanisms. In creep-brittle materials, the summation approach is straightforward when applied to TMF. For creep-ductile materials, the retardation of the crack growth rate due to crack tip blunting, branching, or stress relaxation, has to be taken into account. This is accomplished through the use of a blunting coefficient with its own evolution equations. The methodology is applied to TMF crack growth in a titanium matrix composite by modifying the functional form of the two terms. The cycle-dependent term is taken as a function of temperature, while the time-dependent term has a slight ΔK dependence coupled with the integral of an Arrhenius type term over an entire cycle. For all three materials, the modeling approach provides reasonable predictions of TMF crack growth rates based solely on parameters obtained from isothermal test data.

1. INTRODUCTION

The use of structural materials at high temperatures, such as in turbomachinery, often involve combinations of mechanical as well as thermal cycling, commonly referred to as thermomechanical fatigue (TMF). The introduction of damage tolerant design procedures has necessitated the development of tools to predict the crack growth rate behavior of these high temperature materials in order to determine the component life or the required inspection intervals to insure structural integrity. Of the various conditions which a component is subjected to in service, TMF is one of the most difficult when it comes to predicting crack growth rates. Consequently, there is little information available on which to base a design or predictive procedure.

A review of some of the procedures developed for predicting fatigue crack growth rates under TMF is presented in Ref 1 covering work up through 1989. Presented there, in addition, was an approach based on the concept of linear damage summation of the separate contributions due to purely cycle-dependent and purely time-dependent phenomena. This approach was first postulated by Wei and Landes (Ref 2) and has been applied by several investigators for predicting isothermal fatigue crack growth rates using linear elastic fracture mechanics (Refs 3, 4). The application of the linear damage summation approach to crack growth under TMF is reviewed and demonstrated in a material which is creep brittle, Inconel 718, by Nicholas et al. (Ref 1). This approach, which was developed for use in a nickel-base superalloy (Refs 1, 5), was modified subsequently for use in a creep-ductile material, Ti-24Al-11Nb, under isothermal (Refs 3, 6), non-isothermal (Ref 7) as well as TMF conditions (Refs 8, 9), and ultimately applied to the prediction of crack growth rates in a continuous fiber reinforced metal matrix composite, SCS-6/Ti-6Al-2Sn-4Zr-2Mo, abbreviated hereafter as Ti-6-2-4-2, subjected to TMF (Ref 10). In this paper, the development and use of the linear damage summation approach for the prediction of crack growth rates in these three material classes under TMF is summarized.

2. TMF CRACK GROWTH MODELING

2.1 Creep-brittle materials

Creep-brittle materials can be defined as ones which demonstrate purely time-dependent behavior or purely cycle-dependent behavior, depending on temperature and frequency. The time-dependent behavior is due to environmental effects and results in growth rates which are inversely proportional to frequency as depicted in Fig. 1. In some materials, a mixed mode behavior is observed in the transition region.

For this class of materials, the crack growth rate can be considered to be comprised of two components, one being purely cycle dependent, and one being purely time dependent. The crack growth rate is expressed as

$$\left[da/dN \right]_{tot} = \left[da/dN \right]_{cyc-dep} + \left[da/dN \right]_{time-dep} \quad (1)$$

where the first and second terms on the right hand side represent the behavior under two extremes. The first term implies that a cycle imparts a

18-2

certain amount of damage or crack extension per cycle, and is dependent only on the number of cycles applied, independent of frequency and temperature. In simple terms, "a cycle is a cycle." The second term implies that damage or crack growth rate accumulates due to processes dependent solely on time at temperature under a given stress intensity. Thus, if time-dependent processes were the only ones present, crack growth rate would be inversely proportional to frequency. For this class of creep-brittle materials, and to provide a convenient method of interpolation, the cycle-dependent crack growth rate is written as a function of ΔK and stress ratio, R, in the form of a modified sigmoidal equation (MSE) as described in the Appendix. A similar representation is followed for the time-dependent term in the crack growth rate equation as a function of K and temperature, T. Time-dependent crack growth is represented as growth rate per unit time, da/dt, and is expressed in identical fashion to crack growth per cycle except that da/dN is replaced by da/dt.

The crack growth rate predictions are obtained through the use of eqn (1) in conjunction with the MSE described in the Appendix. For each of a series of values of ΔK, the cycle-dependent term is calculated directly from eqns (A1) through (A5). The time-dependent term is obtained through integration of da/dt over the non-decreasing load part of the TMF cycle. The integration is performed numerically taking into account that both K and temperature change continuously in accordance with the MSE formulation.

The application of this model and the capability to correlate and predict crack growth rates is illustrated in Fig. 2 for sustained load behavior using the MSE. In this figure, growth rates at 538 and 649°C are fit with the MSE, but data at 593°C are predicted based on the interpolative capability of the MSE. The TMF data and isothermal data at max and min temperatures of the TMF cycle are illustrated in Fig. 3 where it can be seen that all of the TMF data are bounded by the two isothermal data sets. The ability of the model to predict the TMF data is shown in Fig. 4 where it can be seen that the data are well represented by the model under all four TMF conditions.

2.2 Creep-Ductile Materials

For materials which cannot be represented as behaving due to a combination of purely cycle-dependent and purely time-dependent processes, a methodology has been developed which accounts for growth rates which are retarded due to the ductility of the material. For this class of creep-ductile materials, the crack growth rate is

considered to be retarded due to a complex phenomenon which is dependent on some combination of crack tip blunting, stress relaxation at the crack tip, crack branching, and possibly other phenomena. The resultant crack growth is considered to be "retarded" from what it would be, hypothetically, if the crack tip were sharp and no blunting, branching, stress relaxation, or other retarding phenomena took place. For this class of materials, crack growth rate is represented by the following equation,

$$\left(da/dN\right)_{tot} = \left(da/dN\right)_{ret\ cd} + \left(da/dN\right)_{ret\ td} \tag{2}$$

where total crack growth rate is represented as the sum of a cycle-dependent (subscript cd) and a time-dependent (subscript td) term, each term, in turn, representing the contribution in an actual condition where crack tip blunting, branching, etc. has occurred, and is denoted in the equation by the subscript "ret" which represents the "retarded" state. A retardation term, β, is introduced, which modifies the crack growth rate to account for the growth rate retardation phenomenon. β can vary from a value of one, which represents the sharp crack state, to zero, which represents total retardation. Then the retarded cycle-dependent crack growth rate term can be expressed as

$$\left(da/dN\right)_{ret\ cd} = \int_0^{t_{ul}} \beta\,(t)\,\left(2/\tau\right)\left(da/dN\right)_{ur\ cd}\,dt \tag{3}$$

where τ is the cycle period, $(da/dN)_{ur\ cd}$ represents the unretarded cycle-dependent crack growth rate at a particular ΔK and temperature, and the upper limit of integration, t_{ul}, represents the uploading time of the cycle, defined as the time required to reach maximum load. The dependence of $(da/dN)_{ur\ cd}$ on temperature is required because of experimental observations as shown in Fig. 5 (Ref 11). Here, it can be seen that crack growth rate decreases to a minimum at approximately 300°C, due primarily to an increase in ductility in the material. As temperature increases further, growth rate increases due to environmental effects, and that growth rate is now sensitive to frequency. Note that in the formulation of eqn (3), the retardation coefficient, β, varies continuously with time during a given cycle as well as from cycle to cycle. In actual calculations, the history of β over a cycle reaches a stable value.

Following a similar procedure, the retarded time-dependent crack growth rate term is written as

$$\left(da/dN\right)_{ret\ td} = \int_0^{t_{nd}} \beta\,(t)\,\left(da/dt\right)_{ur\ td}\,dt \tag{4}$$

where $(da/dt)_{ur\ td}$ is the unretarded time-dependent crack growth rate (per unit time) and t_{nd} is the integration limit corresponding to the point where the load starts to decrease. If there are no hold times in the cycle, then $t_{nd} = t_{ul}$.

The retardation coefficient, β, varies continuously and is calculated as

$$\beta(t) = \beta(t_0) + \int_{t_0}^{t} \frac{d\beta}{dt}\, dt \tag{5}$$

where the evolution equation for β is taken in the form

$$\frac{d\beta}{dt} = \left(\frac{d\beta}{dt}\right)_{inc} + \left(\frac{d\beta}{dt}\right)_{dec} \tag{6}$$

which represents the sum of a crack tip sharpening term (β increasing) and a crack tip blunting term (β decreasing). The increasing term, which corresponds to crack sharpening due to the fatigue process, is taken in the form

$$\left(\frac{d\beta}{dt}\right)_{inc} = \begin{cases} C_1(1-\beta) & \text{for } dP/dt \neq 0 \\ 0 & \text{for } dP/dt = 0 \end{cases} \tag{7}$$

where C_1 is a function of frequency, v. The physical meaning of this term is that during fatigue cycling, the crack tip tends to sharpen, and β should asymptotically approach one. The rate of change of β, therefore, should depend on the cyclic frequency as well as how "blunt" the crack tip is at any instant. The blunting of the crack tip, on the other hand, occurs because the crack tip is subjected to load for periods of time. At higher loads, the crack blunts faster than at lower loads, so a functional form for this is taken as

$$\left(\frac{d\beta}{dt}\right)_{dec} = -C_2 \left(\frac{P}{P_{max}}\right)(\beta - \beta_0) \tag{8}$$

where C_2 is a function of temperature and β_0 is the minimum value that β can achieve. If β_0 is zero, the crack is arrested. In actual computations, β_0 typically has a small, but non-zero value.

The capability of the model to represent the isothermal crack growth rates in Ti-24Al-11Nb is illustrated in Figs. 6 and 7 for variations in frequency and temperature, respectively. The variation in frequency is less than that for a fully time-dependent material (see Fig. 1) over a range of frequencies from 0.001 to 100 Hz, and corresponds to a slope of -0.24 in the mixed mode region of Fig. 1 (Ref 11). It is for this reason that the coefficients C_1 and C_2 introduced into eqns (7) and (8) must have a frequency dependence. The capability of

the model to represent both the frequency and temperature dependence of the isothermal crack growth data is seen to be quite good. Predictions of the in-phase and out-of-phase TMF test data are presented in Fig. 8. The model is seen to provide good correlation with the data.

2.3 Metal matrix composites

The concepts developed for creep-ductile materials, which involves the use of a blunting coefficient, have been extended for use in modeling crack growth in a continuous fiber unidirectional metal matrix composite under TMF (Ref 10). In the material used in that investigation, there was little or no fiber bridging so that the model is restricted to composites under conditions where bridging is not present. The model follows the linear damage summation concept using a cycle-dependent and a time-dependent term, eqn (1).

2.3.1 Cycle-dependent term

Although the cycle-dependent term for a monolithic material is a function of ΔK_{app}, stress ratio, and temperature, the cycle-dependent term for a composite was assumed to be a function of ΔK_{app} only, primarily due to lack of data. Further, only one stress ratio ($R = 0.1$) was used during the study of Blatt and Hartman (Ref 12), and temperature was observed not to influence the matrix crack growth rate markedly.

Although the modeling efforts of Nicholas et al. (Ref 1) for creep-brittle materials, and Pernot et al. (9) for creep-ductile materials, used a modified sigmodial equation (MSE) to describe the cycle-dependent behavior, insufficient data were available to determine the constants for a MSE for the titanium matrix composite in the work by Blatt et al. (Ref 10). Thus, a simple Paris Law was used for the cycle-dependent term which is valid only in Region II and only crack growth data in this region were modeled. Cycle-dependent crack growth rates are thus represented as

$$\frac{da}{dN} = C(\Delta K)^n \tag{9}$$

where C and n are empirical constants. The constant n was determined from the slope of the isothermal and TMF crack growth data where the slope of the linear portion of each data set was similar enough to be considered a constant, $n=2.7$, and not a function of temperature, frequency or phase angle.

2.3.2 Time-dependent term

An expression similar to the fiber damage term in Neu's model (13) for TMF in titanium matrix composites was used to model the time-dependent crack growth behavior. Neu suggested an Arrhenius-type expression to represent the

weakening of a fiber because of time, temperature, and fiber stress. The time-dependent component was chosen in a form similar to Neu's Arrhenius expression, except the fiber-stress component was replaced with an applied ΔK dependence. Because of a strong dependence on temperature and a weaker dependence on K, the ΔK^n term was taken outside the integral. This insures all curves representing time-dependent behavior have the same slope, m. The time-dependent term had the form:

$$\left(\frac{da}{dN}\right)_{time-dep} = \int_{cyc} \frac{da}{dt}dt = (\Delta K)^m \int_0^{t_{nd}} C_1 \, e^{\frac{-C_2}{T_{abs}}} \, dt \tag{10}$$

where C_1 is an empirical constant, T_{abs} is the absolute temperature (T °C + 273) at any instant during the cycle, and m is the exponent of ΔK. Based on the experimental data from a variety of tests involving combinations of cycle- and time-dependent behavior, m was taken to be the same as n because all the da/dN-ΔK curves were essentially parallel. The time, t_{nd}, is the time when the load is non decreasing as in eqn (4).

2.3.3 Effects of frequency

It is to be noted that frequency effects are not explicitly considered in either eqns (9) or (10). As in the two types of monolithic materials considered here, the cycle-dependent term is considered independent of frequency. However, the time-dependent term in eqn (10) is implicit in time (T_{abs} depends on time during a TMF cycle) and thus is a function of frequency. The experimental data revealed that the crack growth behavior was affected by a change in frequency, but the data never exhibited completely time-dependent behavior for the conditions tested. In Fig. 1, this corresponds to all data lying in the mixed mode region as was observed and noted above for Ti-24Al-11Nb (Ref 11). Thus, the procedure used by Nicholas and Mall (Ref 3) was followed where the time-dependent term is modified by a coefficient of the form $t_c^{\gamma-1}$, where t_c is the total cycle time (or period). Whereas they used $\gamma = 0.5$, which yielded a time-dependent term that would vary with frequency as $\sqrt{(t_c)}$, a similar modification was used in the current study to account for frequency effects under different TMF conditions. This is necessary in order to account for micromechanical stresses including thermal residual stresses which differ from one type of TMF test to another. By introducing a coefficient $t_c^{\gamma-1}$, the total crack growth rate equation becomes

$$\left(\frac{da}{dN}\right)_{tot} = C\,(\Delta K)^n + t_c^{\gamma-1}(\Delta K)^m \int_0^{t_{nd}} C_1 \, e^{\frac{-C_2}{T_{abs}}} \, dt \tag{11}$$

A value of γ for each type of test was determined by comparing the total crack growth rates for isothermal, in-phase, and out-of-phase conditions at two different frequencies. The value of γ for the in-phase, isothermal, and out-of-phase conditions was 0.62, 0.57, and 0.52, respectively. The physical explanation for the frequency effect and the different values of γ for each test type are explained further in Ref 10.

After determination of constants for eqn (11), crack growth rates were calculated for each of seven different baseline conditions and then compared to the experimental data to verify the model's ability to correlate the baseline data. The correlation between the three isothermal data sets and results from the model is shown in Fig. 9. As expected, the crack growth rates calculated from the model for each of the isothermal conditions correlate well with the experimental data. The correlation between the two in-phase and two out-of-phase data sets and results from the model is shown in Figs. 10 and 11. Again, the computed crack growth rates correlate well with the experimental data.

To test the predictive capability of the model, a proof test was conducted in which the fatigue cycling starts under isothermal conditions and the minimum temperature is continually decreased throughout the test and finishes under in-phase conditions. In this test, decreasing T_{min} according to a predefined profile produces a constant crack growth rate for the life of the specimen. This is the result of two competing growth rate mechanisms, the increase in stress intensity due to crack extension, and the decrease in minimum temperature which reduces the time-dependent portion of the driving force. To determine the exact T_{min} profile as a function of elapsed cycles for the proof test, the linear summation model, eqn (11), was used. The proof test was started at T=538°C under constant amplitude loading which produced a constant crack growth rate of 1.41×10^{-6} m/cycle. For a predicted range of ΔK from 42 to 80 MPa$\sqrt{m}$, the predicted number of cycles the test would run was 2750.

The crack growth rate is plotted as a function of ΔK_{app} and compared with the growth rate from the predicted simulation in Fig. 12 which shows that the model predicted a slightly decreasing growth rate over the life of the specimen. Nevertheless, the crack growth rates generated during the proof test followed the predicted ones quite closely. These results indicate that the proposed linear summation model successfully captured the primary features which control the crack growth behavior, namely, time-at-temperature. While a single proof test does not

offer absolute evidence that the model is accurate, it strongly supports the fundamental concepts built into the model.

3. DISCUSSION AND CONCLUSIONS

The linear damage summation concept can be applied to the prediction of fatigue crack growth rate in a number of material systems subjected to TMF. For creep-brittle metals, TMF crack growth rates are predicted well using isothermal data obtained at different temperatures and stress ratios. For creep-ductile metals, data must also be obtained at a number of different frequencies in order to establish the degree of crack growth retardation due to blunting. While additional parameters are introduced to account for the combined effects of environment and retardation due to blunting, the predictive capability under TMF is still quite good. For titanium matrix composites, additional terms and factors have to be taken into consideration. In this case, simple TMF data are required to calibrate the model which becomes more correlative than predictive. While the calibration is more complex and requires more data than in the case of pure metals, the model for the composites does not require micromechanical stress analyses. Rather, the effects of micromechanical stresses due to thermal coefficient of expansion mismatch between fiber and matrix are accounted for empirically in a continuum representation of the composite. Nonetheless, the linear summation model appears to have reasonably good capability for prediction and correlation of crack growth rates in all three classes of materials.

ACKNOWLEDGEMENTS

REFERENCES

1. Nicholas, T., Heil, M.L. and Haritos, G.K., Predicting Crack Growth under Thermo-Mechanical Cycling, Int. J. Fracture, *41*, 1989, pp 157-176.

2. Wei, R.P. and Landes, J.D., Correlation Between Sustained-Load and Fatigue Crack Growth in High Strength Steels, Materials Research and Standards, *9*, 1969, pp 25-27, 44, and 46.

3. Nicholas, T. and Mall, S., "Elevated Temperature Crack Growth in Aircraft Engine Materials," *in* Advances in Fatigue Lifetime Predictive Techniques, ASTM STP 1122, M.R. Mitchell and R.W. Landgraf, Eds., American Society for Testing and Materials, Philadelphia, 1992, pp 143-157.

4. Winstone, M.R., Nikbin, K.M. and Webster, G.A., "Modes of Failure under Creep/Fatigue Loading of a Nickel-based Superalloy," Journal of Materials, *20*, 1985, pp 2471-2476.

5. Heil, M.L., Nicholas, T., and Haritos, G.K., "Crack Growth in Alloy 718 Under Thermal-Mechanical Cycling," *in* Thermal Stress, Material Deformation, and Thermo-Mechanical Fatigue, H. Sehitoglu and S.Y. Zamrik, Eds., ASME PVP - Vol. 123, ASME, New York, 1987, pp 23-29.

6. Nicholas, T., "Fatigue Crack Growth Modeling at Elevated Temperatures Using Fracture Mechanics," *in* Elevated Temperature Crack Growth, MD-Vol. 18, S. Mall and T. Nicholas, Eds., American Society of Mechanical Engineers, New York, 1990, pp 107-112.

7. Pernot, J.J., Mall, S. and Nicholas, T., "Crack Growth Rate Behavior of a Titanium-Aluminide Alloy During Isothermal and Non-Isothermal Conditions," ASME J. Eng. Mat. Tech., *117*, 1995, pp 118-126.

8. Mall, S., Nicholas, T., Pernot, J.J. and Burgess, D.G., "Crack Growth in a Titanium Aluminide Alloy under Thermal Mechanical Cycling," Fatigue Fract. Engng. Mater. Struct., *14*, 1991, pp 79-87.

9. Pernot, J.J., Nicholas, T. and Mall, S., "Modelling Thermomechanical Fatigue Crack Growth Rates in Ti-24Al-11Nb," Int. J. Fatigue, *16*, 1994, pp 111-122.

10. Blatt, D., Nicholas, T. and Grandt, A.F.,Jr., "Modeling the Crack Growth Rates of a Titanium Matrix Composite under Thermomechanical Fatigue," *in* Thermo-Mechanical Fatigue Behavior of Materials, ASTM STP 1263, M.J. Verrilli and M.G. Castelli, Eds., ASTM, Philadelphia, 1995.

11. Pernot, J.J., Nicholas, T. and Mall, S., "Crack Growth Rate Behavior in a Titanium-Aluminide Alloy Under Isothermal and Thermomechanical Fatigue," *in* Fracture and Damage, AD-Vol. 27, A. Nagar, Ed.,

American Society of Mechanical Engineers, New York, 1992, pp 109-117.

12. Blatt, D. and Hartman, G. A., "A Methodology for Thermomechanical Fatigue Crack Growth Testing of Metal Matrix Composites," *Experimental Mechanics*, 1995. (in press)

13. Neu, R.W., "A Mechanistic-based Thermomechanical Fatigue Life Prediction Model for Metal Matrix Composites," Fatigue and Fracture of Engineering Materials and Structures, *16*, 1993, pp 811-828.

APPENDIX

The accurate representation of crack growth rate as a function of ΔK as well as methods for representing families of curves as a function of such variables as stress ratio or temperature is a critical part of TMF crack growth modeling using the linear damage summation approach. One method, the modified sigmoidal equation (MSE), has been used for such representations (Refs 1, 9). The equations, and their application to creep-brittle materials (Ref 1) are summarized here for completeness. The MSE has a vertical asymptote at the minimum and maximum values on the ΔK axis and an inflection point somewhere in between. Crack growth rate is expressed in the following manner,

$$da/dN = \exp B' \left(\Delta K/\Delta K_i \right)^P \left[\ln \left(\Delta K/\Delta K^* \right) \right]^Q \left[\ln \left(\Delta K_c/\Delta K \right) \right]^D \tag{A1}$$

where

$$P = \left(da/dN_i \right)' - Q/\ln \left(\Delta K_i/\Delta K^* \right) + D/\ln \left(\Delta K_c/\Delta K_i \right) \tag{A2}$$

$$B' = \ln \left(da/dN_i \right) - Q \ln \left[\ln \left(\Delta K_i/\Delta K^* \right) \right] - D \ln \left[\ln \left(\Delta K_c/\Delta K_i \right) \right] \tag{A3}$$

In these equations, ΔK^* and ΔK_c represent the threshold and critical stress intensity range, respectively. The inflection point on the sigmoidal curve is denoted by the coordinates ΔK_i and (da/dN_i), while the slope at the inflection point is designated $(da/dN_i)'$. The remaining parameters, Q and D, are used for shaping the curve to fit experimental data. For the data reported in (Ref 1), the following relations were established:

$$\Delta K_c = \Delta K_i^2/\Delta K \tag{A4}$$
$$Q = -D = 0.4$$

The following four parameters were determined as a function of stress ratio, R, by the following (matrix) equation which represents a best-fit to a large body of experimental data on Inconel 718 under purely cycle-dependent conditions, namely room temperature, or higher temperature at high frequencies.

$\log \Delta K^*$		1.0866		1.0312		
$\log \Delta K_i$	$=$	1.6299	$+$	0.6068	$\log (1-R)$	(A5)
$\log (da/dN_i)$		-6.2244		0.7690		
$(da/dN_i)'$		3.5896		1.9578		

Using the sigmoidal equation for time-dependent behavior, crack growth per unit time has parameters which are dependent on temperature in the following manner,

$\log K^*$		1.5672		-1.472×10^{-3}		
$\log K_i$	$=$	1.8808	$+$	-9.249×10^{-4}	$(T-538)$	(A6)
$\log (da/dt_i)$		-7.1871		2.008×10^{-2}		
$(da/dt_i)'$		1.2000		1.622×10^{-2}		

where temperature is expressed in °C.
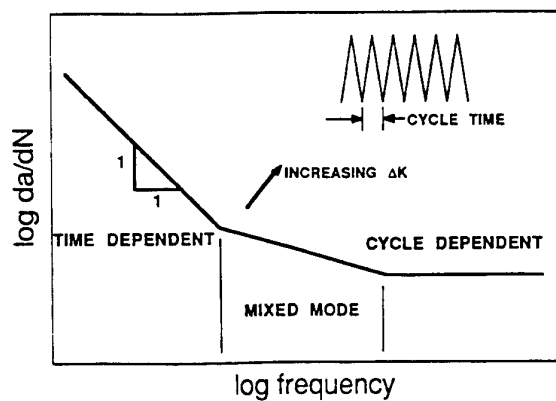
Fig. 1 Schematic of frequency effect on crack growth rate in Inconel 718 at 649°C.
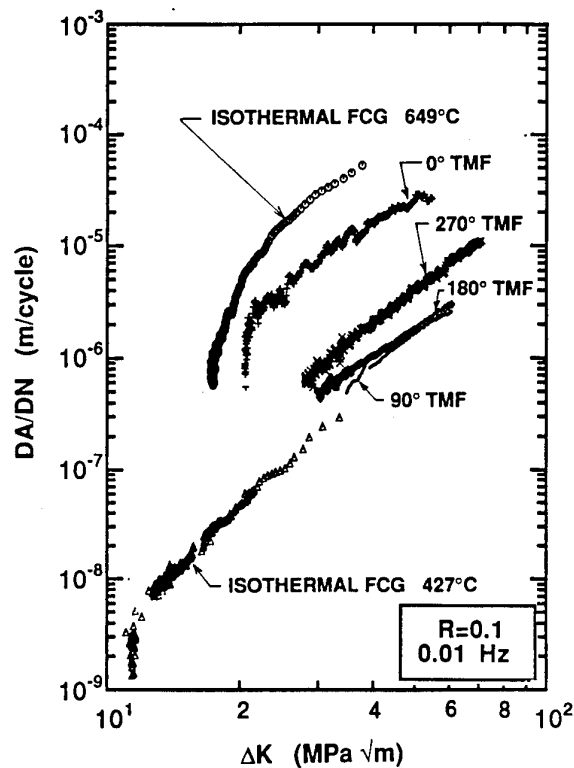
Fig. 3 Experimental crack growth rate data under TMF and isothermal data at max and min temperatures of TMF cycle for Inconel 718.
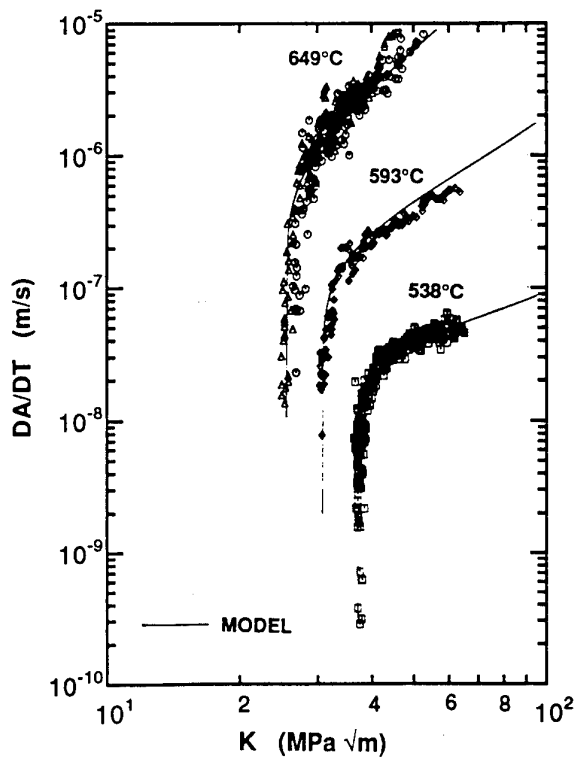
Fig. 2 Sustained load crack growt rates and model predictions in Inconel 718.
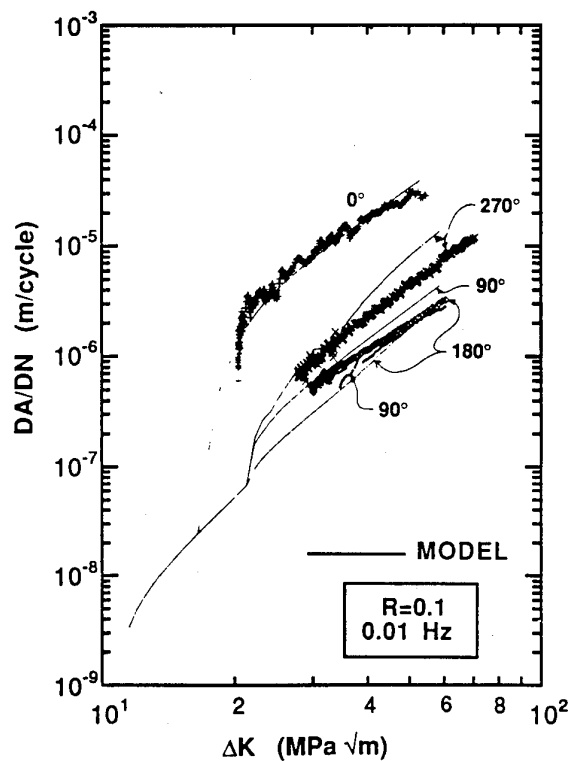
Fig. 4 Experimental data and model predictions for TMF crack growth rates in Inconel 718.
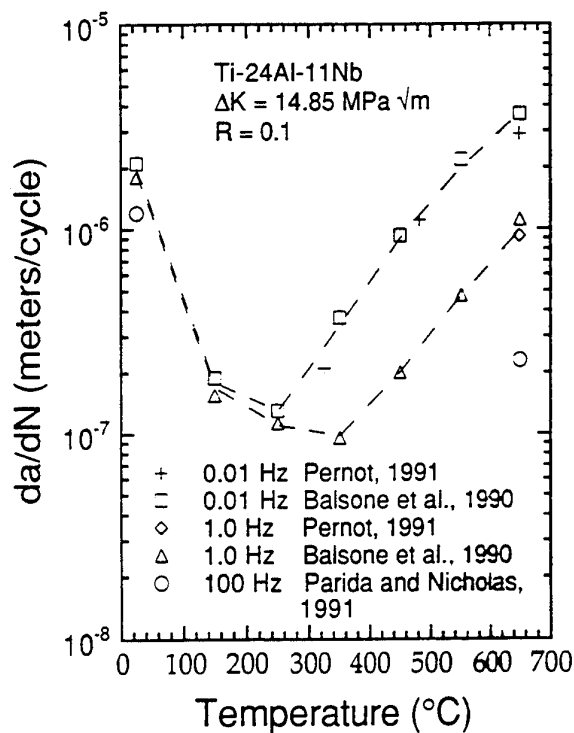
Fig. 5 Effect of temperature on
crack growth rate in Ti-24Al-11Nb
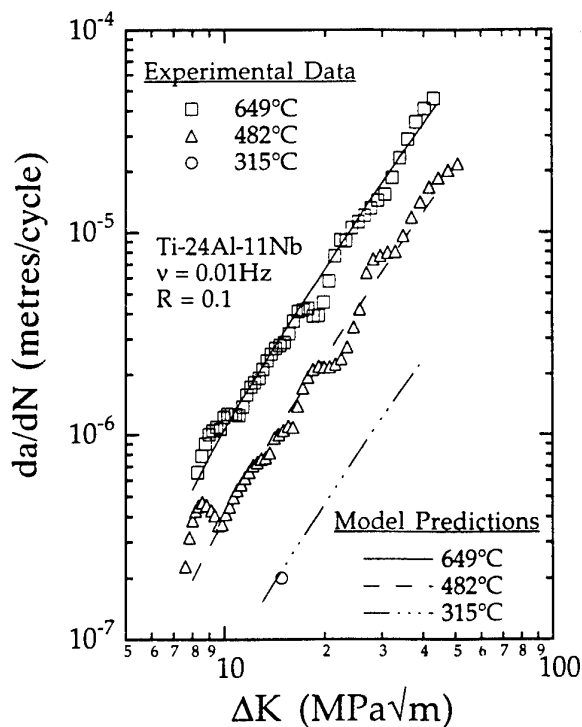
Fig. 7 Crack growth rate predictions in
Ti-24Al-11Nb at different temperatures.
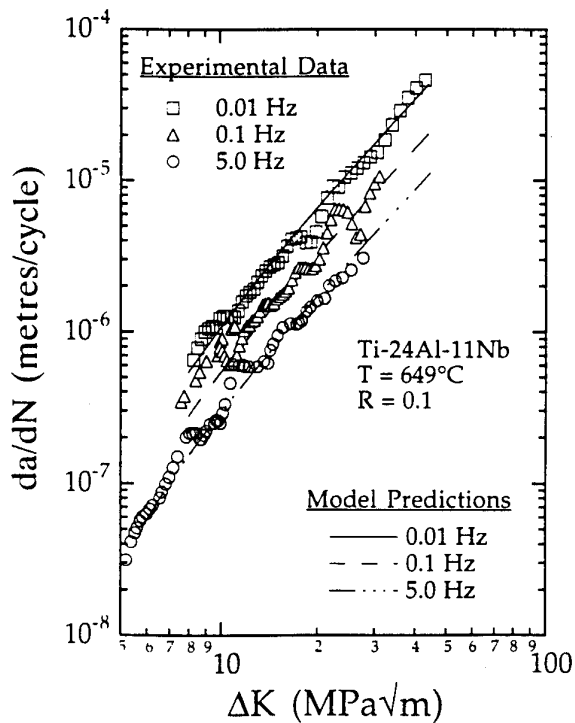
Fig. 6 Crack growth rate predictions in
Ti-24Al-11Nb at different frequencies.
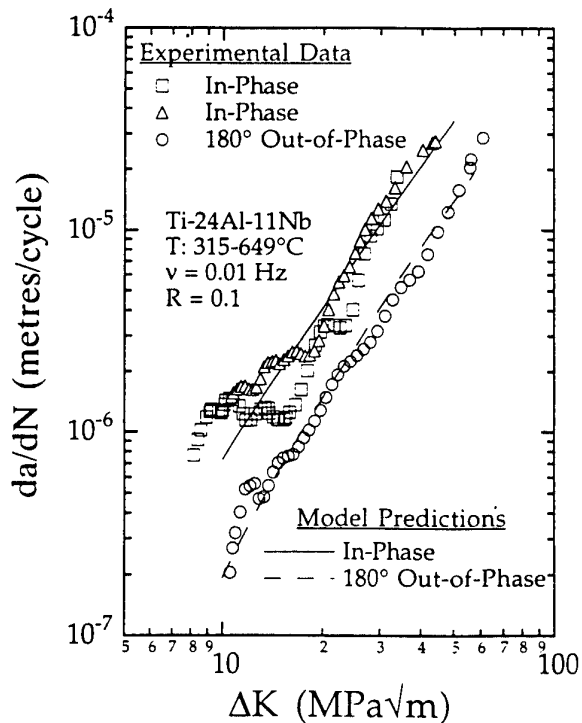
Fig. 8 Crack growth rate predictions in
Ti-24Al-11Nb under IP and OP TMF.
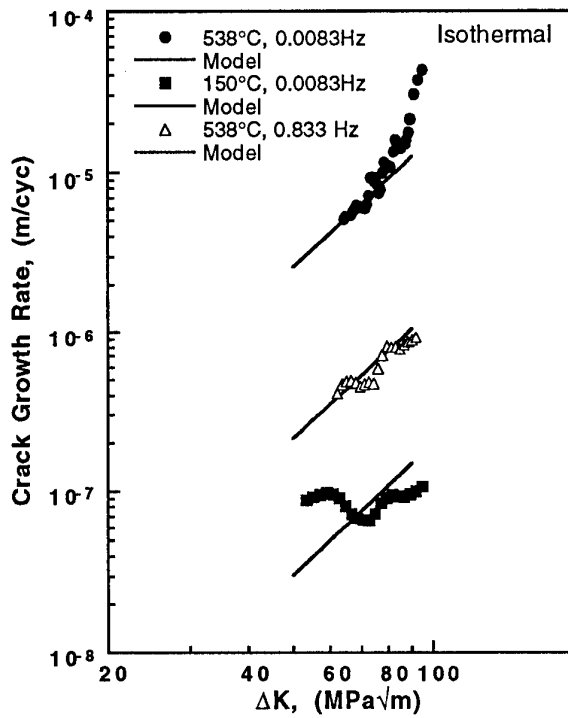
Fig. 9 Correlation between model and SCS-6/Ti-6Al-2Sn-4Zr-2Mo fatigue crack growth data from the isothermal tests at 150°C and 538°C.
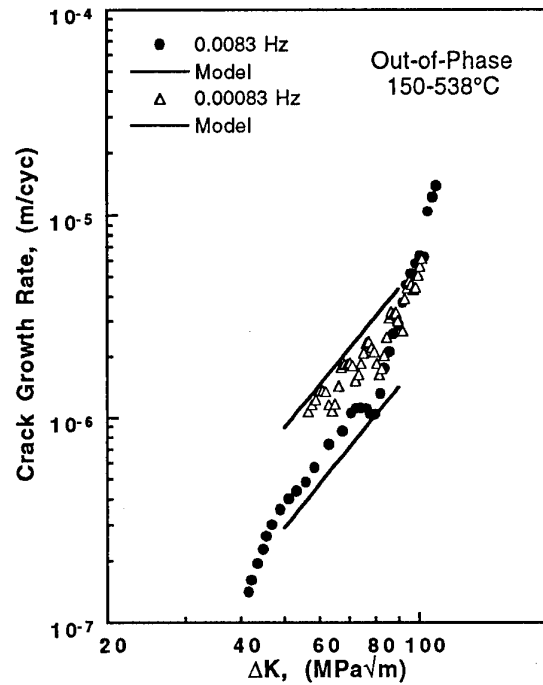
Fig. 11 Correlation between experimental data and model for SCS-6/Ti-6-2-4-2 crack growth rates under out-of-phase TMF at 0.0083 Hz and 0.00083 Hz.
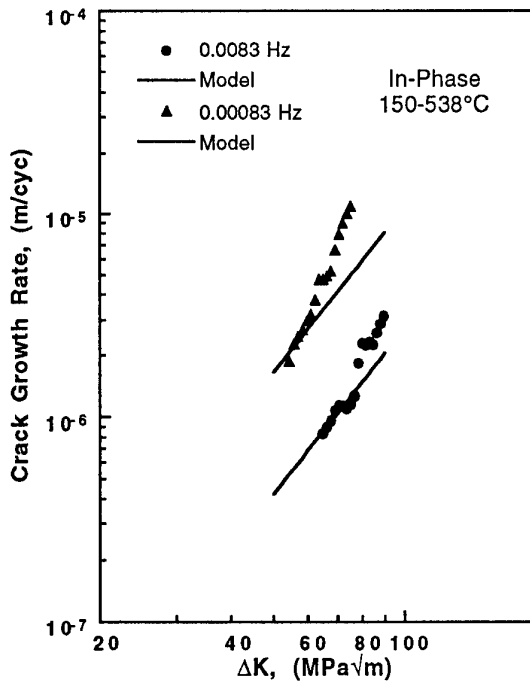
Fig. 10 Correlation between experimental data and model for SCS-6/Ti-6-2-4-2 crack growth rates under in-phase TMF at 0.0083 Hz and 0.00083 Hz
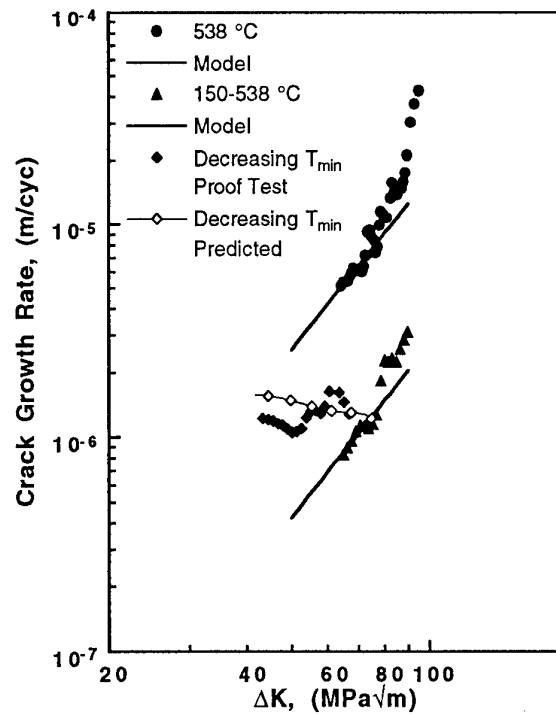
Fig. 12 Experimental data and model predictions for proof test in SCS-6/Ti-6-2-4-2.

THERMO-MECHANICAL BEHAVIOR OF IN 738 LC AND SC 16

J. Meersmann
H. Frenz
J. Ziebs
H.-J. Kühn
S. Forest
Federal Institute for Materials Research and Testing
Unter den Eichen 87
D-12205 Berlin
Germany

SUMMARY
This article describes the study of uniaxial and biaxial thermo-mechanical fatigue (TMF) response of IN 738 LC and the initial experiments of single crystal superalloy SC 16. A life prediction assessment is proposed based on the inelastic work $\Sigma \sigma_{ij} \Delta \sigma_{ij}^{m}$ at $N_f/2$. It is shown that the J_2-theory is applicable to TMF-loadings. Initial experiments on single crystal superalloy SC 16 prove that there is a non-uniform strain distribution in the plastic region along the circumference of [001] orientated specimens. These findings must be weighed when performing TMF-tests.

LIST OF SYMBOLS

|	
A	coefficient, constant
A_1, A_2, A_3	constants
IP	in phase
OP	out of phase
MF	multiaxiality factor
T	temperature
T_o	room temperature
t	time
N_f	cycles to failure
m	exponent
Γ	torsion angle
α (T)	thermal coefficient of expansion
c	strain
$\bar{c}$	equivalent strain
ε_{th}	thermal strain
ε_m	mechanical strain
$\bar{c}_m$, $\Delta \bar{c}_m$	equivalent mechanical strain, strain range
$\dot{c}$	strain rate
$\dot{\bar{c}}_m$	equivalent mechanical strain rate
ε_{45}	readings of 45° strain gauge
γ	torsional strain
σ	axial stress
$\bar{\sigma}$	equivalent stress
τ	shear stress
$\Sigma \sigma_{ij} \Delta \varepsilon_{ij}^{in}$	inelastic work
φ_T	phase angle, c - T
φ_m	phase angle, γ - T

1. INTRODUCTION
Starting and stopping subjects turbine blades to severe cyclic thermal-mechanical loading which can cause thermal-mechanical fatigue damage. In these compo-nents inelasticity does not occur as a result of mechanical loading but is induced mainly through thermal transient cycles and thermal gradients, Figure 1. An added complexity is introduced when the thermal loads and the mechanical loads are not imposed simultaneously. To understand the TMF behavior and the damage mechanisms, it is imperative that extremes in the phasing of temperature and biaxial mechanical loading have to be explored.

This paper represents mainly life prediction assessments carried out as part of a research program aimed at the uniaxial and multiaxial deformation behavior and the development of constitutive equations to describe the elevated temperature stress-strain behavior of single- and polycrystalline superalloys. Parameters used for TMF life prediction include stress, strain, energy or some combination of these [1-5]. It is assumed that the inelastic work $\Sigma \sigma_{ij} \varepsilon_{ij}^{in}$ is the driving force for TMF damage. An additional aspect of this paper is also the applicability of the J_2-theory for TMF tests.

2. MATERIAL DETAILS
The materials studied were the cast nickel base alloys IN 738 LC and SC 16. IN 738 LC is strengthened primarily by a high fraction of gamma-prime particles (43%), and secondarily by grain boundary carbides and solid solution strengthening. The material was solution treated at 1120 °C for two hours, air cooled and then aged at 850 °C for 24 hours. The nominal composition (in wt %) of the material is 0.105 C, 15.999 Cr, 8.7 Co, 1.77 Mo, 1.9 Ta, 3.45 Ti, 3.4 Al, 2.71 W, 0.09 Si, 0.03 Mn, 0.82 Nb, 0.3 Fe, 0.037 Zn and balance Ni.

The single crystals of the alloy SC 16 were provided in the form of rods and tubes with axis parallel to [001] direction. The chemical composition and the heat treatment procedure is given in Table 1.

3. SPECIMEN PREPARATION
Specimen blanks for this testing program were cast under carefully controlled conditions to obtain a grain structure representative of gas turbine buckets (IN 738 LC). The specimen geometry was a hollow cylinder with a gauge section outer diameter of 26.5 mm, a wall thickness 1.25 mm and a gauge length of 50 mm. The
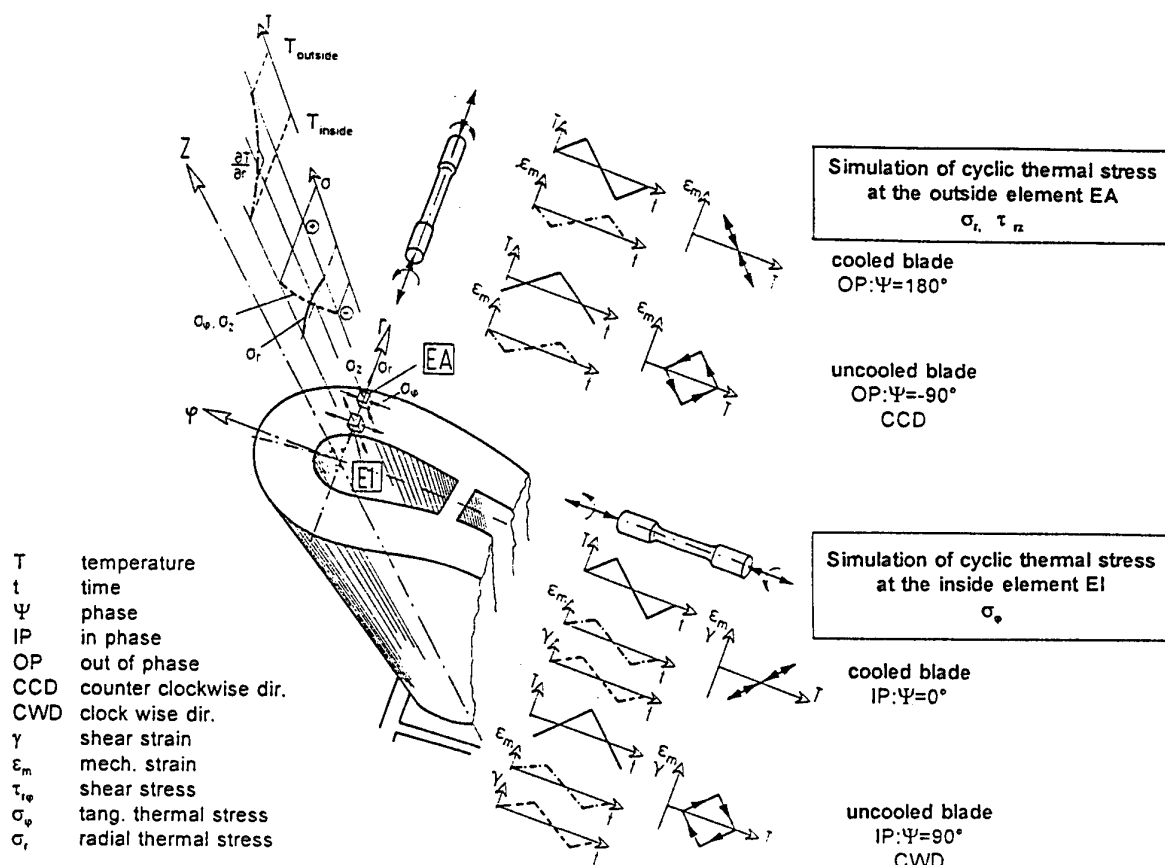
Figure 1 Simulation of cyclic thermal stresses in a blade with simple thermo-mechanical cycles (linear and diamond)

Table 1 Chemical Composition and Heat Treatment Procedure of SC 16

Element	wt. %
Cr	15.40
Mo	2.8
Ta	3.5
Ti	3.48
Al	3.45
Co	0.17
Nb	
V	< 0.003
Mn	
Balance Ni	

Solution treated at 1260 °C for 2 h, Vacuum.
High-temperature aging at 1100 °C for 4 h, Vacuum.
Final aging at 850 °C for 24 h, then finally air cooled.

specimen were finish machined using low stress grinding on the outside and longitudinal honing on the inside.

4. TEST PROGRAM

The TMF-tests were conducted on a tension-torsion-internal pressure closed loop test system under computer control. This system is equipped with an induction heating unit and a temperature monitoring device. Strains were measured with an axial-torsional extensometer over a 25 mm gauge section. The test program comprised two groups of experiments: (1) uniaxial and tension-torsion thermal-mechanical fatigue with linear, diamond and sinusoidal cycles and (2) complex "bucket" uniaxial and tension-torsion thermal-mechanical tests [6], Table 2. As can be seen in Table 2 the TMF-test differ in the ε/T-paths: 1. proportional with phase angles $\varphi_T = 0°$ (In Phase (IP) and $\varphi_T = 180°$ (180° out of phase (180 OP)), 2. non-proportional (diamond, sinusoidal) with $\varphi_T = 90°$ (90 OP). The complex "bucket" thermal-mechanical fatigue tests followed an assumed strain-temperature history representative of the leading edge of the first stage bucket in service. The tests were performed at equivalent strain ranges $\Delta\bar{\varepsilon}_m = 0.6$ %, 0.8 %, 0.9 %, 1.0 %, 1.2 %, equivalent strain rate $\dot{\bar{\varepsilon}}_m = 10^{-4}s^{-1}$ in the temperature range $450° < T < 950°C$ and temperature rate $\dot{T} = 4Ks^{-1}$.

Table 2: Details of simple and complex thermo-mechanical strain paths

Temperature °C			Temperature rate °C s⁻¹		Phase angle °		Strain versus temperature	Symbol used in Fig. 2
T_1	T_2	T_s	$\dot{\varepsilon}=10^{-4}s^{-1}$	$\dot{\varepsilon}=10^{-6}s^{-1}$	ε - T	γ - T		
TMF Tensile-compressive strain				ε_m = 0,6 %, 0,5 %, 0,4 % (CCD, CWD ε_m=0,6 %)				
950	450	700	4,17	0,42	0, 180			□ 0°
850	600	725	2,08	0,21	0, 180			◇ 180°
750	550	650	1,67	0,17	0, 180			
950	450	450	4,17		-90			
850	600	600	2,08		-90			
450	950	950	4,17		90			
600	850	850	2,08		90			
TMF Shear strain				$\gamma/\sqrt{3}$ = 0,6 %, $\dot{\gamma}/\sqrt{3}$ = $\dot{\varepsilon}$				
950	450	700	4,17	0,42		0, 90		
760	450	605	2,58	0,26		0, 90		
450	950	950	4,17	0,42		90		
450	760	760	2,58	0,26		90		
TMF Proportional axial and shear strain				$\bar{\varepsilon}_m$ = 0,6 %				
950	450	700	4,17	0,42	0	0		
760	450	605	2,58	0,26	0	0		
450	950	700	4,17		-90	-90		
450	950	950	4,17	0,42	90	90		
450	760	760	2,58	0,26	90	90		
TMF Nonproportional axial and shear strain				$\bar{\varepsilon}_m$ = 0,4 %, 0,5 %, 0,6 %				
450	950	700	4,17		180	-90		◯
600	850	725	2,08		180	-90		
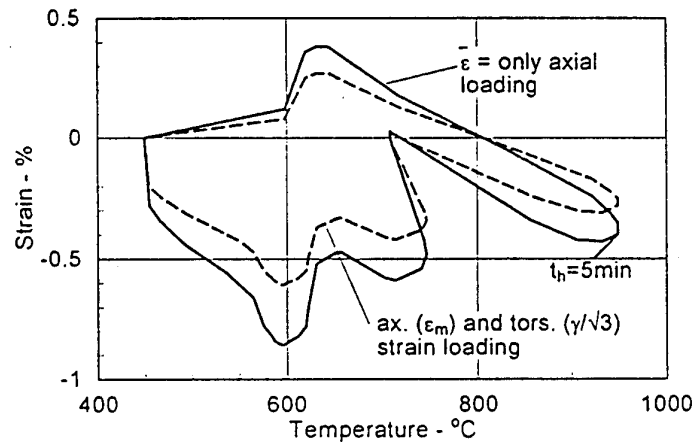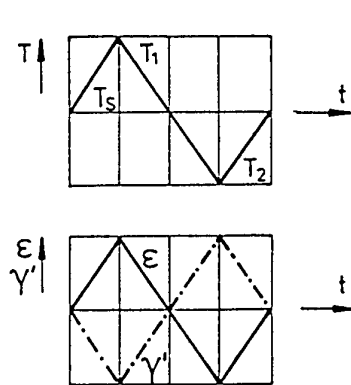
To compare multiaxial with uniaxial tests an equivalent strain range has to be defined.

$$\Delta\bar{\varepsilon}_m = \sqrt{(\Delta\,\varepsilon_m)^2 + \frac{1}{3}(\Delta\,\gamma)^2} \qquad (1)$$

Total specimen strain ε_{tot} was calculated by adding thermal ε_{th} and mechanical strain ε_m. The thermal strain was determined by

$$\varepsilon_{th} = \alpha\,(T)\,(T-T_o) \qquad (2)$$

Based on experimental data α (T) could be approximated by

$$\alpha\,(T) = A_1 + A_2\,(T-T_o) + A_3\,(T-T_o)^2 \qquad (3)$$

5. RESULTS

5.1 Simple TMF Tests

The experiments were designed to investigate two points. Firstly, strain temperature phase effects were studied by using in-phase, out-of-phase and diamond TMF cycles, where the axial strain, shear strain or the axial and shear strain amplitude were held constant, $\varepsilon_m = \bar{c} = 0.4, 0.5$ and 0.6 %. Does this result in dif-

Simple TMF Cycles
450°C - 950°C
☐ ε⊕T ; linear, axial strain
◇ ε⊕T ; linear, axial strain
○ ε⊕T ; sinusoidal ε,T
        non-proportional

Complex TMF Cycles
450°C - 950°C
● axial strain
■ axial and torsional strain
◆ axial and torsional strain
   5 minutes hold time
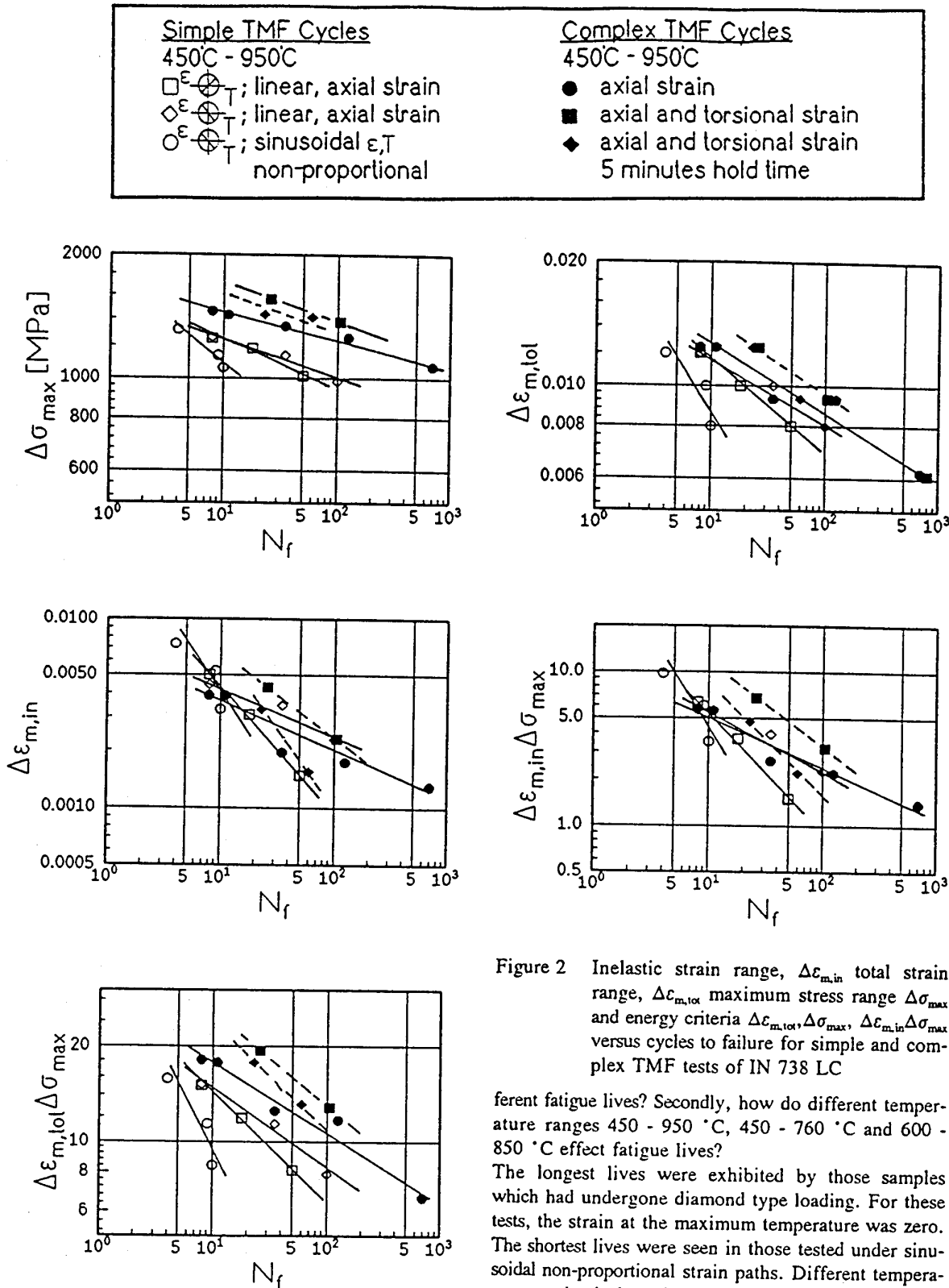
Figure 2 Inelastic strain range, $\Delta\varepsilon_{m,in}$ total strain range, $\Delta\varepsilon_{m,tot}$ maximum stress range $\Delta\sigma_{max}$ and energy criteria $\Delta\varepsilon_{m,tot}\Delta\sigma_{max}$, $\Delta\varepsilon_{m,in}\Delta\sigma_{max}$ versus cycles to failure for simple and complex TMF tests of IN 738 LC

ferent fatigue lives? Secondly, how do different temperature ranges 450 - 950 °C, 450 - 760 °C and 600 - 850 °C effect fatigue lives?

The longest lives were exhibited by those samples which had undergone diamond type loading. For these tests, the strain at the maximum temperature was zero. The shortest lives were seen in those tested under sinusoidal non-proportional strain paths. Different temperature mechanical strain phasing, that is linear out-of-phase or in-phase cycling, had a significant effect on
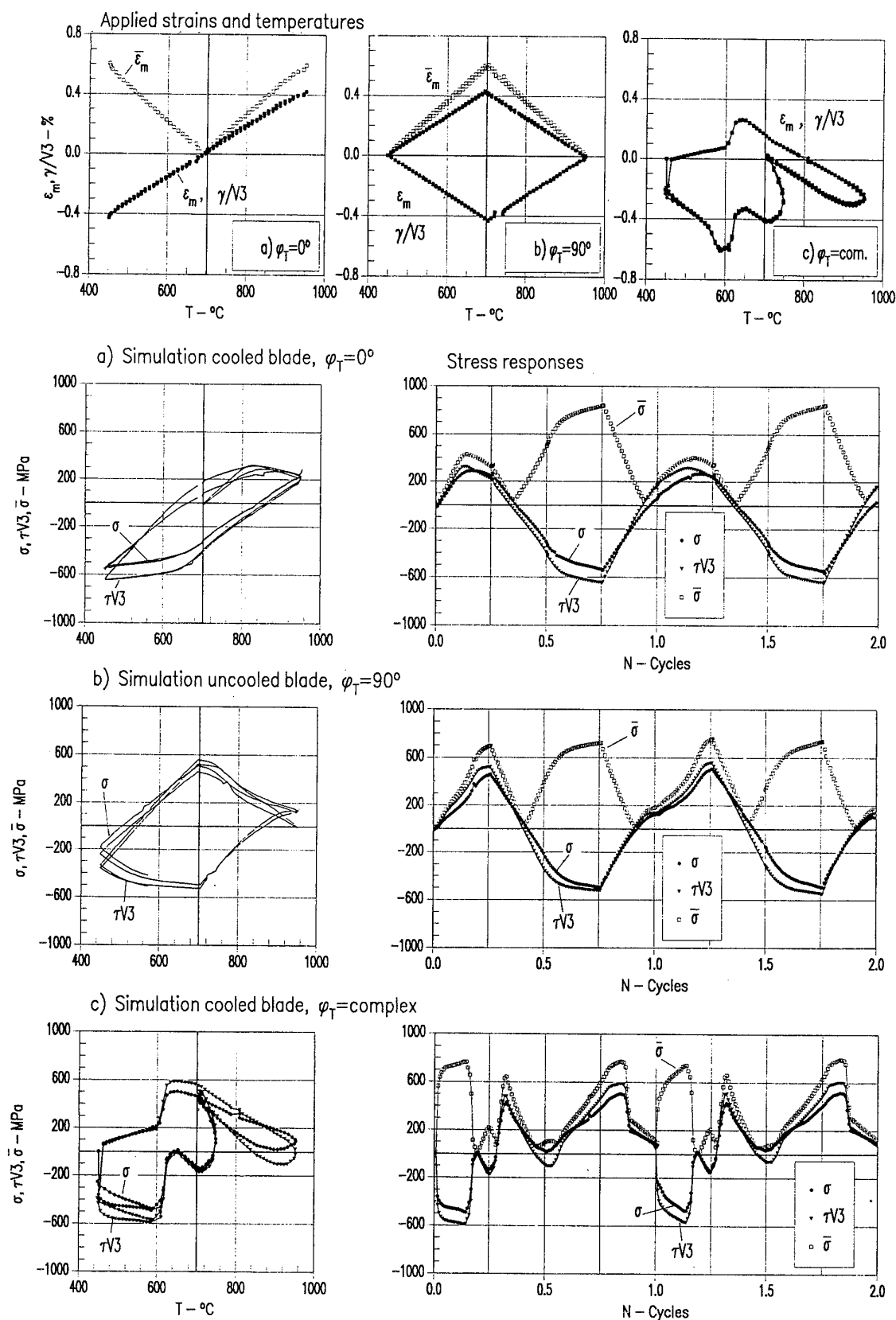
Figure 3   Applied strain and temperature phasings and stress responses for simple and complex TMF tests

fatigue lives in the temperature range 450 °C to 950 °C. A crossover of the linear TMF lines with temperature phasing of 0° or 180° is seen at about 10 cycles to failure, Figure 2.

Fatigue lives for the different TMF cycles are significantly less than for an isothermal cycle at the same maximum temperature [7]. This suggests that the thermal cycling introduces additional damage associated with thermal inhomogeneities, either microscopically or macroscopically.

5.2 Biaxial Stress-Strain Behavior

Only a brief-summary of tension-torsion stress-strain behavior will be given in Figure 3 due to the large variety of TMF cycle shapes which were investigated, Table 2.

The in-phase ($\varphi_T = 0°$) proportional strain-temperature path results in an asymmetric stress response (Figure 3a). In the range of high temperature, 750 $\rightarrow$ 950 °C,
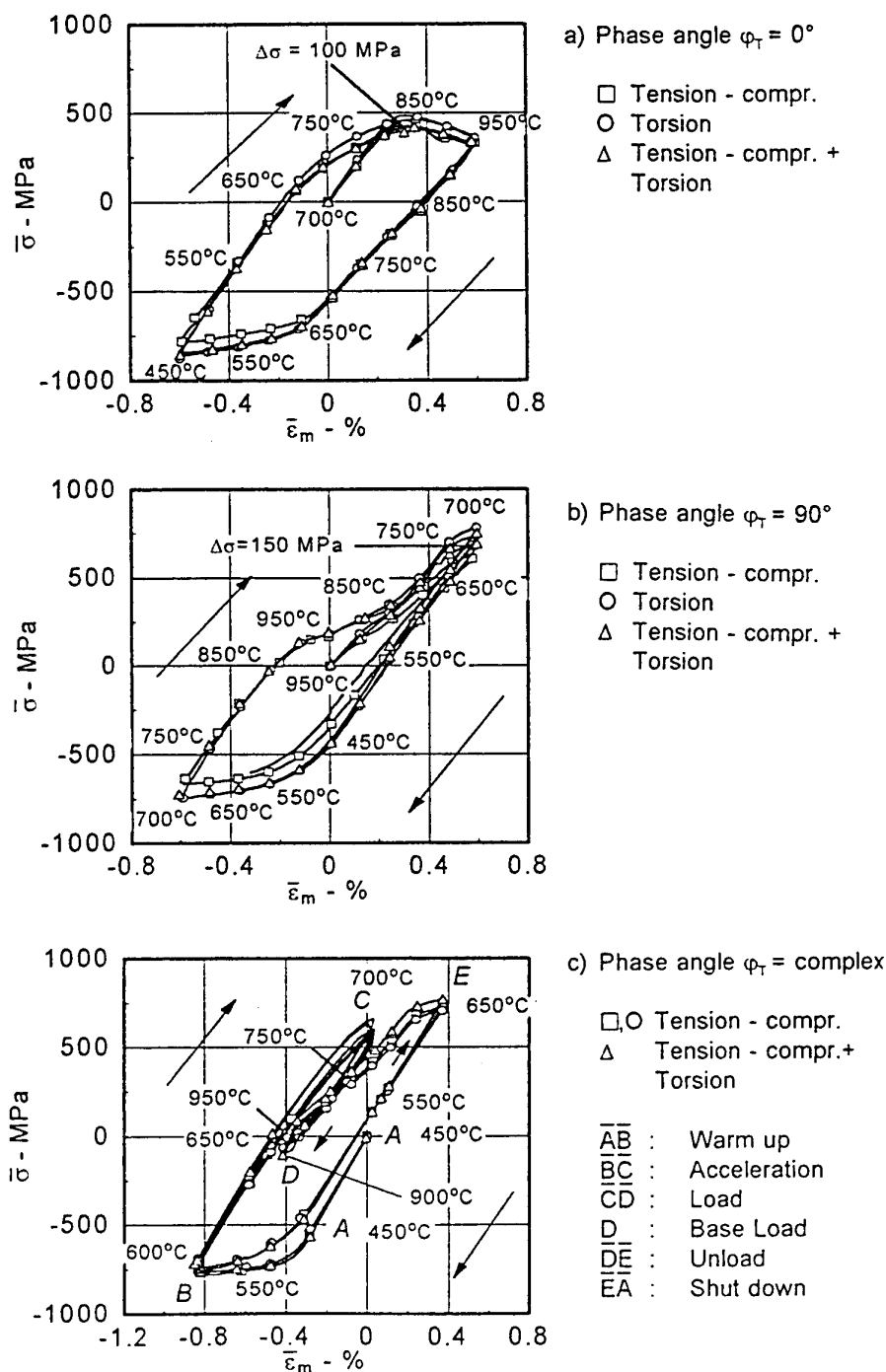
Figure 4   Comparison of uni- and multiaxial TMF-tests 450 °C > T > 950 °C, $\dot{\bar{\varepsilon}}_m = 10^{-4}\,1/s$, $\Delta\bar{\varepsilon}_m = 1.24$ %

a significant stress relaxation is observed due to the time-dependent inelastic strains. The stress response for tension and torsion is similar.

The non-proportional diamond ($\varphi_T = 90°$) strain-temperature path achieves extremes of strains at T = 700 °C, Figure 3b. For temperatures T < 700 °C

mechanical properties are nearly independent of temperatures and strain rates [8]. The TMF stress response meets at comparable mechanical strains the responses of isothermal tests in the temperature range 700 °C → 450 °C → 700 °C. In range 850 °C - 950 °C → 850 °C softening is observed.
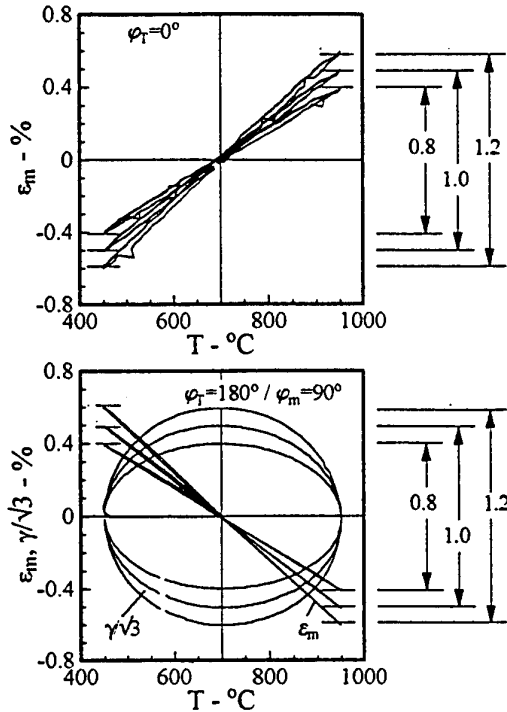
Tension - compression

▽	$\varphi_T =$	0°,	A = 32.87,	m = -0.81
☐	$\varphi_T =$ 180°,		A = 15.88,	m = -0.50
△	$\varphi_T =$ compl,		A = 22.17,	m = -0.66

Tension-compression + Torsion

✳	$\varphi_T =$ compl,	A = 53.16,	m = -0.81	
	$\varphi_m =$	0°, (proportional)		
○	$\varphi_T =$ 180°,	A = 26.31,	m = -0,61	
	$\varphi_m =$	90°, (sinusoidal)		

As shown in Figure 3c compressive stress peaks occur after warm-up, during acceleration and at base load for the blade strain temperature cycles. Tensile peaks occur before "load" and during "unload". The largest inelastic strain is achieved after warm up. It is mainly reduced during the unload phase by tensile stress.

Figure 5 $\Sigma\sigma_{ij}\Delta\varepsilon_{ij}^{in}$ versus number of cycles for different TMF tests including applied strain paths (at the top)

Figure 6   Simulated versus experimental life for different TMF tests

For all examples given above the shear stresses are generally higher than the axial stresses.

6. EXPERIMENTAL VERIFICATION OF THE J_2-THEORY FOR TMF LOADINGS

An investigation into whether or not the J_2-theory may be used to describe the thermomechanical response of IN 738 LC is outlined in this paper.

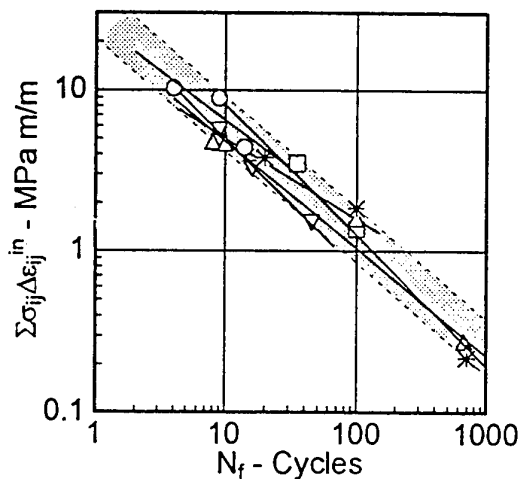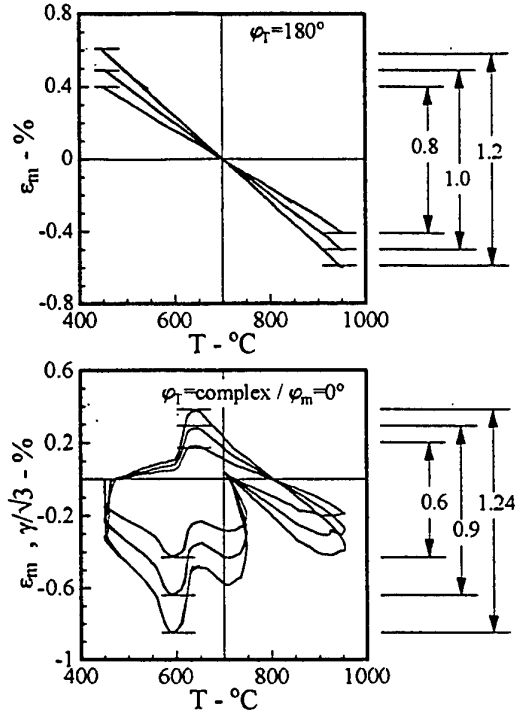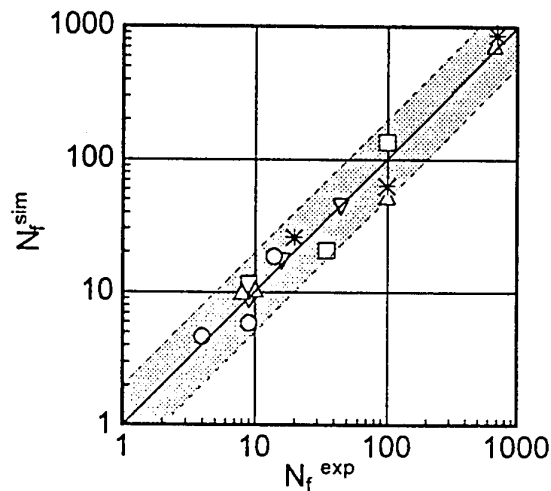Pure Tension-compression- and torsion-tests as well as tension-compression-torsion-tests are compared. Figure 4a represents the IP-path with $\varphi_T = 0$ and Figure 4b the 90 OP-path with $\varphi_T = 90°$ and Figure 4c the complex path. In Figure 4c the pure torsional load is left. The equivalent stress values of pure tension-compression-tests are about 100 MPa lower than the others. These deviations are inside of the scatterband of this material. The equivalent stresses and strains, calculated by the v. Mises relation, of several mechanical loadings are in agreement, thus the J_2-theory is altogether applicable to TMF-loadings.

The curves of equivalent stresses versus equivalent strains lead to very complex shapes because all values are positive. Therefore the curves were changed by signs to get the usual hysteresis loops.

7. LIFE RELATIONS FOR THERMO-MECHANICAL FATIGUE

Life prediction assessments for TMF generally take the form of: strain-life or stress-life approaches or a combination of both [1-5], continuum damage approaches [9/10] and microcrack rate approaches [11]. Of these, the first three approaches may facilitate life prediction for a particular dataset.

Predictions for simple and blade strain temperature TMF cycles are plotted as total mechanical strain range $\Delta\varepsilon_{m,tot}$, maximum stress range $\Delta\sigma_{max}$, mechanical inelastic strain range $\Delta\varepsilon_{m,in}$ and energy criteria $\Delta\sigma_{max} \cdot \Delta\varepsilon_{m,tot}$ and $\Delta\sigma_{max} \cdot \Delta\varepsilon_{m,in}$ versus cycles to failure in Figure 2.

In using stress, strain, energy or some combinations as dominant parameters, the figures do not show a unique curve for the different TMF tests, the parameters classify only the tests.

Fatigue damage is caused by the initiation and propagation of cracks. Within this rough characterization there are many different damage mechanisms which can operate in fatigue conditions, even in the same material. The driving force for the propagation of the nucleated cracks in metals is a function of the shear and normal stresses acting on the crack plane [12]. In multiaxial loading conditions the magnitude of the stresses depends on the strain paths. A global measure which includes all of the above mentioned parameters is the inelastic work $\Sigma\sigma_{ij}\Delta\varepsilon_{ij}^{in}$ at $N_f/2$. Therefore the general form of the criterion is:

$$\Sigma\sigma_{ij}\Delta\varepsilon_{ij}^{in} - A\,N_f^m \qquad (4)$$

where the coefficient A and the exponent m is calculated by linear regression for each TMF history. Figure 5 shows the data of five TMF histories with their straight-lines of regression. The most outside data points limit a scatterband with a N_f - width factor 2.25 with respect to the scatterband midlife. N_f was defined as the cycle at which the maximum stress dropped off to 1 % of a steady-state value including also points behind saturation. As is shown in Figure 5 the results of the uniaxial and biaxial TMF tests fall in a narrow band. The quality of the lifetime prediction is presented in Figure 6. As can be seen the correlation between predicted and actual life is generally within a scatter of ± 2 of the medium.

Manson and Halford [13] proposed a stress based multiaxiality factor MF that modifies the inelastic work. The factor accounts for the change in ductility of a material as the state of stress changes

$$MF\,\Sigma\,\sigma_{ij}\,\Delta\,\varepsilon_{ij}^{in} - A\,N_f^m \qquad (5)$$

where

$$MF - \frac{1}{2-TF},\quad TF \leq 1 \qquad (6)$$

$$MF - TF,\quad TF \geq 1$$

and

$$TF - \frac{\sigma_1 + \sigma_2 + \sigma_3}{\frac{1}{\sqrt{2}}\,\sqrt{(\sigma_1 - \sigma_2)^2 + (\sigma_2 - \sigma_3)^2 + (\sigma_3 - \sigma_1)^2}} \qquad (7)$$

However, this equation estimates the fatigue lives with nearly the same degrees of accuracy as without the multiaxiality factor.

8. BIAXIAL TMF TESTING OF A SINGLE CRYSTAL SUPERALLOY, INFLUENCE OF TEST PARAMETERS, BACKGROUND

In discussing TMF testing on single crystal superalloys it will be necessary to deal with non-uniform strain distribution in the plastic region along the circumference of [001] orientated tubular specimens under torsion or tension-torsion loading.

Local strain measurements by means of eight strain gauge rosettes on tubular specimens, [001], at room temperature prove that four 'soft' zones are present in the specimens near <110> regions and four 'hard' zones in <100> orientations in a torsion test, Figure 7. This fact has already been mentioned by Nonailhas et al. [14]. The strain or stress response in an TMF-torsion test can therefore be very different in dependence of the local behavior.

A completely non-symmetrical, non-homogenous deformation behavior is observed under tension-torsion testing on [001] orientated specimens at room temperature. Eight strain gauge rosettes were attached along the circumference as above. One of them is located near a <100> direction, the others were regularly disposed.
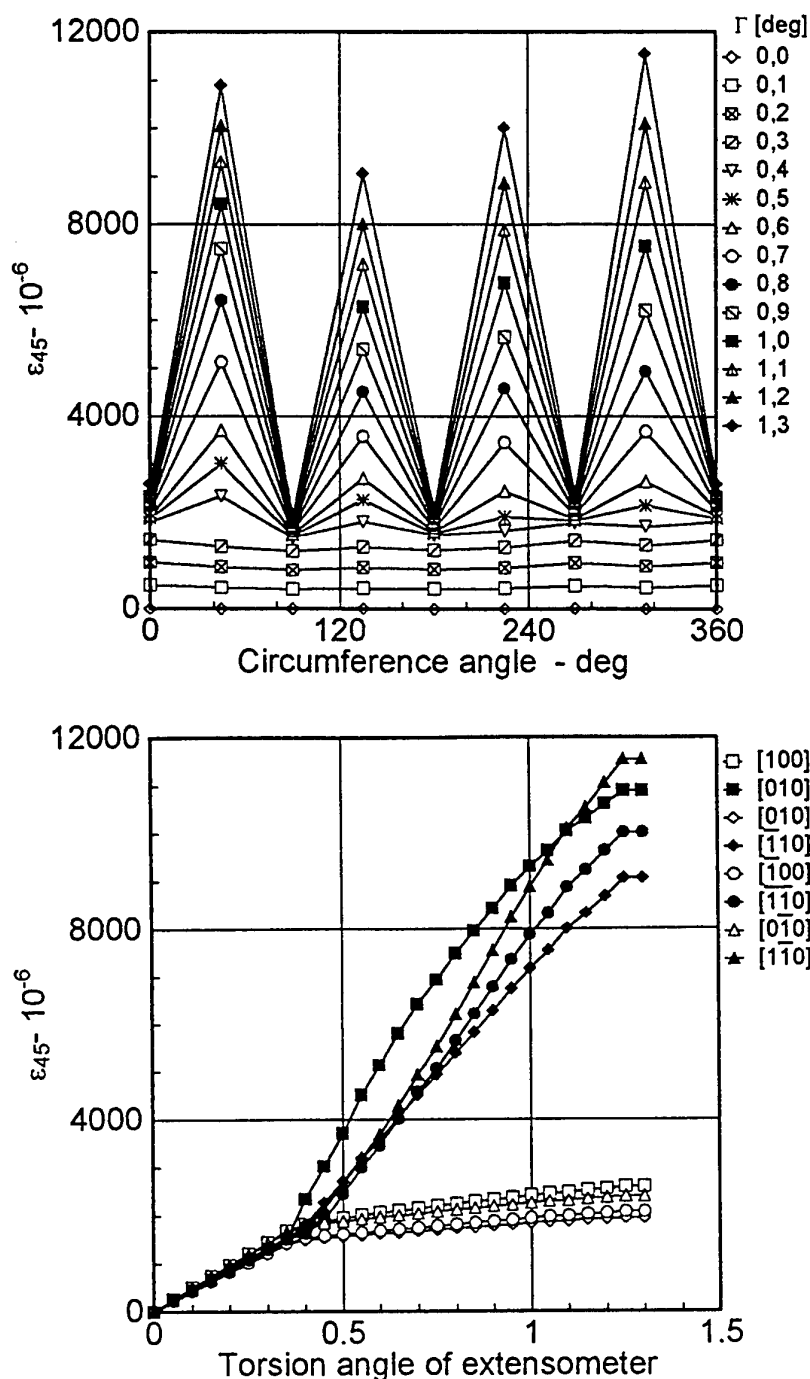
Figure 7 ε_{45}-curves versus the circumference angle (at the top) or torsion angle of extensometer recorded in a torsion test

Axial and torsional strains were also measured by means of an axial-torsional extensometer attached to the specimen near [010]. Figures 8 show the results of the strain gauges in the axial direction and at 45°. Different tension-torsion loading paths were measured.

As can be seen in Figure 8 the deformation is found to be non-uniform and non symmetrical. There are two 'soft' regions. When tension becomes predominant, quasi - uniform straining is obtained only in the axial direction.

The mechanical properties of Ni-base single crystal alloys are highly anisotropic. Dislocation motion (and hence slip) is easiest on closed packed planes and directions. In tension-compression testing of [001] orientated tubular specimens, the resolved shear stresses on the cube slip planes are zero, and only octahedral slip is activated. However, during torsional testing, both the octahedral and cube slip systems are activated. Therefore, tension-torsion tests provide a powerful and easy way to determine the relative proportions of octahedral
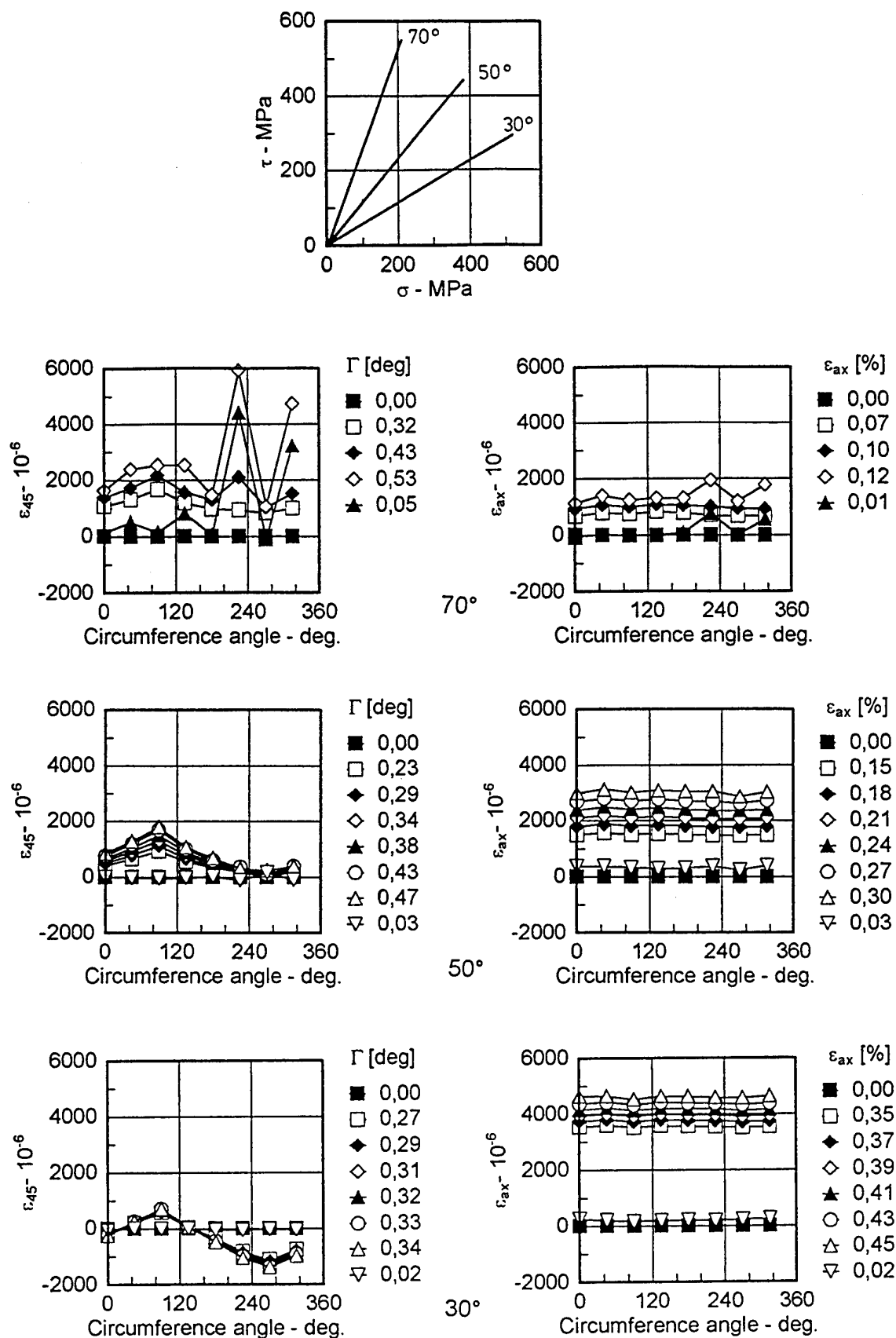
Figure 8   Readings of eight strain gauge rosettes in the axial direction, ε_{ax}, and at 45 ° versus the circumference angle in dependence of the loading paths, 30 °, 50 °, 70 ° (at the top)

and cube slip and the influence of both on the deformations. A prerequisite is that the behavior must be known for both the octahedral and cube slip systems. This behavior varies with temperature.

9. CONCLUSIONS

This study has demonstrated the versatility of the life prediction assessment. It can be applied to any arbitrary temperature-strain phasing. The sinusoidal TMF-time histories show the greatest inelastic works and result in the fewest cycles of failure. The scatterband with a N_f - width-factor is nearly the usual of 2.0.

It was verified by experiments that the v. Mises-hypothesis is altogether applicable to the deformation behavior of IN 738 LC at TMF loading.

Initial experiments on single crystal superalloy SC 16 prove that there is a non-uniform strain distribution in the plastic region along the circumference of [001] orientated specimens under torsion or tension-torsion loading. This fact must be weighed when exact TMF tests are performed. The behavior reported can be explained in terms of slip on a finite number of slip systems.

ACKNOWLEDGEMENTS

REFERENCES

[1] Ellyin, F., "Recent Developments in Predicting Multiaxial Fatigue Failure", Res. Mechanica 25 (1988), pp 1-23

[2] Garud, Y.S., "A New Approach to the Evaluation of Fatigue Under Multiaxial Loading", J. Engng. Mat. Techn., ASME, 103 (1981), pp 118-125

[3] Coffin, L.F., "Overview of Temperature and Environmental Effects on Fatigue of Structural Metals", Fatigue: Environment and Temperature Effects, J.J. Burke and V. Weiss, Eds., Plenum Press, N.Y., 1983, pp 1-40

[4] Ostergren, W.J., "A Damage Function and Associated Failure Equations for Predicting Hold Time and Frequency Effects in Elevated Temperature Low Cycle Fatigue" J. Testing and Evaluation, 4 (1976), pp 327-339

[5] Ellyin, F. and Kujawski, D., "Plastic Strain Energy in Fatigue Failure", J. Press. Vessel Techn., ASME, 106 (1984), pp 342-347

[6] Embley, G.T., Russel, E.S., "Thermal-Mechanical Fatigue of Gas Turbine Bucket Alloys", Proceedings, First Parsons International Turbine Conference, Inst. Mechanical Engineers, London 1984, pp 157-164

[7] Ziebs, J., Meersmann, J., Kühn, H.-J., Hülsmann, N., Olschewski, J., "Multiaxial Thermomechanical Behaviour of IN 738 LC", Fouth International Conference on Biaxial, Multiaxial Fatigue, Vol. II, Societe Française de Metallurgie et de Máteriaux, Europe Structural Integrity Society (ESIS), 1994, pp 247-259

[8] Ziebs, J., Meersmann, J. Kühn, H.-J., Ledworuski, S., "High Temperature Inelastic Deformation of IN 738 LC Under Uniaxial and Multiaxial Loading,", Low Cycle Fatigue and Elasto-Plastic Behaviour of Materials - 3, Ed. K.T. Rie, Elsevier Applied Science 1992, pp. 248-255

[9] Kachanow, L., "Fundamentals of Fracture Mechanics", Nauka, Moscow 1974

[10] Chaboche, J.L., "Continuous Damage Mechanics - A Tool to Describe Phenomena Before Crack Initiation", Nuclear Engr. and Design 64, 1981, pp. 233-247

[11] Bérad, J.Y., McDowell, D.L., Antolovich, S.D., "Damage Observation of a Low Carbon Steel Under Tension-Torsion Low-Cycle Fatigue Advances in Multiaxial Fatigue", ASTM STP 1191, D.L. McDowell and R. Ellis, Eds., ASTM, Philadelphia, 1993, pp. 326-344

[12] Socie, D. "Critical Plane Approaches for Multiaxial Fatigue Damage Assessment", Advances in Multiaxial Fatigue, ASTM STP 1191, D.L. McDowell and R. Ellis, Eds., ASTM, Philadelphia, 1993, pp. 7-35

[13] Manson. S.S. and Halford, G.R., "Discussion, Multiaxial Low Cycle Fatigue of Type 304 Stainless Steel", J. Eng. Mat. Techn., ASME, 99, 1977, pp. 283-286

[14] Nouailhas, D., Pascou, D., Cailletaud, G. Hanriot, F., Rémy, L., "Experimental Study of the Anisotropic Behavior of the CMSX 2 Single-Crystal Superalloy Under Tension-Torsion Loading", Advances in Multiaxial Fatigue, ASTM STP 1191, D.L. McDowell and R. Ellis, Eds., ASTM Philadelphia, 1993, pp. 244-258

TMF LIFE PREDICTION APPROACH FOR TURBINE BLADES

J. E. Heine
E. Ruano
R. E. DeLaneuville
United Technologies Pratt & Whitney
P.O. Box 109600, West Palm Beach, Florida, USA 33410-9600

SUMMARY

Extreme temperature gradients and transients thermally induce the most severe cyclic stresses encountered by turbine airfoils. These thermal stresses combine with mechanically induced centrifugal and bending loads to produce thermomechanical fatigue (TMF) of the airfoil. Anisotropic material properties of advanced turbine blade alloys further complicate analysis and life prediction for these complex loading conditions. Designers and engineers require quick, efficient computational analysis to evaluate airfoil design iterations. A life prediction approach which can be utilized efficiently by designers needs to be relatively simple, but it must capture the first order TMF effects. This paper introduces a life prediction approach that utilizes 3D finite element output and applies a simplified constitutive model to predict the stress extremes of a TMF cycle in an advanced single crystal alloy. An appropriate TMF life relation, such as hysteretic energy, can be use to predict cyclic life.

LIST OF SYMBOLS

σ_i	Stress at time increment
$\sigma_{i,el}$	Elastic stress increment
σ_{ys,T_i}	Yield stress at temperature for the increment
T, T_i	Temperature; Temperature for the increment
σ_{ER}	Exponential stress relaxation stress
m_{LR}	Slope for linear stress relaxation
A, B, C	Stress relaxation constants
$t; t_i$	Time; time increment
$t_{i,1}$	Starting time for stress relaxation
t_a	Time limit for stress relaxation
$t_{i,1}$	Starting time for stress relaxation

1 INTRODUCTION

In advanced military fighter aircraft engines, turbine airfoils experience increasing severe stress and temperature cycles. Higher thrust-to-weight ratios are generally achieved by increasing combustor exit temperatures. Additionally, military air combat missions cycle turbomachinery components more rapidly and frequently, producing more extreme thermal gradients and complex load cycles. Consequently, these combined cyclic thermal, centrifugal, and gas bending loads produce complex stress, strain and temperature cycles that result in turbine airfoil lives limited by thermomechanical fatigue (TMF) [1]. The complex loading conditions are further complicated by the anisotropic nature of

the directionally solidified and single crystal alloys utilized for turbine airfoils. The NASA HOST program explored the mechanics and failure mechanisms of these materials under TMF conditions [2].
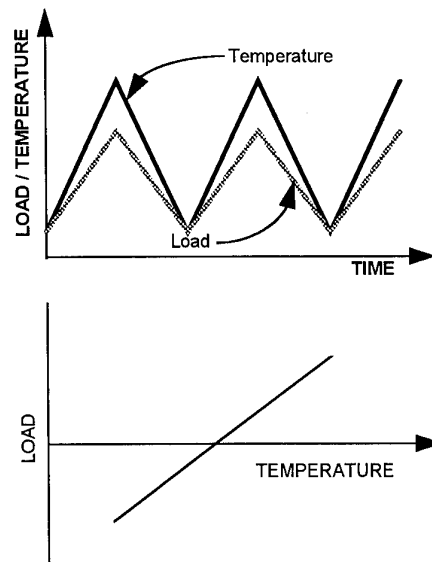
Figure 1. In-phase load and temperature waveform.

A wide variety of thermal and mechanical loading cycles are experienced by turbine airfoils. These are dependent on the location along the airfoil and the speed of the particular power transient. The phasing between thermal and mechanical loads strongly affect the TMF response of the airfoil [3]. The extremes of load-temperature phasing are in-phase (Figure 1) and out-of-phase (Figure 2). In-phase cycles occur when an unconstrained local area of the blade is mechanically loaded at the same time the temperature increases. Out-of-phase cycling occurs when a locally constrained area of the blade tries to expand both mechanically and thermally as temperature increases. This usually causes the blade to go into compression. Out-of-phase cycling is generally the most harmful because stress relaxation at the maximum temperature develops high mean stresses. While actual turbine blade TMF cycles are a combination of in-phase and out-of-phase cycles, TMF characterization of turbine blade materials is generally performed using out-of-phase cycles [1].

Several life prediction approaches for TMF have been introduced [1-8]. Some of these approaches require a large database to define the parameters and constants for accurate life prediction. Additionally, specific test conditions usually limit the predictive capabilities of these models. However, a model using a stress-strain damage parameter, such as hysteretic energy, requires less data and can be used for mission cycle shapes [1, 3]. Most of these models required well defined stress-strain behavior for the TMF cycle.
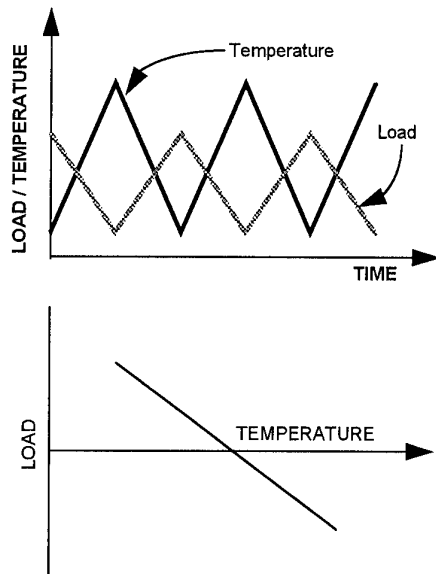
Figure 2. Out-of-phase load and temperature waveforms

TMF life prediction in turbine blades commonly begins with 3D elastic finite element stress analysis. The elastic stresses and strains are combined in a TMF parameter to predict TMF life. Often the finite element analysis identifies the high strain locations within the blade and focuses detailed stress-strain constitutive analysis on those areas. The hysteresis loop predictions are used to define the shakedown stress state which can be applied to an appropriate TMF life prediction technique.

One key to accurate life prediction of components subjected to TMF is reliable prediction of stress and strain. While advanced constitutive models can accurately predict stress and strain, they are too computationally intensive to be used routinely. There is a real need for a computationally efficient method to predict stresses that have experienced plasticity and time dependent relaxation.

An alternate approach uses a simplified constitutive model to predict the hysteresis loops. This simplified constitutive model can use the elastic stress output from the finite element analysis or it can generate stresses from the predicted strains

and temperatures. The model includes first order mechanical and thermal effects. In this paper we will examine the case of a anisotropic turbine blade with an idealized, but representative, TMF mission cycle (Figure 3).
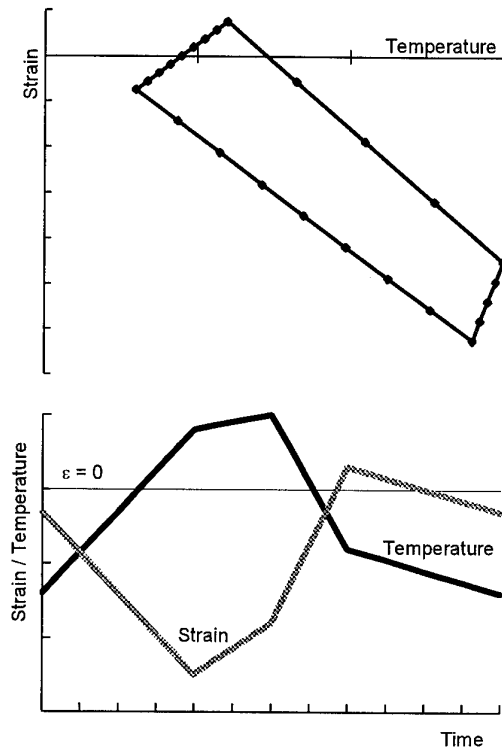
Figure 3. Idealized strain and temperature cycle similar to those seen in turbine blade analysis. Temperature and strain are nearly out-of-phase. The points are individual time steps in the mission.

2   TECHNICAL DISCUSSION

2.1   3D Stress Analysis

TMF cracking occurs at many locations on turbine vanes and blades, including pressure and suction surfaces and leading and trailing edges [2]. In anisotropic structures, cracks are observed both parallel and normal to the casting growth direction (Figure 4). Biaxial loading conditions can cause cracking in orientations counter-intuitive to historical conditions. The anisotropic nature of single crystal and directionally solidified blades make it necessary to perform 3D stress analysis on the airfoil design. Details on how to perform 3D stress analysis can be found in several references [9, 10].

TMF
Cracking
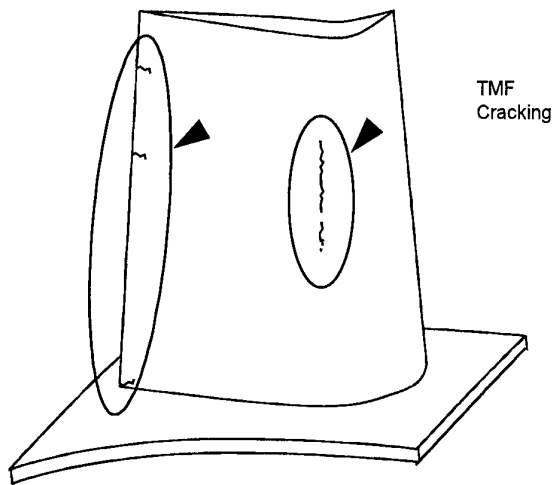
Figure 4. TMF cracking observed on anisotropic turbine blades can occur parallel and perpendicular to the casting solidification direction.

The complexity of turbine blade design makes an elastic-plastic finite element analysis very expensive and time consuming. Generally, the analysis is limited to elastic properties.

Elastic 3D finite element analysis results in a prediction of the full states of stress and strain in the part due to the thermal and mechanical loadings of the mission point being analyzed. The analysis can also provide stress and strain values along arbitrary orientations. Generally, the output is a table of time, temperature and component stresses in the direction of interest.

In our example, the stresses are defined for only one material orientation (Figure 5). The cycle was artificially defined based on testing experience. The stresses are primarily in compression and they exceed the compressive yield strength at the high temperature end of the cycle (Figure 6).

2.2 Hysteresis Loop Prediction

It is assumed that the local region under consideration is constrained by surrounding elastic material and therefore the strains remain unchanged and there is no redistribution of loads. The hysteresis loop analysis is based on breaking up the tabulated finite element output into elastic stress increments. A logical starting point is selected. This is preferably a zero-stress point, but it can be any point in the cycle.

$$\text{Starting point:} \qquad \sigma_{i-1} \qquad\qquad (1)$$

The elastic stress increment is added to the starting stress. This incremented stress value is compared to the yield stress of that orientation and temperature. It is set equal to the yield stress if the incremented stress exceeds the yield stress.

$$\sigma_i = \sigma_{i-1} + \sigma_{i,el} \qquad\qquad (2)$$

$$\text{If:} \qquad \sigma_i \geq \sigma_{ys,T_i} \qquad\qquad (3)$$

$$\text{Then} \qquad \sigma_i = \sigma_{ys,T_i} \qquad\qquad (4)$$

This is an elastic-perfectly plastic assumption. For many single crystal superalloys, this assumption is reasonable because it is representative of the monotonic stress-strain behavior (Figure 7) [3]. Neuber and Glinka offer alternate techniques which represent yielding behavior for materials which do not exhibit elastic-perfectly plastic behavior [11, 12, 13].

In this model, compressive and tensile yielding are assumed to be equal. Isothermal fatigue data for some single crystal materials show isotropic hardening. Kinematic hardening algorithms can be substituted or some combination of isotropic and kinematic hardening can be applied [14].

Time	Temp	Strain	Elastic Stress
0	800	-0.15	-23.00100124
1	937.5	-0.2875	-40.80243385
2	1075	-0.425	-58.08267747
3	1212.5	-0.5625	-74.74497968
4	1350	-0.7	-90.66672815
5	1487.5	-0.8375	-105.6984494
6	1625	-0.975	-119.6638089
7	1762.5	-1.1125	-132.3596108

Figure 5. Example of tabular output from finite element analysis for one material orientation. The conditions were artificially defined based on experience.
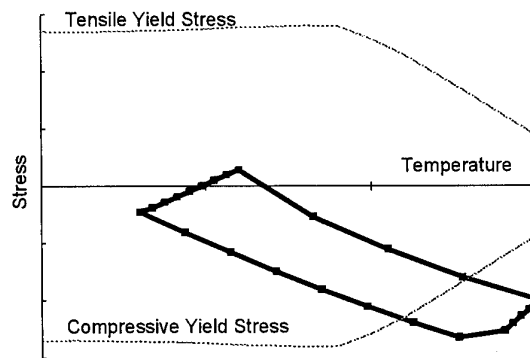

Figure 6. Prediction of elastic stress versus temperature based on modulus at individual temperature along the curve. The elastic stress exceeds the compressive yield stress at high temperatures.
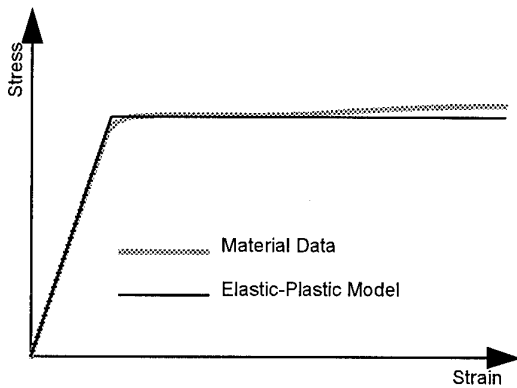
Figure 7. Elastic-perfectly plastic behavior is representative of monotonic stress-strain behavior.

After adjusting the stress for yielding, it is necessary to determine if time dependent stress relaxation occurs at that temperature of the cycle. If the temperature at that point in the cycle is in the stress relaxation regime or creep regime then a stress relaxation model is applied. Stress relaxation for this simplified model is defined in two parts: exponential relaxation and linear relaxation.

Overall stress relaxation is well represented by an exponential regression and can be regressed with a temperature term [3].

$$\sigma_{ER} = \exp(A + BT)t^C \qquad (5)$$

However, for modeling purposes, a stress relaxation curve can be divided into the exponential portion and the linear portion (Figure 8).
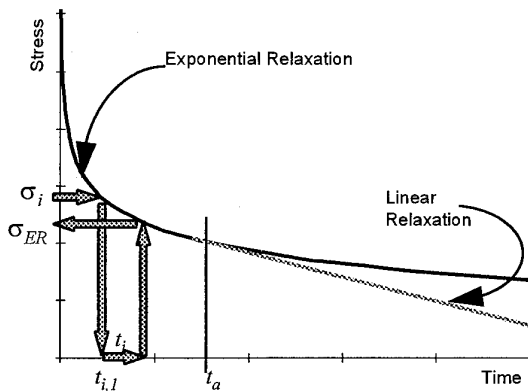

Figure 8. Stress relaxation is divided into exponential and linear regions for modeling.

The exponential portion, represented by equation (5), occurs during the highest stresses for short time periods. The linear region, whose slope is the derivative of equation (5), occurs for times beyond the exponential portion.

$$m_{LR} = C \exp(A + BT)t_a^{C-1} \qquad (6)$$

Stress relaxation occurs over time, therefore, the initial time on the relaxation curve must be determined. The stress for the increment defines the initial time.

$$t_{i,1} = \left(\frac{\sigma_i}{\exp(A+BT)}\right)^{1/C} \qquad (7)$$

If the initial time falls within the exponential region then equation (9) determines the relaxed stress level. If the initial time is greater than the final time for the exponential region, t_a can be defined by the user, then a stress increment using the linear region slope determines the relaxed stress level, equation (10).

If $\qquad\qquad t_{i,1} < t_a$, $\qquad\qquad\qquad (8)$

then $\quad \sigma_i = \sigma_{ER} = \exp(A+BT)(t_{i,1} + t_i)^C \qquad (9)$

else $\quad \sigma_i = \sigma_{LR} = \sigma_i + t_i[C\exp(A+BT)t_a^{C-1}] \qquad (10)$

This loop is repeated until the mean stress of the hysteresis loop becomes stabilized. It has been observed that individual cycles calculations relax at the same rate as specimen tests [3]. Since this can occur over thousands of cycles, the linear stress relaxation is used to accelerate the relaxation simulation, thereby reducing the number of calculations.

Figure 9 illustrates how the example mission is predicted for the first cycle. The modeled, predicted stress follows the elastic stress prediction from the finite element analysis until it exceeds the compressive yield stress. As the cycle progresses to the hottest part of the cycle, stress relaxation occurs, represented in the highlighted gray areas. This is repeated until the hysteresis loop "walks" up to its stabilized position (Figure 10).

When compared to the elastic prediction, significant mean stresses are accumulated due to yielding and stress relaxation. This type of modeling can be applied to isothermal conditions as well. The stress predictions have been verified against strain controlled TMF specimen tests on single crystal material (Figure 11) [3]. The correlation is sufficiently accurate for first order yielding and time dependent effects. It is considerably more accurate than the elastic prediction.

Complex constitutive models have significant data requirements to solve for the necessary constants. As many as twelve constants must be defined [2]. This simplified constitutive model requires standard tensile data for yield

stress and modulus, and stress relaxation data. A technique is being developed to obtain stress relaxation information from creep tests. The data required for the simplified technique is generally available from standard characterization test programs.

TMF life is strongly dependent on the mean stress of the cycle. The accurate prediction of mean stresses is a necessity [3]. The approach discussed above is a efficient method of calculating mean stresses where yielding and creep related stress relaxation are the strongest drivers. Where alternate mechanisms are stronger drivers a comprehensive constitutive model should be used.
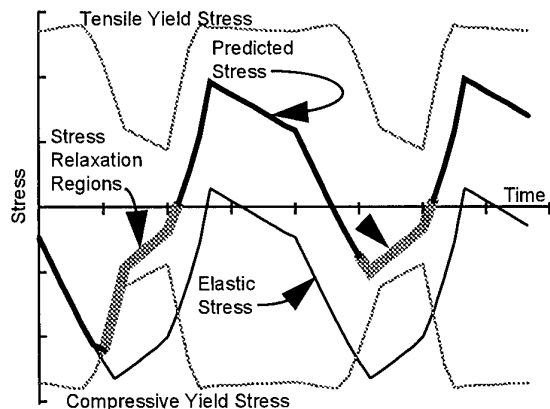
Figure 9. Predicted stresses with yielding and relaxation are significantly higher than the elastic prediction. The predicted stress first exceeds the compressive yield stress and then has stress relaxation. The thick gray areas are times within the cycle where stress relaxation occurs.
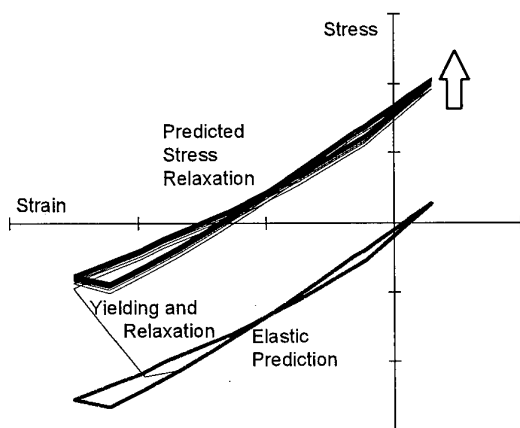
Figure 10. The hysteresis loop prediction shows where stresses yield and relax at high temperatures. This results in significant mean stresses for this cycle.
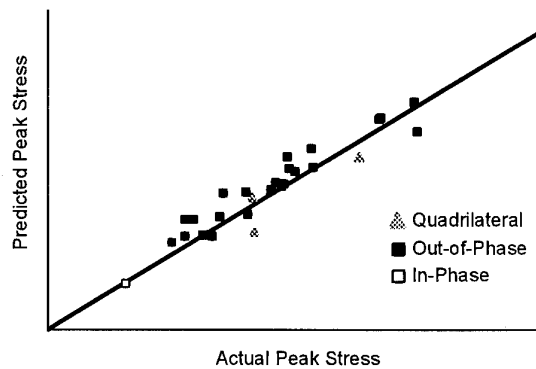
Figure 11. The simplified constitutive model predicted the peak stress of TMF cycles of strain controlled TMF specimens [3].

3 CONCLUSIONS

Turbine blade life prediction requires accurate calculation of stresses and strains. Finite element analysis, a tool routinely used in component design, is the first step in the life prediction. For inelastic conditions, stress relaxation and yielding must be included in the calculation of stress and strain. A simplified constitutive model was demonstrated to capture the first order effects of yielding and time dependent relaxation. First order stress-strain analysis is sufficient for initial design iterations as the detailed transient conditions are not typically fully defined. These types of models can be useful when time constraints limit the use of comprehensive constitutive models.

4 REFERENCES

1. Pejsa, P.N. and Cowles, B.A., "Thermal Mechanical Fatigue Life Prediction for Advanced Anisotropic Turbine Alloys", Journal of Engineering for Gas Turbines and Power, 108, July 1986, pp 504-506.
2. Nissley, D.M., Meyer, T.G., and Walker, K.P., "Life Prediction and Constitutive Models for Engine Hot Section Anisotropic Materials Program", Final Report, NASA CR 189223, September 1992.
3. Heine, J.E., Warren, J.R. and Cowles, B.A., "Thermal Mechanical Fatigue of Coated Blade Materials", Final Report, WRDC-TR-89-4027, June 1989.
4. Jaske, C.E., "Thermal-Mechanical, Low-Cycle Fatigue of AISI 1010 Steel", in Thermal Fatigue of Materials and Components, ASTM STP 612, 1976, pp. 170-198.
5. Fujino, M. and Taira, S., "Effect of Thermal Cycle on Low Cycle Fatigue Life of Steels and Grain Boundary Sliding Characteristics", in Proceedings of the Third International Conference, Cambridge, England, August 20-24, 1979.
6. Halford, G.R. and Manson, S.S., "Life Prediction of Thermal Mechanical Fatigue Using Strain Range

Partitioning", *in* Thermal Fatigue of Materials and Components, ASTM STP 612, 1976, PP. 239-254.

7. Spera, D.A., "Calculation of Thermal Fatigue Life Based on Accumulated Creep Damage", NASA TND-5489, October 1969.

8. McNight, R.L. and Laflen, J.H., "Turbine Blade Non-linear Structural and Life Analysis", *in* AIAA/SAE/ASME Joint Propulsion Conference, Cleveland, OH, June 21-23, 1982, Paper No. 82-1056.

9. Zienkiewicz, O.C., "The Finite Element Method, Third Edition", McGraw-Hill Book Company (UK) Limited, 1985, pp 135-147.

10. Eisley, J.G., "Mechanics of Elastic Structures", Prentice Hall, 1989, pp 366-370.

11. Fuchs, H.O. and Stephens, R.I., "Metal Fatigue in Engineering", John Wiley & Sons, Inc., (ISBN 0-471-05264-7), 1980, pp 135-145.

12. Glinka, G. "Energy Density Approach to Calculation of Inelastic Strain-Stress Near Notches and Cracks", Engineering Fracture Mechanics, *22*, 3, 1985, pp 485-508.

13. Glinka, G. "Relations Between the Strain Energy Density Distribution and Elastic-Plastic Stress-Strain Fields Near Cracks and Notches and Fatigue Life", Low Cycle Fatigue ASTM STP 942, 1988, pp 1022-1047.

14. Fuchs, H.O. and Stephens, R.I., "Metal Fatigue in Engineering", John Wiley & Sons, Inc., (ISBN 0-471-05264-7), 1980, pp 175.

Elevated Temperature Component Fatigue Robustness - An Holistic Approach

P. A. Domas
GE Aircraft Engines
P.O. Box 156301, One Neumann, Way, M/Z Q105
Cincinnati, OH 45215-6301, USA

1. SUMMARY
Fundamental material behavior research in thermal mechanical cycling environments is obviously essential to eventual development and use of thermal mechanical fatigue (TMF) life models in component durability assessments. However, the scope of the research should be guided and focused by experience and issues encountered in actual product usage.

Crack nucleation at surface intersecting ceramic inclusions and degraded low cycle fatigue (LCF) capability of thermally exposed shot peened surfaces are two elements of potential importance to more accurate TMF life prediction of powder metal (PM) nickel base superalloy turbine engine components. Both temperature dependent effects, identified and evaluated in a comprehensive alloy development program, provide significant challenge to conventional, applied engineering fatigue life prediction methodologies. But, never-the-less, such influences must be recognized in design, component manufacture, and field life management.

An overview of observed material fatigue behavior provides an industry example as a basis to illustrate the importance, necessity, and benefit of a fully integrated (holistic) design, material processing, and component manufacturing system approach to obtaining desired product robustness.

2. INTRODUCTION
Increasingly, higher aircraft performance demands and industry economic pressures foster the need for greater realism and accuracy in engine component fatigue life prediction analysis. In addressing this need, improved material behavior mechanistic understanding and refined life prediction models, based on considerable test evidence, are being developed and employed. These models provide a vehicle for quantification of margins and enable greater recognition of the role of uncertainty in establishing mission life limits.

Two recent practical examples, encountered as part of an extensive turbine engine PM alloy development program, that highlight the inherent complexity in more detailed approaches to fatigue behavior modeling and also demonstrate considerable progress being made as the result of Concurrent Engineering, are discussed below.

First, from a design perspective, the quantifiable PM alloy component reliability improvement resulting from cleaner input powder (smaller, less frequent ceramic inclusion content) is illustrated. Assessments using probabilistic engine component life prediction analysis, incorporating carefully measured inclusion size distributions and frequency of occurrence, and recognizing surface and subsurface location variables and changed failure mode sensitivity with temperature, are discussed.

Second, from a manufacturing perspective, the reliability impact associated with limiting the magnitude of surface cold work imparted by the shot peen process (nominally beneficial in retarding surface inclusion initiated fatigue influence) is discussed. Potential fatigue life detriment attributed to an intermittent thermal exposure is highlighted.

3. PM ALLOY CERAMIC INCLUSIONS
In high strength, aircraft turbine engine nickel-base PM alloys, inherent ceramic inclusions can compete with grain facets as potential fatigue crack initiation sites. This competition can be temperature dependent as illustrated by the fatigue test data in Figure 1. In the alloy evaluated, at a comparatively low temperature (204C/400F) cracks in LCF test samples initiate at both inclusions and grains but

resultant fatigue lives are essentially the same for either site and no distinction need necessarily be made between these initiation behaviors when generating or utilizing LCF stress-life (SN) curves in component design.

In contrast, at higher temperature (649C/1200F), crack nucleation at inclusions is predominant. Initiations from surface inclusions in particular lead to much shorter LCF failure lives than initiations at grain facets or subsurface inclusions. Test result scatter is greatly increased (Figure 1). Figure 2 schematically illustrates the results of two fatigue tests run under the same continuously cycled (Rϵ = $\epsilon_{min}/\epsilon_{max}$ = 0.0) loading conditions, one failing from a surface inclusion initiated crack, the other from a subsurface inclusion initiation. The smaller surface inclusion has much shorter LCF life than the twice larger subsurface inclusion.

This temperature dependent nucleation mechanism change presents a significant challenge in component LCF life prediction. Even restricting discussion to isothermal behavior at high temperature provides an example.

3.1 Probabilistic Behavior

The expected LCF life for a given component at the higher temperature condition is probabilistic. It depends not only on the traditional variables of stress and temperature but also on the probability that a potential component fatigue life controlling region contains a ceramic. Other influential variables if a ceramic inclusion (or other imperfection) is present include, for example, its size, whether it is surface intersecting, and its respective propensity to nucleate a crack.

Probabilistic life prediction methods, many fracture mechanics based, are being developed through out the aircraft engine industry to address these issues.[1-4] Resultant life predictions can take the form of component reliability curves such as shown schematically in Figure 3. Probability of fracture is low at comparatively short lives and increases as usage accumulates.

A fundamental input to these analyses are imperfection (e.g. inclusion) frequencies of occurrence and size distributions, measures of powder cleanliness. It is intuitive that the smaller or

less frequent the inherent ceramics, the more robust the component. It is desirable to quantify this benefit.

Techniques for measuring cleanliness have included elutriation, chemical dissolution, micrography, electron beam button melting, ultrasonic inspection[5] and more recently heavy liquid separation (HLS)[6]. The HLS method enables detail sampling of comparatively large quantities (0.23 Kg/0.5 lb.) of each master powder blend (MPB). This is a decided improvement in sampling efficiency and increases confidence in the accuracy of the input distribution. Utilizing HLS to comprehensively examine many MPBs periodically over time, from multiple powder sources reveals cleanliness variations between blends as shown in Figure 4.

Variability in input powder cleanliness translates to component specific predicted LCF life variability as illustrated by an engineering study result for a potential rotating air seal design (Figure 5). Recognition of this type of material behavior and incorporation of the cleanliness variability in the probabilistic life models is a basic part of the overall process to create robust designs and enable confident assessment of safety margins.

3.2 An Holistic Design Approach

This example illustrates how nickel base PM superalloy component LCF life prediction model development has benefited from close integration of:

- a detail *Design* assessment recognizing and addressing the role of stressed volumes and variable fatigue response at different temperatures in a probabilistic life prediction methodology,

- *materials behavior* evaluation including ceramic seeded LCF tests to evaluate inclusion/matrix behavior as a function of inclusion size, frequency of occurrence, applied stress, operating temperature, etc.,

- *powder suppliers and Manufacturing Quality systems* that recognize the need, and provide the ability to monitor and control lot-to-lot production powder inclusion size and frequency, and

- communications with *regulatory agencies and customers* regarding appropriate life limit criteria and emerging fatigue life prediction methods.

Without this Concurrent Engineering approach, the Design life methodology could fail to recognize the material behavior transition with temperature. The Materials Laboratory could be aware of the inclusion behavior at high temperature but not cognizant of the importance of the changed low temperature behavior in mission cycle life analysis. The Quality organization could be confident that large (rogue) ceramic imperfections are detected and culled out by ultrasonic inspections of the extrusions but unaware of the potential impact of less dramatic cleanliness changes resulting from gradual crucible, nozzle, or screen deterioration.

Holistic, boundariless and timely interaction and communication among technically focused Design (including Life Specialists), Manufacturing and Quality organizations and business/industry conscious Systems and Project organizations is essential to identification and resolution of such complex alloy behavior issues through efficiently guided R&D programs.

4. SHOT PEENING COLD WORK

A significantly different example of the importance of an holistic approach, is in evaluation of LCF life capability of shot peened components. Shot peening can provide improved component fatigue life. While exact mechanisms for observed life improvements are not known, compressive surface residual stress and altered surface microstructure are often cited as contributors. Figure 6 illustrates a typical nickel base superalloy residual stress profile and the surface cold work profile imparted by the shot peening (as obtained from X-ray diffraction measurements of shot peened surfaces).

It is known that proper peening can be beneficial and that clearly abusive peening, resulting in surface tears or laps for example, is possible and undesirable. The influence discussed here is more subtle and suggests that certain peening parameters, while not obviously abusive, when mixed with certain operating conditions can be unexpectedly detrimental to LCF life.

4.1 Thermal Exposure Influence

24C (75F) LCF testing of round, moderately shot peened cast and wrought and PM alloy fatigue test samples with and without a non-stressed thermal exposure (538C/1000F, 24 hours) was conducted. Based on preparatory work, there was suspicion that the thermal exposure, in combination with sufficient surface cold work from the shot peening could result in LCF life loss. As the results in Figure 7 show, without thermal exposure, room temperature life was enhanced for the conditions assessed. Subjecting nominally identical test bars to a pre-test, non stressed thermal exposure significantly lowered the life. This behavior is believed related to the amount of surface coldwork imparted by the shot peening. Companion tests found that exposing comparatively cold worked bulk material samples to a thermal activation environment significantly lowered the ductility (Figure 8). This potentially leads to early surface crack initiation and consequent shortened fatigue life.

4.2 Practical Implications

The practical importance of the phenomenon was demonstrated in analyzing shot peened, sub-scale spin pit LCF disk test results compared to longitudinally loaded feature test bars at 399C (750F). Initially, the comparatively short life observed for a spin pit disk bolt hole feature was inconsistent with results from nominally identically manufactured test specimens (Figure 9). It was noted that the disk was heat tinted before and during test (to allow post test crack growth assessment) but the feature specimens were not. When feature test specimens were similarly heat tinted, the results straddled the model disk result.

The relevance of the behavior appears to depend on, at least, the material, shot peening parameters, exposure and application temperatures, and applied stress level. This is an area of ongoing evaluation.

4.3 Holistic Approach Again Needed

Details aside, the role of temperature in changing component behavior in a fairly complex way is again evident. The sub-component disk test result observed by the Design engineer desiring to verify a life prediction method is heavily dependent on details of the component and test vehicle manufacturing process (machine and shot peen) used. This in turn

is significantly influenced by an intriguing phenomenon (coldwork thermal exposure interaction) that is in the traditional domain of the material scientist. When all of the variables are assembled, in an integrated picture, a logical explanation for apparent abnormalities begins to emerge.

5. CLOSING

With increasing emphasis on quantified margins, process control, and robustness, more detailed test programs are revealing significant complications associated with complex interactions of material structure, manufacturing methods, and usage environments.

The aircraft engine component related examples discussed here show that as more sophisticated modeling methods, including TMF models for example, are developed and employed to address these complexities, the importance and benefit of fully integrated design, material processing and component manufacturing systems and organizations is accentuated.

6. ACKNOWLEDGMENTS

7.0 REFERENCES

1. Annis, C.G., Mills, J.S., and Harris, J.A., "Engine Component Retirement for Cause, Vol. II, Life Assessment System Development", AFWAL-TR-87-4069, August 1987.

2. Roth, P.G., "Competition in Probabilistic Life Analysis", in Proceedings of the 1990 USAF Structural Integrity Program Conference, WL-TR-91-4067, August 1991.

3. Bruckner-Foit, A., and Jackels, H., "Prediction of the Lifetime Distribution of High-Strength Components Subjected to Fatigue Loading", Fatigue & Fracture of Engineering Materials & Structures, Vol. 16, No. 8, August 1993.

4. De Bussac, A., and Lautridou, J.C., "A Probabilistic Model for Prediction of LCF Surface Crack Initiation in PM Alloys", Fatigue & Fracture of Engineering Materials & Structures, Vol. 16, No. 8, August 1993.

5. Raisson, G., "The Control of Cleanness in Powder Metallurgy Materials for Turbine Disks", AGARD-R-790, April, 1993.

6. Roth, P.G., Murray, J.C., Morrà, J.E., and Hyzak, J.M., "Heavy Liquid Separation: A Reliable Method to Characterize Inclusions in Metal Powder", Characterization, Testing and Quality Control, Advances in Powder Metallurgy & Particulate Materials - 1994, Vol. 2, Metal Powder Industries Federation, Princeton, N.J.
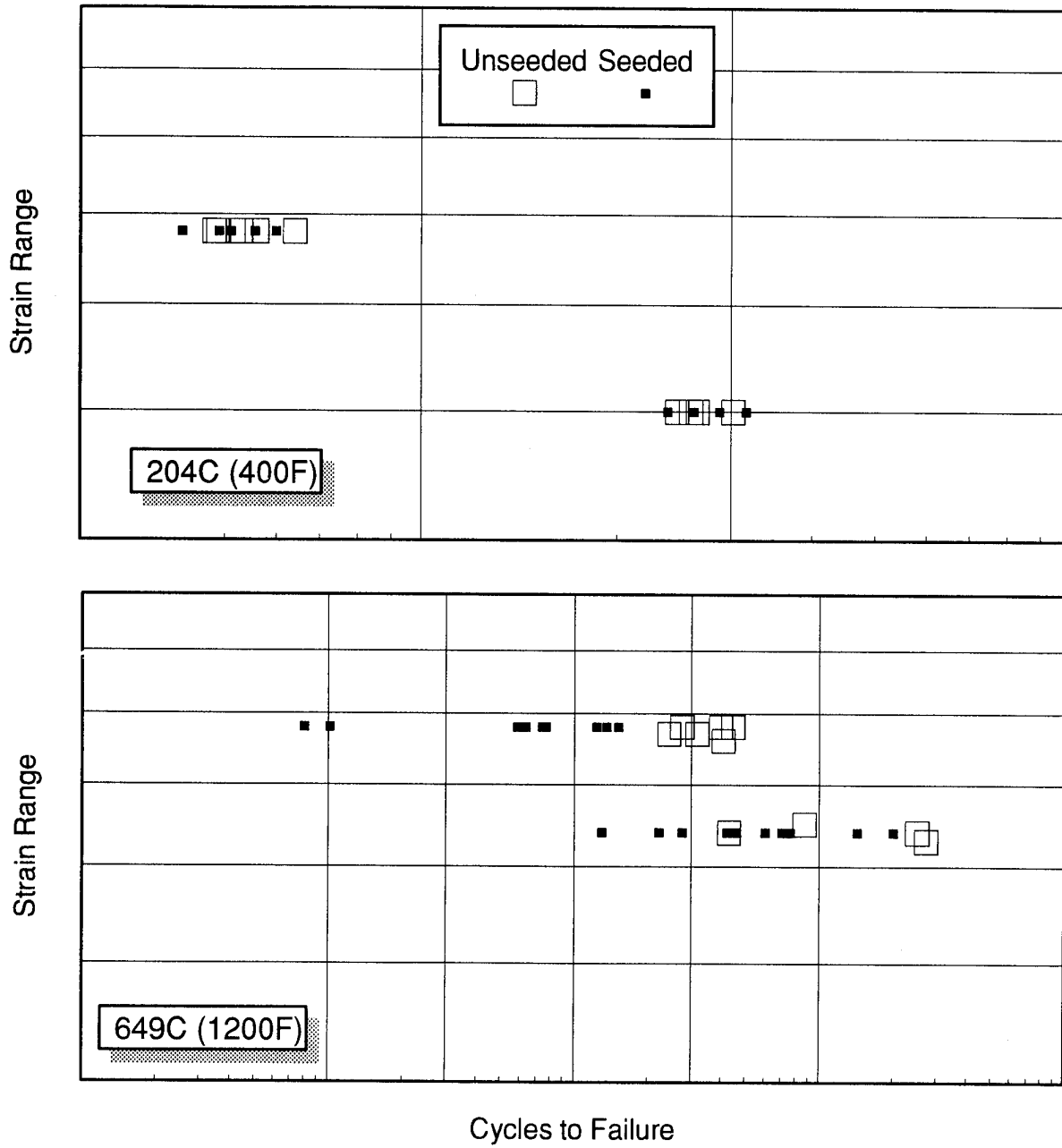
Figure 1: Fatigue test data on non-seeded and ceramic seeded test bars illustrating temperature dependent initiation mode change

Seeded PM Alloy Low Cycle Fatigue

649C (1200F)

Surface initiation
41 mils^2 area
6701 cycles to
failure

Sub-Surface initiation
89 mils^2 area
33,740 cycles to
failure

Specimen Surface

Strain Range

1E+3   1E+4   1E+5

Cycles to failure
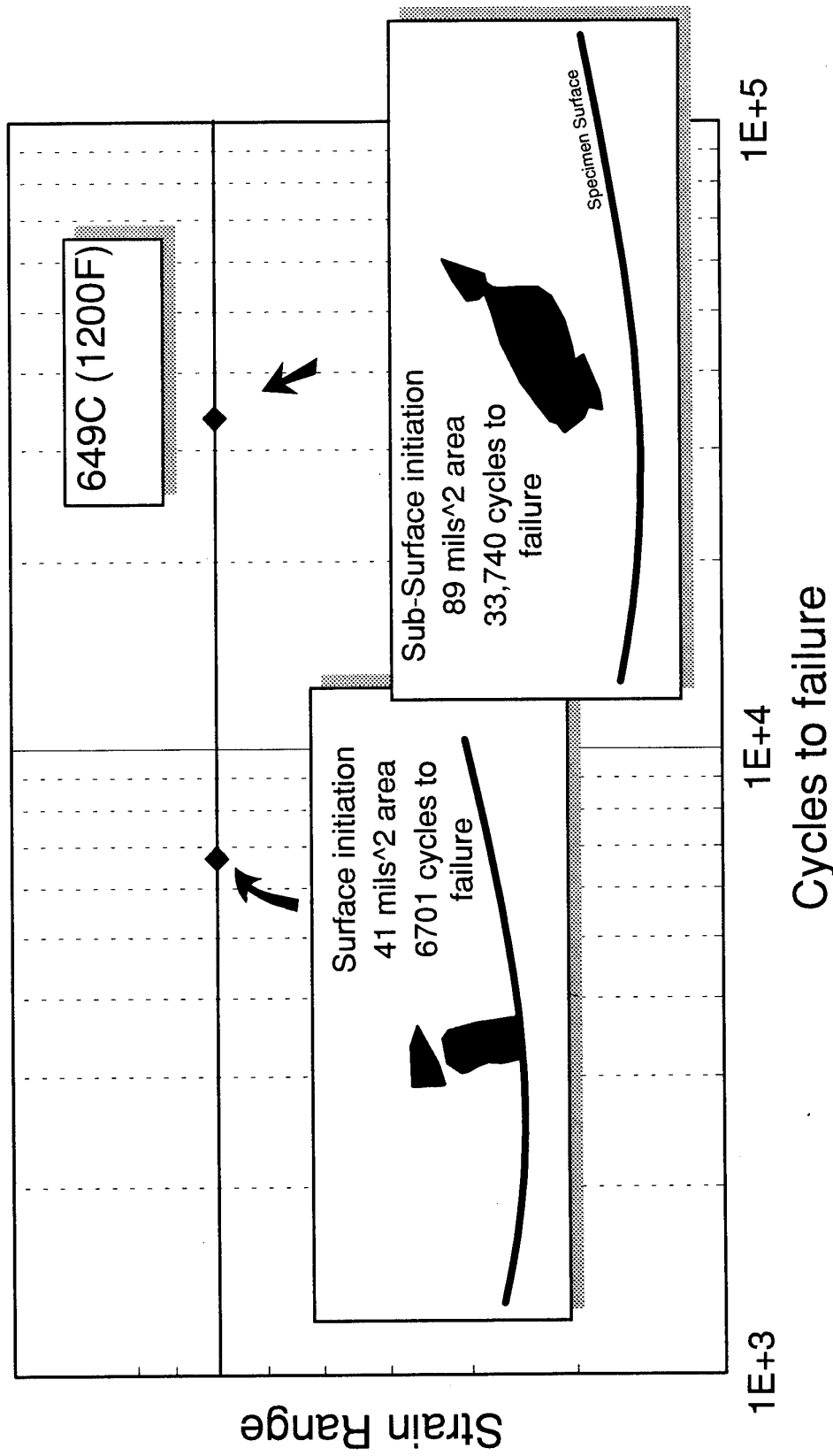
Figure 2: Schematic of PM alloy fatigue test result illustrating that life can be a function of
ceramic inclusion location
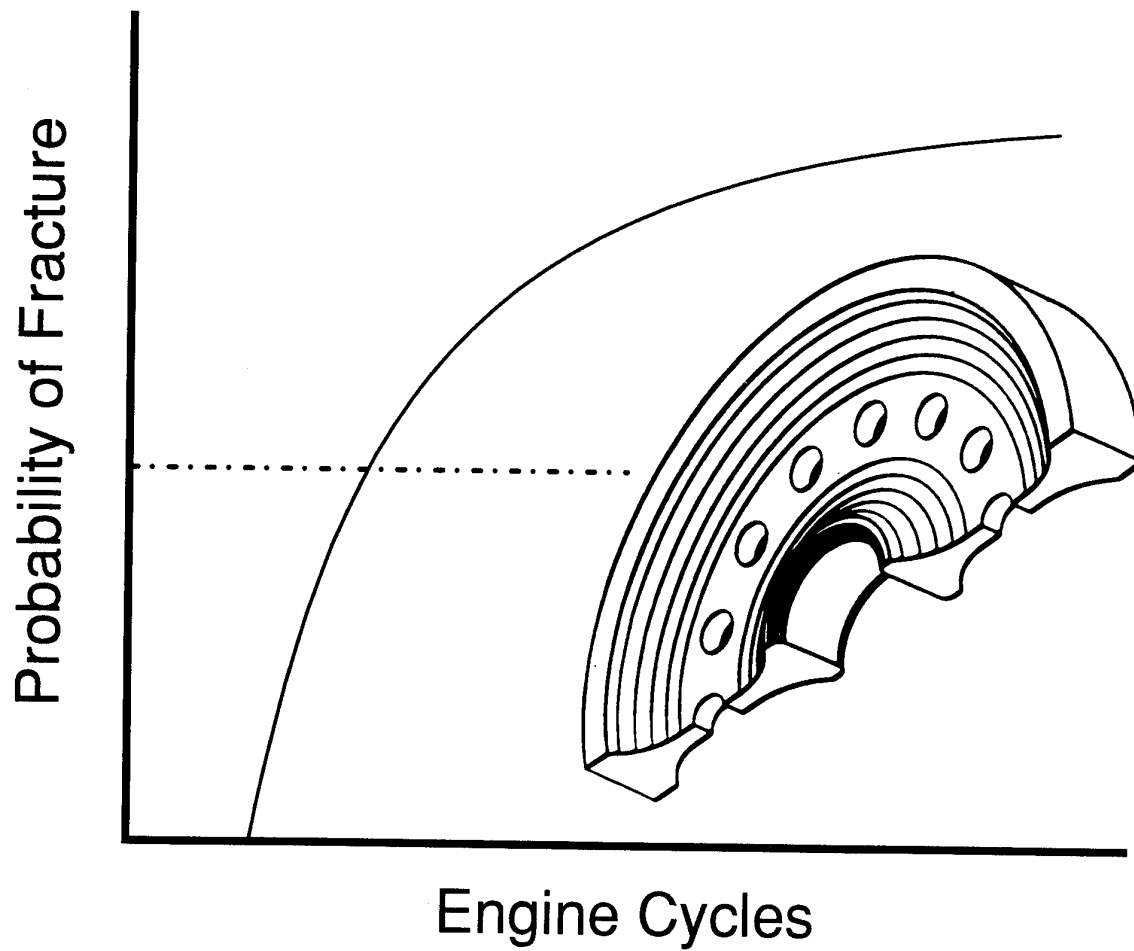
Figure 3: Schematic illustration of component probability of fracture versus usage curve resulting from probabilistic life analysis
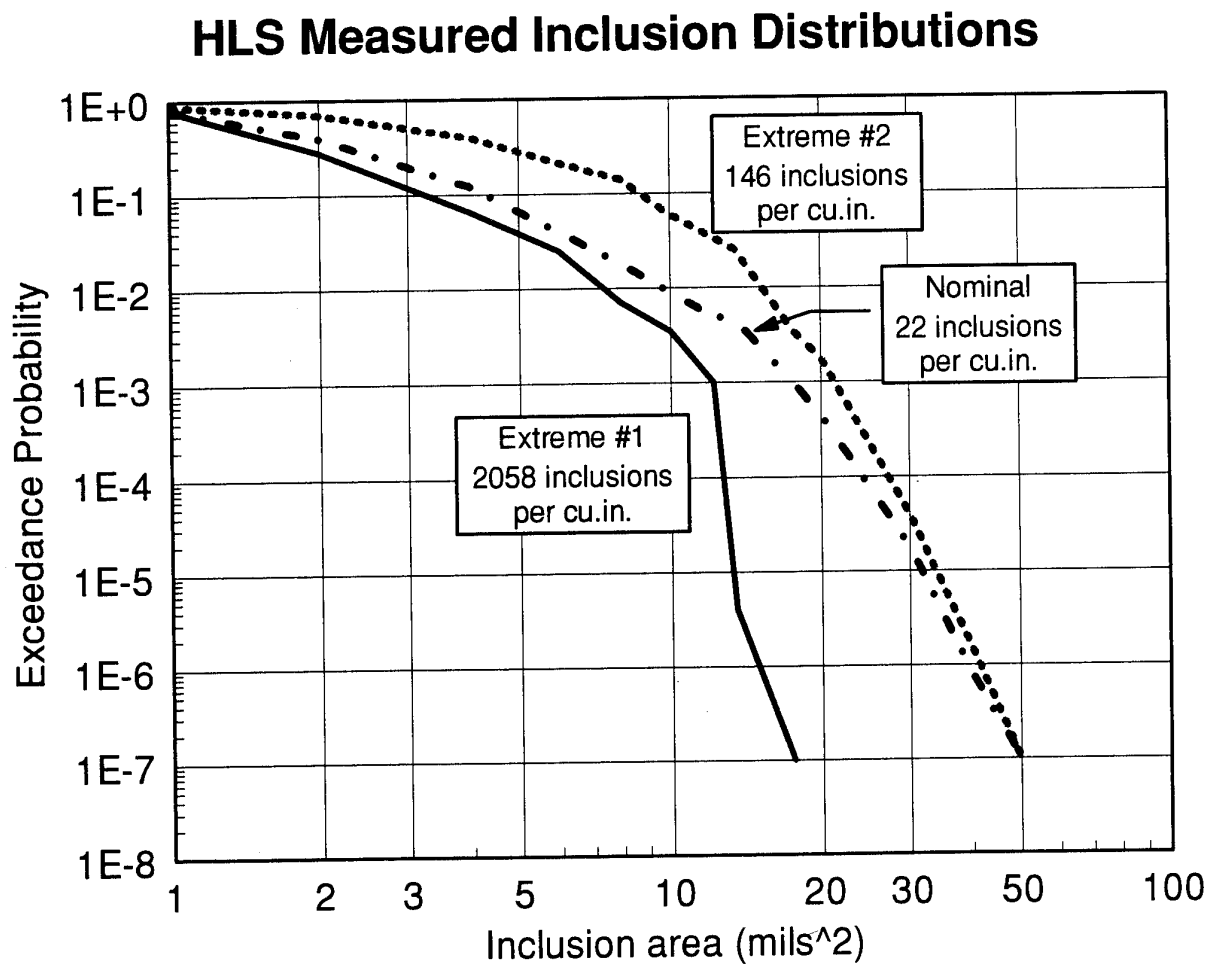
Figure 4: Ceramic inclusion distributions obtained using HLS reveal variability

Engineering Study Of Rotating Air Seal
(Variable inclusion distributions)

Fracture probability

Nominal distribution
22 inclusions
per cu.in.

Extreme #1
2058 inclusions
per cu.in.

Extreme #2
146 inclusions
per cu.in.

20,000   30,000   40,000   50,000   60,000   70,000

Cycles
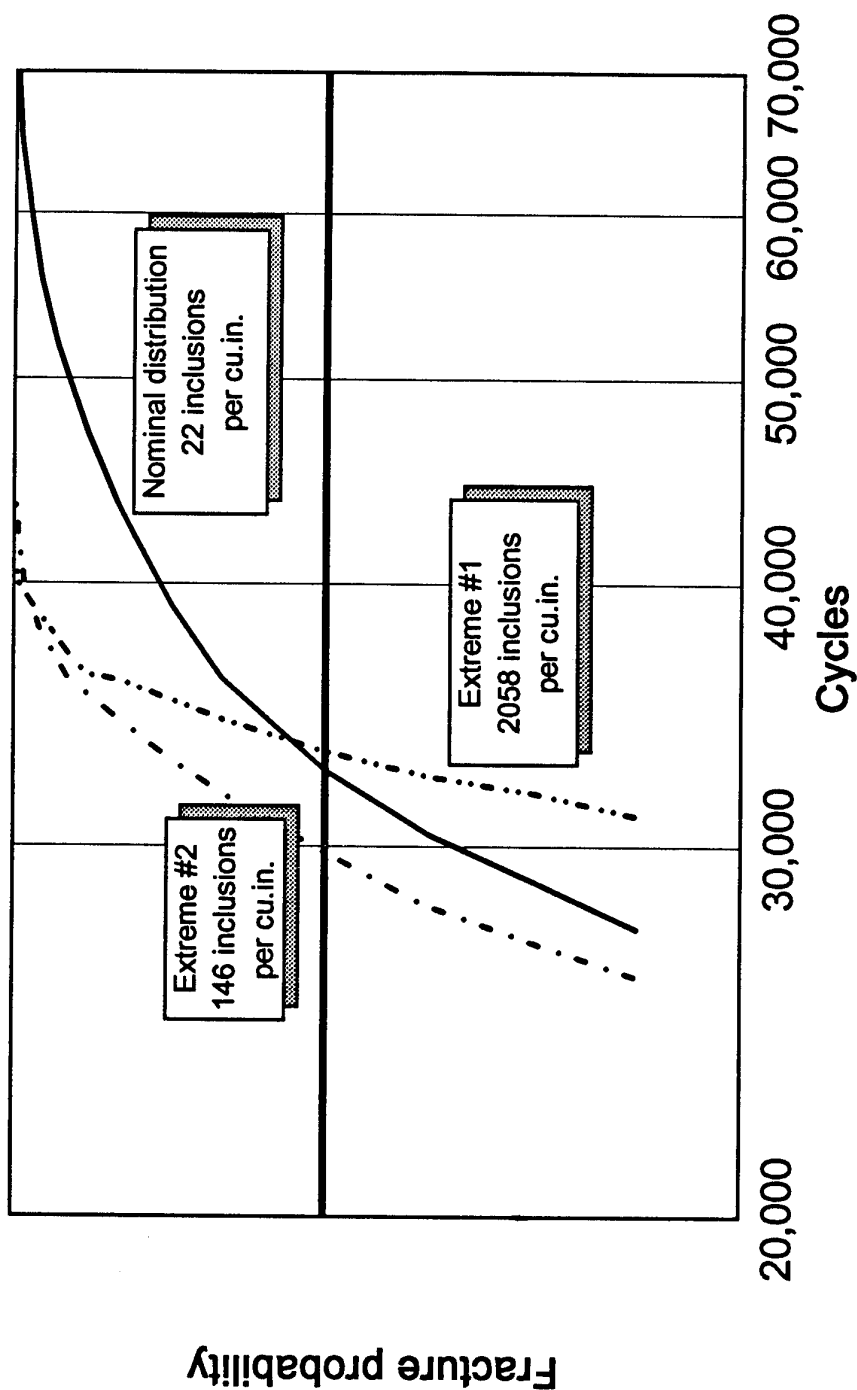
Figure 5:   Analysis results indicate component fatigue life predictions vary based on the inclusion
size distribution and occurrence frequency
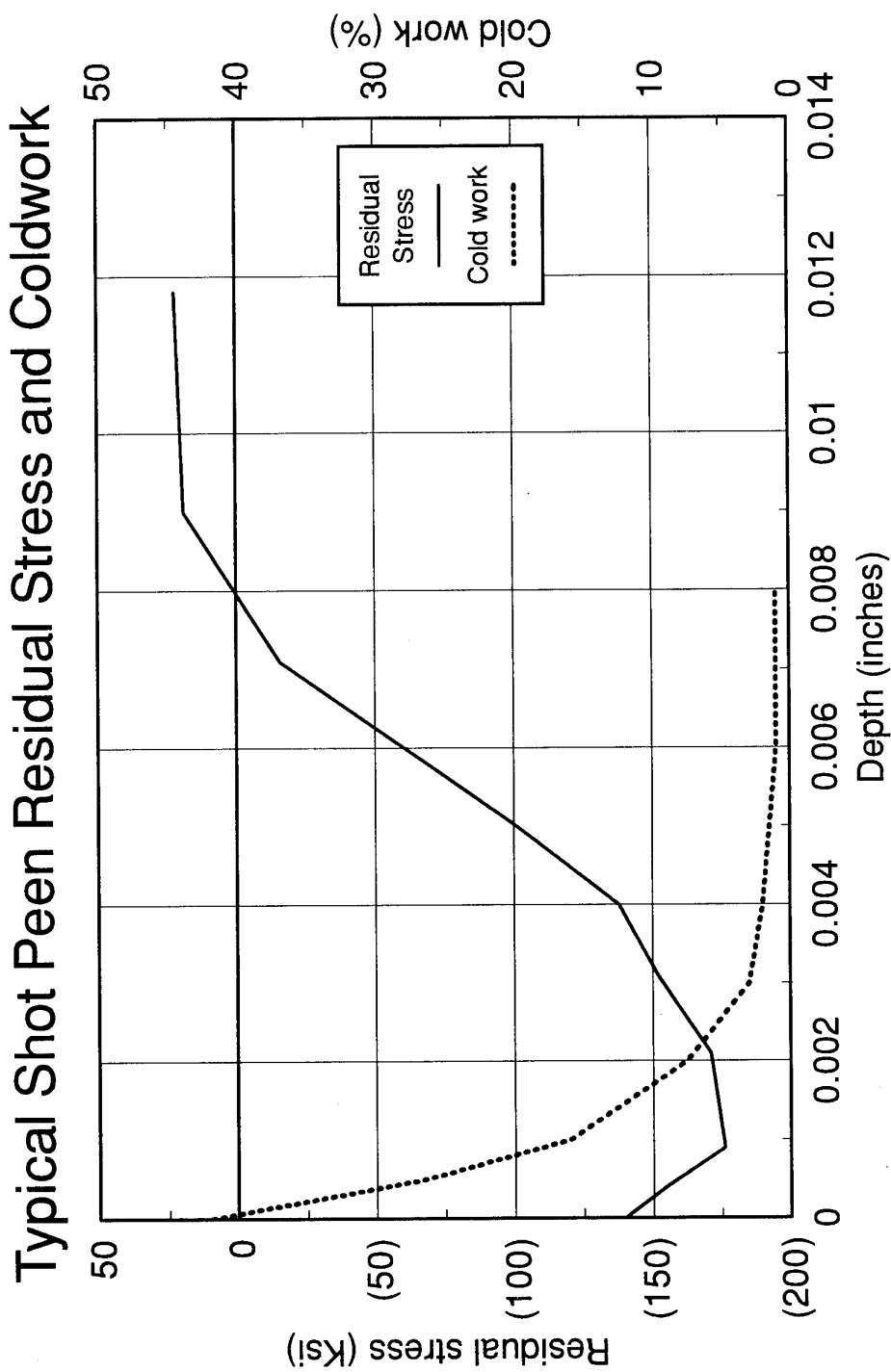
Figure 6: Example residual stress and cold work profiles imparted by shot peening

10A intenstity shot peened thermal exposure data
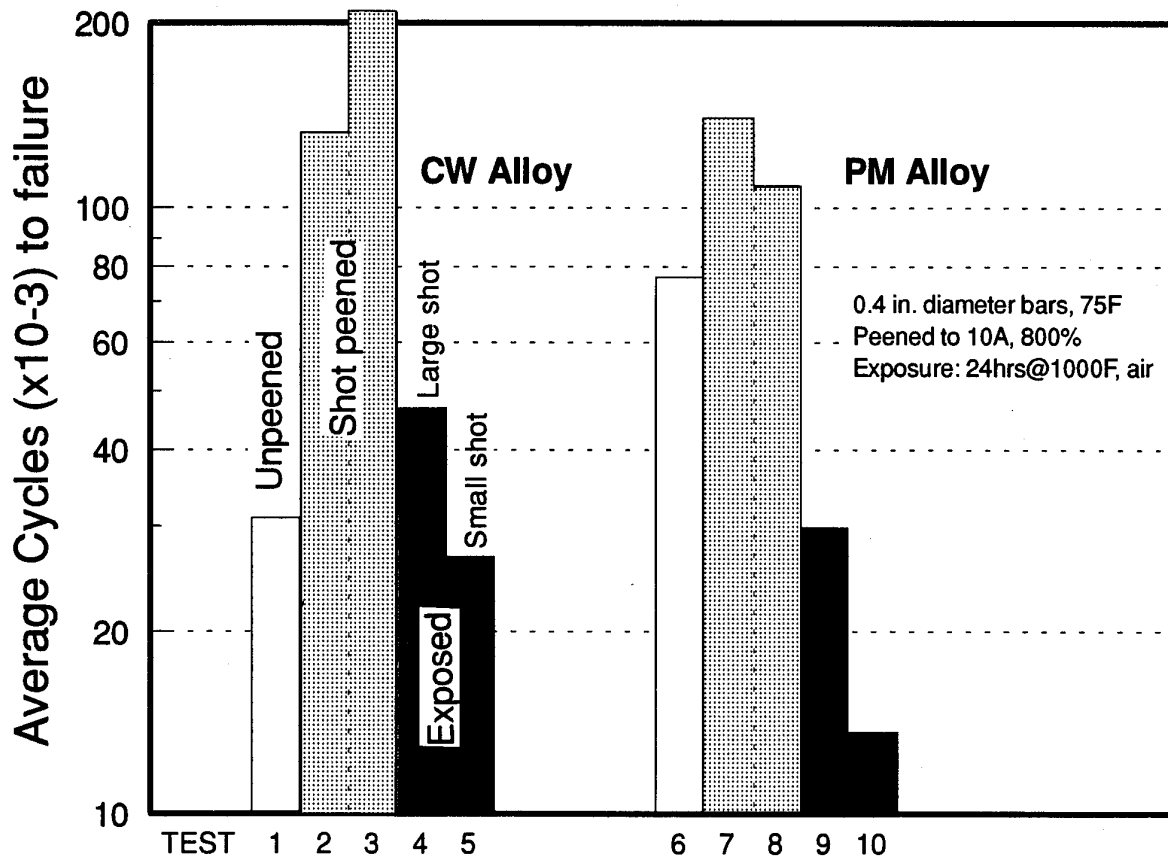
Figure 7: Fatigue test results illustrating potential impact of thermal exposure on shot peened parts

Ductility loss as function of coldwork
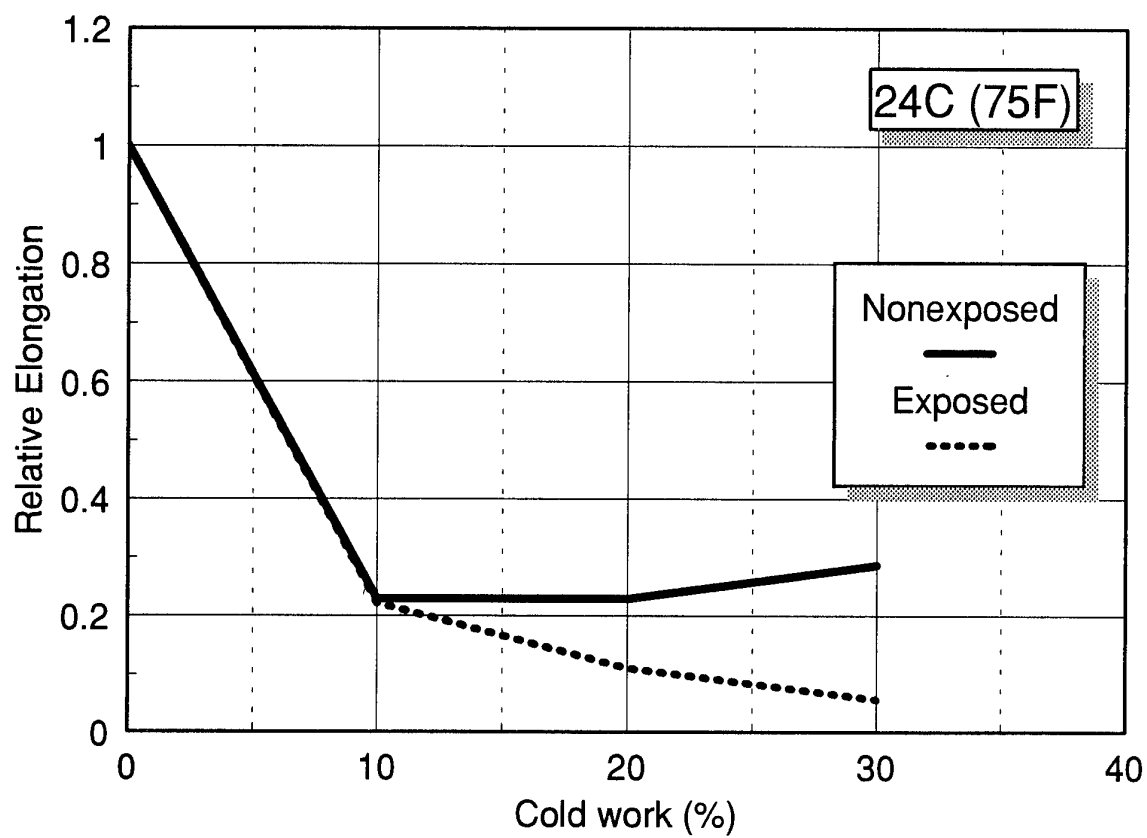
Figure 8: Tensile test results show loss of ductility for thermally exposed cold worked material
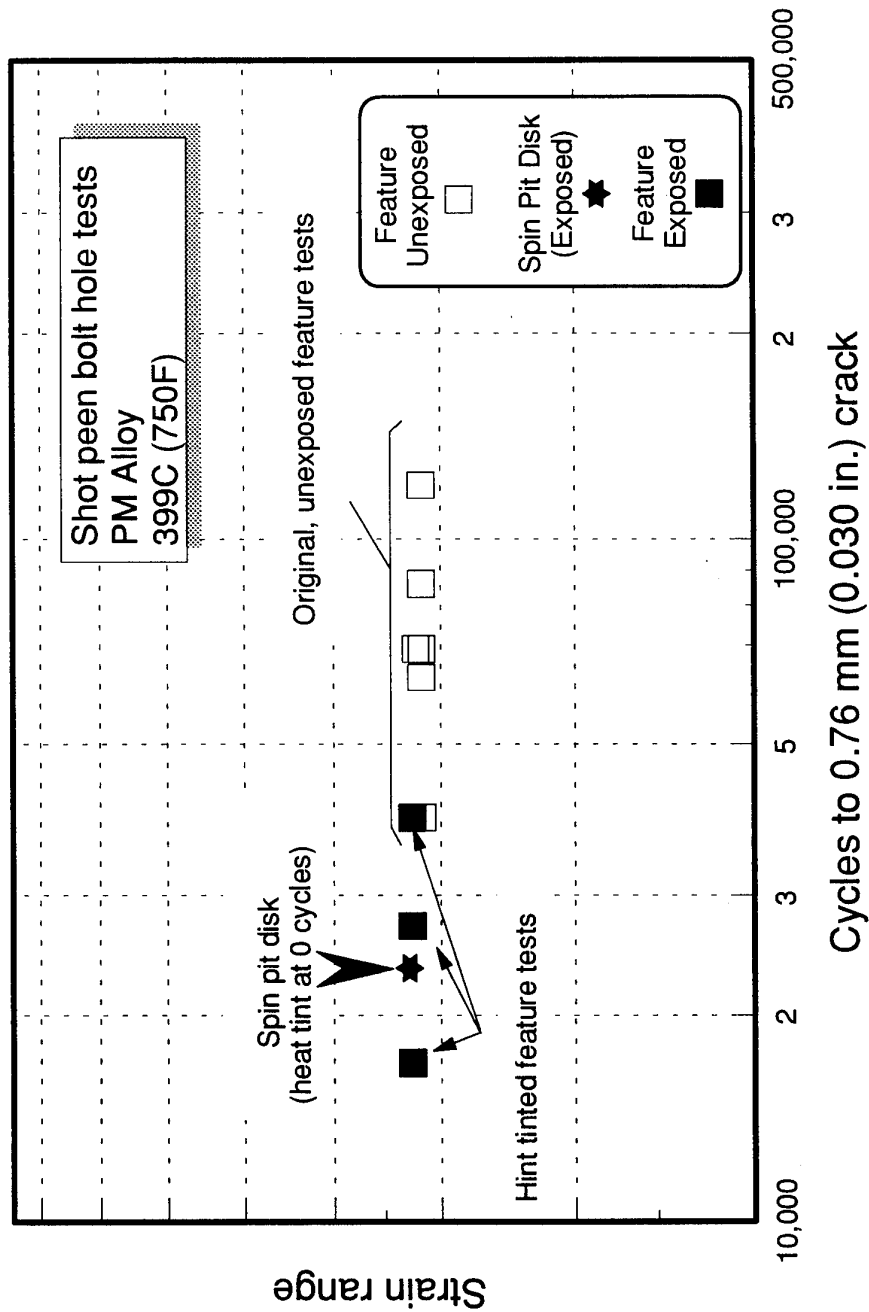
Figure 9: Feature test fatigue results confirm potential for thermal exposure impact

Thermal Mechanical Fatigue of Model Blades made from CC and DS Superalloys

F. Schubert, H.J. Penkalla, D. Frank

Forschungszentrum Jülich GmbH (KFA)
Institute for Materials in Energy Systems (IWE 1)
P.O. Box 19 13, 52425 Jülich
Germany

1. SUMMARY

Thermal mechanical tests with internally cooled model blades of IN 783 LC (conventional casted) and of IN 792 DS (directionally solidified) are experiments to develop non linear elastic analysis methods of stress strain behaviour and life time estimation methods. For the inelastic analysis, a constitutive equation has been developed. This constitutive equation describes the deformation behaviour by using internal variables which concern microstructural features. The constitutive equation has been implemented user materials routines (UMAT) in the finite element code ABAQUS. In the experiment with model blades, loaded periodically in simulating loading cycle of a real working blade for large stationary gas turbine, the temperature distribution are measured by a set of thermal couples around the blade and calculated with using heat transfer estimations for the impact of heat by a high frequency inducion coil and heat consumption by the colling air. Based on the calculated temperature distribution the stress strain behaviour for different point was computed and as far as possible compared with measured strains. The comparison of experimental results with the mathematical prediction showed a fair conformaty.

2. INTRODUCTION

In order to improve the efficiency of land base stationary gas turbines for electrical power supply the burning gas temperature is raised, the turbine rotors are designed for a thermodynamical optimum between aerodynamical efficiency factor and loss due to cooling air. The nowadays modern cooling technology for the first stages of blades of large stationary gas turbines and vanes is as sophisticated as for aircraft turbine engines. More and more modern superalloys, especially optimized for stationary gas turbines, are used in directionally solidified either as columnary or single crystals. The design of such large blades for working temperature higher than 850°C requires beside a suitable material and coatings also suitable methods for the calculation of the stress strain behaviour and for the estimation of life time under realistic multiaxial loading condition. The most important failure type, to be mentioned in life time consideration are

- large inelastic deformation can lead to a loss of function,
- rupture caused by creep or time indepent plastic failure;
- thermal fatigue may leads to local crack initiation and failure.

Not mentioned are in this paper the gas corrosion effects and the erosion.

In a cooperative research programm a deterministic model for estimation of the component behaviour under cyclic thermal mechanical loading has been developed for the superalloy IN 783 LC, conventionally casted (CC) and within the COST-programme 501, II. round modern material such as directionally solidified (DS) and single crystal (SC)-Ni-base alloys with a high level of γ'precipitation are investigated. The development and final formulation of the three dimensional „structurally dependant materials law", as an unified model, are described in /1,2/ and the modification with the Hill-approximation for the anisotropic DS-material are given in /3/. The developed constitutive equation are proved with thermal mechanical tests on model blades of IN 738 LC (CC) and IN 792 DS.

The nominal chemical composition is summerized in Table 1.

specification	IN 738 LC	IN 792 DS	CMSX-4
C	0,10	0,08	0,01
Ni	R	R	R
Cr	16,0	12,5	6,5
Co	8,5	9,0	9,5
Mo	1,7	2,0	0,6
W	2,5	4,1	6,0
Nb	0,8	-	-
Ta	1,7	4,2	6,5
Ti	3,4	3,8	1,0
Al	3,6	3,4	5,6
others	0,01B 0,05Zr	1,0Hf, 0,01B 0,05Zr	3,0Re, 0,10Hf
Vol.γ'	43	49	65

Table 1: Nominal chemical composition of materials for thermal fatigue experiments with model blades

3. THE COMPONENT

In order to calculate the component behaviour by inelastic analysis it is important to consider the component at first. The technical function of the component requires the knowledge of its geometry and the mechanical and thermal loading conditions.

3.1 The geometry

Figure 1 shows an example for a cooled turbine blade. The whole blade, including airfoil, root and shroud is made of superalloys either by conventional casting process or by directionally solidification. The blade is

cooled with 20 cooling holes close underneath the surface. The airfoil dimensions are as follows:

Length, l: approx. 180 mm
Width, w: approx. 110 mm
Wall thickness, h: minimum 1.2 mm
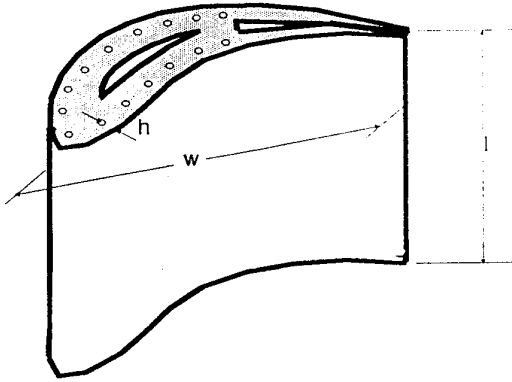(between hot outer surface and cooling holes)

Fig. 1: Siemens blade for COST 501
        Schematic airfoil geometry

3.2 The loading conditions

The loadings of the turbine blade can be classified in different types:

Steady state conditions:
During stationary service stresses are given by the centrifugal load and the steady state temperature gradients trough the thickness.

The centrifugal force gives rise the stress in the radial direction, i.e. along the blade. The resulting stress σ_c is in the range 100 - 150 MPa, both at the hot surface and around the cooling holes.

From the steady state boundary conditions, temperature and stress and stress distribution are related for the special type of blade shown in Fig. 1. The temperature gradient between the hot outer side and the inner surface of the cooling channels leads to the radial stress σ_r, i.e. the principal stress along the blade, which is the stress component with the highest value in the temperature analysis. Both stresses, σ_c and σ_r constitute the same stress component, which is of importance when calculating the stress range for the loading cycle.

Transient conditions:
For the cooled blade considered here, the thermal strains increase or decrease monotonously at loading and normal deloading (shut down). The conditions for this procedures are so defined that the material will not experience higher strains during the transients than the thermal strains at steady state. This is true for normal start of an industrial gas turbine, with blade size considered here. A baseload trip will create higher strains during the transients than the thermal strains at steady state. However, this event will occur very seldom and is therefore not included in the design principles.

Dynamic stresses:
Dynamic stresses, generated from gas pressure variations over the blade and increased when running close to

resonances, are less than about 50 MPa. The maximal stress occur at the hot surface.

Local stresses:
Stress concentrations appear in the transition regions from airfoil to shroud and from airfoil to root. To prevent stress peaks, the wall thickness is increasing continuously there, so that the stress concentrations that will appear in these regions are small.

Load history:
The most common load cycle consists of start up loading, followed by the steady state centrifugal and temperature load and normal shut down. Disregarding creep and plasticity effects, representative stress cycle is shown schematically in Figure 2.

The operation time at steady state will vary between 1 and 2 hours at peak load plants and about 10 hours or more at combined cycle plants. The latter is expected to be the most common in the future. During these hold times, the thermal stresses will relax and by this will cause creep strains.

The present life time requirements are 100,000 hours at base load or 10,000 load cycles.
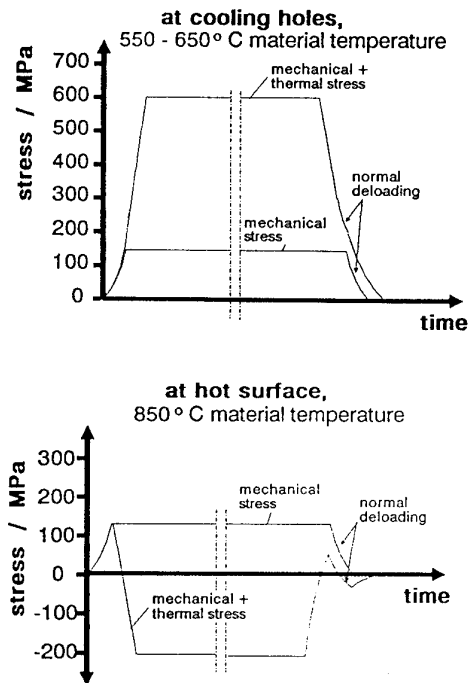
Fig. 2: Representative stress cycle on DS blade, disregarding creep and plasticity

3.3 The model-blades

The geometry of the model blade has derived from this and other kinds of internal cooled blades in order to simplify the experimental procedure and non linear elastic analysis. The used model-blades of IN 783 LC (CC) has been casted by usual vacuum investment cast process with material of the same master heat as the specimens, which has been tested under complex loading conditions for finally fitting the parameters of the constitutive equation /3/. The blade contains three

cooling channels and the wall thickness was 2 resp. 3 mm (compare Fig. 3).

Fig. 3: Drawing of the used model blade for IN 738 LC

During the test work with this modell blade we learnt, that it would be easier to simplify the top and foot region for experimental reasons and three dimensional finite element calculation. The 3D-finite element model is shown in Fig. 4.

Fig. 4: 3D-finite element model for the DS-blades of IN 792 DS

3.4 Test facility and test parameters

The blade was axial loaded by 120 MPa resp. 180 MPa in a servohydraulic test facility to simulate the centrifugal forces. A high sophisticated high frequency heating system has been developed which allows, by using the skin effect, to generate the heat in the region of the blade surface and to generate a thermal gradient of about 50°C across the wall and along the blade shape (compare Fig. 5). The temperature distribution in the blade was claculated using the measurements of thermocouples on the blade, results of former

temperature distribution measurements and estimations by heat transfer coefficient. The blades were exposed to temperature cycles, heating up in 15 to 20 sec. to a medium temperature of about 900°C and 950°C resp. on the blade surface, holding this temperature for 200 and 1800 sec. resp. and cooling down. The elongation was measured by an extensiometer gripped at the outlet trailing edge of the model-blade.

Fig. 5: Test arrangement for the model blade of IN738LC

4. RESULTS OF THE ANALYSIS

The temperatures of the thermocouples, the elongation of the total blade and the measured strain at the outlet trail are continously written on two multichannel data recorder. The temperature distribution was calculated from the measured temperatures on the heat input using the heat transition coefficience of the inner side of the wall. Based on the calculated temperature distribution, the stress and the strain distributions were computed using either a two dimensional finite element mesh net gernalized plain strain element, which allows a calculation in all three dimension or the shown three dimensional finite element mesh net. Both elastic and inelastic analysis are computed. For the inelastic analysis the „microstructural materials law", a unified model has been used.

4.1 The constitutive equation

4.1.1 Principles

The visco-elastic material behaviour at high temperature can be described by a flow equation which is given in an uniaxial form as the power law in form of

$$\dot{\varepsilon}_i = K(\sigma - \sigma_i)^N \qquad (4.1)$$

$\dot{\varepsilon}_i$ is the inelastic strain rate, σ the external stress, and σ_i is the internal stress which controls the hardening and softening of the material at high temperature. σ_i can be interpreted as the resistance of the material against deformation caused by different mechanisms of deformation. In the following consideration these mechanisms are subdivided in two parts, defined as "conservative" part and "dissipative" part. Both parts are represented in the formulation of σ_i by the simple equation

$$\sigma_i = \sigma_b + \rho \qquad (4.2)$$

The order of dislocations to subgrains and meshes in the subgrain boundaries is load dependent and leads to an internal back stress σ_b. If the external load disappears after service the order of dislocations is resolved and the back stress decreases. Therefore, the back stress is declared as conservative and describes the cinematic hardening. The evolution of the back stress is written by

$$\dot{\sigma}_b = \lambda_0 \dot{\varepsilon}_i (\overline{\sigma}_b - \sigma_b) \qquad (4.3)$$

$\dot{\sigma}_b$ is the back stress rate and $\overline{\sigma}_b$ is the stationary value, reached if the inelastic strain rate is in equilibrium (e.g. stationary creep). The difference $(\overline{\sigma}_b - \sigma_b)$ can be interpreted as the distance to the equilibrium state and as the driving force for the change of the back stress. The inelastic strain rate represents the compliance of the material.

The interaction between the dislocations and the γ'-particles is defined as the dissipative part of the internal stress and can be declared as friction stress or drag stress ρ. Dependent on the particle size a single dislocation or a dislocation pair can cut a particle, envelop it by Orowan mechanism or climb the particle.

For low sizes the strain rate a function of $1/r$ and for a radius greater than a critical value r_s the resulting strain rate is given as a function of r. From an extensive derivation the friction stress ρ is given

$$\rho = \sigma \cdot [1 - (\frac{k \cdot R}{K} \cdot \sigma^{n-N} \cdot \exp\{\alpha \cdot \sigma\})^{1/N}]..$$
$$- \sigma_b$$

$$(4.4)$$

with $R = r/r_0$ for $r < r_s$ and $R = r_0 r/r_s^2$ for $r >= r_s$. r_0 is the initial γ'-particle radius, r_s the critical radius and r the current radius. The time dependent change of the friction stress ρ is determined by the growth of the γ'-particles described by the Ostwald ripening. For a constant temperature the average Volumerate $\dot{V}$ is constant. Therefore, the evolution equation for the radius is given by

$$r = (r_0^3 + \frac{3}{4\pi} \int_0^t \dot{V} dt)^{1/3} \qquad (4.5)$$

4.1.2 The basis of formalism

In order to estimate the general internal stress (sum of both parts) it is assumed that under creep conditions the duration of primary creep is limited related to the whole creep time. After primary creep the process of dislocation order in the matrix is finished and the creep rate respective the internal stress should be in the stationary state. The evaluation of the minimum creep rate, can be compared with the flow equation, with $\overline{\sigma}_i$ as the equilibrium value of the internal stress.

$$k \cdot \sigma^n \cdot \exp\{\alpha \cdot \sigma\} = K \cdot (\sigma - \overline{\sigma}_i)^N \qquad (4.6)$$

This leads e.g. for CC and DS material to the equation for $\overline{\sigma}_i$ in form of

$$\overline{\sigma}_i = \sigma \cdot (1 - (\frac{k}{K} \cdot \sigma^{n-N} \cdot \exp\{\alpha\sigma\})^{1/N}) \qquad (4.7)$$

In order to calculate the constants K and N (k, n, and a are known from the evaluation of $\dot{\varepsilon}$ min) two additional boundary conditions must be considered. In general the internal stress is lower than the external stress, but for $\sigma \to 0$ the internal stress must be $\sigma_i \to \sigma$. For stresses equal or higher than the yield stress σ_y the internal stress reaches a maximum. Both conditions can be written as

$$\frac{d\sigma_i}{d\sigma} = \text{max für } \sigma \to 0 \qquad \text{and}$$

$$\frac{d\sigma_i}{d\sigma} = 0 \text{ für } \sigma \geq \sigma_y \qquad (4.8)$$

Both parts of the internal stress can be written by the proportionality

$$\rho = q_0 \cdot \sigma_i \quad \text{and} \quad \sigma_b = (1 - q_0) \cdot \sigma_i \qquad (4.9)$$

The dependency of q_0 on σ can be calculated from the initial strain rate in a creep test. At the time $t = 0$ it is assumed that the back stress will be zero, therefore, the internal stress at $t = 0$ is identical the friction stress r. Therefore, the proportionality q_0 is given by

$$q_0 = \frac{\sigma \cdot (\frac{\dot{\varepsilon}_{init}}{K})^{1/N}}{\sigma \cdot [1 - (\frac{k}{K} \cdot \sigma^{n-N} \exp\{\alpha\sigma\})^{1/N}]} \qquad (4.10)$$

This formula requires an evaluation of $\dot{\varepsilon}_{init}$ in dependence on the external stress. For the materials considered in this report the formula

$$q_0 = 1 - A \cdot \left|\frac{\sigma}{\sigma_y}\right|^p$$

$$(4.11)$$

will be a good approach.

4.1.3 The multiaxial formulation

For a multiaxial formulation, the difference of external and internal stress is called the effective stress $\sigma - \sigma_i = \sigma_e$. For a general description of deformation the inelastic strain rate tensor is defined as the derivation of a flow potential $\Phi(S)$ to all components of the effective stress tensor $\{\sigma_{e,kl}\}$ ($\{..\}$ describes the complete tensor)

$$\{\dot{\varepsilon}_{i,kl}\} = \frac{d\Phi(S)}{dS} \cdot \{\frac{\partial S}{\partial \sigma_{e,kl}}\}. \qquad (4.12)$$

S is a suitable invariant of the effective stress tensor. Because of the volume constance under plastic deformation the derivation of S to all components $\sigma_{e,kl}$ can be set proportionally to the deviator $\{\sigma^*_{e,kl}\}$

$$\{\frac{\partial S}{\partial \sigma_{e,kl}}\} = 3 \cdot \{\sigma^*_{e,kl}\} \qquad (4.13)$$

For isotropic CC material the deviator is given by the expression

$$\{\sigma^*_{kl}\} = \{s^*_{kl}\} = \{\sigma_{kl} - (\frac{1}{3}\sigma_{ij} \cdot \delta_{ij}) \cdot \delta_{kl}\} (4.14)$$

and the invariant S as result of equation 4.13 can be written as

$$S = \frac{3}{2} s^*_{kl} \cdot s^*_{kl}. \qquad (4.14)$$

which is proportional to the second invariant of the deviator. (Note, that in these formulations Einstein's sum convention is provided. That means, all terms with the same indices are added for all values of the indices). The property of S to be invariant against co-ordinate transformations leads to the definition of a deviatoric stress resp. effective stress by von Mises as

$$\sigma_v = \sqrt{S} \qquad (4.15)$$

Therefore, in multiaxial formulation the inelastic strain rate tensor can be written as the multiaxial flow equation

$$\{\dot{\varepsilon}_{i,kl}\} = \frac{3}{2} \cdot K\sigma_{e,v}^{N-1} \cdot \{\sigma^*_{e,kl}\} \qquad (4.16)$$

For anisotropic material such as DS or SC alloys the deviator $\{\sigma^*_{kl}\}$ and the invariant S can be modified by the Hill anisotropy tensor of 4. order $\{A_{ijkl}\}$ in form of

$$\{\sigma^*_{kl}\} = \{A_{ijkl}\}\{s^*_{ij}\} \text{ and } \qquad (4.17)$$

$$S = \frac{3}{2} A_{ijkl} s^*_{ij} \cdot s^*_{kl}. \qquad (4.18)$$

$$A_{ijkl} \cdot \delta_{ij} = 0 \text{ (volume constance)} \qquad (4.19)$$

The considered anisotropic materials can be classified in two special cases of orthotropy:
- transversely isotropy and
- cubic orthotropy.

DS material show a transversely isotropic behaviour that means only one main anisotropy direction is indicated. In this case only three coefficients of the anisotropy tensor must be known and it follows:

$$F = G, L = M \text{ and } N = H + 2G \qquad (4.20)$$

For DS material it was found that the coefficients of the anisotropy tensor can be defined as time and stress independent. The material show a temperature dependent change of the direction of highest strength at a temperature of about 800 °C.

SC material can be described by cubic orthotropy because all cubic axes must show the same stress strain behaviour and by the symmetry of the crystal lattice only the range between the (100), (110) and (111) directions must be considered (see fig. 4). Therefore, only two coefficients of the anisotropy tensor must be known..

$$F = G = H \text{ and } L = N = M \qquad (4.21)$$

Combined with the elastic strain tensor, the complete set of equations for the material law is given by

$$\{\dot{\varepsilon}_{kl}\} = \{S_{ijkl}\} \cdot \{\sigma_{ij}\} + \frac{3}{2} \cdot K\sigma_{e,v}^{N-1} \cdot \{\sigma^*_{e,kl}\}$$
$$(4.22)$$

$$\{\dot{\sigma}_{b,kl}\} = \lambda_0 \dot{\varepsilon}_{eff} \{\overline{\sigma}_{b,kl} - \sigma_{b,kl}\} \qquad (4.23)$$

$$\{\overline{\sigma}_{b,kl}\} = (1 - q_0) \cdot \{\sigma_{kl}\} \cdot [1 - (\frac{k}{K} \cdot \sigma_v^{n-N} \dots \\ \cdot \exp\{\alpha \cdot \sigma_v\})^{1/N}]$$
$$(4.24)$$

$$\{\rho_{kl}\} = \{\sigma_{kl}\} \cdot [1 - (\frac{k \cdot R}{K} \cdot \sigma_v^{n-N} \\ \cdot \exp\{\alpha \cdot \sigma\})^{1/N}] . - \{\overline{\sigma}_{b,kl}\}$$
$$(4.25)$$

$$q_o = 1 - A \cdot \left|\frac{\sigma_v}{\sigma_y}\right|^p \qquad (4.26)$$

$$r = (r_0^3 + \frac{3}{4\pi} \int_0^t \dot{V}dt)^{1/3} \text{ (ro = initial radius)}$$
$$(4.27)$$

$$r_s = r_0 \cdot [z + B \cdot \left|\frac{\sigma_v - \sigma_y}{\sigma_r}\right|^\beta] \qquad (4.28)$$

The values k, K, a, n, N, A, B, z and σ_r are material and temperature dependent constants. $\{S_{ijkl}\}$ is the compliance tensor describing the elastic part of deformation.
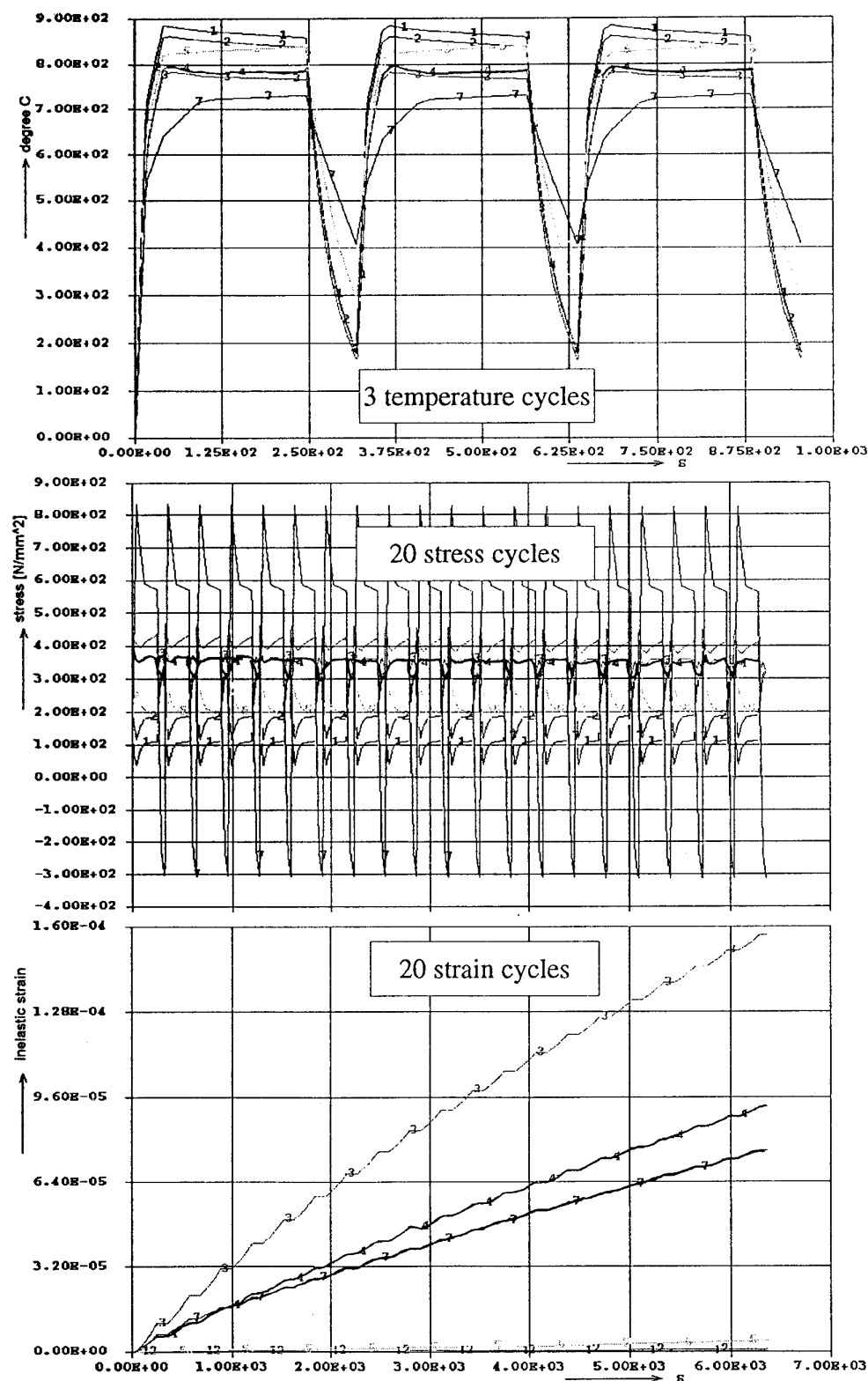
Fig. 6a: Temperatures stresses and strains at three points in the structure of the model blade (hold time 246s)
3 middle of the first cooling rib
4 middle of the second cooling rib
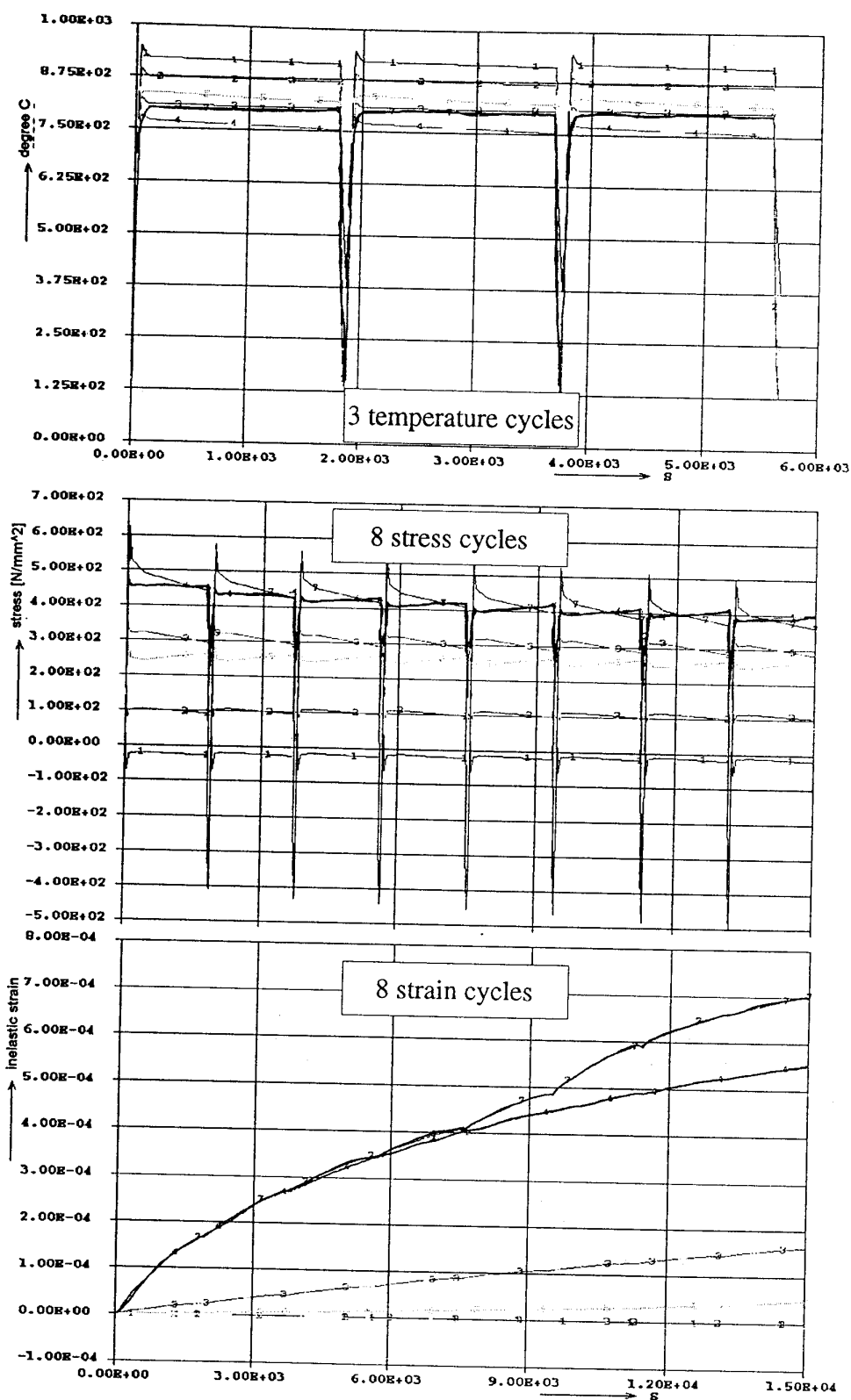7 close to the trailing edge

Fig. 6b: Temperatures stresses and strains at three points in the structure of the model blade (hold time 1800s)
3 middle of the first cooling rib
4 middle of the second cooling rib
7 close to the trailing edge

22-8

4.2 Results for IN 738 LC blades

Based on the calculated temperature distribution, the stress and the strain distribution was computed using a two dimensional finite element mesh net generalized plain strain element, which allows a calculation in all 3 dimensions. The results for two different hold on temperature times (246 and 1800 sec) are shown in Figures 6a and 6b.

The influence of the holding time can be seen in the time dependent stress tension amplitude. During the short time calculation the amplitude is nearly constant. Only in the very good cooled and high loaded ribs (lines 3 and 4) a sinking of the (mean stress) can be observed. In contrast during the long time calculation a changement of the amplitudes and of the mean stress occurs.

The influence of the holding time can also be seen in figure 7. In this picture, the cycles to failure measured in the experiments are compared with calculated cycles. The calculation is based on the strain amplitude out of the ABAQUS computing and cycle to failure diagrams including a hold time.

The measured cycles are laying in the range of the calculated. With the short time loaded blade condures 3058 cycles, the long time loaded blade failed after 1245 cycles. The crack were initiated in the trailing edge caused by the temperature distribution induced highest local stress range.
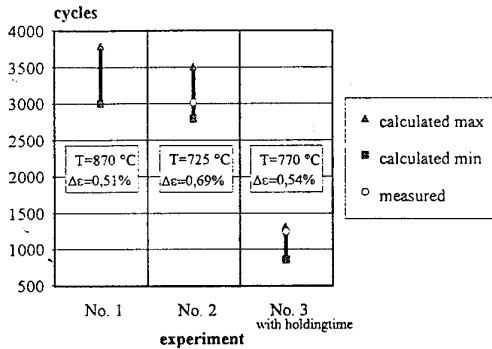

Fig. 8: Measured remaining strain at the outlet trailing edge of the DS-model blade

Fig. 7: Comparison of the calculated and measured number of cycles to failure

Fig. 9a/b: Elastically (a) and inelastically calculated stresses (b) for the inlet trailing edge (Meßstelle 6) and the midst of the first internal cooling rib (vorderer Steg) calculated stress

4.3 Results for IN 792 DS-blades

In the same manner as for the CC-blades, the model blade of IN 792 DS was loaded axial and thermocycled. The mean axial stress has been raised in the first test run up to 190 MPa, the second test was run with a constant load of 90 kN with is equal a mean stress of 190 MPa. In Fig. 9 the measured remaining accumulated strain is given. The temperature distribution seemed to be more homogeneous in this blades. Again the elastically and inelastically finite element analysises used the ABAQUS programme in which the „anisotropic structural materials law" has been implemented by on USER programm.

Compared with the elastically approach (Fig. 9a), the inelastic analysis (Fig. 9b) described the relaxation and redistribution of stresses during the holding time (more precisely). In Fig. 9 for the inlet trailing edge (Meßstelle 6) and for the midst of the first cooling rib (vorderer Steg) the calculated stresses are documented, that the secondary thermal induced stresses are relaxed versus the medium primary stress due to the axial loading.
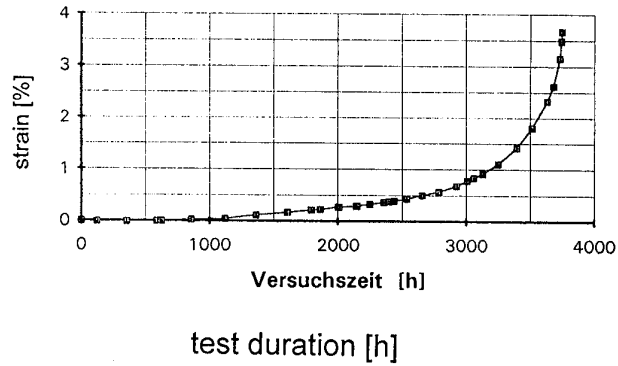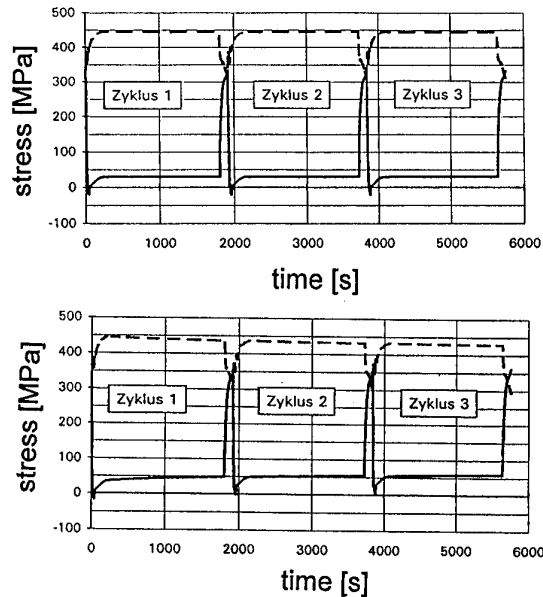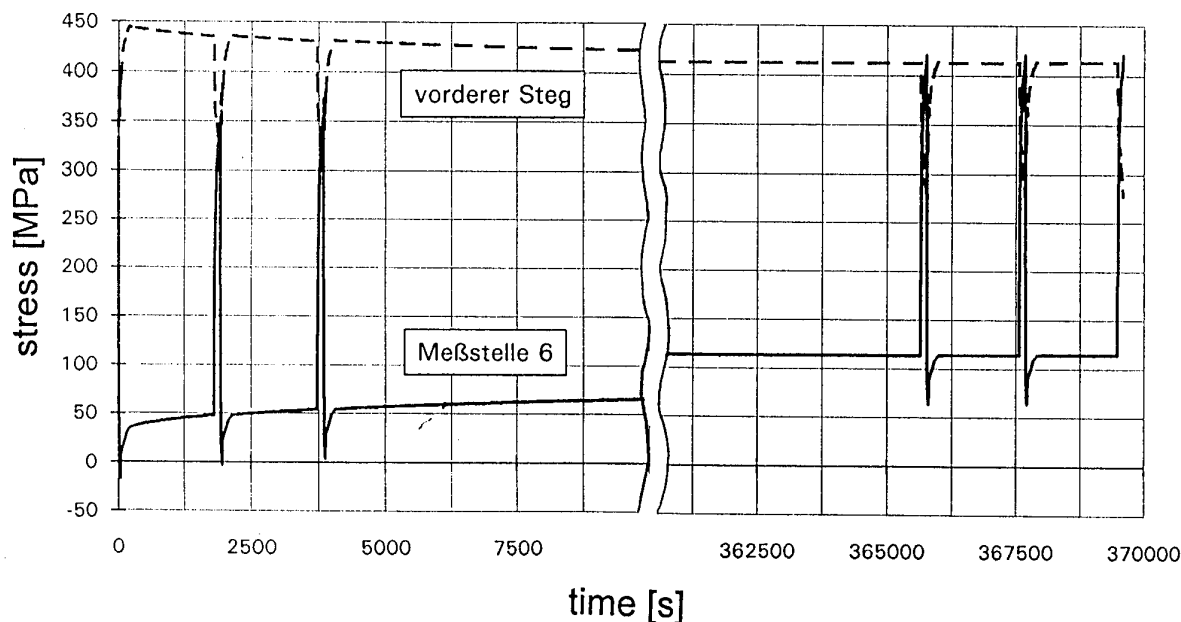
Fig. 10: Stress redistribution at the inlet-trailing edge (Meßstelle 6) and at the cooling rip (vorderer Steg) of the model blade of IN782DS

5. CONCLUDING REMARKS

The thermal mechanical experiments with the CC and DS-model blades demonstrated, that with for estimation of the stress strain distribution per loading cycle and for the different numbers of loading cycles an inelastic analysis with the developed „structural dependent material laws" is necessary to understand the stress redistribution in a blade. These experimental work and analytical work will be go on with single-crystal model blades made of CMSX-4.

Acknowledgement

The authors thanks to the colleague of the national funded programme (IN 738 LC) and the COST 501 (WP1) action for the grateful cooperation.

6. REFERENCES

1. Schubert, F.; Penkalla, H.J.; Nickel, H.:
   „Ein strukturabhängiges Werkstoffmodell für innengekühlte Gasturbinenschaufeln"
   Z. Metallkd. 83 (1992) 6, p. 416-422

2. Beckmöller, S.; Wolters, J.; Breitbach, G.; Penkalla, H.J.; Schubert, F.:
   „Microstructural dependent constitutive equation for inelastic analysis of internally cooled IN738LC turbine blades"
   Proc. of the 5th Liège-Conf.: „Materials for Advanced Power Engineering" (1994), Kluwer Academic Publishers, Part 1, p. 829-839

3. Penkalla, H.J.; Schubert, F.; Janson, J.:
   „Life time prediction of blading materials"
   Proc. of the 5th Liège-Conf.: „Materials for Advanced Power Engineering" (1994), Kluwer Academic Publishers, Part 1, p. 675-684

REPORT DOCUMENTATION PAGE

1. Recipient's Reference	2. Originator's Reference AGARD-CP-569	3. Further Reference ISBN 92-836-1031-8	4. Security Classification of Document UNCLASSIFIED/ UNLIMITED

5. Originator	Advisory Group for Aerospace Research and Development North Atlantic Treaty Organization 7 rue Ancelle, 92200 Neuilly-sur-Seine, France

6. Title	Thermal Mechanical Fatigue of Aircraft Engine Materials

7. Presented at/sponsored by	The 81st Meeting of the AGARD Structures and Materials Panel, held in Banff, Canada 2-4 October 1995.

8. Author(s)/Editor(s) Multiple	9. Date March 1996

10. Author's/Editor's Address Multiple	11. Pages 232

12. Distribution Statement	There are no restrictions on the distribution of this document. Information about the availability of this and other AGARD unclassified publications is given on the back cover.

13. Keywords/Descriptors

Aircraft engines	Thermal fatigue
Military aircraft	Thermal stresses
Turbine blades	Mechanical properties
Materials	Stresses
Fatigue (materials)	Environments
Cracking (fracturing)	Damage
Crack propagation	Tests
Service life	

14. Abstract

Aircraft engine components experience severe operating conditions, often involving complex combinations of cyclic mechanical stress, cyclic temperature and varying environmental conditions.

At the 81st Meeting of the AGARD Structures and Materials Panel, the SMP held a Specialists' Meeting on Thermal Mechanical Fatigue of Aircraft Engine Materials to review the state-of-the-art experience in experimental methods as well as approaches to analytical modelling of damage accumulation and growth in metallic gas turbine engine materials under TMF conditions.

AGARD

NATO -⊕- OTAN

7 RUE ANCELLE • 92200 NEUILLY-SUR-SEINE

FRANCE

Télécopie (1)47.38.57.99 • Télex 610 176

DIFFUSION DES PUBLICATIONS

AGARD NON CLASSIFIEES

Aucun stock de publications n'a existé à AGARD. A partir de 1993, AGARD détiendra un stock limité des publications associées aux cycles de conférences et cours spéciaux ainsi que les AGARDographies et les rapports des groupes de travail, organisés et publiés à partir de 1993 inclus. Les demandes de renseignements doivent être adressées à AGARD par lettre ou par fax à l'adresse indiquée ci-dessus. *Veuillez ne pas téléphoner.* La diffusion initiale de toutes les publications de l'AGARD est effectuée auprès des pays membres de l'OTAN par l'intermédiaire des centres de distribution nationaux indiqués ci-dessous. Des exemplaires supplémentaires peuvent parfois être obtenus auprès de ces centres (à l'exception des Etats-Unis). Si vous souhaitez recevoir toutes les publications de l'AGARD, ou simplement celles qui concernent certains Panels, vous pouvez demander à être inclu sur la liste d'envoi de l'un de ces centres. Les publications de l'AGARD sont en vente auprès des agences indiquées ci-dessous, sous forme de photocopie ou de microfiche.

<u>CENTRES DE DIFFUSION NATIONAUX</u>

ALLEMAGNE
Fachinformationszentrum Karlsruhe
D-76344 Eggenstein-Leopoldshafen 2

BELGIQUE
Coordonnateur AGARD-VSL
Etat-major de la Force aérienne
Quartier Reine Elisabeth
Rue d'Evere, 1140 Bruxelles

CANADA
Directeur, Services d'information scientifique
Ministère de la Défense nationale
Ottawa, Ontario K1A 0K2

DANEMARK
Danish Defence Research Establishment
Ryvangs Allé 1
P.O. Box 2715
DK-2100 Copenhagen Ø

ESPAGNE
INTA (AGARD Publications)
Pintor Rosales 34
28008 Madrid

ETATS-UNIS
NASA Headquarters
Code JOB-1
Washington, D.C. 20546

FRANCE
O.N.E.R.A. (Direction)
29, Avenue de la Division Leclerc
92322 Châtillon Cedex

GRECE
Hellenic Air Force
Air War College
Scientific and Technical Library
Dekelia Air Force Base
Dekelia, Athens TGA 1010

ISLANDE
Director of Aviation
c/o Flugrad
Reykjavik

ITALIE
Aeronautica Militare
Ufficio del Delegato Nazionale all'AGARD
Aeroporto Pratica di Mare
00040 Pomezia (Roma)

LUXEMBOURG
Voir Belgique

NORVEGE
Norwegian Defence Research Establishment
Attn: Biblioteket
P.O. Box 25
N-2007 Kjeller

PAYS-BAS
Netherlands Delegation to AGARD
National Aerospace Laboratory NLR
P.O. Box 90502
1006 BM Amsterdam

PORTUGAL
Estado Maior da Força Aérea
SDFA - Centro de Documentação
Alfragide
2700 Amadora

ROYAUME-UNI
Defence Research Information Centre
Kentigern House
65 Brown Street
Glasgow G2 8EX

TURQUIE
Millî Savunma Başkanliği (MSB)
ARGE Dairesi Başkanliği (MSB)
06650 Bakanliklar-Ankara

Le centre de distribution national des Etats-Unis ne détient PAS de stocks des publications de l'AGARD.

D'éventuelles demandes de photocopies doivent être formulées directement auprès du NASA Center for AeroSpace Information (CASI) à l'adresse ci-dessous. Toute notification de changement d'adresse doit être fait également auprès de CASI.

<u>AGENCES DE VENTE</u>

NASA Center for
AeroSpace Information (CASI)
800 Elkridge Landing Road
Linthicum Heights, MD 21090-2934
Etats-Unis

ESA/Information Retrieval Service
European Space Agency
10, rue Mario Nikis
75015 Paris
France

The British Library
Document Supply Division
Boston Spa, Wetherby
West Yorkshire LS23 7BQ
Royaume-Uni

Les demandes de microfiches ou de photocopies de documents AGARD (y compris les demandes faites auprès du CASI) doivent comporter la dénomination AGARD, ainsi que le numéro de série d'AGARD (par exemple AGARD-AG-315). Des informations analogues, telles que le titre et la date de publication sont souhaitables. Veuiller noter qu'il y a lieu de spécifier AGARD-R-nnn et AGARD-AR-nnn lors de la commande des rapports AGARD et des rapports consultatifs AGARD respectivement. Des références bibliographiques complètes ainsi que des résumés des publications AGARD figurent dans les journaux suivants:

Scientific and Technical Aerospace Reports (STAR)
publié par la NASA Scientific and Technical
Information Division
NASA Headquarters (JTT)
Washington D.C. 20546
Etats-Unis

Government Reports Announcements and Index (GRA&I)
publié par le National Technical Information Service
Springfield
Virginia 22161
Etats-Unis
(accessible également en mode interactif dans la base de données bibliographiques en ligne du NTIS, et sur CD-ROM)

AGARD

NATO ⊕ OTAN

7 RUE ANCELLE • 92200 NEUILLY-SUR-SEINE

FRANCE

Telefax (1)47.38.57.99 • Telex 610 176

DISTRIBUTION OF UNCLASSIFIED

AGARD PUBLICATIONS

AGARD holds limited quantities of the publications that accompanied Lecture Series and Special Courses held in 1993 or later, and of AGARDographs and Working Group reports published from 1993 onward. For details, write or send a telefax to the address given above. *Please do not telephone.*

AGARD does not hold stocks of publications that accompanied earlier Lecture Series or Courses or of any other publications. Initial distribution of all AGARD publications is made to NATO nations through the National Distribution Centres listed below. Further copies are sometimes available from these centres (except in the United States). If you have a need to receive all AGARD publications, or just those relating to one or more specific AGARD Panels, they may be willing to include you (or your organisation) on their distribution list. AGARD publications may be purchased from the Sales Agencies listed below, in photocopy or microfiche form.

NATIONAL DISTRIBUTION CENTRES

BELGIUM
Coordonnateur AGARD — VSL
Etat-major de la Force aérienne
Quartier Reine Elisabeth
Rue d'Evere, 1140 Bruxelles

CANADA
Director Scientific Information Services
Dept of National Defence
Ottawa, Ontario K1A 0K2

DENMARK
Danish Defence Research Establishment
Ryvangs Allé 1
P.O. Box 2715
DK-2100 Copenhagen Ø

FRANCE
O.N.E.R.A. (Direction)
29 Avenue de la Division Leclerc
92322 Châtillon Cedex

GERMANY
Fachinformationszentrum Karlsruhe
D-76344 Eggenstein-Leopoldshafen 2

GREECE
Hellenic Air Force
Air War College
Scientific and Technical Library
Dekelia Air Force Base
Dekelia, Athens TGA 1010

ICELAND
Director of Aviation
c/o Flugrad
Reykjavik

ITALY
Aeronautica Militare
Ufficio del Delegato Nazionale all'AGARD
Aeroporto Pratica di Mare
00040 Pomezia (Roma)

LUXEMBOURG
See Belgium

NETHERLANDS
Netherlands Delegation to AGARD
National Aerospace Laboratory, NLR
P.O. Box 90502
1006 BM Amsterdam

NORWAY
Norwegian Defence Research Establishment
Attn: Biblioteket
P.O. Box 25
N-2007 Kjeller

PORTUGAL
Estado Maior da Força Aérea
SDFA - Centro de Documentação
Alfragide
2700 Amadora

SPAIN
INTA (AGARD Publications)
Pintor Rosales 34
28008 Madrid

TURKEY
Millî Savunma Başkanliği (MSB)
ARGE Dairesi Başkanliği (MSB)
06650 Bakanliklar-Ankara

UNITED KINGDOM
Defence Research Information Centre
Kentigern House
65 Brown Street
Glasgow G2 8EX

UNITED STATES
NASA Headquarters
Code JOB-1
Washington, D.C. 20546

The United States National Distribution Centre does NOT hold stocks of AGARD publications.

Applications for copies should be made direct to the NASA Center for AeroSpace Information (CASI) at the address below. Change of address requests should also go to CASI.

SALES AGENCIES

NASA Center for
AeroSpace Information (CASI)
800 Elkridge Landing Road
Linthicum Heights, MD 21090-2934
United States

ESA/Information Retrieval Service
European Space Agency
10, rue Mario Nikis
75015 Paris
France

The British Library
Document Supply Centre
Boston Spa, Wetherby
West Yorkshire LS23 7BQ
United Kingdom

Requests for microfiches or photocopies of AGARD documents (including requests to CASI) should include the word 'AGARD' and the AGARD serial number (for example AGARD-AG-315). Collateral information such as title and publication date is desirable. Note that AGARD Reports and Advisory Reports should be specified as AGARD-R-nnn and AGARD-AR-nnn, respectively. Full bibliographical references and abstracts of AGARD publications are given in the following journals:

Scientific and Technical Aerospace Reports (STAR)
published by NASA Scientific and Technical
Information Division
NASA Headquarters (JTT)
Washington D.C. 20546
United States

Government Reports Announcements and Index (GRA&I)
published by the National Technical Information Service
Springfield
Virginia 22161
United States
(also available online in the NTIS Bibliographic
Database or on CD-ROM)